Asteroseismology in Binary Stars with Applications of Bayesian Inference Tools

by

Zhao Guo

Under the Direction of Douglas R. Gies

ABSTRACT

Space missions like *Kepler* have revolutionized asteroseismology, the science that infers the stellar interiors by studying oscillation frequency spectra of pulsating stars.

Great advancements have been made in understanding solar-like oscillators. However, this is not the case for variable stars of intermediate masses, such as δ Scuti and γ Doradus variables. By studying these stars in eclipsing binaries (EBs), model independent fundamental parameters such as mass and radius can be inferred. On one hand, this synergy constrains the parameter space and facilitates the asteroseismic modeling, and this is shown for the δ Scuti type pulsating EB KIC 9851944. On the other hand, studies of binary stars must address the complexities such as mass transfer. KIC 8262223 is such an example, which

consists of a mass-gaining δ Scuti primary and a pre-He white dwarf secondary. Some of the eccentric binary systems, the 'heartbeat' stars, show tidally excited oscillations. After briefly reviewing the linear theory of tidally forced stellar oscillations, we study the tidal pulsating binary KIC 3230227 and demonstrate that both amplitude and phase can be used to identify the tidally excited pulsation modes. We also discuss the variability of a Slowly Pulsating B-star KOI-81 and a Cataclysmic variable KIC 9406652.

In the second part of this dissertation, we apply Bayesian statistics to some problems in binaries and asteroseismology with the help of packages BUGS and JAGS. Special attention is paid to the inverse problems (tomography) encountered in studying the double-line spectroscopic binaries.

INDEX WORDS: astronomy, asteroseismology, binaries, binaries: spectroscopic, binaries: eclipsing stars: oscillations, stars: variables: delta Scuti, stars: individual: (KIC 9851944), stars: individual: (KIC 8262223), stars: individual: (KIC 3230227), methods: statistical

Asteroseismology in Binary Stars with Applications of Bayesian Inference Tools

by

Zhao Guo

A Dissertation Submitted in Partial Fulfillment of the Requirements for the Degree of

Doctor of Philosophy

in the College of Arts and Sciences

Georgia State University

2016

Asteroseismology in Binary Stars with Applications of Bayesian Inference Tools

by

Zhao Guo

Committee Chair: Douglas R. Gies

Committee: Richard H. D. Townsend

Fabien Baron

Russel J. White

Harold A. McAlister

Electronic Version Approved: Vadym Apalkov

Office of Graduate Studies

College of Arts and Sciences

Georgia State University

December 2016

TABLE OF CONTENTS

LIST OF TABLES

LIST OF FIGURES

CHAPTER 1

An Introduction to δ Scuti /γ Doradus Variables and Solar-like Oscillating Stars

1.1 Pulsating Stars On The H-R diagram

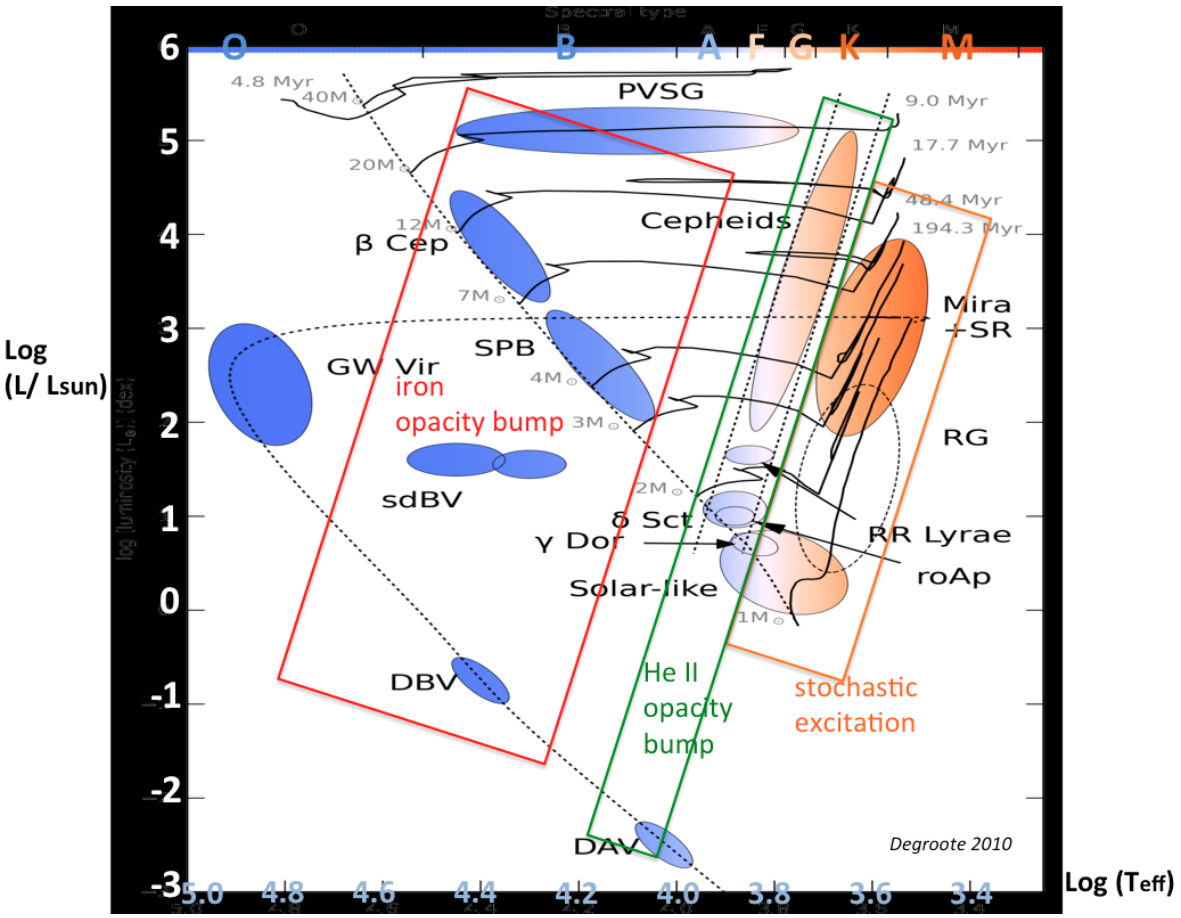

Figure 1.1 An overview of pulsating stars on the H-R diagram, taken from Degroote (2010). Different classes of variables are indicated by ellipses, and these ellipses are filled with colors in accordance with their spectral-types (effective temperatures). The rectangles mark the positions of pulsators driven by different mechanisms (see text).

Stars pulsate at various stages of their evolution. Figure 1.1 shows the positions of different classes of pulsating stars in temperature and luminosity space. Due to their large pulsation amplitudes, giant stars like Cepheids, Miras, and Semi-regular variables were discovered first. They have long pulsation periods ($\approx 1 - 100$ days). The Cepheids are located in the classical instability strip (between the straight dotted lines in Figure 1.1), and the strip intercepts with the Main Sequence (MS) at a position where we find the δ Scuti variables (periods of $0.6 - 6$ hours). Lower on the MS at cooler temperatures, we find γ Doradus variables (periods of $\approx 0.3 - 3$ days) and solar-like oscillators (periods of a few minutes). Red giants also show solar-like oscillations. Massive stars like β Cephei variables (periods of a few hours) and Slowly Pulsating B-stars (SPB) (periods of half to a few days) are located on the upper main sequence. Even more massive stars like supergiants can also pulsate. At late stages of evolution, various classes of white dwarfs (GW Vir, DBV, DAV) pulsate with very short periods ($\approx 2 - 15$ minutes). There are also special classes of variables such as the sub-dwarf B stars, probably the results of binary evolution, which can pulsate with both high frequency p-modes (periods of ≈ 1 hour) and low frequency g-modes (periods of $1 - 6$ minutes).

In Figure 1.1, the β Cephei, SPB, sdB, and DBV stars, located inside the red rectangle, are driven by the opacity mechanism due to the bump of iron elements. The same mechanism, but mainly driven by He II ionization, works for classical Cepheids, RR-Lyrae stars, δ Scuti stars, and DAV white dwarfs (green rectangle). The cooler stars, including solar-like stars, red-giants, Mira variables and semi-regular variables are driven by stochastic motions in

their convection zones (orange rectangle). Note that γ Doradus pulsations are mainly driven by the convective blocking mechanism (although they are located in the green rectangle).

There are pulsators that are not shown in Figure 1.1, for instance, the pre-MS δ Scuti stars (Zwintz et al. 2014). Some O-type stars are found to show p-mode pulsations (Mahy et al. 2009; Degroote et al. 2010). There is a possible class of pulsators located between SPB and δ Scuti stars. Giant planets are believed to show pulsations. There are discoveries of p-mode pulsations in Jupiter and indirect evidence of g-mode pulsations of Saturn that manifest themselves in its rings (Gaulme et al. 2015).

The aforementioned pulsations are all self-driven. Recent observations especially those from space have confirmed that stars can also show externally-driven (e.g., tidal force) pulsations, and some of these so-called heartbeat stars are detailed in Chapter 6. Stars can also interact with the accretion disks and produce more complicated pulsational phenomenon, e.g., white dwarfs in cataclysmic variables. An example of such a system will be discussed in Chapter 7.

The focus of this dissertation is the properties of pulsating stars in eclipsing binaries in which combined light curve and radial velocity analysis yields precise estimations of stellar mass, radius, and effective temperature. We develop the tools to facilitate the analysis of the observations and to explain the observed properties in the framework of theoretical modes of stellar interiors and atmospheres. Chapter 2 briefly describes MESA stellar evolution models and the effects on the evolutionary tracks of changing several physical parameters. The linear theories of free and forced stellar oscillations are presented in Chapter 3. We

apply these theories to *Kepler* field of view δ Scuti/γ Dor binaries as well as tidally induced pulsators (heartbeat stars) in Chapter 5 and Chapter 6, respectively. The modeling tools of binary stars are described in Chapter 4. Other routines encountered in analyzing binary stars, such as fitting radial velocity data, and separating double-lined spectra, are dealt with in a Bayesian framework in Chapter 8 and Chapter 9 with the help of the statistical package BUGS/JAGS.

1.2 δ Scuti Stars

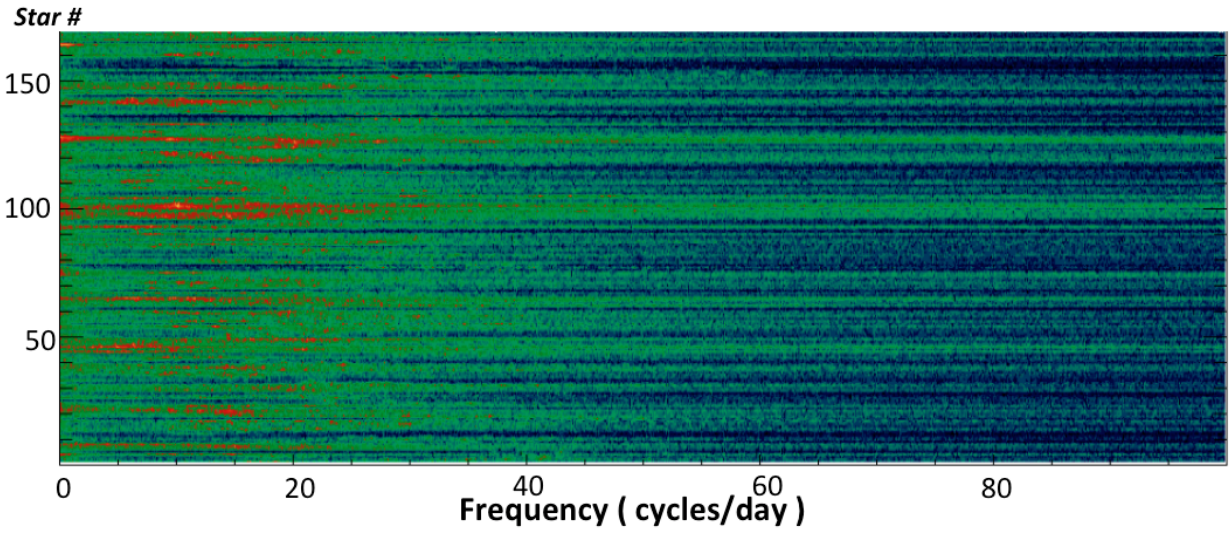

Figure 1.2 An overview of the pulsation spectra of 170 δ Scuti stars observed by *Kepler* in short cadence mode. Targets are selected from Uytterhoeven et al. (2011). The colors (from no amplitude at blue to large amplitude as red) indicate the strength of the oscillations as a function of frequency, where each row corresponds to a particular stars.

δ Scuti stars are radial and non-radial p-mode pulsators. As shown in Figure 1.2, most of the pulsational frequencies appear in the range from 4 to 30 d^{-1}. Some of δ Scuti stars can pulsate at frequencies as high as 60 d^{-1} or higher. δ Scuti stars are within the mass range of 1.5 to 2.5 $M_{\odot}$ and of spectral type A2-F5. Their p-mode pulsations are driven by the κ (opacity) mechanism, mainly due to the opacity bump that occurs at a depth corresponding to the He II ionization zone. The convective blocking mechanism, which drives the γ Doradus pulsations, also works for the cool δ Scuti stars. Almost all δ Scuti stars show low-frequency pulsations, and all of them can be called δ Scuti and γ Dor hybrids (Balona 2010).

The observed frequency distributions of δ Scuti stars observed by the NASA *Kepler* spacecraft in 10 different locations on the H-R diagram are shown in Figure 1.3. The range of unstable modes from the current linear non-adiabatic theory seems agree more or less with observations. However, strong differences still exist for the cool δ Scuti stars, and we cannot explain the observed pulsations at very high frequencies either. For comparison of individual frequencies, we still lack a mode selection mechanism. This problem may be partially resolved with non-linear pulsation analysis which still awaits its development and application to δ Scuti stars.

δ Scuti stars are generally fast rotators, with a mean projected rotational velocity of $v \sin i$ of 120 km s^{-1}. They can even rotate at velocities close to critical value. This makes the asteroseismic modeling much more difficult. Some slow or intermediate-rotating δ Scuti stars have been studied in detail (FG Vir, 44 Tau, 29 Cygni, etc.). There are efforts of modeling Altair ($v \sin i \approx 200$ km s^{-1}) by using one-dimensional (1-D) stellar models and

perturbative approximation of rotation to the second order (Suárez et al. 2005). More appropriate treatment needs 2-D stellar models so that the rotational distortion can be fully taken into account. Such frontier modeling have been applied to α Oph (Deupree 2011; Deupree et al. 2012), one of the fast rotating δ Scuti stars that have been imaged with optical interferometry and observed by satellite. The lesson learned is that theory predicts many more modes than observations, and better constraints on the stellar parameters are needed (although this star is already the best known so far).

Magnetic fields have been found on the δ Scuti star HD 188774 (Neiner & Lampens 2015). And spots generated by the B-field can mimic the signature of g-mode γ Dor type pulsations. This suggests that the nature of δ Scuti and γ Dor hybrids may be more complicated.

δ Scuti stars in eclipsing binaries are the best laboratories to develop and test our pulsation theory for these stars. Although additional factors like eclipses and tidal effects need to be taken into account, the trade-off is that masses and radii can be determined accurately (to $\approx$1 %). In Chapter 5, we will present detailed studies for a few such systems. And indeed, in one system, the fundamental radial mode can be identified from single-band photometry thanks to its binary nature.

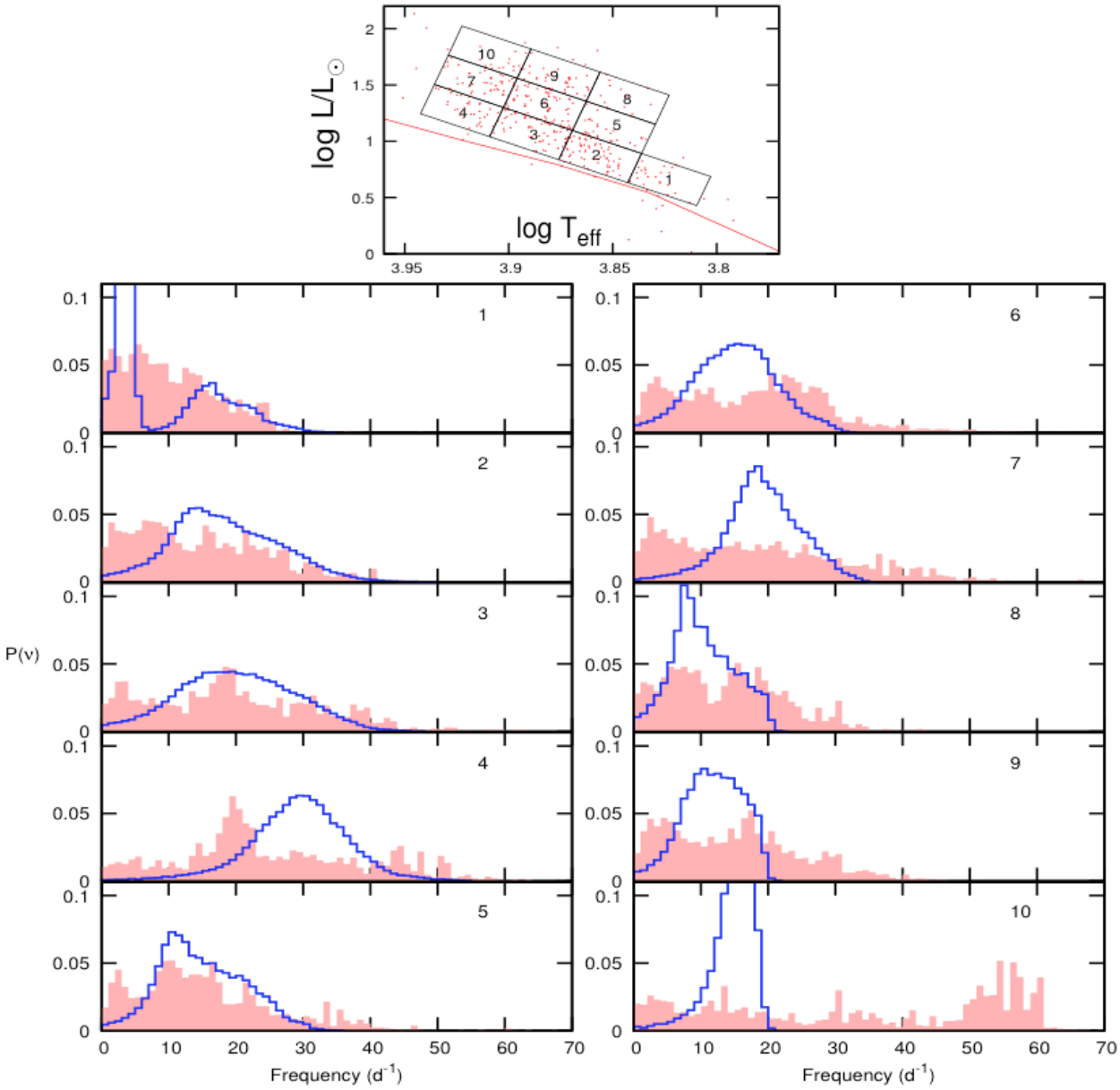

Figure 1.3 The observed (filled) and theoretical (solid blue curves) frequency distributions of δ Scuti stars. Only unstable modes with degrees, $l \leq 6$ are considered, and the mode frequencies have been corrected for rotational effects with perturbation theory to the third order. All models have metal abundance Z = 0.015. The lower 10 panels correspond to the labeled regions on the H-R diagram shown in the upper panel. Figure is taken from Balona et al. (2015).

1.3 γ Doradus Stars

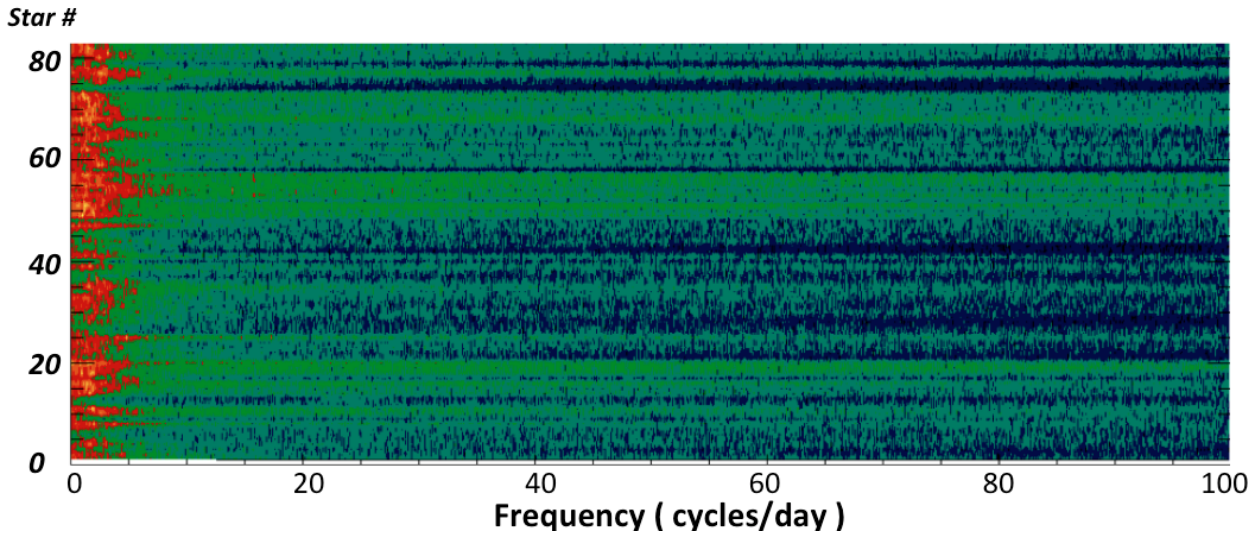

Figure 1.4 An overview of the pulsation spectra of 85 γ Doradus stars observed by *Kepler*, in the same format as Figure 1.2. Targets are selected from Uytterhoeven et al. (2011).

γ Doradus stars are a relatively new class of variable (Balona et al. 1994). Figure 1.4 shows the Fourier spectra of 85 γ Dor stars observed by *Kepler*. It can be seen that their pulsations are mainly at low frequencies ($<\approx 5$ d^{-1}). They are intermediate-mass ($\approx 1.2-2.0 M_{\odot}$) stars with spectral type of F. On the H-R diagram, they are located in a small region on or just above the main sequence. Their pulsations modes are driven by the modulation of radiative flux by the convection zone (Guzik et al. 2000).

As γ Doradus pulsations are high-order g-modes in the asymptotic regime, we expect to find near-equally spaced modes in period. Systematic studies can be found in Van Reeth et al. (2015a, 2015b). Due to rotation, some of the observed period spacings, when plotted as a function of period, show a linear slope. This can be used as a diagnostic to study their

internal rotational distribution (Ouazzani et al. 2016).

1.4 Solar-like Oscillating Stars

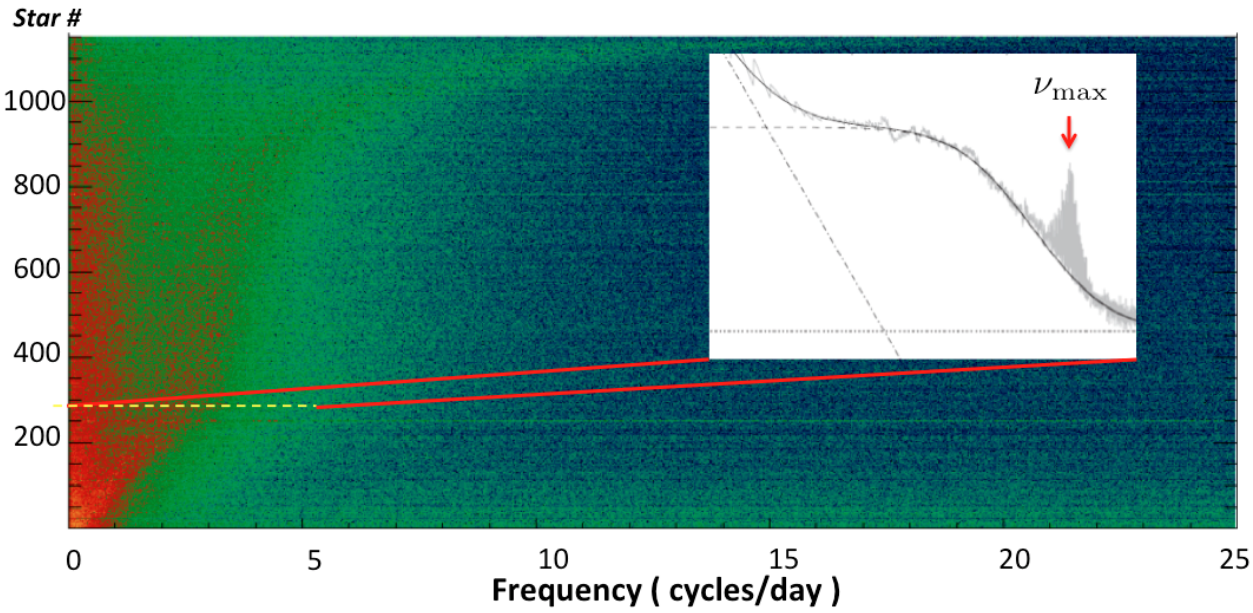

Figure 1.5 An overview of the pulsation spectra of 1300 solar-like oscillating red-giant stars observed by *Kepler*, in the same format as Figure 1.2. Targets are selected from Hekker et al. (2011). The inset shows the power spectrum of one particular star with the oscillation frequency of maximum power (ν_{max}) marked by the red arrow. The oscillation spectrum is shown as a Gaussian like power excess on top of the smooth trend signal due to the noise background. The oscillations of each star form the visible red ridge extending from the lower left to the upper right since the star numbers are sorted by their ν_{max}.

The solar-like oscillators include main sequence stars with spectral type later than about F4, sub-giant stars, and red-giants. They show pressure-mode oscillations stochastically driven

by convection. I calculated the power spectrum of 1300 solar-like oscillating red-giant stars in Hekker et al. (2011). In Figure 1.5, each spectrum is represented as a horizontal density plot. The oscillation amplitudes increase from blue to green to yellow and to red. As shown in the inset of Figure 1.5, the power spectrum of a typical solar-like oscillator is composed of a broad smooth trend and a Gaussian-like power excess due to oscillations. The trend is caused by the noise and stellar activity, and it is often modeled by several components such as granulation, Harvey-like profiles, etc., (shown as dashed lines). The oscillations reach the maximum power at a frequency defined as ν_{max}. The oscillation spectrum is usually analyzed after subtracting the background signal. Note that the oscillation frequency peaks are nearly equally-spaced with a spacing of about $0.5\Delta\nu$, and this can be seen in the inset of Figure 1.6. This inset panel shows that the Sun has a large frequency separation ($\Delta\nu$) of 135 μHz, which is the spacing between frequencies of consecutive radial orders.

There are scaling relations between quantities (Figure 1.6) of the oscillations and ν_{max}. Such quantities include $\Delta\nu$, mean mode amplitude at ν_{max} (H_{max}), stellar background at ν_{max} (B_{max}), stellar radius (R), effective temperature ($T_{\rm eff}$), etc. (Mosser et al. 2013). In other words, all these quantities are proportional to ν_{max} in the log-log plot. And these relations hold from MS stars to red-giants on the tip of RGB. The period-luminosity relation of evolved giants is actually a direct reflection of these scaling relations, although for these stars, we can only observe one or two frequencies.

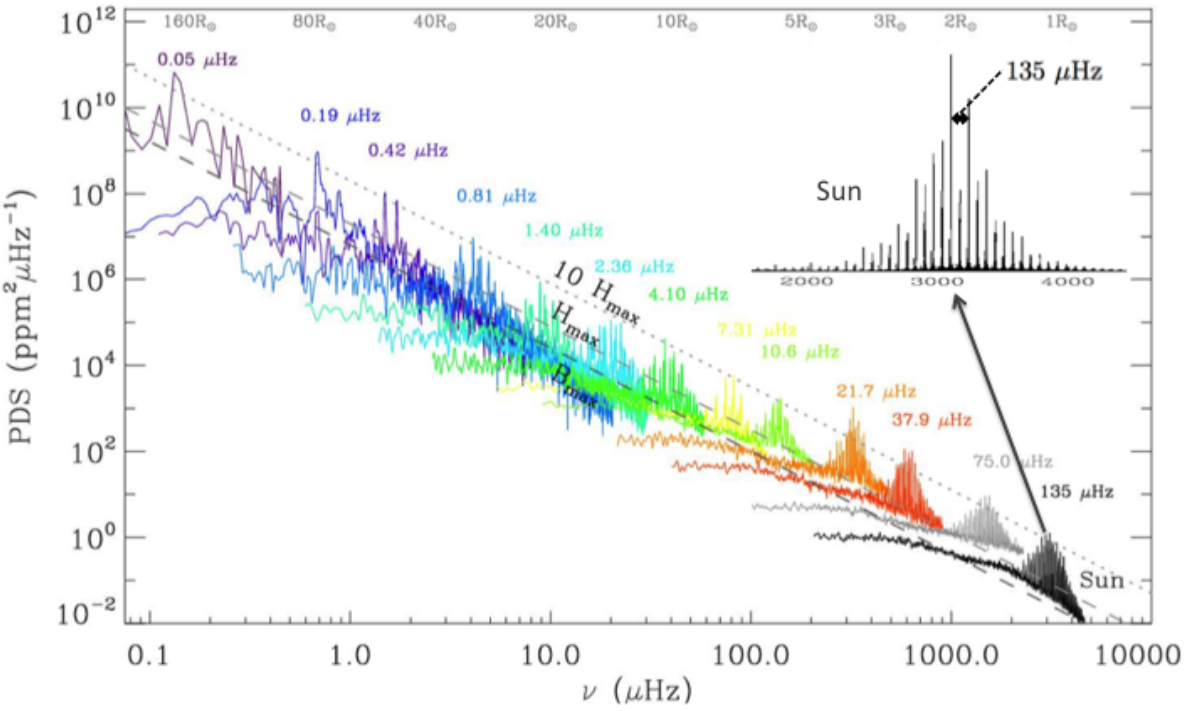

Figure 1.6 The power density spectrum of solar-like oscillating stars from the Main Sequence (grey and black), to the bottom (red and orange) and then to the tip of RGB (purple). The spectra are identified by their $\Delta\nu$ marked on top. The blow-up inset shows the oscillations of the Sun, and its large frequency separation $\Delta\nu$ =135 μHz is labeled. Figures are taken from Mosser et al. (2013) and Aerts et al. (2010).

In the analysis of power spectrum of red-giants, we firstly determine the global parameters $\Delta\nu$ and ν_{max} from techniques such as autocorrelation (Huber et al. 2009). Then we get the ratio $n_{max} = \nu_{max}/\Delta\nu$, which is a proxy for the radial order n at maximum power. And

since the oscillation spectra of red-giant stars follow a universal pattern, the modes with frequencies $\nu_{n,l}$ can be identified by the relation in Mosser et al. (2011):

$$\frac{\nu_{n,l}}{\Delta\nu} = n + \frac{l}{2} + \varepsilon(\Delta\nu) - d_{0l}(\Delta\nu) + \frac{\alpha_l}{2}(n - n_{max})^2 \quad \text{for } l = 2, 0, 3, 1 \tag{1.1}$$

The $\varepsilon(\Delta\nu)$, $d_{0l}(\Delta\nu)$ are functions of $\Delta\nu$ given by the empirical relations:

$$\begin{aligned} d_{0,2} &= (0.14) + (-0.033)\log_{10}(\Delta\nu) \\ d_{0,0} &= 0.0 \\ d_{0,3} &= (0.28) + (0.0)\log_{10}(\Delta\nu) \\ d_{0,1} &= (-0.056) + (-0.002)\log_{10}(\Delta\nu) \\ \varepsilon &= (0.634) + (0.546)\log_{10}(\Delta\nu) \end{aligned} \tag{1.2}$$

and α_l are given by:

$$\begin{aligned} \alpha_2 &= 0.005 \\ \alpha_0 &= 0.008 \\ \alpha_3 &= 0.005 \\ \alpha_1 &= 0.003 \end{aligned} \tag{1.3}$$

Note that these values are given in the order of l as $[l = 2, l = 0, l = 3, l = 1]$ for convenience, since modes in the observed spectra follow this order in frequency repeatedly.

We usually calculate the theoretical mode positions for a series of n (around n_{max}), and then compare with observed mode positions for identification.

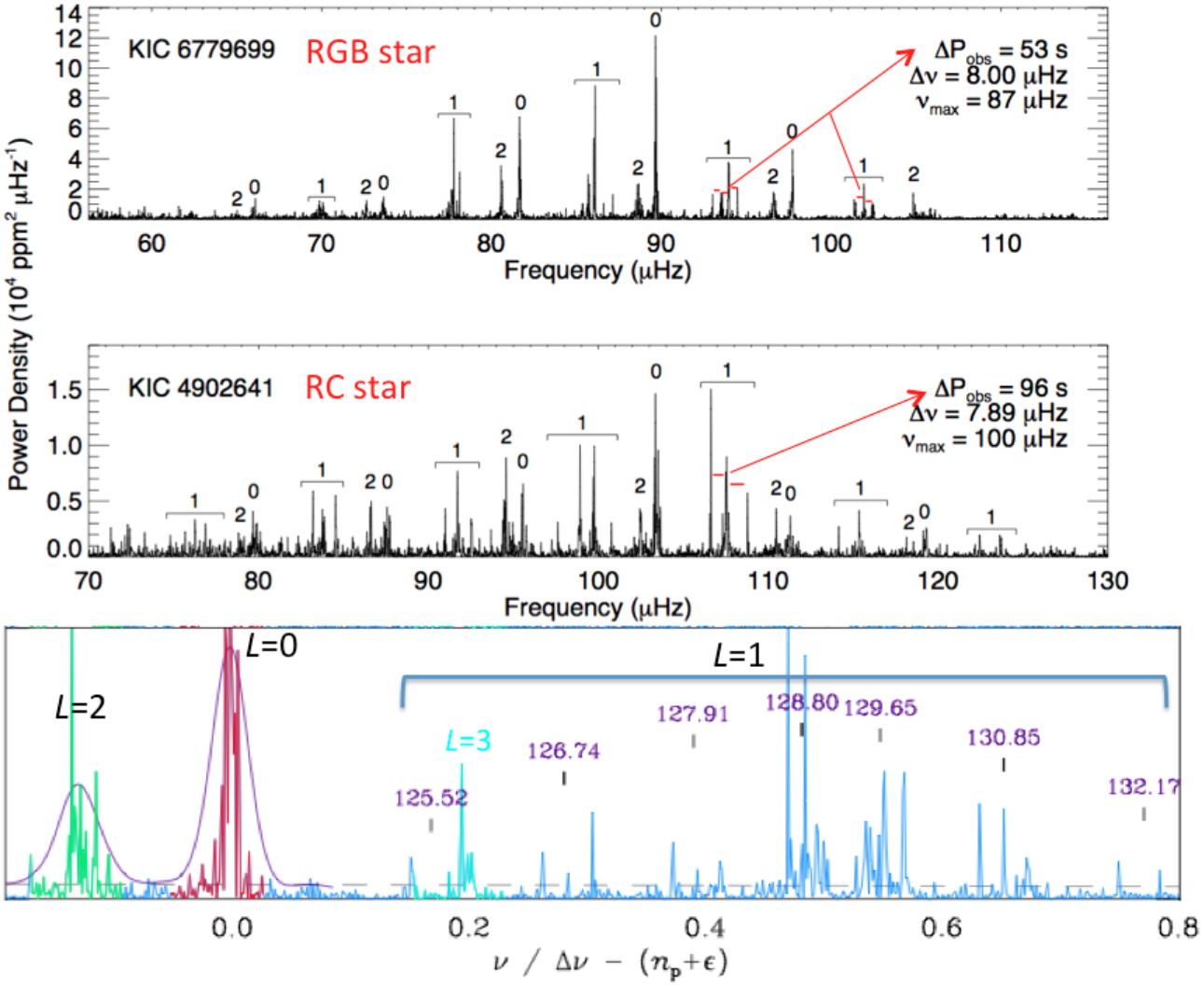

Figure 1.7 **Upper panel**: The power density spectrum of a hydrogen-burning RGB star and a Red Clump (RC) star, which is burning He in the core. The short red lines associated with the $l = 1$ modes indicate the spacing between the series of mixed $l = 1$ modes. **Lower panel**: The power spectrum of a red-giant star which shows rotational splittings in the $l = 1$ mixed modes (light blue). The $l = 2$, $l = 0$ and $l = 3$ modes are highlighted in green, red and cyan, respectively. The purple numbers are the theoretical positions of $l = 1$ modes in μHz. Figures are taken from Bedding et al. (2011) and Mosser et al. (2012).

The $l = 2, 0$ and $l = 1$ modes usually have higher amplitudes in the power spectrum, and $l = 3$ modes have low amplitudes and sometimes are not visible at all. Due to the mode coupling (between p-modes in the convective envelope and g-modes in the radiative core), $l = 1$ modes are sometimes mixed p- and g-modes. And in this case there will be a series of $l = 1$ mixed modes, instead of just one peak predicted by the above equation for universal pattern. As shown in the upper two panels of Figure 1.7, by measuring the spacing of these $l = 1$ mixed modes in period, the evolutionary stage (RGB stars or Red Clump stars) of red-giant can be determined (Bedding et al. 2011). We can sometimes even see rotational splittings in these series of mixed modes (the lower panel in Figure 1.7), and this can provide us with information on the rotation of the core. The core is found to be rotating a few times faster than the envelope (Beck et al. 2012), and similar results have been found for some sub-giant oscillators as well (Deheuvels et al. 2012). Mosser et al. (2012) found that the spin of the core increases slightly for stars ascending the RGB, and then slows down for red-clump stars.

Interestingly, some of the red-giants stars have unusual $l = 1$ modes with very low amplitudes. Recent studies suggest that these modes are likely suppressed by the internal magnetic field which is presumably dipolar (Fuller et al. 2015; Stello et al. 2016).

CHAPTER 2

Stellar Evolutionary Models

Modules for Experiments in Stellar Astrophysics (MESA) offer researchers a one-dimensional, open-source stellar evolution code (Paxton et al. 2011, 2013), developed by a team of astrophysicists since 2009. A large scientific community has been formed, which continuously maintains and improves the code. Various numerical improvements in the code enable it to model the evolution of a star from pre-Main Sequence to White Dwarf phase, bypassing the difficulties in calculating the He-burning phase (He-flash). This is not possible in many other stellar evolution codes, e.g., the Aarhus STellar Evolution Code (ASTEC), Warsaw-New Jersey Stellar Evolution Code, etc. MESA is designed to be very user-friendly and fast. Evolving a model for a low-mass star like the Sun from the pre-MS to the WD stage takes about $3-4$ hours on a personal laptop. It is usually sufficient to evolve a star from pre-MS to the base of Red Giant Branch, and this only takes about several minutes.

The capabilities of MESA include modeling of mass loss, element diffusion, gravitational settling, rotation, binary evolution, and many more. This chapter includes the modeling of an eclipsing binary KIC 9851944 with MESA, and comparison of different stellar evolutionary models. MESA is also used for modeling the non-conservative mass transfer in the EL CVn type binary KIC 8262223 (Chapter 5) as well as the heartbeat star KIC 3230227 (Chapter 6). The coupling of MESA with stellar oscillation package GYRE (Townsend & Teitler 2013) makes it possible to analyze the oscillations in the aforementioned systems.

2.1 MESA Evolutionary Models and Applications to KIC 9851944

The fundamental parameters of the primary and secondary star of KIC 9851944 have been determined from a combined analysis of the *Kepler* light curve and ground-based spectroscopy (Guo et al. 2016). This short-period ($P = 2.16$ d) eclipsing binary has a circular orbit and is composed of two A-type stars. We only briefly summarize the results in the following Table 2.1. Details of the derivations are presented in Chapter 5. The modeling process is elaborated in this section.

Table 2.1: Fundamental Parameters of KIC 9851944

Parameters	Primary	Secondary
Mass ($M_\odot$)	1.76 ± 0.07	1.79 ± 0.07
Radius ($R_\odot$)	2.27 ± 0.03	3.19 ± 0.04
$T_{\rm eff}$ (K)	7026 ± 100	6902 ± 100
$\log g$ (cgs)	3.96 ± 0.03	3.69 ± 0.03

The accurate stellar parameters that can be derived from eclipsing binaries offer us opportunities to confront our current stellar structure and evolution theories with observations. We adopted a forward modeling approach and computed non-rotating models with the stellar evolution code MESA with different stellar physics. Convection is described by the mixing length theory (Böhm-Vitense 1958), with the value of mixing length parameter $\alpha_{\rm MLT}$ fixed to 1.8. Convective core overshoot is described by the exponentially decaying prescription of Herwig (2000). The OPAL opacity tables (Iglesias & Rogers 1996) and the MESA equation-of-state are used. The default solar mixtures of Grevesse & Sauval (1998) are adopted as

they are close to the solar mixture used in our spectroscopic analysis (see Chapter 5). Note that the updated solar mixtures in Asplund et al. (2009) have a slightly lower metallicity.

We scanned the mass range from 1.7 to 1.9 $M_{\odot}$ in steps of $0.01 M_{\odot}$, which covers the 1 sigma uncertainty box of both stars. The exponentially decaying overshooting parameter (f_{ov}) was varied in the range from 0.0 to 0.02 in steps of 0.005, which corresponds to the traditional step-wise overshoot parameter of $\alpha_{ov} \in [0.0, 0.2]$ expressed in terms of the local pressure scale height H_p. The metal mass fraction (Z) was also varied from 0.01 to 0.02 with a step of 0.002, with the helium mass fraction fixed to Y= 0.28. Note the solar metal mass fraction $Z_{\odot}$ we adopted in MESA is 0.02.

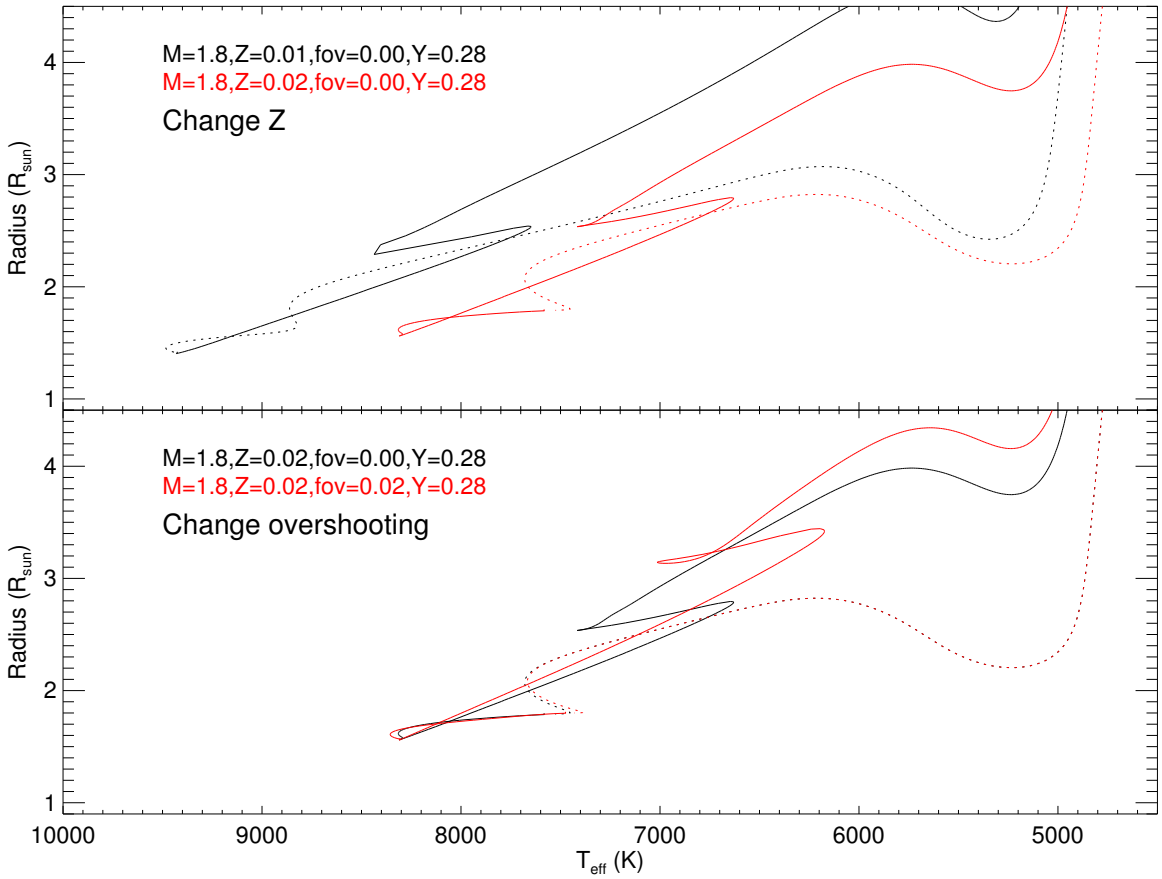

Figure 2.1 The evolutionary tracks for stellar models with $M = 1.8M_{\odot}$ and $Y = 0.28$. The upper panel illustrates the effect of changing the metal mass fraction from $Z = 0.01$ to $Z = 0.02$. The lower panel shows the result of changing convective core overshooting parameter f_{ov} from 0.00 to 0.02. For clarity, most of the pre-MS tracks are indicated by dotted lines.

Here, we show the effect on the evolutionary tracks of changing various physical parameters for a typical δ Scuti star ($M = 1.8M_{\odot}$). Note in the upper panel of Figure 2.1, the

effect of decreasing metal mass fraction ($Z = 0.02 \rightarrow 0.01$) is a near horizontal shift of the tracks to lower effective temperatures. Increasing the convective overshooting parameter of the core ($f_{ov} = 0.00 \rightarrow 0.02$), the evolutionary tracks show a prolonged main sequence (MS) in the $R - T_{\rm eff}$ plane. The main sequence tracks with higher f_{ov} are generally above those with lower f_{ov} values, and the effects of f_{ov} on pre-MS tracks are small.

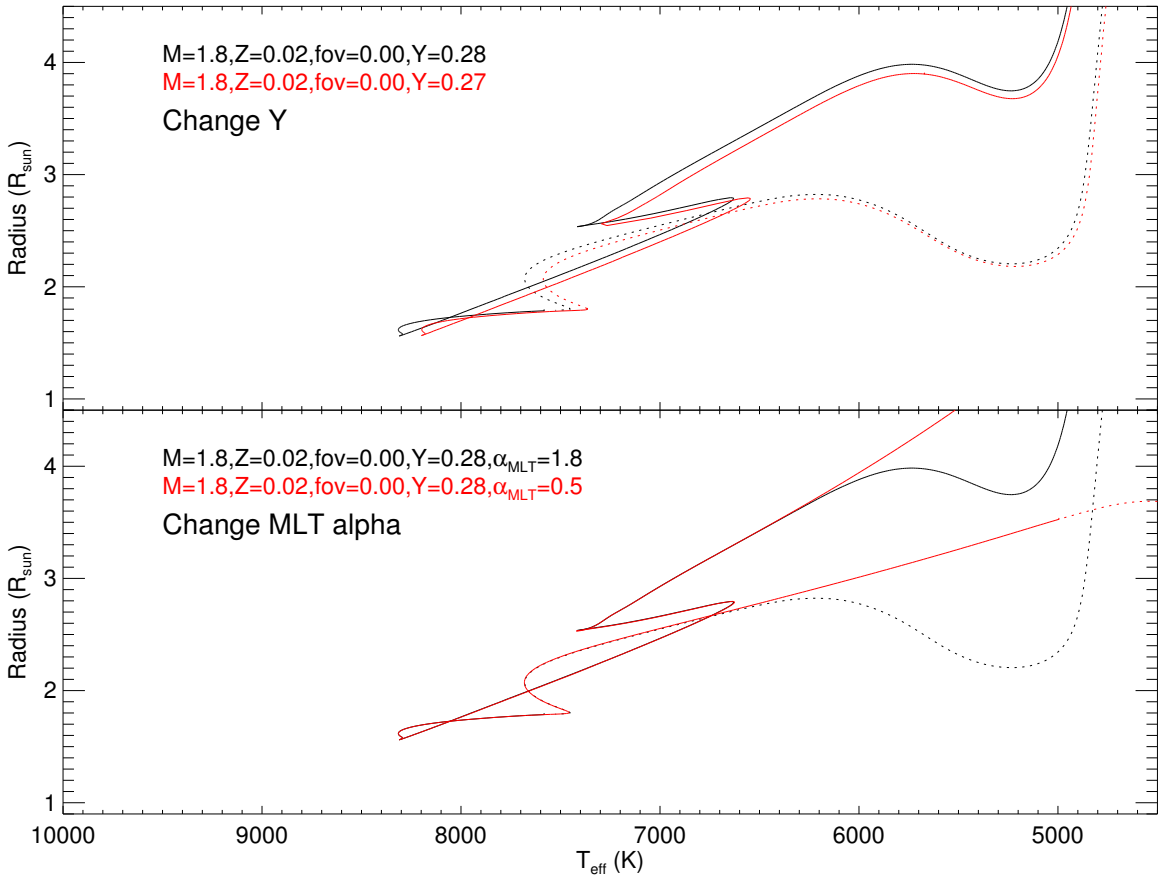

Figure 2.2 The evolutionary tracks for stellar models with $M = 1.8M_{\odot}$, $Z = 0.02$ and $f_{ov} = 0.00$. The upper panel illustrates the effects of changing the initial He abundance from $Y = 0.28$ to $Y = 0.27$. The lower panel shows the result of changing the Mixing Length parameter $\alpha_{\rm MLT}$ from 0.5 to 1.8. For clarity, most of the pre-MS tracks are indicated by dotted lines.

As shown in the upper panel of Figure 2.2, an increase of initial He abundance (Y) from 0.27 to 0.28 shifts the evolutionary track to the left (region with higher temperatures). The

effect of coefficient $\alpha_{\rm MLT}$ in Mixing Length Theory is only important when stars are closer to the Hayashi line when they have large fractional convective envelopes (lower panel).

In the modeling of KIC 9851944, more than 30000 structure models were computed. Out of these models, we choose a pair of models with the same age and metal mass fraction (Z) which represent the primary and secondary star, respectively. All coeval models which fall within the 2σ error box of the observed effective temperature and radius of the two stars have been selected. We use a χ^2 like cost function as the criterion to characterize the goodness of fit:

$$\chi^2 = \sum_{i=1}^{2}((\frac{T_i - T_{obs,i}}{\sigma_{T_{obs,i}}})^2 + (\frac{R_i - R_{obs,i}}{\sigma_{R_{obs,i}}})^2 + (\frac{M_i - M_{obs,i}}{\sigma_{M_{obs,i}}})^2).$$

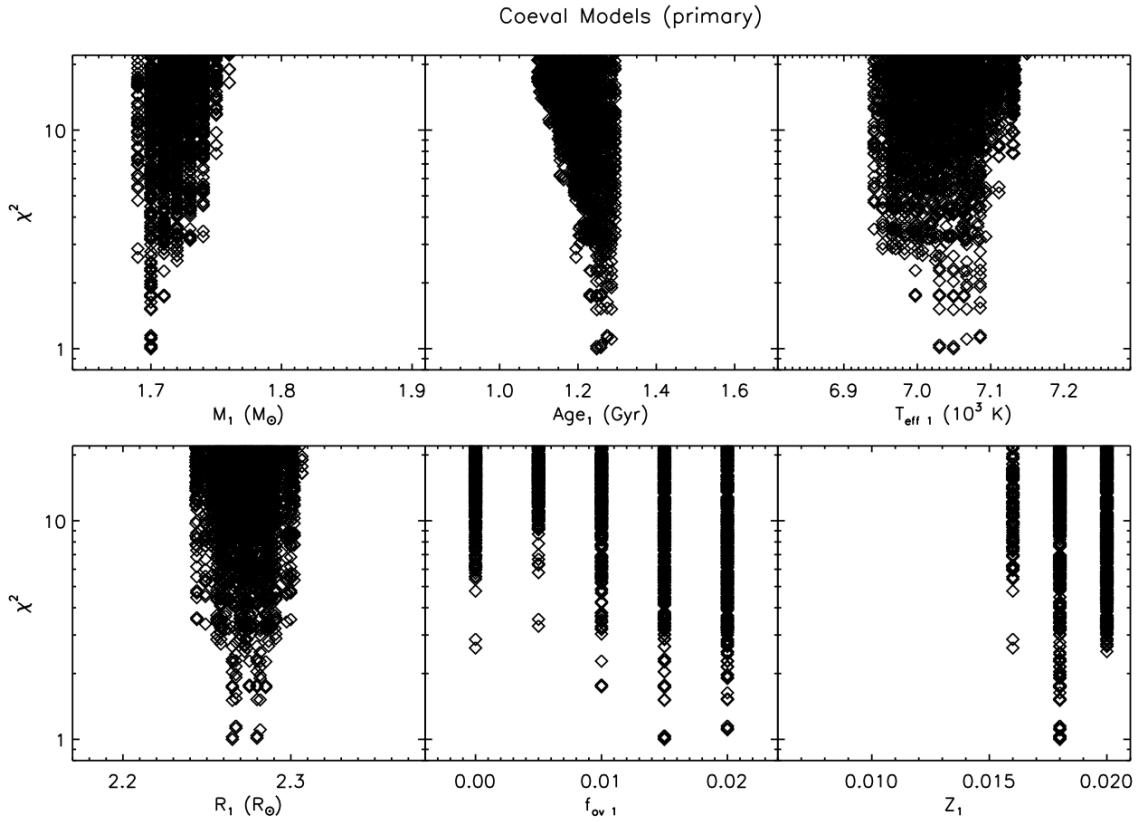

Figure 2.3 The distribution of physical parameters of coeval MESA models for the primary star. The minimum of χ^2 has been normalized to 1.

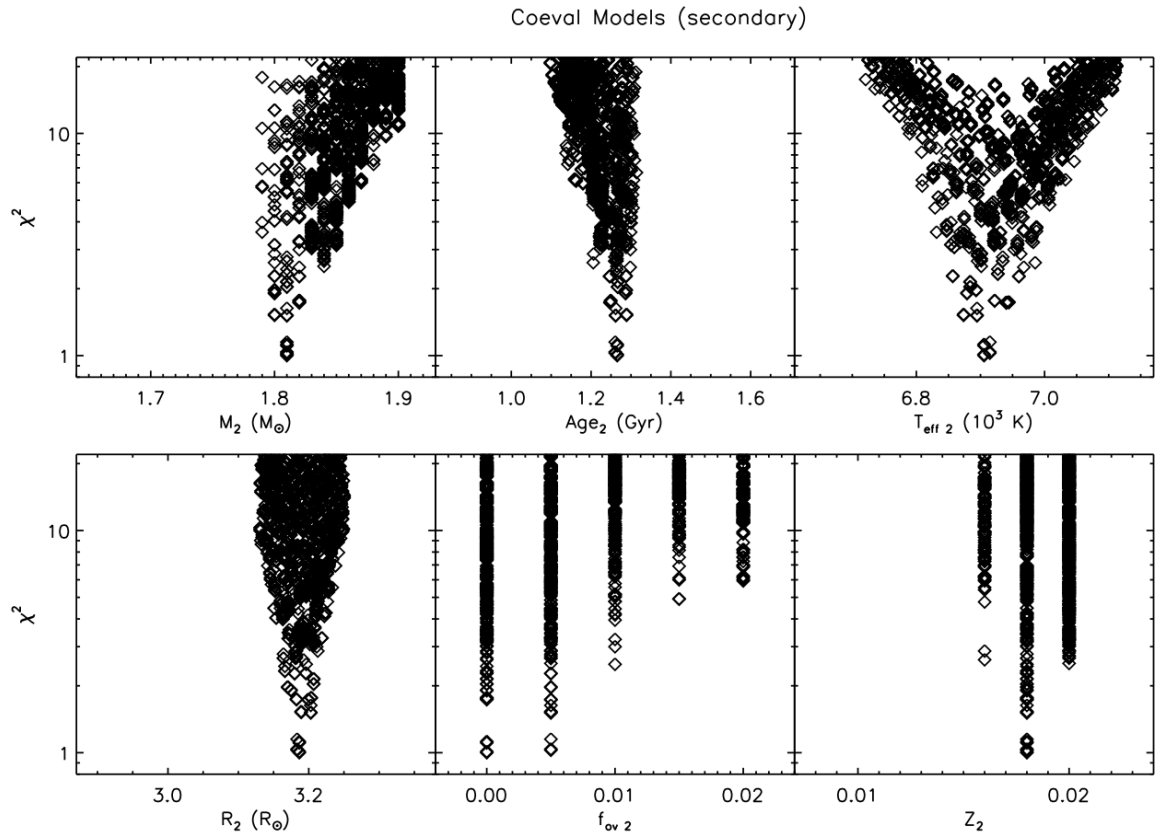

Figure 2.4 The distribution of physical parameters of coeval MESA models for the secondary star. The minimum of χ^2 has been normalized to 1.

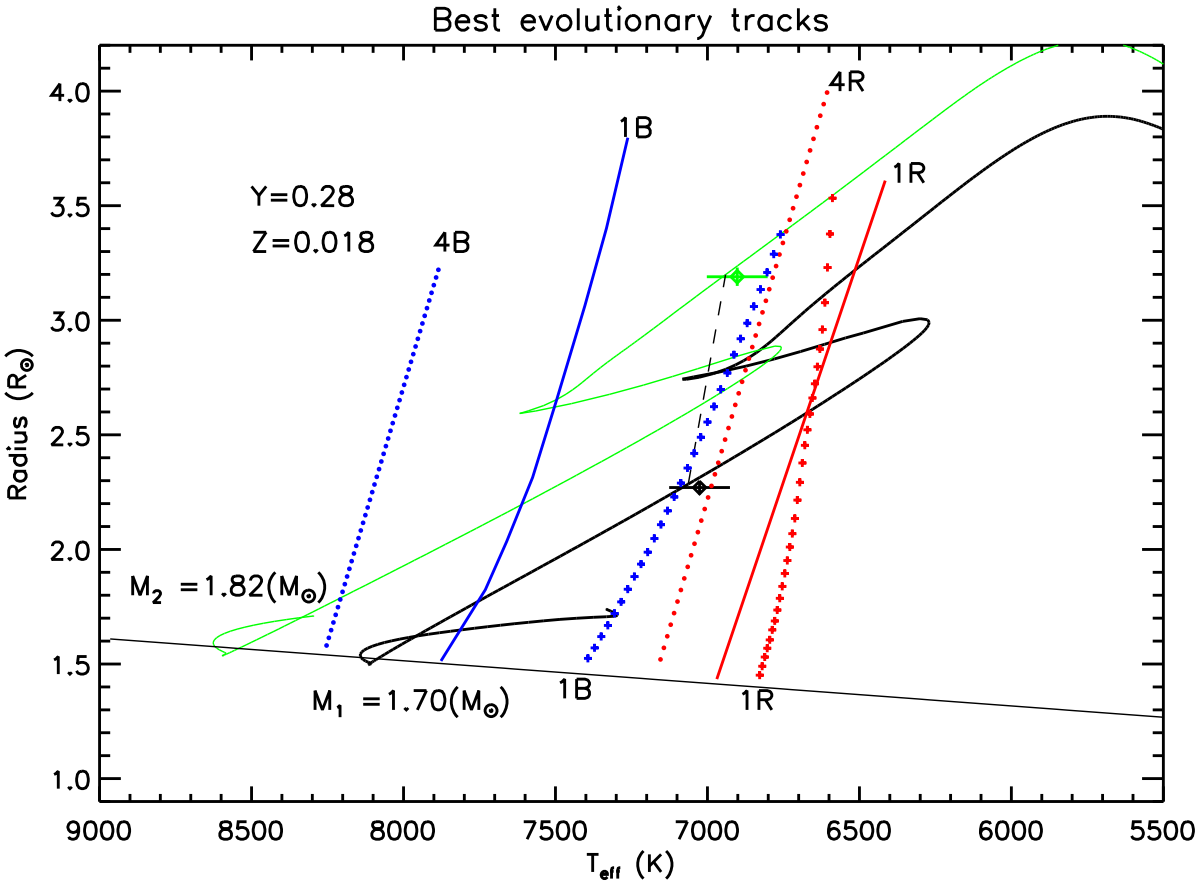

Figure 2.5 Best coeval MESA models in the $T_{\rm eff}$-R plane. The evolutionary tracks of the primary ($M = 1.70 M_{\odot}$) and the secondary ($M = 1.82 M_{\odot}$) are indicated by the black and green solid curves, respectively. Two diamonds indicate the observational estimates for the primary and secondary stars. The long dash line connecting two models in the tracks represents an isochrone of 1.23 Gyr. The thin black solid line shows the Zero-Age Main Sequence. The radial fundamental red and blue edges (1R, 1B) and the 4th overtone radial red and blue edges (4R, 4B) of the δ Scuti instability strip are indicated by the blue/red solid and dotted lines. The cross lines are the red and blue edges of the γ Dor instability strip ($l = 1$ and mixing length $\alpha_{\rm MLT} = 2.0$) (Dupret et al. 2005).

Figures 2.3 and 2.4 show the χ^2 of a grid of fundamental stellar parameters (mass, effective temperature, radius, and age) and two stellar physics parameters (metal mass fraction Z and overshooting parameter f_{ov}). The best coeval models have a mass of $1.70 M_{\odot}$, radius of $2.27 R_{\odot}$ and effective temperature of 7049 K for the primary, and $1.81 M_{\odot}$, $3.19 R_{\odot}$, 6906 K for the secondary, with an age of about 1.25 Gyr. The corresponding evolutionary tracks and the δ Scuti and γ Doradus instability strips are shown in Figure 2.5. The primary is a hydrogen-burning main sequence star located in the middle of the MS phase. The secondary is more evolved and has exhausted the central hydrogen. After a short contraction it is now in the expanding hydrogen shell burning post-MS phase. Only models with metal fraction Z of 0.018 or 0.020 can fit the two data points simultaneously, so this suggests that the bulk metallicity of both stars is close to the solar value. The convective overshooting parameter f_{ov} of the primary star is not well constrained (note the broad lower envelope in Fig. 2.3) but the model seems to favor a higher value from 0.010 to 0.015. For the secondary star, no overshooting or low overshooting (f_{ov} less than 0.005) can fit the observations well. The best fitting model pair has a mass ratio of 1.06 which is higher than the observed 1.01 ± 0.03 at the 1.6σ level. However, we do acknowledge that if the radii are more similar to each other (suggested by spectroscopy, detailed in Chapter 5), then a mass ratio closer to 1.0 does fit the evolutionary tracks in Figure 2.5.

We also fit the two stars individually, relaxing the constraints of coevality. The single best-fit models for the primary have a mass range of $1.74 - 1.75 M_{\odot}$, an age range of $1.1 - 1.2$ Gyr, an overshooting parameter of $0.00 - 0.005$, and metallicity of 0.018 or 0.02. For the

secondary star, mass is constrained as $\approx 1.84 M_{\odot}$, age as of $1.2 - 1.4$ Gyr. The overshooting parameter is poorly constrained, but favors a higher value $0.015 - 0.02$. The metallicity is also poorly constrained. Both stars can be fitted reasonably well with an isochrone of solar-metallicity.

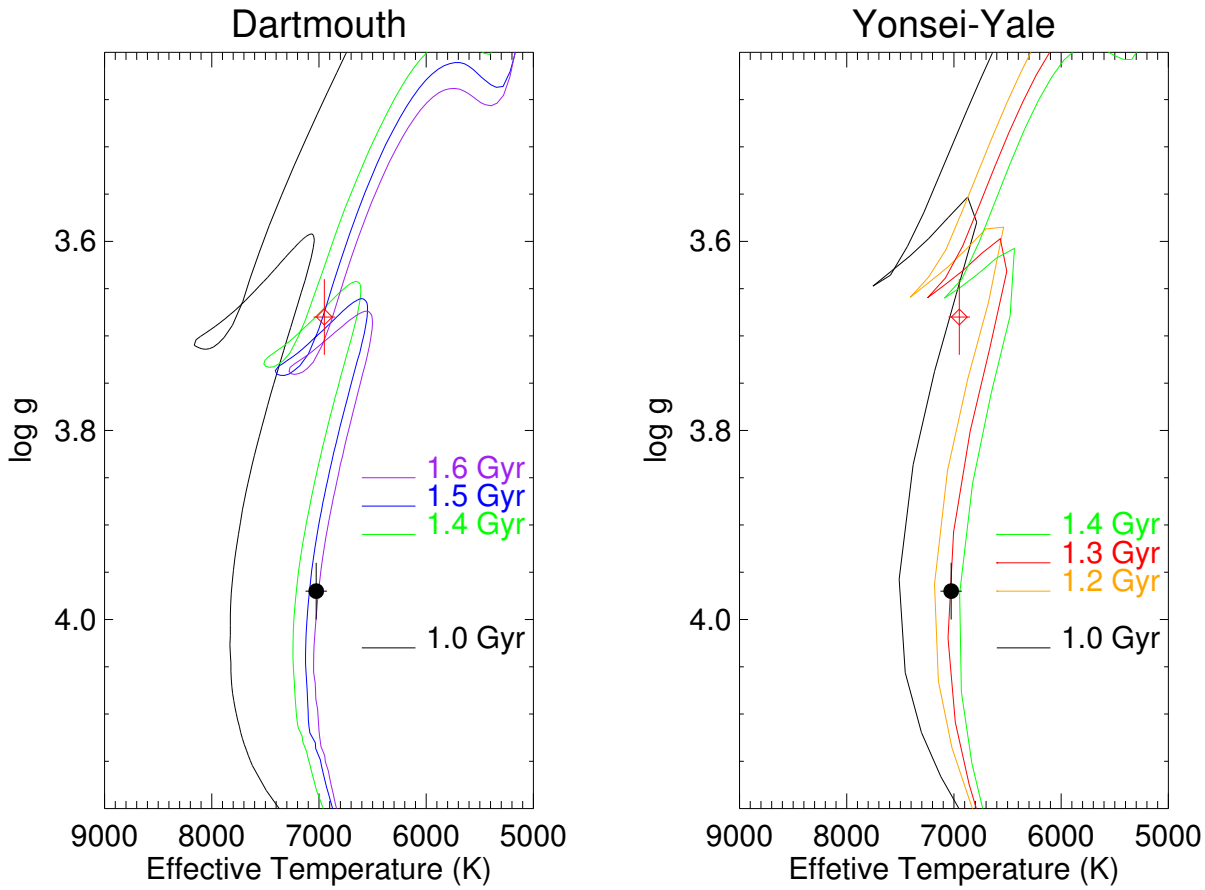

Figure 2.6 Comparison of observations with the Dartmouth and Yonsei-Yale isochrones in the $T_{\rm eff}$-$\log g$ plane. The primary and secondary star are indicated by filled dots and open diamonds, respectively.

We also compare the observations with two other stellar evolutionary models: the Dartmouth model (Dotter et al. 2008) and Yonsei-Yale (Y^2) model (Yi et al. 2001). In the $\log g$-$T_{\rm eff}$ plane (Fig. 2.6), Dartmouth isochrones of $\approx 1.4 - 1.6$ Gyr can fit the observations of the two stars well, while the best fitting Yonsei-Yale isochrones have ages of $1.2 - 1.4$ Gyr. In both cases, solar metallicity agrees with the observations well. However, the same mass discrepancy exists: the best fitting Dartmouth isochrone intersects the observation box at masses of $1.65M_{\odot}$ and $1.80M_{\odot}$,and this gives an even higher mass ratio of 1.09. This is not surprising because these two evolutionary models have only fixed physics, while in MESA models we can partially alleviate this discrepancy by evoking different overshooting parameters in the two stars.

2.2 Bayesian Isochrone Fitting

As shown in the last section, isochrone fitting is an important way of inferring the age of stars. The traditional method of χ^2 minimization neglects some important prior information, e.g., stars spend more time on the main sequence than in the sub-giant phase. We show two examples in Figure 2.7. A rough comparison with the isochrones suggests that a much more constrained age can be derived for star A. However, for star B, nearly all isochrones young enough can match its position. We need a way to determine the distribution of probable age instead of just a point estimate from χ^2_{min}.

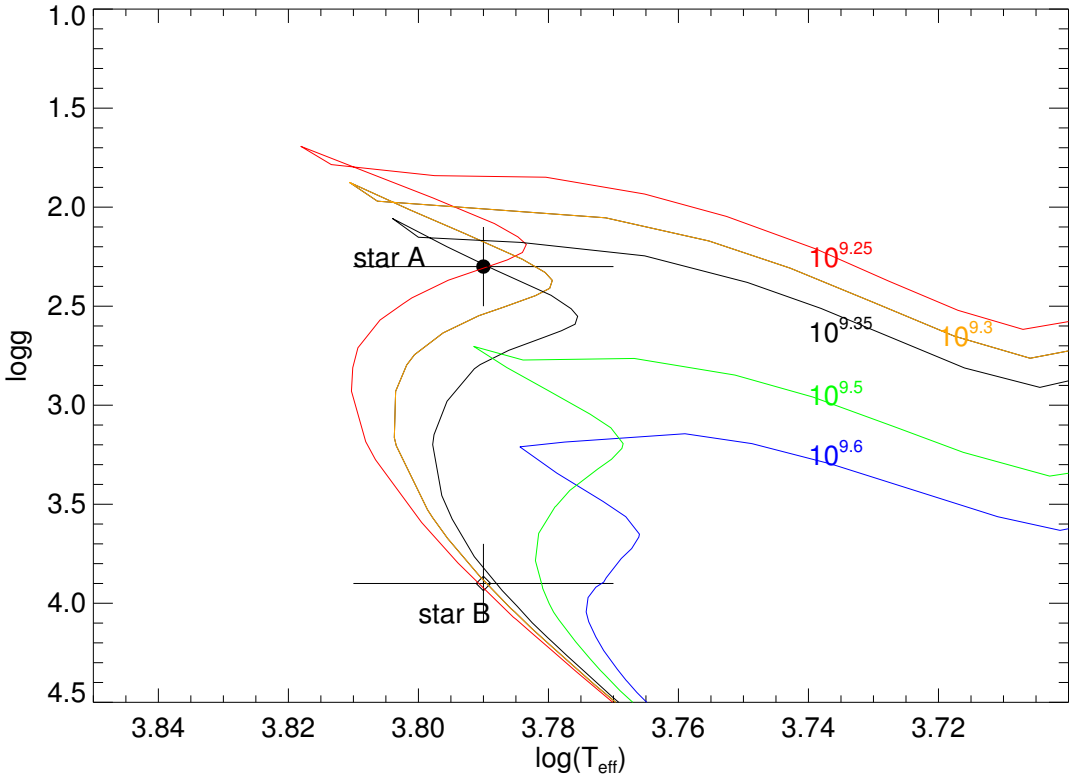

Figure 2.7 Padova isochrones (Bressan et al. 2012) on the $\log T_{\rm eff} - \log g$ plane with age labeled. The filled circle and diamond mark the positions of two hypothetical stars for which we want to determine their ages. The assumed 1σ error bars of $\log(T_{\rm eff})$ for both stars are 0.02, and similarly $\sigma(\log g) = 0.2$.

Here, we follow the method of Bayesian isochrone fitting introduced in Jørgensen & Lindegren (2005). This method takes into account priors such as the initial mass function, evolutionary speed, etc., and can generate the posterior probability distributions instead of just one point estimate.

We briefly summarize the algorithm here. For simplicity and without loss of generality,

we only consider models with solar metallicity here. The stellar evolutionary models provide a mapping from the parameter space $\boldsymbol{p} = (\tau, m)$ to the data space $\boldsymbol{q} = (\log g, T_{\rm eff})$. τ and m are the age and initial mass, respectively. We can treat the observed quantities $\boldsymbol{q}_{obs}$ as functions of parameters of interest $\boldsymbol{p}$ plus some Gaussian noise, $\boldsymbol{q}_{obs} = \boldsymbol{q}(\boldsymbol{p}) + \boldsymbol{e} = \boldsymbol{q}(\tau, m) + \boldsymbol{e}$. We want to get the posterior probability distribution of parameters of interest $p((\tau, m)|\boldsymbol{q}_{obs})$, which is $\propto p(\boldsymbol{q}_{obs}|\tau, m)p(\tau, m)$ following Bayes' rule.

$p(\boldsymbol{q}_{obs}|\tau, m)$ is the likelihood function. Assuming independent uncertainties in $\log g$ and $T_{\rm eff}$, it can be expressed as:

$$\begin{aligned} p(\boldsymbol{q}_{obs}|\tau, m) &= \boldsymbol{N}(\boldsymbol{q}(\tau, m), \boldsymbol{C_q}) = \prod_i^I N(q_i(\tau, m), \sigma_i) \\ &= \left(\prod_i^I \frac{1}{\sqrt{2\pi\sigma_i^2}} \right) \exp(-\chi^2/2) \end{aligned} \tag{2.1}$$

where

$$\chi^2 = \sum_i^I \left(\frac{q_i^{obs} - q_i(\tau, m)}{\sigma_i} \right)^2 \tag{2.2}$$

$N(q, \sigma)$ and $\boldsymbol{N}(\boldsymbol{q}, \boldsymbol{C_q})$ are normal distribution and multivariate normal distribution, respectively. σ is the standard deviation of q and $\boldsymbol{C_q}$ is the covariance matrix of $\boldsymbol{q}$. I is the number of data points (or stars) on the $\log g - T_{\rm eff}$ plane, with i as an index.

$p(\tau, m)$ is the prior distribution of parameters. Assume that age and initial mass are independent, the prior is then $p(\tau)p(m)$. The prior on stellar age $p(\tau)$ relates to the star formation rate, and we use a flat distribution for convenience. For the prior on stellar initial mass $p(m)$, we use $p(m) \sim m^{-2.7}$, which corresponds to a Salpeter initial mass function.

Thus the posterior is $p((\tau, m)|\boldsymbol{q}_{obs}) \propto p(\boldsymbol{q}_{obs}|\tau, m)p(m)$. If we need the posterior of one

parameter, for example, the age τ, we can marginalize over other parameters, m:

$$p(\tau|\boldsymbol{q}_{obs}) \propto \int p((\tau, m)|\boldsymbol{q}_{obs})dm \propto \int p(\boldsymbol{q}_{obs}|\tau, m)p(m)dm \tag{2.3}$$

Numerically, we can evaluate the above equation for each age τ_i as

$$p(\tau_i|\boldsymbol{q}_{obs}) \propto \sum_k p(\boldsymbol{q}_{obs}|\tau_i, m_{i,k})p(m_k)\Delta m_k. \tag{2.4}$$

This is a sum for each mass m_k on the isochrone of age τ_i, and Δm_k is the grid spacing in mass. For the extension of this equation to include metallicity, see eq.(11) in the original paper (Jørgensen & Lindegren 2005). We can of course select different parameters in parameter space and data space (Prada Moroni et al. 2012).

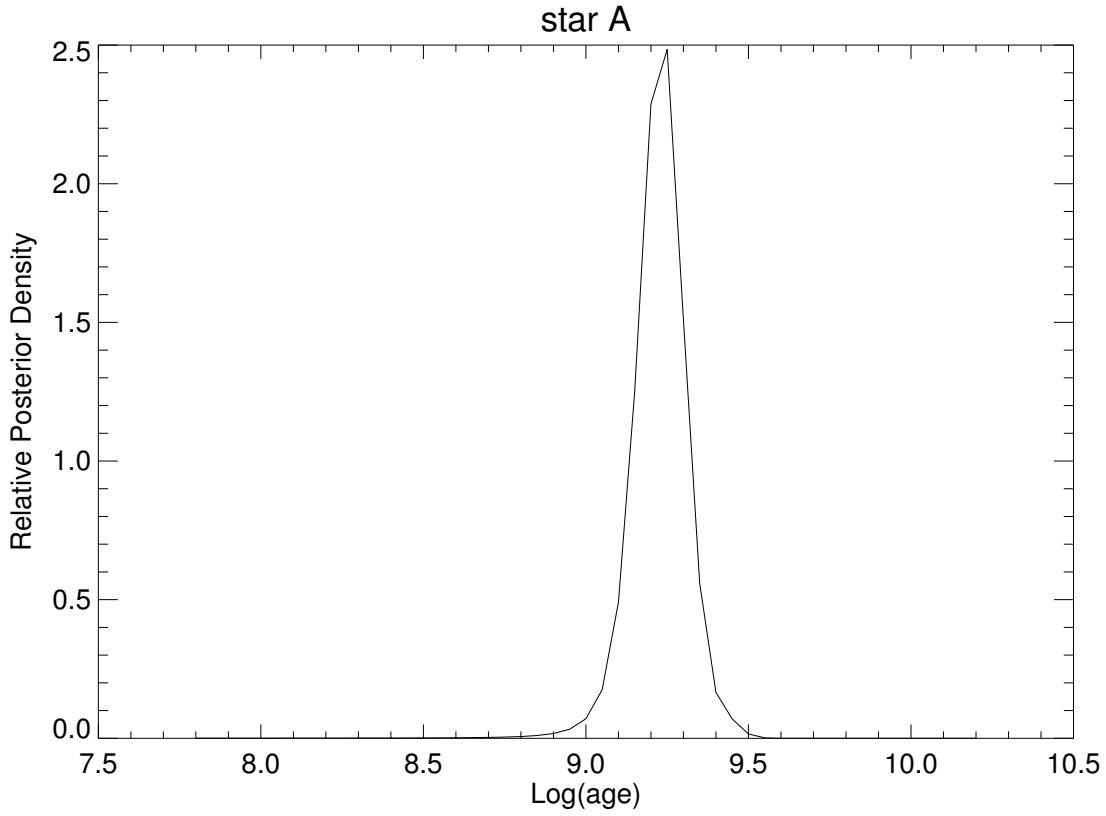

Figure 2.8 The relative posterior probability density of age for star A.

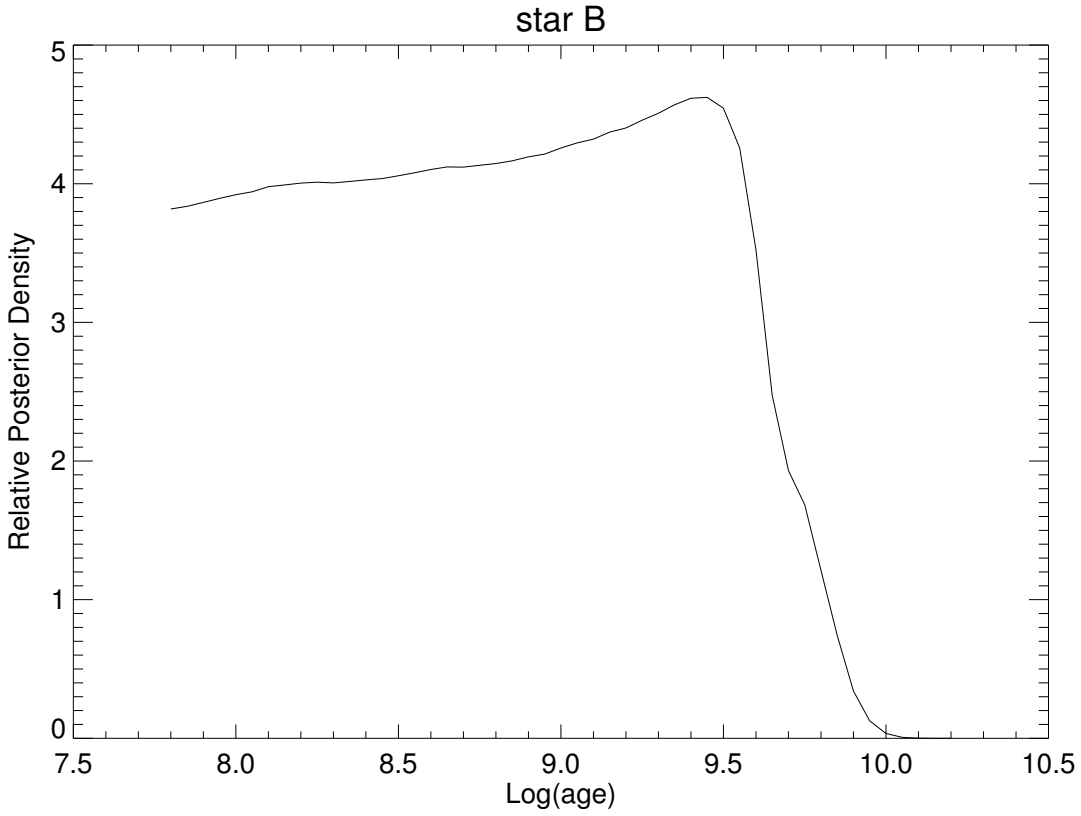

Figure 2.9 The relarive posterior probability density of age for star B.

We have implemented the above algorithm with the Padova evolutionary models (Girardi et al. 2000), and the IDL source code has been included in the appendix. In Figure 2.8 and 2.9, we show the results of Bayesian isochrone fitting for star A and star B, respectively. Note that the age of star A is much better constrained and the distribution for the age of star B is very broad.

We show similar calculations for the eclipsing binary KIC 9851944 in Figure 2.10 and 2.11. Note that the posterior distribution of age is sharper when we consider the two components simultaneously, assuming that the two components are coeval.

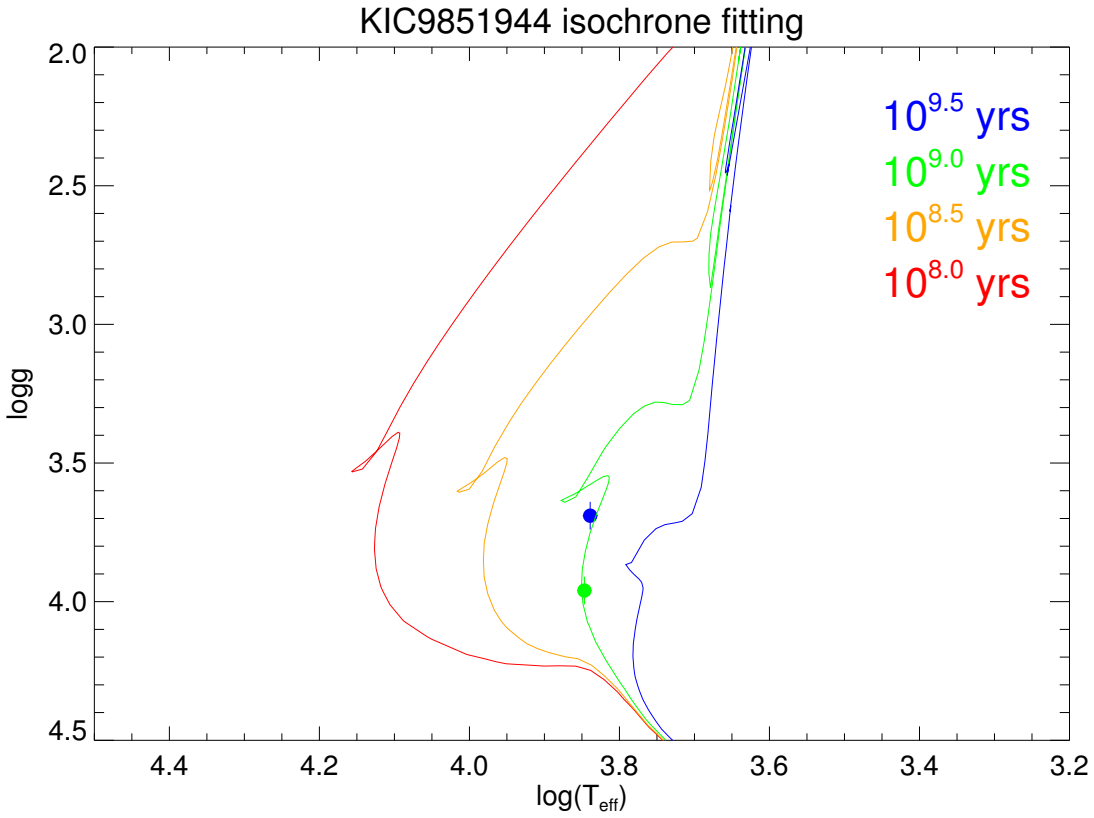

Figure 2.10 Position of KIC 9851944 on the $\log T_{\rm eff} - \log g$ plane. The primary and secondary star are indicated by the green and blue symbol, respectively. Padova isochrones are overlayed for comparison.

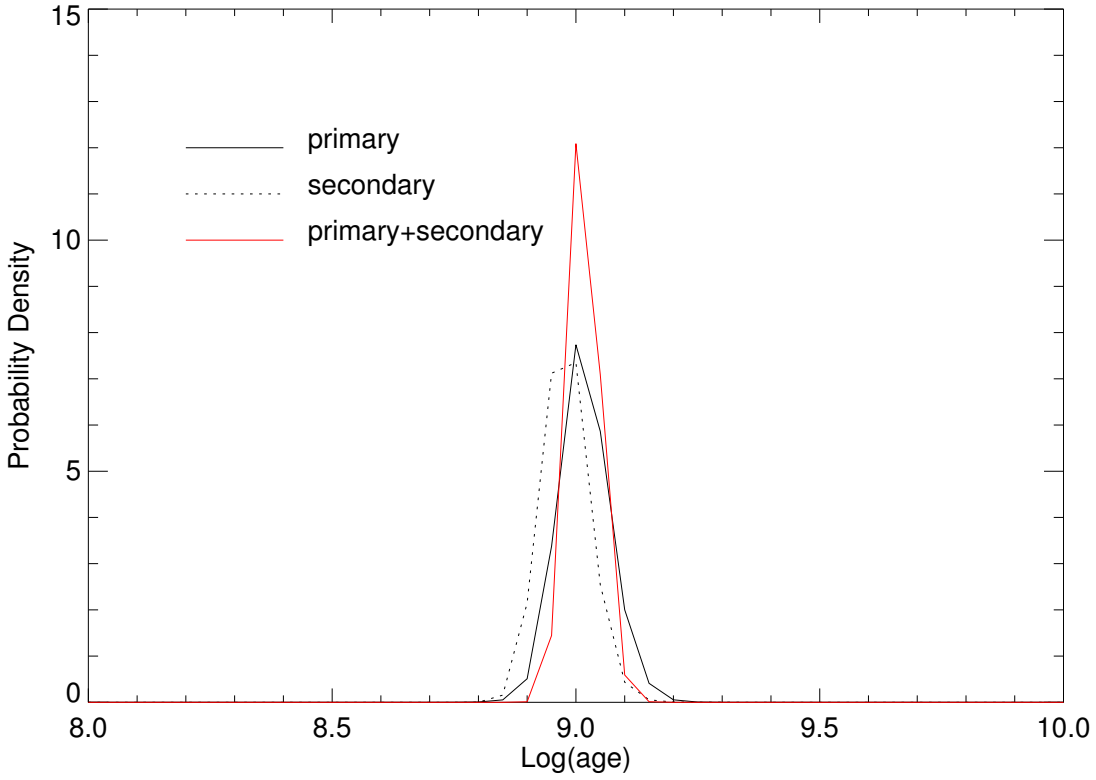

Figure 2.11 The posterior probability distributions of age for KIC 9851944. The solid and dotted line are the results from fitting the observed ($\log T_{\rm eff}$, $\log g$) of the primary and secondary, respectively. The much sharper distribution in red is the result of considering the two components simultaneously, assuming coevality.

2.3 Differences between Y^2 and Dartmouth Isochrones for Low Mass Stars

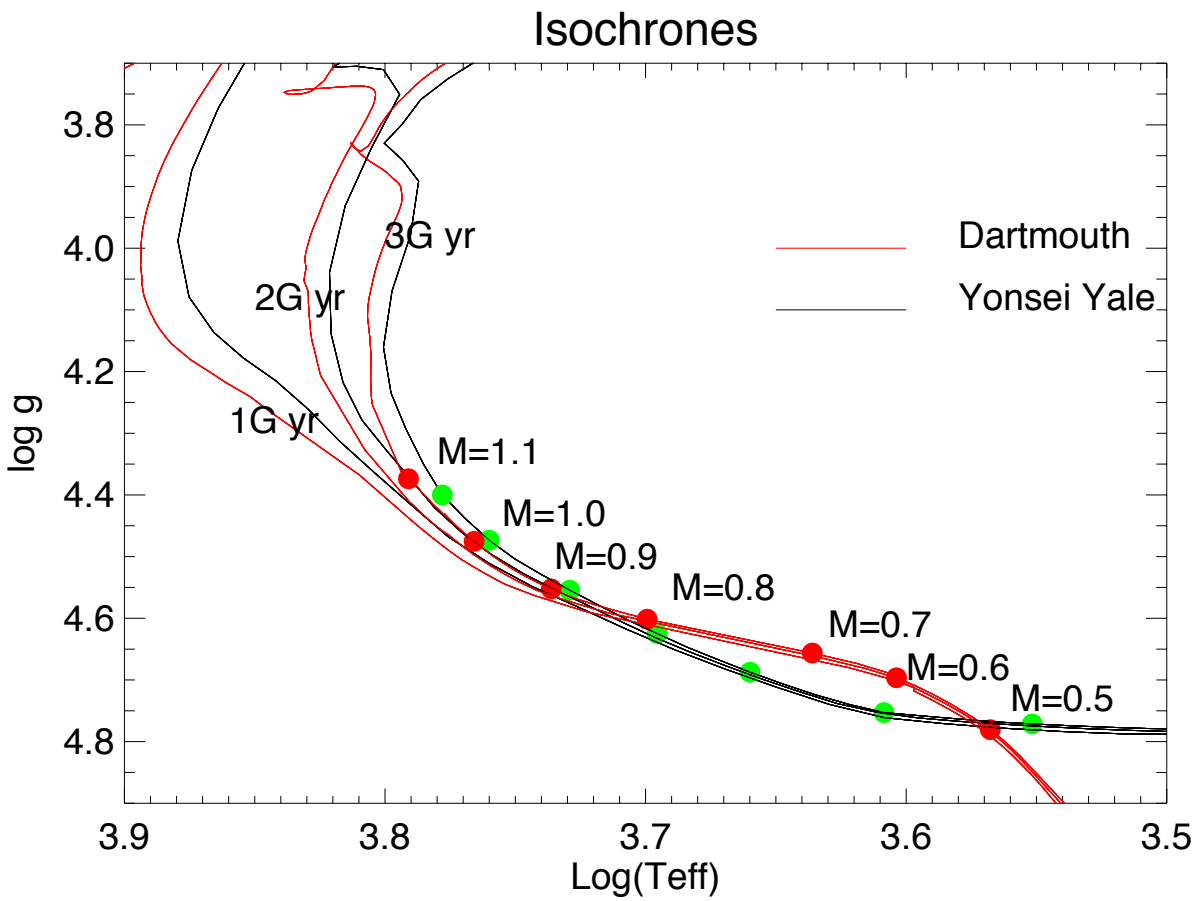

Figure 2.12 The isochrones from Dartmouth (red) and Yonsei-Yale (black) evolutionary models on the $\log g - \log T_{\rm eff}$ plane. The masses on isochrones are labeled respectively by the red and green dots.

We rely heavily on stellar evolutionary models for inference of fundamental parameters. In most observational work, only one model is considered and differences between different evolutionary models are not taken into account.

Figure 2.6 in the last section already shows the differences between Yonsei-Yale (Y^2)

and Dartmouth evolutionary models (DSEP) for KIC 9851944. In Figure 2.12, we show the isochrones from these two models again but for low mass stars. The most distinct differences are for stars with masses lower than $0.8M_{\odot}$. The Dartmouth isochrones have systematically higher surface gravities. This difference will affect the derived masses and radii of exoplanets as discussed below.

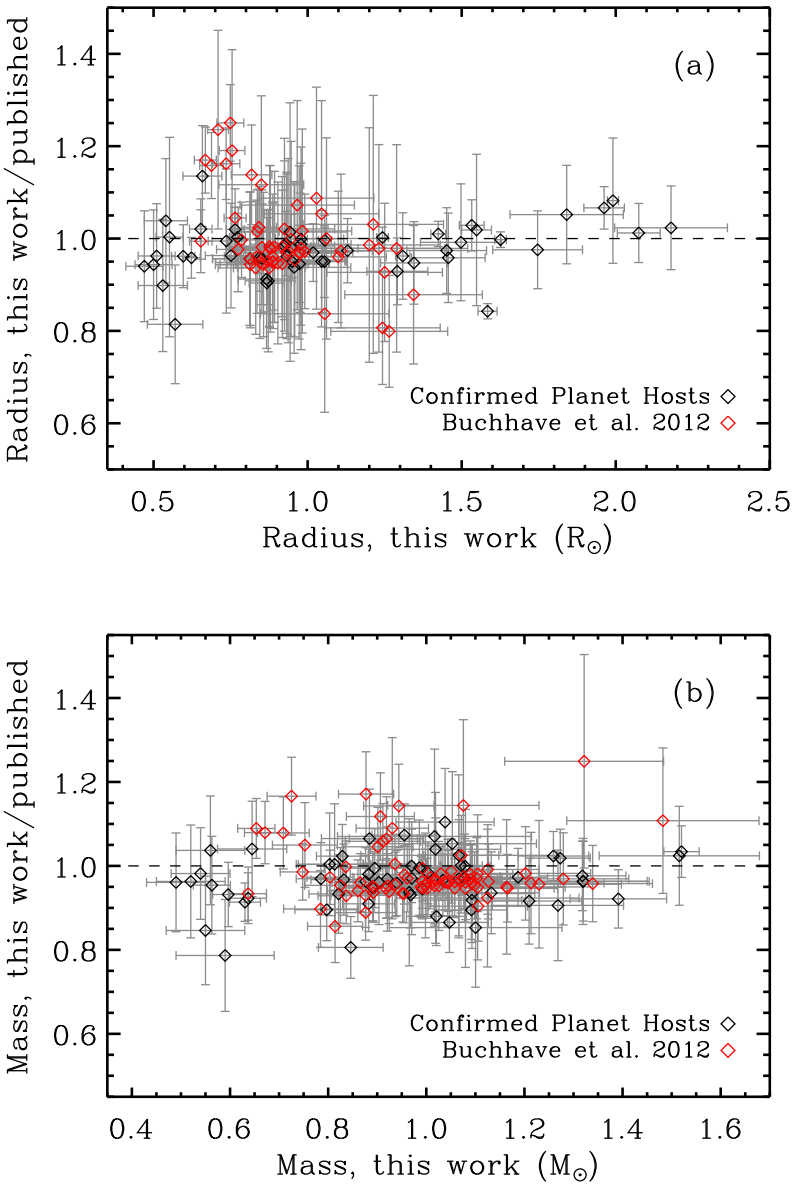

Figure 2.13 (a) Fractional difference between published radii and masses derived in Huber et al. (2014) for confirmed planet host stars (black) and planet-candidate host stars analyzed by Buchhave et al. (2012) (red). (b) Same as panel (a) but for stellar masses. Figure is taken from Huber et al. (2014).

Figure 2.13 shows a comparison for confirmed Kepler planet host stars taken from the NASA exoplanet archive (black), as well as the larger sample of planet-candidate host stars by Buchhave et al. (2012) (red). In both cases the majority of the radii and masses were derived using Yonsei-Yale (Y^2) evolutionary models. Overall the residuals show an offset of 1% for radius and an offset of 3% for mass. We observe systematic differences at the low-mass end ($\leq 0.8 M_{\odot}$), resulting in a 'kink' with higher DSEP masses and radii between $\approx 0.6 - 0.8 M_{\odot}$, and lower DSEP masses and radii for $\leq 0.6 M_{\odot}$.

Table 2.2 presents the differences in the adopted stellar physics between these two models. $M_{\rm critical}$ is the mass when stars start to develop a convective core. For [Fe/H] = 0 and [α/Fe] = 0, $M_{\rm critical}$ is about $1.2 M_{\odot}$. Most of the listed physics is similar. The difference in the treatment of convective core overshooting has nothing to do with low-mass stars ($\leq 0.8 M_{\odot}$). The aforementioned observed systematic differences for the low-mass stars is thus likely due to different equations of state adopted.

Table 2.2: Comparison of Yonsei-Yale and Dartmouth

Models

Input Physics	Yonsei-Yale	Dartmouth
Opacity Table	OPAL opacities	OPAL opacities
	Alexander&Ferguson 1994 for lower $T_{\rm eff}$	Ferguson 2005 for lower $T_{\rm eff}$
Equation of State (EOS)	($M > 0.75M_{\odot}$) Saha-solver	($M \geq 0.8M_{\odot}$), general ideal gas EOS
	+Debye-Huckel approximation	+Debye-Huckel correction
	(others) OPAL EOS	(others) Free EOS
Diffusion	based on Thoul et al. 1994	based on Thoul et al. 1994
Convective Overshooting	$0.2H_p$ for age $\leq$ 2 Gyr	$0.05H_p$ for $M \approx M_{cirital}$
		$0.1H_p$ for $M \in M_{\rm critical} + [0.05, 0.1]$
		$0.2H_p$ for $M \in M_{\rm critical} + [0.1, 0.2]$

CHAPTER 3

Linear Oscillation Theory

This chapter contains the theory of linear stellar oscillations. The theory of free oscillations with and without rotation is from Unno et al. (1989) and Townsend (1997). The linear tidal oscillation theory without rotation is mainly from Fuller & Lai (2012), Burkart et al. (2012), and Valsecchi et al. (2013). Although most of the content is a review of the theory in the literature, I summarize and present them in a general framework following the formulism used in GYRE (Townsend & Teitler 2013). The Hough function, used in the traditional approximation, is discussed in detail and presented graphically. I have tried to fill in the gaps in the derivations especially for the tidal oscillation theory. All figures are based on my own calculations and the adiabatic and non-adiabatic tidal eigenfunctions are the main contributions.

This chapter is directly related to Chapter 1 and Chapter 5, in which we utilize the results from solving the free oscillation equations. In Chapter 6, we apply the amplitude and phase equations of tidally forced oscillations to *Kepler* heartbeat stars.

The variables and terms used in the adiabatic and non-adiabatic stellar oscillations in this chapter are listed in Table 3.1, and some of them are also listed in Valsecchi et al. (2013).

Table 3.1: Definition of Variables

Symbol	Expression/Description
$\delta\rho$	Lagrangian density perturbation
ρ'	Eulerian density perturbation
$\delta\boldsymbol{r}$ or $\boldsymbol{\xi}$	Lagrangian displacement
$\boldsymbol{\xi}_R$ or $\boldsymbol{\xi}_r$	radial part of the Lag. displacement
$\boldsymbol{\xi}_S$	horizontal part of the Lag. displacement

$\boldsymbol{v}$	velocity
Φ	gravitational potential
Φ' or $\delta\Phi$	Eulerian gravitational potential perturbation
δp	Lag. pressure perturbation
p'	Eulerian pressure perturbation
$\Gamma_1 = (\frac{\partial \ln p}{\partial \ln \rho})_s$	adiabatic index
V_g	$\frac{V}{\Gamma_1} = gr/c_s^2$
V	$-d\ln P/d\ln r = GM_r\rho/rp$
c_1	$(\frac{r}{R})^3 \frac{M}{M_r}$
N^2	Brunt-Väisälä frequency $= g(\frac{1}{\Gamma_1}\frac{d\ln p}{dr}\frac{d\ln \rho}{dr})$
A^*	$rg^{-1}N^2$
U	$\frac{d\ln M_r}{d\ln r} = \frac{4\pi\rho r^3}{M_r}$
M_r	mass contained within a radius of r
M_* or M	total mass of the star
R_* or R	radius of the star
δS	Lag. entropy perturbation
c_P	specific heat at constant pressure
δL_R	Lag. perturbation of radiative luminosity
L_R	radiative luminosity
κ	Opacity
κ_T	$(\frac{\partial \ln \kappa}{\partial \ln T})_\rho$
κ_ρ	$(\frac{\partial \ln \kappa}{\partial \ln \rho})_T$
S	Specific entropy
κ_{ad}	$(\frac{\partial \ln \kappa}{\partial \ln p})_S = \kappa_T\nabla_{ad} + \frac{\kappa_\rho}{\Gamma_1}$
κ_s	$c_P(\frac{\partial \ln \kappa}{\partial S})_p = \kappa_T - \nu_T\kappa_\rho$
∇	$\frac{d\ln T}{d\ln p}$
∇_{ad}	$(\frac{d\ln T}{d\ln p})_S$
c_2 or c_{kap}	$(\kappa_{ad} - 4\nabla_{ad})V\nabla + \nabla_{ad}(\frac{d\ln \nabla_{ad}}{d\ln r} + V)$
c_3	$\frac{4\pi r^3\rho\epsilon_N}{L_R}$
c_4	$\frac{4\pi r^3\rho T c_P}{L_R}\sqrt{\frac{GM}{R^3}}$
ν_T	$c_P\nabla_{ad}\frac{\rho T}{p}$
ϵ_N	Nuclear generation rate
ϵ_T	$(\frac{\partial \ln \epsilon_N}{\partial \ln T})_\rho$
ϵ_ρ	$(\frac{\partial \ln \epsilon_N}{\partial \ln \rho})_T$
ϵ_{ad}	$(\frac{\partial \ln \epsilon_N}{\partial \ln p})_S = \epsilon_T\nabla_{ad} + \frac{\epsilon_\rho}{\Gamma_1}$
g	gravitational acceleration
c	speed of light
G	gravitational constant

3.1 Free Oscillations

3.1.1 Without Rotation

The basic hydrodynamic equations describing stellar structures include the conservation of mass, momentum, and energy, supplemented with the Poisson equation for the gravitational potential, equations of state, equations for energy generation rate and opacity (Unno et al. 1989). Ignoring the effects of magnetic field and rotation, we then get the linearized equations for adiabatic (entropy perturbation is zero) non-radial oscillations:

$$\begin{aligned} &\frac{\delta\rho}{\rho} + \nabla\cdot(\delta\boldsymbol{r}) = 0 \\ &\frac{\partial\boldsymbol{v}}{\partial t} = -\nabla\Phi' - \frac{\rho'}{\rho}\nabla\Phi - \frac{1}{\rho}\nabla p' \\ &\frac{\delta p}{p} = \Gamma_1\frac{\delta\rho}{\rho} \\ &\nabla^2\Phi' = 4\pi G\rho' \end{aligned} \tag{3.1}$$

where ρ and p are density and pressure, Φ and Φ' are gravitational potential and its perturbation, Γ_1 is adiabatic index equal to $(\frac{\partial p}{\partial\rho})_s$, and $\boldsymbol{v}$ is velocity of the fluid element. These equations correspond to the mass conservation equation, the equation of motion, the adiabatic state equation, and the Poisson equation, respectively. δ refers to Lagrangian perturbations, and prime means Euler perturbations. The Lagrangian description is a way of looking at fluid motion where the observer follows an individual fluid parcel as it moves through space and time. The Eulerian specification focuses on specific fixed locations in the space through

which the fluid flows as time passes. The Lagrangian displacement vector $\delta\boldsymbol{r}$ is often written as $\boldsymbol{\xi}$ in literature. Expressing these equations in spherical coordinates, and utilizing variable separation, the displacement vector is :

$$\boldsymbol{\xi} = \delta\boldsymbol{r} = \left[\xi_R(r), \xi_S(r)\frac{\partial}{\partial\theta}, \xi_S(r)\frac{\partial}{\sin\theta\partial\phi}\right] Y_l^m(\theta,\phi)e^{-i\sigma t}, \tag{3.2}$$

where $\xi_R(r)$ and $\xi_S(r)$ refer to the radial part of the radial and horizontal displacement, respectively. Perturbations of various variables can be expressed as, for example, the pressure perturbation,

$$p'(r,\theta,\phi,t) = p'(r)Y_l^m(\theta,\phi)e^{-i\sigma t}. \tag{3.3}$$

For numerical convenience, Dziembowski (1971) first introduced the dimensionless dependent variables. Following the treatment of Townsend & Teilter (2013) and inspired by private communications with Joshua Burkart, the linearized dimensionless oscillation equations can be written as:

$$\frac{d\boldsymbol{y}}{dx} = A(x,\omega)\boldsymbol{y} \tag{3.4}$$

where ω is the eigenvalue (dimensionless oscillation frequency) and vector $\boldsymbol{y}$, as functions of dimensionless radial coordinates $x = \ln x' = \ln(r/R)$ and ω, is the eigenfunction, representing various oscillation variables (e.g., ξ_r/r, etc.).

In the adiabatic case, the eigenfunction vector can be written as (Dziembowski 1971):

$$\boldsymbol{y} = \begin{pmatrix} y^{(1)} \\ y^{(2)} \\ y^{(3)} \\ y^{(4)} \end{pmatrix} \tag{3.5}$$

where

$$\begin{aligned} y^{(1)} &= \frac{\xi_r}{r} \\ y^{(2)} &= \frac{1}{gr}(\frac{p'}{\rho} + \Phi') \\ y^{(3)} &= \frac{1}{gr}\Phi' \\ y^{(4)} &= \frac{1}{g}\frac{d\Phi'}{dr}. \end{aligned} \tag{3.6}$$

$A(r, \omega)$ is the coefficient matrix (4 by 4 for adiabatic case). The inner ($r = 0$) and outer ($r = R$) boundary conditions (BCs) are:

$$B_{in}\boldsymbol{y}(0) = 0, \quad B_{out}\boldsymbol{y}(R) = 0 \tag{3.7}$$

where B_{in} and B_{out} are 2 by 4 matrices for adiabatic oscillations.

We begin with a stellar equilibrium model that is given on a depth grid from center to surface with index $1 \leq i \leq N$. The various physical quantities are evaluated at the i^{th} grid point (or perhaps taken as the average of values at grid points i and $i + 1$). Define the increment $\Delta x_i = x_{i+1} - x_i$. Then we can assume the coefficient matrix A is constant at each i^{th} grid point, and thus we have the Taylor expansion:

$$\begin{aligned}\boldsymbol{y}(x_i + \Delta x_i) &= \boldsymbol{y}(x_i) + \frac{d\boldsymbol{y}}{dx}\Delta x_i + \frac{1}{2!}\frac{d^2\boldsymbol{y}}{dr^2}\Delta x_i^2 + \cdots \\ &= (1 + A_i\Delta x_i + \frac{1}{2!}A_i^2\Delta x^2 + \cdots)\boldsymbol{y}(x_i) \\ &= \exp(A_i\Delta x)\boldsymbol{y}(x_i).\end{aligned} \tag{3.8}$$

Further define the matrix $T_i = \exp(A_i\Delta r_i)$, and the above equations can then be written as $\boldsymbol{y}_{i+1} = T_i\boldsymbol{y}_i$. We can then connect each individual grid value by applying the this relation repeatedly (from $i = 1$ to N), along with the boundary conditions from equation (3.7). We thus have:

$$\boldsymbol{y}_N = (T_1T_2\cdots T_N)\boldsymbol{y}_1 = T\boldsymbol{y_1} \tag{3.9}$$

and

$$B_{in}\boldsymbol{y}_1 = B_{out}T\boldsymbol{y}_1 = 0. \tag{3.10}$$

For convenience we define a vector:

$$\boldsymbol{u} = \begin{pmatrix} \boldsymbol{y_1} \\ \vdots \\ \boldsymbol{y}_N \end{pmatrix} \tag{3.11}$$

and the above two equations (3.9) and (3.10) can then be summarized into:

$$\begin{bmatrix} B_{in} & & & & & \\ T_1 & -1 & & & & \\ & T_2 & -1 & & & \\ & & & \ddots & & \\ & & & & T_{N-1} & -1 \\ & & & & & B_{out} \end{bmatrix} \begin{pmatrix} \boldsymbol{y}_1 \\ \boldsymbol{y}_2 \\ \boldsymbol{y}_3 \\ \vdots \\ \boldsymbol{y}_{N-1} \\ \boldsymbol{y}_N \end{pmatrix} = S\boldsymbol{u} = 0. \tag{3.12}$$

For this homogeneous system of linear equations to have non-zero solutions of $\boldsymbol{u}$, it must

satisfy:

$$det(S) = 0. \tag{3.13}$$

Thus, the eigenvalues (oscillation frequencies) are the roots of the above equation. For each eigenvalue, we solve the corresponding eigenvector (eigenfunction) $\boldsymbol{u}$. This can be achieved by LU decomposition or Singular Value Decomposition of matrix S.

In the adiabatic case, the coefficient matrix A_i is given by Unno et al. (1989):

$$A_i = \begin{bmatrix} V_g - 3 & \frac{l(l+1)}{c_1\omega^2} - V_g & V_g & 0 \\ c_1\omega^2 - A^* & A_* - U + 1 & -A^* & 0 \\ 0 & 0 & 1 - U & 1 \\ UA^* & UV_g & l(l+1) - UV_g & -U \end{bmatrix} \tag{3.14}$$

where

$$\begin{aligned} V &= -\frac{d\ln p}{d\ln r} \\ A^* &= \frac{1}{\Gamma_1}\frac{d\ln p}{d\ln r} - \frac{d\ln \rho}{d\ln r} \\ U &= \frac{d\ln M_r}{d\ln r} \\ c_1 &= \frac{r^3}{R_*^3}\frac{M_*}{M_r} \\ V_g &= \frac{V}{\Gamma_1} = -\frac{1}{\Gamma_1}\frac{d\ln p}{d\ln r} = \frac{gr}{c^2} \\ \omega^2 &= \frac{\sigma^2}{GM/R^3} \text{ (dimensionless frequency)} \end{aligned} \tag{3.15}$$

The inner BC is:

$$B_{in} = \begin{bmatrix} c_1\omega^2 & -l & 0 & 0 \\ 0 & 0 & l & -1 \end{bmatrix} \tag{3.16}$$

The Dziembowski-type outer BC is

$$B_{out} = \begin{bmatrix} (a) & -1 & (b) & 0 \\ 0 & 0 & l+1 & 1 \end{bmatrix} \tag{3.17}$$

where

$$\begin{aligned} (a) &= 1 + \left[\frac{l(l+1)}{\omega^2} - 4 - \omega^2\right]\frac{1}{V} \\ (b) &= 1 + \left[\frac{l(l+1)}{\omega^2} - l - 1\right]\frac{1}{V}. \end{aligned} \tag{3.18}$$

In the limit that the surface pressure vanishes, $1/V \to 0$, and we have the the 'zero' outer BC

$$B_{out} = \begin{bmatrix} 1 & -1 & 1 & 0 \\ 0 & 0 & l+1 & 1 \end{bmatrix} \tag{3.19}$$

The derivation of these boundary conditions are detailed in Unno et al. (1989) and Townsend (1997), which involves some algebraic manipulation and physical intuition. Here, we use a general representation derived by Joshua Burkart based on matrix diagonalization. Utilizing the capability of symbolic computation of *Mathematica*, these derivations can be simplified.

Using the denotation $x = r/R$, the linear oscillation equations in eq. (3.4) are ,

$$x\frac{d\boldsymbol{y}}{dx} = A\boldsymbol{y}. \tag{3.20}$$

At the stellar center ($r \to 0$), $U \to 3$, $V \to 0$, and $A^* \to 0$. Then the equations become

$$x\frac{d\boldsymbol{y}}{dx} = A_{r\to 0}\boldsymbol{y} \tag{3.21}$$

where the constant matrix $A_{r\to 0}$ is

$$A_{r\to 0} = \begin{bmatrix} -3 & \frac{l(l+1)}{c_1\omega^2} & 0 & 0 \\ c_1\omega^2 & -2 & 0 & 0 \\ 0 & 0 & -2 & 1 \\ 0 & 0 & l(l+1) & -3 \end{bmatrix}. \tag{3.22}$$

We perform an eigendecomposition of $A_{r\to 0} = SDS^{-1}$, where $S = (\boldsymbol{\xi}_1, \boldsymbol{\xi}_2, \cdots, \boldsymbol{\xi}_n)$ is the eigenvector matrix and $D = (\lambda_1, \lambda_2, \cdots, \lambda_n)$ is the eigenvalue matrix which is diagonal. Then the equations at $x \to 0$ are,

$$\begin{aligned} x\boldsymbol{y}' &= SDS^{-1}\boldsymbol{y} \\ xS^{-1}\boldsymbol{y}' &= DS^{-1}\boldsymbol{y} \\ x\boldsymbol{z}' &= D\boldsymbol{z} \\ &(\text{define} \quad S^{-1}\boldsymbol{y} = \boldsymbol{z}) \end{aligned} \tag{3.23}$$

Note that $\boldsymbol{y}'$ denotes $d\boldsymbol{y}/dx$. The solution for each eigenvalue λ_i is then

$$z_i = C_i x^{\lambda_i}. \tag{3.24}$$

However, we need to reject certain λ on physical grounds, and the corresponding undetermined constant C_i then needs to be zero since x^{λ_i} diverges. If one of these is λ_m, then $z_m = C_m x^{\lambda_m} = 0x^{\lambda_m} = 0$ and this yields the boundary condition

$$S^{-1}_{mn} y_n = 0. \tag{3.25}$$

For the matrix $A_{x\to 0}$, a *Mathematica* symbolic calculation yields:

$$\begin{aligned} &\text{Eigenvalues}[\{-3, l*(l+1)/a, 0, 0\}, \{a, -2, 0, 0\}, \{0, 0, -2, 1\}, \{0, 0, l*(l+1), -3\}] \\ &= \{l-2, l-2, -3-l, -3-l\} \end{aligned} \tag{3.26}$$

which is the matrix D in the above equation 3.23 and we have used the notation $a = c_1\omega^2$. We need to reject the eigenvalue $l-2$ since x^{l-2} diverges with increasing x. The corresponding inverse of eigenvector matrix of S is S^{-1}, given by,

$$\text{Inverse[Eigenvectors}[\{-3, l*(l+1)/a, 0, 0\}, \{a, -2, 0, 0\}, \{0, 0, -2, 1\}, \{0, 0, l*(l+1), -3\}]] \tag{3.27}$$

$$= \begin{pmatrix} 0 & \frac{s}{g} & 0 & -\frac{s}{g} \\ 0 & -\frac{(l+1)s}{ag} & 0 & \frac{\frac{1}{a}(1+\frac{l}{l+1})}{g} \\ \frac{\frac{1}{a}(2l+1)}{g} & 0 & \frac{\frac{1}{a}(2l+1)}{-g} & 0 \\ \frac{\frac{1}{(l+1)a}(2l+1)}{g} & 0 & \frac{\frac{1}{a}(2+\frac{1}{l})}{g} & 0 \end{pmatrix}^T \tag{3.28}$$

where $s = \frac{1}{l} + \frac{1}{l+1}$ and $g = \frac{2}{a} + \frac{1}{al} + \frac{1}{a(1+l)} + \frac{2l}{a(1+l)}$.

Thus one of the boundary condition from $S^{-1}\boldsymbol{y} = 0$ at $x \to 0$ is

$$\frac{s}{g}y_1 + (\frac{-\frac{1}{a}(1+\frac{l}{l+1})}{g})y_2 + 0y_3 + 0y_4 = 0 \tag{3.29}$$

which reduces to $y_1 = \frac{l}{a}y_2$. The other inner BC from the same equation is $ly_3 = y_4$. These are the same results as eq. 18.29 and 18.30 in Unno et al. (1989) and eq. 3.8 and 3.13 in Townsend (1997).

In the non-adiabatic case (Unno et al. 1989),

$$\boldsymbol{y} = \begin{pmatrix} y^{(1)} \\ y^{(2)} \\ y^{(3)} \\ y^{(4)} \\ y^{(5)} \\ y^{(6)} \end{pmatrix} \tag{3.30}$$

where

$$\begin{aligned} y^{(1)} &= \frac{\xi_r}{r} \\ y^{(2)} &= \frac{1}{gr}(\frac{p'}{\rho} + \Phi') \\ y^{(3)} &= \frac{1}{gr}\Phi' \\ y^{(4)} &= \frac{1}{g}\frac{d\Phi'}{dr} \\ y^{(5)} &= \frac{\delta S}{c_P} \\ y^{(6)} &= \frac{\delta L_R}{L_R}. \end{aligned} \tag{3.31}$$

where δS is entropy perturbation, and δL_R is the perturbation of radiative luminosity. The coefficient matrix A_i is:

$$A_i = \begin{bmatrix} V_g - 3 & \frac{l(l+1)}{c_1\omega^2} - V_g & V_g & 0 & \nu_t & 0 \\ c_1\omega^2 - A^* & A_* - U + 1 & -A^* & 0 & \nu_t & 0 \\ 0 & 0 & 1 - U & 1 & 0 & 0 \\ UA^* & UV_g & l(l+1) - UV_g & -U & -U\nu_t & 0 \\ V(c) & V(d) & Vc_2 & V\nabla_{ad} & V\nabla(4 - \kappa_s) & -V\nabla \\ (e) & (f) & (g) & 0 & (h) & -\frac{d\ln L_R}{d\ln r} \end{bmatrix} \tag{3.32}$$

The inner BC is

$$B_{in} = \begin{bmatrix} c_1\omega^2 & -l & 0 & 0 & 0 & 0 \\ 0 & 0 & l & -1 & 0 & 0 \\ 0 & 0 & 0 & 0 & 1 & 0 \end{bmatrix}. \tag{3.33}$$

The outer BC is

$$B_{out} = \begin{bmatrix} (a) & -1 & (b) & 0 & 0 & 0 \\ 0 & 0 & l+1 & 1 & 0 & 0 \\ 2 - 4\nabla_{ad}V & 4\nabla_{ad}V & -4\nabla_{ad}V & 0 & 4 & -1 \end{bmatrix}, \tag{3.34}$$

where (a) and (b) are given in eq. (3.18) and others are

$$
\begin{aligned}
(c) &= \left[\nabla_{ad}(U - c_1\omega^2) - 4(\nabla_{ad} - \nabla) + c_{kap}\right] \\
(d) &= \left[\frac{l(l+1)}{c_1\omega^2}(\nabla_{ad} - \nabla) - c_{kap}\right] \\
(e) &= \left[l(l+1)\frac{\nabla_{ad} - \nabla}{\nabla} - \epsilon_{ad}c_3V\right] \\
(f) &= \left[\epsilon_{ad}c_3V + l(l+1)(-\frac{\nabla_{ad}}{\nabla} + \frac{c_3}{c_1\omega^2})\right] \\
(g) &= \left[l(l+1)\frac{\nabla_{ad}}{\nabla} - \epsilon_{ad}c_3V\right] \\
(h) &= \left[\epsilon_s c_3 - \frac{l(l+1)}{V\nabla} - i\omega c_4\right].
\end{aligned}
\tag{3.35}
$$

Please refer to Table 3.1 for the definitions of all variables.

3.1.2 Rotation with the Traditional Approximation

In the previous section, the oscillation equations are solved for each spherical degree l, and the oscillations are degenerate with respect to the azimuthal number m in the non-rotating case. The traditional approximation (TA), first applied in geophysics, can be used to study the effects of rotation to low frequency g-modes. This approximation is valid for g-modes for which $\omega \ll N$ and $\Omega_s \ll N$ (where ω is mode frequency in rotating frame, N is the Brunt-Väisälä frequency, and Ω_s is rotational frequency). With treatment of rotation in TA, the eigenfrequencies and eigenfunctions are now functions of spin parameter $\nu = 2\Omega_s/\omega$. With rotation, we can think of a g-mode with (l) in the non-rotating case becomes (l_j, m),

given by:

$$\begin{aligned} l_j &= |m| + 2(j-1), \text{ for even modes} \\ l_j &= |m| + 2j - 1, \quad \text{for odd modes} \\ (j &= 1, 2, 3, ..., \infty). \end{aligned} \tag{3.36}$$

The radial Lagrangian displacement and Eulerian pressure perturbation are given by:

$$\begin{aligned} \xi_r(\boldsymbol{r}) &= \xi_r(r) H_{l_j,m}(\theta) e^{im\phi} \\ p'(\boldsymbol{r}) &= p'(r) H_{l_j,m}(\theta) e^{im\phi} \end{aligned} \tag{3.37}$$

where $H_{l_j,m}(\theta)$ are Hough functions (Aerts et al. 2010; Townsend 2003). Note that we still have the separation of variables for r, θ, and ϕ. The eigenfrequencies and then the r dependent eigenfunctions ($\xi_r(r)$, $p'(r)$, etc.) are solved in the following. We consider the simplest case for adiabatic non-radial oscillations with the Cowling approximation, i.e., neglect of the variations in the gravitational potential. For each l_j, the oscillation equations in traditional approximation are

$$\begin{aligned} \frac{dy_1^j}{dx} &= (V_g - 3) y_1^j + (\frac{l_j(l_j+1)}{c_1\omega^2} - V_g) y_2^j \\ \frac{dy_2^j}{dx} &= (c_1\omega^2 - A^*) y_1^j + (1 - U + A^*) y_2^j. \end{aligned} \tag{3.38}$$

The inner BC is $c_1\omega^2 y_1^j - l_j y_2^j = 0$.

The outer BC is $y_1^j - y_2^j = 0$.

y_1 and y_2 are the same with those in eq. (3.31) but with $\Phi' = 0$. Comparing with eq.

(3.14), (3.16), and (3.19), we can see that the differential equations and boundary conditions are identical to the non-rotating case. Details of the derivation can be found in the PhD thesis of Townsend (1997). Note that there is a typo in his eq. 6.72 on page 120 which should read $c_1\omega^2(\boldsymbol{Z}_1)_j - l_j(\boldsymbol{Z}_2) = 0$. The equations for non-adiabatic case in TA are given by Townsend (2005a).

The only difference is that we need to replace l with the effective $l_j = \frac{\sqrt{1+4\lambda^m_{lj}}-1}{2}$, which is the root of equation $l_j(l_j+1) = \lambda^m_{lj}$, where $\lambda^m_{l_j}$ for each j is one of the eigenvalues of matrix $\boldsymbol{W}$. The elements of its inverse matrix $\boldsymbol{W^{-1}}$ are given in an explicit form (eq. 34.29 and eq. 34.30 in Unno et al. 1989). Note that the eigendecompositions have the properties: $\boldsymbol{W} = \boldsymbol{B\Lambda B^{-1}}$ and $\boldsymbol{W^{-1}} = \boldsymbol{B\Lambda^{-1}B^{-1}}$, where $\boldsymbol{\Lambda}$ is the diagonal matrix whose diagonal elements are the corresponding eigenvalues of $\boldsymbol{W}$ and $\boldsymbol{B}$ is the square matrix whose columns are the eigenvectors of $\boldsymbol{W}$. In practical calculations, we get the eigenvalues $1/\lambda^m_{l_j}$ and corresponding eigenvectors from $\boldsymbol{W^{-1}}$.

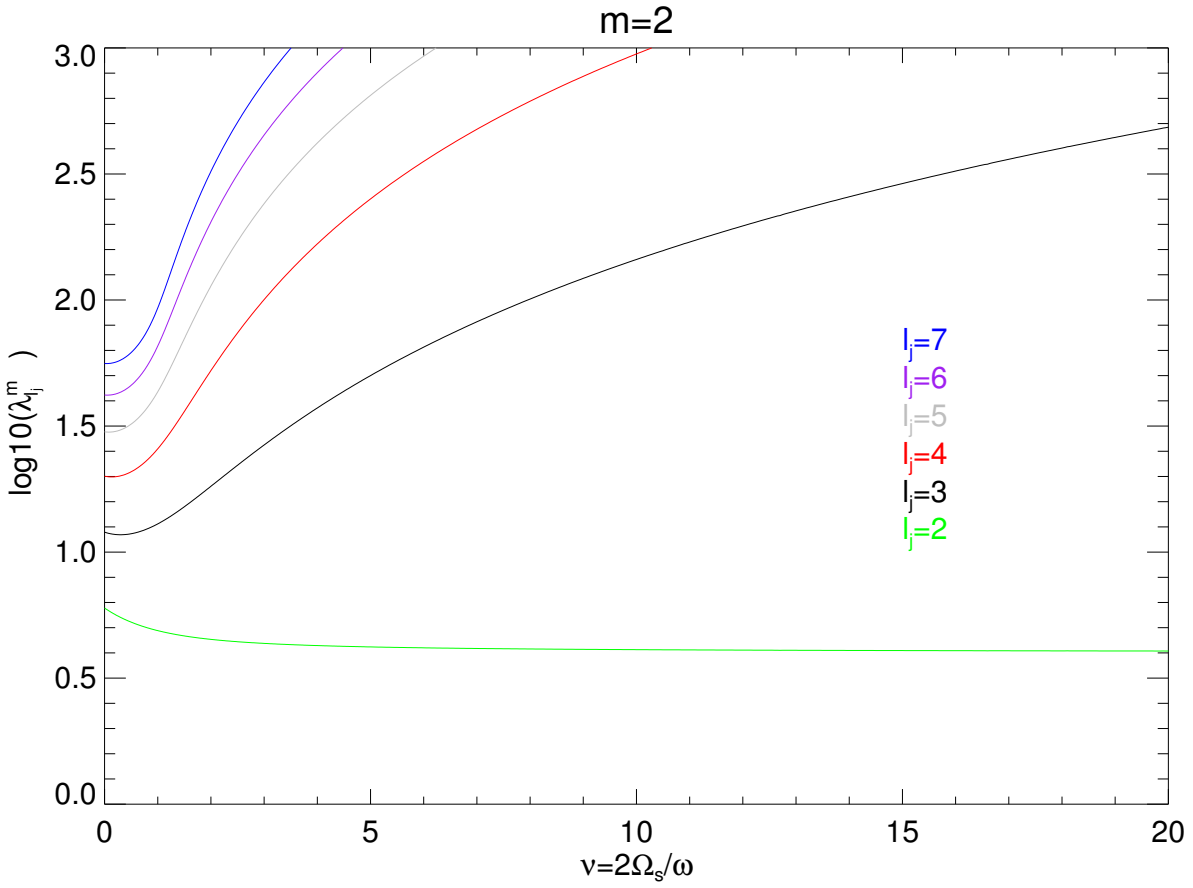

Figure 3.1 The eigenvalues λ_{lj}^m for $m = 2$ g-modes. The lines from top to bottom represent the eigenvalues for $l_j = 7$ to $l_j = 2$ modes.

In Figure 3.1, we show the variations of eigenvalues λ_{lj}^m for $m = 2$ modes as ν increases. In the oscillation code GYRE (Townsend & Teitler 2013), the eigenvalues λ_{lj}^m are pre-calculated and tabulated in grids of ν. For a given rotational frequency, they are interpolated and the corresponding l_j^m is used for solving the oscillation equations. Note that l_j^m can be treated as a function of radial coordinate r, thus we can assign different rotational velocities for different r and analyze the effects of radial differential rotation.

The aforementioned θ-dependent Hough functions $H_{l_j,m}(\theta)$ can be expressed as the sum of associated Legendre polynomials,

$$H_{l_j,m}(\theta) = \sum_{j=1}^{\infty} \gamma_{l_j}^m(\nu) \tilde{P}_{l_j}^m(\cos\theta) \tag{3.39}$$

The expansion coefficients $\gamma_{l_j}^m(\nu)$ for $(j = 1, 2, 3, ...)$ form the eigenvector of $\boldsymbol{W}$ with respect to index j (the jth column of matrix $\boldsymbol{B}$), and $\tilde{P}_{l_j}^m(\cos\theta)$ is the normalized associated Legendre function given by

$$\tilde{P}_{l_j}^m(\cos\theta) = \sqrt{\frac{2l+1}{4\pi}\frac{(l-m)!}{(l+m)!}} P_{l_j}^m(\cos\theta). \tag{3.40}$$

Note that the spherical harmonics $Y_l^m(\theta,\phi) = \tilde{P}_l^m(\cos\theta)e^{im\phi}$. In the zero-rotation limit, for $j = 1, 2, 3, ...$, $\gamma_{l_j}^m(\nu \to 0) = (1, 0, 0, ...)$ so that $H_{l_j,m}(\theta)e^{im\phi}$ becomes $Y_l^m(\theta,\phi)$.

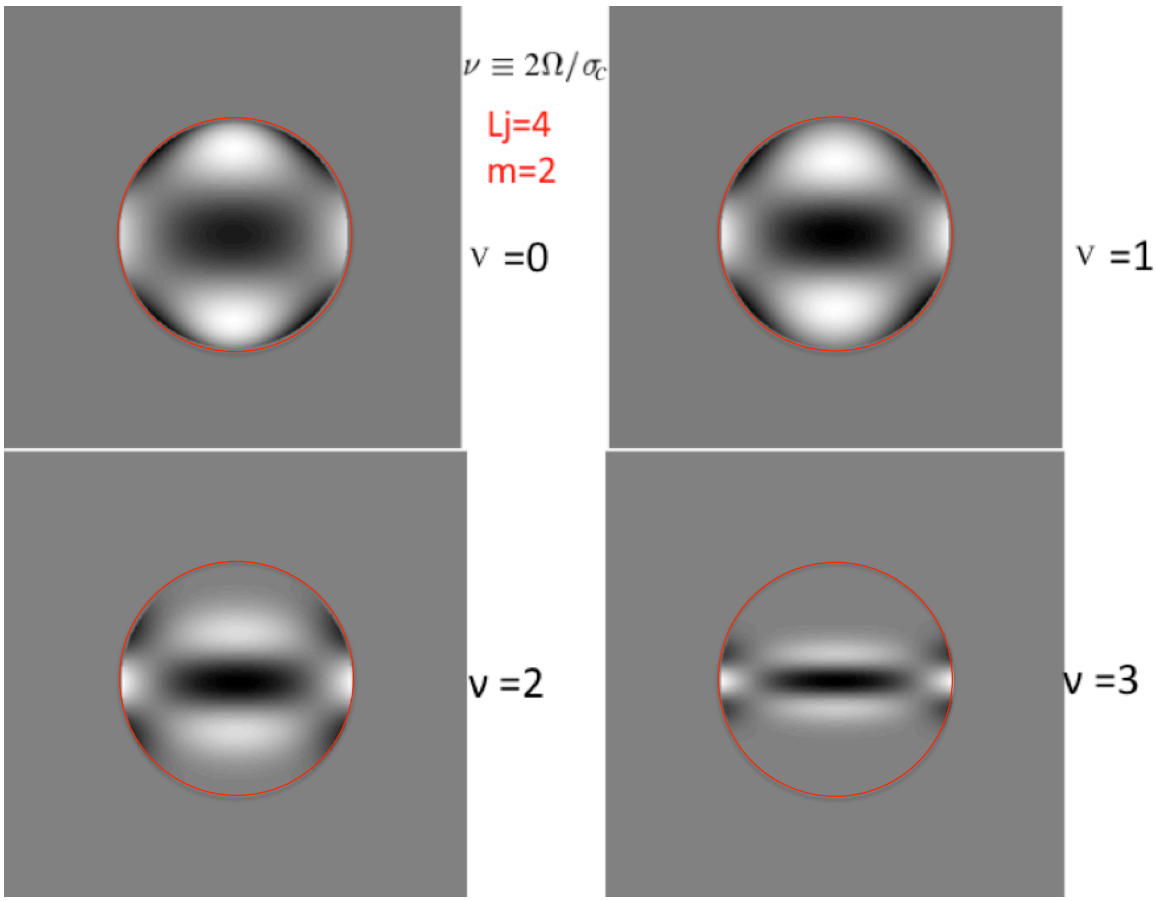

Figure 3.2 Representation of $H_{l_j,m}(\theta)e^{im\phi}$ on the stellar surface of a $(l_j = 4, m = 2)$ mode. Inclination angle of the star is 90 degrees (edge-on view). As the rotational frequency Ω increases, the mode is compressed to the equator.

The angular dependence of $\xi_r(\boldsymbol{r})$ is expressed as $H(\theta)e^{im\phi}$ which is associated with the expansion matrix $\boldsymbol{B}$ (coefficients $\gamma_{l_j}^m$). In Figure 3.2, we present these angular functions for an $l_j = 4, m = 2$ mode with different values of spin parameter ν on a sphere. The mode-compression effect of rotation can be clearly seen that localizes the amplitude to the vicinity of the equator.

The expansion coefficients $\gamma_{l_j}^m$ of Hough function $H(\theta)$ for a $(l = 2, m = 2)$ mode are shown in Figure 3.3, which are calculated with the *astro_hough* subroutine of GYRE. In the zero-rotation limit ($\nu = 0$), the base coefficient $\gamma_{l_j=2}^{m=2} = 1$ and all other coefficients $\gamma_{l_j=4}^{m=2}, \gamma_{l_j=6}^{m=2}, ...$ are zero. This is just a non-rotating $(l = 2, m = 2)$ mode. As rotational frequency increases, the amplitude of base coefficient $\gamma_{l_j=2}^{m=2}$ decreases, and other higher j coefficients begin to gain importance. This illustrates the effect of rotation: high $l_j = 4, 6, 8, ...$ modes begin to couple with the base $l_j = 2$ mode.

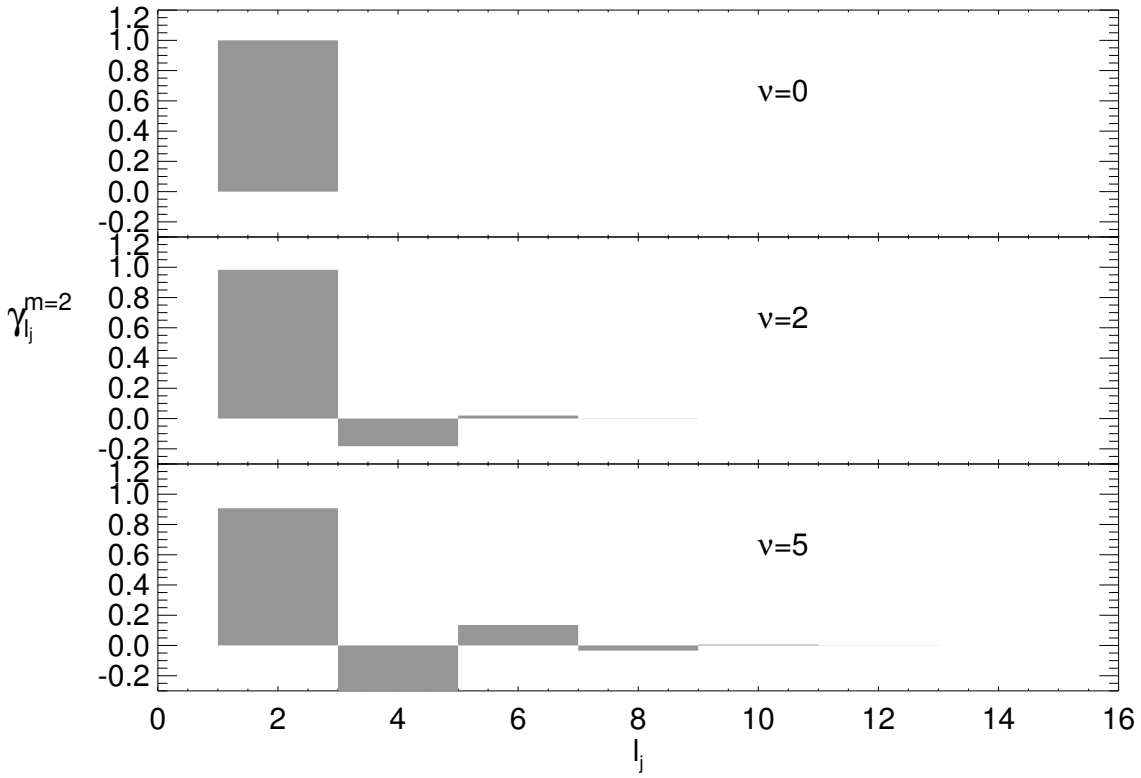

Figure 3.3 The expansion coefficients $\gamma_{l_j}^m$ of the Hough function $H(\theta)$ for a $(l = 2, m = 2)$ mode for three spin parameters $\nu = 0, 2, 5$ (from top to bottom, respectively).

The horizontal and toroidal displacements $\xi_h(\boldsymbol{r})$, $\xi_t(\boldsymbol{r})$ need extra calculations, and their associated expansion matrices $\boldsymbol{Q}$ and $\boldsymbol{R}$ are detailed in Townsend (1997, eq. $6.80 - 6.83$). Except for the rotationally-modified g-modes mentioned above, there are also Rossby modes (r-modes) that do not have non-rotating counterparts and only m (instead of l, m) can be assigned to these modes. The limitations of the traditional approximation are described in Gerkema et al. (2008) in a geophysical and astrophysical prospective.

3.2 Tidally Forced Oscillations

3.2.1 Directly Solving Tidal Oscillation Equations

Following Fuller & Lai (2012), we set up a spherical coordinate system with the origin on the center of the primary star of mass M_1. The companion (or secondary) is orbiting in the plane $\theta = \pi/2$, perpendicular to the rotation axis $\theta = 0$, with the temporally varying azimuthal angle $\phi = f(t)$.

The gravitational potential due to the secondary of mass M_2, experienced by the primary M_1, is given by:

$$U(\mathbf{r}_i, t) = \frac{-GM_2}{|\mathbf{D}(t) - \mathbf{r}|} \tag{3.41}$$

where $\mathbf{r}_i = (r, \theta, \phi_i = \phi + \Omega_s t)$ is a position vector relative to the center of the primary star, the azimuthal angle ϕ is measured in the rotating frame of the star, with the rotation frequency Ω_s and the rotation axis aligned with the orbital angular momentum. The azimuthal angle ϕ_i is in the inertial frame (observer's frame).

$\mathbf{D}(t) = [D(t), \pi/2, f(t)]$ specifies the position vector of the companion M_2, which is treated as a point mass. $D(t)$ is binary separation, $f(t)$ is true anomaly.

Following the treatment in Jackson (2006) (eq. 3.70) and with the help of the additional theorem of spherical harmonics, this gravitational potential generated by M_2 (also denoted by M') experienced by M_1 can be expanded as

$$U(\mathbf{r}_i, t) = -GM' \sum_{l=2}^{\infty} \sum_{m=-l}^{m=+l} W_{lm} \frac{r^l}{D(t)^{l+1}} e^{-imf(t)} Y_{lm}(\theta, \phi_i) \tag{3.42}$$

where $W_{lm} = \frac{4\pi}{2l+1} Y^*_{lm}(\frac{\pi}{2}, 0) = (-1)^{\frac{l+m}{2}} [\frac{4\pi}{2l+1}(l+m)!(l-m)!]^{\frac{1}{2}} [2^l (\frac{l+m}{2})!(\frac{l-m}{2})!]^{-1}$. For $l = 2$,

$W_{20} = -\sqrt{\pi/5}$ and $W_{2\pm2} = \sqrt{3\pi/10}$.

The true anomaly $f(t)$ represents the temporal dependence of an eccentric orbit with orbital frequency $\Omega_{orb} = 2\pi/P_{orb}$, and it can be decomposed as the sum of infinite number ($k = -\infty, ..., +\infty$) of time-invariant circular orbits each with the frequency of an orbital harmonic $k\Omega_{orb}$. The Fourier decomposition (Burkart et al. 2012) is:

$$\left(\frac{a}{D(t)}\right)^{l+1} e^{-imf(t)} = \sum_{k=-\infty}^{+\infty} X_{lm}^{k} e^{-ik\Omega_{orb}t} \tag{3.43}$$

or equivalently,

$$\left(\frac{D_{peri}}{D(t)}\right)^{l+1} \exp[-imf(t)] = \sum_{k=-\infty}^{+\infty} X_{lm}^{k}(1-e)^{l+1} \exp(-ik\Omega_{orb}t). \tag{3.44}$$

Note that $D_{peri} = a(1-e)$ is the distance at periastron and e is the orbital eccentricity. We use $e^{\cdots}$ or $\exp(\cdots)$ for exponential function and it should not be confused with the orbital eccentricity e. The Hansen coefficients $X_{lm}^{k}(e)$ are functions of e and (l, m, k), and they satisfy:

$$\sum_{k=-\infty}^{+\infty} X_{lm}^{k}(1-e)^{l+1} = 1 \tag{3.45}$$

They can be calculated numerically as the following integral of the eccentric anomaly E (Burkart et al. 2012):

$$X_{lm}^{k} = \frac{1}{\pi}\int_{0}^{\pi} (1 - e\cos E)^{-l} \cos\left[k(E - e\sin E) - 2m \ \arctan\left(\sqrt{\frac{1+e}{1-e}}\tan(E/2)\right)\right] \ dE. \tag{3.46}$$

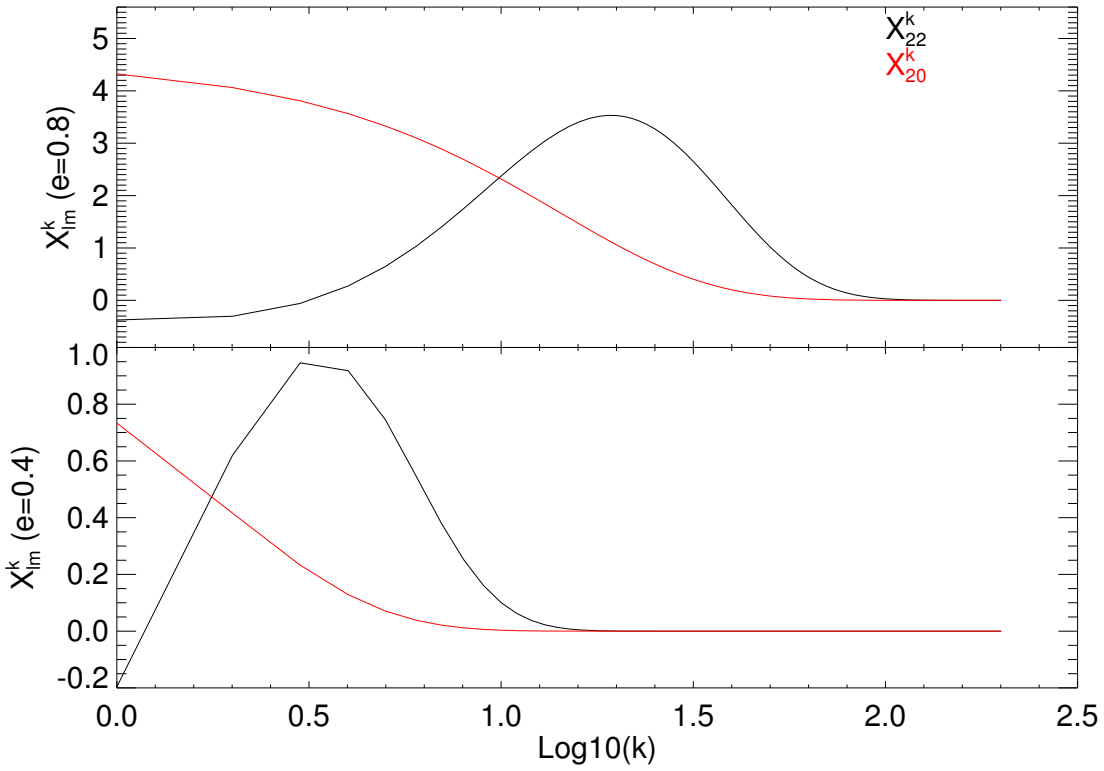

Figure 3.4 The Hansen coefficients X^k_{lm} for $e = 0.8$ and $e = 0.4$. The black and red lines correspond to $(l = 2, m = 2)$ and $(l = 2, m = 0)$, respectively.

The coefficients $X^k_{2m}(e)$ of $m = 0$ and $m = 2$ are shown in Figure 3.4 for two eccentricities $e = 0.4$ and $e = 0.8$. Note the Hansen coefficients are generally larger at higher k for higher eccentricity. More examples can be found in Figure 3 of Willems (2003).

Inserting eq. (3.43) into eq. (3.42), we can find that the tidal potential $U(\mathbf{r}_i, t)$ can be written as the sum of terms with respect to (l, m, k), where (l, m) corresponds to spatial decomposition and k is the index of temporal decomposition. By using the decomposition

of tidal force and following the treatment of Valsecchi et al. (2013), for each set of (l, m, k), the forced oscillation equations are just the free oscillation equations (their eq. $1-5$, or our equations 3.31, 3.32, 3.33, 3.34) with an extra gravitational potential term ($\epsilon_T W$) added to the momentum equation (their eq. 2). If we group the perturbation of the stars gravitational potential (Φ') and the tide-generating potential ($\epsilon_T W$) into the total perturbation of the gravitational potential defined as $\Psi = \Phi' + \epsilon_T W$, then the inhomogenous forced oscillation equations can be reduced to the following homogenous equations in the same form of the original free oscillation equations $d\boldsymbol{y}/dx = A\boldsymbol{y}$.

In the adiabatic case, the dependent variable $\boldsymbol{y}$ is,

$$\boldsymbol{y} = \begin{pmatrix} y^{(1)} \\ y^{(2)} \\ y^{(3)} \\ y^{(4)} \\ y^{(7)} \\ y^{(8)} \end{pmatrix} \tag{3.47}$$

where

$$\begin{aligned} y^{(1)} &= \frac{\xi_r}{r} \\ y^{(2)} &= \frac{1}{gr}\left(\frac{p'}{\rho} + \Psi\right) \\ y^{(3)} &= \frac{1}{gr}\Psi \\ y^{(4)} &= \frac{1}{g}\frac{d\Psi}{dr} \\ y^{(7)} &= const. \\ y^{(8)} &= const. \end{aligned} \tag{3.48}$$

where $y^{(7)}$ and $y^{(8)}$ are two auxiliary constant dependent variables (added so that the bound-

ary conditions also become homogeneous). The coefficient matrix A_i at the ith grid point is,

$$A_i = \begin{bmatrix} V_g - 3 & \frac{l(l+1)}{c_1\omega^2} - V_g & V_g & 0 & 0 & 0 \\ c_1\omega^2 - A^* & A_* - U + 1 & -A^* & 0 & 0 & 0 \\ 0 & 0 & 1 - U & 1 & 0 & 0 \\ UA^* & UV_g & l(l+1) - UV_g & -U & 0 & 0 \\ 0 & 0 & 0 & 0 & 0 & 0 \\ 0 & 0 & 0 & 0 & 0 & 0 \end{bmatrix} \tag{3.49}$$

The inner BC is:

$$B_{in} = \begin{bmatrix} c_1\omega^2 & -l & 0 & 0 & 0 & 0 \\ 0 & 0 & l & -1 & 0 & 0 \\ 0 & 0 & 0 & 0 & 1 & -1 \end{bmatrix} \tag{3.50}$$

The outer BC (eq. 18, 53, 20 in Valsecchi et al. 2013) is:

$$B_{out} = \begin{bmatrix} (a) & -1 & (b) & 0 & 0 & 0 \\ \frac{4\pi\rho}{g} & 0 & l+1 & 1 & 0 & \frac{\varepsilon_T(2l+1)c_{lmk}}{g} \\ 0 & 0 & 0 & 0 & 1 & -1 \end{bmatrix} \tag{3.51}$$

where (a) and (b) are given in the last section (eq. 3.18). The dimensionless parameter ε_T is defined by $\varepsilon_T = (\frac{R_1}{a})^3(\frac{M_2}{M_1})$. ρ and g are dimensionless density and surface gravity, defined as $\rho_{cgs}/(M_1/R_1^3)$ and $g_{cgs}/(GM_1/R_1^2)$, respectively.

Following Willems (2000), c_{lmk} is defined as:

$$c_{lmk} = \frac{(l-|m|)!}{(l+|m|)!} P_l^{|m|}(0) \left(\frac{R_1}{a}\right)^{l-2} X_{lm}^k \tag{3.52}$$

where $P_l^{|m|}(0)$ is:

$$P_l^{|m|}(0) = \frac{2^{|m|}}{\sqrt{\pi}} \frac{\Gamma[(l+|m|+1)/2]}{\Gamma[(l-|m|+2)/2]} \cos[\frac{\pi}{2}(l+|m|)]. \tag{3.53}$$

Note that we use the notation in Burkart et al. (2012) the for Hansen coefficient X_{lm}^k, which is the same as Willems' $X_k^{-(l+1),-m}$.

In the non-adiabatic case, the dependent variable $\boldsymbol{y}$ is,

$$\boldsymbol{y} = \begin{pmatrix} y^{(1)} \\ y^{(2)} \\ y^{(3)} \\ y^{(4)} \\ y^{(5)} \\ y^{(6)} \\ y^{(7)} \\ y^{(8)} \end{pmatrix} \tag{3.54}$$

where

$$\begin{aligned} y^{(1)} &= \frac{\xi_r}{r} \\ y^{(2)} &= \frac{1}{gr}(\frac{p'}{\rho} + \Psi) \\ y^{(3)} &= \frac{1}{gr}\Psi \\ y^{(4)} &= \frac{1}{g}\frac{d\Psi}{dr} \\ y^{(5)} &= \frac{\delta S}{c_P} \\ y^{(6)} &= \frac{\delta L_R}{L_R} \\ y^{(7)} &= const. \\ y^{(8)} &= const. \end{aligned} \tag{3.55}$$

and the coefficient matrix A is

$$A_i = \begin{bmatrix} V_g - 3 & \frac{l(l+1)}{c_1\omega^2} - V_g & V_g & 0 & \nu_T & 0 & 0 & 0 \\ c_1\omega^2 - A^* & A^* - U + 1 & -A^* & 0 & \nu_T & 0 & 0 & 0 \\ 0 & 0 & 1 - U & 1 & 0 & 0 & 0 & 0 \\ UA^* & UV_g & l(l+1) - UV_g & -U & -U\nu_T & 0 & 0 & 0 \\ V(c) & V(d) & Vc_2 & V\nabla_{ad} & V\nabla(4 - \kappa_s) & -V\nabla & 0 & 0 \\ (e) & (f) & (g) & 0 & (h) & -\frac{d\ln L_R}{d\ln r} & 0 & 0 \\ 0 & 0 & 0 & 0 & 0 & 0 & 0 & 0 \\ 0 & 0 & 0 & 0 & 0 & 0 & 0 & 0 \end{bmatrix}. \tag{3.56}$$

The inner BCs matrix is:

$$B_{in} = \begin{bmatrix} c_1\omega^2 & -l & 0 & 0 & 0 & 0 & 0 & 0 \\ 0 & 0 & L & -1 & 0 & 0 & 0 & 0 \\ 0 & 0 & 0 & 0 & 1 & 0 & 0 & 0 \\ 0 & 0 & 0 & 0 & 0 & 0 & 1 & -1 \end{bmatrix} \tag{3.57}$$

The outer BCs matrix is:

$$B_{out} = \begin{bmatrix} (a) & -1 & (b) & 0 & 0 & 0 & 0 & 0 \\ \frac{4\pi\rho}{g} & 0 & l+1 & 1 & 0 & 0 & 0 & \frac{\varepsilon_T(2l+1)c_{lmk}}{g} \\ 2-4\nabla_{ad}V & 4\nabla_{ad}V & -4\nabla_{ad}V & 0 & 4 & -1 & 0 & 0 \\ 0 & 0 & 0 & 0 & 0 & 0 & 1 & -1 \end{bmatrix} \tag{3.58}$$

where (a),(b),(c),(d),(e),(f),(g),(h) are given in eq. (3.18) and eq. (3.35).

In the previous section, we see that the free oscillation equations finally reduce to a homogenous algebraic equation $S\boldsymbol{u} = 0$. The eigenfrequencies are the roots of $det(S) = 0$ and eigenfunctions are the non-zero solutions $\boldsymbol{u}$. For the tidally forced oscillation equations discussed above, the final form is also $S\boldsymbol{u} = 0$. The difference is that the eigenfrequencies are just driven frequencies and we naturally have $det(S) = 0$. Thus we only need to solve for the eigenfunctions on a grid of given driven frequencies.

Here we show the tidal eigenfunctions of a star with mass of $M_1 = 5M_\odot$ and radius of $R_1 = 2.62R_\odot$ in a binary system. The companion is treated as a point mass with $M_2 = 5M_\odot$. The orbit has an eccentricity $e = 0.4$ and orbital period P. This is the same example presented by Valsecchi et al. (2013). By solving the free oscillation equations, we find the star has a $n = 9$ g-mode with period of $P_{n_g=9} = 44448.89$ seconds. We vary the orbital period of the binary so that the tidal forcing frequency becomes comparable to this natural frequency. For $(l = 2, m = 0, k = 1)$, we solve the forced oscillation equations (3.48, 3.49, 3.50, 3.51) for the adiabatic eigenfunctions (y_1, y_2, y_3, y_4) with LU decomposition for 4 orbital

periods $P_1 = 44448.00$s, $P_2 = 44448.67$s, $P_3 = 44449.33$s, and $P_4 = 44450.00$s. These tidal eigenfunctions are shown in Figure 3.5, 3.6, 3.7, and 3.8. It can be seen that the mode amplitude sensitively depends on the detuning parameter, which is the difference between the driving frequency and natural frequency (or the driving period and the natural period). It is apparent that P_2 is closest to the natural period $P_{n_g=9} = 44448.89$ and thus has a very large amplitude. A smaller detuning parameter suggests a larger mode amplitude, especially at the stellar surface. The mode amplitudes (as a function of driving frequency) form a Lorentzian-like profile, with the peak at the natural frequency (Figure 5 in Valsecchi et al. 2013).

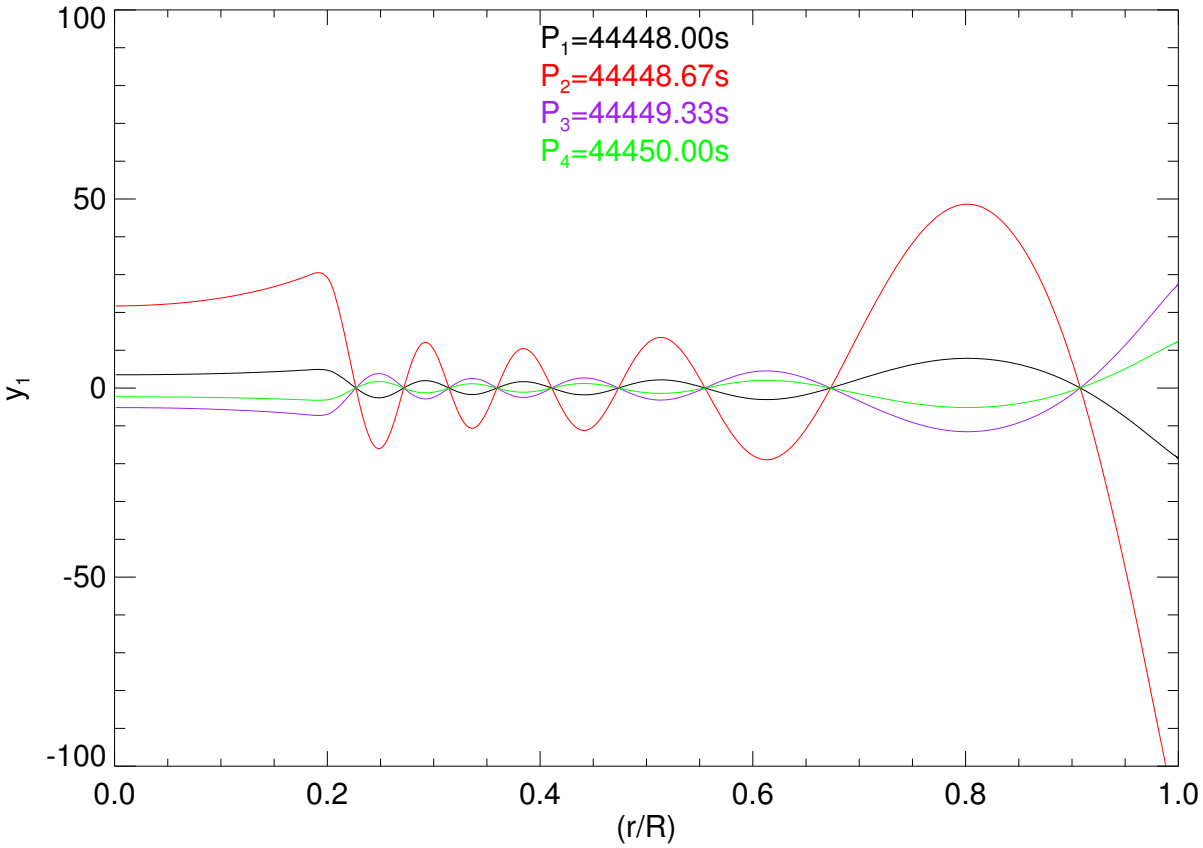

Figure 3.5 The adiabatic tidal eigenfunction $y_1 = \xi_r(r)/r$ for four driving frequencies which correspond to periods of P_1, P_2, P_3, P_4 labeled in the figure.

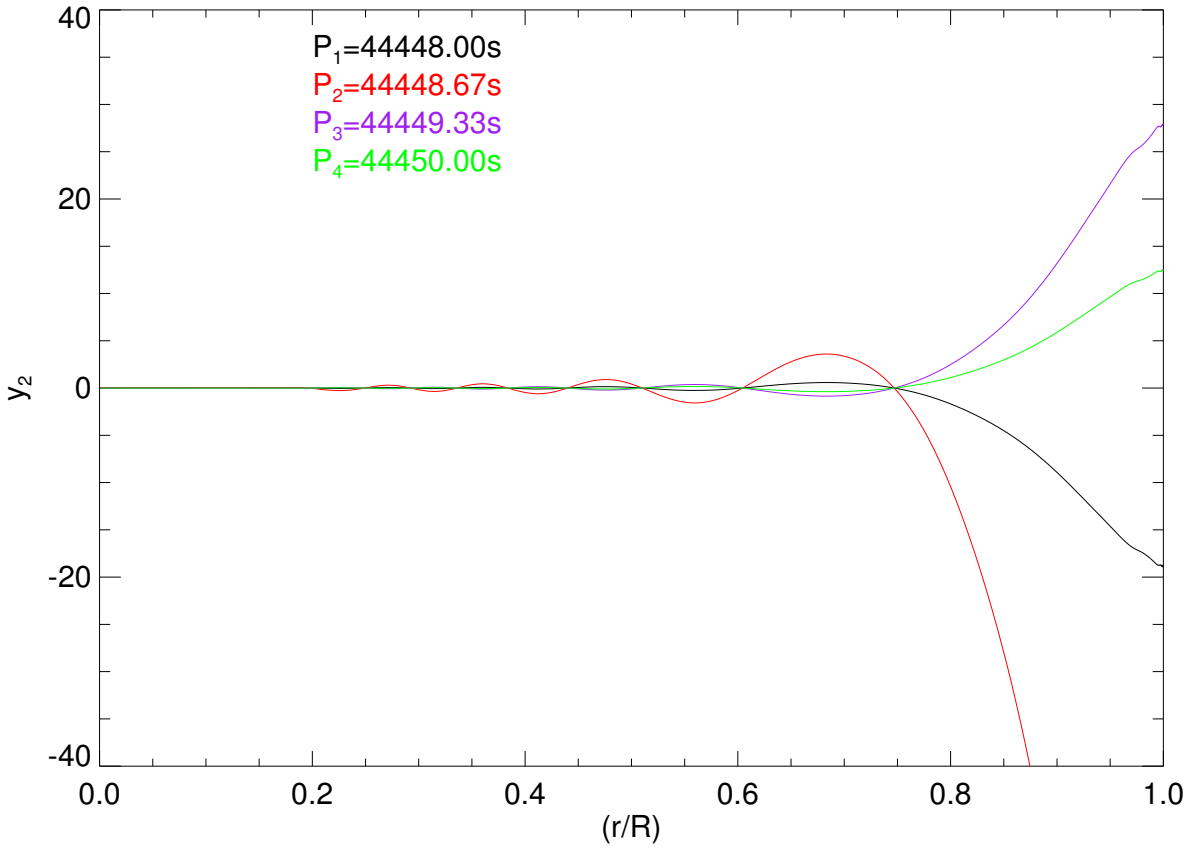

Figure 3.6 The adiabatic tidal eigenfunction $y_2 = \frac{1}{gr}(\frac{p'}{\rho} + \Phi')$ for four driving frequencies which correspond to the labeled periods of P_1, P_2, P_3, P_4.

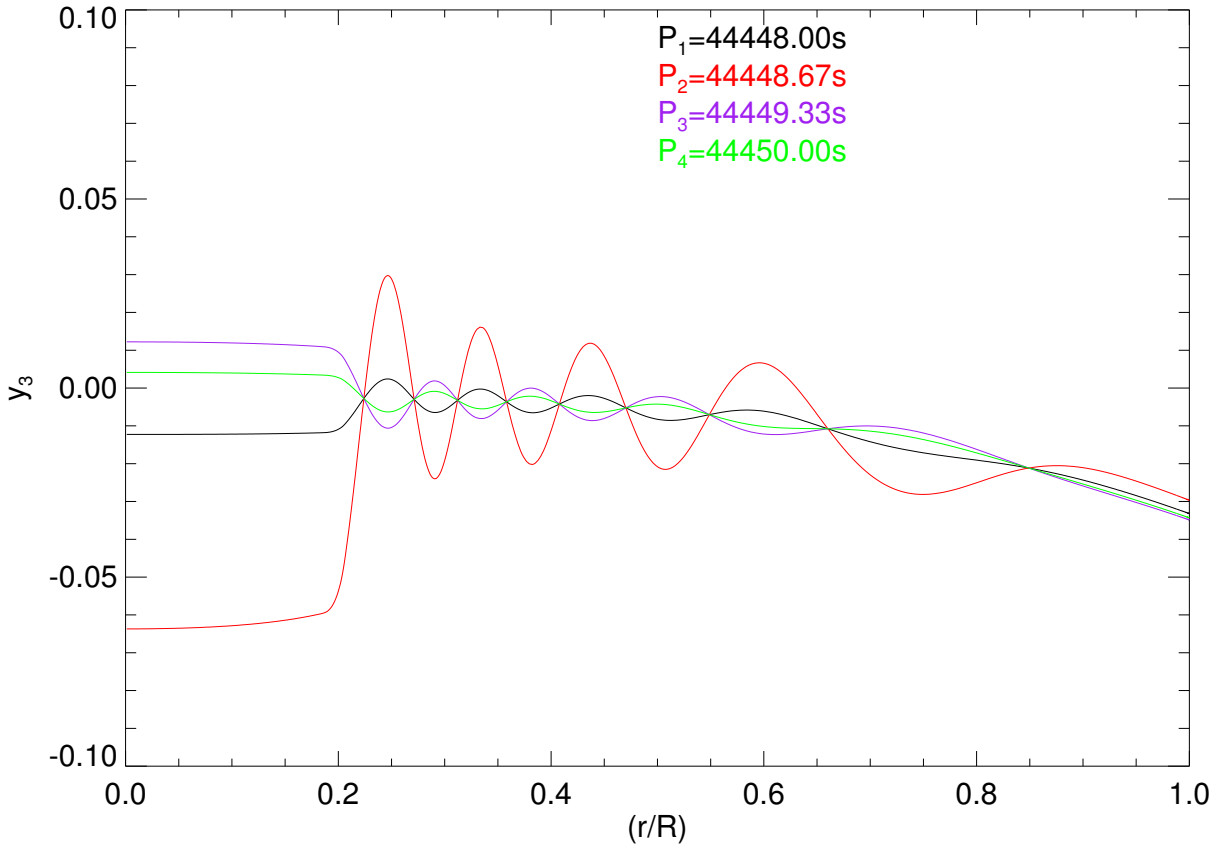

Figure 3.7 The adiabatic tidal eigenfunction $y_3 = \frac{1}{gr}\Phi'$ for four driving frequencies which correspond to the labeled periods P_1, P_2, P_3, P_4

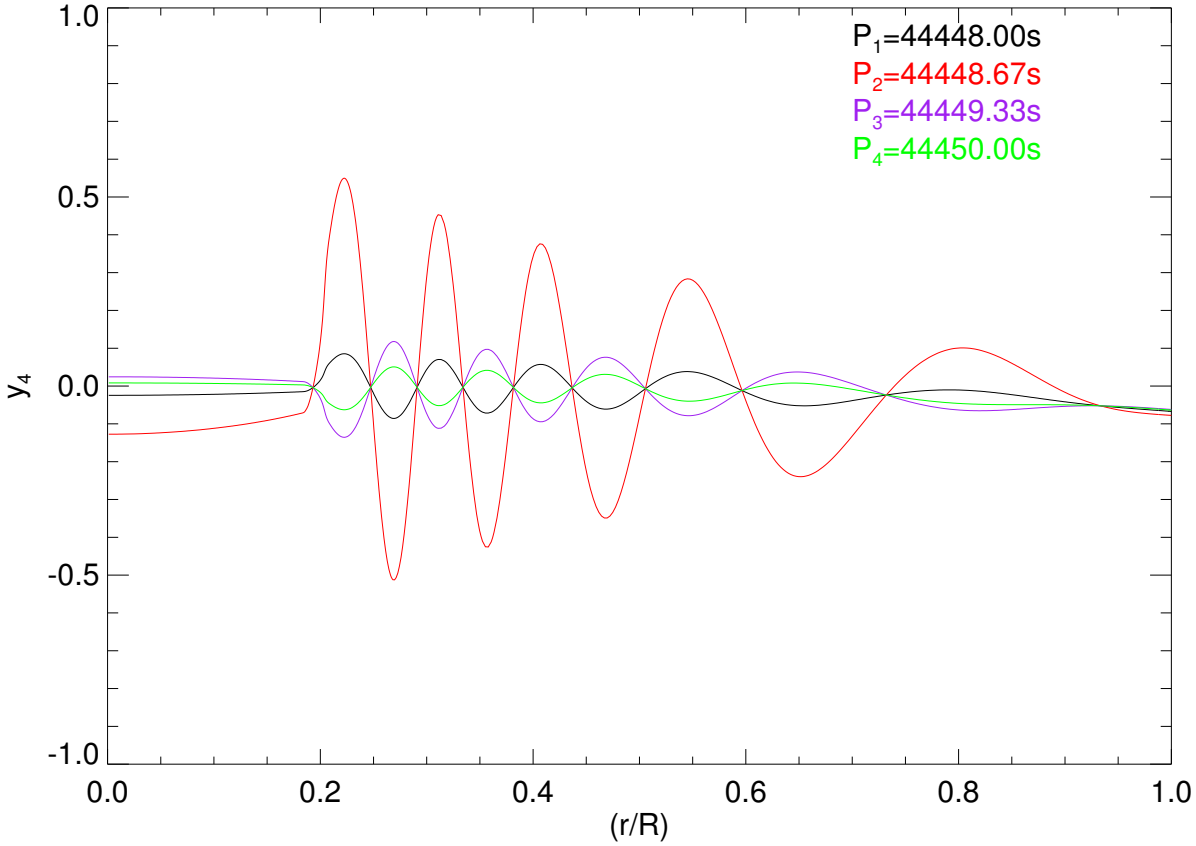

Figure 3.8 The adiabatic tidal eigenfunction $y_4 = \frac{1}{g}\frac{d\Phi'}{dr}$ for four driving frequencies which correspond to the labeled periods P_1, P_2, P_3, P_4.

No need to use ad. freqs as approximation in nad gyre_nad.fpp
call scan_search(ad_bp, omega, md) -> call scan_search(nad_bp, omega, md)
call prox_search(nad_bp, md)
Skip the root finding in gyre_nad_bvp.fpp
mode (change omega_root to forcing freq)
Change Ba and Bb in gyre_nad_bound.fpp
init (change to n_i = 4,n_o = 4)
innerbound (change to 4x8)
outer_bound_dziem (change to 4x8)
Change A in gyre_nad_jacobian.fpp
init (change n_e=8)
eval_logx (change to 8x8)

Figure 3.9 Changes made to subroutines of GYRE to calculate tidal eigenfunctions.

For the non-adiabatic calculations, we find that the previous method based on LU decomposition does not work. It is probably due to difficult numerical properties of matrix S. We resort to the GYRE oscillation code, which uses a better algorithm (Wright 1994) for solving the free oscillation equations $S\boldsymbol{u} = 0$. To extend GYRE's capability to solve the tidal oscillation equation, we need to change the matrix S, which means we need to change the coefficient matrix A_i at each layer and the two boundary conditions B_{in} and B_{out}. We also need to skip the root-finding step in solving $det(S) = 0$ as it is not needed for solving tidal oscillation frequencies (they are equal to the driving frequencies). The changes made to the subroutines in GYRE are briefly summarized in Figure 3.9.

In Figure 3.10, 3.11, 3.12, and 3.13, we show the non-adiabatic eigenfunctions for the same example above calculated with GYRE and the CAFein code (Valsecchi et al. 2013). Our eigenfunctions calculated with GYRE are generally in agreement with those from CAFein. The differences seem to be significant for $y_{3,R}$, $y_{4,R}$ and $y_{6,R}$. For all the eigenfunctions, there

seems to be a scaling factor difference, which is probably due to some scaling mistakes in evaluating the coefficients of differential equations. We are still in the process of analyzing this issue. Nevertheless, this work is very promising. The CAFein code is much slower than GYRE, and it usually needs $\sim$ 10 minutes to calculate eigenfunctions for one oscillation mode, whereas, GYRE can calculate eigenfunctions for tens of modes in several seconds.

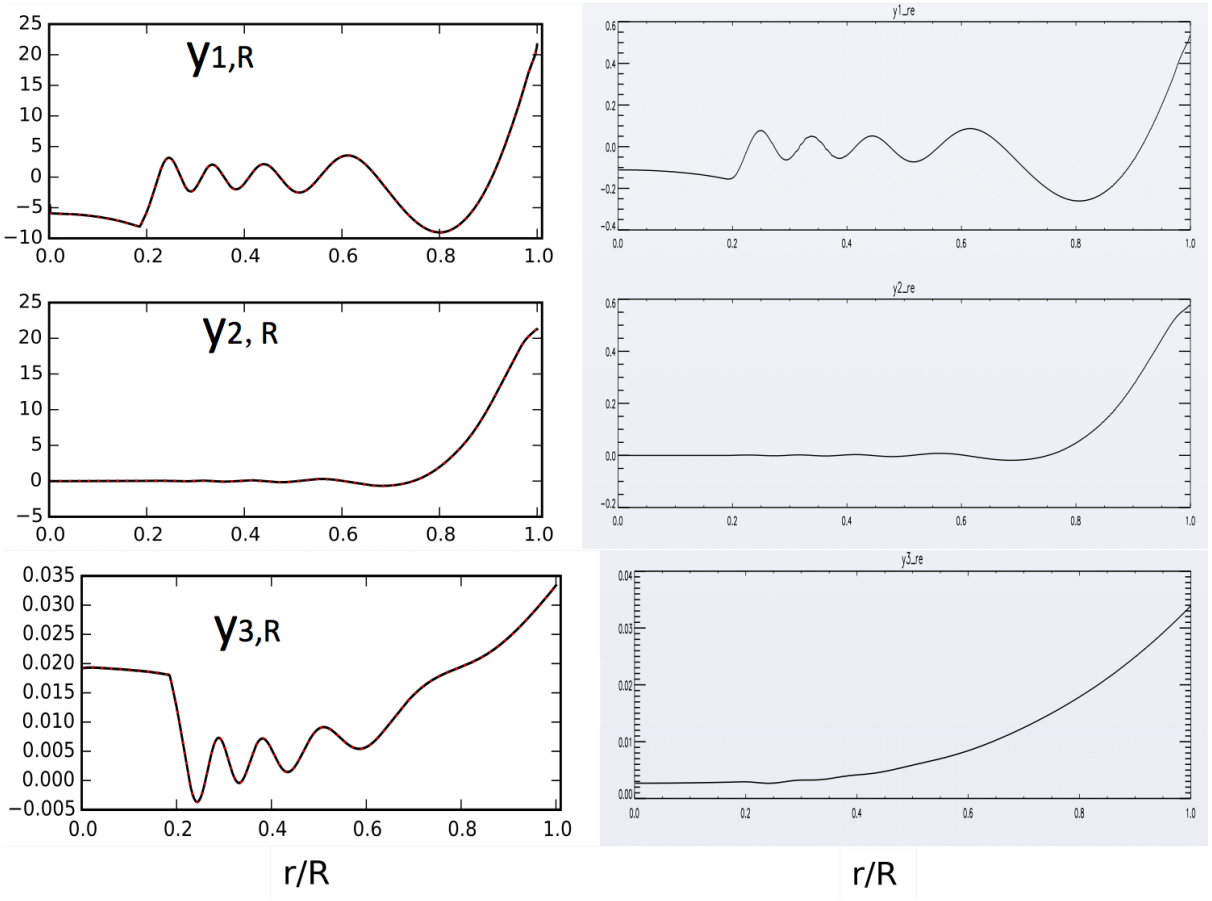

Figure 3.10 Real part of the non-adiabatic tidal eigenfunctions $y_1 = \frac{\xi_r}{r}, y_2 = \frac{1}{gr}(\frac{p'}{\rho} + \Psi), y_3 = \frac{1}{gr}\Psi$. The left and right panels are results from the CAFein and GYRE codes, respectively.

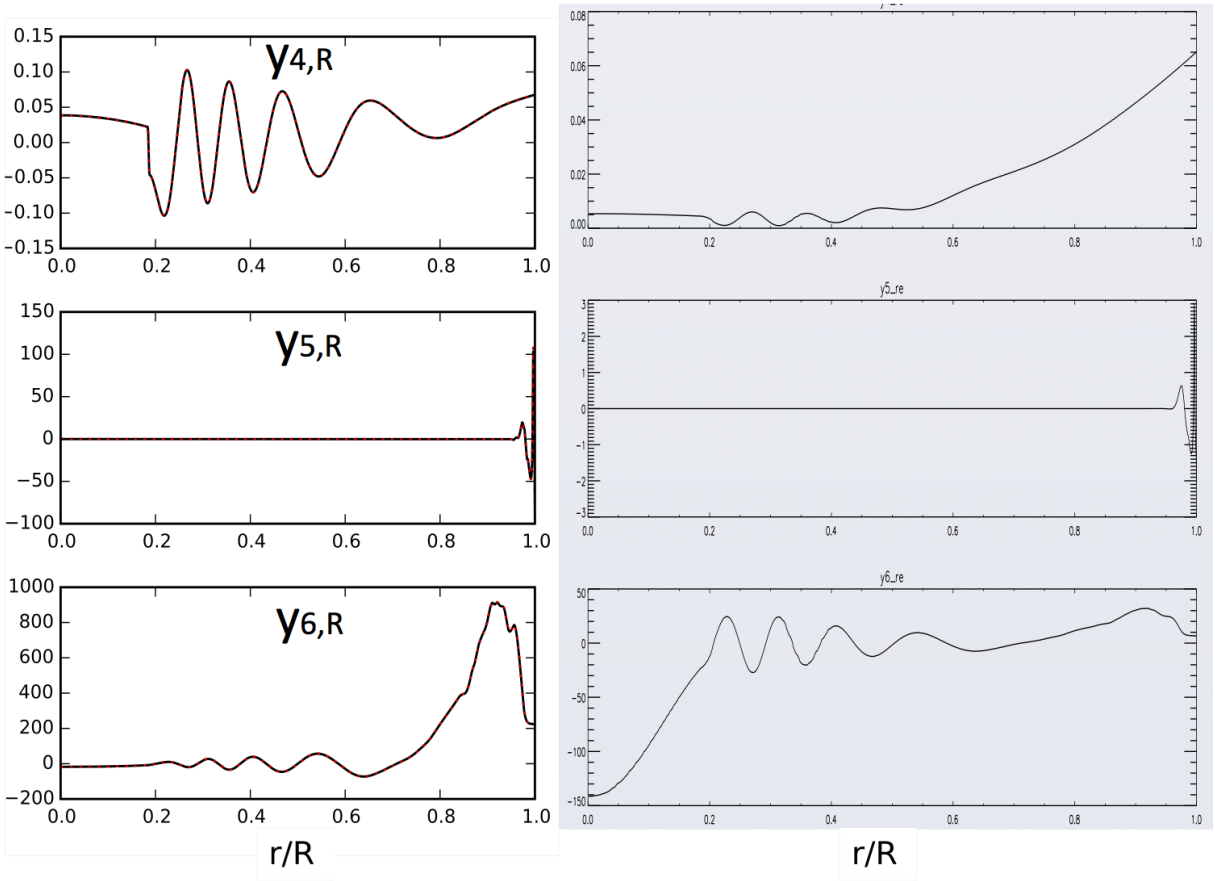

Figure 3.11 Real part of the non-adiabatic tidal eigenfunctions $y_4 = \frac{1}{g}\frac{d\Psi}{dr}, y_5 = \frac{\delta S}{c_P}, y_6 = \frac{\delta L_R}{L_R}$.The left and right panels are results from the CAFein and GYRE codes, respectively.

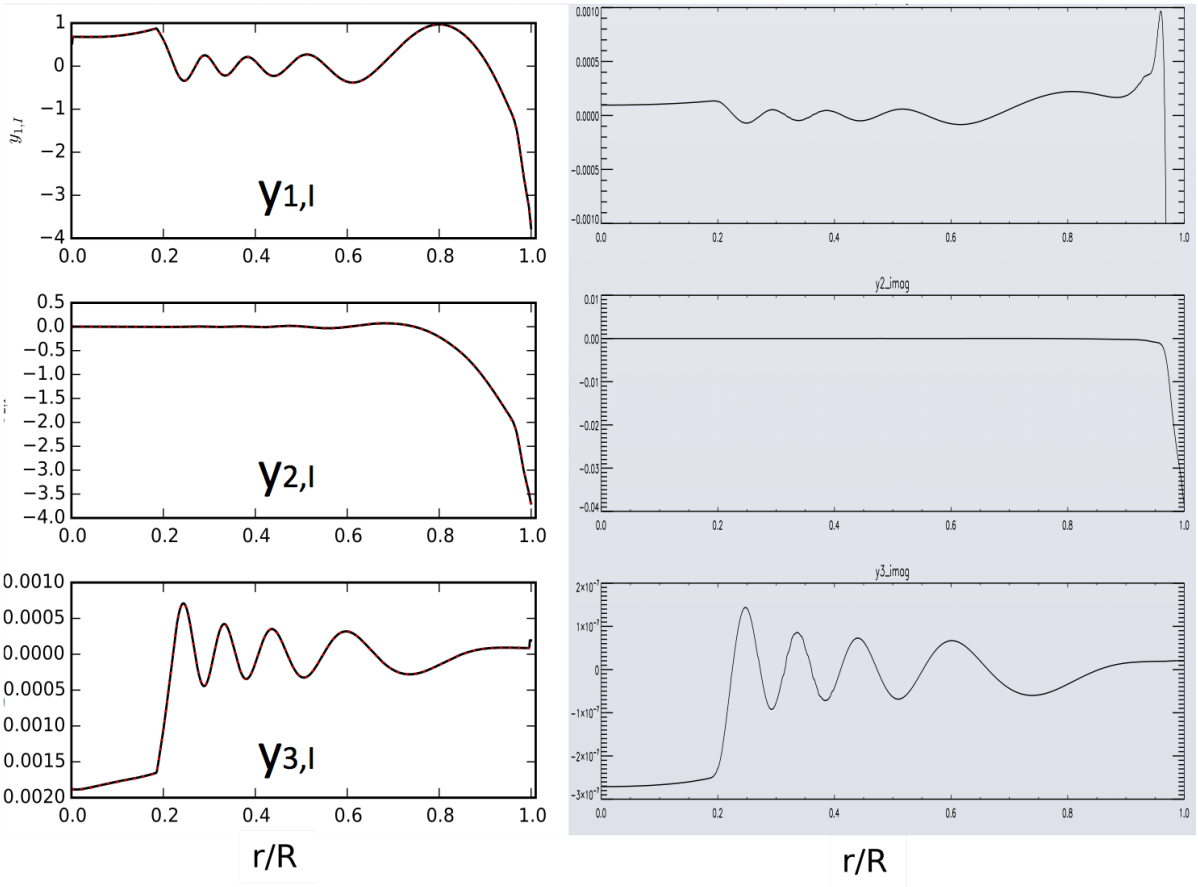

Figure 3.12 Imaginary part of the non-adiabatic tidal eigenfunctions $y_1 = \frac{\xi_r}{r}, y_2 = \frac{1}{gr}(\frac{p'}{\rho} + \Psi), y_3 = \frac{1}{gr}\Psi$. The left and right panels are results from the CAFein and GYRE codes, respectively.

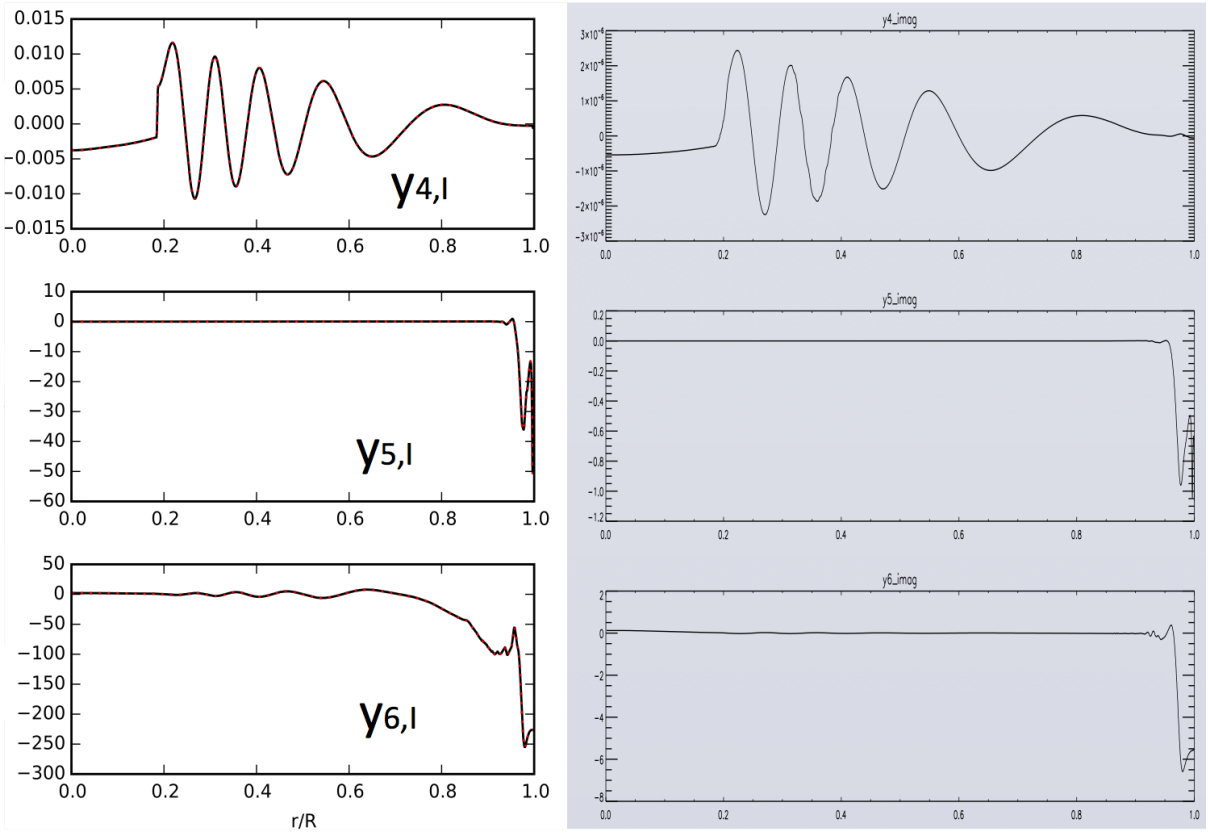

Figure 3.13 Imaginary part of the non-adiabatic tidal eigenfunctions $y_4 = \frac{1}{g}\frac{d\Psi}{dr}, y_5 = \frac{\delta S}{c_P}, y_6 = \frac{\delta L_R}{L_R}$. The left and right panels are results from the CAFein and GYRE codes, respectively.

The discussions above are all for cases without rotation. The forced oscillation equations with rotation in the Cowling and traditional approximation are given in the Appendix of Burkart et al. (2012). These inhomogenous equations can also be solved by the aforementioned algorithm, and the equations are reduced to the final form of $\boldsymbol{Ax} = \boldsymbol{b}$. Thus the solution is just the sum of general solution to the homogenous equation $\boldsymbol{Ax} = \boldsymbol{0}$ and the particular solution $\boldsymbol{A}^{-1}\boldsymbol{b}$. In practice, if we know the modes are tidally excited, we can just use the particular solution $\boldsymbol{A}^{-1}\boldsymbol{b}$ for comparison with observations. The matrix inversion $\boldsymbol{A}^{-1}$ can be derived with various decomposition algorithms, including the method used in GYRE (Wright 1994). It is interesting to note that the free oscillation equations when considering the lowest order non-linear term (the quadratic term) can also take the form of $\boldsymbol{Ax} = \boldsymbol{b}$ (eq. 6 in Kurtz et al. 2015). Thus the study of solving the forced oscillation equations can improve our understanding of the non-linear oscillation equations, which generate combination frequencies.

3.2.2 Expansions as Summation of Free Oscillations

Instead of directly solving the tidal oscillation equations, we can study the tidal responses by just using the eigenfunctions from the free oscillation equations.

Let us define the spherical harmonics as

$$Y_{lm}(\theta, \phi) = \sqrt{\frac{2l+1}{4\pi}\frac{(l-m)!}{(l+m)!}} P_l^m(\cos\theta) e^{im\phi}. \tag{3.59}$$

Using this definition, the normalization and orthogonality conditions are:

$$\int_0^{2\pi} d\phi \int_0^{\pi} \sin\theta d\theta \; Y^*_{l',m'}(\theta, \phi) Y_{l,m}(\theta, \phi) = \delta_{l',l}\delta_{m',m} \tag{3.60}$$

where $\delta_{i,j}$ represents the Kronecker delta function which is unity if $i = j$ or zero if $i \neq j$. The spherical harmonics also satisfy the following identity:

$$\int_0^{2\pi} d\phi \int_0^{\pi} \sin\theta d\theta \ [r\nabla_\perp Y^*_{l',m'}(\theta,\phi)][r\nabla_\perp Y_{l,m}(\theta,\phi)] = l(l+1)\delta_{l',l}\delta_{m',m}. \tag{3.61}$$

Note that the integral covers all solid angle $\int d\Omega = \int_0^{2\pi} d\phi \int_0^{\pi} \sin\theta d\theta$ and $\nabla_\perp$ is defined below. Spherical harmonics form an orthonormal basis of functions on the unit sphere. Any (square-integrable) function on the unit sphere can be expanded as a linear combination of spherical harmonics, and this is shown graphically in Appendix A.

In non-rotating case, the Lagrangian displacement $\boldsymbol{\xi}_\alpha(\mathbf{r})$ of a particular free normal mode with mode indices $\alpha = (n, l, m)$ can be written as the sum of radial and poloidal parts:

$$\boldsymbol{\xi}_\alpha(r,\theta,\phi) = \boldsymbol{\xi}_\alpha(\mathbf{r}) = \boldsymbol{\xi}_{nlm}(\mathbf{r}) = [\xi^R_{nl}(r)\mathbf{e_r} + \xi^S_{nl}(r) r\nabla_\perp] Y_{lm}(\theta,\phi) \tag{3.62}$$

where $\mathbf{e_r}$ is the unit vector in radial direction. It is convenient to write the operator ∇ as the sum of a radial and a horizontal part $\nabla = \nabla_r + \nabla_\perp$, where $\nabla_r = \mathbf{e_r}\frac{\partial}{\partial r}$ and $\nabla_\perp = (\mathbf{e}_\theta \frac{1}{r}\frac{\partial}{\partial\theta} + \mathbf{e}_\phi \frac{1}{r\sin\theta}\frac{\partial}{\partial\phi})$. We assume the temporal dependence is $\propto e^{-i\omega_\alpha t}$, so that the Lagrangian displacement is $\boldsymbol{\xi}_\alpha(\mathbf{r},t) = \boldsymbol{\xi}_\alpha(\mathbf{r}) e^{-i\omega_\alpha t}$. ω_α is the angular frequency of a mode with indices $\alpha = (n,l,m)$ in the co-rotating frame, and in inertial frame the mode frequency is $\sigma_\alpha = \omega_\alpha + m\Omega_s$, where Ω_s is the angular frequency of rotation. The Lagrangian displacement of a free oscillation mode $\boldsymbol{\xi}_\alpha(\boldsymbol{r},t)$ satisfies the equation of motion in the co-rotating frame:

$$\frac{\partial^2 \boldsymbol{\xi}_\alpha(\boldsymbol{r},t)}{\partial t^2} + 2\Omega_s \times \frac{\partial \boldsymbol{\xi}_\alpha(\boldsymbol{r},t)}{\partial t} + \boldsymbol{C}\boldsymbol{\xi}_\alpha(\boldsymbol{r},t) = 0, \tag{3.63}$$

where the operator $\boldsymbol{C}$ includes the perturbation of density and pressure and its expression

can be found at eq. 22, 23, 25, 26, 30 in Lynden-Bell & Ostriker (1967) and eq. 2.9, 2.11, 2.13, 2.14 in Schenk et al. (2002).

We take the derivatives with respect to time $\frac{\partial}{\partial t} = -i\omega_\alpha$, and the equation becomes:

$$-\omega_\alpha^2 \boldsymbol{\xi}_\alpha(\boldsymbol{r}) - 2i\omega_\alpha \boldsymbol{\Omega}_s \times \boldsymbol{\xi}_\alpha(\boldsymbol{r}) + \boldsymbol{C}\boldsymbol{\xi}_\alpha(\boldsymbol{r}) = 0. \tag{3.64}$$

Following Lai (1997), Lai & Wu (2006), and Fuller & Lai (2012), if we take the tidal force of the companion into account, the linear tidal response of the star M_1 (forced oscillation) is specified by the Lagrangian displacement $\boldsymbol{\xi}(\boldsymbol{r}, t)$, and it satisfies the equation of motion

$$\frac{\partial^2 \boldsymbol{\xi}(\boldsymbol{r}, t)}{\partial t} + 2\Omega_s \times \frac{\partial \boldsymbol{\xi}(\boldsymbol{r}, t)}{\partial t} + \boldsymbol{C}\boldsymbol{\xi}(\boldsymbol{r}, t) = -\nabla U. \tag{3.65}$$

Note that the tidal response $\boldsymbol{\xi}(\boldsymbol{r}, t)$ can be written as the sum of the free mode displacements $\boldsymbol{\xi}(\boldsymbol{r}, t) = \sum_\alpha c_\alpha(t)\boldsymbol{\xi}_\alpha(\boldsymbol{r})$, and each has an amplitude of $c_\alpha(t)$. To be more exact, the following is the phase space mode expansion from Schenk et al. (2002):

$$\begin{bmatrix} \boldsymbol{\xi}(\boldsymbol{r}, t) \\ \dfrac{\partial \boldsymbol{\xi}(\boldsymbol{r}, t)}{\partial t} \end{bmatrix} = \sum_\alpha c_\alpha(t) \begin{bmatrix} \boldsymbol{\xi_\alpha}(\boldsymbol{r}) \\ -i\omega_\alpha \boldsymbol{\xi_\alpha}(\boldsymbol{r}) \end{bmatrix}. \tag{3.66}$$

Thus we also have

$$\frac{\partial \boldsymbol{\xi}(\boldsymbol{r}, t)}{\partial t} = \sum_\alpha c'_\alpha(t)\boldsymbol{\xi}_\alpha(\boldsymbol{r}) = \sum_\alpha (-i\omega_\alpha c_\alpha(t))\boldsymbol{\xi}_\alpha(\boldsymbol{r}). \tag{3.67}$$

We define the inner product as $\langle \boldsymbol{A}, \boldsymbol{B} \rangle = \int d^3x \rho \boldsymbol{A}^* \cdot \boldsymbol{B} = \int_0^{2\pi} d\phi \int_0^\pi \sin\theta d\theta \int_0^R r^2 dr \rho(r) \boldsymbol{A}^* \cdot \boldsymbol{B}$.

Then the mode normalization becomes

$$
\begin{aligned}
&\langle \boldsymbol{\xi_\alpha}(\boldsymbol{r}), \boldsymbol{\xi_\alpha}(\boldsymbol{r})\rangle = \int d^3x\rho(r)\boldsymbol{\xi^*_\alpha}(\boldsymbol{r})\cdot\boldsymbol{\xi_\alpha}(\boldsymbol{r}) \\
&= \int d^3x\rho(r)[\xi^R_{nl}(r)\mathbf{e_r} + \xi^S_{nl}(r)r\nabla_\perp]Y^*_{lm}(\theta,\phi)\cdot[\xi^R_{nl}(r)\mathbf{e_r} + \xi^S_{nl}(r)r\nabla_\perp]Y_{lm}(\theta,\phi) \\
&= \int d^3x\rho(r)\left\{[\xi^R_{nl}(r)^2Y^*_{lm}Y_{lm}] + [\xi^S_{nl}(r)^2(r\nabla_\perp Y^*_{lm})(r\nabla_\perp Y_{lm})]\right\} \\
&= \int_0^R r^2dr\rho(r)\xi^S_{nl}(r)^2\int d\Omega Y^*_{lm}Y_{lm} + \int_0^R r^2dr\rho(r)\xi^R_{nl}(r)^2\int d\Omega(r\nabla_\perp Y^*_{lm})(r\nabla_\perp Y_{lm}) \\
&= \int_0^R r^2dr\rho(r)\xi^R_{nl}(r)^2\cdot 1 + \int_0^R r^2dr\rho(r)\xi^S_{nl}(r)^2\cdot l(l+1) \\
&= \int_0^R r^2dr\rho(r)\left\{\xi^R_{nl}(r)^2 + l(l+1)\xi^S_{nl}(r)^2\right\} \\
&= MR^2
\end{aligned}
\tag{3.68}
$$

That is, the mode has unit inertia in the natural units of the star M_1 (using M, R, $\sqrt{R^3/GM}$ as the unit for mass, length, and time, respectively) as in Press & Teukolsky (1977) and Valsecchi et al. (2013).

From eq. (3.63), (3.64), (3.65) and utilizing the property of inner product $\langle\boldsymbol{\xi}_\alpha, 2i\boldsymbol{\Omega}_s\times\boldsymbol{\xi}_{\alpha'}\rangle+(\omega_\alpha+\omega_{\alpha'})\langle\boldsymbol{\xi}_\alpha,\boldsymbol{\xi}_{\alpha'}\rangle = 0$, we can find that the mode amplitude $c_\alpha(t)$ satisfies the following equation (Schenk et al. 2002; Fuller & Lai 2012; Fuller et al. 2013):

$$
\begin{aligned}
\frac{dc_\alpha(t)}{dt} + (i\omega_\alpha+\gamma_\alpha)c_\alpha(t) &= \frac{i}{2\varepsilon_\alpha}\langle\boldsymbol{\xi}_\alpha(\boldsymbol{r}), -\nabla U\rangle \\
&= \frac{iGM'W_{lm}Q_\alpha}{2\varepsilon_\alpha D(t)^{l+1}}e^{im\Omega_s t - imf(t)}
\end{aligned}
\tag{3.69}
$$

where Q_α is defined below in eq. (3.73). We have written ω_α as $\omega_\alpha - i\gamma_\alpha$, where γ_α is the mode damping rate, and it is the (negative) imaginary part of mode frequencies in the non-

adiabatic calculation. ε_α is the unperturbed frequency for a non-rotating star, defined by $\varepsilon_\alpha \equiv \omega_\alpha + \langle \boldsymbol{\xi}_\alpha, i\boldsymbol{\Omega}_s \times \boldsymbol{\xi}_\alpha \rangle$. It is often convenient to adopt the perturbative approximation for rotation, which is valid when $\Omega_s < \omega_\alpha^0$. Then $\langle \boldsymbol{\xi}_\alpha, i\boldsymbol{\Omega}_s \times \boldsymbol{\xi}_\alpha \rangle = \int d^3x \rho \boldsymbol{\xi}_\alpha^* \cdot (i\boldsymbol{\Omega}_s \times \boldsymbol{\xi}_\alpha) = mC_{nl}\Omega_s$. C_{nl} is the Ledoux constant (Aerts et al. 2010, eq. 3.361). Assume the mode eigenfunctions are unchanged by stellar rotation, but the mode frequencies are modified as $\omega_\alpha = \omega_\alpha^0 - mC_{nl}\Omega_s$ in the co-rotating frame, and $\sigma_\alpha = \omega_\alpha^0 - m(1 - C_{nl})\Omega_s$ in the inertial frame. In this approximation, $\varepsilon = \omega_\alpha^0$, which is the mode frequency in the zero-rotation limit.

Using the Fourier decomposition of $e^{-imf(t)}$ in the last section (eq. 3.43) which relates the time varying distance $D(t)$ to the semi-major axis a, the above equation can be written as:

$$\frac{dc_\alpha(t)}{dt} + (i\omega_\alpha + \gamma_\alpha)c_\alpha(t) = \left[\frac{iGM'W_{lm}Q_\alpha}{2\varepsilon_\alpha a^{l+1}}\right] \sum_{k=-\infty}^{+\infty} X_{lm}^k e^{i(m\Omega_s - k\Omega_{orb})t}. \tag{3.70}$$

To solve for the mode amplitude $c_\alpha(t)$, just assume the time dependence:

$$c_\alpha(t) \propto e^{i(m\Omega_s - k\Omega_{orb})t} \tag{3.71}$$

since the solution has the same time dependence as the driving force on the right side of the equation. So the solution for the mode amplitude c_α is:

$$c_\alpha(t) = \left[\frac{GM'W_{lm}Q_\alpha}{2\varepsilon_\alpha a^{l+1}}\right] \sum_{k=-\infty}^{+\infty} \frac{X_{lm}^k e^{i(m\Omega_s - k\Omega_{orb})t}}{(\sigma_\alpha - k\Omega_{orb}) - i\gamma_\alpha}. \tag{3.72}$$

The key term here in the expression is the overlap integral:

$$\begin{aligned} Q_\alpha &= \left\langle \boldsymbol{\xi}_\alpha(\boldsymbol{r}), \nabla(r^l Y_{lm}) \right\rangle \\ &= \int d^3x \rho(r) \boldsymbol{\xi}_\alpha(\boldsymbol{r}) \cdot \nabla(r^l Y^*_{lm}) \end{aligned} \tag{3.73}$$

Note that :

$$\begin{aligned} &\boldsymbol{\xi}_\alpha(\boldsymbol{r}) \cdot \nabla(r^l Y^*_{lm}) \\ &= [\xi^R_{nl}(r)\boldsymbol{e_r} + \xi^S_{nl}(r) r\nabla_\perp] Y_{lm} \cdot [\nabla_r(r^l Y^*_{lm}) + \nabla_\perp(r^l Y^*_{lm})] \\ &= [\xi^R_{nl}(r)\boldsymbol{e_r} + \xi^S_{nl}(r) r\nabla_\perp] Y_{lm} \cdot [l r^{l-1} Y^*_{lm}\boldsymbol{e_r} + r^l \nabla_\perp(Y^*_{lm})] \\ &= l r^{l-1} \xi^R_{nl} Y_{lm} Y^*_{lm} + 0 + 0 + \xi^S_{nl}(r) r^{l-1} (r\nabla_\perp Y_{lm})(r\nabla_\perp Y^*_{lm}) \end{aligned} \tag{3.74}$$

so that:

$$\begin{aligned} Q_\alpha &= \int d^3x \rho(r) \boldsymbol{\xi}_\alpha(\boldsymbol{r}) \cdot \nabla(r Y^*_{lm}) \\ &= \int d^3x \rho(r) [l r^{l-1} \xi^R_{nl} Y_{lm} Y^*_{lm} + \xi^S_{nl}(r) r^{l-1} (r\nabla_\perp Y_{lm})(r\nabla_\perp Y^*_{lm})] \\ &= \int_0^R r^2 dr \rho(r) \xi^R_{nl}(r) l r^{l-1} \int d\Omega Y_{lm} Y^*_{lm} + \int_0^R r^2 dr \rho(r) \xi^R_{nl}(r) r^{l-1} \int d\Omega (r\nabla_\perp Y_{lm})(r\nabla_\perp Y^*_{lm}) \\ &= \int_0^R r^2 dr \rho(r) \xi^R_{nl}(r) l r^{l-1} + \int_0^R r^2 dr \rho(r) \xi^R_{nl}(r) r^{l-1} l(l+1) \\ &= \int_0^R r^2 dr \rho(r) l r^{l-1} [\xi^R_{nl}(r) + (l+1)\xi^S_{nl}(r)]. \end{aligned} \tag{3.75}$$

It can also be shown that there are equivalent expressions for Q_α (Burkart et al. 2012):

$$
\begin{aligned}
Q_\alpha &= \int_0^R r^2 dr \rho(r) l r^{l-1} [\xi_\alpha^R(r) + (l+1)\xi_\alpha^S(r)] \\
&= \int_0^R \delta\rho_\alpha r^{l+2} dr \\
&= -\frac{2l+1}{4\pi} \delta\phi_\alpha(R)/\omega_\alpha^2.
\end{aligned}
\tag{3.76}
$$

To show the units more explicitly, the expressions for the dimensionless Q_α are:

$$
\begin{aligned}
Q_\alpha &= \frac{1}{MR^l} \int_0^R dr \rho(r) l r^{l+1} [\xi_{nl}^R(r) + (l+1)\xi_{nl}^S(r)] \\
&= \frac{1}{MR^l} \int_0^R \delta\rho_\alpha r^{l+2} dr \\
&= -\frac{R}{GM} \frac{2l+1}{4\pi} \delta\phi_\alpha(R)/\omega_\alpha^2
\end{aligned}
\tag{3.77}
$$

where $\delta\rho_\alpha$ is the Lagrangian displacement of density of the mode with indices $\alpha = (n, l, m)$. $\delta\phi_\alpha(R)$ is the Eulerian perturbation of gravitational potential of the mode at the stellar surface ($r = R$) which needs to be calculated without the Cowling approximation. In practice, the third expression has better numerical performance especially for high order g-modes for which Q_α is very small and hard to calculate accurately from the first two expressions.

After we get the mode amplitude for each mode α, the total tidal response is just the sum of each mode $\boldsymbol{\xi}(\boldsymbol{r}, t) = \sum_\alpha c_\alpha(t)\boldsymbol{\xi}_\alpha(\boldsymbol{r})$. To compare directly with observations, we need to write the expression of tidal response in the inertial frame $\boldsymbol{r}_i = (r, \theta, \phi_i)$, so just use $\phi_i = \phi + m\Omega_s t$.

$$
\begin{aligned}
\boldsymbol{\xi}(\boldsymbol{r},t) &= \sum_{\alpha} c_{\alpha}(t)\boldsymbol{\xi}_{\alpha}(\boldsymbol{r}) \\
&= \sum_{\alpha}\left\{\left[\frac{GM'W_{lm}Q_{\alpha}}{2\varepsilon_{\alpha}a^{l+1}}\right]\sum_{k=-\infty}^{+\infty}\frac{X_{lm}^{k}e^{i(m\Omega_s-k\Omega_{orb})t}}{(\sigma_{\alpha}-k\Omega_{orb})-i\gamma_{\alpha}}\right\}\boldsymbol{\xi}_{\boldsymbol{\alpha}}(\boldsymbol{r}) \\
&= \sum_{\alpha}\left\{\left[\frac{GM'W_{lm}Q_{\alpha}}{2\varepsilon_{\alpha}a^{l+1}}\right]\sum_{k=-\infty}^{+\infty}\frac{X_{lm}^{k}e^{i(m\Omega_s-k\Omega_{orb})t}}{(\sigma_{\alpha}-k\Omega_{orb})-i\gamma_{\alpha}}\right\}\boldsymbol{\xi}_{\boldsymbol{\alpha}}(\boldsymbol{r_i})e^{-im\Omega_s t} \\
&= \sum_{\alpha}\left\{\left[\frac{GM'W_{lm}Q_{\alpha}}{2\varepsilon_{\alpha}a^{l+1}}\right]\sum_{k=-\infty}^{+\infty}\frac{X_{lm}^{k}e^{-ik\Omega_{orb}t}}{(\sigma_{\alpha}-k\Omega_{orb})-i\gamma_{\alpha}}\right\}\boldsymbol{\xi}_{\boldsymbol{\alpha}}(\boldsymbol{r_i}) \\
&= \sum_{\alpha}\sum_{k=-\infty}^{+\infty}B_{\alpha,k}\boldsymbol{\xi}_{\boldsymbol{\alpha}}(\boldsymbol{r_i}).
\end{aligned}
\tag{3.78}
$$

where $B_{\alpha,k}$ is the amplitude of each contribution and is equivalent to the A_{nlmk} discussed below.

It is convenient to write the expression for each orbital harmonic k by switching the order of the two summations:

$$
\begin{aligned}
&= \sum_{k=-\infty}^{+\infty}\sum_{\alpha}\left\{\left[\frac{GM'W_{lm}Q_{\alpha}}{2\varepsilon_{\alpha}a^{l+1}}\right]\frac{X_{lm}^{k}e^{-ik\Omega_{orb}t}}{(\sigma_{\alpha}-k\Omega_{orb})-i\gamma_{\alpha}}\right\}\boldsymbol{\xi}_{\boldsymbol{\alpha}}(\boldsymbol{r_i}) \\
&= \sum_{k=-\infty}^{-1}\sum_{\alpha}\left\{\left[\frac{GM'W_{lm}Q_{\alpha}}{2\varepsilon_{\alpha}a^{l+1}}\right]\frac{X_{lm}^{k}e^{-ik\Omega_{orb}t}}{(\sigma_{\alpha}-k\Omega_{orb})-i\gamma_{\alpha}}\right\}\boldsymbol{\xi}_{\boldsymbol{\alpha}}(\boldsymbol{r_i}) \\
&+ \sum_{k=1}^{+\infty}\sum_{\alpha}\left\{\left[\frac{GM'W_{lm}Q_{\alpha}}{2\varepsilon_{\alpha}a^{l+1}}\right]\frac{X_{lm}^{k}e^{-ik\Omega_{orb}t}}{(\sigma_{\alpha}-k\Omega_{orb})-i\gamma_{\alpha}}\right\}\boldsymbol{\xi}_{\boldsymbol{\alpha}}(\boldsymbol{r_i}) \\
&= \sum_{k=1}^{+\infty}\sum_{\alpha}\left\{\left[\frac{GM'W_{lm}Q_{\alpha}}{2\varepsilon_{\alpha}a^{l+1}}\right]\left[\frac{X_{lm}^{-k}e^{+ik\Omega_{orb}t}}{(\sigma_{\alpha}+k\Omega_{orb})-i\gamma_{\alpha}}+\frac{X_{lm}^{k}e^{-ik\Omega_{orb}t}}{(\sigma_{\alpha}-k\Omega_{orb})-i\gamma_{\alpha}}\right]\right\}\boldsymbol{\xi}_{\boldsymbol{\alpha}}(\boldsymbol{r_i}).
\end{aligned}
\tag{3.79}
$$

3.2.3 Flux variations of Tidally Forced Oscillations

We need to translate the displacement field on the stellar surface to a corresponding disk-averaged observed flux perturbation δJ in the observed passband. Here we present two methods from Dziembowski (1977) and from Buta & Smith (1979), respectively. Both treatments have approximations.

Method (1), the Dziembowski method:

Following Dziembowski (1977), Pfahl et al. (2008), and Burkart et al. (2012), if there is a radial displacement field ξ_r and a Lagrangian perturbation to the emitted flux ΔF on the stellar surface due to a mode α, then the fractional observed flux variation $\delta J/J$ to the first order is given by:

$$\begin{aligned}\frac{\delta J}{J} &= [(2b_l - c_l)\frac{\xi_{r,\alpha}(R)}{R} + \beta(T)b_l\frac{\Delta F_\alpha(R)}{F(R)}]Y_{lm}(\theta_0,\phi_0) \\ &= \left[(2b_l - c_l)\frac{\xi_r(R)}{R}\right]Y_{lm}(\theta_0,\phi_0) + \left[\beta(T)b_l\frac{\Delta F_\alpha(R)}{F(R)}\right]Y_{lm}(\theta_0,\phi_0) \\ &= (\frac{\delta J}{J})_G + (\frac{\delta J}{J})_T\end{aligned} \tag{3.80}$$

The subscripts G and T refer to flux variations due to geometry effects and temperature changes, respectively. In terms of magnitude variations, a small fractional flux variation yields

$$\delta\text{mag} = -\frac{2.5}{\ln 10}\frac{\delta J}{J} = -1.0857\frac{\delta J}{J}. \tag{3.81}$$

The bolometric Lagrangian flux perturbation $\Delta F/F$ can be computed from $\Delta F/F = \Delta L/L_r - 2\xi_r/r$, so that when evaluated at the surface $\Delta F(R)/F(R) = \Delta L(R)/L_r(R) -$

$2\xi_r(R)/R$. $\Delta L/L_r$ is relative radiative Lagrangian luminosity perturbation and ξ_r/r is relative Lagrangian radial displacement, and they are both the outputs of GYRE. The disk-integral factors are:

$$b_l = \int_0^1 \mu P_l(\mu) h(\mu) d\mu \tag{3.82}$$

and

$$c_l = \int_0^1 \left[2\mu^2 \frac{dP_l}{d\mu} - (\mu - \mu^3) \frac{d^2 P_l}{d\mu^2} \right] h(\mu) d\mu \tag{3.83}$$

where $h(\mu)$ is the limb darkening function, which is normalized as $\int_0^1 \mu h(\mu) d\mu = 1$. $P_l(\mu)$ is the Legendre polynomial. $\beta(T)$ is the correction factor for the observed passband (e.g., *Kepler*), so that the bandpass-corrected flux perturbation $(\Delta F/F)_{corrected} = \beta(T)(\Delta F/F)_{bol}$, and $(\Delta F/F)_{bol}$ is the bolometric Lagrangian flux perturbation from GYRE calculations.

This method is further developed on the basis of the original treatment by Dziembowski and described in series of papers (Cugier et al. 1994; Cugier & Daszyńska 2001; Stamford & Watson 1981; Watson 1988; Daszyńska-Daszkiewicz et al. (2002). The asteroseismic software *FAMIAS* (Zima 2008) used the expressions in Daszyńska-Daszkiewicz et al. (2002) for the mode identification from multicolor photometry. The calculation was extended to include rotation in the traditional approximation by Townsend (2003).

Method(2), the BS79 method:

Following Buta & Smith (1979), see also Fuller & Lai (2012), the total magnitude variation is the sum of variation due to temperature changes and due to geometric changes:

$$\Delta \text{mag} = (\Delta \text{mag})_T + (\Delta \text{mag})_G \tag{3.84}$$

The magnitude variation due to temperature change has the following expression assuming the pulsations are adiabatic and using the blackbody radiation approximation:

$$
\begin{aligned}
&(\Delta\text{mag})_T = -1.0857\varepsilon F_\lambda \gamma_l \; Y_{lm}(i_s, \phi_0) e^{i\sigma t} \\
&= -1.0857 \frac{\delta R}{R} \left[\frac{x e^x}{e^x - 1} \frac{\Gamma_2 - 1}{\Gamma_2} \left(\frac{l(l+1)}{\omega^2} - 4 - \omega^2 \right) \right] \gamma_l \sqrt{\frac{(2l+1)(l-m)!}{4\pi(l+m)!}} P_l^m(\cos i_s) e^{im\phi_0} e^{i\sigma t}
\end{aligned}
\tag{3.85}
$$

Note $\varepsilon = \frac{\delta R}{R}$ is the amplitude of fractional displacement, i_s is the orbital inclination, $\Gamma_2 \approx 5/3$ is adiabatic index and ω is dimensionless mode frequency given by $\omega = \omega_\alpha / \sqrt{GM/R^3}$. Note the term F_λ is related to the relative temperature perturbations, relative pressure perturbations, and relative radius perturbations as (Buta & Smith 1979) :

$$
\begin{aligned}
F_\lambda(l, \omega^2, T) &= \frac{x e^x}{e^x - 1} [F_T(l, \omega^2, T)] \\
&= \frac{x e^x}{e^x - 1} \left[\frac{\Gamma_2 - 1}{\Gamma_2} (F_p(l, \omega^2)) \right] \\
&= \frac{x e^x}{e^x - 1} \left[\frac{\Gamma_2 - 1}{\Gamma_2} \left(\frac{l(l+1)}{\omega^2} - 4 - \omega^2 \right) \right]
\end{aligned}
\tag{3.86}
$$

and,

$$
\begin{aligned}
&\frac{\delta P}{P} = F_p(l, \omega^2) \frac{\delta R}{R}, \\
&\frac{\delta T}{T} = \left(\frac{\Gamma_2 - 1}{\Gamma_2} \right) \frac{\delta P}{P} \\
&= \left(\frac{\Gamma_2 - 1}{\Gamma_2} \right) F_p(l, \omega^2) \frac{\delta R}{R} \\
&= \left(\frac{\Gamma_2 - 1}{\Gamma_2} \right) \left(\frac{l(l+1)}{\omega^2} - 4 - \omega^2 \right) \frac{\delta R}{R}
\end{aligned}
\tag{3.87}
$$

where $F_p(l, \omega^2)$ refers to the ratio of relative pressure perturbation and relative radius per-

turbation. δR is the same as the radial displacement evaluated at the stellar surface $\xi_r(R)$. We consider the pulsation semi-amplitude from maximum to mid-point, so set $e^{im\phi_0}e^{i\sigma t} = 1$. For an $l = 2, m = 0$ mode,

$$\begin{aligned}
&(\Delta\text{mag})_T^{m=0} \\
&= -1.0857\frac{\delta R}{R}\left[\frac{xe^x}{e^x-1}\frac{\Gamma_2-1}{\Gamma_2}\left(\frac{l(l+1)}{\omega^2}-4-\omega^2\right)\right]\gamma_l\ \sqrt{\frac{5}{4\pi}}(0.5)(3\cos^2 i_s - 1) \\
&= -1.0857\gamma_l\left[\sqrt{\frac{5}{4\pi}}(0.5)\right]\frac{xe^x}{e^x-1}\left[\frac{\Gamma_2-1}{\Gamma_2}\left(\frac{l(l+1)}{\omega^2}-4-\omega^2\right)\right](3\cos^2 i_s - 1)\frac{\delta R}{R} \qquad (3.88)\\
&= -1.0857\cdot 0.32\cdot 3.44\gamma_l\left[\frac{\Gamma_2-1}{\Gamma_2}\left(\frac{l(l+1)}{\omega^2}-4-\omega^2\right)\right](3\cos^2 i_s - 1)\frac{\delta R}{R} \\
&= -1.2\gamma_l\left[\frac{\Gamma_2-1}{\Gamma_2}\left(\frac{l(l+1)}{\omega^2}-4-\omega^2\right)\right](3\cos^2 i_s - 1)\frac{\delta R}{R}.
\end{aligned}$$

where γ_l is the bolometric limb darkening coefficient defined below, i_s is the stellar inclination angle. x is $hc/\lambda kT_{\text{eff}}$, with Boltzmann constant k, Planck constant h, passband wavelength λ, speed of light c, and effective temperature of the star T_{eff}. This is the expression for the amplitude of magnitude variation due to effect of temperature changes.

Similarly, for $l = 2$, $m = 2$ modes:

$$\begin{aligned}
&(\Delta\text{mag})_T^{m=2} \\
&= -1.0857\frac{\delta R}{R}\left[\frac{xe^x}{e^x-1}\frac{\Gamma_2-1}{\Gamma_2}\left(\frac{l(l+1)}{\omega_\alpha^2}-4-\omega_\alpha^2\right)\right]\gamma_l\ \sqrt{\frac{5}{4\pi}\frac{1}{24}}(3\sin^2 i_s) \\
&= -1.0857\gamma_l\left[\sqrt{\frac{5}{4\pi}\frac{1}{24}}(3)\right]\frac{xe^x}{e^x-1}\left[\frac{\Gamma_2-1}{\Gamma_2}\left(\frac{l(l+1)}{\omega_\alpha^2}-4-\omega_\alpha^2\right)\right](\sin^2 i_s)\frac{\delta R}{R} \qquad (3.89)\\
&= -1.0857\cdot 0.39\cdot 3.44\gamma_l\left[\frac{\Gamma_2-1}{\Gamma_2}\left(\frac{l(l+1)}{\omega_\alpha^2}-4-\omega_\alpha^2\right)\right](\sin^2 i_s)\frac{\delta R}{R} \\
&= -1.5\gamma_l\left[\frac{\Gamma_2-1}{\Gamma_2}\left(\frac{l(l+1)}{\omega_\alpha^2}-4-\omega_\alpha^2\right)\right](\sin^2 i_s)\frac{\delta R}{R}.
\end{aligned}$$

The magnitude variation due to geometric effects (cross section changes, surface norm changes) satisfies:

$$\begin{aligned}(\Delta\text{mag})_G &= -1.0857\varepsilon(\alpha_l+\beta_l)\ Y_{lm}(i_s,\phi_0)e^{i\sigma t} \\ &= -1.0857\frac{\delta R}{R}(\alpha_l+\beta_l)\ \sqrt{\frac{(2l+1)(l-m)!}{4\pi(l+m)!}}P_l^m(\cos i_s)\cdot e^{im\phi_0}e^{i\sigma t}.\end{aligned} \tag{3.90}$$

For $l=2$, $m=0$ modes,

$$\begin{aligned}&(\Delta\text{mag})_G^{m=0} \\ &= -1.0857\frac{\delta R}{R}(\alpha_l+\beta_l)\ \sqrt{\frac{5}{4\pi}}0.5(3\cos^2 i_s-1)\cdot 1 \\ &= \left[-1.0857\cdot\sqrt{\frac{5}{4\pi}}0.5\right](\alpha_l+\beta_l)(3\cos^2 i_s-1)\frac{\delta R}{R} \\ &= [-0.34](\alpha_l+\beta_l)(3\cos^2 i_s-1)\frac{\xi_{r,\alpha}(R)}{R}.\end{aligned} \tag{3.91}$$

For $l=2, m=2$ modes,

$$\begin{aligned}&(\Delta\text{mag})_G^{m=2} \\ &= \left[-1.0857\cdot\sqrt{\frac{5}{4\pi}\frac{1}{24}}\cdot 3\right](\alpha_l+\beta_l)\sin^2 i_s\frac{\delta R}{R} \\ &= [-0.42](\alpha_l+\beta_l)\sin^2 i_s\frac{\xi_{r,\alpha}(R)}{R}\end{aligned} \tag{3.92}$$

where α_l, β_l and γ_l are bolometric limb darkening coefficients defined in eq. (37, 38, 39) of Buta & Smith (1979). They are equivalent to the b_l and c_l used in Dziembowski (1977) and

Burkart et al. (2012) by the following relations:

$$\begin{aligned} \alpha_l + \beta_l &= 2b_l - c_l \\ \gamma_l &= b_l. \end{aligned} \tag{3.93}$$

For A stars and the *Kepler* passband, $\alpha_l + \beta_l \approx -1.2$ and $\gamma_l \approx 0.3$. Burkart et al. (2012) listed values of b_l and c_l for $l = 0 - 5$ modes in the *Kepler* passband in their Table 3.

Here we show that the two expressions for magnitude variations due to geometry effect (cross section changes) from Burkart et al. (2012) $(\delta\text{mag})_G$ and from Fuller & Lai (2012) $(\Delta\text{mag})_G$ are identical.

For $l = 2, m = 0$ modes,

$$\begin{aligned} (\delta\text{mag})_G^{m=0} &= -1.0857 \left(\frac{\delta J}{J}\right)_G \\ &= -1.0857 \left[(2b_l - c_l)\frac{\xi_r(R)}{R}\right] Y_{lm}(\theta_0, \phi_0) \\ &= -1.0857 \left[(-1.3)\frac{\xi_r(R)}{R}\right] Y_{20}(i_s, \phi_0) \\ &= -1.0857 \left[(-1.3)\frac{\xi_r(R)}{R}\right] \left[0.5\sqrt{\frac{5}{4\pi}}(3\cos^2 i_s - 1)\right] \\ &= (-1.3)(-1.0857 \cdot 0.5\sqrt{\frac{5}{4\pi}})(3\cos^2 i_s - 1)\frac{\xi_r(R)}{R} \\ &= (-1.3)(-0.34)(3\cos^2 i_s - 1)\frac{\xi_r(R)}{R} \\ &= -0.34(\alpha_l + \beta_l)(3\cos^2 i_s - 1)\frac{\xi_{r,\alpha}(R)}{R} \\ &= (\Delta mag)_G^{m=0}. \end{aligned} \tag{3.94}$$

Similarly, for $l = 2, m = 2$ modes,

$$\begin{aligned}
(\delta\text{mag})_G^{m=2} &= -1.0857\left[(-1.3)\frac{\xi_r(R)}{R}\right] Y_{22}(i_s,\phi_0) \\
&= -1.0857\left[(-1.3)\frac{\xi_r(R)}{R}\right]\left[\sqrt{\frac{5}{4\pi}\frac{1}{24}}(3\sin^2 i_s)\right] \\
&= (-1.3)(-1.0857\cdot 3\sqrt{\frac{5}{4\pi}\frac{1}{24}})(\sin^2 i_s)\frac{\xi_r(R)}{R} \\
&= (-1.3)(-0.42)(\sin^2 i_s)\frac{\xi_r(R)}{R} \\
&= -0.42(\alpha_l+\beta_l)\sin^2 i_s\frac{\xi_{r,\alpha}(R)}{R} \\
&= (\Delta mag)_G^{m=2}.
\end{aligned} \tag{3.95}$$

After we get the magnitude variation for one normal mode, the total magnitude variation due to the tidal response for each orbital harmonic k can be calculated.

For magnitude variations of the k^{th} orbital harmonic due to the temperature perturbation :

$$\begin{aligned}
&(\Delta\text{mag})_{k,T} \\
&= -1.0857\sum_\alpha\left\{\left[\frac{GM'W_{lm}Q_\alpha}{2\varepsilon_\alpha a^{l+1}}\right]\left[\frac{X_{lm}^{-k}e^{+ik\Omega_{orb}t}}{(\sigma_\alpha+k\Omega_{orb})-i\gamma_\alpha}+\frac{X_{lm}^{k}e^{-ik\Omega_{orb}t}}{(\sigma_\alpha-k\Omega_{orb})-i\gamma_\alpha}\right]\right\}\frac{\delta R}{R}F_\lambda\gamma_l\ Y_{lm}(i_s,\phi_0) \\
&= -1.0857\sum_\alpha\left\{\left[\frac{GM'W_{lm}Q_\alpha}{2\varepsilon_\alpha a^{l+1}}\right]\left[\frac{X_{lm}^{-k}e^{+ik\Omega_{orb}t}}{(\sigma_\alpha+k\Omega_{orb})-i\gamma_\alpha}+\frac{X_{lm}^{k}e^{-ik\Omega_{orb}t}}{(\sigma_\alpha-k\Omega_{orb})-i\gamma_\alpha}\right]\right\} \\
&\quad\times\frac{\delta R}{R}\left[\frac{xe^x}{e^x-1}\frac{\Gamma_2-1}{\Gamma_2}(\frac{l(l+1)}{\omega^2}-4-\omega^2)\right]\gamma_l\sqrt{\frac{(2l+1)(l-m)!}{4\pi(l+m)!}}P_l^m(\cos i_s).
\end{aligned} \tag{3.96}$$

For variations due to the geometry perturbation:

$$
\begin{aligned}
&(\Delta\mathrm{mag})_{k,G} \\
&= -1.0857 \sum_{\alpha} \left\{ \left[\frac{GM' W_{lm} Q_{\alpha}}{2\varepsilon_{\alpha} a^{l+1}} \right] \left[\frac{X_{lm}^{-k} e^{+ik\Omega_{orb}t}}{(\sigma_{\alpha} + k\Omega_{orb}) - i\gamma_{\alpha}} + \frac{X_{lm}^{k} e^{-ik\Omega_{orb}t}}{(\sigma_{\alpha} - k\Omega_{orb}) - i\gamma_{\alpha}} \right] \right\} \\
&\quad \times \frac{\delta R}{R} (\alpha_l + \beta_l)\ Y_{lm}(i_s, \phi_0) \qquad (3.97) \\
&= -1.0857 \sum_{\alpha} \left\{ \left[\frac{GM' W_{lm} Q_{\alpha}}{2\varepsilon_{\alpha} a^{l+1}} \right] \left[\frac{X_{lm}^{-k} e^{+ik\Omega_{orb}t}}{(\sigma_{\alpha} + k\Omega_{orb}) - i\gamma_{\alpha}} + \frac{X_{lm}^{k} e^{-ik\Omega_{orb}t}}{(\sigma_{\alpha} - k\Omega_{orb}) - i\gamma_{\alpha}} \right] \right\} \\
&\quad \times \frac{\delta R}{R} (\alpha_l + \beta_l)\ \sqrt{\frac{(2l+1)(l-m)!}{4\pi(l+m)!}} P_l^m(\cos i_s).
\end{aligned}
$$

Burkart et al. (2012) gave an equivalent expression for the tidal response. For any perturbation variable denoted as δX such as the Lagrangian density perturbation $\Delta\rho$, the radial Lagrangian displacement ξ_r, etc., the tidal response is a sum over mode indices $\alpha = (n, l, m)$ and temporal Fourier expansion indices k:

$$
\delta X(r, \theta, \phi, t) = \sum_{\alpha} \sum_{k=-\infty}^{+\infty} A_{\alpha,k} \delta X_{\alpha}(r) e^{-ik\Omega_{orb}t} Y_{lm}(\theta, \phi) \qquad (3.98)
$$

where the sum of α includes the sum of $|n| < +\infty$, $2 \leq l < +\infty$, and $-l \leq m \leq l$. Ω_{orb} is angular frequency of the orbit. The amplitude for each contribution is:

$$
A_{\alpha,k} = A_{nlmk} = \frac{2\varepsilon_l Q_{nl} X_{lm}^{k} (1-e)^{l+1} W_{lm} \Delta_{nlmk}}{E_{nl}}. \qquad (3.99)
$$

The terms are defined previously, except for the tidal parameter ε_l

$$
\varepsilon_l = \left(\frac{M'}{M} \right) \left(\frac{R}{a(1-e)} \right)^{l+1}, \qquad (3.100)
$$

and the Lorentzian factor Δ_{nlmk}

$$\Delta_{nlmk} = \frac{\omega_{nl}^2}{(\omega_{nl}^2 - \sigma_{km}^2) - 2i\gamma_{nl}\sigma_{km}} \tag{3.101}$$

where $\sigma_{km} = k\Omega_{orb} - m\Omega_s$ is the driving frequency in the co-rotating frame, and Ω_s is the spin frequency. The Lorentzian factor (as well as Q_{nl}) has a slightly different form with eq. (25) since Burkart et al. (2012) set the mode energy equal to 1, while Fuller & Lai (2012) use unit mode inertia as normalization (eq. 68). The mode normalization by mode energy E_{nl} is,

$$E_{nl} = 2\left(\frac{\omega_{nl}^2 R}{GM^2}\right)\int_0^R (\xi_{r,nl}^2 + l(l+1)\xi_{h,nl}^2)\rho(r)r^2 dr = 1. \tag{3.102}$$

Note that since the modes are normalized to have unit energy instead of inertia, the mode amplitude expression A_{nlmk} in Burkart et al. (2012) has a slightly different form with that in Fuller & Lai (2012).

Following O'Leary & Burkart (2014), the observed phase of the tidally induced pulsations with frequency of k^{th} orbital harmonics is

$$\delta_{\rm phase} = \arg(\delta J_k/J_k) = \arg(A_{nlmk}) + \arg(Y_{lm}(\theta_0, \phi_0)) = \psi_{nlmk} + m\phi_0 \tag{3.103}$$

and if assuming the mode eigenfunctions have phases close to zero (for adiabatic normal modes the eigenfunctions are purely real, so the phases are zero; a fully non-adiabatic calculation will introduce local phases, but they are usually very small). Then we can evaluate ψ_{nlmk} by

$$
\begin{aligned}
\psi_{nlmk} &= \arg(A_{nlmk}) \\
&= \arg(Q_{nl}\Delta_{nlmk}) \\
&\approx \arg(\Delta_{nlmk}) \\
&= \arg(\frac{1}{(\omega_{nl}^2 - \sigma_{km}^2) - 2i\gamma_{nl}\sigma_{km}}) = \arg((\omega_{nl}^2 - \sigma_{km}^2) + 2i\gamma_{nl}\sigma_{km}) \\
&= \pi/2 - \arctan\left(\frac{(\omega_{nl} - \sigma_{km})(\omega_{nl} + \sigma_{km})}{2\gamma_{nl}\sigma_{km}}\right) \\
&= \pi/2 - \arctan\left(\frac{\delta\omega(\omega_{nl} + \sigma_{km})}{2\gamma_{nl}\sigma_{km}}\right) \\
&\approx \pi/2 - \arctan\left(\frac{\delta\omega}{\gamma_{nl}}\right)
\end{aligned}
\tag{3.104}
$$

where $\delta\omega = \omega_{nl} - \sigma_{km}$ and we have used the assumption $\omega_{nl} \approx \sigma_{km}$. These equations are only valid for standing waves (the imaginary part of the flux perturbation is small relative to the real part). The observed time dependence is

$$
\cos[k\Omega_{orb}t - (\psi_{nlmk} + m\phi_0)]. \tag{3.105}
$$

.

In asteroseismology, the observed pulsations are often described as the sum of sine functions, so in the form of a sine function,

$$
\begin{aligned}
&\cos[k\Omega_{orb}t - (\psi_{nlmk} + m\phi_0)] \\
&= \sin[\pi/2 - (k\Omega_{orb}t - (\psi_{nlmk} + m\phi_0))] \\
&= \sin[-k\Omega_{orb}t + (\pi/2 + \psi_{nlmk} + m\phi_0)].
\end{aligned}
\tag{3.106}
$$

The sign of k is unknown and $t = 0$ corresponds to the time of periastron passage. Note if the phases are in units of 2π, the dependence becomes $\sin[-k\Omega_{orb}t + (1/4 + \psi_{nlmk} + m\phi_0)]$.

Thus the observed phase in units of 2π is then :

$$\delta_{\rm phase} = \left(\frac{1}{4} + \psi_{nlmk} + m\phi_0\right) \mod \frac{1}{2} \tag{3.107}$$

and

$$\phi_0 = \frac{1}{4} - \frac{\omega_p}{2\pi} \tag{3.108}$$

where ω_p is argument of periastron. In the limit of poor tuning, i.e., the detuning parameter is much larger than mode damping rate, $|\delta\omega| \gg \gamma_{nl}$,

$$\psi_{nlmk} \approx \left[\pi/2 - \arctan\left(\frac{\delta\omega}{\gamma_{nl}}\right)\right]/(2\pi) = \left[\pi/2 - \pi/2\right]/(2\pi) = 0 \tag{3.109}$$

and the observed phase is then

$$\delta_{\rm phase} = \left(\frac{1}{4} + m\phi_0\right) \mod \frac{1}{2} \tag{3.110}$$

Note that if using a magnitude variation, the phase will be off by π (or by 1/2 if in units of 2π), since $\delta{\rm mag} \propto -\delta J/J$. As pointed out by Burkart et al. (2012), we only observe $|k|$ in observations and thus the sign of k cannot be determined. We cannot tell whether the mode is prograde ($m > 0$) or retrograde ($m < 0$) (when the time dependence is $e^{-i\omega t + m\phi}$).

In Chapter 6, we apply the linear tidal theory in this section to several *Kepler* binaries with tidally induced oscillations.

CHAPTER 4

Light Curve Modeling of Binary Stars

This chapter contains the descriptions of modeling tools for binary stars and star-planet systems. It is related directly to Chapter 5 and Chapter 6, in which we apply these tools to *Kepler* filed of view binary stars. A review of these tools is presented in Section 4.1. For most of the packages, I have shown explicitly the input parameters and the code flow. A detailed binary modeling with the ELC code is given in Section 4.2, where I show the light curves, radial velocity curves, and the synthetic spectra of the binary. For usage of the ELC, please refer to the appendix.

4.1 Introduction to Modeling Tools

Space missions like *Kepler* (Borucki et al. 2010), CoRoT (Baglin et al. 2006), and BRITE (Weiss et al. 2014) have produced more than 10^5 light curves of various kinds of stars. As most stars are within binary or multiple systems, it is important to model their time series to learn about their dimensions and physical properties. Here we briefly summarize the current tools of modeling light curves of binary stars and star-planet systems.

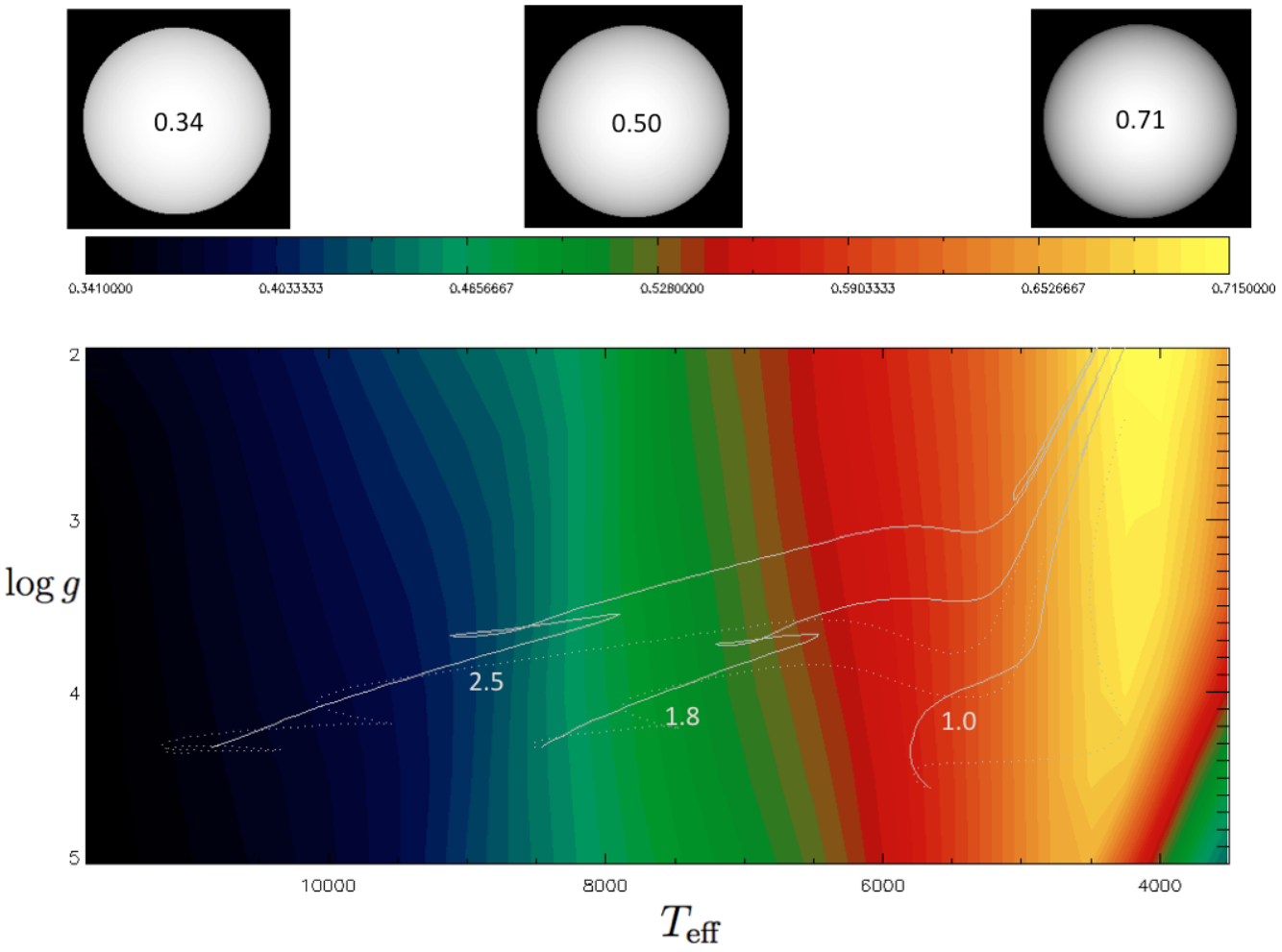

Figure 4.1 a) The top panel shows the specific intensity of stellar disks for three values of linear limb darkening coefficients indicated in the center. b) The lower panel is a contour plot of linear limb darkening coefficients for *Kepler* passband based on models with solar metallicity over a grid of effective temperature and gravity. These coefficients are interpolated from the grids in PHOEBE package (Prsa & Zwitter 2005). The evolutionary tracks for $1.0M_{\odot}, 1.8M_{\odot}, 2.5M_{\odot}$ stellar models from the Dartmouth models (Dotter et al. 2008) are over-plotted from right to left, respectively. The pre-main-sequence part of the tracks are shown as a dotted line, while main sequence (MS) and post-MS stages are shown as a solid line.

Light curve modeling tools of binary stars or star-planet systems can be classified into two kinds: two-dimensional (2-D) models and three-dimensional (3-D) models.

(1): 2-D models: Stars (or planets) are treated as limb-darkened circular disks. The simplest description of the surface brightness is to use the linear limb darkening law for the specific intensity I:

$$I(\cos\theta) = I_0(1 - \varepsilon + \varepsilon\cos\theta) \tag{4.1}$$

where θ is the angle between the surface normal and the line of sight. The specific intensity varies from I_0 at disk center to $I_0(1-\epsilon)$ at the extreme limb. The variations of linear limb darkening coefficient ε as a function of atmospheric parameters are shown in Figure 4.1. It shows that ε is primarily a function of $T_{\rm eff}$, with smaller value for hotter stars and vice versa. Better limb darkening functions like logarithm, quadratic, or non-linear law can be adopted (Claret & Bloemen 2011). The 2-D disk is the projected image of the three-dimensional star onto the sky plane. Analytical expressions exist for the fractional loss of fluxes in eclipses for these circular disk cases.

(1a) Transits by a dark exoplanet: The treatment of Mandel & Agol

The most popular analytical method for exoplanet transit light curve modeling is presented in Mandel & Agol (2002), where the star is a limb-darkened disk and the planet is treated as an opaque circular disk. The model has the following eight parameters:

p: Radius ratio between planet and star.

a: Semi-major axis of planetary orbit [in units of stellar radii].

i: Inclination of orbit in degrees (90 deg is edge-on view).

linLib: Linear limb-darkening coefficient.

quadLimb: Quadratic limb-darkening coefficient.

T_0: Time of transit center.

per: Period of planetary orbit.

b: Describes the flux ratio between a stellar companion and the main star (default is 0).

The final analytical expressions involve Beta functions and hypergeometric functions. This model has been widely used in modeling transit light curves.

(1b) Mutual eclipses of stars: The treatment of Kopal and Gimenez

A more general treatment of the flux loss is given by Gimenez (2006a, b). Their expressions apply to both binary stars and star-planet systems. An analytical formula for the Rossiter-McLaughlin (RM) effect in radial velocities is also presented.

This method is based on the original formulation in Kopal (1979) who considered the problem of evaluating the fractional loss of light in a binary or star-planet system in the Fourier domain and linked the fractional loss of light to the diffraction patterns of the two apertures as described in physical optics. The final expressions take advantage of the mathematical tools such as diffraction integrals and involve Bessel functions of the first kind and Jacobi polynomials.

The five model parameters are:

r_s: The relative radius of the companion star (radius divided by semimajor axis);

$k = r_p/r_s$: The ratio of radii;

i: The orbital inclination;

u_a and u_b: The limb-darkening coefficients (quadratic law).

This model is implemented in the ELC code (see below) as the 'Fast Analytic Mode'.

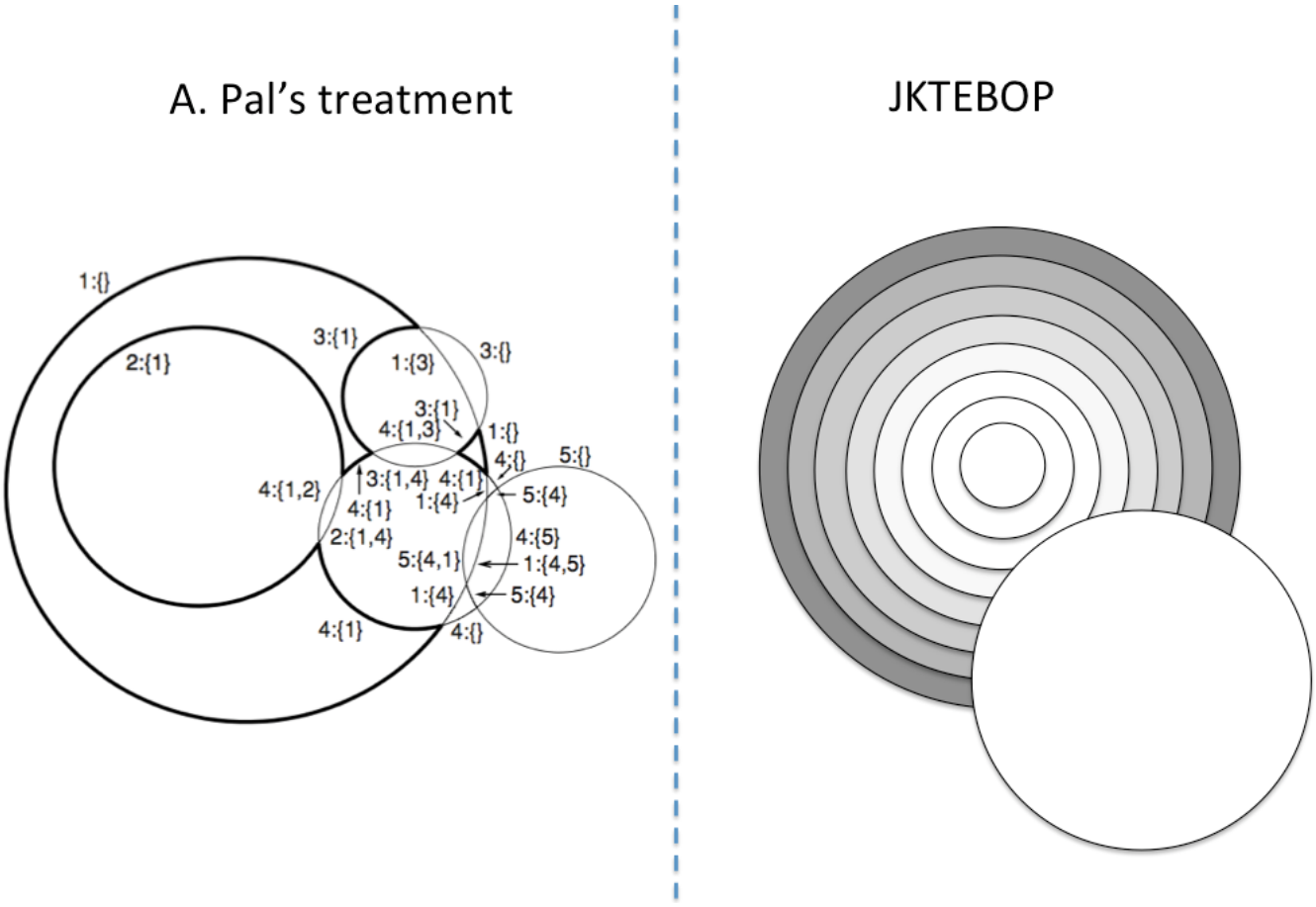

Figure 4.2 Treatment of light curve calculation in Pál (2012) for multiple objects (left panel) and JKTEBOP for binaries (right panel).

(1c) Multiple transiting exoplanets: The treatment of Pál and Carter

The analytical expressions for more complicated cases involving three or more bodies (all treated as circular disks) were studied in Pál (2012) and were applied to circumbinary exoplanet systems in a series of papers (Carter et al. 2011; Welsh et al. 2012; etc.).

In the so-called photometric-dynamic modeling, the orbit has to be determined from an N-body numerical integration. Once the positions of multiple objects are calculated in each time step, the intensities on the visible part of the disks are integrated. The observed flux is just an integral of the surface brightness (the limb-darkening law for each object, treated as a vector field $\boldsymbol{F}$) over the visible part of the disks. By using the Stoke's theorem, the problem can be cast as an integral of another vector field $\boldsymbol{f}$ along the boundary of the visible surface (a series of arcs on multiple disks, see left panel in Figure 4.2). This clever idea thus replaces the original complicated surface integral $\int \boldsymbol{F} \cdot \boldsymbol{dS}$ by a much easier curvilinear integral $\int \boldsymbol{f} \cdot \boldsymbol{dl}$ along the arcs. The key step is to find $\boldsymbol{f}$ from $\boldsymbol{F}$ so that it satisfies $\nabla \times \boldsymbol{f} = \boldsymbol{F}$, and this can be achieved by solving a simple differential equation.

The model parameters for the photometric modeling include the mass, radius, flux and limb-darkening coefficient for each object. For the orbit determination from N-body integration, the model parameters are the $N - 1$ Jacobian Keplerian elements.

(1d) Numerical integrations: The method of surface discretization

In this straightforward method, each circular disk is treated as a series of concentric rings and a numerical integration of the visible part of the rings is performed (Fig. 4.2, right panel). This is the method used in the EBOP code (Etzel 1993) with the further development in JKTEBOP code[1] (Southworth et al. 2005).

For example, in the JKTEBOP code, there are about 19 model parameters:

Integration ring size;

Sum of the radii; Ratio of the radii;

[1]http://www.astro.keele.ac.uk/jkt/codes/jktebop.html

Orbital inclination; Mass ratio;

Orbital eccentricity: e; Periastron longitude: ω;

Gravity darkening coefficient (star A and star B);

Surface brightness ratio; Amount of third light;

Linear limb-darkening coefficient (star A and star B);

Nonlinear limb-darkening coefficient (star A and star B);

Reflection effect star A; Reflection effect star B;

Phase shift of primary minimum; Light scale factor (mag);

Orbital period of eclipsing binary system;

Reference time of primary minimum.

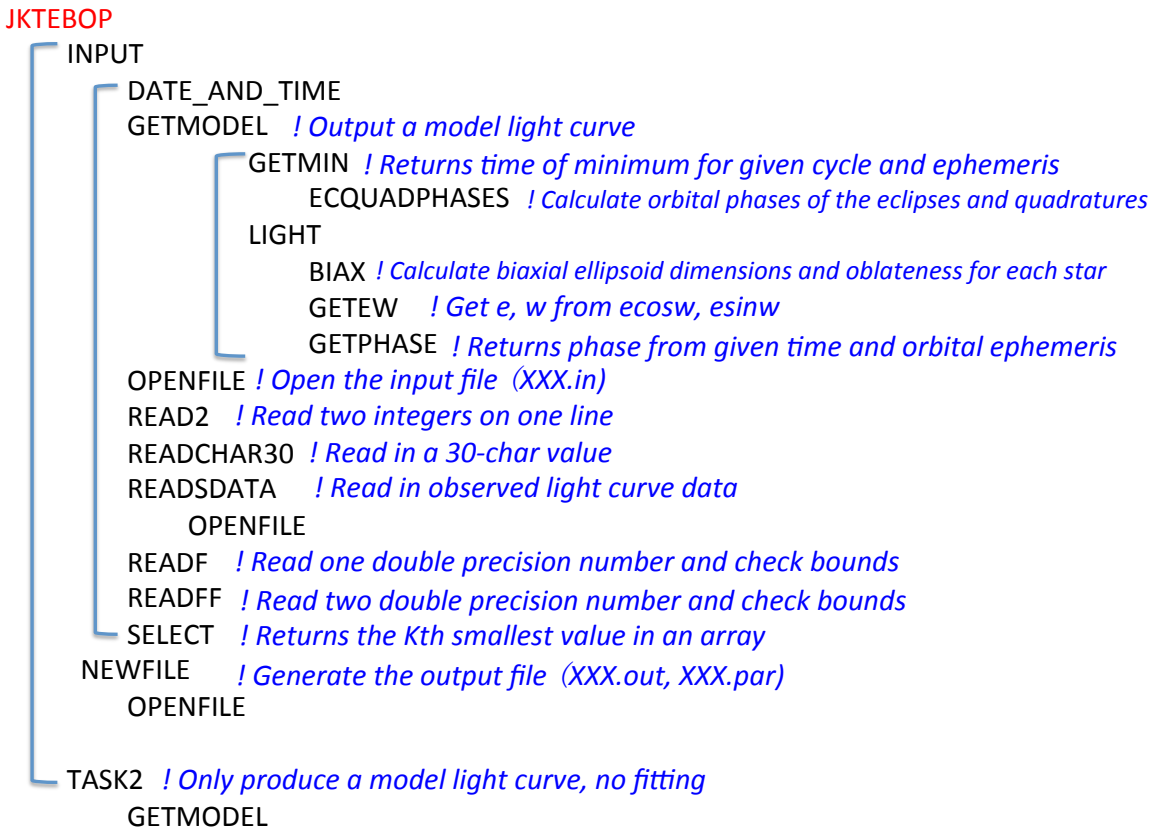

Figure 4.3 The call tree of the JKTEBOP code. TASK2 in JKTEBOP is for calculating the light curve. Other tasks are mainly for parameter optimization and are not shown.

In Figure 4.3, we show the call tree of this code, which is produced by the static analyzer for Fortran programs *ftnchek*[2]. JKTEBOP has been widely used for detached eclipsing binaries as well as exoplanet transit light curve modeling. Although the ellipsoidal and reflection effects in close binaries can be partially and approximately accounted for using biaxial spheroids in JKTEBOP, a more realistic treatment is to use the three-dimensional

[2]http://www.dsm.fordham.edu/ftnchek/

Roche model (see next section).

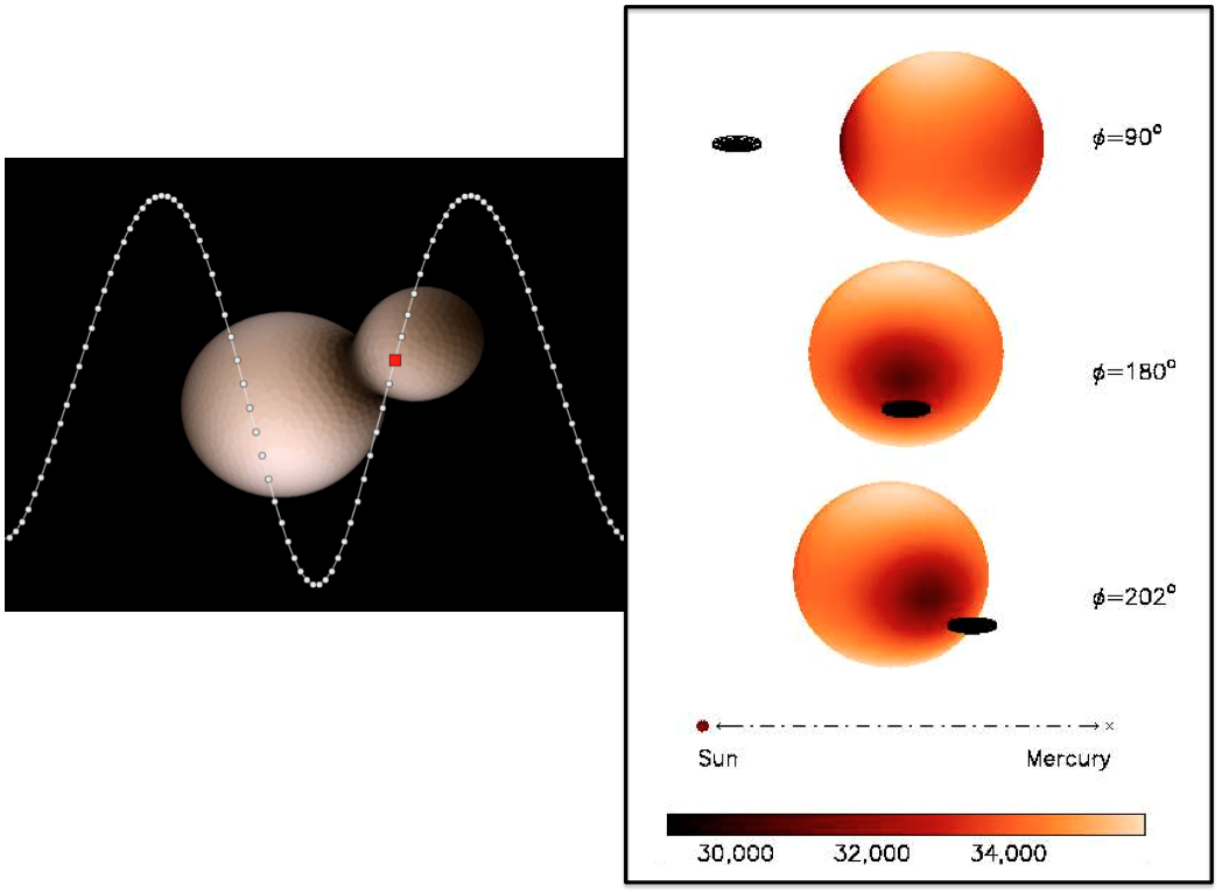

Figure 4.4 3-D model of the contact binary EE Ceti (left panel); Model of M33-X7, an eclipsing binary with a black hole (right panel).

(2): 3-D models: The 3-D codes model the surface of the star as the equipotential surface of a Roche potential, taking into account both rotation and orbital motion. The surface is discretized into grid elements each with its coordinates (r_i, θ_i and ϕ_i). Accretion disks can be included, usually using a simple geometry such as a cylinder. The eclipse horizon is calculated and intensities of the visible part of the surface are integrated. This step is

then repeated for each new orbital phase. Figure 4.4 shows two examples of such models: the contact binary EE Ceti (taken from Phoebe 2 webpage[3]) and an eclipsing binary with an accretion disk around a black hole (Orosz et al. 2007).

(2a) Wilson-Devinney code [4](WD) and PHOEBE[5] (Prša, Degroote and others)

One of the widely used packages is the Wilson-Devinney code (Wilson & Devinney 1971; Wilson 1979, 1990; Wilson & Liou 1993). This package models the shapes of stars by using the Roche geometry and fully takes the gravitational darkening, limb-darkening and reflection effects into account. Both the light curve and radial velocity curve can be simulated with the LC part of the code. The model parameters can be optimized with a differential corrections algorithm (the DC part) by comparing with observations.

[3]http://phoebe-project.org/docs/2.0b/
[4]http://www.astro.ufl.edu/∼kallrath/WD2007.html
[5]http://phoebe-project.org

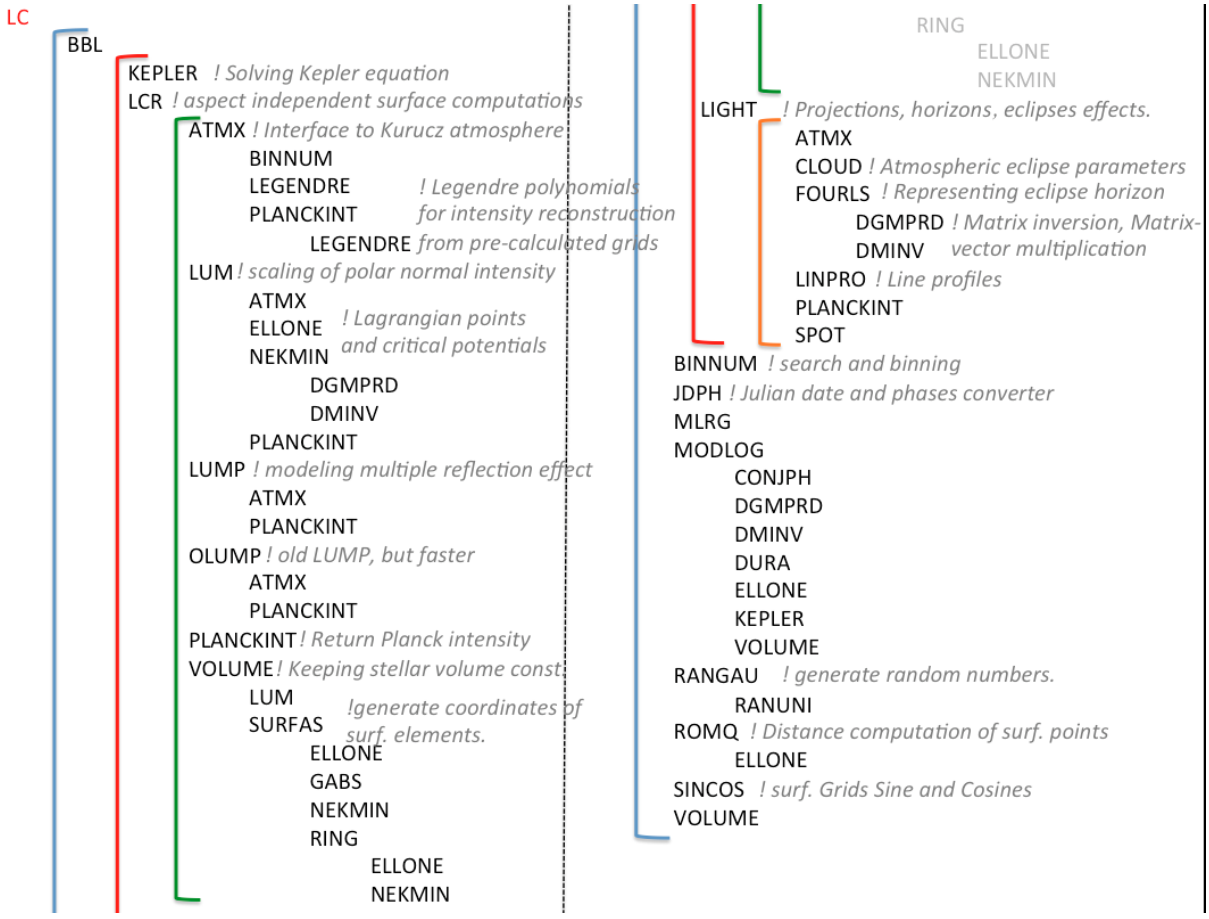

Figure 4.5 Call tree of the LC (Light Curve) part of the WD code (version 2003). The DC part (differential corrections for parameter optimization) is not shown.

The call tree of WD2003 is shown in the above diagram (Figure 4.5). The top subroutine is the Basic Block (BBL), which includes three subroutines KEPLER, LCR and LIGHT. Detailed descriptions of other subroutines can be found in the Appendix of Kallrath & Milone (2009).

Prša & Zwitter (2005) wrote a graphical user interface PHOEBE for the WD code with a few innovations including a new optimizer based on the global downhill simplex algorithm.

The PHOEBE team led by Pieter Degroote has developed a new version of light curve synthesis code PHOEBE2 in python. With the help of external optimizers/samplers, the parameter optimization process is much easier and robust. Several new functionalities, such as Doppler boosting and multi-sinusoidal modeling of pulsations, were included to deal with the precise photometric data from space missions.

A detailed description of binary modeling process using Roche geometry can be found in the Phoebe scientific reference by A. Prša[6].

(2b) Eclipsing Light Curve (ELC) code by Jerome Orosz

Based on the original code by Yorham Avni which was used to model ellipsoidal light curve of X-ray binaries, Jerome Orosz rewrote and developed the near completely new code ELC (Orosz & Hauschildt 2000). This code can model the light curve and radial velocity curve of circular and eccentric binaries, except for over-contact binaries.

With the advent of space missions like *Kepler*, further development of the code now includes the subtle effects like Doppler boosting (van Kerkwijk et al. 2010), more accurate integration during eclipses/transit, integration with specific intensities of Phoenix[7] (Husser et al. 2013), Kurucz[8], Lanz-Hubeny[9] (Lanz & Hubeny 2007) atmosphere models, N-body numerical integration and mutual eclipses of multiple objects (using the previous mentioned algorithm by A. Pál), multi-sinusoidal modeling of pulsations (so called ELCsinus), etc. Many optimization algorithms are implemented including Levenberg-Marquardt, amoeba,

[6]phoebe-project.org/1.0/docs/phoebe_science.pdf
[7]http://phoenix.astro.physik.uni-goettingen.de/
[8]http://kurucz.harvard.edu/grids.html
[9]http://nova.astro.umd.edu/

genetic algorithm, Markov Chain Monte Carlo (MCMC), differential-Monte Carlo (de-MC), etc. The most recent development of the code includes parallel computing using GPUs.

The applications of ELC to X-ray and eclipsing binaries can be found in Orosz et al. (2007), Bass et al. (2012), and Rawls et al. (2016), to exoplanet transits in Wittenmyer et al. (2005), Welsh et al. (2010), to circum-binary planet transits in Orosz et al. (2012), Welsh et al. (2012), and Kostov et al. (2014), to pulsations in heartbeat stars in Welsh et al. (2011), etc. A detailed description of its usage can be found in the Appendix .

Note that the WD code cannot be used to model exoplanet transit light curves (or other systems with extreme ratios of radii). For heartbeat stars (binaries with large orbital eccentricity), the subtle effects such as tidal distortion and reflection on the light curve also require high integration accuracy. The advancement in the accuracy of intensity integration of ELC is described in the appendix of Orosz & Hauschildt (2000). There is also an option in ELC to account for fractional surface elements in eclipse with the Monte Carlo method using the Sobol sequence (Sobol 1967) (better than the ordinary random numbers). These advances enable its application in exoplanet systems and heartbeat stars. From direct comparison, we found that ELC shows advantages over the WD or PHOEBE code in modeling these systems, especially for modeling the low-amplitude ellipsoidal variations and reflections.

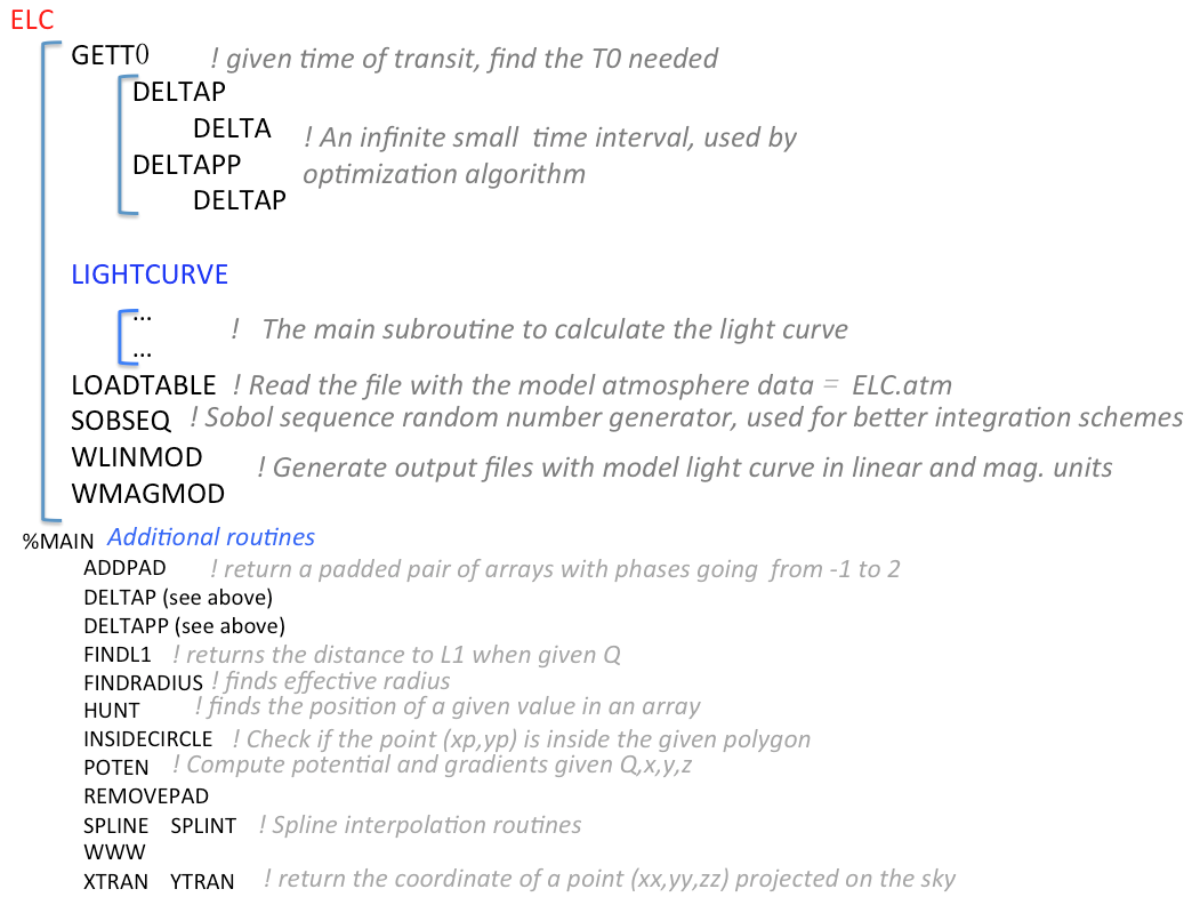

Figure 4.6 The call tree of ELC.

We show the code flow of ELC in Figure 4.6. The call tree of the main subroutine LIGHTCURVE is quite long (243 lines), and can be found in the **Appendix**.

4.2 An Example of the ELC model

As an example, we show the ELC model of a simulated eclipsing binary system with parameters of KIC 9851944. The binary has a circular orbit with period of 2.189 days. The mass, radius and effective temperature of the primary and secondary star are $(1.76, 1.79 M_{\odot})$,

$(2.27, 3.19 R_{\odot})$ and $(7026, 6950 K)$, respectively. We have changed the orbital inclination to 90° so that the Rossiter-McLaughlin effect can be shown more clearly in the RV curves. The rotation rate is assumed to be synchronous with orbital motion.

We show the light curve and flux-weighted radial velocity curve of this simulated binary system in Figure 4.7. Note that we adopt the progression of orbital phase in degrees, and the primary and secondary eclipses correspond to phases of 180 and 0 degrees, respectively. Note that the larger, cooler star is the secondary, and its RV curve is marked with several diamonds. The RV curve of the smaller, hotter primary is marked with crosses.

For a series of selected phases, marked as diamonds and crosses, we show the positions of the two components on the sky (normalized by semi-major axis) in Figures 4.8 and 4.9. In the same figures, we also show the synthetic composite spectrum from a simple spectral synthesis. We assume that the primary and secondary star contribute to 70% and 30% of flux in the spectra, respectively. The intrinsic line profile for each surface element is assumed to be a pure Gaussian shape with $\sigma = 1$ pixel and is independent of $T_{\rm eff}$ and $\log g$. We then calculate the radial velocity of each surface element on the visible part of each star and Doppler shift these intrinsic profiles accordingly (assuming 1 pixel $\approx$ 16 km s^{-1}). Finally, we sum up all these profiles to generate the observed composite spectra.

The Rossiter-McLaughlin effect is clearly seen in Figure 4.7, and this can be understood with the help of Figure 4.8 and Figure 4.9. At phases $0^{\circ} - 30^{\circ}$, the larger secondary is in eclipse. From $4^{\circ} - 30^{\circ}$, mainly the right hemisphere, which is rotating away from the observer (positive RVs), is blocked by the primary, thus the observed RVs of the secondary (crosses)

are smaller (more negative) than the Keplerian values. Similarly, from $150° - 172°$, the left hemisphere of smaller primary star is in eclipse, and since this hemisphere is approaching the observer (negative RV), the measured RVs of the primary (diamonds) are larger. This can also be seen in the synthetic spectra, e.g., the spectra of the primary at phase 170° is narrower (less rotational broadening) and its centroid is more to the right (negative RV).

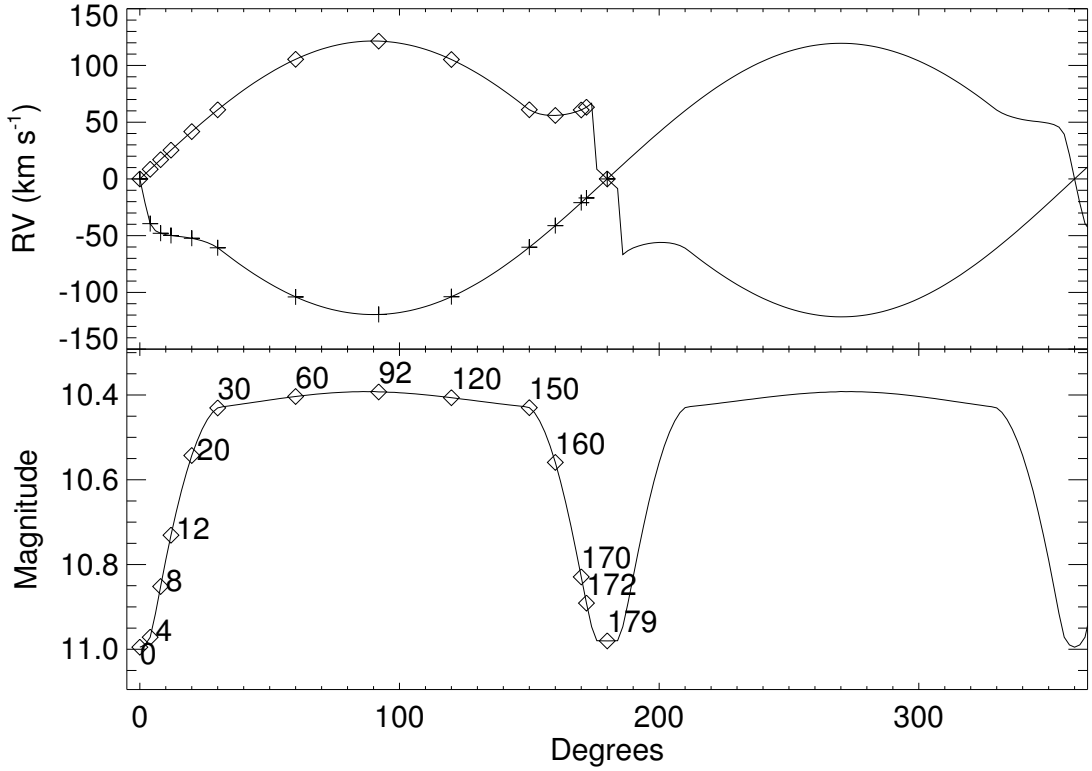

Figure 4.7 The model RV curve (upper panel) and light curve (lower panel) of an eclipsing binary star from ELC (See text for details). The diamonds and crosses mark the phases at which we show detailed sky positions and synthetic spectra in the following two figures. Note that we use degrees (0 to 360) instead of orbital phases (0 to 1).

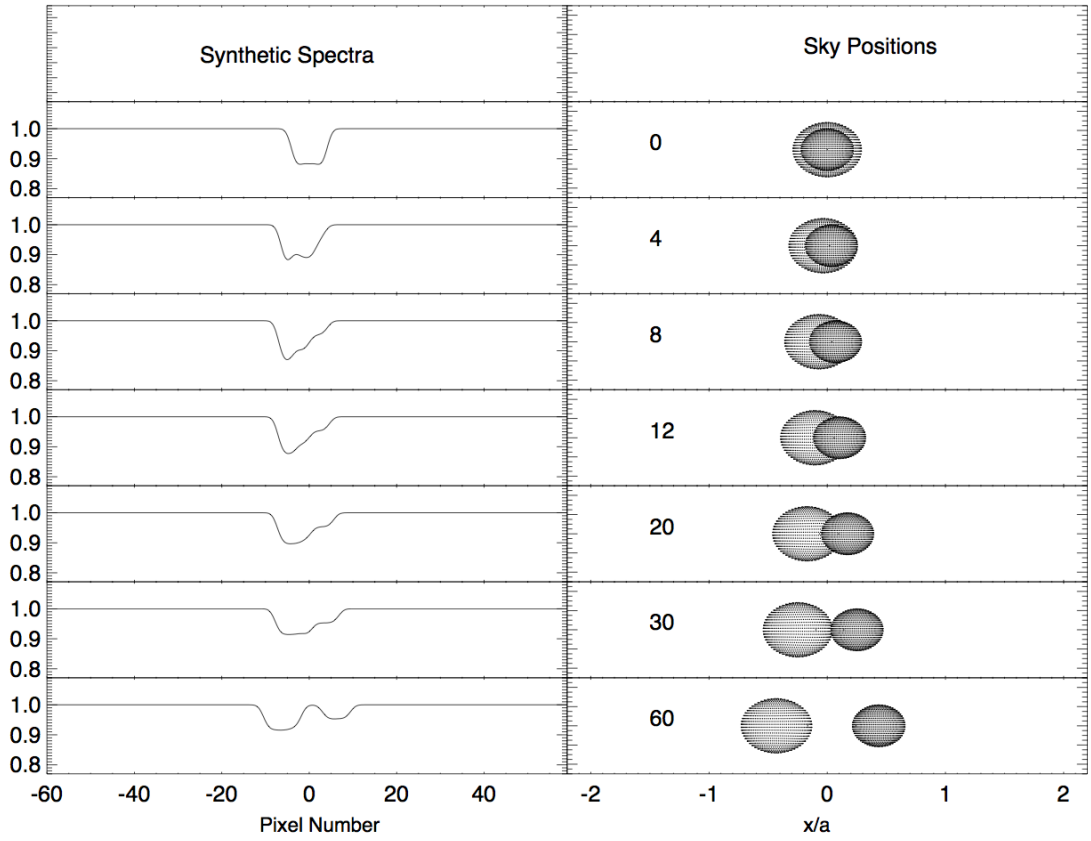

Figure 4.8 The synthetic spectra and stellar positions on the sky for seven different phases $(0, 4, 8, 12, 20, 30, 60$ in degrees). One pixel step in the left panel corresponds to a Doppler shift of ~ 16 km s^{-1}.

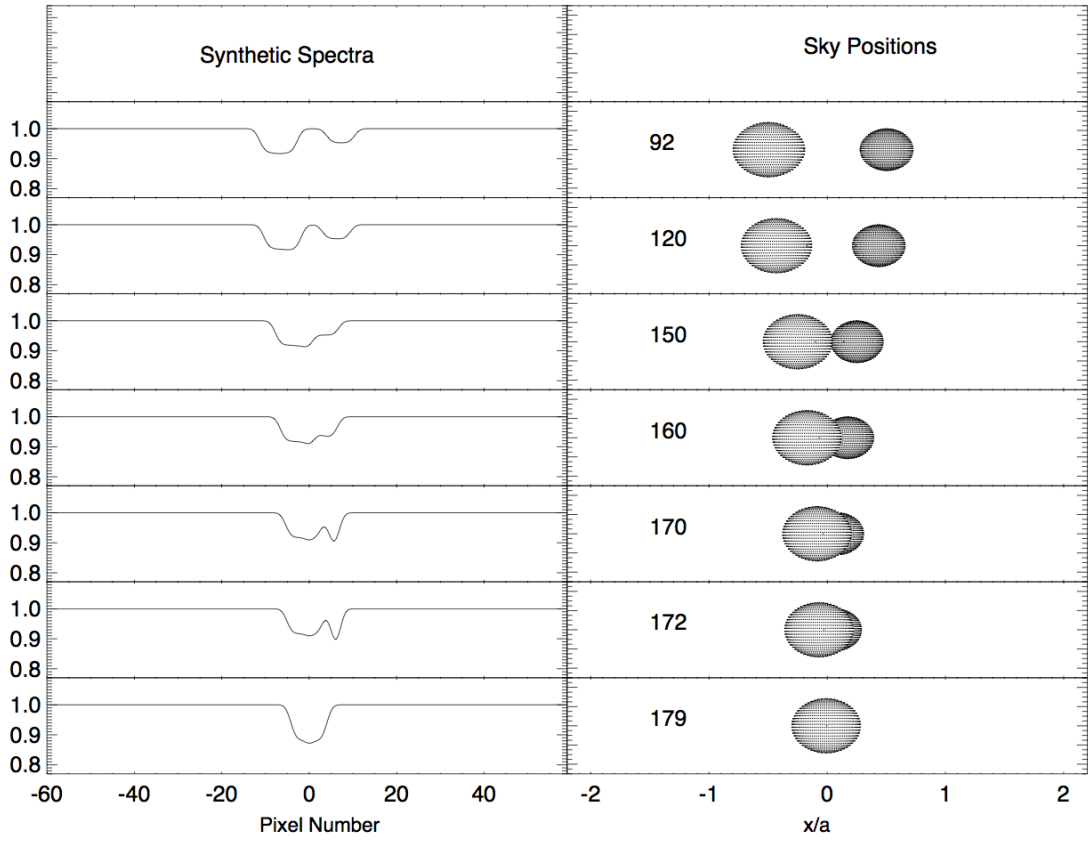

Figure 4.9 The same as Figure 8, but for phases at $92, 120, 150, 160, 170, 172, 179$ degrees.

The main model parameters of ELC are listed in Table 4.1. The results from fitting the light curves of KIC 9851944, KIC 8262223, KIC 3230227 are also presented. Details of modeling these binaries can be found in later sections (Chapters 5 and 6). A light curve gallery of heartbeat stars is presented in Chapter 6.

Other light curve modeling packages of binary stars are described by Kallrath & Milone (2009). Light curve modeling of more complicated objects such as asteroids requires better discretization schemes (e.g., spherical t-design) of surfaces and descriptions of shapes with spherical harmonic expansions (Kaasalainen & Torppa 2001).

Table 4.1: Main Model Parameters of ELC

Parameters	Primary	Secondary
	Tuning Parameters	
inclination (deg)	orbital inclination	$[0-90]$
mass ratio (q)	M_2/M_1	dimensionless
f1	filling factor[1](star1)	$[0.0-1.0]$, counterpart of Ω_1
f2	filling factor[1](star2)	$[0.0-1.0]$, counterpart of Ω_2
o1	$\Omega_{rot}/\Omega_{orb}$ (star1)	1 for synchronous rotation
o2	$\Omega_{rot}/\Omega_{orb}$ (star2)	1 for synchronous rotation
T1 (K)	$T_{\rm eff}$ (star1)	
T2 (K)	$T_{\rm eff}$ (star2)	
separation ($R_\odot$)	a	
eccentricity	e	$[0-1]$
argper (deg)	argument of periastron (star1), ω	$[0-360]$
pshift	phase shift	for convenience
period (day)	orbital period	-
T0 (day)	time of inferior conjunction of star1	secondary minimum in LC
-	time of periastron passage (eccentric orbits)	-
l1	bolometric albedo (star1)	usually $[0-1]$
l2	bolometric albedo (star2)	usually $[0-1]$
gamma (km s^{-1})	systemic velocity	
oc	$e\cos\omega$	estimated from LC
os	$e\sin\omega$	estimated from LC
contam	Kepler contamination[2]	from KIC
e1	beaming factor (star1)	van Kerkwijk et al. 2010
e2	beaming factor (star2)	van Kerkwijk et al. 2010
tconj	time of primary eclipse	alternative to T0
density	density can constrain q and f	
ai	the inclination of rotational axis star 1	axis_I
ab	the angle of rotation axis w.r.t orbit	axis_beta
temprat	temperature ratio, $T_{\rm eff2}/T_{\rm eff1}$	
pm ($M_\odot$)	primary mass	
pr ($R_\odot$)	primary radius	
pk (km s^{-1})	primary semi-amplitude	from RV
ratrad	radius ratio, R_1/R_2	

q1	frac1, R_1/a	fractional radii (star1)
q2	frac2, R_2/a	fractional radii (star2)
	Fixed Parameters	
Nalpha1, Nbet1	No. of grid elements	star1
Nalpha2, Nbet2	No. of grid elements	star2
dphase (deg)	step size used in LC calculation	computation time
Tgrav1,Tgrav2	gravity darkening exponent	0.25 (radiative),0.08(convective)
ilaw	limb darkening law,1:linear,2:log	3:sqrt,4:quadratic
Disk	parameters not listed here	
Spot	parameters not listed here	
	KIC 9851944 (tuning parameters)	Comments
f1	0.432	$e \equiv 0.0$, $P \equiv 2.16390189$ d
f2	0.627	Tgrav1$\equiv$ 0.08,Tgrav2$\equiv$ 0.08
temprat	0.982	*l1*$\equiv$ 0.5, *l2*$\equiv$ 0.5,*T1*$\equiv$ 7026K
inclination	74.52°	$K_1 \equiv 121.95$ km s^{-1} (from RV)
T0	55341.03987	$q \equiv 1.014$ (from RV)
	KIC 8262223 (tuning parameters)	Comments
f1	0.314	$e \equiv 0.0$, $P \equiv 1.61301476$ d
f2	0.672	Tgrav1$\equiv$ 0.25,Tgrav2$\equiv$ 0.08
temprat	0.78	$K_1 \equiv 21.4$ km s^{-1} (from RV)
inclination	75.203°	$q \equiv 0.104$ (from RV)
T0	55431.716337	beaming effect included
l2	0.22	$T_{\rm eff1} =$*T1* is fixed (9128K)
	KIC 3230227 (tuning parameters)	Comments
T0	54958.7916213	$P \equiv 7.047106$ d
q1	0.085	Tgrav1$\equiv$ 0.25,Tgrav2$\equiv$ 0.25
q2	0.071	$K_1 \equiv 98.5$ km s^{-1} (from RV)
temprat	1.022	$q \equiv 0.95$ (from RV)
inclination	73.42°	*l1*$\equiv$ 1.0, *l2*$\equiv$ 1.0
eccentricity	0.60	$T_{\rm eff1} =$*T1* is fixed (8000K)
argper	293°	-

[1]The Roche lobe filling factor (f_1, f_2) is defined as the ratio of the radius of the star toward the inner Lagrangian point (L1) to the distance to L1 from the center of the star, $f = x_{point}/x_{L_1}$

[2]Keper contamination factor is defined as the fraction of flux from other sources

CHAPTER 5

δ Scuti/γ Doradus Stars in Eclipsing Binaries

5.1 Introduction

The analysis of eclipsing binaries (EBs) with the simple geometric effect and Kepler's 3rd Law offers us a means to determine accurate stellar masses and radii. Asteroseismology, the study of stars through their oscillation frequencies, also provides us with accurate stellar parameters. The pulsating eclipsing binaries are thus the best laboratories to test and refine our knowledge of stellar structure and evolution.

δ Scuti stars are radial and non-radial p-mode pulsators with frequencies from 4 to 60 d^{-1}. γ Doradus variables are main sequence high order g-mode pulsators with pulsation periods from 0.3 to 3 days. There are δ Scuti/γ Dor hybrids, where both p and g-modes are present (Grigahcène et al. 2010; Uytterhoeven et al. 2011). Recent space observations suggest that the hybrid behavior is normal in most of these stars and essentially all δ Scuti stars are found to show low frequency pulsations (Balona 2010).

The early studies of pulsating eclipsing binaries found many pulsating Algol (oEA) systems (Mkrtichian 2002, 2003), most of which are δ Scuti pulsators. Soydugan (2006) made a list of 25 confirmed such systems. Christiansen et al. (2007) discovered the first high amplitude δ Scuti star in an EB. These early studies are nearly all observational, with the detections of a few oscillation frequencies. Thanks to the space missions like *CoRoT* and *Kepler*, the number of known pulsating EBs increased greatly. The Kepler Eclipsing Binary Catalog[1] has more than 2600 entries, and many of them show signals of pulsations. Recent studies of pulsating EBs with δ Scuti/γ Doradus

[1] http://keplerebs.villanova.edu/

components include CoRoT 102918586 (Maceroni et al. 2013), KIC 11285625 (Debosscher et al. 2013), KIC 10661783 (Southworth et al. 2011; Lehmann et al. 2013), KIC 4844587 (Hambleton et al. 2013), DY Aqr (Alfonso-Garzon et al. 2014), KIC 3858884 (Maceroni et al. 2014), CoRoT 105906206 (da Silva et al. 2014), and KIC 8569819 (Kurtz et al. 2015a). These works mostly focus on the binary properties, with mass and radius determination to a few percent and detections of tens of pulsational frequencies. For a general review of pulsating EBs with other type of pulsators, please refer to Huber (2015) and Southworth (2015).

The asteroseismic modeling and mode identification of δ Scuti stars are notoriously difficult. The fast rotation generally requires 2-D structure models. There are efforts of seismic modeling of single δ Scuti stars using 1-D stellar models such as Suárez et al. (2005) on Altair, where rotation is treated as a perturbation to the second order. δ Scuti stars in eclipsing binaries are rarely modeled. The exception is the work by Maceroni et al. (2014) on KIC 3858884, in which the authors identified the g-modes with the Frequency Ratio Method (Moya et al. 2005) and identified a possible fundamental radial p-mode with the help of the frequency regularity. The seismic modeling using 2-D models is still the frontier of asteroseismology and mostly adiabatic (Reese et al. 2008; Deupree 2011; Ouazzani et al. 2012).

5.2 KIC 3858884

This section is based on my work published in Maceroni et al. (2014), A&A, 563, 59.

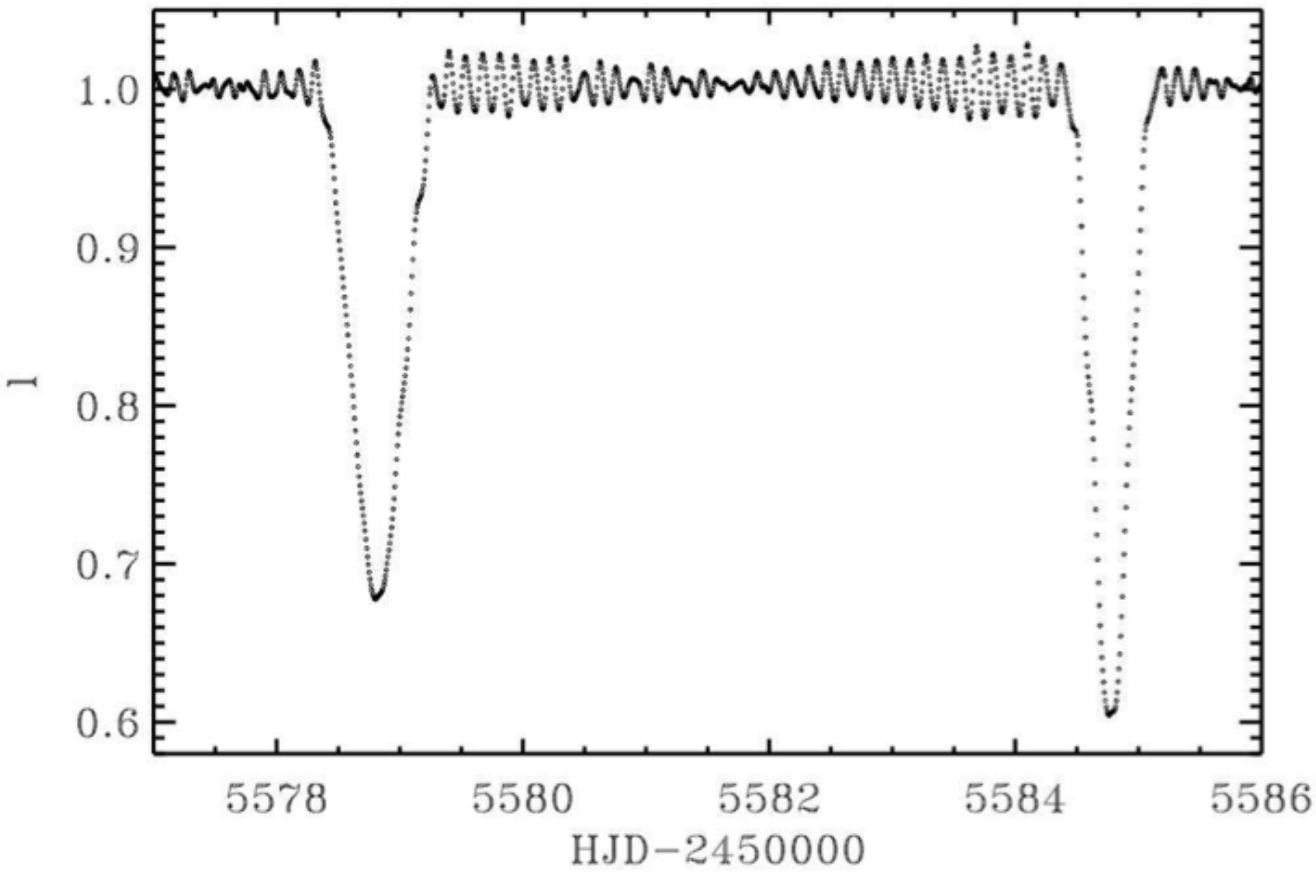

Figure 5.1 The detrended and normalized light curve of KIC 3858884 from *Kepler*, taken from Maceroni et al. (2014).

Table 5.1: Fundamental Parameters of KIC 3858884

Parameters	Primary	Secondary
Mass ($M_\odot$)	1.88 ± 0.03	1.86 ± 0.04
Radius ($R_\odot$)	3.45 ± 0.01	3.05 ± 0.04
$T_{\rm eff}$ (K)	6800 ± 70	6606 ± 70
$\log g$ (cgs)	3.63 ± 0.01	3.74 ± 0.01
	Oscillation Frequency(d^{-1})	Oscillation Amplitude (10^{-3})
f_1	7.2306 ± 0.0001	10.15 ± 0.21
f_2	7.4734 ± 0.0001	9.10 ± 0.15
f_3	9.8376 ± 0.0001	1.96 ± 0.07
f_4	7.5125 ± 0.0002	1.75 ± 0.06
f_5	6.7358 ± 0.0002	1.55 ± 0.05
f_6	9.5191 ± 0.0002	1.24 ± 0.04
f_7	14.7041 ± 0.0002	1.15 ± 0.04
f_8	11.7257 ± 0.0002	1.02 ± 0.04

KIC 3858884 is an eclipsing binary with an eccentric orbit ($e \approx 0.46$) and an orbital period of 25.952 days. This system was observed by *Kepler* satellite and was studied in depth by Maceroni et al. (2014). The fundamental parameters they derive are listed in Table 1. The binary components have very similar masses (1.88 and 1.86 $M_\odot$) and effective temperatures (6800 and 6600 K), but different radii (3.45 and 3.05 $R_\odot$). The de-trended light curve is shown in Figure 5.1. Obvious δ Scuti type pulsations can be seen, and the Fourier amplitude spectrum is presented in Figure 5.2.

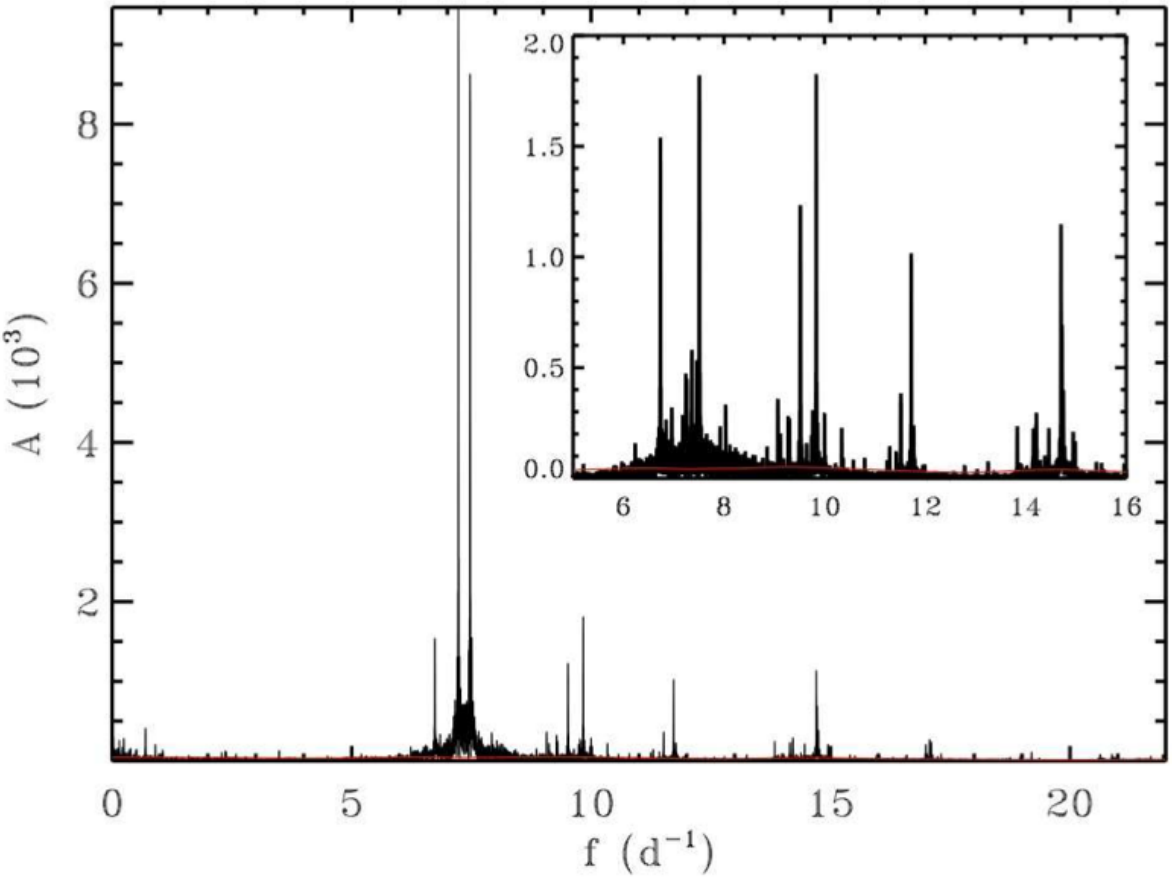

Figure 5.2 The oscillation spectrum of KIC 3858884, taken from Maceroni et al. (2014). The inset is a blow up of the region from 5 to 16 d^{-1} with two the strongest peaks pre-whitened. The frequencies seem to form about 4 clusters. The frequency spacing can be found in the next figure, showing the frequency difference histogram.

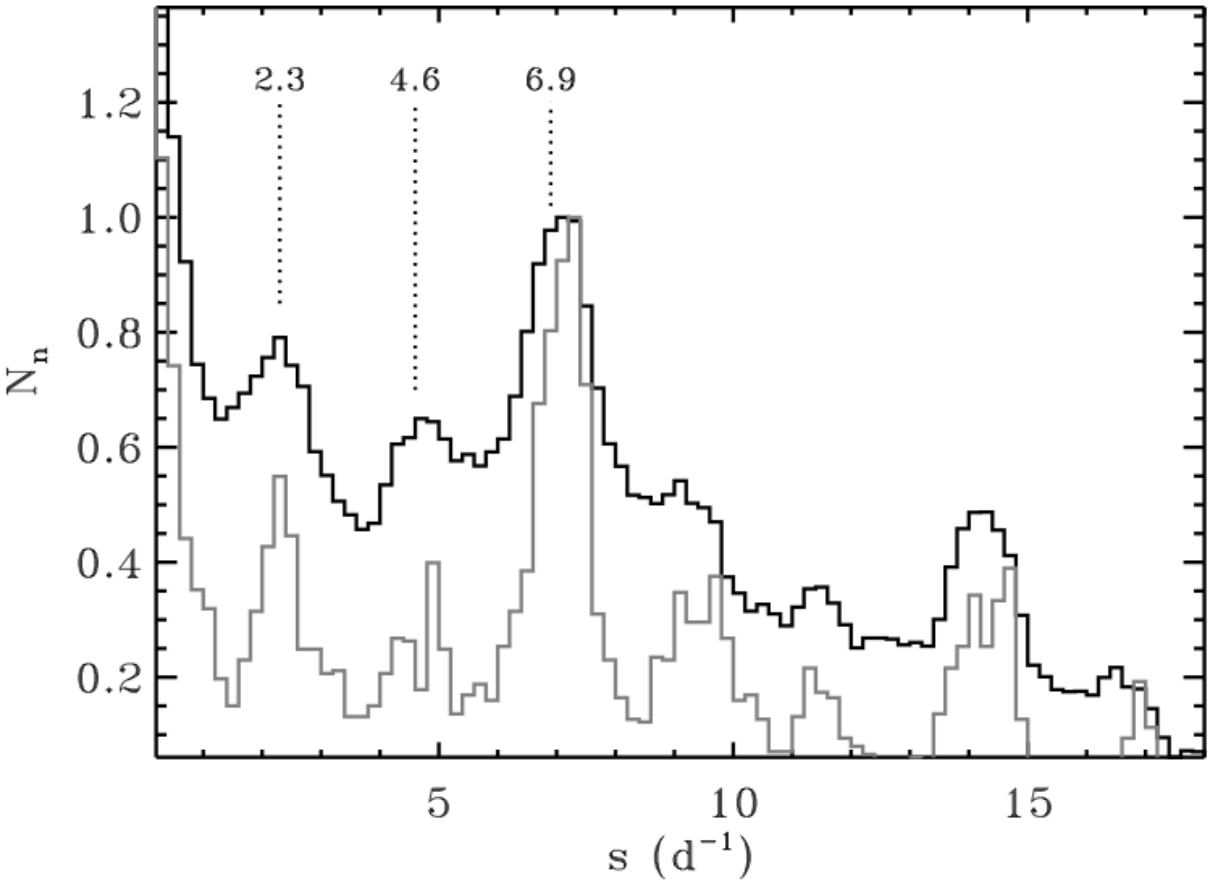

Figure 5.3 The histogram of frequency differences (every frequency was subtracted from all the others and the plot is restricted to the positive values). For easier comparison each histogram is normalized to the local maximum around 7 d^{-1}. The black line refers to the whole set of 403 frequencies, the gray line to those with amplitude larger than 10^{-4}. The histograms show that there is a preferred spacing around 2.3 d^{-1} which is clearly visible in both distributions. According to (Breger et al. 2009) the spacing corresponds to that between radial modes. The multiples of the spacing are also indicated by dotted lines.

As shown in Figure 5.2, the observed pulsational frequencies seem to form clusters. As Breger et al. (2009) pointed out, the numerous observed frequencies of δ Sct stars often appear in groups which cluster around the frequencies of radial modes and show some regularity in spacing. The grouping is probably related to mode trapping in the envelope which increases the probability of detection (Dziembowski & Krolikowska 1990). These modes are the non-radial counterparts of the acoustic radial modes and, for low l degree, have frequencies close to those of radial modes. In the case of δ Sct pulsators, theory predicts a much higher efficiency of mode trapping for $l = 1$ modes, see also Breger et al. (2009).

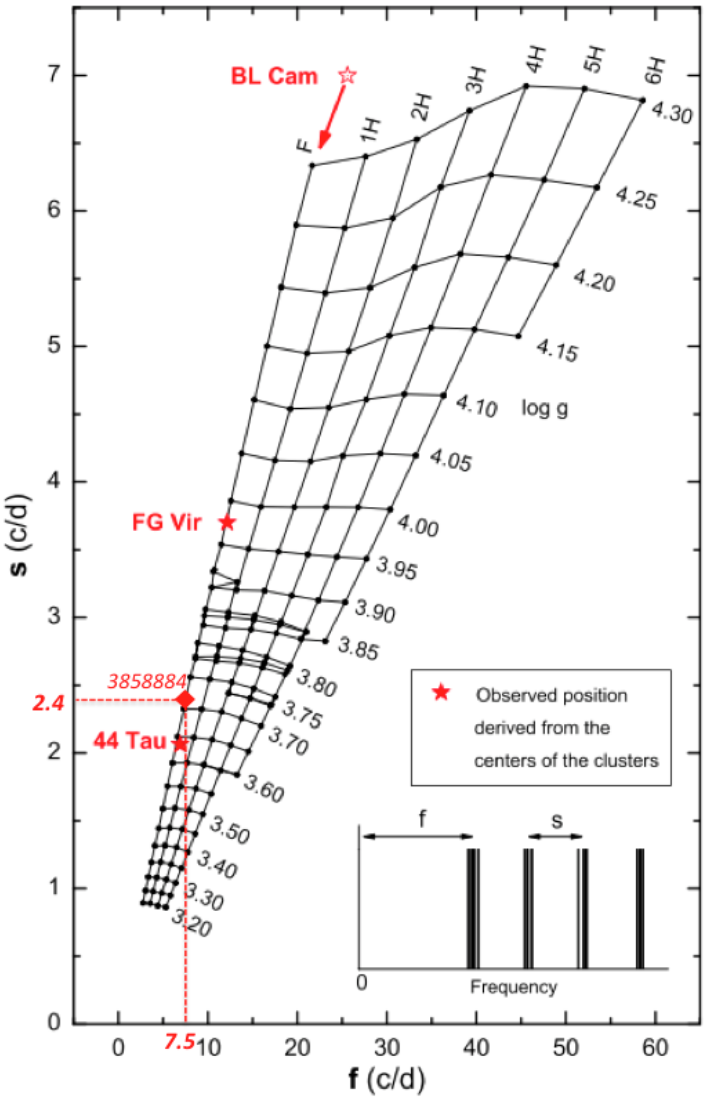

Figure 5.4 The $s-f$ (frequency spacing vs. lowest unstable radial mode frequency) diagram from Breger et al. (2009). The position of KIC 3858884 is marked by the red diamond. The grid shows the predicted lowest radial mode frequency and frequency spacing as functions of gravity ($\log g$) and harmonic overtone (top).

Breger et al. (2009) introduced a theoretical diagram displaying the average separation of the radial frequencies versus the frequency of the lowest-frequency unstable radial mode (Fig.

5.4, the $s-f$ diagram). The values are arranged on a grid with the different radial modes and surface gravity as parameters. The location of a pulsator in that diagram allows, therefore, to estimate its surface gravity (if the radial mode is assumed or known). The histogram of the frequency difference is shown in Figure 5.3 both for the whole set of frequencies and for those with an amplitude $A > 10^{-4}$ ($\sim$ 100 frequencies). There is an evident pattern, indicating a separation of the radial modes of $s \approx 2.3 - 2.4$ d^{-1}. This frequency regularity can be interpreted as the large frequency separation, i.e., the spacing between consecutive radial orders. One sees in fact a first peak at $2.3 - 2.4$ d^{-1} and others at approximately two and three times the value (the separation of radial modes is not exactly constant with increasing order). As we already have a precise estimate of the gravity, we can use the value of s to derive the frequency of the fundamental radial mode of the secondary, which is ~ 7.5 d^{-1}, i.e., very close to the value of f_2 (Table 5.1). We know that both f_1 and f_2 belong to the secondary component; if - as plausible - we assume that f_2 is its fundamental radial mode, then f_1 should be a non-radial one. The lower frequencies in the same domain could be either non-radial modes of the secondary or radial/non-radial modes of the primary component.

We see that the eclipsing binary nature of KIC 3858884 enables the identification of f_2 as the fundamental radial mode. The asteroseismic modeling of KIC 3858884 in Maceroni et al. (2014) did not take advantage of the observed frequency spacing at $2.3 - 2.4$ d^{-1}, and this should be performed in future studies of this system. This regularity is in fact a proxy for the mean stellar density as will be elaborated in later sections.

5.3 KIC 9851944

This section is partially based on my work published in Guo et al. (2016), ApJ, 826, 69.

5.3.1 Introduction

KIC 9851944 (K_p=11.249, α_{2000}=19:56:09.732, δ_{2000}=+46:39:40.19) was first discovered to be an eclipsing binary with an Algol type light curve in the All Sky Automated Survey (Pigulski et al. 2009) with an orbital period of 2.1639 days. It was later included in the Kepler Eclipsing Binary Catalog of Prša et al. (2011) and Slawson et al. (2011) as a detached eclipsing binary. Gies et al. (2012) calculated the eclipse times by using the long cadence *Kepler* light curve data from quarter 0 through quarter 9. They also noted that this system displays near harmonic pulsational variability, possibly on both stars, as evident in their grey scale residual images. Recently, Gies et al. (2015) updated their calculations by using all *Kepler* quarters. The $O-C$ curve is essentially flat around zero and shows no evidence of a third body or apsidal motion. They determined the orbital period as 2.16390177 $\pm$0.00000005 days from the primary eclipses and 2.16390178$\pm$0.00000004 days from the secondary eclipses. Conroy et al. (2014) reported the eclipse times of 1279 *Kepler* eclipsing binaries with short periods including KIC 9851944. Armstrong et al. (2014) used a model of the binary Spectral Energy Distribution (SED) to fit the photometry from Everett, Howell, & Kinemuchi (2012), Greiss et al. (2012a,b), and 2MASS (Skrutskie et al. 2006). They derived the effective temperature of the primary and the secondary as $T_{pri} = 6549 \pm 409$K and $T_{sec} = 6256 \pm 638$K.

5.3.2 Observations: Kepler Photometry and Ground-based Spectroscopy

KIC 9851944 was observed by the *Kepler* satellite from 2009 to 2013. Short cadence data (sampling rate of 58.8488 seconds) were obtained during Quarter (Q) 0, Q12 through 14 and Q16 − 17. In long cadence mode (29.4244 minutes sampling), there are data in every quarter from 0 to 17 except for Q7, Q11, and Q15[2].

[2]The *Kepler* Data Release (DR) 23 was used here. Note the short cadence data in the DR24 cannot be used in projects requiring high photometric precision. There is another issue related to the smear corrections of the short cadence light curves in all data releases announced on 2016 Feb 5. We evaluated this effect by comparing the target pixel files of the long cadence data (which are not affected) with those of short cadence data and found that this effect is negligible in the case of KIC 9851944.

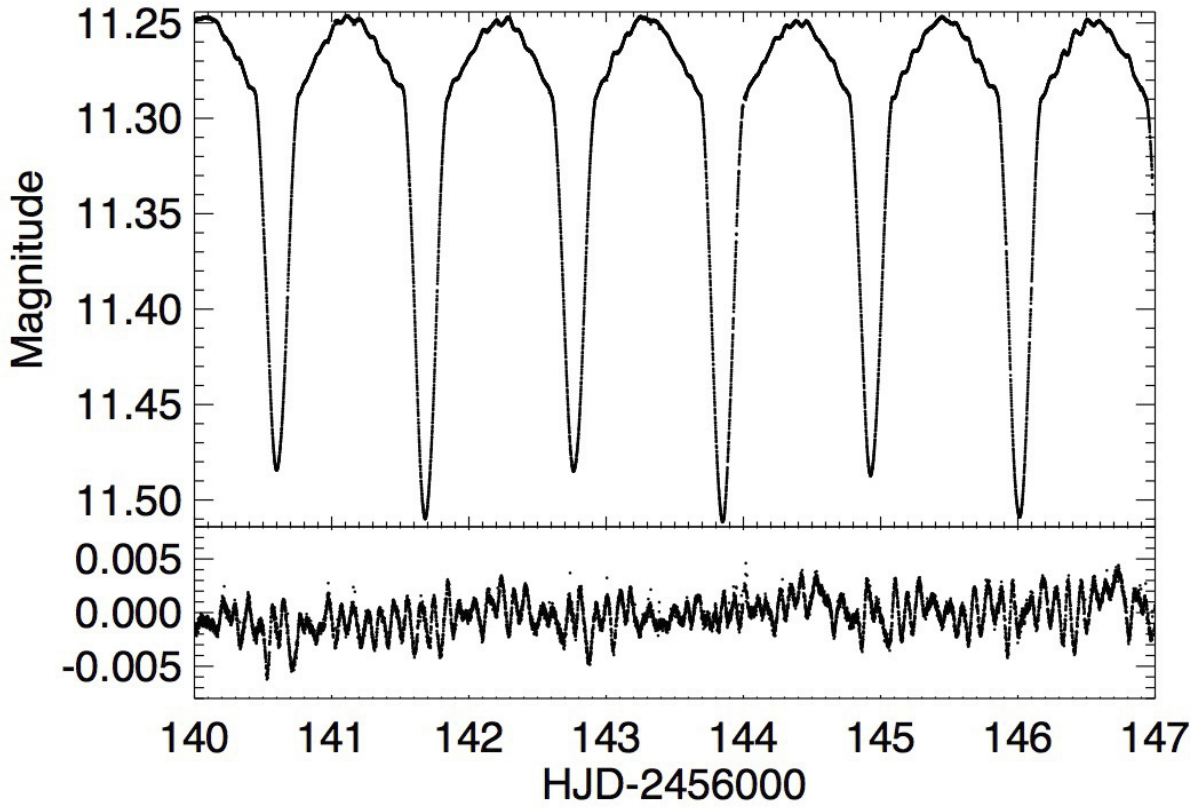

Figure 5.5 The de-trended light curve of KIC 9851944 during Q13 from short cadence measurements. The lower panel shows the pulsations after subtracting the best binary light curve model.

A preliminary examination of the *Kepler* light curves (Figure 5.5) shows that this eclipsing binary has evident ellipsoidal variations and pulsations with periods ≈ 2 hours. The Simple Aperture Photometry (SAP) light curves were used for analysis. The outliers were removed by a 5 sigma criterion. Median differences in quarters were normalized to the same flux. In order to remove the long term trend, a spline curve was used to fit the binned light curve of the out-of-eclipse envelope of the original light curve. This was the method used in Gies et

al. (2012) and was similar to the de-trending process in Hambleton et al. (2013) who used a polynomial fit to the out-of-eclipse envelope of the light curve. We de-trended the raw light curve of each month and chose the best bin size as the one that minimizes standard deviation of the out-of-eclipse part of the folded light curve. If the dataset contains gaps, we treat each segment separately. We also checked the Fourier transform of the spline trend to make sure we did not remove any intrinsic variations of this system.

As part of the program of spectroscopic follow up studies to the 41 *Kepler* eclipsing binaries in Gies et al. (2012), we obtained 10 moderate resolution spectra with the R-C Spectrograph on the Kitt Peak National Observatory (KPNO) 4-meter Mayall telescope and 3 spectra from the DeVeny Spectrograph on the 1.8-meter Perkins telescope at Anderson Mesa of Lowell Observatory between 2010 and 2011. We used the BL380 grating (1200 grooves mm^{-1}) on the R-C Spectrograph at KPNO and this provided wavelength coverage of $3930-4610$Å. For the DeVeny Spectrograph at Lowell, a 2160 grooves mm^{-1} grating was used and the wavelength range was $4000-4530$Å. Both instrument setups provided a resolving power of $R = \lambda/\delta\lambda \sim 6000$. The calibration exposures at KPNO used HeNeAr lamps and those at Lowell used HgNeSrCd Pen-Ray lamps. Flat-field and bias spectra were obtained nightly. Standard IRAF[3] routines were used to reduce, extract, and calibrate each spectrum. However, wavelength calibrations for spectra from Lowell Observatory were performed using late-giant stars with known velocities as described in Matson et al. (2016) since the available Pen-Ray lamps provide insufficient emission lines for a dispersion solution. Finally, all spectra

[3]IRAF is distributed by the National Optical Astronomy Observatory, which is operated by the Association of Universities for Research in Astronomy (AURA), Inc., under cooperative agreement with the National Science Foundation

were normalized to the local continuum and put onto a common heliocentric wavelength grid with uniform $\log \lambda$ spacing. At the observed wavelength range, the mean signal-to-noise ratios (S/N) of the KPNO spectra were about $70 - 120$ and the Lowell spectra have lower S/N of about $30 - 40$.

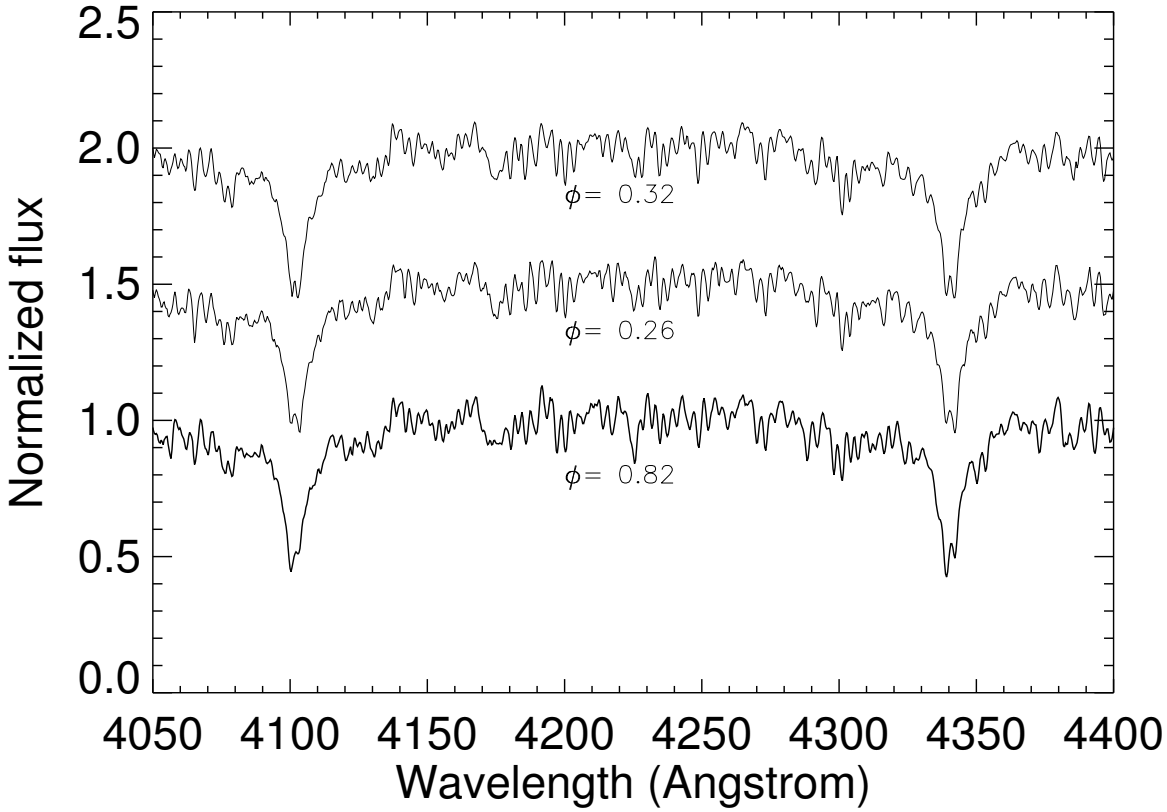

Figure 5.6 The observed composite spectra in the region between Hδ and Hγ lines. The two components are resolved in the cores of these Balmer lines at times of the velocity extrema. The orbital phases (ϕ) are labeled for each spectrum. For better visibility, the spectra at $\phi = 0.26$ and $\phi = 0.32$ have been shifted upwards by 0.5 and 1.0, repectively.

The reduced spectra showed that the two components have similar flux contribution and spectral type. As shown in Figure 5.6, the clear double lines in the composite spectra indicated that the two components are resolved near the Doppler shift extrema.

5.3.3 Data Analysis

5.3.3.1 Orbital Elements and Tomographic Reconstruction

The observed composite spectra were cross-correlated with two templates for the primary and secondary star to get radial velocities (RVs) and their uncertainties (Zucker 2003) which are listed in Table 5.2. The templates were constructed from the UVBLUE spectral grid (Rodríguez-Merino et al. 2005) using preliminary parameters based on the Kepler Eclipsing Binary Catalog of Slawson et al. (2011). UVBLUE is a library of theoretical stellar spectra computed with the ATLAS9 and SYNTHE codes developed by R. L. Kurucz, with a spectral resolving power $\lambda/\Delta\lambda = 50,000$. It covers the short wavelength range ($850-4700$Å) which is ideal for our studies. The RVs derived from KPNO and Lowell spectra have similar statistical uncertainties. However, the Lowell RVs show larger systematic uncertainties which is likely due to the imprecise wavelength calibration.

Table 5.2: Radial Velocities

Time (BJD-2400000)	Phase	V_r(pri) (km s^{-1})	V_r(sec) (km s^{-1})	Observation Source
55367.6938	0.32	-113.5 ± 3.2	105.2 ± 4.7	KPNO
55368.6869	0.78	117.4 ± 3.0	-117.8 ± 4.7	KPNO
55368.7235	0.79	115.9 ± 3.2	-109.6 ± 4.8	KPNO
55368.7705	0.82	108.5 ± 3.2	-105.1 ± 4.9	KPNO
55368.8208	0.84	95.7 ± 3.0	-99.5 ± 4.3	KPNO
55369.6816	0.24	-128.9 ± 3.2	114.9 ± 4.8	KPNO
55369.7259	0.26	-126.8 ± 3.4	118.7 ± 5.5	KPNO

55369.7869	0.29	-120.9 ± 3.2	117.2 ± 4.6	KPNO
55369.8234	0.30	-120.3 ± 3.1	111.5 ± 4.3	KPNO
55434.8181	0.34	-106.6 ± 2.7	99.1 ± 4.1	KPNO
55449.9141	0.31	-101.3 ± 3.1	136.4 ± 4.7	Lowell
55463.8100	0.74	129.4 ± 3.2	-104.3 ± 5.1	Lowell
55755.9599	0.75	106.6 ± 3.2	-127.9 ± 4.9	Lowell

At first we used templates with atmospheric parameters and projected rotational velocity of $T_{\rm eff}, \log g, v \sin i$ =[6200K, 4.4, 23 km s^{-1}] for the primary, and [6000K, 4.4, 23 km s^{-1}] for the secondary, with a flux ratio of F_2/F_1=0.72 and solar metallicity. The templates were later updated to [7026K, 4.0, 52 km s^{-1}] and [6950K, 3.7, 70 km s^{-1}] for the primary and secondary, respectively, and with a flux ratio of 1.3 after we performed the preliminary analysis of the separated component spectra (see below).

We derived the orbital elements by fitting the radial velocities with the non-linear, least squares fitting program of Morbey & Brosterhus (1974). The orbital period was fixed to the value in Gies et al. (2012) as $P = 2.16390189 \pm 0.00000008$ days, which was the same within uncertainties as from later eclipse time measurements (Gies et al. 2015). The fitting parameters included T_0 (time of maximum velocity), K_1 (semi-amplitude velocity of the primary), γ (system velocity) for the primary star and K_2, T_0 and γ for the secondary. The eccentricity was fixed to 0.0. We search for a circular orbital solution since the *Kepler* light curve suggests that the eccentricity is essentially zero. The system is probably old enough to have completed the circularization.

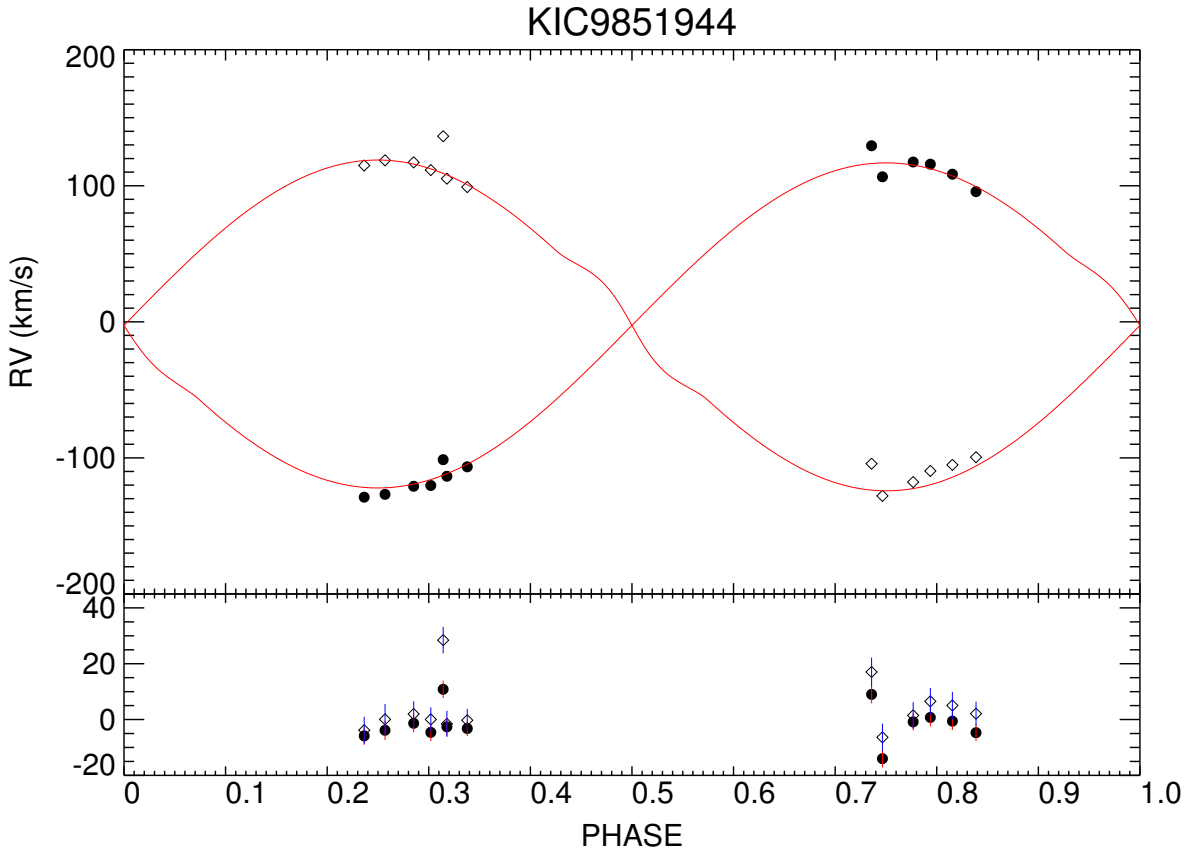

Figure 5.7 The radial velocities (V_r) derived from the cross correlation technique and the best fitting model from ELC. The primary and secondary are indicated by the filled dots and open diamonds, respectively. The bottom panel shows the residuals.

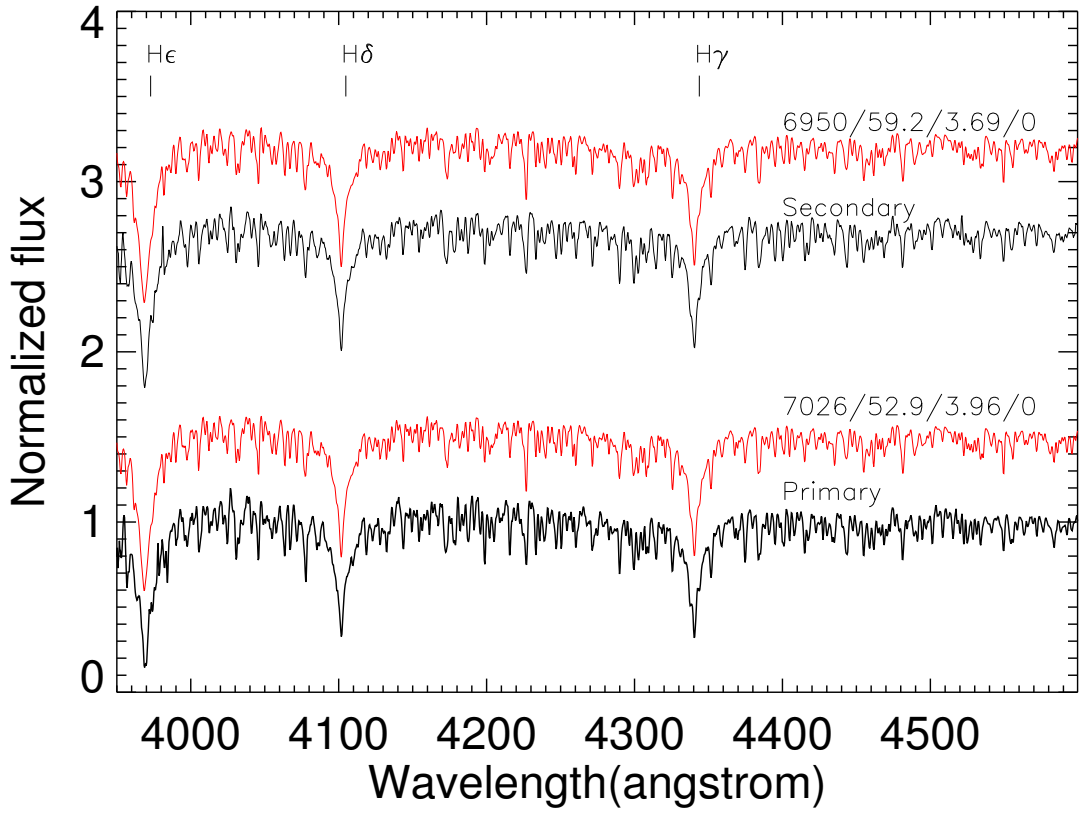

Figure 5.8 The reconstructed component spectra of the two components (primary : lower part; secondary : upper part) (black) and the corresponding best synthetic spectra from UVBLUE (red). The effective temperature ($T_{\rm eff}$), projected rotational velocity ($v \sin i$), surface gravity ($\log g$) and metallicity ([Fe/H]) are labeled above the synthetic models.

The best fitting orbital solutions based on all RVs are shown in Figure 5.7. These solutions were used to determine the pixel shifts for each spectrum. We then applied the Doppler tomography program (Bagnuolo et al. 1994) to get the individual spectrum of each component (Fig. 5.8). In the reconstruction process, we treated the mean flux ratio of

the two components in the observed spectral range as a free parameter (F_2/F_1), and the reconstructed spectra were subsequently compared with synthetic spectra from the UVBLUE library. The best mean monochromatic flux ratio was determined as the one that gives the minimum chi square from the spectra residuals of both the primary and the secondary, which was $F_2/F_1 = 1.34 \pm 0.03$. The spectra from UVBLUE were normalized and convolved with the instrumental broadening and rotational kernel (Gray 2008) before comparing with observational spectra.

Our goal is to determine the stellar properties of each star from the reconstructed spectra. It is helpful to set the gravity $\log g$ in the analysis from the masses and radii determined from a combined spectroscopic and light curve fit (see section 5.3).

Table 5.3: Fundamental Parameters of KIC 9851944

Parameters	Primary[2]	Secondary[2]	Primary[3]	Secondary[3]
$T_{\rm eff}$ (K)	7026 ± 50	6950 ± 50	7018 ± 76	6881 ± 70
$\log g$ (cgs)	3.96[1]	3.69[1]	3.96[1]	3.69[1]
$v \sin i$ (km s^{-1})	53 ± 7	59 ± 3	56 ± 10	71 ± 10
[Fe/H]	0.0[a]	0.0[a]	-0.06 ± 0.05	-0.04 ± 0.05

[1]Fixed.
[2]From genetic algorithm.
[3]From Levenberg-Marquardt algorithm.

An initial light curve fitting was performed with ELC (see next section for details) and the primary velocity semi-amplitude K_1, systemic velocity γ, and mass ratio were fixed to the values from the radial velocity curve fitting mentioned above. $T_{\rm eff}$ of the primary was initially fixed to the value from Armstrong et al. (2014) and adjusted later. We found that in the light curve fitting process, when we changed the primary temperature to 6200K and 7200K, the best fitted inclination only changed by less than 0.4%, and the $\log g$ only changes by 0.9%. Thus, the $\log g$ values from the light curve and radial velocity curve modeling were more accurate and so were adopted in fitting the spectra by atmosphere models. A well known problem in spectroscopic analysis is the parameter degeneracy. While the effective temperature and projected rotational velocity $v \sin i$ are usually well constrained, the parameters $\log g$ and metallicity are more difficult to pinpoint and both correlate with $T_{\rm eff}$. Thus, setting $\log g$ from the combined analysis will greatly reduce the parameter degeneracy. This procedure was also adopted by Maceroni et al. (2014).

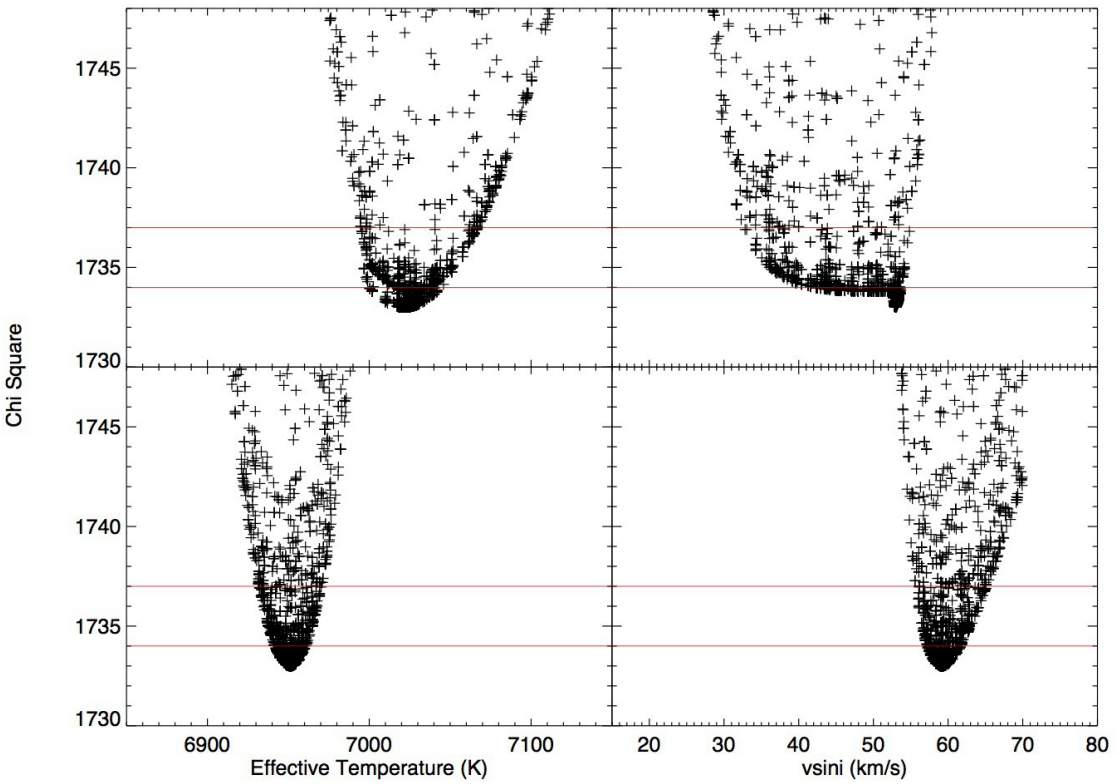

Figure 5.9 The χ^2 of stellar atmosphere parameters, $T_{\rm eff}$ and $v \sin i$ from the genetic algorithm. The gravity $\log g$ is fixed to ELC values of 3.96 and 3.69, and the metallicity is fixed to the solar value. The χ^2 have been scaled so that $\chi^2_{min} \approx \nu$ (the degree of freedom). The two red lines indicate the level of $\chi^2_{min} + 1.0$ and $\chi^2_{min} + 4.0$. The upper (lower) panels correspond to fits of the reconstructed primary (secondary) spectra.

To get the atmospheric parameters of both components, we adopted two different techniques. First, the genetic algorithm *pikaia* (Charbonneau 1995) was used. This optimizer is able to explore a broad parameter space and is good at finding the global minimum. The fitting parameters were $T_{\rm eff}$ and $v \sin i$, while the logarithmic metallicity referenced to the Sun [Fe/H] was fixed to 0.0. The parameters were allowed to vary in broad ranges. The $T_{\rm eff}$ boundaries for the primary and the secondary star were $6500 - 7500$K and $6200 - 7200$K, respectively. The $v \sin i$ values of both stars were allowed to very from 10 to 100 km s^{-1}. In Figure 5.9 we show the χ^2 as a function of atmospheric parameters ($T_{\rm eff}$, $v \sin i$) of both stars. The χ^2 has been scaled so that $\chi^2_{min} \approx \nu$, where ν is the degree of freedom. We use the intersections of the lower envelope of χ^2 samples and the level of $\chi^2_{min} + 1$ as the $\pm 1\sigma$ parameter bounds, the derived uncertainties are shown in Table 5.3. Note this approach probably underestimates the uncertainties due to parameter correlations as the residuals are not independent Gaussian distributions. The 1σ errors of effective temperatures are quite small (25K and 15K for the primary and secondary, respectively), and we conservatively adopt one tenth of the UVBLUE grid step size ($\Delta T_{\rm eff} = 50$K) as the final uncertainties. A comparison of the reconstructed component spectra with synthetic spectra is shown in Figure 5.8.

In the second approach, we determine the atmospheric parameters successively (except for the $\log g$, which is always fixed to the value determined from the combined fit). First, a preliminary tomographic reconstruction was performed with the effective temperatures of the two components fixed to [7026K, 6900K] and an estimated mean flux ratio of 1.3.

Since the hydrogen lines are dominated by Stark (pressure) broadening and less sensitive to rotation, we selected six different spectral ranges with least blended metallic lines (4010 − 4040, 4041 − 4080, 4130 − 4210, 4220 − 4250, 4260 − 4290 Å) and determined the best $v \sin i$ by comparing the reconstructed component spectra with a grid of synthetic template spectra of different rotational broadening. The optimal values of $v \sin i$ are found to be [55.8 km s^{-1}, 70.5 km s^{-1}], which are not sensitive to the initial fixed value of effective temperature and flux ratio. Then the $v \sin i$ estimates are fixed to the best values and the spectral separations are performed again over a grid of mean flux ratios, and for each flux ratio we determine the [Fe/H] and effective temperature by minimizing the χ^2 with a Levenberg-Marquardt algorithm implemented in the package MPFIT (provided by Craig B. Markwardt, NASA/GSFC). The error estimates from MPFIT are formal errors based on the covariance matrix which are probably underestimated. The final results are summarized in Table 5.3.

The flux ratio and atmospheric parameters from the above two techniques agree very well. We adopted the projected rotational velocities from the second method which are very close to the expected synchronized values. Please note the ELC synchronous rates are given in Table 5.4. According to Zahn's (1977) theory of radiative damping of dynamic tides for early-type close binaries, the orbital circularization timescale t_{cir} follows the relation (Khaliullin & Khaliullina 2010): $1/t_{cir} = 1/t_{cir1} + 1/t_{cir2}$, where $t_{cir,i} = 10.5(GM_i/R_i^3)^{0.5} q(1 + q)^{11/6} E_{2,i}(R_i/a)^{10.5}$ with $i = 1, 2$. If we adopt the averaged tidal torque constant E_2 of a $1.8 M_\odot$ star on the main sequence $\approx 10^{-8.37}$(Claret 2004), then the calculated circularization

timescale for a binary system like KIC 9851944 is about 6×10^8 years. The synchronization timescale is an order of magnitude shorter than the circularization timescale and both timescales are shorter than the age of this system (see the isochrone fitting in Section 5.4). This system is expected to have synchronized rotation. Our derived $v \sin i$ values, especially those from the metal lines using the Levenberg-Marquardt algorithm, are very close to the synchronized value within uncertainties of about 0.8σ and 0.3σ. In the later binary modeling process, we adopt this synchronization assumption. The observed projected rotational velocities are lower than the average $v \sin i$ in single δ Scuti stars which is around 120 km s^{-1}. It is plausible that diffusion can take place more easily for δ Scuti stars within close binaries and this may explain the observed non-solar metallicity in some close binaries. However, for KIC 9851944 the derived metallicity is essentially within the 1σ error box of solar.

5.3.3.2 Binary Modeling

We use the *Kepler* short cadence data to perform the light curve modeling. There are 15 months of SC data, one month in Q0, three months each in Q12, Q13, Q14, Q16 and two months in Q17. We fit the light curve of each month separately as this will account for the possible systematic uncertainties from imperfect de-trending and differences in the photometric aperture definition. The Eclipsing Light Curve (ELC) code (Orosz & Hauschildt 2000) is used to find orbital and astrophysical parameters for KIC 9851944. ELC utilizes the Roche model and NextGen model atmospheres to synthesize the binary light curve with the effects of gravity darkening and reflection included. This code[4] has been used to analyze

[4]This proprietary Fortran code is maintained by Jerome Orosz. Detailed documentation is available on request.

Kepler eclipsing binaries (Bass et al. 2012; Sandquist et al. 2013; Rawls et al. 2016), heartbeat stars (Welsh et al. 2011), transiting exoplanets (Wittenmyer et al. 2005), and circumbinary planets (Orosz et al. 2012), etc. The version revised especially for *Kepler* data integrates the stellar Spectral Energy Distribution in the *Kepler* passband and also incorporates subtle effects such as contamination, relativistic beaming, and finite integration. ELC can fit the radial velocities (RVs) and the light curves (LC) simultaneously, as done in Williams (2009).

Due to the sharp difference between the quality of *Kepler* photometry and our spectroscopic data, we decide to fit the RVs and LC separately. The RVs were fit first as mentioned in the last section and the corresponding parameters K_1 (velocity semi-amplitude), q (mass ratio), and γ (system radial velocity) were used to fit the LC data in ELC as these parameters have no affect on the light curves (only very weakly on q). After fitting the light curve, the output RV curves from ELC are compared with observed RVs to make sure we have a consistent model.

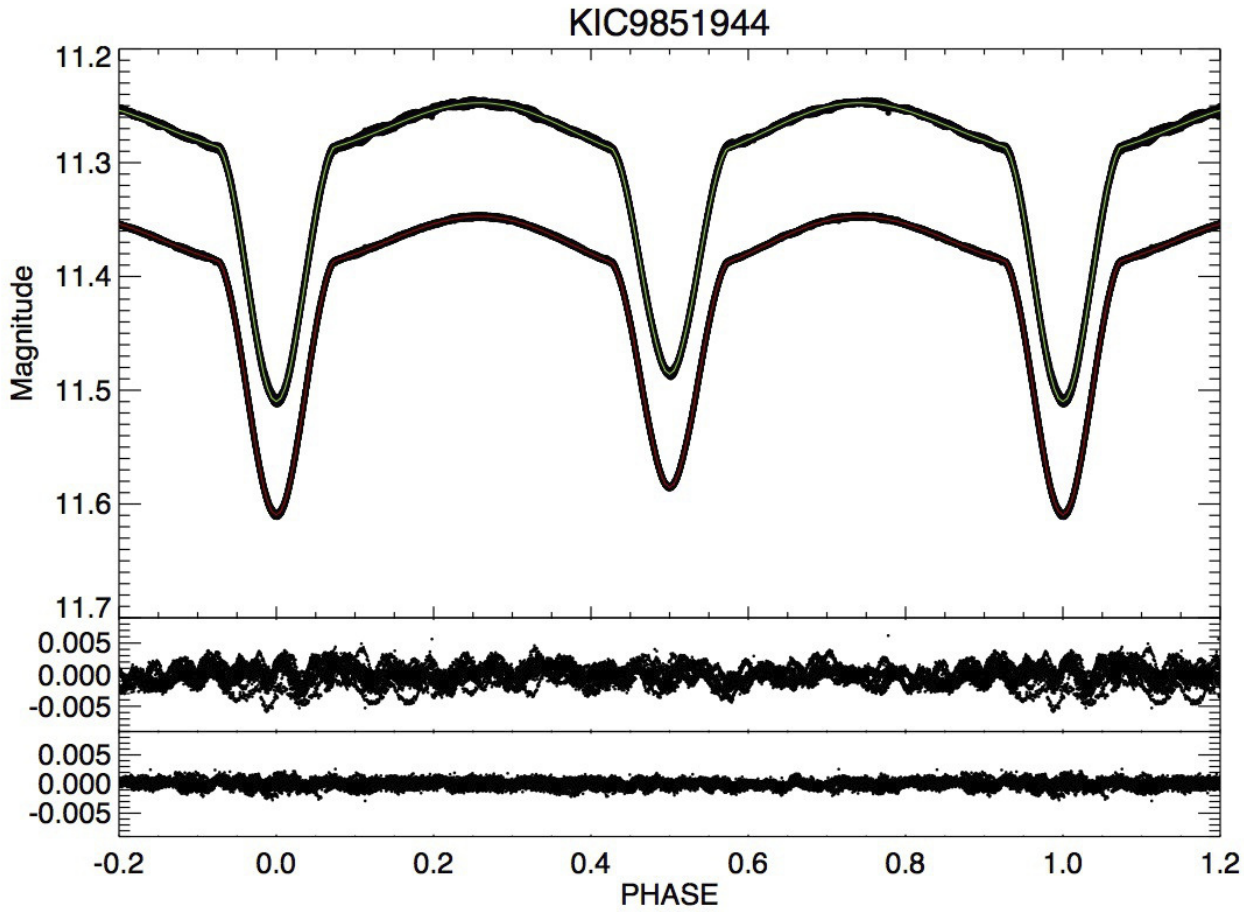

Figure 5.10 A fit to the eclipsing binary light curve of KIC9851944 before (above) and after (below) the pre-whitening of pulsations from the dataset of quarter Q12b. The model light curves are indicated by the green and red solid lines. The lower two panels show the corresponding residuals.

The original de-trended *Kepler* light curve is fit first and the residuals still show strong signals of pulsations (Fig. 5.10). To pre-whiten the pulsational signal in the light curve, we use the SigSpec package (Reegen 2007) to find significant frequencies in the Fourier spectrum of the residuals down to a signal to noise ratio ≈ 4 (spectral significance in SigSpec ≈ 5).

We compare the Fourier spectrum of the residuals in consecutive months, and the peaks that appear in both datasets within the frequency resolution were selected. This can prevent us from selecting frequencies that are due to imperfect de-trending and binary light curve modeling. We only choose the frequencies that have amplitudes larger than about 40 ppm, because there are many lower peaks below this level that may be unrelated to pulsation. The pulsation signal is then represented by a sum of sinusoids of these selected frequencies and is subtracted from the original *Kepler* light curves.

This pre-whitened light curve is fit with ELC again. We use both the genetic algorithm based on *pikaia* (Charbonneau 1995) and the Monte Carlo Markov Chain (MCMC) (Tegmark et al. 2004) to find the global minimum in parameter space. The parameters for the light curve fitting are i (orbital inclination), f_1 (filling factor of the primary), f_2 (filling factor of the secondary), T_0 (time of the secondary minimum) [5] , and $T_{\rm eff2}/T_{\rm eff1}$ (effective temperature ratio). The Roche lobe filling factor (f_1, f_2) is defined as the ratio of the radius of the star toward the inner Lagrangian point (L1) to the distance to L1 from the center of the star, $f = x_{point}/x_{L_1}$. The filling factors determine the stellar radii, and they are the functional counterpart of the surface effective potential (Ω_1, Ω_2) in W-D program (Wilson & Devinney 1971) and PHOEBE (Prša & Zwitter 2005). The orbital period is also adjusted at first and fixed later on since the converged value is almost identical to the values given by Gies et al. (2012). The primary effective temperature is fixed to the value from spectroscopy as $T_{\rm eff1} = 7026K$. The Kepler contamination factor k is the percent of contamination light from

[5]Throughout the paper, the epoch we adopted is the time of primary minimum T_0. The only exception is during the light curve fitting process where ELC uses T_0 as the time of secondary minimum.

other stars in the photometric aperture. In ELC, this effect is accounted for by subtracting an offset determined by multiplying the median value of the light curve by $k/(1-k)$. For KIC 9851944, this k factor, taken from the *Kepler* Input Catalog, varies from 0.005 to 0.01 in different quarters and has only negligible effect on the light curve modeling. More than 10^5 models are calculated and the corresponding parameters and their corresponding χ^2 are recorded. The Markov chains generally converge after about a few 10^4 iterations. The histogram for each fitting parameter and the correlation of each parameter pair is shown in Figure 5.11.

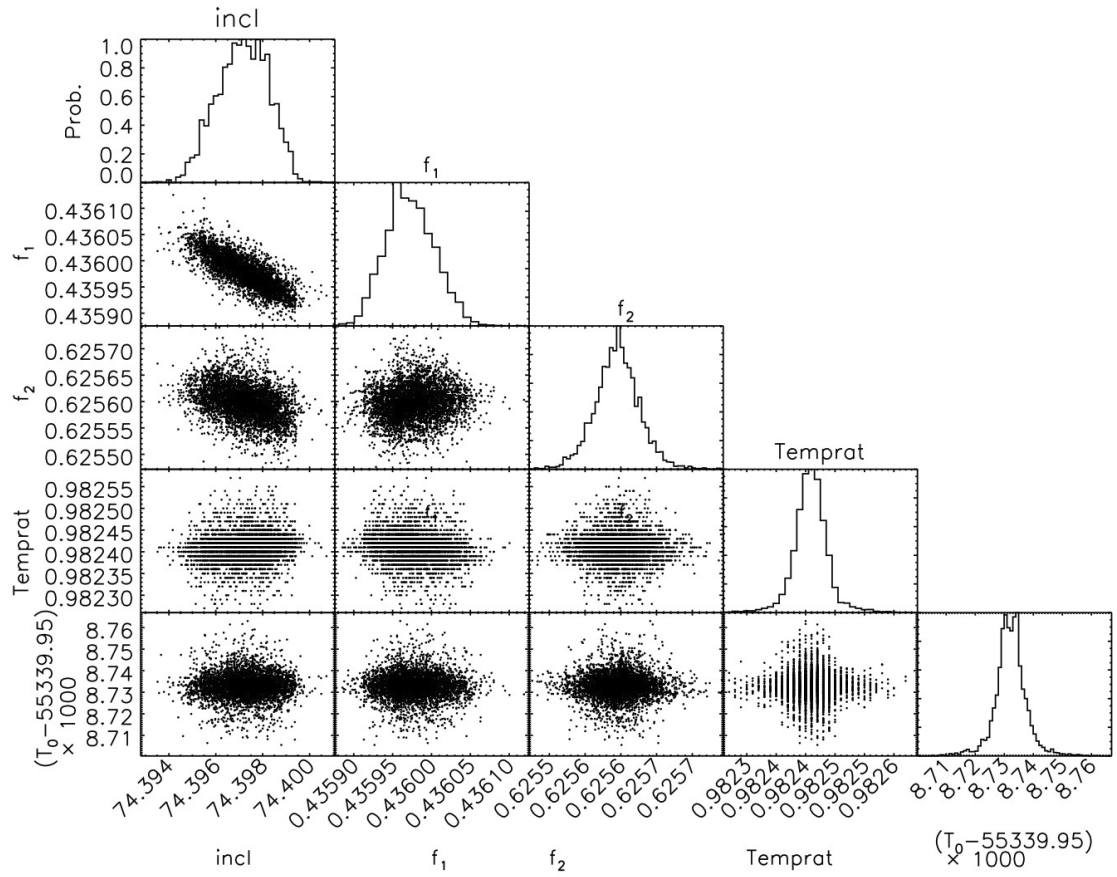

Figure 5.11 The parameter correlations from the MCMC analysis of dataset Q14. The fitting parameters are *incl* (inclination), f_1, f_2 (filling factor), temprat ($T_{\rm eff,2}/T_{\rm eff,1}$) and T_0 (time of secondary minimum). The histograms have been normalized to have a maximum peak of unity. There is a clear correlation between inclination and filling factor, as larger filling factor can be accounted for by a smaller inclination.

We adopt the final fitting parameters as the average value of all MCMC solutions in

different quarters, and their standard deviations as the final systematic error bar. Note the statistical error bars from the light curve fitting in each quarter are much smaller than the systematic error bars we adopted from the quarter-to-quarter differences.

Our final result shows that a circular orbit with two synchronized rotating components can fit both the light curve and radial velocity curve very well.

We define the distortion to the shape of the star as $D = (R_e - R_p)/R_e$, where R_p and R_e are polar radius and the radius pointing to L1, respectively. The secondary star fills the Roche lobe more and D is much larger (8.5%) compared with that of the primary (2.7%).

The circular orbit solution is sufficient, as our final residuals of light curve fit still show pulsations at 10^{-3} magnitude level. The circular orbit solution will be undistinguishable with a plausible better fit with very small eccentricity. We explore the possibility of smaller eccentricity of this system by examining the published eclipse timings in Gies et al. (2015) and Conroy et al. (2014). For a circular orbit, the phase difference between the secondary and primary eclipse times ($\delta\phi$) is exactly 0.5, and a deviation from this value can be shown to be equal to $\frac{1}{\pi}(1 + \frac{1}{\sin i})e\cos\omega$ (Kallrath & Milone 2009) where i is the orbital inclination. This can give us a lower limit on the eccentricity. For KIC 9851944, the median $0.5 - \delta\phi$ of all cycles is 0.000057 and this suggests $e \geq |e\cos\omega| \approx 0.0001$. Strictly speaking, the time difference between the secondary and primary eclipse times is also affected by the light travel time effect, which is primarily a function of semi-velocity amplitude and mass ratio (see eq. 3 in Bass et al. 2012). Since the mass ratio of KIC 9851944 is very close to 1.0, this light travel effect is very small (0.3 seconds) and can be neglected.

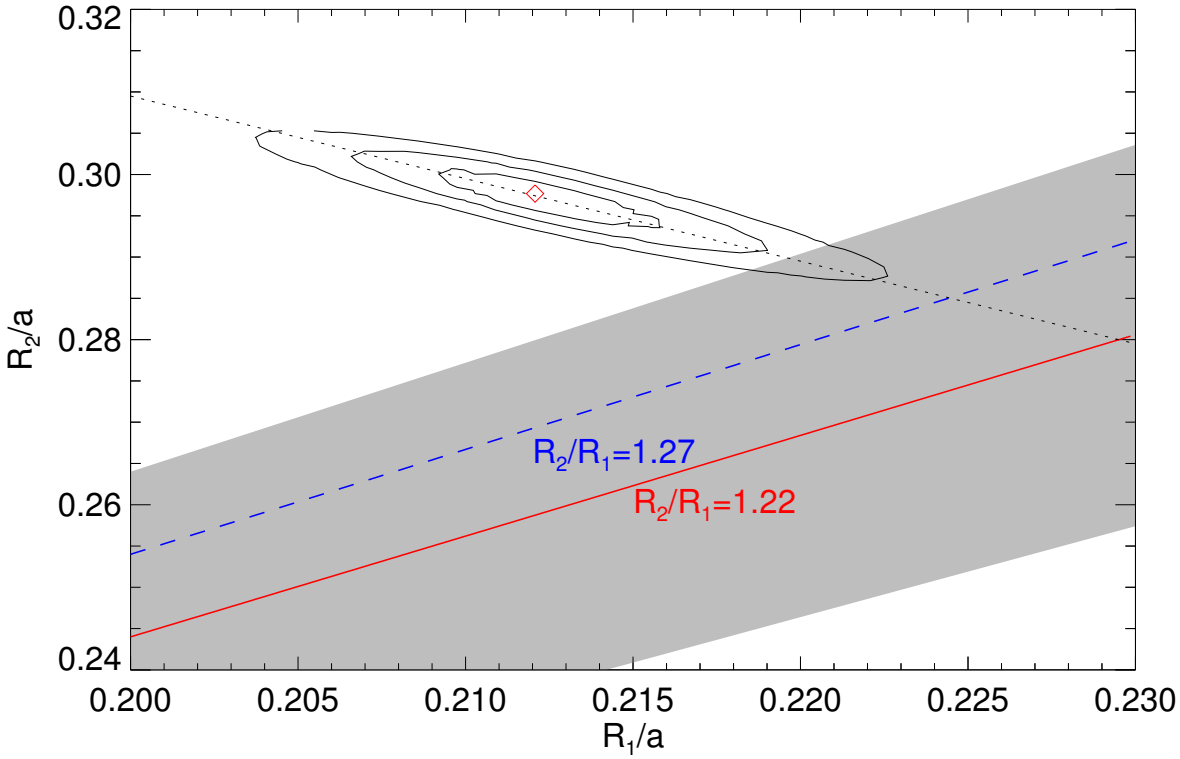

Figure 5.12 The radius ratio from spectroscopy and binary modeling. The contours show the 1σ, 2σ, and 3σ credible regions of the radius R_1/a and R_2/a from the light curve modeling. The final adopted value is indicated as the diamond. The dark dotted line which crosses the contours corresponds to $R_1/a + R_2/a = 0.51$. It indicates the valley of possible solutions for partial eclipsing systems from the light curve modeling. The radius ratio from spectroscopy is $R_2/R_1 = 1.22 \pm 0.05$, shown as the red solid line, and the gray shaded area is the corresonding 2σ credible region. The blue dashed line shows the ratio of $v \sin i$

To check if the results from spectroscopy and the binary light curve modeling are consistent (Rozyczka et al. 2014), we show the radius ratio of two stars in Figure 5.12. We obtain a mean flux ratio $F_2/F_1 = 1.34 \pm 0.03$ from the blue spectra (at $\approx$ 4275Å) in the spectral tomography analysis. Thus, we can calculate the observed flux ratio from the projected areas and surface flux ratio per unit area (f_2/f_1) assuming the stars are spherical: $F_2/F_1 = (f_2/f_1)(R_2/R_1)^2$, where $f_2/f_1 = 0.92$ is from the Kurucz models using the atmosphere parameters of the two stars. The radius ratio derived this way is $R_2/R_1 = 1.22 \pm 0.05$, and this is shown as the red solid line and the corresponding 2σ credible region is indicated as the gray shaded region. Another way to estimate the radius ratio is directly from the $v \sin i$ measurements since the system is probably synchronized, so that $R_2/R_1 = (v \sin i_2)/(v \sin i_1) = 71/56 = 1.27 \pm 0.29$, and this ratio is indicated as the blue dashed line. The radius ratio from the binary modeling (corresponding to the filling factor ratio) is indicated by the red diamond and the contours. The result $R_2/R_1 = 1.40$ is larger than that from spectroscopy ($R_2/R_1 = 1.22$ and 1.27) indicating a discrepancy. For partial eclipsing binaries, there exists a family of comparable solutions to the light curve modeling. These solutions fall in a valley which satisfies $R_1/a + R_2/a = constant$, and this is represented as the black dotted line. We tentatively adopt the radii associated with the best fit of the light curve (Table 5.4) as it is less model dependent, but we discuss below the implications of solutions with a smaller ratio of R_2/R_1.

Table 5.4: Model Parameters

Parameters	Primary	Secondary	System
Period (days)			2.16390189[1]$\pm$ 0.0000008
Time of primary minimum (HJD-2400000)			55341.03987 ± 0.00004
Mass ratio q=M_2/M_1			1.01 ± 0.03
Orbital eccentricity, e			0.0[1]
γ velocity (km s^{-1})			-1.3 ± 0.7
Orbital inclination (degree), i			74.52 ± 0.02
Semi-major axis ($R_\odot$), a			10.74 ± 0.14
Mass ($M_\odot$)	1.76 ± 0.07	1.79 ± 0.07	
Radius ($R_\odot$)	2.27 ± 0.03	3.19 ± 0.04	
Filling factor, f	0.432 ± 0.003	0.627 ± 0.001	
Gravity brightening, β	0.08[1]	0.08[1]	
Bolometric albedo	0.5[1]	0.5[1]	
$T_{\rm eff}$ (K)	7026[1]$\pm$ 100	6902 ± 100	
$\log g$ (cgs)	3.96 ± 0.03	3.69 ± 0.03	
Synchronous $v \sin i$ (km s^{-1})	51.4 ± 0.7	72.1 ± 0.9	
Velocity semiamplitude K (km s^{-1})	121.9 ± 1.3	120.2 ± 1.7	
rms of V_r residuals (km s^{-1})	6.2	9.7	

[1]Fixed.

5.3.4 Comparision with Evolutionary Models

This part is described in Chapter 2 in the context of stellar evolutionary models.

5.3.5 Interpretation of Pulsations

There has been significant advancement in the field of asteroseismology. However, most of these achievements focus on solar-like oscillators (Bedding et al. 2011; Beck et al. 2011; Mosser et al. 2012). The A-F type pulsators, mostly δ Scuti and γ Dor stars still require a better theory to explain observations. Even the first step of asteroseismology, that is mode identification, is notoriously difficult due to our lack of knowledge of crucial stellar physics such as mode excitation, nonlinear effects, and the treatment of rotation.

We analyzed the residuals of the binary light curve to investigate the pulsational properties. We found that masking the eclipses generates strong aliases in the Fourier spectrum and thus the whole residual lightcurves were used in the analysis. A standard pre-whitening procedure was performed with the *Period* 04 package (Lenz & Breger 2005) to all long cadence data as well as short cadence data with the fitting formula $Z+\sum_i A_i \sin(2\pi(\Omega_i t+\Phi_i))$, where Z, A_i, Ω_i, Φ_i are the zero-point shift of the residuals, pulsational amplitudes, frequencies and phases, respectively, and time $t = \mathrm{BJD} - 2,400,000$. The calculation was performed to the long and short cadence Nyquist frequencies (24.47 d^{-1} and 734 d^{-1}, respectively). No peaks were found beyond the frequency ≈ 25 d^{-1} in the short cadence spectrum. The envelope of the pre-whitened amplitude spectrum was adopted as a conservative noise level. We extracted the final frequencies from the long cadence data as they have a longer timespan and

better frequency resolution. These frequencies have signal to noise ratios (S/N) larger than 4.0 and are reported in Table 5.5. We estimated the uncertainties of frequencies, amplitudes, and phases following Kallinger et al. (2008). We show the Fourier amplitude spectrum with the window function, the noise spectrum after pre-whitening 89 significant peaks and the extracted frequency peaks in the upper, middle and lower panels of Figure 5.13, respectively. A remarkable feature in extracted frequencies was that many of them are related to the orbital frequency $f_{orb} = 0.46213$ d^{-1} in the form of $f_i \pm k f_{orb}$ ($k = 1, 2, 3, ...$). We list these frequencies and other combination frequencies in the form of $mf_i \pm nf_j$ (we restricted to $m, n = 1$ or 2) in the second half of Table 5.5, while the independent frequencies are listed in the first half.

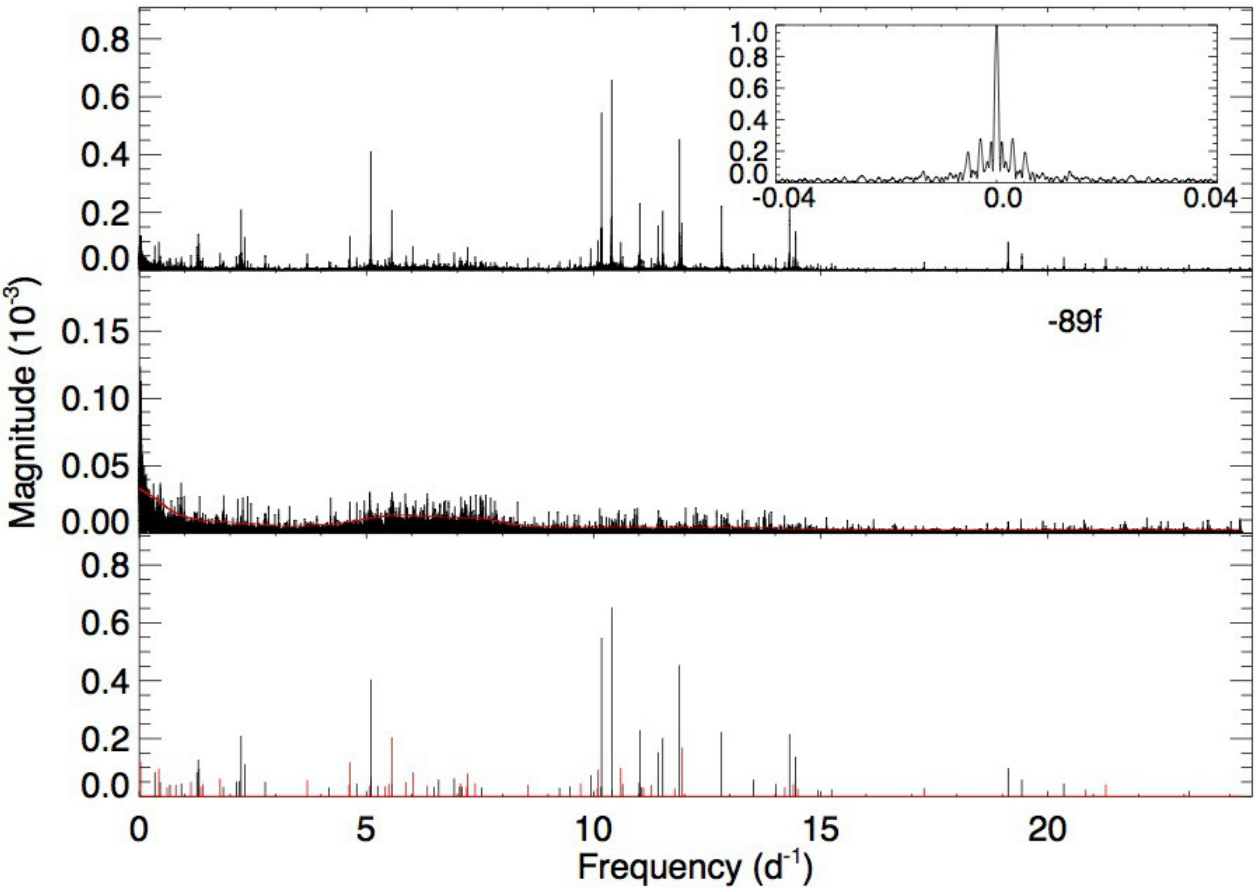

Figure 5.13 **Upper panel:** The amplitude spectrum of the residual light curve of long cadence data ($Q0-10, 12, 13, 14, 16, 17$) without masking the eclipses. The spectral window is shown in the upper right inset. **Middle panel:** The spectrum after subtracting 89 frequencies. The solid red curve represents the adopted noise level. **Bottom panel:** The extracted significant frequencies with S/N > 4.0 as listed in Table 5.5 (black: independent frequencies; red: combination frequencies).

Table 5.5: Significant oscillation frequencies

	Frequency (d^{-1})	Amplitude (10^{-3})	Phase (rad/2π)	S/N	Comment
f_1	10.399692 ± 0.000002	0.653 ± 0.008	0.343 ± 0.006	132.5	
f_2	10.176019 ± 0.000002	0.548 ± 0.008	0.764 ± 0.007	114.1	
f_3	11.890476 ± 0.000002	0.454 ± 0.008	0.249 ± 0.008	100.6	
f_4	5.097099 ± 0.000007	0.404 ± 0.019	0.002 ± 0.022	35.6	
f_5	11.018543 ± 0.000005	0.229 ± 0.008	0.124 ± 0.016	49.0	
f_6	12.814916 ± 0.000005	0.223 ± 0.008	0.259 ± 0.016	50.2	
f_7	14.315078 ± 0.000004	0.216 ± 0.006	0.493 ± 0.013	60.3	
f_8	2.23970 ± 0.00001	0.210 ± 0.013	0.373 ± 0.029	27.9	
f_{10}	11.52231 ± 0.00001	0.202 ± 0.008	0.998 ± 0.018	45.0	
f_{12}	11.41981 ± 0.00001	0.153 ± 0.008	0.565 ± 0.023	34.0	
f_{13}	14.44808 ± 0.00001	0.137 ± 0.006	0.852 ± 0.020	39.4	
f_{14}	1.29699 ± 0.00002	0.127 ± 0.018	0.190 ± 0.064	12.4	
f_{16}	2.31972 ± 0.00002	0.112 ± 0.013	0.091 ± 0.052	15.2	
f_{18}	19.12671 ± 0.00001	0.098 ± 0.004	0.104 ± 0.021	38.4	
f_{21}	1.26807 ± 0.00003	0.084 ± 0.018	0.350 ± 0.099	8.0	
f_{23}	7.22672 ± 0.00003	0.079 ± 0.020	0.242 ± 0.118	6.8	
f_{25}	5.09657 ± 0.00004	0.066 ± 0.019	0.573 ± 0.137	5.8	
f_{26}	6.93255 ± 0.00004	0.063 ± 0.020	0.173 ± 0.150	5.3	
f_{28}	6.59001 ± 0.00005	0.059 ± 0.021	0.992 ± 0.167	4.8	
f_{29}	19.42781 ± 0.00001	0.058 ± 0.004	0.124 ± 0.035	22.5	
f_{31}	3.69704 ± 0.00002	0.056 ± 0.010	0.196 ± 0.082	9.7	$8f_{orb}$
f_{32}	2.20292 ± 0.00003	0.053 ± 0.013	0.573 ± 0.113	7.0	
f_{33}	2.13439 ± 0.00003	0.052 ± 0.013	0.151 ± 0.120	6.7	
f_{34}	5.09768 ± 0.00005	0.051 ± 0.019	0.259 ± 0.176	4.5	
f_{35}	1.13657 ± 0.00005	0.051 ± 0.019	0.712 ± 0.179	4.5	
f_{37}	11.00534 ± 0.00002	0.047 ± 0.008	0.270 ± 0.079	10.1	
f_{40}	4.78514 ± 0.00005	0.044 ± 0.016	0.139 ± 0.171	4.7	
f_{41}	14.01095 ± 0.00002	0.043 ± 0.007	0.760 ± 0.071	11.2	
f_{44}	14.39802 ± 0.00002	0.043 ± 0.006	0.690 ± 0.066	12.1	
f_{46}	8.55119 ± 0.00003	0.040 ± 0.010	0.875 ± 0.112	7.1	
f_{47}	11.27238 ± 0.00003	0.040 ± 0.008	0.638 ± 0.090	8.8	
f_{50}	10.16680 ± 0.00003	0.033 ± 0.008	0.981 ± 0.115	7.0	$22f_{orb}$
f_{52}	14.21085 ± 0.00003	0.032 ± 0.006	0.909 ± 0.090	8.8	
f_{56}	17.27820 ± 0.00002	0.029 ± 0.005	0.286 ± 0.075	10.7	
f_{58}	11.78608 ± 0.00004	0.028 ± 0.008	0.447 ± 0.129	6.2	
f_{59}	14.49315 ± 0.00003	0.027 ± 0.006	0.124 ± 0.101	7.9	
f_{60}	11.43813 ± 0.00004	0.027 ± 0.008	0.212 ± 0.134	5.9	
f_{61}	12.35236 ± 0.00004	0.027 ± 0.008	0.847 ± 0.138	5.8	
f_{63}	10.50479 ± 0.00004	0.026 ± 0.008	0.536 ± 0.150	5.3	

f_{65}	11.42880 ± 0.00004	0.025 ± 0.008	0.108 ± 0.145	5.5	
f_{67}	20.82350 ± 0.00003	0.023 ± 0.005	0.910 ± 0.097	8.2	
f_{70}	10.40016 ± 0.00005	0.023 ± 0.008	0.109 ± 0.172	4.6	
f_{72}	9.59225 ± 0.00005	0.022 ± 0.008	0.934 ± 0.174	4.6	
f_{73}	11.36517 ± 0.00005	0.021 ± 0.008	0.461 ± 0.168	4.8	
f_{77}	23.10643 ± 0.00003	0.019 ± 0.005	0.636 ± 0.113	7.1	$50f_{orb}$
f_{79}	13.61003 ± 0.00005	0.019 ± 0.007	0.636 ± 0.171	4.7	
f_{81}	14.20153 ± 0.00005	0.018 ± 0.006	0.645 ± 0.168	4.8	
f_{82}	14.83255 ± 0.00005	0.015 ± 0.006	0.387 ± 0.170	4.7	
f_{84}	14.69435 ± 0.00005	0.015 ± 0.006	0.090 ± 0.175	4.5	
f_{86}	21.25792 ± 0.00004	0.015 ± 0.005	0.208 ± 0.147	5.4	$46f_{orb}$
f_{88}	21.52354 ± 0.00005	0.012 ± 0.005	0.640 ± 0.183	4.4	
f_{89}	21.24588 ± 0.00005	0.012 ± 0.005	0.918 ± 0.183	4.4	
f_{24}	9.93762 ± 0.00001	0.073 ± 0.008	0.004 ± 0.051	15.6	$f_1 - f_{orb}$
f_{49}	9.47544 ± 0.00003	0.035 ± 0.008	0.468 ± 0.111	7.2	$f_1 - 2f_{orb}$
f_{64}	11.32396 ± 0.00004	0.026 ± 0.008	0.087 ± 0.139	5.7	$f_1 + f_{orb}$
f_{39}	9.71393 ± 0.00002	0.045 ± 0.008	0.774 ± 0.084	9.5	$f_2 - f_{orb}$
f_{42}	10.63815 ± 0.00003	0.043 ± 0.008	0.692 ± 0.091	8.8	$f_2 + f_{orb}$
f_{54}	9.25177 ± 0.00004	0.030 ± 0.008	0.736 ± 0.129	6.2	$f_2 - 2f_{orb}$
f_{55}	11.10030 ± 0.00004	0.030 ± 0.008	0.172 ± 0.125	6.4	$f_2 + 2f_{orb}$
f_{68}	11.56241 ± 0.00004	0.023 ± 0.008	0.048 ± 0.153	5.2	$f_2 + 3f_{orb}$
f_{83}	22.06649 ± 0.00004	0.015 ± 0.005	0.694 ± 0.144	5.6	$f_2 + f_3$
f_9	5.55917 ± 0.00002	0.205 ± 0.023	0.987 ± 0.052	15.3	$f_4 + f_{orb}$
f_{15}	4.63503 ± 0.00002	0.118 ± 0.015	0.526 ± 0.057	13.9	$f_4 - f_{orb}$
f_{22}	6.02135 ± 0.00004	0.083 ± 0.023	0.547 ± 0.129	6.2	$f_4 + 2f_{orb}$
f_{53}	4.17286 ± 0.00005	0.031 ± 0.012	0.043 ± 0.173	4.6	$f_4 - 2f_{orb}$
f_{11}	11.94281 ± 0.00001	0.169 ± 0.008	0.732 ± 0.021	37.3	$f_5 + 2f_{orb}$
f_{20}	10.09429 ± 0.00001	0.093 ± 0.008	0.443 ± 0.041	19.5	$f_5 - f_{orb}$
f_{66}	15.23934 ± 0.00003	0.025 ± 0.005	0.148 ± 0.099	8.0	$f_7 + 2f_{orb}$
f_{75}	13.39085 ± 0.00005	0.019 ± 0.007	0.472 ± 0.170	4.7	$f_7 - 2f_{orb}$
f_{78}	13.85292 ± 0.00005	0.019 ± 0.007	0.462 ± 0.168	4.7	$f_7 - f_{orb}$
f_{80}	14.77724 ± 0.00004	0.019 ± 0.006	0.639 ± 0.141	5.7	$f_7 + f_{orb}$
f_{19}	1.31541 ± 0.00002	0.095 ± 0.017	0.551 ± 0.085	9.4	$f_8 - 2f_{orb}$
f_{27}	1.77756 ± 0.00003	0.061 ± 0.015	0.285 ± 0.112	7.1	$f_8 - f_{orb}$
f_{17}	10.59808 ± 0.00001	0.098 ± 0.008	0.794 ± 0.040	19.9	$f_{10} - 2f_{orb}$

f_{51}	11.06020 ± 0.00003	0.033 ± 0.008	0.900 ± 0.113	7.0	$f_{10} - f_{orb}$
f_{74}	11.98450 ± 0.00005	0.021 ± 0.008	0.152 ± 0.170	4.7	$f_{10} + f_{orb}$
f_{30}	13.52384 ± 0.00002	0.058 ± 0.007	0.278 ± 0.056	14.2	$f_{13} - 2f_{orb}$
f_{43}	1.39544 ± 0.00005	0.043 ± 0.017	0.963 ± 0.180	4.4	$f_{16} - 2f_{orb}$
f_{38}	20.35207 ± 0.00001	0.045 ± 0.005	0.444 ± 0.049	16.4	$f_{29} + 2f_{orb}$
f_{45}	21.27632 ± 0.00002	0.041 ± 0.005	0.963 ± 0.053	15.0	$f_{29} + 4f_{orb}$
f_{36}	2.77282 ± 0.00003	0.051 ± 0.011	0.450 ± 0.102	7.8	$f_{31} - 2f_{orb}$
f_{48}	4.62129 ± 0.00005	0.040 ± 0.014	0.117 ± 0.169	4.7	$f_{31} + 2f_{orb}$
f_{62}	8.78964 ± 0.00004	0.027 ± 0.009	0.296 ± 0.155	5.2	$f_{31} - f_{45}$
f_{57}	10.08109 ± 0.00004	0.029 ± 0.008	0.291 ± 0.131	6.1	$f_{37} - 2f_{orb}$
f_{71}	14.93516 ± 0.00003	0.023 ± 0.005	0.626 ± 0.113	7.0	$f_{41} + 2f_{orb}$
f_{85}	15.32227 ± 0.00005	0.015 ± 0.005	0.396 ± 0.164	4.9	$f_{44} + 2f_{orb}$
f_{76}	13.28659 ± 0.00005	0.019 ± 0.007	0.966 ± 0.175	4.6	$f_{52} - 2f_{orb}$
f_{87}	17.74031 ± 0.00005	0.013 ± 0.004	0.613 ± 0.163	4.9	$f_{56} + f_{orb}$
f_{69}	12.35302 ± 0.00005	0.023 ± 0.008	0.872 ± 0.158	5.0	$f_{65} + 2f_{orb}$

In the low frequency region ($f < 4$ d^{-1}), the peaks seem to cluster around 1.3 d^{-1} and 2.3 d^{-1}. Almost all δ Scuti stars observed by *Kepler* show low frequency peaks, and this star is no exception. The primary star is located inside the γ Doradus instability strip and the secondary star is just hotter than the blue edge of this strip, so these low frequency peaks are possibly g-mode pulsations.

In the frequency region (4 d^{-1} $\leq f \leq$ 8 d^{-1}), there is a quintuplet $f_9, f_{15}, f_{22}, f_{53}$ around $f_4 = 5.097$ d^{-1}: $f_9 = f_4 + f_{orb}$, $f_{15} = f_4 - f_{orb}$, $f_{22} = f_4 + 2f_{orb}$, $f_{53} = f_4 - 2f_{orb}$. In the high frequency region (8 d^{-1} $\leq f \leq$ 24 d^{-1}), nearly all the strong peaks are within the range 10 to 15 d^{-1}, with several lower peaks near 20 d^{-1}. These frequencies correspond to p-mode pulsations of δ Scuti stars. We find splittings to many of these p-modes including

$f_1 \rightarrow (f_{24}, f_{49}, f_{64})$, $f_2 \rightarrow (f_{39}, f_{42}, f_{54}, f_{55}, f_{68})$, $f_5 \rightarrow (f_{11}, f_{20})$, $f_7 \rightarrow (f_{66}, f_{75}, f_{78}, f_{80})$, $f_8 \rightarrow (f_{19}, f_{27})$, $f_{10} \rightarrow (f_{17}, f_{51}, f_{74})$, $f_{29} \rightarrow (f_{38}, f_{45})$ and $f_{31} \rightarrow (f_{36}, f_{48})$ (see the second half of Table 4). These splittings are all related $f_{orb} = 0.46213$ d^{-1} and are likely the result of amplitude modulation from eclipses. Due to the different cancellation effects, modes of different spherical degree l have different amplitude modulation. It is possible to identify the modes from these amplitude modulations, the so called *eclipse mapping* method described by Reed et al. (2005) and Bíró & Nuspl (2011). KIC 9851944 has a circular orbit, and the tidal effect is from the equilibrium tide which is confined to the first and second orbital harmonics. It is surprising to find that $f_{31} = 8f_{orb}$, $f_{50} = 22f_{orb}$, $f_{77} = 50f_{orb}$ and $f_{86} = 46f_{orb}$ are large multiple integer times of orbital frequency as such high orbital harmonics are usually found in very eccentric systems such as heartbeat stars (Welsh et al. 2011; Hambleton et al. 2013). Note that da Silva et al. (2014) also find a pulsation frequency at 19 times of orbital frequency in the circular eclipsing binary CoRoT 105906206.

There are other combination frequencies like $f_{23} = f_2 + f_3$, and these can be explained by nonlinear mode coupling as proposed by Weinberg et al. (2013). It is possible to extract information on the mode identification from the combination frequencies (Balona 2012). Recent study emphasizes the importance of combination frequencies as they provide a simple interpretation of the complex spectra of many γ Dor and SPB stars (Kurtz et al. 2015b).

As a preliminary attempt to identify pulsation modes, we chose representative structure models among the best coeval MESA models which fit the observed R, $T_{\rm eff}$ and M. The detailed modeling is presented separately in Chapter 2. Since the models favor a higher

mass ratio, we choose $1.70M_{\odot}$ and $1.77M_{\odot}$ as the possible lower and upper mass limits of the primary; for the secondary the limits of 1.79 and $1.86M_{\odot}$ are adopted. We calculated the non-rotating non-adiabatic frequencies for all models within a 1σ error box of the observed radius with the GYRE code (Townsend & Teitler 2013).

The calculated frequencies need to be corrected for the effect of rotation. To the first order, each $l > 0$ mode will split in to $2l+1$ components with $m = -l, \cdots, l$. The frequencies of the split modes follow the relation: $\omega_{lm} = \omega_0 + (1 - C_{nl})m\bar{\Omega} + O(\bar{\Omega}^2)$, where C_{nl} is the Ledoux constant (Ledoux 1951) which depends on the eigenfunction of the mode. $\bar{\Omega}$ is the mean rotational frequency for the mode. For KIC 9851944, the C_{nl} are directly computed in GYRE from mode eigenfunctions. The $l = 1, 2$ modes of the primary have C_{nl} about $0.1 - 0.3$. For the $l = 1, 2$ modes of the secondary star, the C_{nl} are about $0.4 - 0.6$ and 0.2, respectively.

The relative amplitudes of rotational splitting components to the central $m = 0$ mode depend on the inclination of the pulsation axis (Gizon & Solanki 2003). If the pulsation axis is aligned with the orbital and rotation axis, then at an inclination of 75 degrees, the $l = 1, m = 0$ mode has a very small amplitude and the $l = 1$ modes with $m = \pm 1$ are more likely to be observed. Similarly, the $l = 2, m = \pm 2$ modes and $l = 2, m = 0$ modes are more likely to be observed.

Both stars in KIC 9851944 rotate at an intermediate value, with $v \sin i \approx 60$ km s^{-1}. Even at this rotation rate, the rotational splitting may already start to deviate from the above simple first order equation (Dziembowski & Goode 1992; Goupil et al. 2000; Suarez

et al. 2006). Here we made an order of magnitude estimation of the second order effect by interpolating the coefficients in Table 1 in Saio (1981) assuming a polytropic model with $n = 3$ following Pérez Hernández et al. (1995). For the pure $l = 1$ p-mode in the observed frequency range, this correction is ≈ 0.03 d^{-1}. A similar estimation for the high order p-modes can be made by using the equation 3.381 in Aerts et al. (2010). For the $l = 1$ and $l = 2$ p-modes in the observed frequency range, we get similar results, changes of $0.02 - 0.03$ d^{-1} for the primary star. The distortion due to the centrifugal force also alters the oscillation frequencies and it is also a second order effect. We neglect this effect in this analysis as well as the similar effect from the tidal distortion of stars. Another effect of rotation is the mode degenerate coupling (Goupil et al. 2000; Zwintz et al. 2014), e.g, between $l = 0$ and $l = 2$ modes if their frequencies are very close. For low radial orders, the effect is smaller than $\approx 1\mu$ Hz $= 0.086$ d^{-1} at $v \leq 70$ km s^{-1} (Goupil 2011). We also neglect this effect in the analysis.

We plot the theoretical frequencies of unstable modes of $l = 0, 1, 2$ for the above mentioned representative models and the observed frequencies in Figure 5.14. Theoretical frequencies of the primary star are from models of $M_1 = 1.70 M_\odot$ and $M_1 = 1.77 M_\odot$. Similarly, we show frequencies from models of $M_2 = 1.79 M_\odot$ and $M_2 = 1.86 M_\odot$ for the secondary star. Radial, dipole and quadrupole modes are indicated by black, green and red dots, respectively. Due to the extreme denseness of the theoretical frequencies, the rotational splittings are not shown for the secondary star. The symbol size has been scaled to be proportional to the expected mode visibility S_{nl} according to the expressions given by Handberg & Campante

(2011).

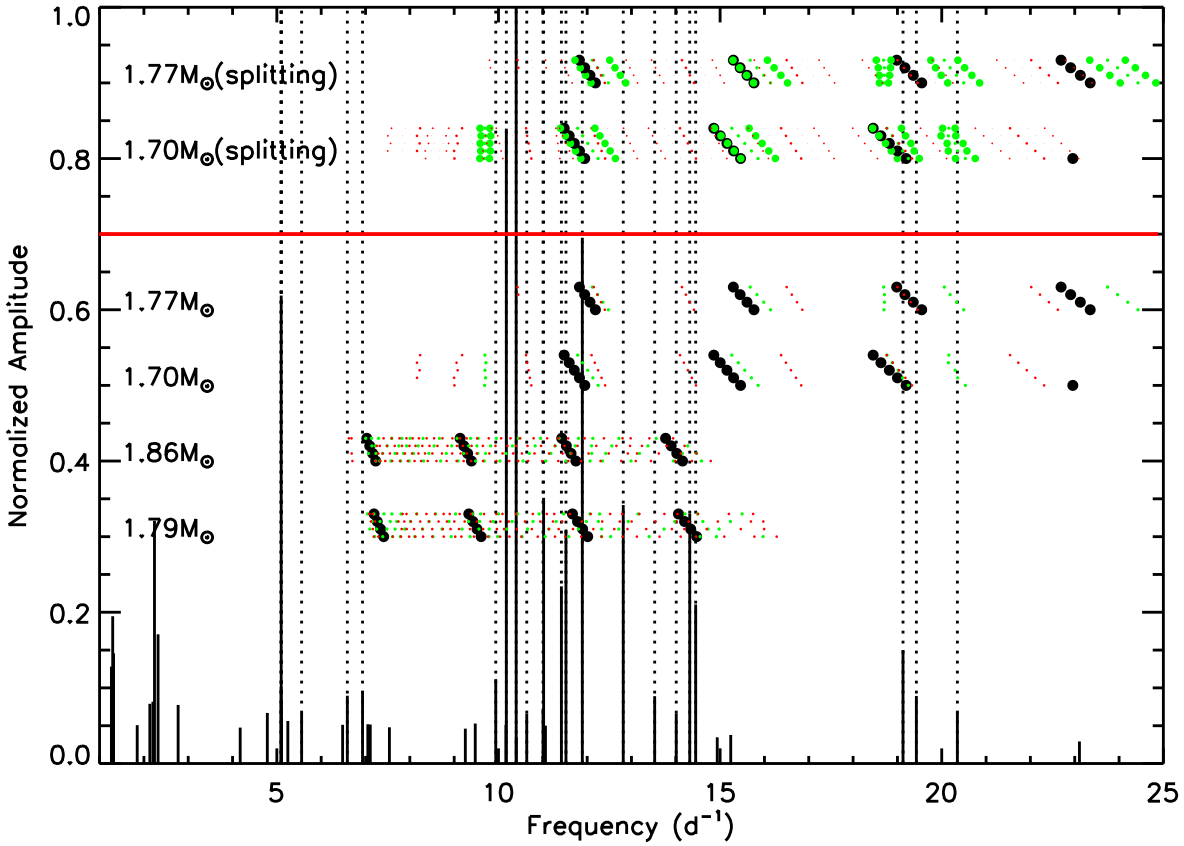

Figure 5.14 A comparison of the observed independent frequencies (solid lines, extended as dotted lines for comparison) with theoretical oscillation frequencies (symbols) from models. Theoretical frequencies of the primary star are from models of 1.70 $M_{\odot}$ and 1.77 $M_{\odot}$ (lower and upper mass limit) for two cases: (1) the frequencies corrected for the 1st order rotational splitting (above the horizontal red line); (2) those without rotational splittings (below the red line). The model frequencies of the secondary star are derived from models of 1.79 $M_{\odot}$ and 1.86 $M_{\odot}$ (lower and upper mass limit). Note there are four or five models within the 1σ error box of radius with a fixed mass. Due to the extreme denseness of the modes of the sub-giant secondary, only frequencies without rotational splitting are shown. Black dots are radial modes. Green dots are $l = 1$ dipole modes, and $l = 2$ modes are indicated as red dots. The symbol size is proportional to the theoretical predicted mode visibility (see text).

The primary star is still on the main sequence, which shows a clear and sparse spectrum. The fundamental to the 2nd or 3rd overtone radial modes are predicted to be unstable. The frequencies above the horizontal red line have taken into account the 1st order rotational splitting assuming that the mean rotational frequency $\bar{\Omega}$ is equal to the orbital frequency. The secondary star has an instability range from the fundamental to the the 3rd overtone radial mode. The highest two peaks $f_1 = 10.3997$ d^{-1} and $f_2 = 10.1760$ d^{-1} are likely to be $l = 1$ or $l = 2$ modes of the secondary. Frequency peaks $f_{18} = 19.1267$ d^{-1}, $f_{29} = 19.4278$ d^{-1} and $f_{67} = 20.8235$ d^{-1} are located only in the unstable range of the primary and probably stem from the primary. f_{18} and f_{29} fall into possible range of the second overtone radial mode. f_{12}, f_{10} and f_3 can be the fundamental radial mode of the primary or the second overtone radial mode of the secondary. The high peak f_4 at 5.0971 d^{-1} does not seem to be explained by our unstable p-mode frequencies, and could be a g-mode. We assume the observed frequencies are from $l = 0, 1, 2$, but it is possible that the $l = 3$ or even higher order modes can also be observed. The range of unstable frequencies agrees roughly with the observations. The theory predicts many more excited modes than the observations reveal, but some observed modes are not predicted to be excited. We can see that even with the constrained mass, radius and effective temperature, the mode identification is still difficult.

5.3.6 Conclusions

Thanks to the unprecedented light curves from the *Kepler* satellite, we are discovering more eclipsing binaries with pulsating components. Eclipsing binaries and pulsating frequencies are the only two sources where we can get accurate, model independent fundamental stellar

parameters such as mass and radius. Pulsating eclipsing binaries with δ Scuti and γ Doradus stars are the key to our improvement of understanding the mode excitation mechanisms in these intermediate mass stars, and this advancement can only be made after we have a statistically large sample of such systems. Here we add one more system to the list, KIC 9851944, two F stars in a circular orbit with a period of 2.1639 days. The two components have similar masses and effective temperatures but very different radii. We try to match the observations with models of different stellar physics and parameters. Both stars probably show δ Scuti type p-mode pulsations as well as low frequencies pulsations. We made an attempt to understand the general pulsational spectrum of δ Scuti stars within this mass range. The observed pulsations can be explained by the low order p-modes of the primary and the secondary or the g-mode and mixed modes of the secondary. This work is an effort of preliminary seismic modeling of δ Scuti stars in eclipsing binaries using 1-D stellar models. We note that even with the mass and radius constrained to 3.9% and 1.3%, respectively, the mode identification for δ Scuti stars from single band photometry of *Kepler* is still inconclusive. This is general problem for all δ Scuti stars. Accurate multicolor photometry and high cadence data of line profile variations will help to overcome partially this difficulty. It is also desirable to analyze the system with 2-D structure models taking into account the rotational and tidal distortion. The real advancements call for better theoretical understanding of the effects of convection, rotation, tidal interactions and non-linearity on pulsations, which are still the frontiers of asteroseismology.

5.4 KIC 8262223

5.4.1 Introduction

KIC 826223 (K_p=12.146, α_{2000}=20:01:19.788, δ_{2000}=+44:08:38.90) is included in the Kepler Eclipsing Binary Catalog (Prša et al. 2011; Slawson et al. 2011). It is described as a semi-detached eclipsing binary with an orbital period of 1.612 days, a near circular orbit, and a high inclination ($\sin i = 0.97$). The eclipse timing analysis of this system was performed by Gies et al. (2012, 2015) and Conroy et al. (2014). The flat $O - C$ diagram of the timings indicates that this circular binary is not likely to have a nearby third companion. Gies et al. (2012) also noticed a pulsation signal in near resonance with the orbit in the light curve. Armstrong et al. (2014) estimated the effective temperatures of the primary and secondary as $T_{\rm eff1} = 9325 \pm 428$ K and $T_{\rm eff2} = 6791 \pm 642$ K, respectively, based on their fit of the binary spectral energy distribution (SED).

5.4.2 Photometric and Spectroscopic Observations

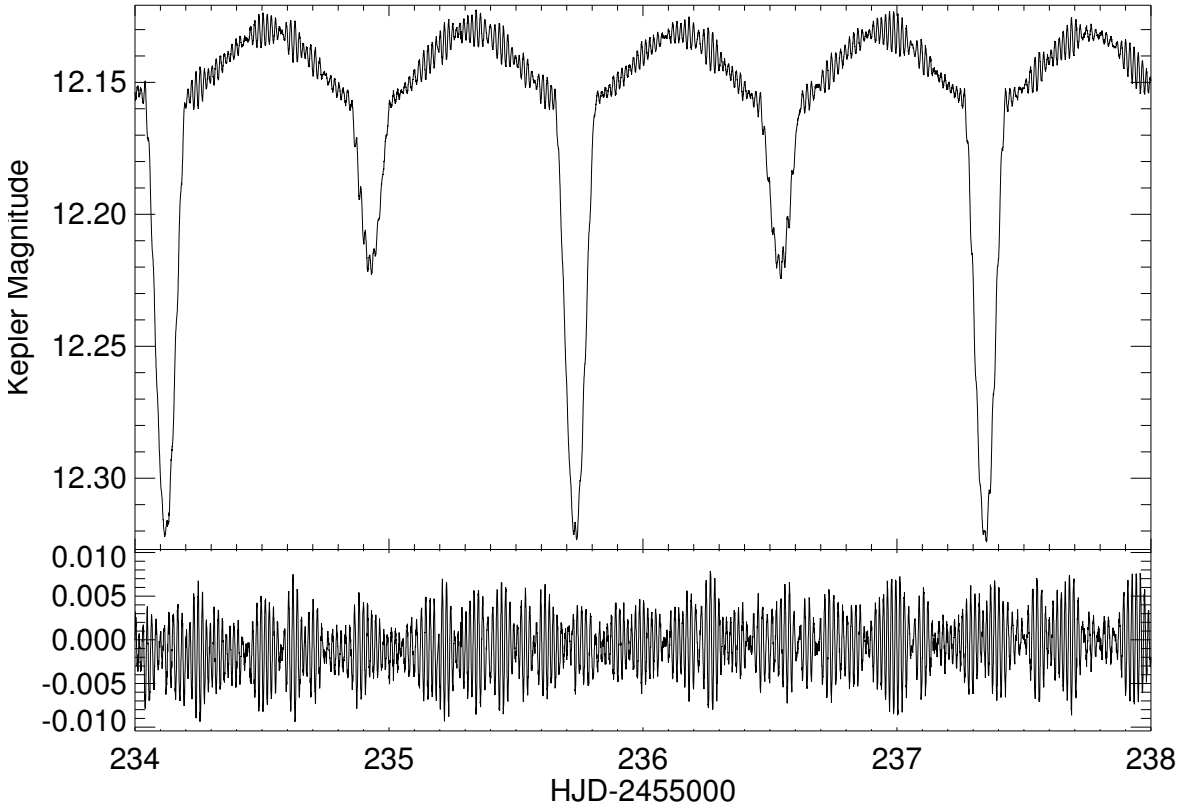

Figure 5.15 The de-trended short cadence light curve of KIC 8262223 during Quarter 4. The lower panel shows the residuals after subtracting the best binary light curve model.

Simple Aperture Photometry (SAP) data (Data Release 23) from the *Kepler* satellite were retrieved from the MAST Archive. There are 18 quarters (Q0-17) of long cadence data and 1 quarter (Q4) of short cadence data. The aperture contamination is lower than 0.7% in all quarters except for Q12 (1.3%). The light curve shows deep eclipses, ellipsoidal variations

and coherent pulsations at frequency about 65 d^{-1} as apparent in the short cadence data. A sample of the short cadence light curve is shown in Figure 5.15. As the main pulsational frequency is well above the Nyquist frequency (≈ 24 d^{-1}) of long cadence data (30 minutes sampling), these pulsations are essentially all cancelled out in the long cadence measurements. Thus we used the long cadence data for binary light curve modeling and the light curve residuals of short cadence data for pulsational analysis.

We also obtained ground-based spectra of moderate resolving power ($R \approx 6000$) from the R-C Spectrograph on Kitt Peak National Observatory (KPNO) 4-meter Mayall telescope from 2010 to 2013 (Figure 5.16). More information about the instrument and spectra can be found in Matson et al. (2016).

5.4.3 Spectroscopic Orbit and Atmospheric Parameters

The radial velocities (RVs) were determined following the same cross-correlation technique described by Matson et al. (2016) and Guo et al. (2016). Two templates from atmospheric model grids UVBLUE (Rodríguez-Merino et al. 2005) were cross-correlated with the observed spectra to obtain the radial velocities presented in Table 5.6. The derived RVs were fitted to get the orbital parameters $(K_1, K_2, \gamma_1, \gamma_2, T_0)$, where K_1, K_2 and γ_1, γ_2 are semi-amplitude velocities and system velocities of the primary and secondary star, respectively; T_0 is time epoch of the primary minimum. We searched for a circular orbital solution ($e = 0$) and the orbital period was fixed to the value from eclipse timing measurements in Gies et al. (2015) as $P = 1.61301476$ days. We then used the tomography algorithm (Bagnuolo et al. 1994) to reconstruct the individual component spectra of two stars. These spectra were compared

with a grid of UVBLUE synthetic spectra and the best atmospheric parameters ($T_{\rm eff}$, $\log g$, [Fe/H] and $v \sin i$) were determined from a grid search followed by a local optimization with the Levenberg-Marquardt algorithm. To break the degeneracy in fitting five atmospheric parameters, the $v \sin i$ values were initially estimated from the metal lines in five different spectral sections and the $\log g$ value was fixed to the result from the binary modeling (see next section). Note that the uncertainties were estimated from the covariance matrices, and these can be somewhat underestimated. The procedures mentioned above are iterative, and in each step the templates and RVs were updated from previous determinations. We adopted the final values when the parameters converge.

Table 5.6: Radial Velocities

Time (BJD-2400000)	Phase	V_r(pri) (km s^{-1})	$O-C$ (km s^{-1})	V_r(sec) (km s^{-1})	$O-C$ (km s^{-1})	Observation Source
55369.9232	0.19	1.5 ± 1.7	-0.9	215.4 ± 4.3	0.4	KPNO
55732.8574	0.19	2.6 ± 1.7	0.4	213.5 ± 4.5	-3.3	KPNO
55815.8979	0.68	42.7 ± 1.9	0.2	-159.2 ± 5.9	-2.1	KPNO
56077.9534	0.14	6.2 ± 1.7	0.8	185.0 ± 4.7	4.2	KPNO
56078.7629	0.64	42.3 ± 2.4	2.0	-144.2 ± 7.0	-11.9	KPNO
56078.8440	0.79	42.0 ± 1.8	-1.2	-163.3 ± 5.7	1.9	KPNO
56078.9357	0.75	45.8 ± 1.9	1.6	-183.5 ± 5.6	-3.9	KPNO
56079.7925	0.28	9.3 ± 3.4	7.2	220.4 ± 10.7	-6.4	KPNO
56081.9642	0.63	34.8 ± 2.9	-4.2	-103.3 ± 6.4	15.5	KPNO
56082.8204	0.16	3.1 ± 1.8	-1.0	195.2 ± 4.7	0.9	KPNO
56082.8833	0.20	1.7 ± 1.7	-0.4	217.2 ± 4.7	-0.0	KPNO
56082.9468	0.23	0.6 ± 2.0	-0.8	227.5 ± 5.6	-1.2	KPNO

Spectral disentangling (Hadrava1995) is another way to derive orbital parameters. For spectroscopic binaries, we observe the linear combination of two component spectra with different Doppler shifts. Given the radial velocities of the two stars and their mean flux ratio, we can form a coefficient matrix A. Then we can separate the component spectra by solving the linear inverse problem $y = Ax$, where y and x are vectors formed by concatenating the observed composite spectra and the individual component spectra (see Hensberge at al. 2008). If the RVs used in the coefficient matrix are calculated from orbital parameters, we can find the optimized orbital parameters by minimizing the χ^2 differences of the observed and synthetic composite spectra, $|y-AX|^2$. We implemented this method with the FDBinary code (Ilijic et al. 2004). Note that the code uses a downhill simplex optimizer and regrettably does not provide uncertainty estimates.

The final orbital parameters are summarized in Table 5.7. The orbital parameters from the two techniques agree very well (Figure 5.17). The results show that the system has a very small mass ratio ($q = 0.104$), and the systemic velocities from fitting RVs of primary and secondary (γ_1, γ_2) agree within uncertainties. Table 5.8 contains the optimal atmospheric parameters. This binary consists of a hot A-type primary ($T_{\rm eff1} = 9128$ K) and a much cooler secondary ($T_{\rm eff2} = 7119$ K). Both stars have metallicities slightly lower than solar. The projected rotational velocity of the primary star ($v \sin i = 37 \pm 13$ km s^{-1}) is a little lower than the synchronized value at 50 km s^{-1} (see Table 5.9 in next section). The $v \sin i$ of the secondary matches the synchronized value very well. Note that each pixel in our spectra is equal to 26.25 km s^{-1} in velocity space, and we cannot reliably measure small rotational

velocities ($v \sin i < 30$ km s^{-1}). In Figure 5.18, we show the reconstructed component spectra of the two stars and the best matching model spectra. The mean flux ratio (F_2/F_1) in the observed spectral range (≈ 4225 Å) is 0.21 ± 0.02 which amounts to percentage contributions of 82.6% and 17.4% for the primary and secondary, respectively.

Table 5.7: Orbital Parameters

Parameters	RVs	Spectral Disentangling
T_0(primary minimum) (HJD-2,400,000)	55690.5 ± 0.1	55690.605
K_1 (km s^{-1})	21.4 ± 1.0	21.5
K_2 (km s^{-1})	204.8 ± 3.2	201.4
γ_1 (km s^{-1})	22.8 ± 0.6	...
γ_2 (km s^{-1})	25.1 ± 1.7	...
e	0.0	0.0
rms_1 (km s^{-1})	2.6	...
rms_2 (km s^{-1})	6.3	...

Table 5.8: Atmospheric Parameters

Parameters	Primary	Secondary
$T_{\rm eff}$ (K)	9128 ± 130	7119 ± 150
$\log g$ (cgs)	4.3[a]	3.5[a]
$v \sin i$ (km s^{-1}) ...	37 ± 13	35 ± 10
[Fe/H]	-0.05 ± 0.1	-0.05 ± 0.1
Flux Contribution	82.6%	17.4%

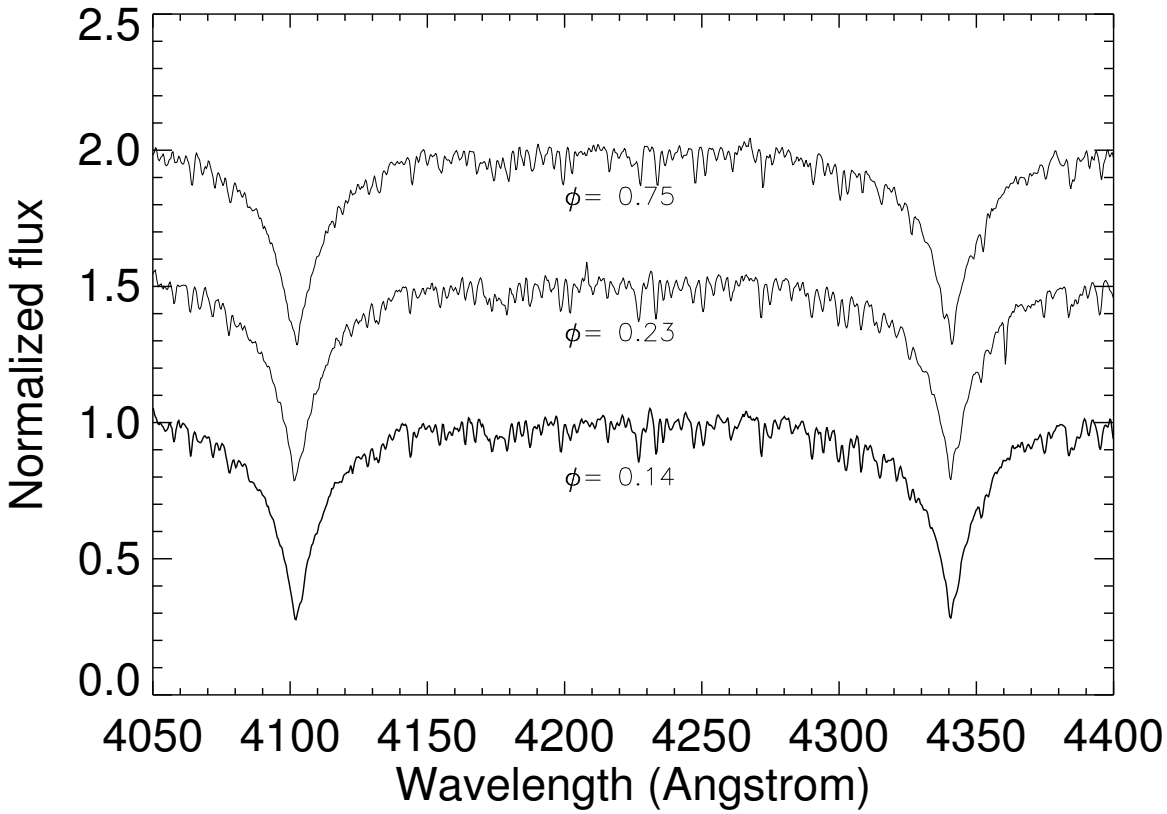

Figure 5.16 The observed composite spectra of KIC 8262223. For clarity, the spectra at orbital phases $\phi = 0.23$ and 0.75 have been shifted upwards by 0.5 and 1.0, respectively.

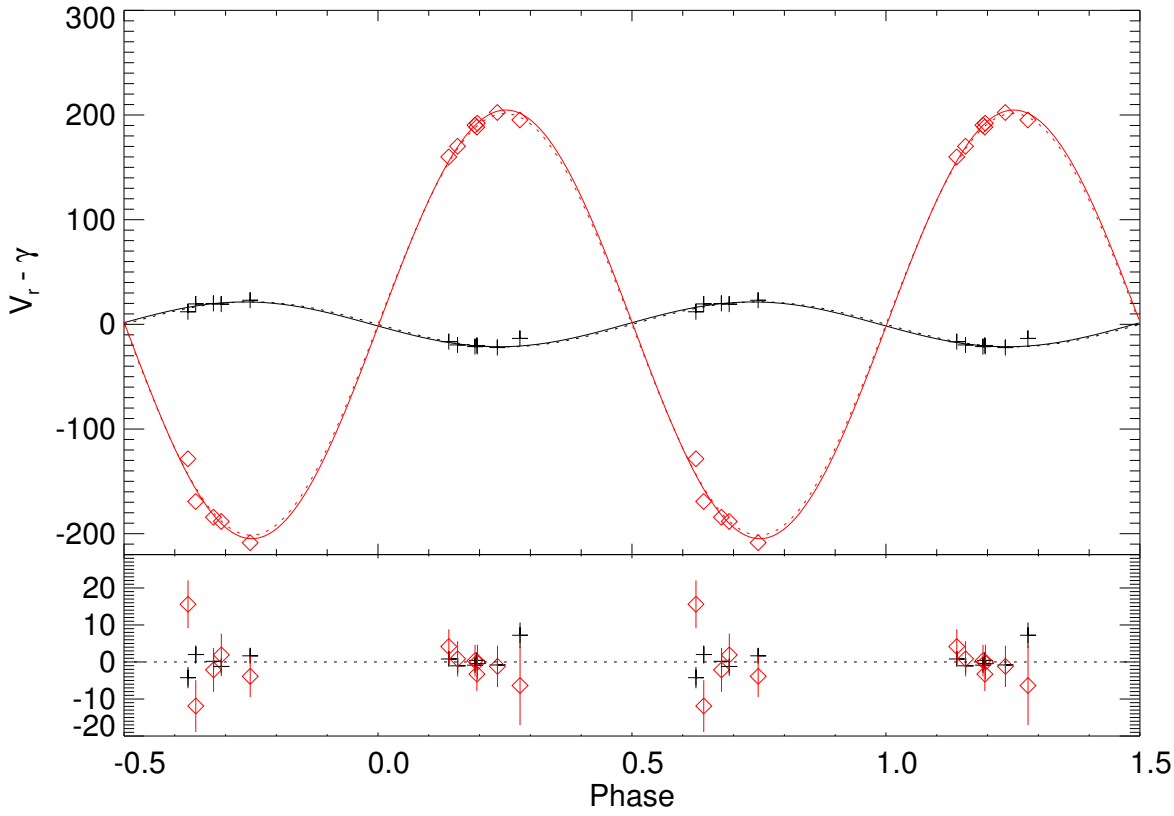

Figure 5.17 Radial velocities (RVs) in km s^{-1} and circular orbital solutions of KIC 8262223. The observed RVs of the primary and the secondary star from cross correlation are shown as black crosses and red diamonds, respectively. The black and red solid lines are the best-fit radial velocity curves for the primary and secondary, respectively. The lower panel shows the corresponding residuals. The RV models from the spectral disentangling technique by FDBinary are indicated as black and red dashed lines.

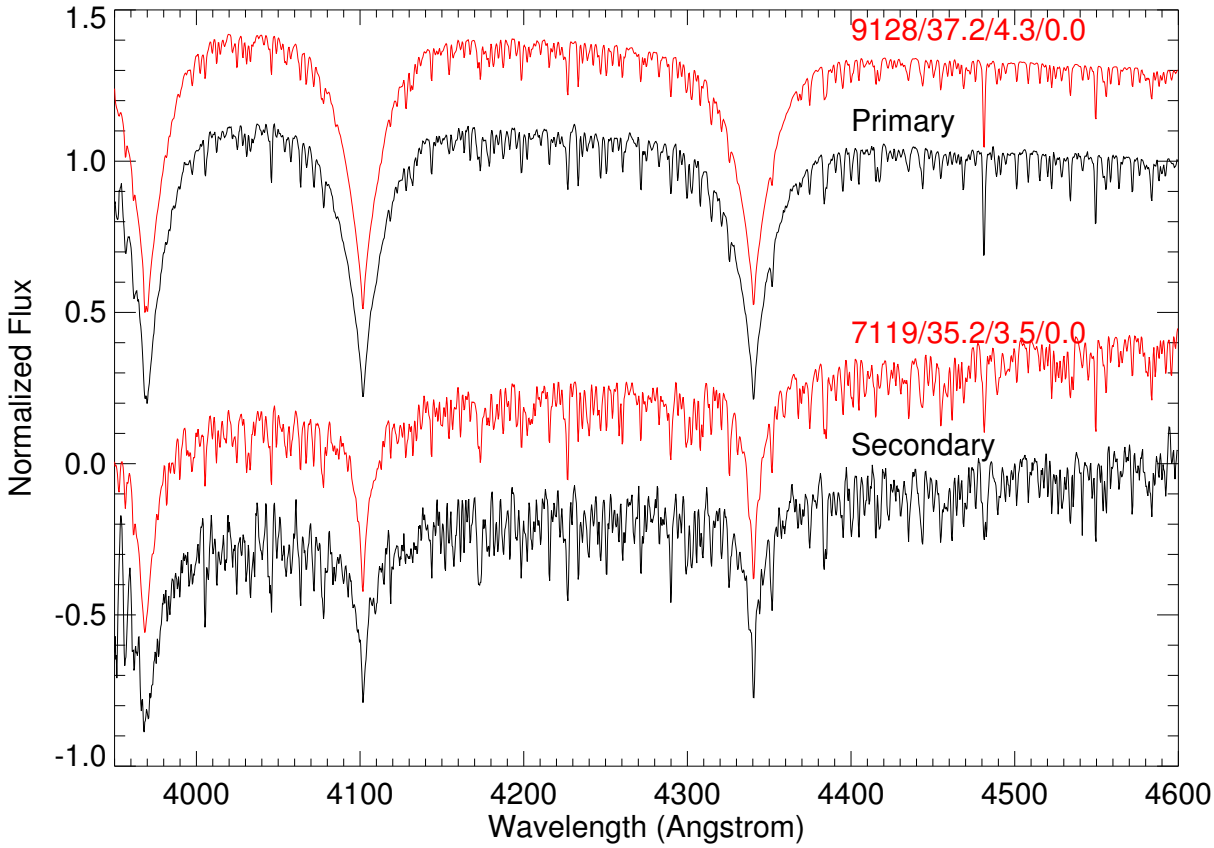

Figure 5.18 The reconstructed individual spectra of the primary (upper) and secondary (lower) of KIC 8262223. The best matching atmospheric models from UVBLUE are shown as red spectra, and the corresponding parameters $T_{\rm eff}$(K), $v \sin i$(km s^{-1}), $\log g$(cgs) and [Fe/H] are labeled.

5.4.4 ELC Binary Models

We used the *Kepler* long cadence data to perform our light curve modeling. The preparation of the raw data, which was detailed in Guo et al. (2016), includes de-trending and outlier

removal. We divided the 18 quarters into eight sections ($Q0-Q2$, $Q3-4$, $Q5-6$, $Q7-8$, $Q9-10$, $Q11-12$, $Q13-14$, $Q15-17$) and fitted the light curve of each individually. The standard deviations of the best fitting parameters from these eight datasets are adopted as the final uncertainties.

We used the Eclipsing Light Curve (ELC) code by Jerome Orosz (Orosz & Hauschildt 2000) to model the binary light curve. The code implements the Roche model and synthesizes the binary light curve and radial velocity curve by integrating the specific intensity and flux-weighted RVs of each segment on the stellar surface.

We optimized the following fitting parameters: orbital inclination (i), temperature ratio ($temprat = T_{\rm eff2}/T_{\rm eff1}$), filling factors ($f_1, f_2$) and time of primary minimum (T_0) by implementing the genetic algorithm PIKAIA (Charbonneau 1995). We set broad search ranges for these parameters: $i \in [50, 90]$(degrees), $temprat \in [0.6, 0.9]$, $f_1, f_2 \in [0.1, 0.8]$, $T_0 \in [55431.7, 55433.3]$(HJD-2,400,000). The orbital period was fixed to 1.61301476 days as found by Gies et al. (2015). The effective temperature of the primary was fixed to the value from spectroscopy (9128 K) as it is well known that the light curve is only sensitive to the temperature ratio. We assumed the binary has a circular orbit and the two components have synchronized rotation as indicated from spectroscopy. The parameters mass ratio ($q = M_2/M_1$), velocity semi-amplitude (K_1) and systemic velocity (γ) were fixed to values from spectroscopic orbital solutions as they have little affect on the light curve. The gravity brightening coefficients (β) were fixed to the canonical values of 0.25 for radiative atmospheres and 0.08 for convective atmospheres. Similarly, the surface bolometric albe-

dos (l_1, l_2) were set to 1.0 and 0.5 for radiative and convective atmospheres, respectively. However, the light curve residuals from the parameter settings above still show obvious variations. We found that by setting l_2 as a free parameter the light curve fit is much better. The optimal value of l_2 is 0.22, which is much lower than the canonical value of 0.5. Note Matson et al. (2016) also found a lower albedo (0.33) for the F stars in KIC 5738698. If we let the albedo of the primary star (l_1) vary, the best value is very close to 1.0, and the light curve fit is not improved.

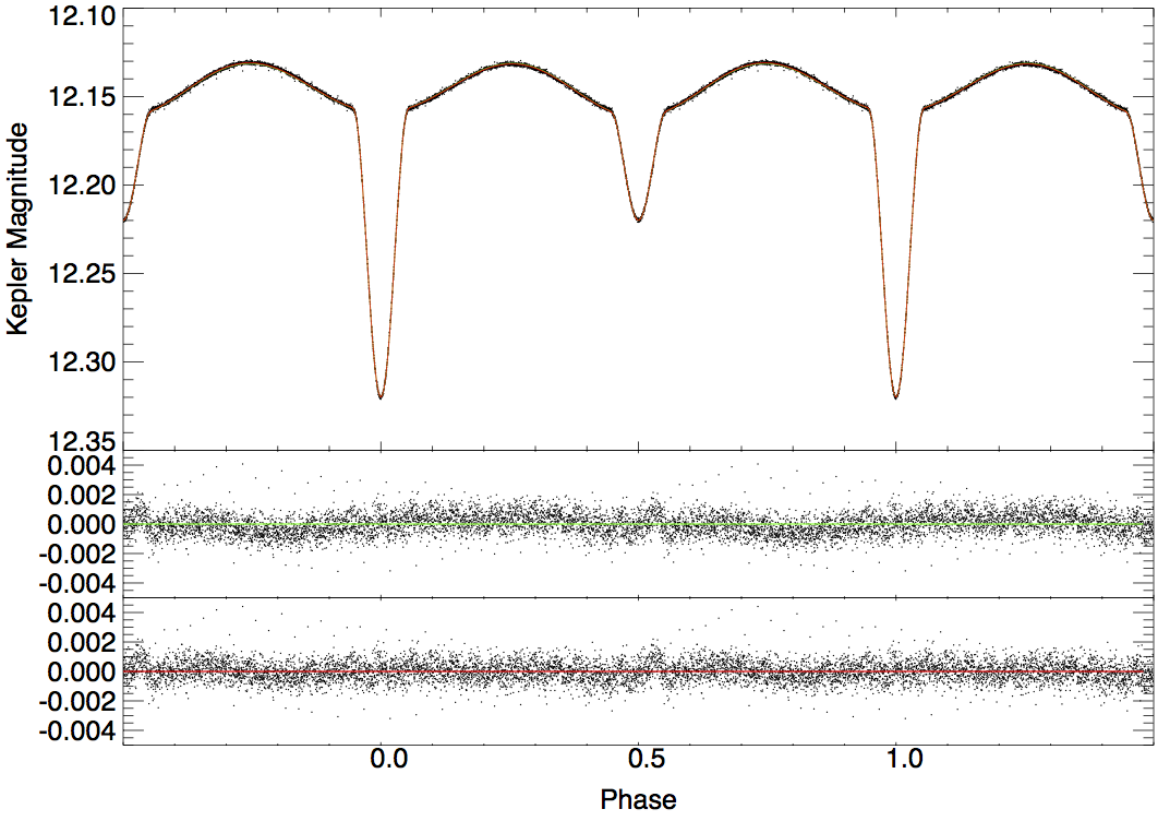

Figure 5.19 **Top panel**: The phase-folded long cadence light curve of KIC 8262223 (dots) in Quarter 4 and 5 and the best-fit model from ELC (red and green solid line) when the bolometric albedo of the secondary star (l_2) is allowed to vary. **Middle and Lower panel**: The corresponding residuals without and with the Doppler beaming effect taken into account, respectively.

Doppler boosting or beaming is a relativistic effect, in which the observer will receive a higher photon rate from a star moving towards him or her, and vice versa. The fractional change of photon rate is $\Delta n_\lambda / n_\lambda = f_{DB} v_\lambda / c$, where v_λ is radial velocity of the star and c is speed of light. Thus, the key parameters are the mass and flux ratios. If the two stars have

similar temperature, then the beaming effect will be canceled out if they have a mass ratio of 1. For systems with a very small mass ratio, the Doppler beaming effect is expected to play an important role. A measurement of the beaming amplitude from the light curve can provide an independent estimation of the orbital parameters. This was performed in many beaming binaries such as KOI-74, KOI-81 (van Kerkwijk et al. 2010) and KIC 11558725 (Telting et al. 2012). In the ELC code, the Doppler beaming effect is accounted for following the treatment in van Kerkwijk et al. (2010). The beaming parameter f_{DB} is estimated as the wavelength average of $xe^x/(e^x-1)$ in the *Kepler* passband, where $x = hc/(\lambda kT)$. The estimated values are 2.76 and 3.48 for the primary and secondary, respectively, and are fixed in the fitting process. In Figure 5.19, we show the best light curve solution and corresponding residuals with (Red) and without (Green) Doppler beaming. It can be seen in the bottom panel that the residuals are more symmetric around the zero horizontal line if the beaming effect is included.

In Table 5.9, we list the final model parameters of KIC 8262223. The parameters of the primary are typical for a mid-A type ZAMS star ($M_1 = 1.94M_\odot$, $R_1 = 1.67R_\odot$, $T_{\rm eff1} = 9128K$). The secondary has a very low mass ($M_2 = 0.20M_\odot$) and very discrepant radius ($R_2 = 1.31R_\odot$) and effective temperature ($T_{\rm eff2} = 6849K$). This suggests that this system has gone through the binary evolution with mass transfer. The implications and possible evolutionary scenarios are discussed in section 5.6.

The optimal effective temperature ratio ($T_{\rm eff2}/T_{\rm eff1}$) from fitting the light curve is 0.75, and this gives $T_{\rm eff2} = 6849K$ which is $\approx 300K$ cooler than that from spectroscopy ($T_{\rm eff2} = 7119K$).

This discrepancy can be explained by our adopted lower albedo $l_2 = 0.22$. There is a correlation between $T_{\rm eff2}$ and bolometric albedo l_2. If we fixed l_2 to the canonical value of $0.5 - 0.6$, then the optimal $T_{\rm eff2}/T_{\rm eff1}$ value is much higher (0.78), which agrees well with the spectroscopic result. As we cannot get a very good light curve fit with l_2 fixed to 0.5, we seem to have a dilemma. It is known that the bolometric albedo is difficult to pin point and is usually treated as a free parameter. Sometimes even values as high as 2.46 are used (e.g., star A in KIC 10661783; Lehmann et al. 2013). Note that the effective temperature of KIC 3858884 star B from spectroscopy by Maceroni et al. (2014) is also $\approx 300K$ different from that from the light curve solution. Thus, we think this minor discrepancy is not an unexpected problem for our analysis.

Table 5.9: Model Parameters

Parameters	Solution
Period (days)	1.61301476^{1}
Time of primary minimum (HJD-2400000)	$55432.522844 \pm 0.000007$
Mass ratio $q = M_2/M_1$	0.104 ± 0.002
Orbital eccentricity e	0.0^{1}
Orbital inclination i (degree)	75.203 ± 0.007
Semi-major axis a ($R_\odot$)	7.45 ± 0.11
M_1 ($M_\odot$)	1.94 ± 0.06
M_2 ($M_\odot$)	0.20 ± 0.01
R_1 ($R_\odot$)	1.67 ± 0.03
R_2 ($R_\odot$)	1.31 ± 0.02
Filling factor f_1	0.314 ± 0.003
Filling factor f_2	0.672 ± 0.001
Gravity brightening, β_1	0.25^{1}
Gravity brightening, β_2	0.08^{1}
Bolometric albedo 1	1.0^{1}
Bolometric albedo 2	0.22
Beaming parameter 1	2.76^{1}
Beaming parameter 2	3.48^{1}
$T_{\rm eff1}$ (K)	9128^{1}
$T_{\rm eff2}$ (K)	6849 ± 15
$\log g_1$ (cgs)	4.28 ± 0.04
$\log g_2$ (cgs)	3.51 ± 0.06
Synchronous $v \sin i_1$ (km s^{-1})	50.6 ± 0.9
Synchronous $v \sin i_2$ (km s^{-1})	39.6 ± 0.6

5.4.5 Pulsational Characteristics

Only the short cadence data can be used to study the pulsations of this system. We calculated the Fourier spectrum of the light curve residuals with the *Period 04* package (Lenz & Breger 2005) with all eclipses truncated. The calculation was performed to the short cadence Nyquist frequency (≈ 734 d^{-1}). No significant peaks were found beyond 70 d^{-1}. All frequencies with $S/N > 4$ are reported in Table 5.10 and the Fourier spectrum is shown in Figure 5.20. The uncertainties were calculated following Kallinger et al. (2008).

Almost all the pulsations are in the range of $50 - 65$ d^{-1}. There appears to be some low amplitude peaks at $100 - 130$ d^{-1} (not shown in Figure 5.20), which are exactly twice the main pulsation range. We interpret these peaks as the harmonics of the main pulsations rather than some high intrinsic pulsation frequencies. This indicates that the pulsations are to some extent non-sinusoidal. The primary star contributes much more light (83% in the wavelenth range of our spectra), and its fundamental parameters ($M_1 = 1.94 M_\odot$, $R_1 = 1.67 R_\odot$, $T_{\rm eff1} = 9128K$) also agree with those of a typical δ Scuti pulsator. It is, thus, very likely that the pulsations stem from the primary. The pulsations at $50 - 65$ d^{-1} can be well explained as high order ($n_p \approx 6, 7$) radial and non-radial p-modes.

In the low frequency region, there are two peaks $f_{20} = 1.2397$ d^{-1} and $f_{58} = 0.79928$ d^{-1}. f_{20} is equal to twice of orbital frequency $2f_{orb} = 2 \times 0.61996$ d^{-1} within uncertainties and is likely the result of imperfect light curve fitting (e.g., ellipsoidal variations). f_{58} is probably a g-mode.

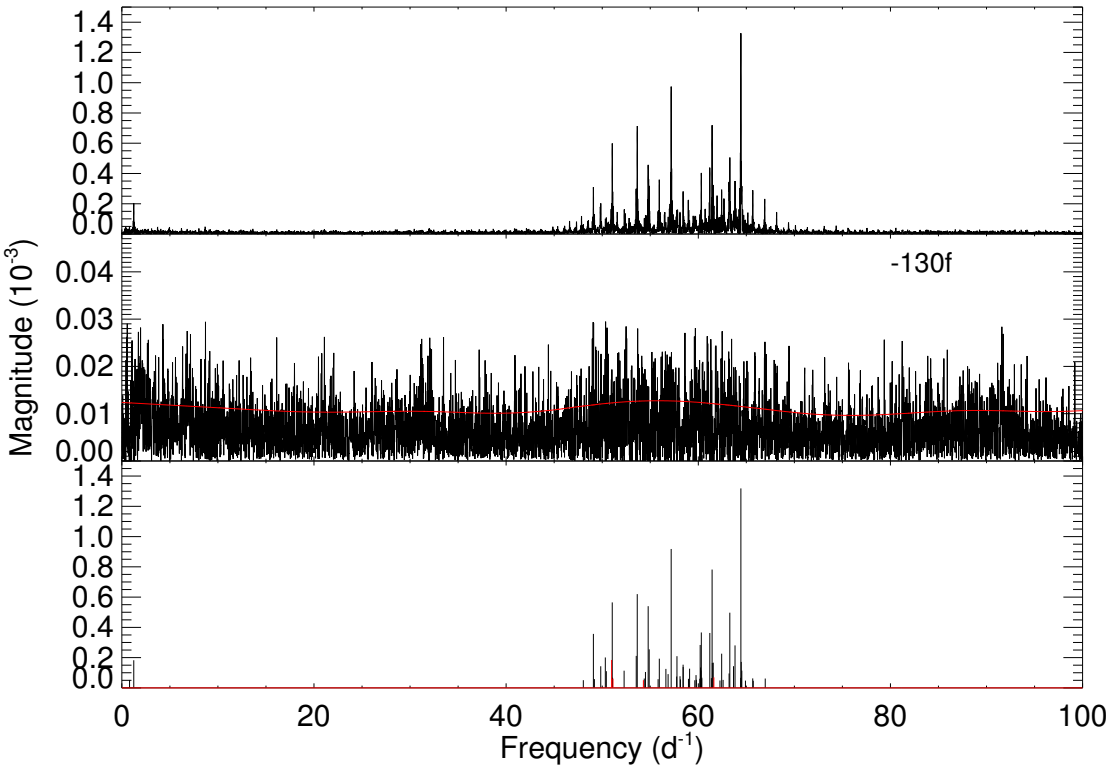

Figure 5.20 **Top panel:** The amplitude spectrum of the residual light curve of short cadence data (Q4) with eclipses masked. **Middle panel:** The noise spectrum after subtracting 130 frequencies. The solid red curve represents the adopted noise level. **Bottom panel:** The 64 extracted significant frequencies with S/N $>$ 4.0 as listed in Table 5.10 (black: independent frequencies; red: combination frequencies).

As the star is pulsating at relatively high radial orders, which are closer to the asymptotic regime, we can expect to find some frequency regularities similar to those observed in solar-like oscillators. García Hernández et al. (2015) found the signature of frequency regularities in six δ Scuti stars in eclipsing binaries by analyzing the Fourier Transform (FT) of the p-mode frequencies. These frequency patterns are close to the large frequency separation which is related to the mean stellar density. We applied the same FT technique to the frequencies in Table 5.10, and the Fourier spectrum is presented in Figure 5.21. The periodicity at 39.9μHZ$= 0.5\Delta\nu_{obs}$ is related to the large frequency separation. From the mean density of the primary, we can deduce the expected large separation ($\Delta\nu$) by using the linear relation between $\log\Delta\nu$ and $\log\rho$ (Suárez et al. 2014; García Hernández et al. 2015). The expected $\Delta\nu$ is 70.7 μHZ, which is similar to but smaller than the observed value $\Delta\nu_{obs} = 2 \times 39.9 =$ 79.8 μHZ. Paparo et al. (2016a, b) found the signatures of the large frequency separation in 90 δ Scuti stars observed by *CoRoT* satellite, and except for showing regularities of $\Delta\nu$, some of them show patterns which approximately agree with $\Delta\nu \pm \Omega_{rot}$ or $\Delta\nu \pm 2\Omega_{rot}$. If we adopt the synchronous rotational frequency $\Omega_{rot} = 5.2\mu$HZ, the corresponding rotational splittings for the high order p-modes are $m(1 - C_{nl})\Omega_{rot} \approx m\Omega_{rot}$, and $m = \pm 1$ and $m = \pm 1, \pm 2$ for $l = 1$ and $l = 2$ modes, respectively. We thus conclude that the observed pattern $\Delta\nu_{obs}$ agrees with the theoretical large frequency separation with rotational effect taken into account. Indeed, the highest peak in the Fourier spectrum in Figure 5.21 is at about 7.07μHZ which is only slightly smaller than the orbital frequency $f_{orb} = 7.176\mu$HZ, and thus this regularity is likely the result of rotational splitting.

To check whether the pulsation range can be explained by the non-adiabatic theory, we model the evolution of some single non-rotating stellar models with MESA (Paxton et al. 2011, 2013) and calculate their pulsation frequencies in the range of $20 - 70$ d^{-1} with GYRE (Townsend & Teitler 2013). We set the mixing length parameter $\alpha_{\rm MLT}$ to 1.8 and used the OPAL opacity tables (Iglesias & Rogers 1996). Solar mixtures in Grevesse & Sauval (1998) were adopted for the assumed solar composition. The results are presented in Figure 5.22. The pulsation modes ($l = 0, 1, 2$) from the equilibrium model with $M = 1.94 M_{\odot}$, $R = 1.67 M_{\odot}$, $Y = 0.28$, and $Z = 0.02$ are all stable ($\eta < 0$). However, we note that the peak of the instability parameter η (the normalized growth-rate defined in Stellingwerf 1978) is at $60 - 65$ d^{-1} which roughly agrees with the observed unstable range $50 - 65$ d^{-1}. Note that modes from a similar but slightly less massive model with $M = 1.79 M_{\odot}$, $R = 1.67 R_{\odot}$, $Y = 0.28$, and $Z = 0.02$ can produce unstable p-modes (positive η) in the range of $55 - 60$ d^{-1}. We have to be cautious in interpreting the above analysis based on single star evolution, because the real inner structure of the δ Scuti type primary may have different pulsation properties due to past mass transfer in the binary.

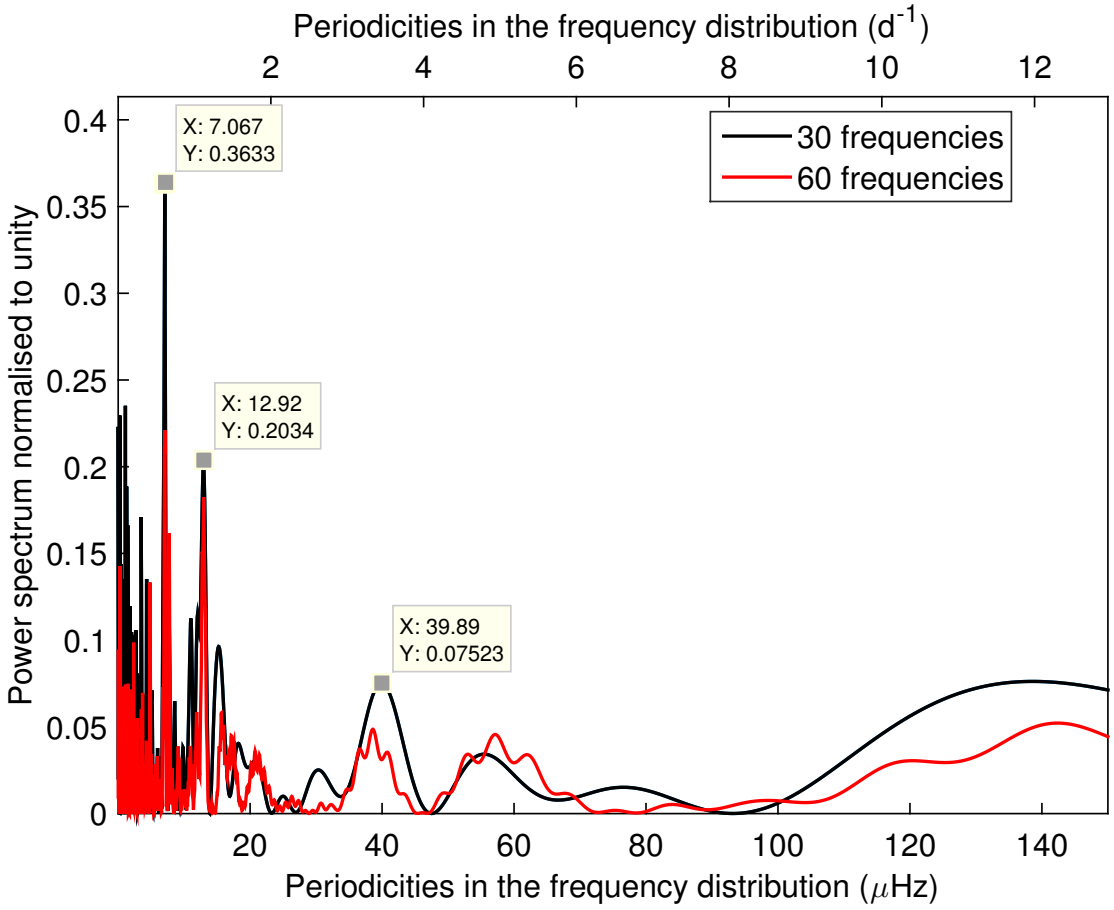

Figure 5.21 The Fourier spectrum of the reported oscillation frequencies in Table 4. The black and red lines are the results of using 30 and 60 highest frequencies, respectively. The highest peak at 7.067μHZ is likely the result of rotational splitting. The pattern at 39.89μHZ is related to the large frequency separation $\Delta\nu$. Please see text for more details.

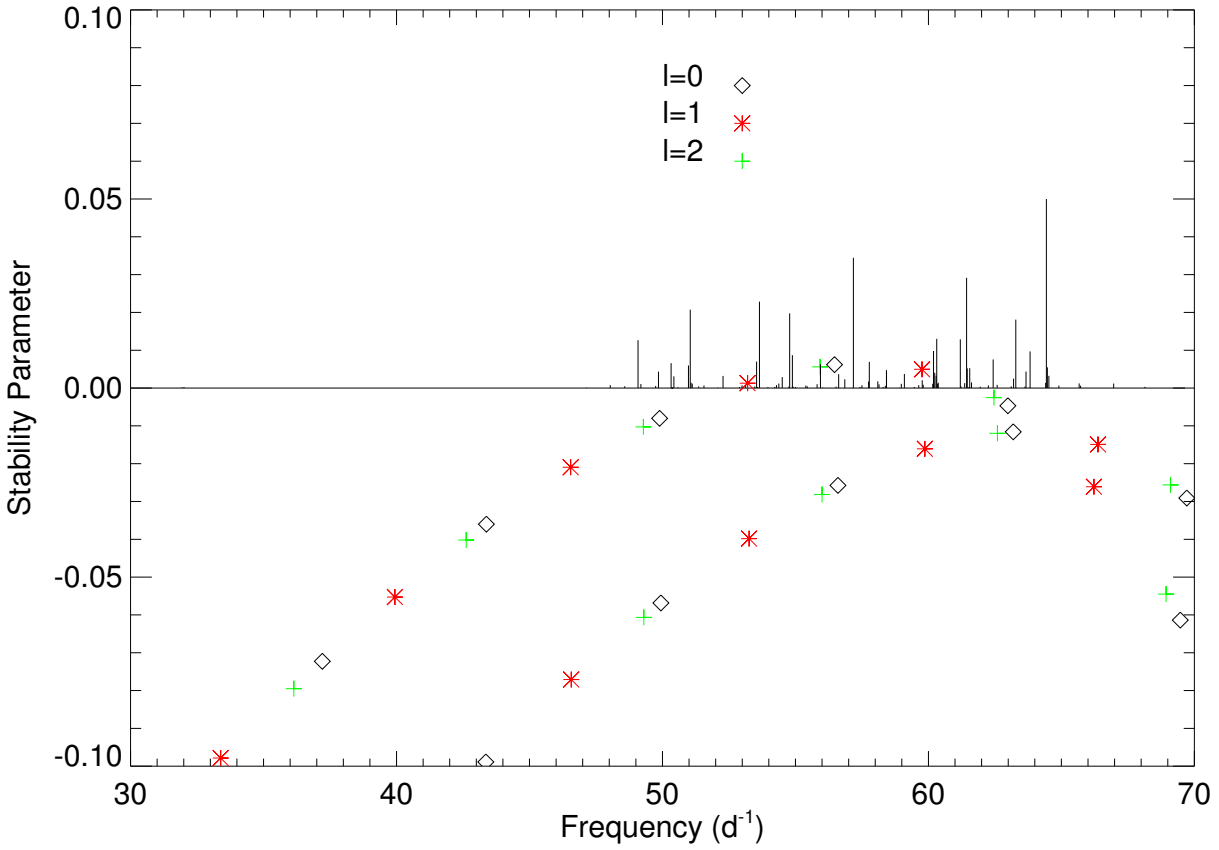

Figure 5.22 The stability parameter η of p-modes ($l = 0, 1, 2$) of two models for the primary star calculated with MESA and GYRE. The equilibrium models have the following parameters: (a) $M_1 = 1.79 M_\odot$, $R_1 = 1.66 R_\odot$; (b) $M_1 = 1.94 M_\odot$, $R_1 = 1.67 R_\odot$. Both models have the same $Z = 0.02$ and $Y = 0.28$. Modes of Model (a) are unstable (positive stability parameters) in the frequency range $53 - 62$ d^{-1} and all modes of model (b) are stable. The observed frequencies of KIC 8262223 are overplotted and re-scaled for clarity.

Table 5.10: Significant oscillation frequencies

	Frequency (d^{-1})	Amplitude (10^{-3})	Phase (rad/2π)	S/N	Comment
f_1	64.43390 ± 0.00010	1.319 ± 0.020	0.896 ± 0.007	114.5	
f_2	57.17794 ± 0.00016	0.918 ± 0.022	0.313 ± 0.011	72.3	
f_3	61.43616 ± 0.00018	0.782 ± 0.021	0.190 ± 0.012	64.4	
f_4	53.64792 ± 0.00024	0.620 ± 0.022	0.345 ± 0.016	49.0	
f_5	51.04548 ± 0.00026	0.565 ± 0.021	0.281 ± 0.017	46.0	
f_6	54.78183 ± 0.00028	0.540 ± 0.022	0.368 ± 0.019	42.5	
f_7	63.28439 ± 0.00028	0.497 ± 0.020	0.516 ± 0.019	42.2	
f_8	60.31265 ± 0.00040	0.366 ± 0.021	0.949 ± 0.027	29.7	
f_9	61.19863 ± 0.00040	0.363 ± 0.021	0.896 ± 0.027	29.8	
f_{10}	49.08047 ± 0.00039	0.357 ± 0.020	0.218 ± 0.027	30.1	
f_{11}	60.19302 ± 0.00052	0.284 ± 0.021	0.669 ± 0.035	22.9	
f_{12}	63.82187 ± 0.00049	0.281 ± 0.020	0.947 ± 0.033	24.1	
f_{13}	54.88585 ± 0.00059	0.255 ± 0.022	0.607 ± 0.040	20.0	
f_{14}	62.43309 ± 0.00063	0.226 ± 0.020	0.717 ± 0.042	18.9	
f_{15}	53.54042 ± 0.00071	0.212 ± 0.022	0.134 ± 0.048	16.7	
f_{16}	57.77610 ± 0.00071	0.210 ± 0.022	0.885 ± 0.048	16.6	
f_{17}	50.32422 ± 0.00071	0.201 ± 0.021	0.513 ± 0.048	16.6	
f_{18}	55.94001 ± 0.00078	0.193 ± 0.022	0.050 ± 0.053	15.2	
f_{19}	50.97786 ± 0.00079	0.185 ± 0.021	0.755 ± 0.053	15.1	
f_{21}	64.47378 ± 0.00079	0.172 ± 0.020	0.584 ± 0.053	14.9	
f_{22}	61.55406 ± 0.00086	0.167 ± 0.021	0.746 ± 0.058	13.7	
f_{23}	61.46043 ± 0.00087	0.165 ± 0.021	0.255 ± 0.059	13.6	
f_{24}	58.42108 ± 0.00097	0.153 ± 0.022	0.494 ± 0.066	12.2	
f_{25}	63.66929 ± 0.00096	0.144 ± 0.020	0.252 ± 0.065	12.3	
f_{26}	49.85027 ± 0.00100	0.143 ± 0.021	0.713 ± 0.067	11.9	
f_{27}	58.42454 ± 0.00108	0.138 ± 0.022	0.593 ± 0.073	10.9	
f_{28}	60.23810 ± 0.00108	0.135 ± 0.021	0.568 ± 0.073	10.9	
f_{29}	59.09553 ± 0.00117	0.127 ± 0.021	0.757 ± 0.079	10.1	
f_{30}	56.62486 ± 0.00120	0.126 ± 0.022	0.992 ± 0.081	9.9	
f_{31}	60.28838 ± 0.00126	0.116 ± 0.021	0.751 ± 0.085	9.4	
f_{32}	64.52926 ± 0.00119	0.114 ± 0.020	0.752 ± 0.080	9.9	
f_{33}	52.27648 ± 0.00130	0.114 ± 0.021	0.204 ± 0.088	9.1	
f_{34}	50.42825 ± 0.00130	0.111 ± 0.021	0.808 ± 0.088	9.1	
f_{35}	54.50442 ± 0.00142	0.105 ± 0.022	0.515 ± 0.096	8.3	
f_{36}	63.20290 ± 0.00146	0.096 ± 0.020	0.717 ± 0.099	8.1	
f_{37}	56.85719 ± 0.00165	0.091 ± 0.022	0.197 ± 0.111	7.2	
f_{38}	59.76651 ± 0.00174	0.084 ± 0.021	0.690 ± 0.118	6.8	
f_{40}	57.75009 ± 0.00199	0.075 ± 0.022	0.430 ± 0.134	5.9	
f_{41}	61.62167 ± 0.00207	0.069 ± 0.021	0.177 ± 0.139	5.7	

f_{42}	60.36814 ± 0.00215	0.068 ± 0.021	0.742 ± 0.145	5.5	
f_{43}	51.07405 ± 0.00215	0.068 ± 0.021	0.854 ± 0.145	5.5	
f_{44}	64.40949 ± 0.00205	0.067 ± 0.020	0.325 ± 0.138	5.8	
f_{45}	61.36160 ± 0.00222	0.065 ± 0.021	0.574 ± 0.150	5.3	
f_{46}	65.66649 ± 0.00212	0.063 ± 0.019	0.513 ± 0.143	5.6	
f_{47}	66.96511 ± 0.00209	0.062 ± 0.019	0.258 ± 0.141	5.7	
f_{48}	54.37597 ± 0.00243	0.062 ± 0.022	0.028 ± 0.164	4.9	
f_{49}	51.11913 ± 0.00237	0.061 ± 0.021	0.195 ± 0.160	5.0	
f_{50}	60.16181 ± 0.00242	0.060 ± 0.021	0.567 ± 0.163	4.9	
f_{51}	60.34386 ± 0.00242	0.060 ± 0.021	0.157 ± 0.163	4.9	
f_{52}	58.97922 ± 0.00247	0.060 ± 0.021	0.686 ± 0.167	4.8	
f_{54}	55.81344 ± 0.00262	0.057 ± 0.022	0.227 ± 0.177	4.5	
f_{55}	58.14367 ± 0.00266	0.056 ± 0.022	0.960 ± 0.179	4.5	
f_{56}	59.80451 ± 0.00275	0.054 ± 0.021	0.532 ± 0.185	4.3	
f_{58}	0.79928 ± 0.00277	0.052 ± 0.021	0.658 ± 0.187	4.3	
f_{59}	54.28582 ± 0.00294	0.051 ± 0.022	0.767 ± 0.199	4.0	
f_{60}	48.03643 ± 0.00270	0.051 ± 0.020	0.140 ± 0.182	4.4	
f_{61}	59.63633 ± 0.00291	0.051 ± 0.021	0.109 ± 0.197	4.1	
f_{62}	62.25437 ± 0.00288	0.049 ± 0.021	0.425 ± 0.194	4.1	
f_{63}	64.90535 ± 0.00281	0.048 ± 0.020	0.340 ± 0.190	4.2	
f_{64}	65.72024 ± 0.00282	0.047 ± 0.019	0.585 ± 0.190	4.2	
f_{20}	1.23967 ± 0.00079	0.183 ± 0.021	0.027 ± 0.053	14.9	$2f_{orb}$
f_{39}	58.09686 ± 0.00194	0.077 ± 0.022	0.993 ± 0.131	6.1	$f_{37} + 2f_{orb}$
f_{53}	49.18796 ± 0.00242	0.058 ± 0.020	0.677 ± 0.163	4.9	$f_{34} - 2f_{orb}$
f_{57}	62.58379 ± 0.00267	0.053 ± 0.020	0.528 ± 0.180	4.4	$f_{36} - f_{orb}$

5.4.6 Evolution

The primary star of KIC 8262223 appears like a normal A-type dwarf near the zero age main sequence (ZAMS) (slightly overluminous), while the low-mass secondary is noticeably over-sized and over-luminous. The classical scenario for the formation of this type of cool Algol system involves the mass transfer (probably case B) from the original massive primary (donor) to the original less massive secondary, leading to a mass reversal (Paczynski 1971; Nelson & Eggleton 2001; Eggleton & Kiseleva- Eggleton 2002).

KIC 8262223 is likely to evolve into a typical EL CVn system, which consists of a normal A- or F-type dwarf and a low mass ($\approx 0.2M_{\odot}$) helium white dwarf precursor (pre-He WD). Maxted et al. (2014) presented 17 EL CVn systems discovered by the WASP survey. KIC 8262223 closely resembles the cool Algol system KIC 10661783 described by Southworth et al. (2011) and Lehmann et al. (2013). The latter authors also discussed several similar systems such as AS Eri (Mkrtichian et al. 2004) and V228 (Kaluzny et al. 2007). Sarna et al. (2008) found that a system with similar initial masses and slightly longer period ($M_{10} = 0.88M_{\odot}, M_{20} = 0.85M_{\odot}, P = 1.35$d) can evolve to the current state of V228 ($M_2 = 0.20M_{\odot}, M_1 = 1.51M_{\odot}, P = 1.15$d) through non-conservative case B mass transfer. For better comparison, we list the parameters of four systems KIC8262223, KIC10661783, AS Eri, and V228 in Table 5.11. All these binaries consist of a low mass secondary ($\approx 0.2M_{\odot}$) and may have similar evolutionary history as detailed below.

Table 5.11: Fundamental

Name	M_1 ($M_\odot$)	M_1 ($M_\odot$)	R_1 ($R_\odot$)	R_2 ($R_\odot$)	$T_{\rm eff1}$ (K)	$T_{\rm eff1}$ (K)	Period (days)	Pulsation (d^{-1})	Remark
KIC8262223	1.94	0.20	1.67	1.31	9128	6849	1.61	$50-65$	detached
KIC10661783	2.05	0.20	2.56	1.12	7760	5980	1.23	$20-30$	detached
AS Eri	1.92	0.21	1.50	1.15	7290	4250	2.66	≈ 60	semi-detached
V228	1.51	0.20	1.36	1.24	8070	5810	1.15	...	semi-detached

Chen et al. (2016) found that EL CVn type binaries can result from non-conservative binary evolution with long-term stable mass transfer between low-mass stars and that avoided a rapid common-envelope evolution. They did thorough simulations with the MESA code to analyze the evolution channel of EL CVn stars from low mass progenitors ($M_{10} \in [0.9, 2.0]M_{\odot}$ and $q_0 = M_{10}/M_{20} \in [1.1, 4.0]$). The parameters of the secondary star of KIC 8262223 ($R_2/a = 0.176$, $T_{\rm eff2} = 6849K$) fit their $R_2/a - T_{\rm eff2}$ relation for pre-He WD very well (see their Fig. 9). They also found a tight correlation between orbital periods and WD masses as shown in their Fig. 10. Our observed values ($P = 1.6$d, $M_2 = 0.20M_{\odot}$) also nicely match their theoretical relations. According to their Figure 7, the pre-He WD in KIC 826223 with a mass of $0.2M_{\odot}$ has an envelope mass of $0.02M_{\odot}$.

To form EL CVn stars from two low mass progenitors, the initial orbital period has to be slightly longer than 'the bifurcation period' (P_b) between the contact and non-contact systems. The mass donor will evolve to the cooler, less luminous part of the H-R diagram when mass transfer starts and eventually enter into a long-lived phase at nearly constant luminosity (pre-He WD phase). The donor in systems with shorter periods ($P < P_b$) will evolve to a state of very low luminosity, and the systems will experience a common envelope evolution or merger.

Due to the uncertainties in the treatment of mass loss and angular momentum loss of binary evolution, we do not attempt to find a best matching evolution history for KIC 8262223. Instead, we show that this binary as well as other binaries in Table 5.11 can be qualitatively explained by the aforementioned formation channel. We used the binary module of

MESA (v7624) (Paxton et al. 2011, 2013) and evolved two systems: (1) $M_{10} = 1.35M_{\odot}$, $M_{20} = 1.15M_{\odot}$ and $P_0 = 2.89$ d; (2) $M_{10} = 1.0M_{\odot}$, $M_{20} = 0.9M_{\odot}$ and $P_0 = 3.0$d. The metallicities were set to the solar value ($Z = 0.02$) and initial helium abundances were fixed to $Y = 0.28$. The evolutionary tracks were assumed to be non-conservative. Following the assumptions in Chen et al. (2016), half of the mass lost from the vicinity of the donor is accreted by the gainer while the other 50% leaves the system as a fast wind, carrying away the same angular momentum of the donor.

The evolutionary paths are shown in the H-R diagram in Figure 5.23. The black and red tracks are for the donor and gainer in model (1), respectively. In Figure 5.24 we show the evolution of parameters of model (1). The system starts with an orbital period of 2.89 d, and the two stars follow their single star evolutionary tracks and the orbit slightly shrinks. The mass transfer begins when the primary evolves to the sub-giant stage and its radius reaches its Roche lobe (at $t = 3.32$ Gyr, marked by the filled circles). During the mass transfer, the radius of the donor is the same or slightly larger than the Roche lobe (to a few percent). The orbital period gets shorter and the system shrinks until the two stars have equal masses ($t = 3.85$ Gyr, marked by the filled triangles), after which the orbit begins to expand. At an age of 4.18 Gyr as indicated by the filled stars, the mass transfer stops. At the same time, the radius of the donor star reaches a maximum, and it then begins to contract, cool, and evolve to a He WD precursor. The system ends up with parameter values $M_1 = 0.218M_{\odot}, M_2 = 1.716M_{\odot}$, and $P = 3.59$d.

We also present the evolution of the initial primary and secondary star (gray and light

red lines, respectively) of model (2) in Figure 5.23. The filled circles in gray and light red indicate the onset of mass transfer. The final status of this system has parameters of $M_1 = 0.20 M_\odot, M_2 = 1.30 M_\odot, P = 1.06$d.

We have over-plotted the observed positions of the four systems mentioned above in the H-R diagram in Figure 5.23. The low mass secondary which was the previous mass donor is indicated by black open symbols. The mass gainers evolve along the red tracks to the upper left and arrive at the observed locations of the A- or F-type dwarfs (red open symbols). For KIC 8262223, the secondary seems to be a star that has just finished its mass transfer and is contracting (i.e., from filling its Roche lobe to under-filling its Roche lobe). It may evolve to an EL CVn star after further contraction.

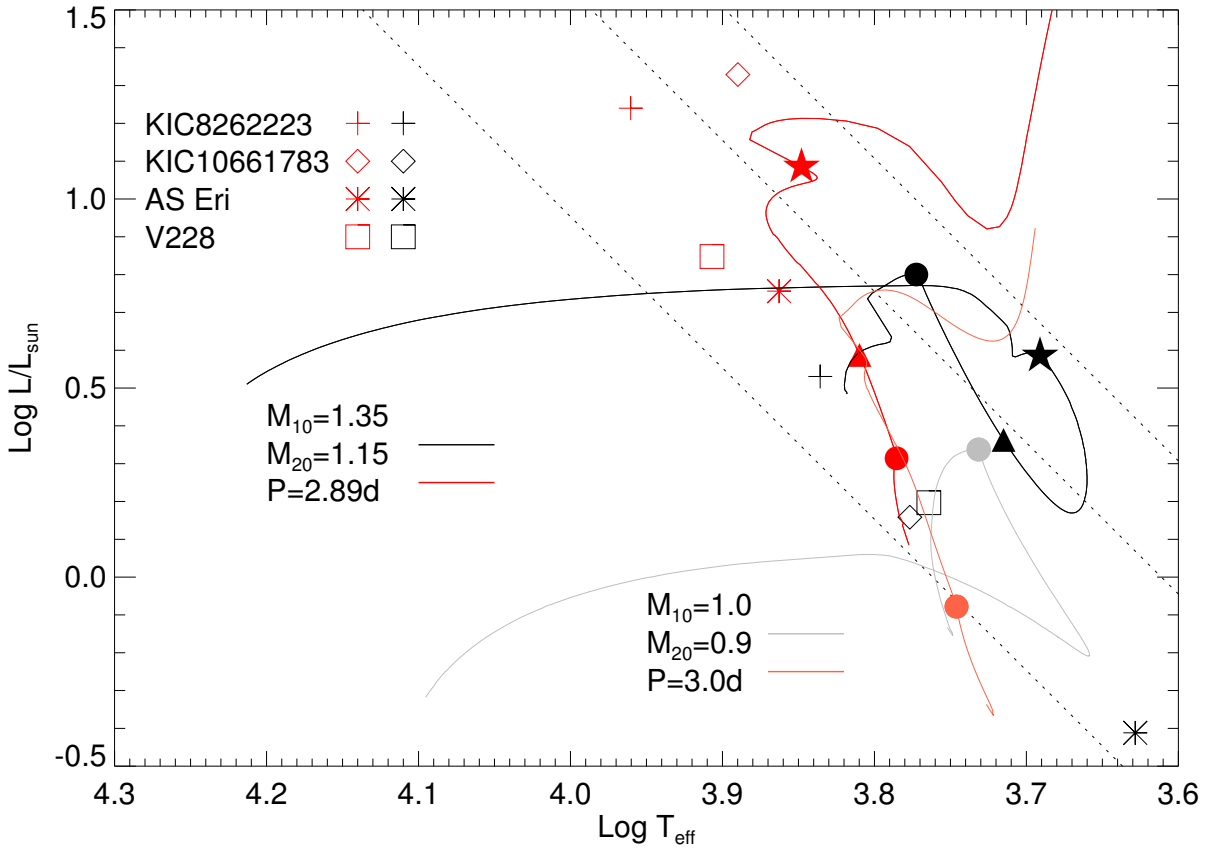

Figure 5.23 Evolution tracks for two binary models in the H-R diagram. Model (1): $M_{10} = 1.35M_{\odot}, M_{20} = 1.15M_{\odot}, P = 2.89$d. Model (2): $M_{10} = 1.0M_{\odot}, M_{20} = 0.9M_{\odot}, P = 3.0$d. The evolutionary tracks for the initial primary and secondary of model (1) are shown as red and dark solid lines, respectively. The corresponding tracks for models (2) are indicated as gray and light red lines. The locations of four cool Algols in Table 5.11 are shown as open symbols. Three moments in the evolution are marked for model (1): the onset of mass transfer (filled circle), orbital period reaches minimum (filled triangle) and the end of mass transfer (filled star). For model (2), only the onset of mass transfer is labeled.

It is interesting to note that the dwarf stars in these systems are often pulsating (all but V228, which has a mass too low to be a δ Scuti pulsator). As can be seen in Table 5.11, these systems can pulsate at low ($20 - 30$ d^{-1}) as well as high frequencies ($50 - 60$ d^{-1}). It is known that the unstable range of pulsations will vary as the star evolves off the ZAMS. For example, for a δ Scuti star with $M = 1.8 M_{\odot}$, the p-modes $n_p = 4 - 7$ ($45 - 60$ d^{-1}) are unstable for young models close to ZAMS. The unstable range moves to $5 - 25$ d^{-1} for models near TAMS which are low order p-modes and g-modes (Dupret 2002). Asteroseismology has the potential of determining the ages of the δ Scuti pulsators in these EL CVn binaries. Not only the dwarfs, but the pre-He WD precursor can also show pulsations. And these pulsations enabled the discovery of a thick hydrogen envelope on the pre-He WD J0247-25B (Maxted et al. 2013). More information can be extracted from these pulsations, which may lead to great advancements in our understanding of the evolution of low mass close binaries.

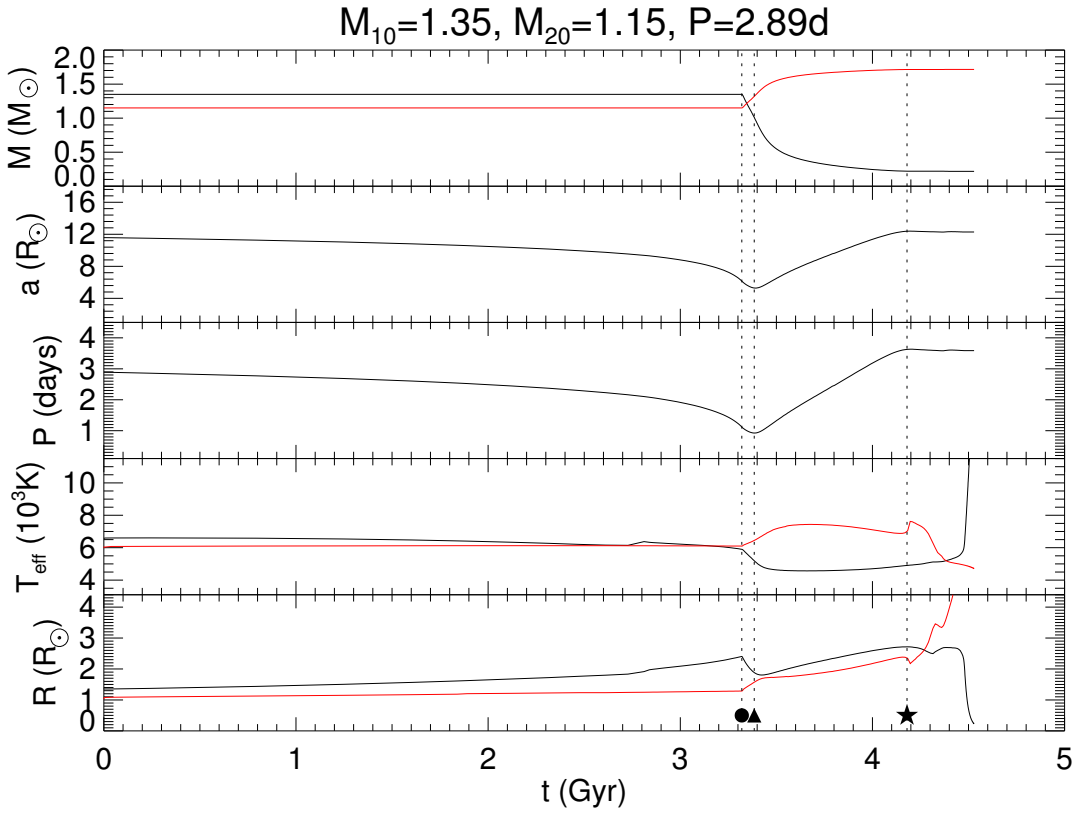

Figure 5.24 The evolution of a close binary system with initial masses $M_{10} = 1.35M_{\odot}$, $M_{20} = 1.15M_{\odot}$ and initial period $P = 2.89$ days. The parameters mass (M), semi-major axis (a), period (P), effective Temperature ($T_{\rm eff}$), and radius (R) are shown as a function of time (t). The initial more massive star (donor) is indicated as black solid line and the mass gainer is shown in red. The vertical dashed lines label three important moments in the evolution: the onset of mass transfer (filled circle), orbital period reaches minimum (filled triangle), and the end of mass transfer (filled star). Please see text for more details.

5.4.7 Conclusions and Prospects

Utilizing the accurate *Kepler* photometric data and our ground-based spectroscopic data, we determined the fundamental parameters of KIC 8262223, an eclipsing binary system with an orbital period of 1.6 days which contains an A-type dwarf and an oversized low mass secondary star. The light curve shows high frequency pulsations at about 60 d^{-1}. These δ Scuti type pulsations are likely from the primary star and can be explained as radial and non-radial p-modes. We discussed possible evolutionary scenarios and showed that this system and several other very similar binaries can be explained by the non-conservative evolution of close binaries with low mass progenitors as detailed in Chen et al. (2016). KIC 8262223 also poses some challenges to our non-adiabatic theory of stellar pulsations as the modes calculated from the equilibrium model which match the observed modes of the primary are stable. A future spectroscopic follow up covering the full orbit could help pin point accurate masses and rotational alignment.

Asteroseismic modeling has not yet been applied to δ Scuti stars in pulsating Algols (oEAs) due to the complex nature of these systems. As a prerequisite, it is possible to identify the pulsation modes through high cadence and high resolution spectroscopy. The eclipse mapping method (Reed et al. 2005; Bíró & Nuspl 2011) is also promising but still awaits application to a real object. Several hundreds of δ Scuti variables are already detected by the *Kepler* satellite, and future missions like *TESS* will provide more systems. A complete analysis of their pulsational properties will require a better understanding of close binary tidal interactions and binary evolution.

5.5 Other δ Scuti and γ Doradus EBs

The two systems KIC 9851944 and KIC 8262223 are among the 41 eclipsing binaries for which we started the ground-based spectroscopic follow-up observations. Among these, we briefly summarize the characteristics of 10 δ Sct or γ Dor pulsating eclipsing binaries in Table 5.12. The effective temperatures are taken from Armstrong et al. (2014). We then show their light curves and oscillation spectra (Figure $5.25 - 5.34$) calculated from the residuals after subtracting a binned model light curve. The detailed analysis of their light curves and spectra is still in process. Descriptions of each system are presented in the captions. The spectroscopic orbits were derived for most of these systems and will be presented by R. Matson (2016, in preparation).

Table 5.12: Parameters of Other Pulsating EBs

Name	$T_{\rm eff1}$ (K)	$T_{\rm eff2}$ (K)	Period (days)	Frequency Range (d^{-1})	Main Frequency (d^{-1})	Pulsation Class
KIC 3858884	6800 ± 70	6606 ± 70	25.95200	$(< 3), (7 - 15)$	7.23	δ Sct/γ Dor
KIC 9851944	7026 ± 70	6902 ± 70	2.1639019	< 16	10.40	δ Sct/γ Dor
KIC 8262223	9128 ± 150	7719 ± 150	1.6130147	$50 - 65$	64.43	δ Sct
KIC 4851217	7022 ± 373	6804 ± 587	2.4702807	$15 - 21$	19.09	δ Scuti
KIC 7368103	10098 ± 457	6699 ± 704	2.182516	$20 - 30$	28.58	δ Scuti
KIC 8553788	10028 ± 483	6939 ± 570	1.506504	$40 - 60$	58.26	δ Scuti
KIC 9159301	7257 ± 373	3540 ± 541	3.044770	$26 - 30$	27.36	δ Scuti
KIC 10619109	7441 ± 391	3824 ± 571	2.0451612	$20 - 50$	42.80	δ Scuti
KIC 10686876	10230 ± 1039	6475 ± 817	2.6184292	$20 - 24$	23.08	δ Scuti
KIC 12071006	9634 ± 413	5721 ± 601	6.096022	$14 - 24$	15.16	δ Scuti
KIC 10736223	10388 ± 416	6148 ± 592	1.1050920	$15 - 21$	25.04	δ Scuti
KIC 9592855	7934 ± 381	7805 ± 570	1.2193248	< 24	2.23	δ Sct/γ Dor
KIC 10486425	7494 ± 360	5916 ± 642	5.2748069	< 3	1.32	γ Dor

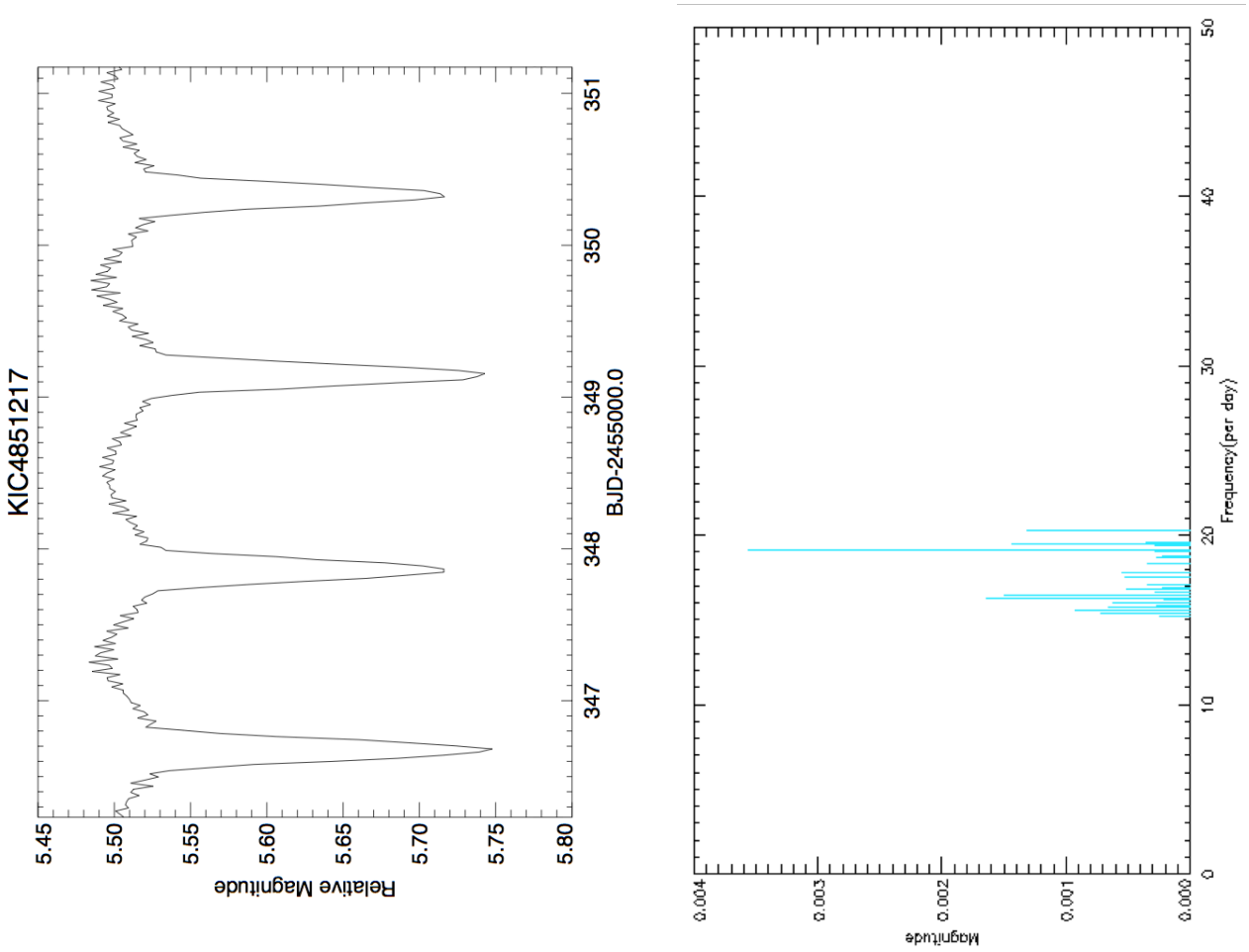

Figure 5.25 The light curve and oscillation spectrum of KIC 4851217 calculated by using the short cadence data. The pulsation range is from 15 to 21 d^{-1} with the highest pulsation frequency at 19.09 d^{-1}.

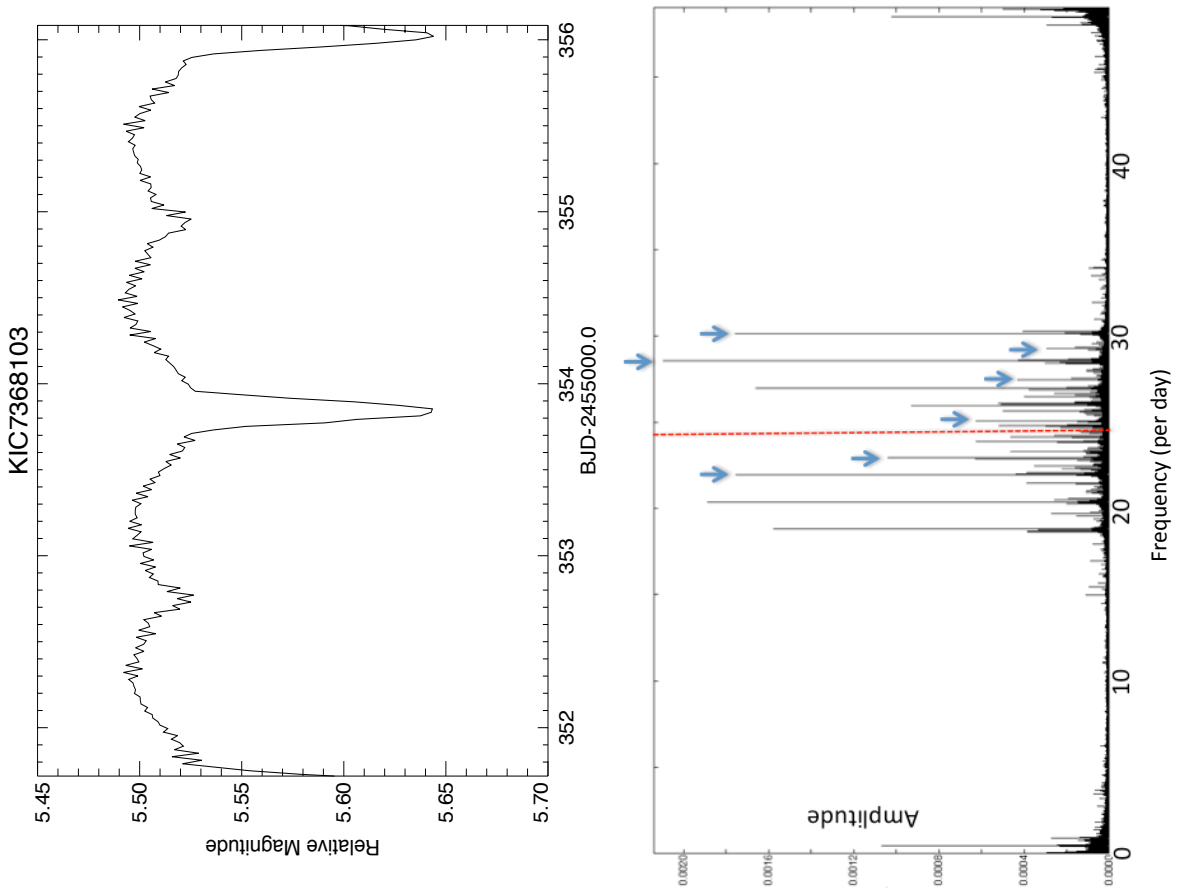

Figure 5.26 The light curve and oscillation spectrum of KIC 7368103. Only long cadence data are available, but the super-Nyquist frequencies ($> f_{Nyquist} \sim 24$ d^{-1}) can be identified following the method in Murphy et al. (2012). The arrows mark the real frequencies, and the corresponding aliases are symmetric to the Nyquist frequency indicated by the red dashed line. The highest pulsation frequency occurs at about 28.58 d^{-1}.

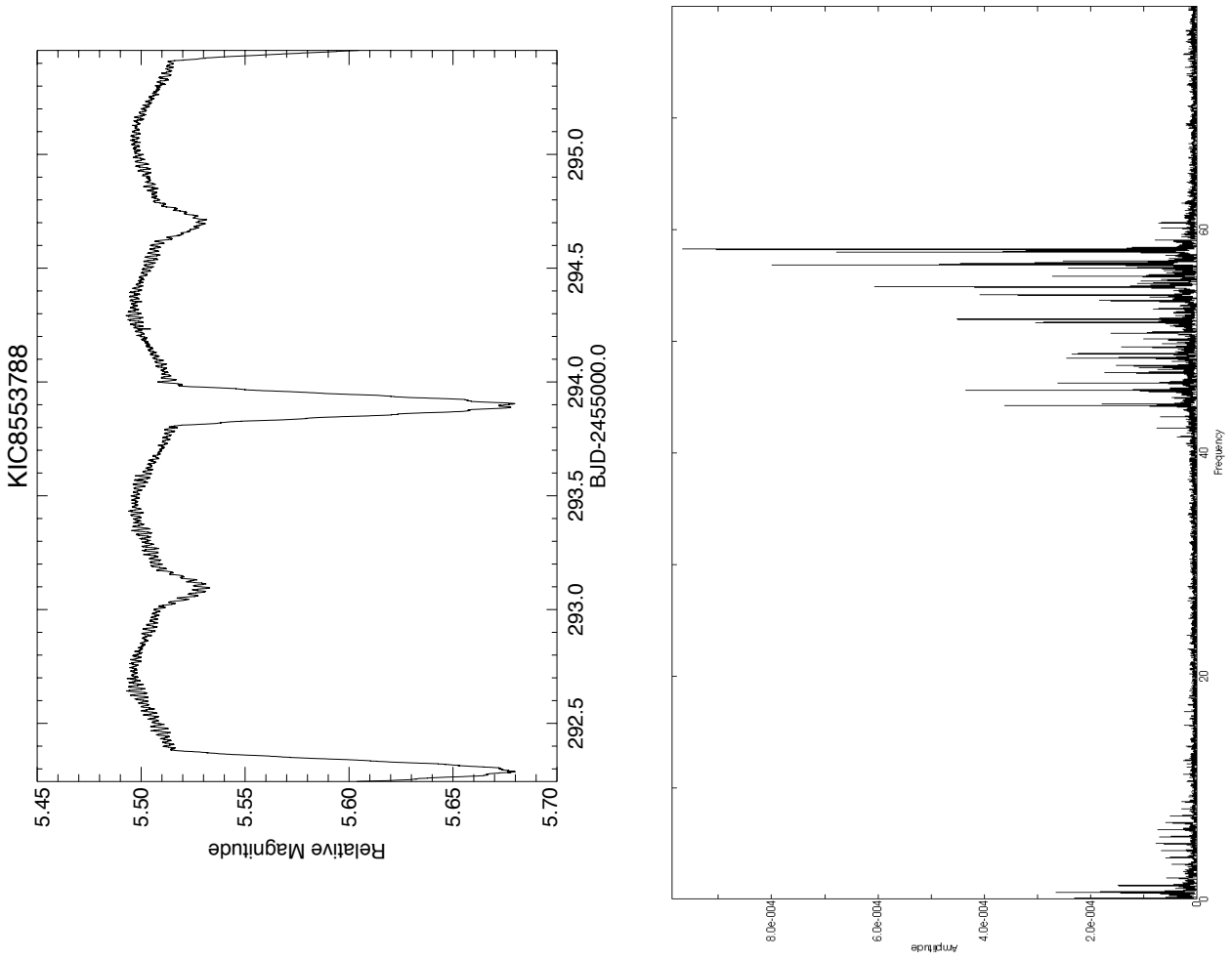

Figure 5.27 The light curve (short cadence) and oscillation spectrum of KIC 8553788. The high frequency oscillations can only been seen the short cadence data. Most of the pulsations occur over the frequency range of $40 - 60$ d^{-1}. The strongest pulsation has a frequency of 58.26 d^{-1}. Both the binary light curve and pulsation spectrum resemble those of KIC 8262223 discussed in the last section. It is thus possible that KIC 8553788 is an oscillating Algol.

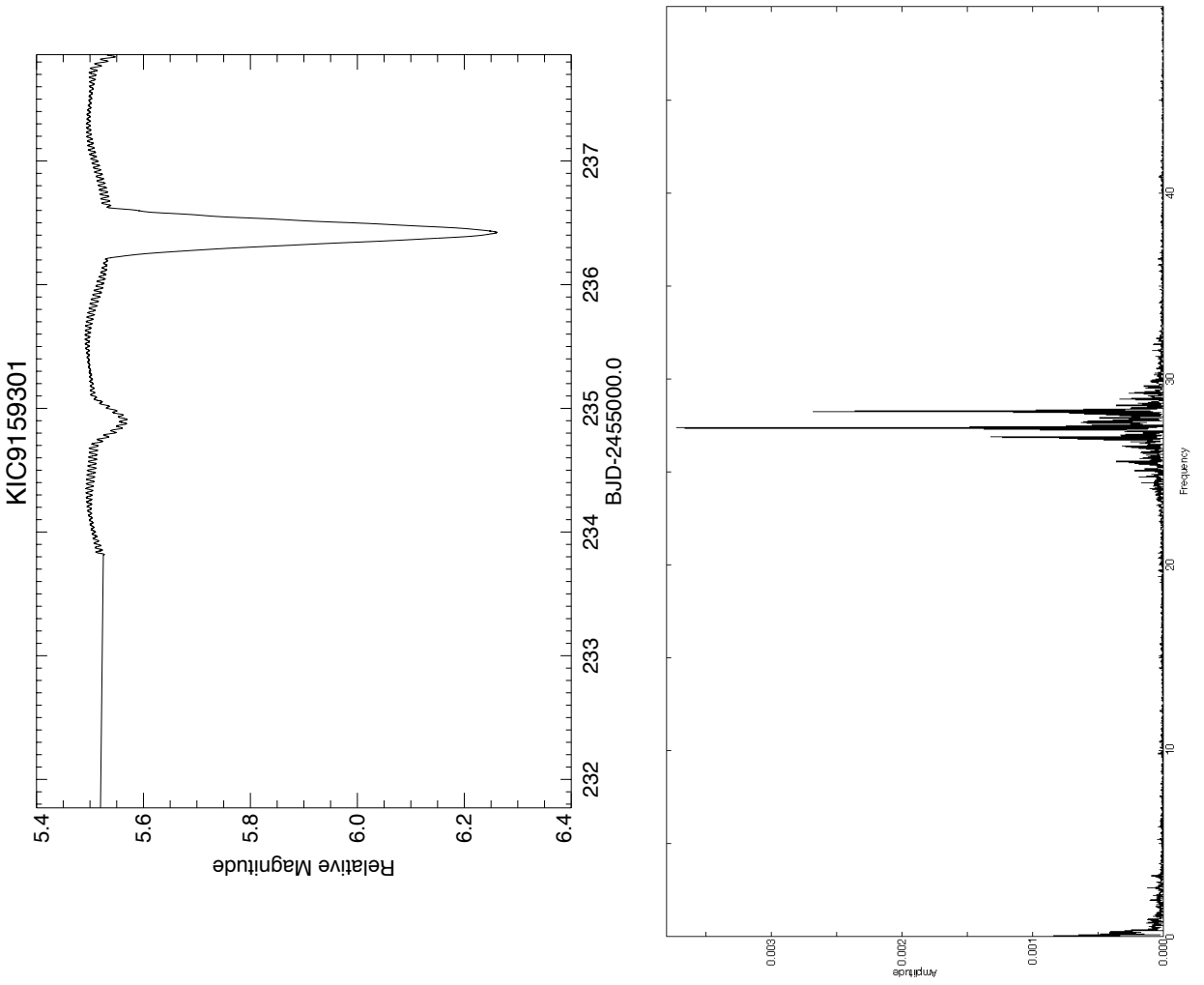

Figure 5.28 The light curve (short cadence data) and oscillation spectrum of KIC 9159301. The three strongest pulsations occur at frequencies of $f_1 = 27.36$, $f_2 = 28.25$, $f_3 = 26.87$ d^{-1}, which are in the decreasing order of amplitude. A small mass ratio $q = M_2/M_1 \approx 0.25$ is derived from RVs. The secondary star has a low effective temperature ($T_{\rm eff} \approx 3000 - 4000$ K).

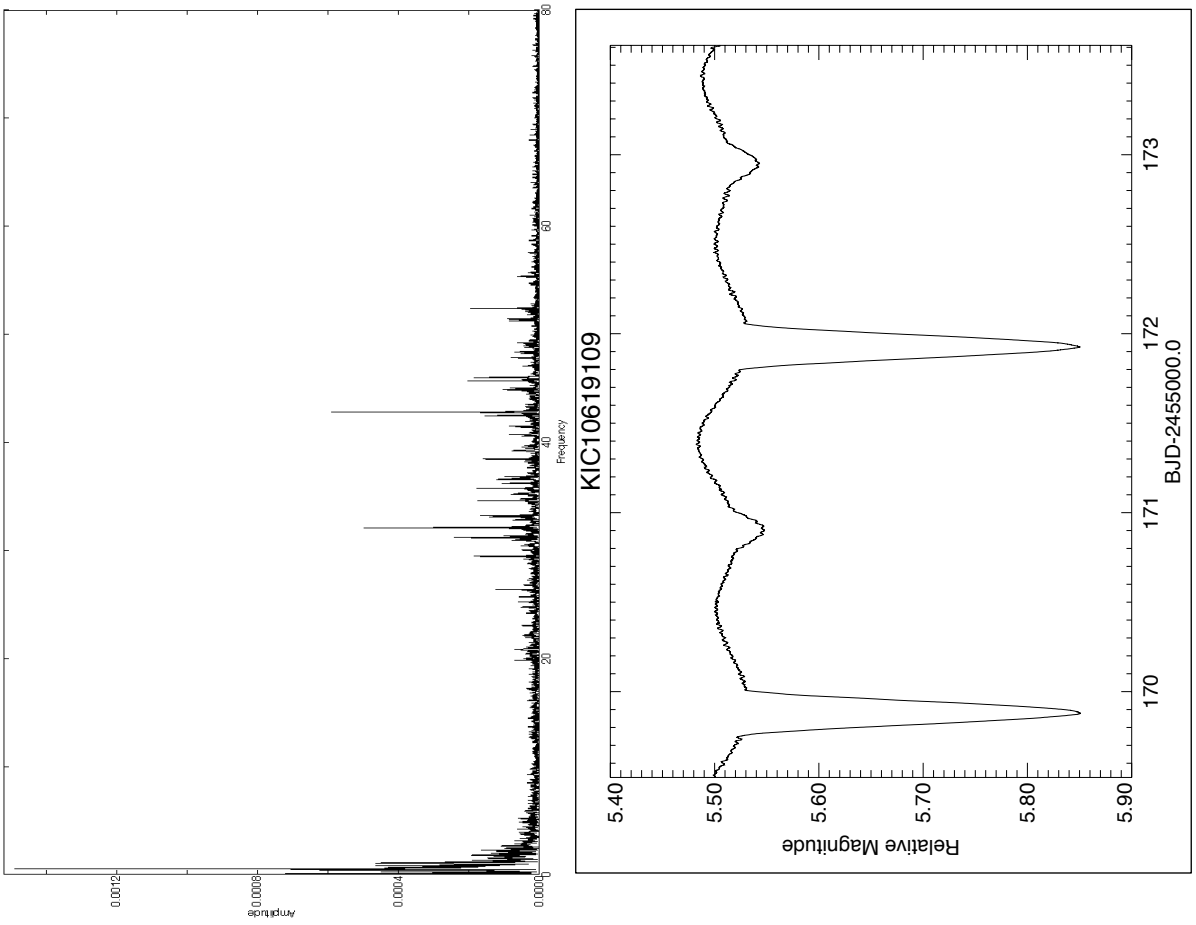

Figure 5.29 The light curve and oscillation spectrum of KIC 10610109. The two highest pulsations are at 42.80 and 32.09 d^{-1}. The two maxima at the quadrature phases have very different amplitudes, which is probably due to the O'Connell effect, i.e., long-lived starspots (see also Figure 1.36 in Gies et al. 2012).

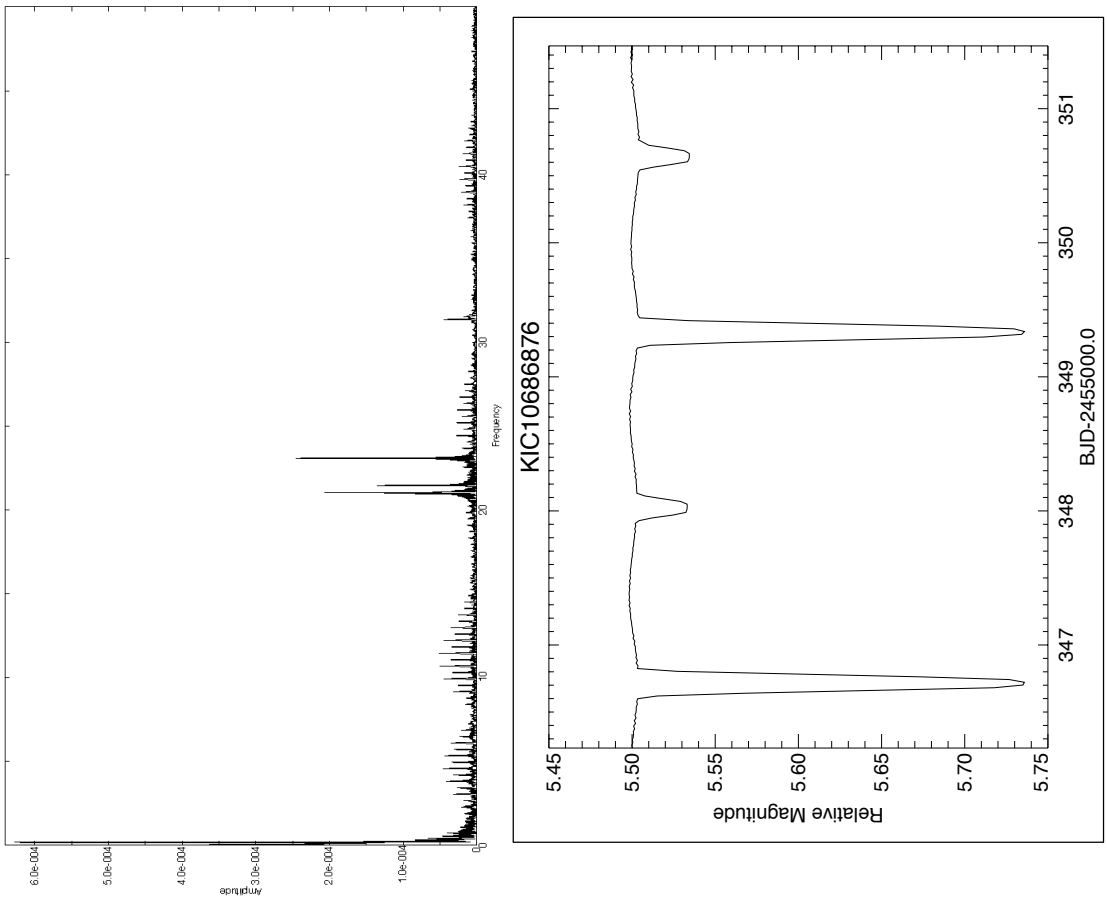

Figure 5.30 The light curve and oscillation spectrum of KIC 10686876. The three strongest pulsations have frequencies of 23.08, 21.03, and 21.46 d^{-1}. There are also a series of peaks with equal spacings due to the imperfect subtraction of the binary light curve.

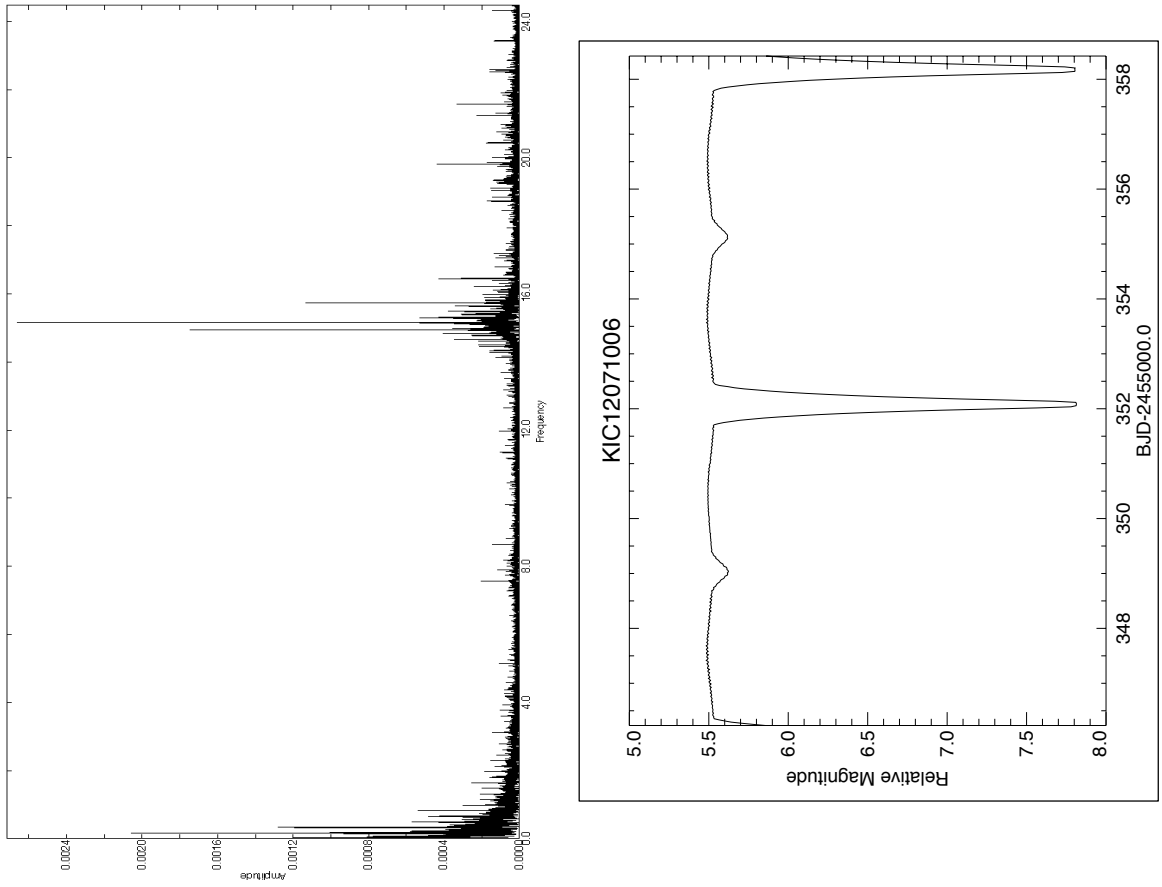

Figure 5.31 The light curve and oscillation spectrum of KIC 12071006. The dominant pulsation has a frequency of 15.156 d^{-1}.

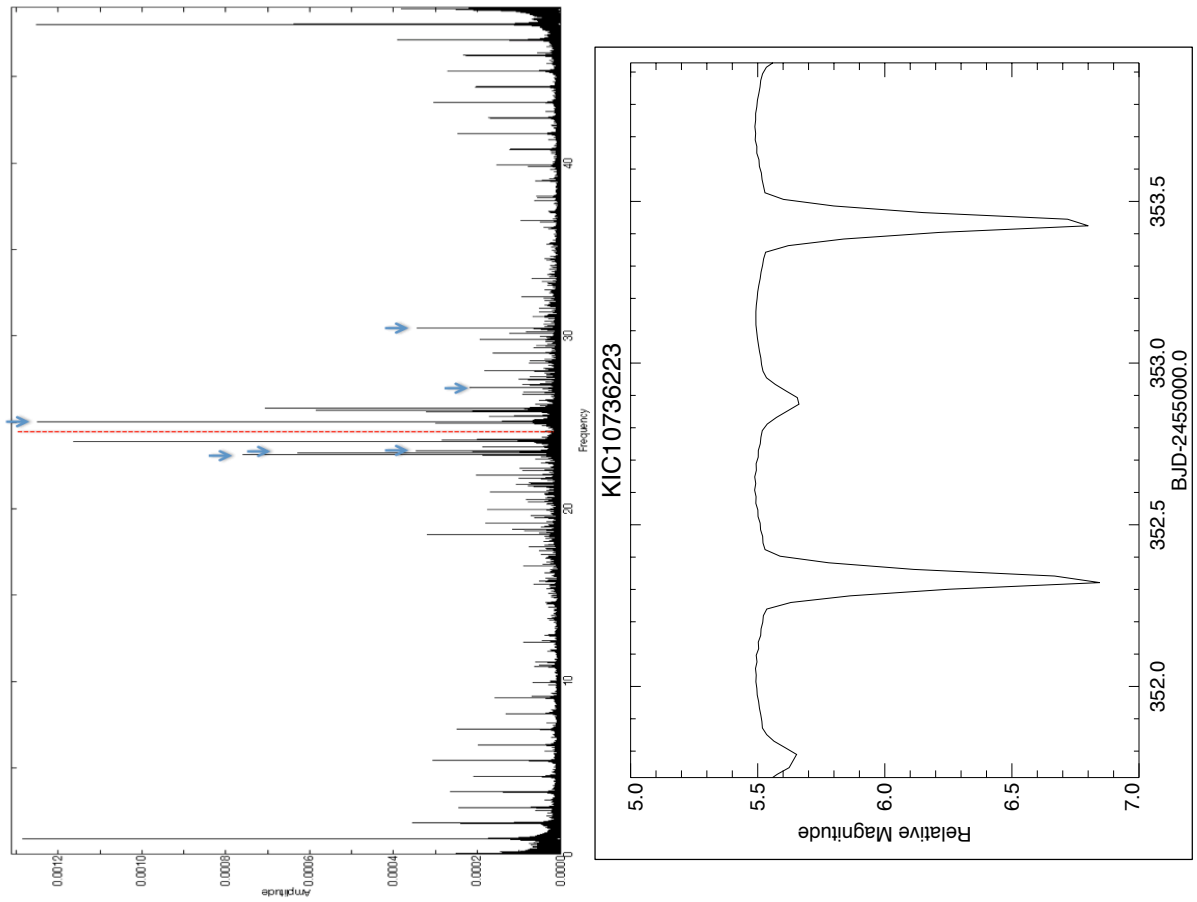

Figure 5.32 The light curve and oscillation spectrum of KIC 10736223. The frequency peaks at $\sim 20 - 30$ d^{-1} are due to pulsations. The arrows mark the real frequencies, and the corresponding aliases are symmetric to the Nyquist frequency indicated by the red dashed line. The equally spaced frequencies at $\sim< 11$ d^{-1} (and their reflections at about > 39 d^{-1}) are due to the imperfect removal of the binary light curve.

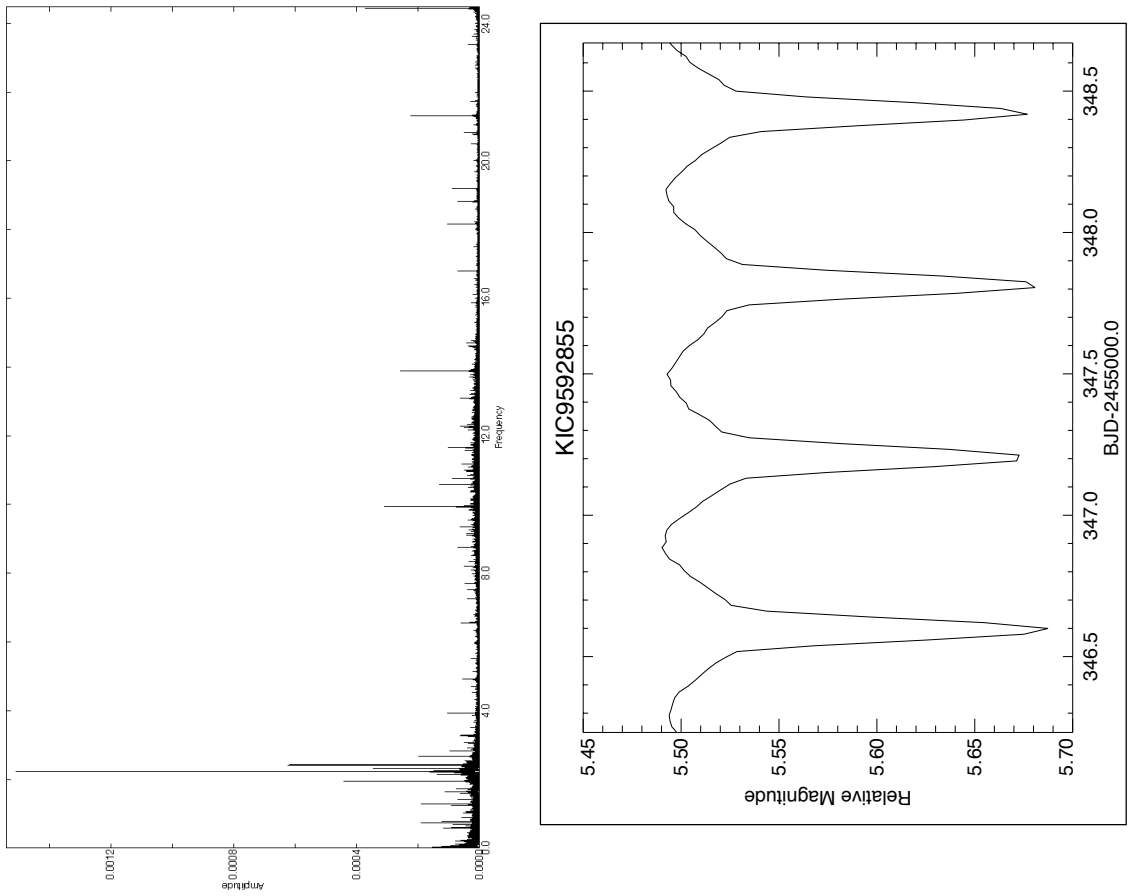

Figure 5.33 The light curve and oscillation spectrum of KIC 9592855. Both γ Dor type low-frequency peaks at around 2.23 d^{-1} and δ Scuti type high frequencies are present.

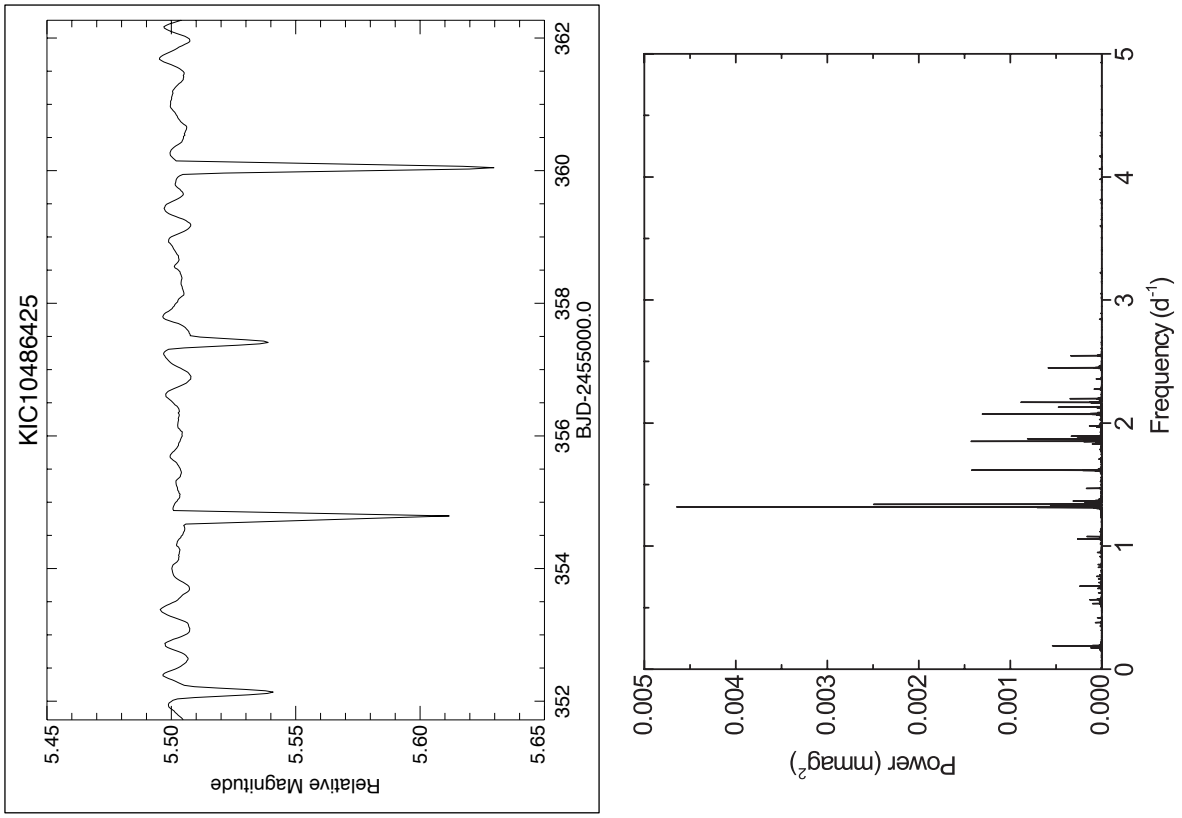

Figure 5.34 The light curve and oscillation spectrum of KIC 10486425. The power spectrum is taken from Aliçavuş & Soydugan (2014). The pulsation are of γ Dor type and the dominant pulsation has a frequency of about 1.319 d^{-1}. This binary is probably a triple system suggested from spectroscopy.

5.6 Frequency Regularities in δ Scuti Stars

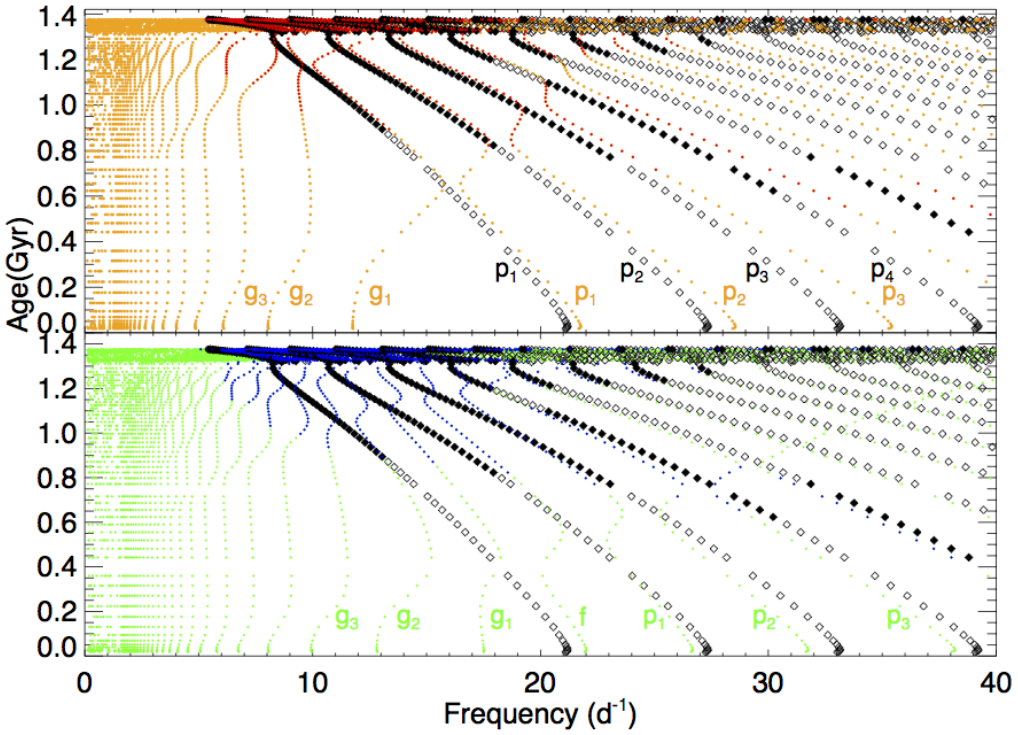

Figure 5.35 Evolution of oscillation frequencies from ZAMS to post-MS for a $1.8M_{\odot}$ star, with $Z = 0.018$, $Y = 0.28$, $f_{ov} = 0.005$. The upper panel shows the radial ($l = 0$, diamond) and dipole ($l = 1$, orange/red dots) modes, the lower panel shows the radial ($l = 0$, diamond) and quadruple ($l = 2$, green/blue dots) modes. The corresponding radial orders (n) are labeled for p-modes (p_n), g-modes (g_n) and f-modes (only for $l = 2$). The filled symbols, red dots, and blue dots indicate unstable modes of $l = 0, 1, 2$, respectively. Due to the denseness of high order g-modes, the calculated frequencies less than ≈ 2 d^{-1} are not reliable.

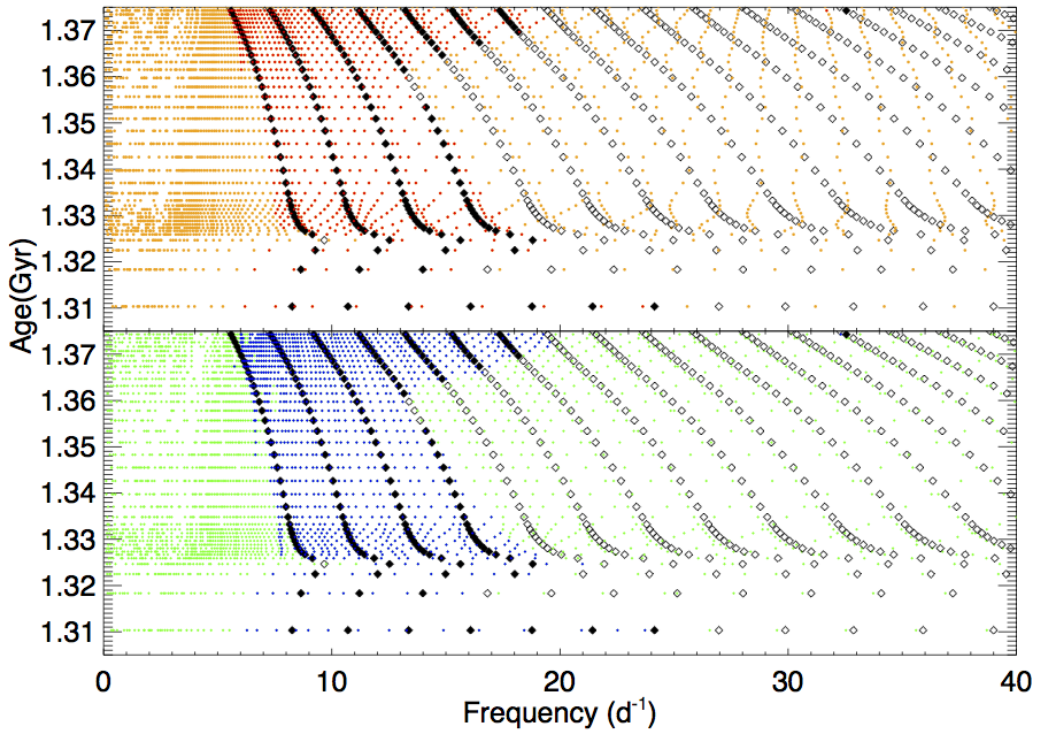

Figure 5.36 The evolution of oscillation frequencies from near TAMS to post-MS for a $1.8M_{\odot}$ star. Note the extreme denseness of modes. The upper panel shows the radial ($l = 0$, diamond) and dipole ($l = 1$, orange/red dots) modes, the lower panel shows the radial ($l = 0$, diamond) and quadruple ($l = 2$, green/blue dots) modes. The filled symbols, red dots and blue dots are unstable modes of $l = 0, 1, 2$, respectively. Due to the denseness of high order g-modes, the calculated frequencies less than ≈ 5 d^{-1} are not reliable.

We show the evolution of pulsational frequencies of $l = 0, 1, 2$ modes of a $1.8M_{\odot}$ star from Zero Age Main Sequence (ZAMS) to post-MS phases in Figures 5.35 and 5.36. A similar diagram can be found in Dupret (2002). These modes suffer from less cancellation effects in broadband photometry like that from *Kepler*, and thus are most likely to be observed.

The stellar structure models are calculated from MESA with solar metallicity, overshooting parameter $f_{ov} = 0.005$, and helium fraction Y=0.28. The pulsating frequencies are calculated with GYRE (Townsend & Teitler 2013) in the non-adiabatic mode.

In Figure 5.35, the star evolves upwards from the bottom of the plot at ZAMS (0.017 Gyr). The fundamental radial mode (p_1) and 1st overtone radial mode (p_2)(diamonds) have frequencies around 21 d^{-1} and 27 d^{-1}, with a frequency separation of 6 d^{-1} (this separation is essentially constant as we move to higher frequency). As the star slowly expands, the frequencies of radial modes decrease monotonically, forming the inclined diamond ridges. At about 1.3 Gyr, hydrogen in the core is exhausted as the star reaches the Terminal Age Main Sequence (TAMS). After TAMS, as mixed modes appear, the spectrum becomes extremely dense (Fig. 5.36).

As the behaviors of radial modes are the simplest, we can compare the position of the $l = 1$ and $l = 2$ modes with the radial ones to get some insight into the relative positions of different modes. For most of the time on main sequence (upper panel in Fig. 5.35), the positions of $l = 1$ dipole modes (orange p_1 and p_2 dots) are very close to radial modes (black p_1 and p_2 diamonds) at low radial order. The exceptions due to avoided crossings happen at advanced stages only for very short time intervals. As we move to higher frequency, the $l = 1$ modes (orange p_3 dots) move gradually to the middle of two consecutive $l = 0$ diamond ridges (p_3 and p_4). Similarly, in the lower panel of Figure 5.35, we can often observe two close $l = 0$ (diamonds) and $l = 2$ modes (green dots) at a wide range of frequencies.

All the above descriptions support the argument that we can often observe regular fre-

quency separations in δ Scuti stars. The theoretical mode frequencies in Figure 5.35 and 5.36 are calculated from non-rotating stellar structure models and are very simplified. δ Scuti stars usually have fast rotation and the rotational splitting and rotation generated modes can greatly alter the spectrum. However, the regular patterns can be preserved even with fast rotation (Reese et al. 2008). Breger et al. (2009) proposed a method to search for regularities by observing the frequency difference histogram. Handler et al. (1997) and García Hernández et al. (2009, hereafter GH09) searched for regularities by performing a Fourier transform of the observed p-mode frequencies, and the latter authors also assumed all frequencies have amplitudes of unity (hereafter, the FT method). Maceroni et al. (2014) applied the method of Breger et al. (2009) to the pulsational frequencies of the eclipsing binary KIC 3858884 and identified the position of the fundamental radial mode of the secondary component. Recently, García Hernández et al. (2015, hereafter GH15) applied the FT method to δ Scuti stars in seven systems which have accurately determined masses and radii (six eclipsing binaries and the angular resolved star Rasalhague), and they found regular frequency patterns in all of them (see Figure 5.37). The regular frequency spacings are found to be related to the large frequency separation. They also confirmed that the large frequency separation follows a linear relation with the logarithm of the mean density as shown by Suárez et al. (2014), and this relation seems to be independent of rotational velocity.

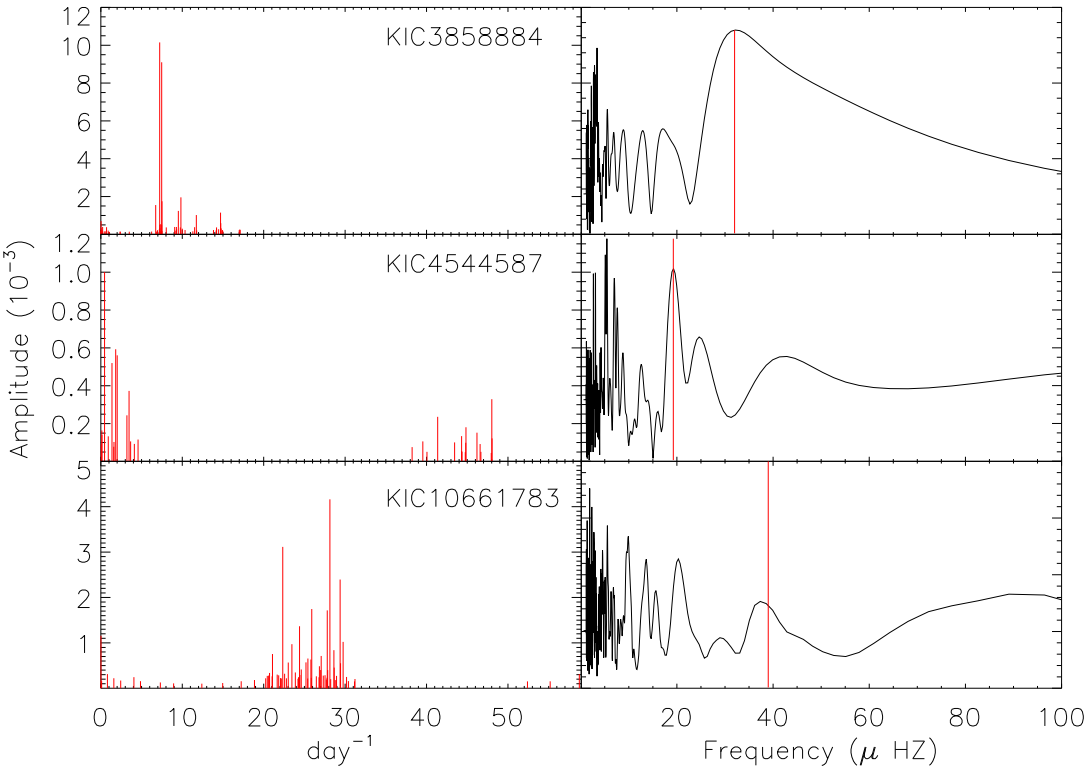

Figure 5.37 Left column: The observed oscillation spectrum of three δ Scuti stars in eclipsing binary system. Right column: The corresponding Fourier spectrum of p-mode frequencies. The frequency regularities that agree with mean densities are labeled by the vertical red lines.

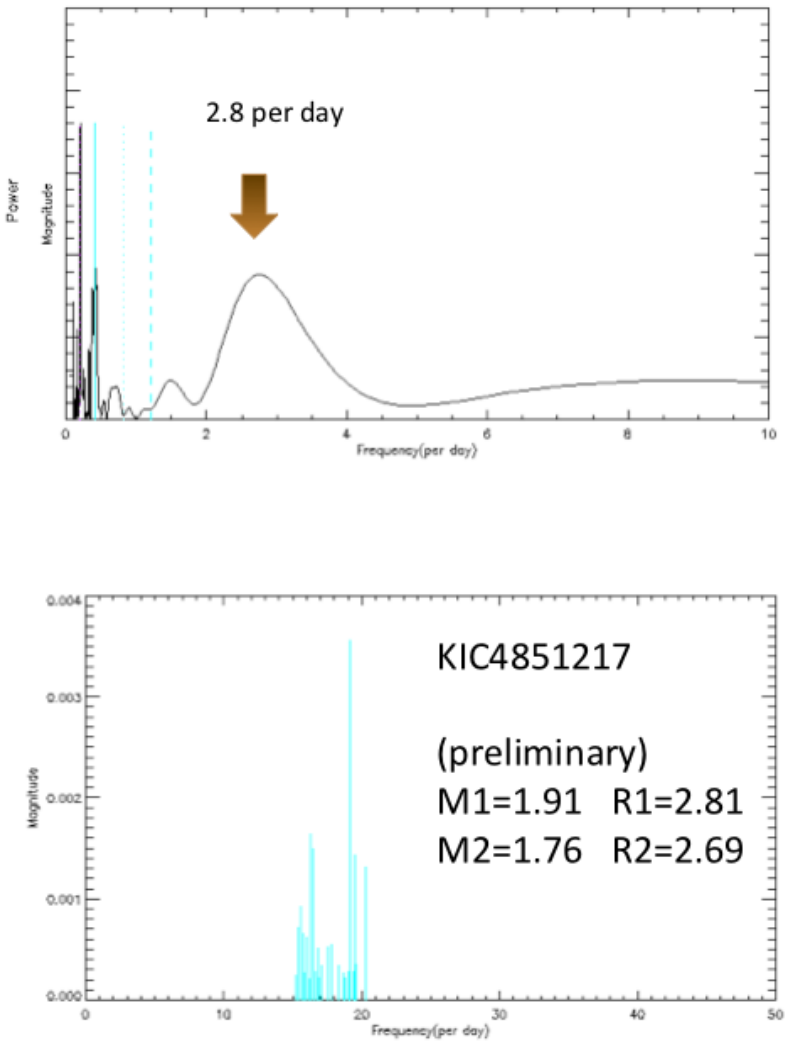

Figure 5.38 The lower right panel shows the oscillation spectrum of KIC 4851217. The upper left panel presents the Fourier spectrum of the p-mode frequencies. A regularity of 2.8 d^{-1} is marked by the arrow.

We applied the FT method to the independent p-mode frequencies of KIC9851944, and

although there seems to be a regularity of 2.3 d^{-1}, which is close to the spacing of consecutive radial modes of the secondary star (2.4 d^{-1}). For KIC 4851217, a frequency spacing of about 2.8 d^{-1} was found from preliminary analysis.

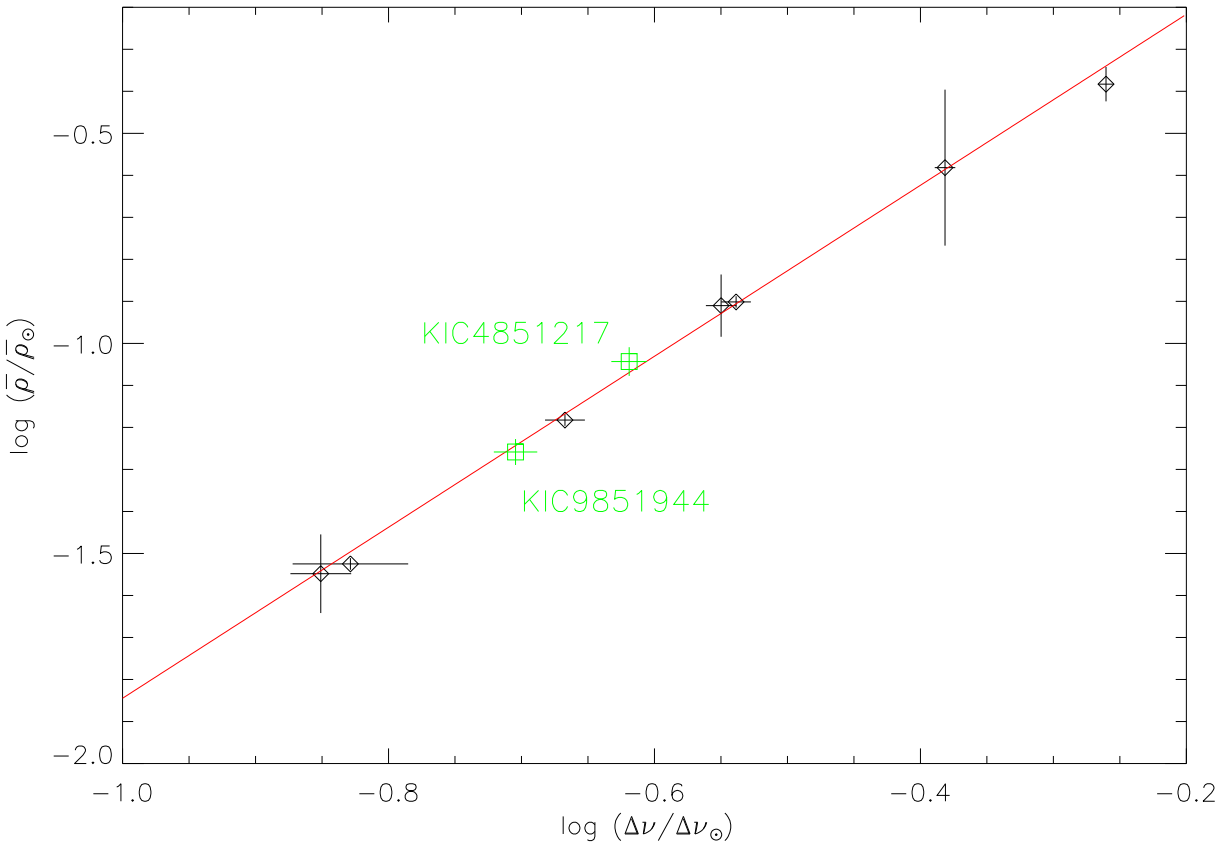

Figure 5.39 The observed frequency spacing (labeled as $\Delta\nu$) and mean densities ($\bar{\rho}$) of nine δ Scuti stars. Diamonds indicate the seven δ Scuti stars in GH15, and the red line is the linear fit from the same paper.

The observed frequency regularities in δ Scuti stars (7 systems from GH15, with KIC 9859144 and KIC 4851217) are shown in Figure 5.39 as a function of the mean density. Al-

though the result of KIC 4851217 needs further refinement, the observed frequency spacings seem to follow the relation $\Delta\nu \propto \sqrt{\rho}$ very well.

Paparo et al. (2016a, b) analyzed the Fourier spectrum of a large sample ($\sim$ 90) of δ Scuti stars, and found regular spacings in the majority of them (77). The observed frequency regularities ($\Delta\nu_{obs}$) scale with mean stellar densities but can be affected by rotation (Figure 5.40), so that $\Delta\nu_{obs}$ can be close to $\Delta\nu \pm \Omega$ or even $\Delta\nu \pm 2\Omega$. Castañeda & Deupree (2016) calculated theoretical oscillation frequencies using their 2-D stellar models for a series of δ Scuti stars with rotation, and found that the large separation scales approximately with the root mean density regardless of rotation. They essentially confirmed the former discoveries from more realistic calculations.

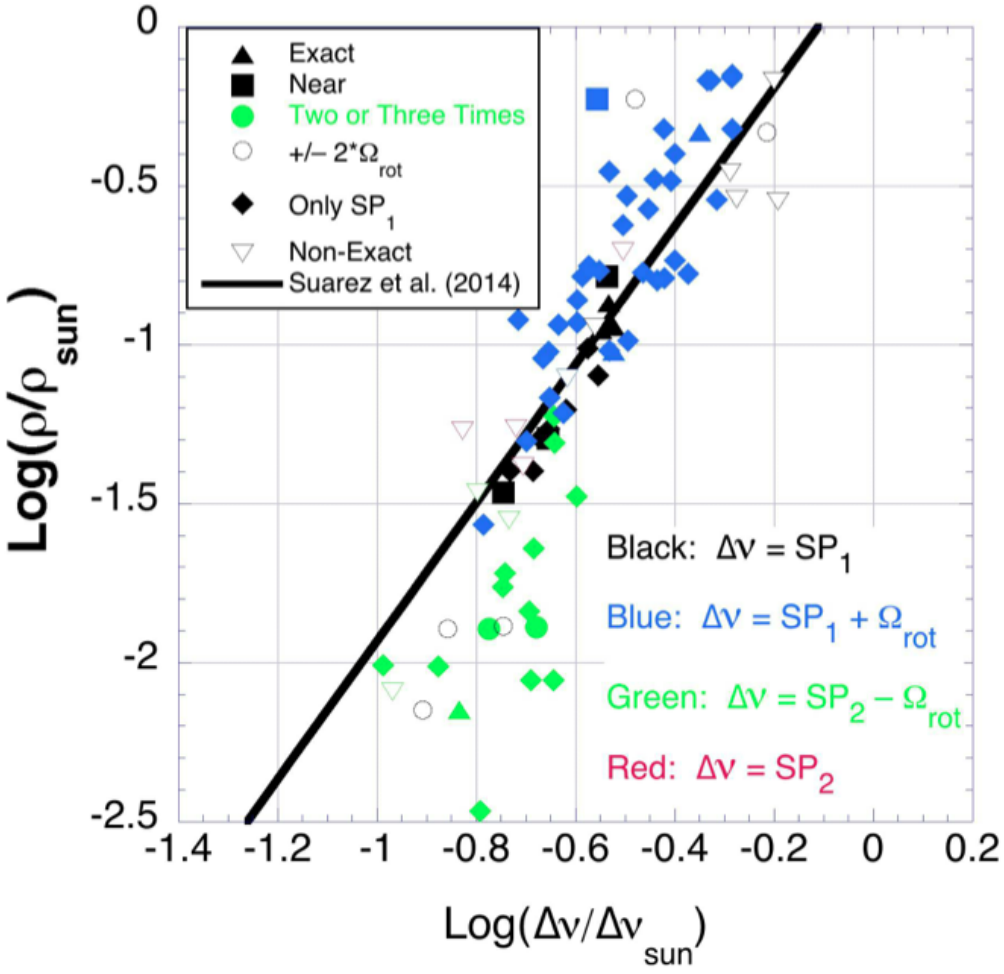

Figure 5.40 The observed frequency spacing (labeled as $\Delta\nu$) and mean densities ($\bar{\rho}$) of ~ 90 δ Scuti stars observed by CoRoT. The figure is taken from Paparo et al. (2016b).

CHAPTER 6

Heartbeat Stars

This chapter discusses the heartbeat stars, i.e., a class of eccentric binaries with tidally induced oscillations. It is the direct application of the linear forced oscillation theory discussed in Chapter 3. After a review of their properties and light curves in section 6.1 and 6.2, the details of observations and modeling of two particular heartbeat stars, KOI-54 and KIC 3230227 are contained in section 6.3 and 6.4. The preliminary results of another four systems are presented in section 6.5.

6.1 Overview of Heartbeat Stars

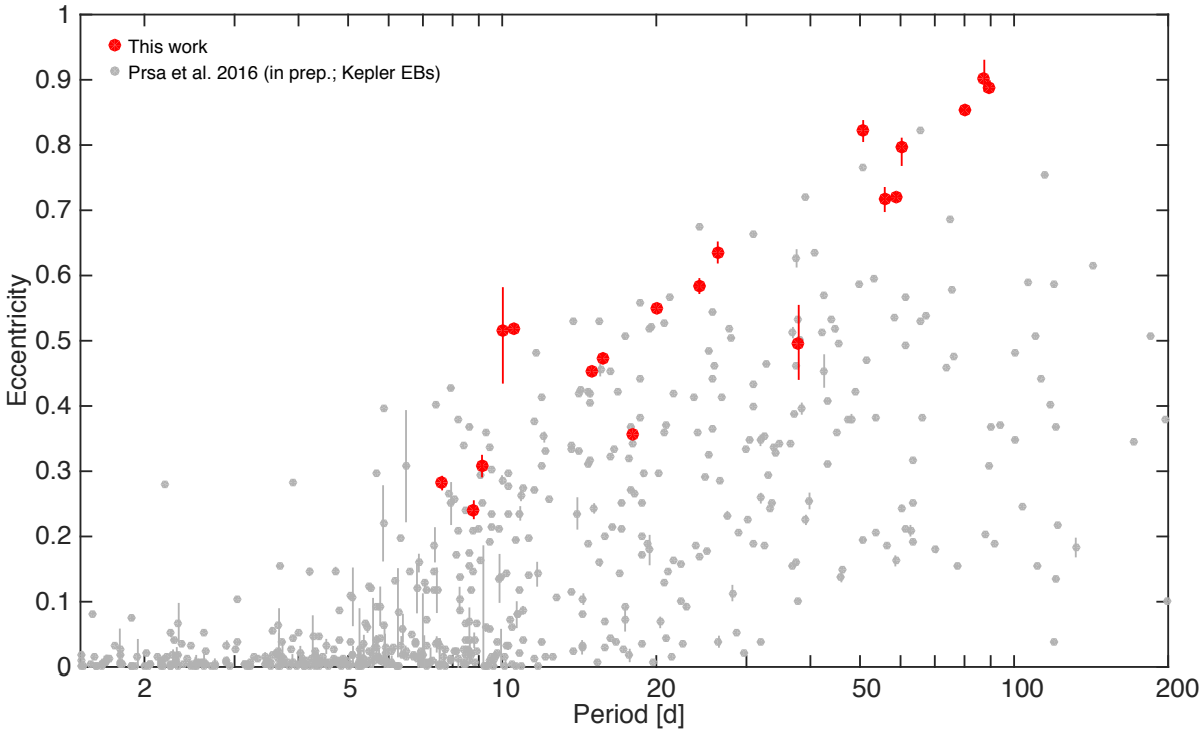

Figure 6.1 The eccentricity and orbital period of *Kepler* eclipsing binaries (gray dots) and 19 heartbeat stars (red dots); taken from Shporer et al. (2016).

The heartbeat stars (HBs), named after the resemblance between their light curves and electrocardiograms, are binary or multiple systems with very eccentric orbits. The HBs that have been studied in detail include the late B stars in Maceroni et al. (2009), A or F stars in Handler et al. (2002), Welsh et al. (2011), Hambleton et al. (2013), Smullen & Kobulnicky (2015) and red giant stars in Beck et al. (2014). Recently, Shporer et al. (2016) presented the spectroscopic orbits for 19 single-lined HBs. The *Kepler* eclipsing catalog[1] includes over

[1]http://keplerebs.villanova.edu/

150 of these stars with the flag 'HB'. We show the distribution of eccentricity (e) and orbital period (P) for *Kepler* eclipsing binaries and the 19 HBs monitored in Shporer et al. (2016) in Figure 6.1. Note that the HBs seem to outline the upper envelope of the $e - P$ diagram.

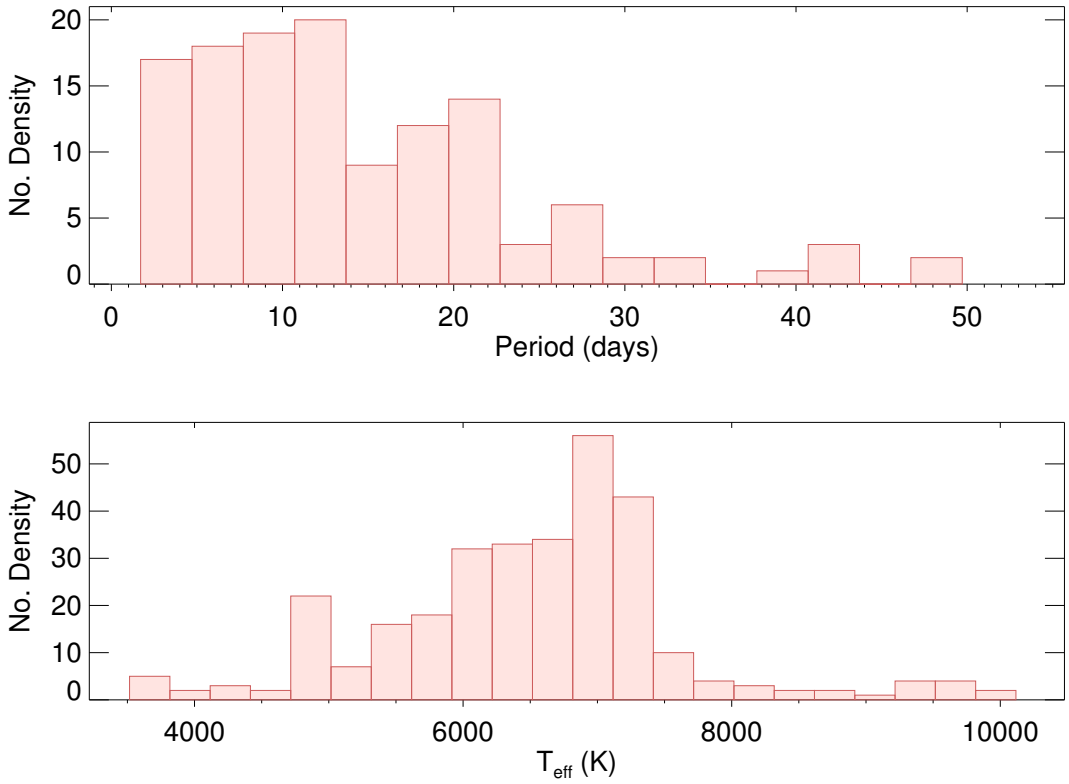

Figure 6.2 Distribution of orbital period (upper panel) and effective temperature (lower panel) for 150 HBs in *Kepler* eclipsing binary catalog.

The distributions of period and $T_{\rm eff}$ of 150 HBs are shown in Figure 6.2. The effective temperatures are taken from Armstrong et al. (2014). The majority of HBs seem to have orbital periods shorter than 30 days. Their range of effective temperatures ($\sim 5000 - 7500$ K) suggests that most of them are of spectral type earlier than G (mostly G, F, and A types).

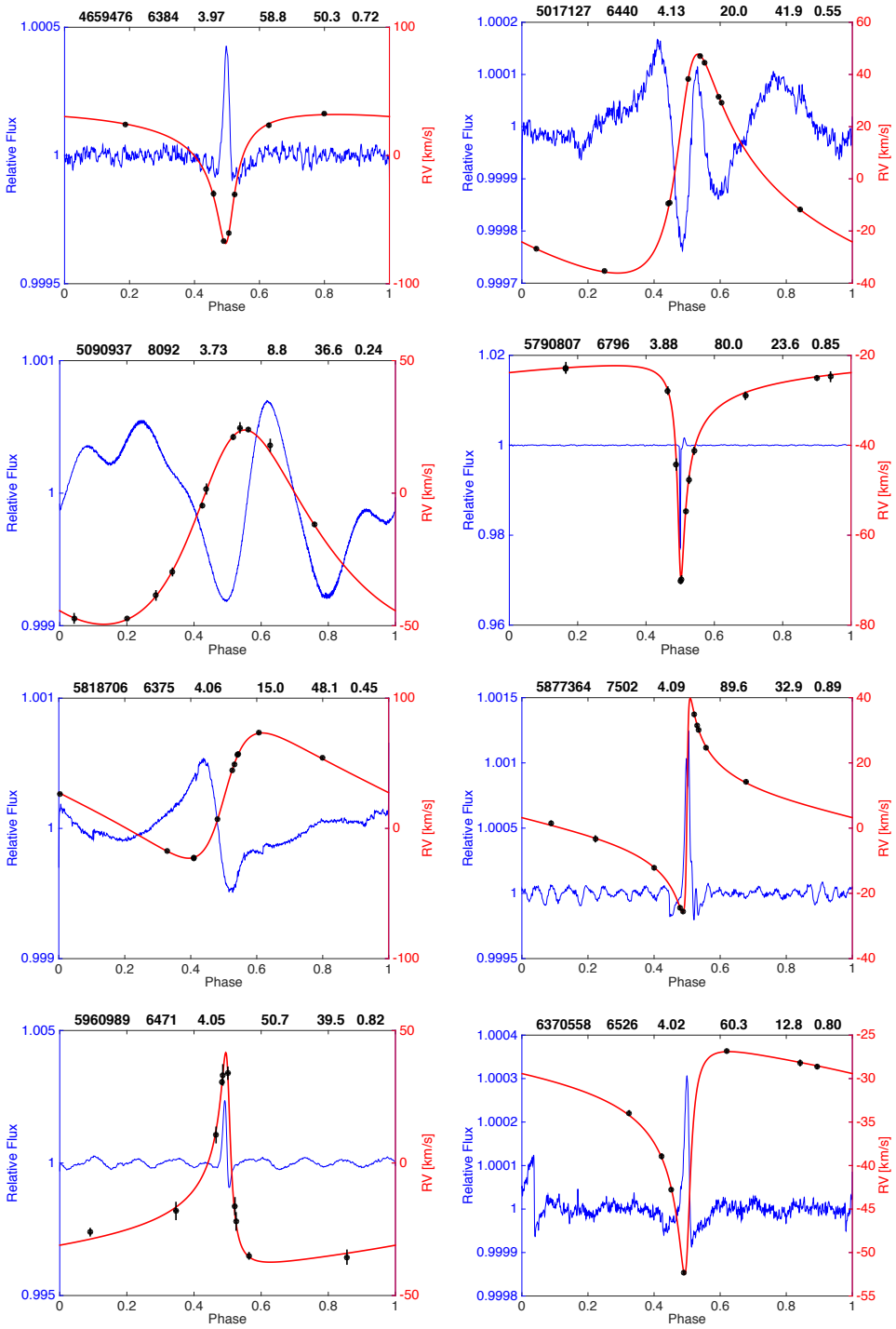

Figure 6.3 The Kepler light curves (red) and radial velocity curves (blue) of a sample of heartbeat stars; taken from Shporer et al. (2016).

Figure 6.3 displays the light curves and radial velocity (RV) curves of 8 single lined HBs, taken from Shporer et al. (2016). The title of each panel lists, from left to right, the KIC ID, $T_{\rm eff}$ (K), $\log g$, orbital period (d), semi-amplitude of RVs (K in km s^{-1}), and eccentricity. The light curves usually show a peak or 'heartbeat' at periastron passage (zero phase in RVs), and sometimes eclipses are present (e.g., KIC 5790807). The brightness increase at periastron is the result of tidal stellar deformation as well as the reflection effect from heating. The special shape of HB light curves can provide us with valuable information on the orbital parameters such as inclination, eccentricity and argument of periastron according to the theoretical work by Kumar et al. (1995). The fractional flux variation is given by (see Kumar et al. eq. 44)

$$\frac{\delta F}{F} = S\frac{1-3\sin^2(i)\sin^2[f(t)-\omega]}{[r(t)/a]^3} + C \tag{6.1}$$

where S is a free scale parameter, and C is a free offset parameter. Other parameters include: orbital inclination (i), true anomaly (f), argument of periastron (ω), semi-major axis (a) and distance between two stars (r). In practice, a grid of eccentric anomaly (E) is evaluated, and the correspondence between f and r is calculated from:

$$\begin{aligned} f &= 2\arctan\left(\sqrt{\frac{1+e}{1-e}}\tan(E/2)\right) \\ r &= a(1-e\cos E). \end{aligned} \tag{6.2}$$

Using this theoretical model for light curves (Kumar model hereafter), Thompson et al. (2012) analyzed the light curves of 17 HBs, and some of their derived orbital parameters were later refined from RV monitoring by Smullen & Kobulnicky (2015). It is important to

note that the Kumar light curve model does not take into account the reflection effect and eclipses. The orbital parameters derived by fitting the light curve with Kumar model can be treated as good estimates, but can also be off by a large margin especially the orbital inclination if the reflection effect is important and/or eclipses occur.

A better treatment of light curve modeling of HBs was performed for KOI-54 by Welsh et al. (2011). This system is nearly face-on, with an orbital inclination of 5.5°, and thus no eclipses are present. The authors modeled the light curve and radial velocity curve simultaneously, taking advantage of their binary modeling tool (ELC). Stellar distortions are fully modeled with the Roche equipotential, and the reflection effect from mutual irradiation heating is also included. Thompson et al. (2012) displayed various light curve shapes by using the Kumar model. Here we present a gallery of heartbeat star light curves in section 2, modeled with the ELC code.

Sometimes pulsations can also be seen in the light curve, such as observed in the stars KIC 4659476, KIC 5877364 and KIC 5960989 (Figure 5.3). The pulsations of HBs can be attributed to intrinsic pulsations (mostly γ Dor/δ Scuti type), tidally induced pulsations, or both. We will discuss the tidally induced oscillations shown in KOI-54 and KIC 3230227 in sections 6.3 and 6.4. In section 6.5, we will present four more HBs and illustrate that heartbeat stars can also show intrinsic pulsations.

6.2 Light Curve Gallery of Heartbeat Stars

We consider a binary system similar to KIC 3230227 as discussed in the next section. The binary has an orbital period of 7 days, and the two components have same effective temperatures $T_{\rm eff} = 8000$K. We then simulate light curves of heartbeat stars for a grid of different e, ω, and inclination values. The light curves are shown from Figures 6.4 to Figure 6.9, with orbital phase on the horizontal axis, and magnitude on the vertical axis. The mean flux of light curves has been normalized to 1.0.

At low inclinations ($i = 10°, 20°$, Figure 6.4 and 6.5), the light curves are more symmetric about the periastron, and the amplitudes of the light curves essentially increase with increasing eccentricity. Light curves with high eccentricities are similar, with a dominant brightening feature at periastron. Light curves of circular orbits show low amplitude ellipsoidal variations.

At intermediate inclinations ($i = 40°, 60°$) as shown in Figures 6.6 and 6.7, the light curves start to become asymmetric about periastron. The shape and amplitude of periastron brightening essentially depend on ω and e, respectively. Light curves with $\omega = 180° \pm \delta\omega$ are mirror reflections of each other. At high eccentricities, eclipses begin to appear.

At high inclinations ($i = 80°$), if e is not too small, the light curves are dominated by eclipses (Figure 6.8). When orbits become very edge-on ($i = 85°$), there are two deep eclipses in one orbital period regardless of eccentricity (Figure 6.9).

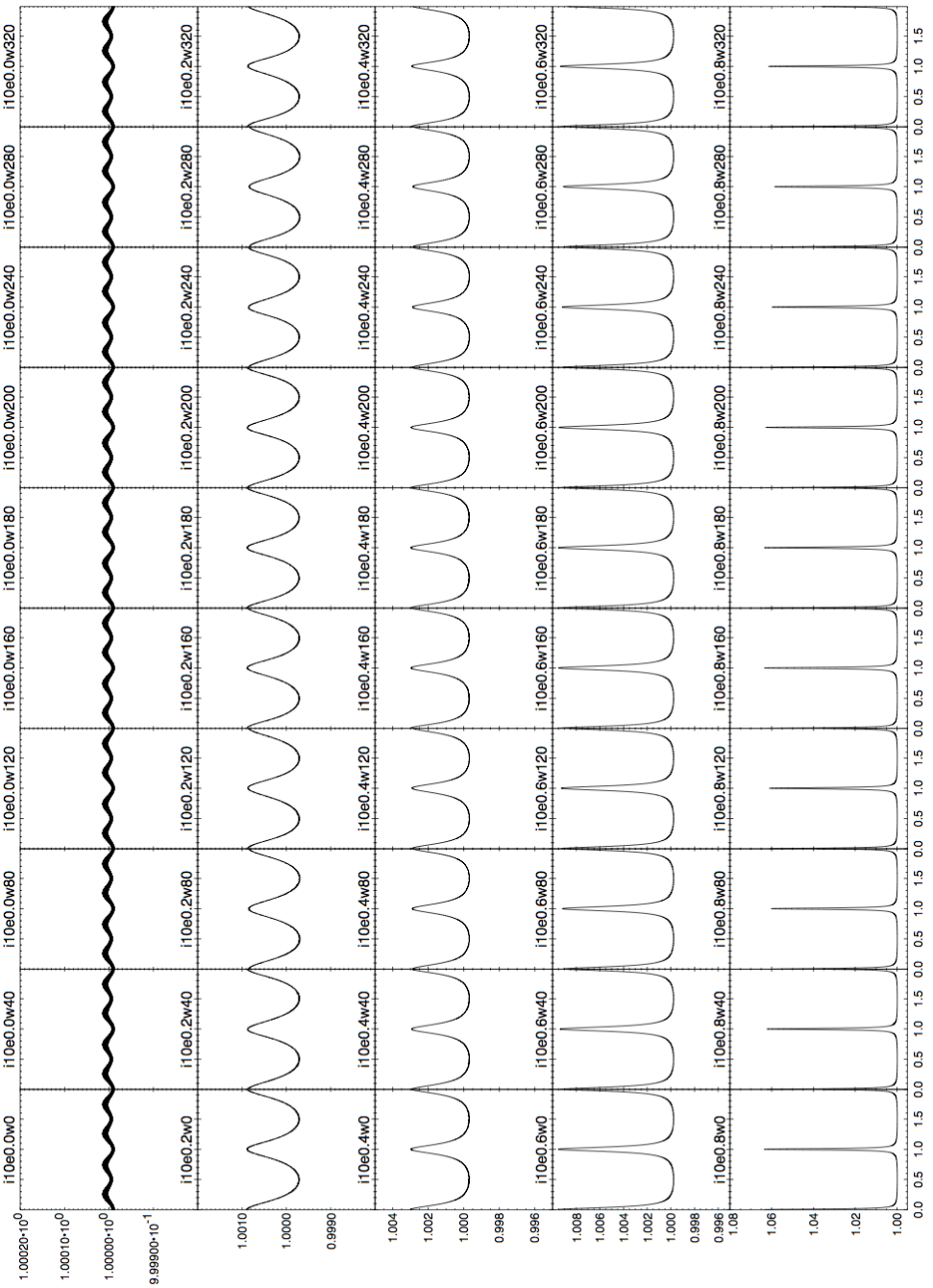

Figure 6.4 Simulated light curves of heartbeat stars for a grid of e and ω values labeled on the top of each panel. The orbital inclination is fixed to 10°.

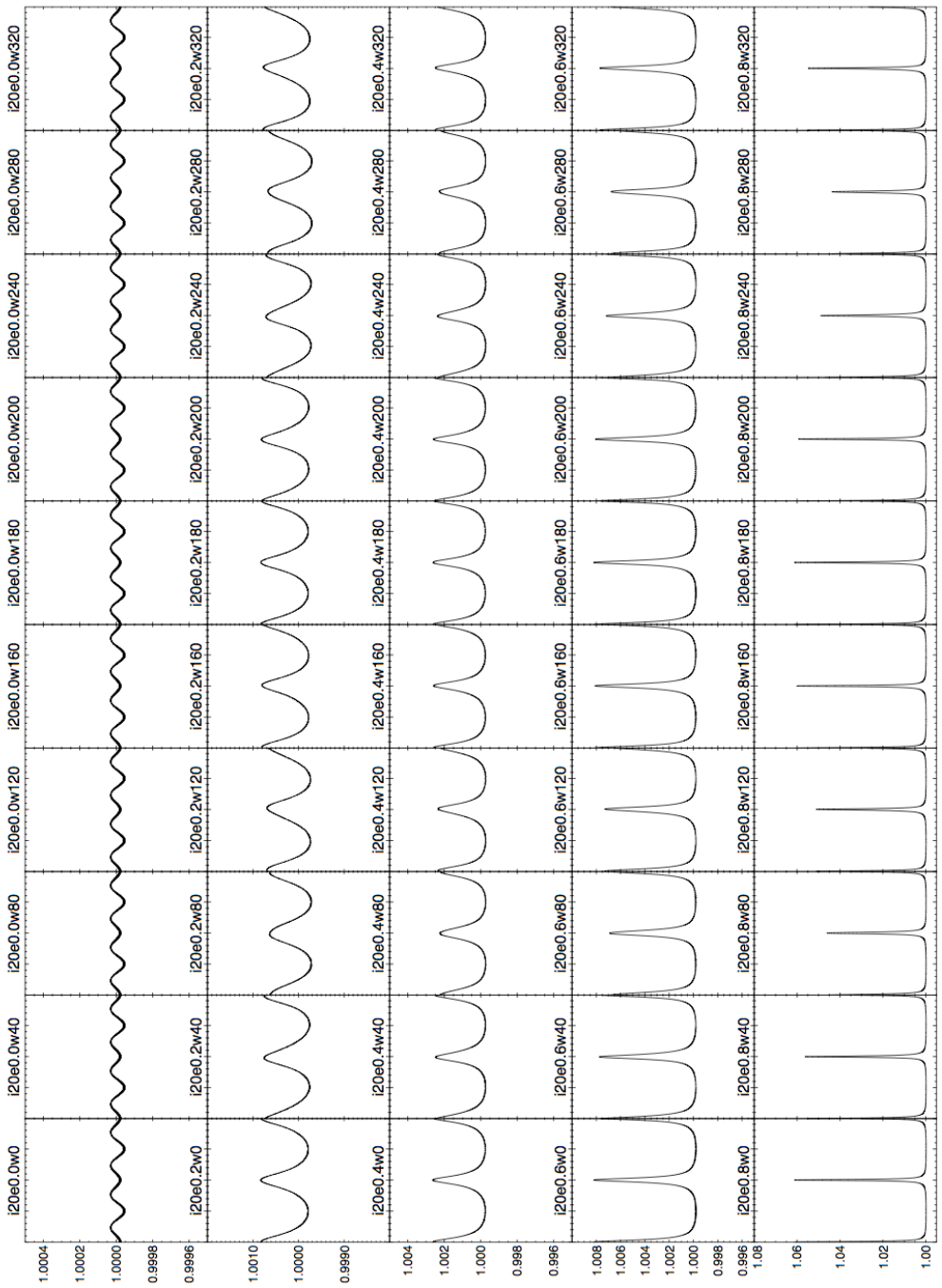

Figure 6.5 Simulated light curves of heartbeat stars for a grid of e and ω values labeled on the top of each panel. The orbital inclination is fixed to 20°.

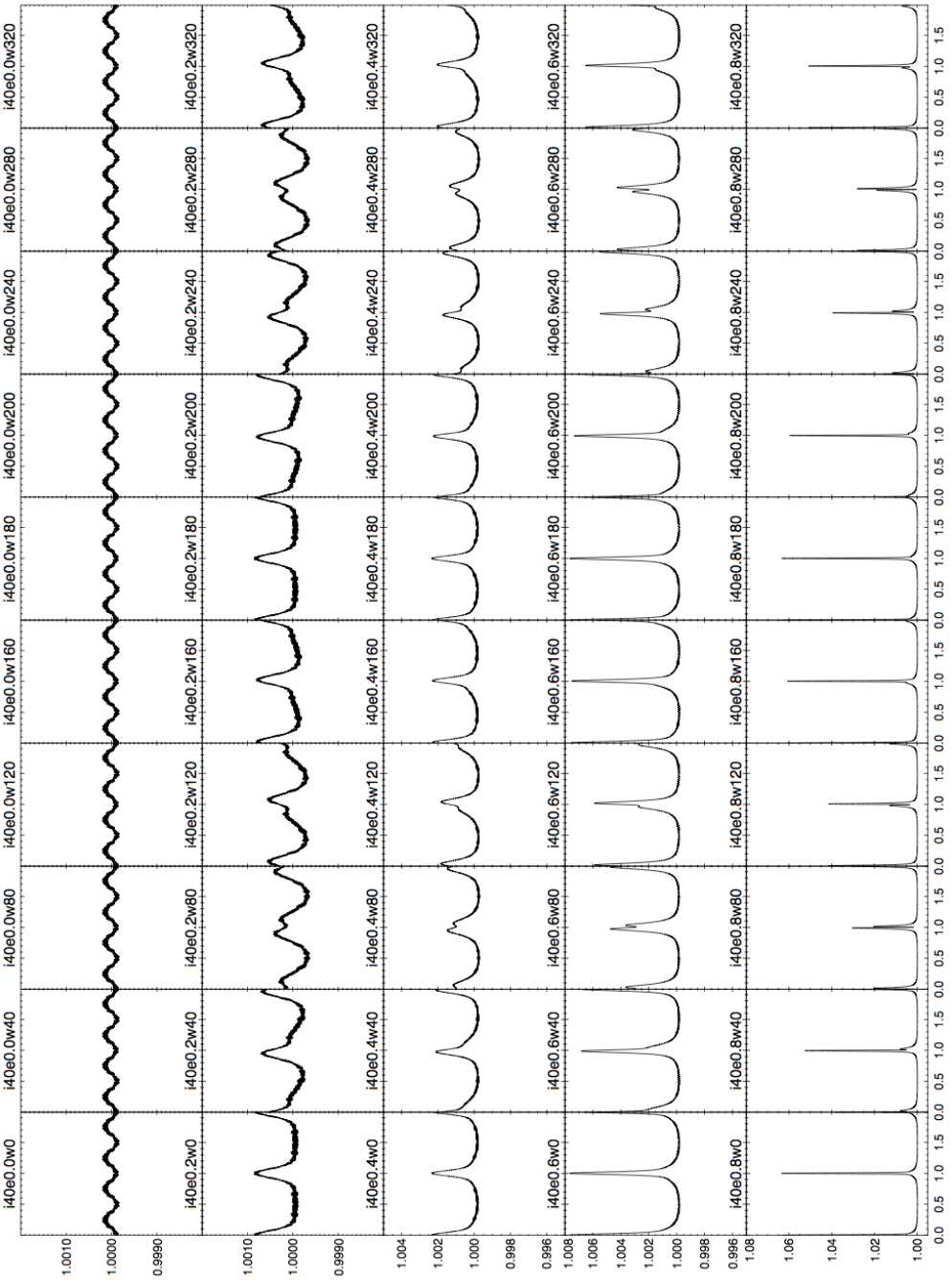

Figure 6.6 Simulated light curves of heartbeat stars for a grid of e and ω values labeled on the top of each panel. The orbital inclination is fixed to 40°.

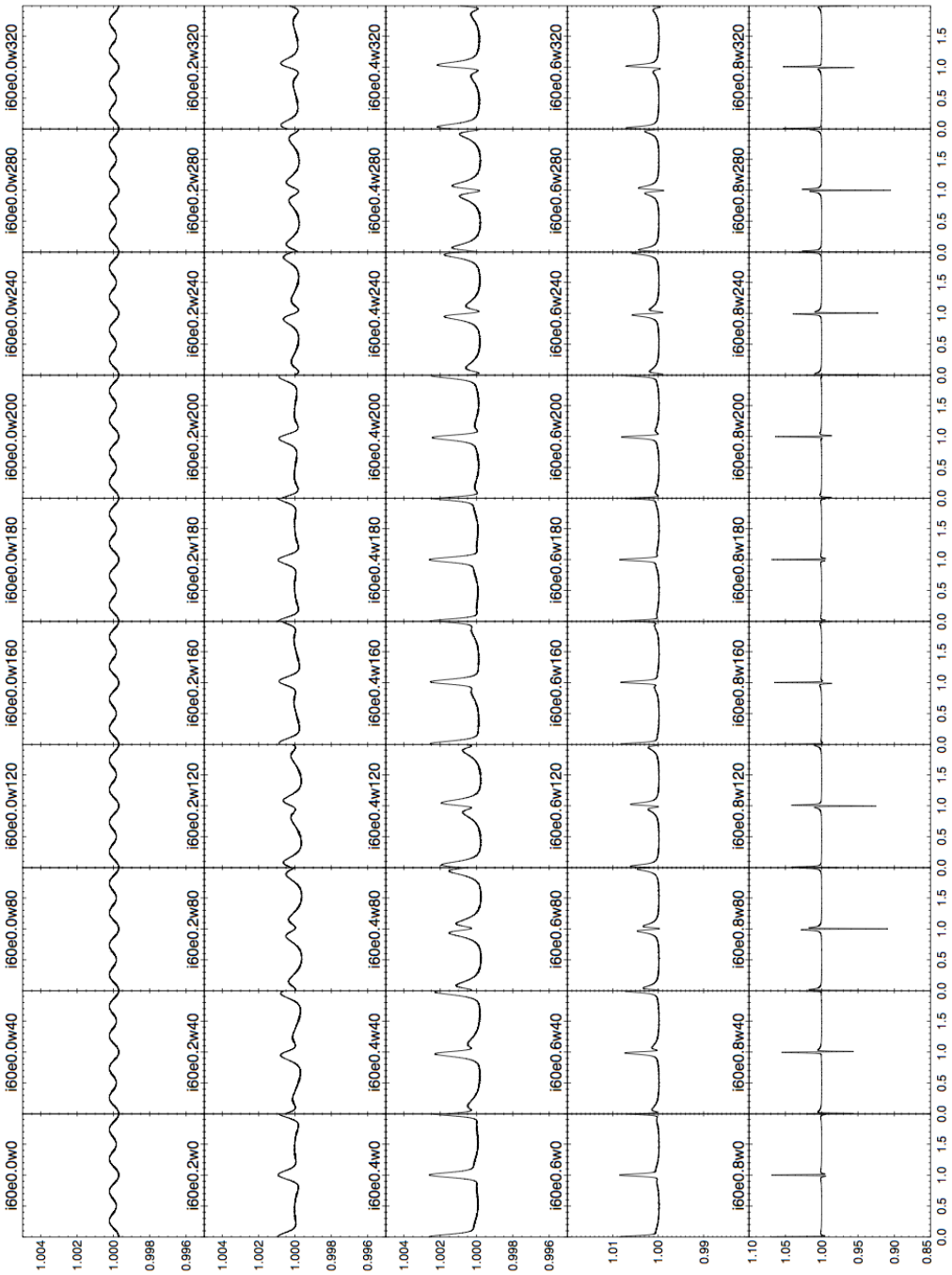

Figure 6.7 Simulated light curves of heartbeat stars for a grid of e and ω values labeled on the top of each panel. The orbital inclination is fixed to 60°.

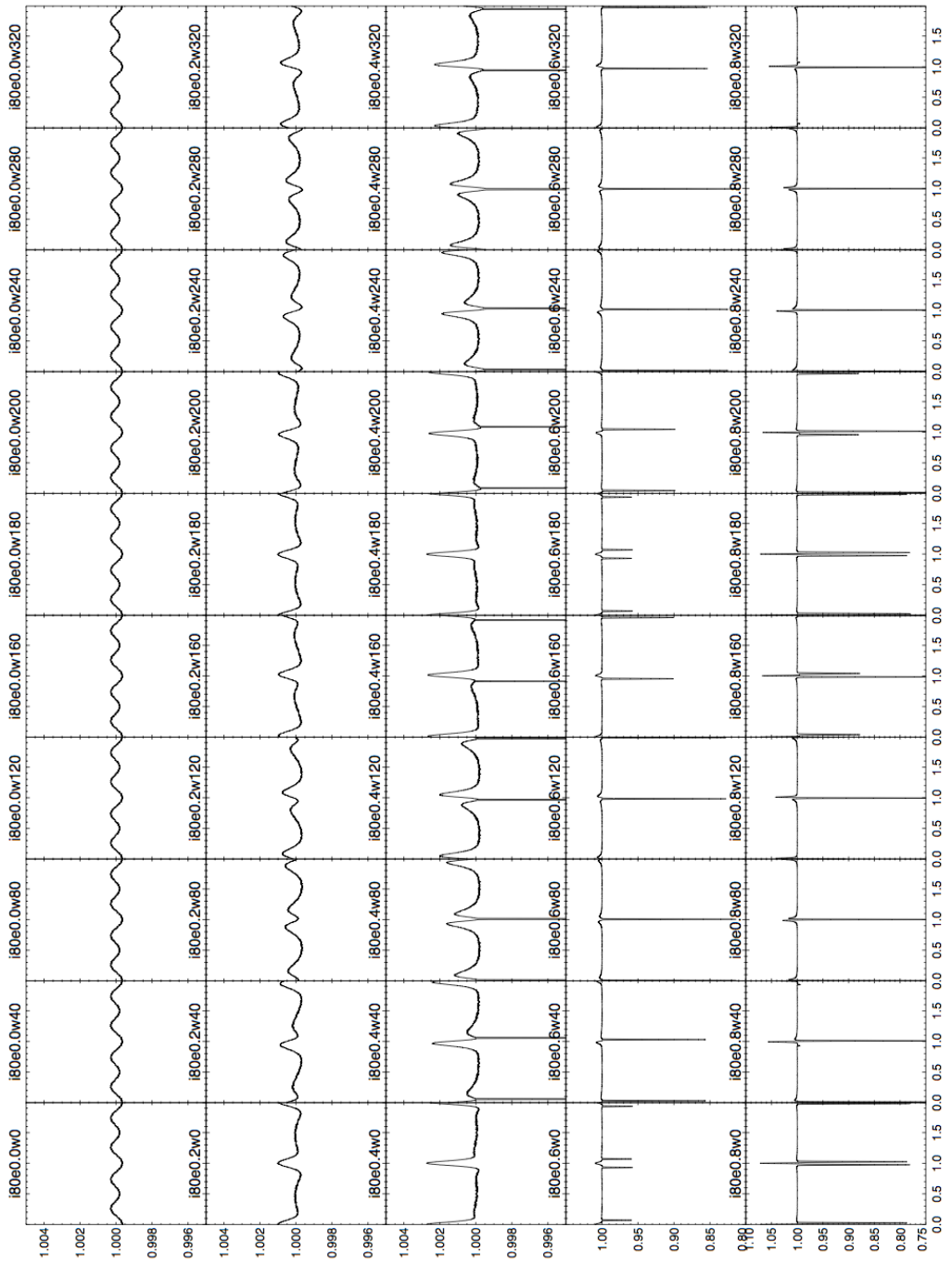

Figure 6.8 Simulated light curves of heartbeat stars for a grid of e and ω values labeled on the top of each panel. The orbital inclination is fixed to 80°.

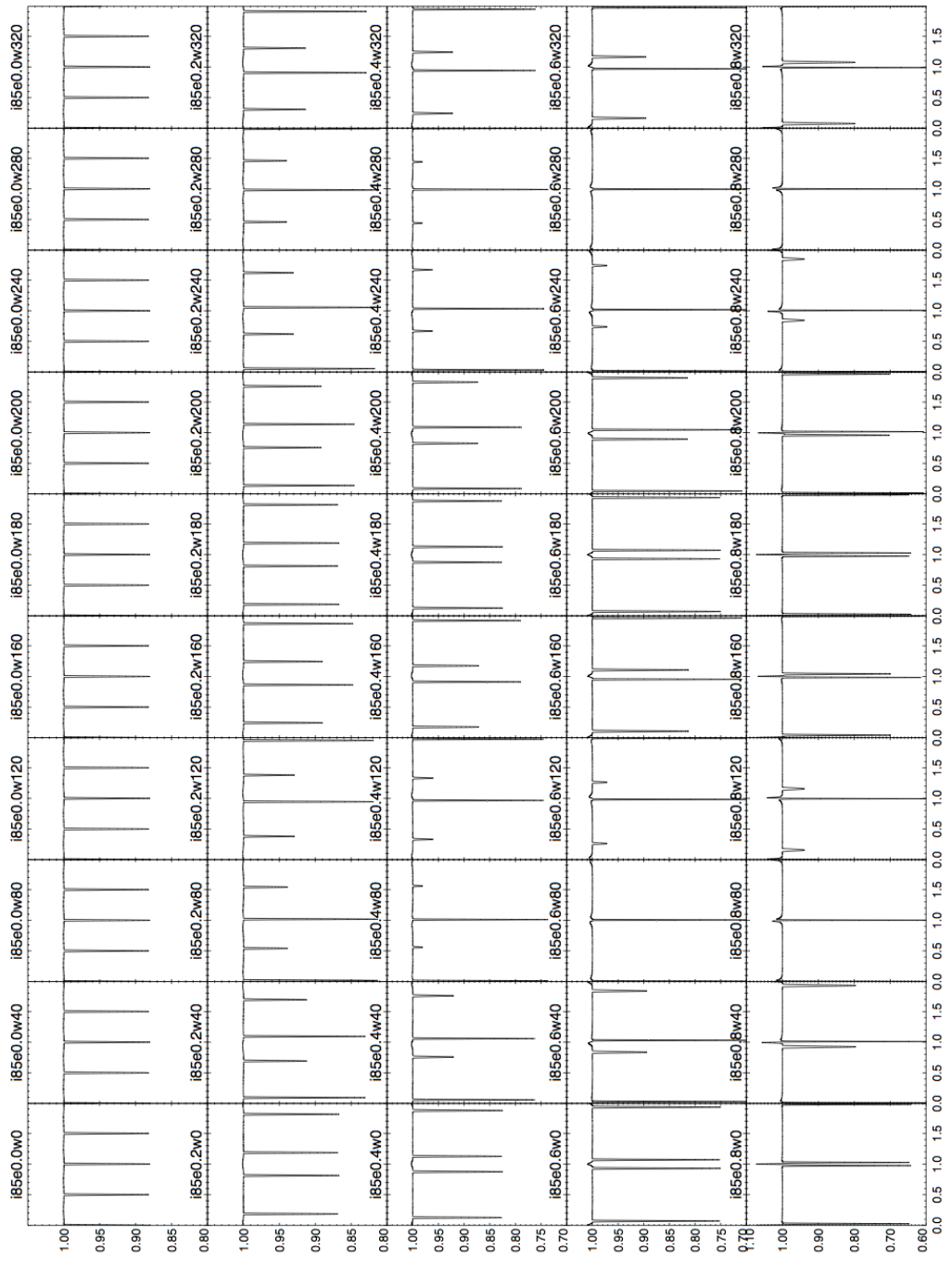

Figure 6.9 Simulated light curves of heartbeat stars for a grid of e and ω values labeled on the top of each panel. The orbital inclination is fixed to 85°.

6.3 A Recap of KOI-54

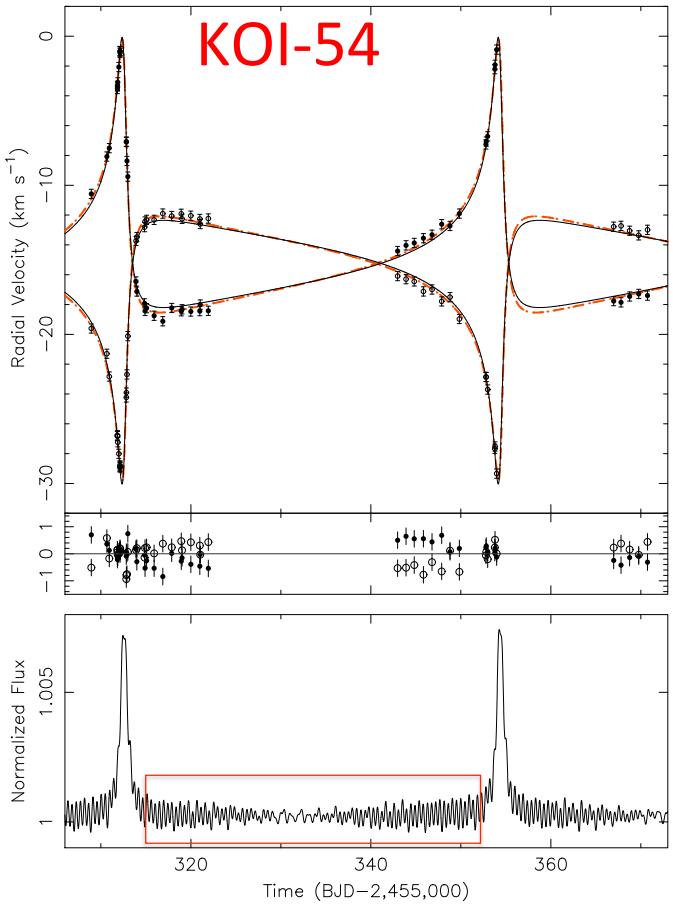

Parameter	Value	Uncertainty	Unit
Star 1 temperature: T_1	8500	200	K
Star 2 temperature: T_2	8800	200	K
log g_1	3.8	0.2	(cgs)
log g_2	4.1	0.2	(cgs)
Luminosity ratio: L2/L1	1.22	0.04	
Star 1 $V_{\rm rot} \sin i_1$	7.5	4.5	km s^{-1}
Star 2 $V_{\rm rot} \sin i_2$	7.5	4.5	km s^{-1}
Star 1 [Fe/H]$_1$	0.4	0.2	
Star 2 [Fe/H]$_2$	0.4	0.2	
Fitting RV only:			
K_1	9.16	0.10	km s^{-1}
K_2	8.85	0.10	km s^{-1}
Mass ratio, $q = M_2/M_1$	1.034	0.016	
Systemic velocity, γ	−15.257	0.035	km s^{-1}
Orbital period, P	41.805	0.014	days
Epoch of Periastron, T_p	2455103.5973	0.0074	BJD
Orbital eccentricity, e	0.8315	0.0032	
Arg. periastron, ω	39.46	0.51	deg
Fitting RV + light curve:			
K_1	9.04	0.07	km s^{-1}
K_2	8.82	0.09	km s^{-1}
Mass ratio, $q = M_2/M_1$	1.024	0.013	
Systemic velocity, γ	−15.239	0.034	km s^{-1}
Orbital period, P	41.8050	0.0003	days
Epoch of periastron, T_p	2455103.5490	0.0010	BJD
Orbital eccentricity, e	0.8335	0.0005	
Arg. periastron, ω	36.70	0.90	deg
Orbital inclination, i	5.50	0.10	deg
Semimajor axis, a	0.3956	0.008	AU
Star 1: Ω_1	3.5	2.3	···
Star 2: Ω_2	1.0	0.9	···
Star 1 mass: M_1	2.33	0.10	$M_\odot$
Star 2 mass: M_2	2.39	0.12	$M_\odot$
Star 1 radius: R_1	2.20	0.03	$R_\odot$
Star 2 radius: R_2	2.33	0.03	$R_\odot$

Welsh et al. 2011

Figure 6.10 Radial velocity curve (upper left) and light curve (lower left) and the fundamental parameters (right) of KOI-54. The figure is taken from Welsh et al. (2011).

KOI-54 is a binary system with an eccentric orbit ($e = 0.83$) and a low orbital inclination ($i = 5.5°$). It is composed of two similar A-type stars. The *Kepler* light curve shows a remarkable feature, with a periodic brightness increase of about 0.7% every 41.8 days. At first it was speculated to be a candidate of black hole, but later spectroscopic observations

revealed its binary nature. Welsh et al. (2011) modeled the light curve and radial velocity curve with the ELC code. The radial velocity and light curves are shown in Figure 6.10 along with the fundamental parameters. Figure 6.11 shows simulated light curves of KOI-54 at different inclination angles that were simulated with ELC.

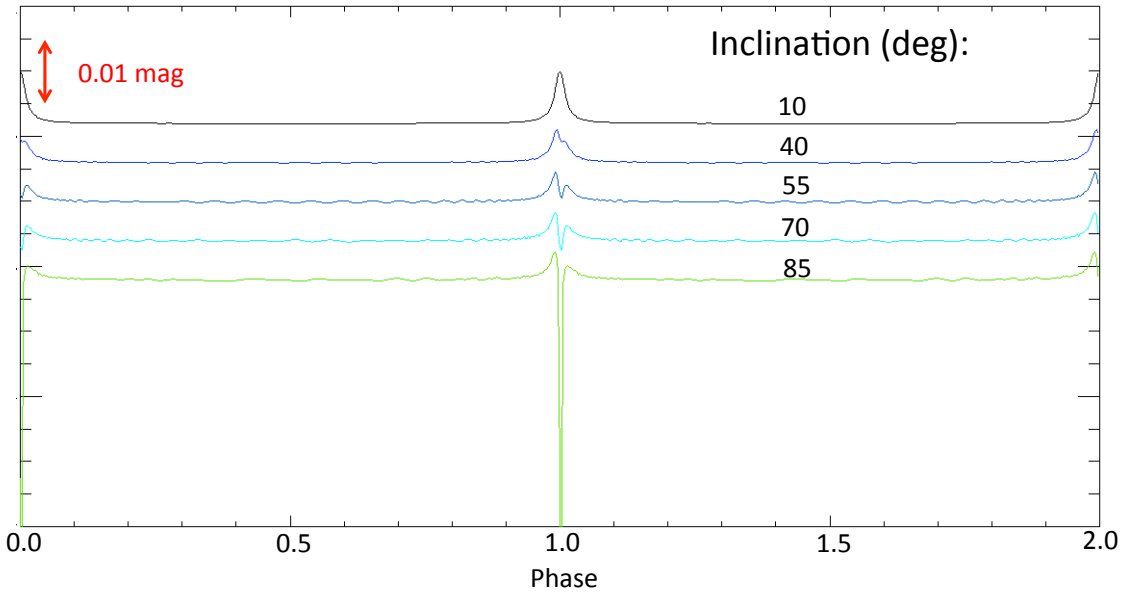

Figure 6.11 Simulated light curves of KOI-54 as observed from different inclinations (with $e = 0.83$ and $\omega = 36.7°$ from the combined light and radial velocity curve solution), calculated from ELC. The light curves have been shifted vertically for clarity. The 'pulsation-like' signals at phases away from 0 and 1 are not real, but are due to the limited numerical accuracy of the flux integration.

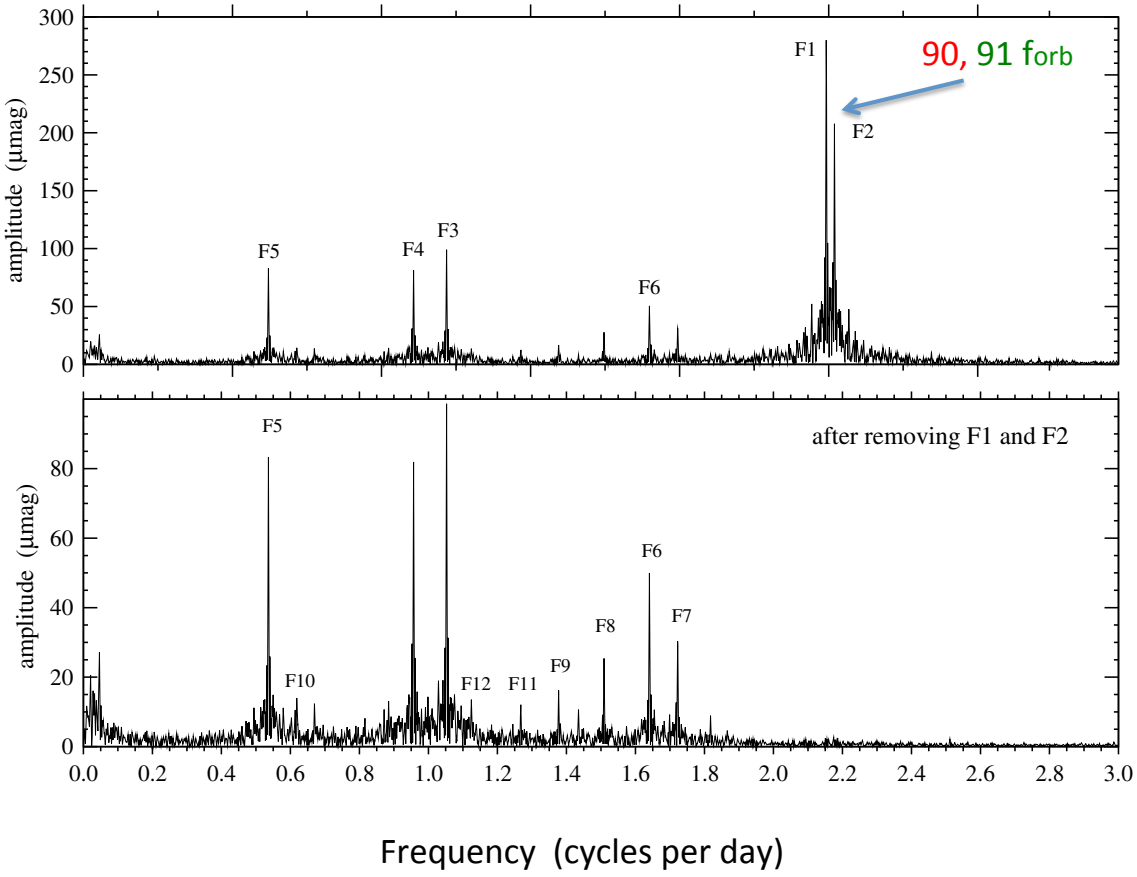

Figure 6.12 The Fourier spectrum of oscillations in KOI-54, taken from Welsh et al. (2011). The two dominant pulsational frequencies (F1, F2) are exactly 90 and 91 times of orbital frequency (f_{orb}).

As shown in Figure 6.10, the light curve shows obvious coherent pulsations. Figure 6.12 displays the oscillation spectrum. Two dominant pulsations (F1, F2) have frequencies that are exact 90 and 91 times of orbital frequency. Other frequencies include F3, F4, F7, F8, F10, F11, F12 that are also integer multiple times of the orbital frequency. This is clearly evidence of tidally induced pulsations. Fuller & Lai (2012) and Burkart et al. (2012)

presented theoretical analyses of such tidal oscillations. The predicted amplitude of tidal oscillations were calculated from linear tidal theory, although they used two different methods discussed in Chapter 3. Fuller & Lai (2012) suggested that the two dominant pulsations are $l = 2, m = 2$ modes, since their frequencies seem to agree with the possible range for mode resonance locking. However, Burkart et al. (2012) identified them as more likely $l = 2, m = 0$ modes. Subsequently, O'Leary & Burkart (2014) examined the phases of tidal oscillations and confirmed that the two dominant frequencies (F1, F2) are really $l = 2, m = 0$ modes.

Here we calculate the theoretical amplitude of magnitude variation following the same method in Fuller & Lai (2012). First, a stellar model with $M = 2.35 M_\odot$ and solar metallicity was evolved. The equilibrium stellar model was adopted when the radius of the star reached $R = 2.34 R_\odot$. The eigenfrequencies and eigenfunctions of oscillations were calculated with the GYRE code in the non-adiabatic mode. The mode damping rates are thus directly the imaginary part of eigenfrequencies, and the approximation of using radiative diffusion can be avoided as was done in Fuller & Lai (2012). We need to pay special attention to the mode amplitude normalization. Different versions of GYRE adopt different normalization schemes. The early versions (2.0, 2.3) use the formula $(4\pi)^2 \int [(\xi_r^2 + l(l+1)\xi_h^2)\rho r^2 dr] = MR^2$, and the latest versions (4.0, 4.3) adopt the normalization as $(4\pi) \int [(\xi_r^2 + l(l+1)\xi_h^2)\rho r^2 dr] = MR^2$. Thus, in order to use directly the formulation of tidal oscillation amplitude in Schenk et al. (2002) and Fuller & Lai (2012), the mode eigenfunctions need to be renormalized as $\int [(\xi_r^2 + l(l+1)\xi_h^2)\rho r^2 dr] = MR^2$. I appreciate the help from Jim Fuller in resolving this issue.

The results are presented in Figure 6.13. All the red crosses refer to the observed magnitude variations of tidal oscillations. Comparing with the original diagram (Figure 3 in Fuller & Lai 2012), the amplitudes from our non-adiabatic calculations are lower, but seem to have better overall agreement with observations.

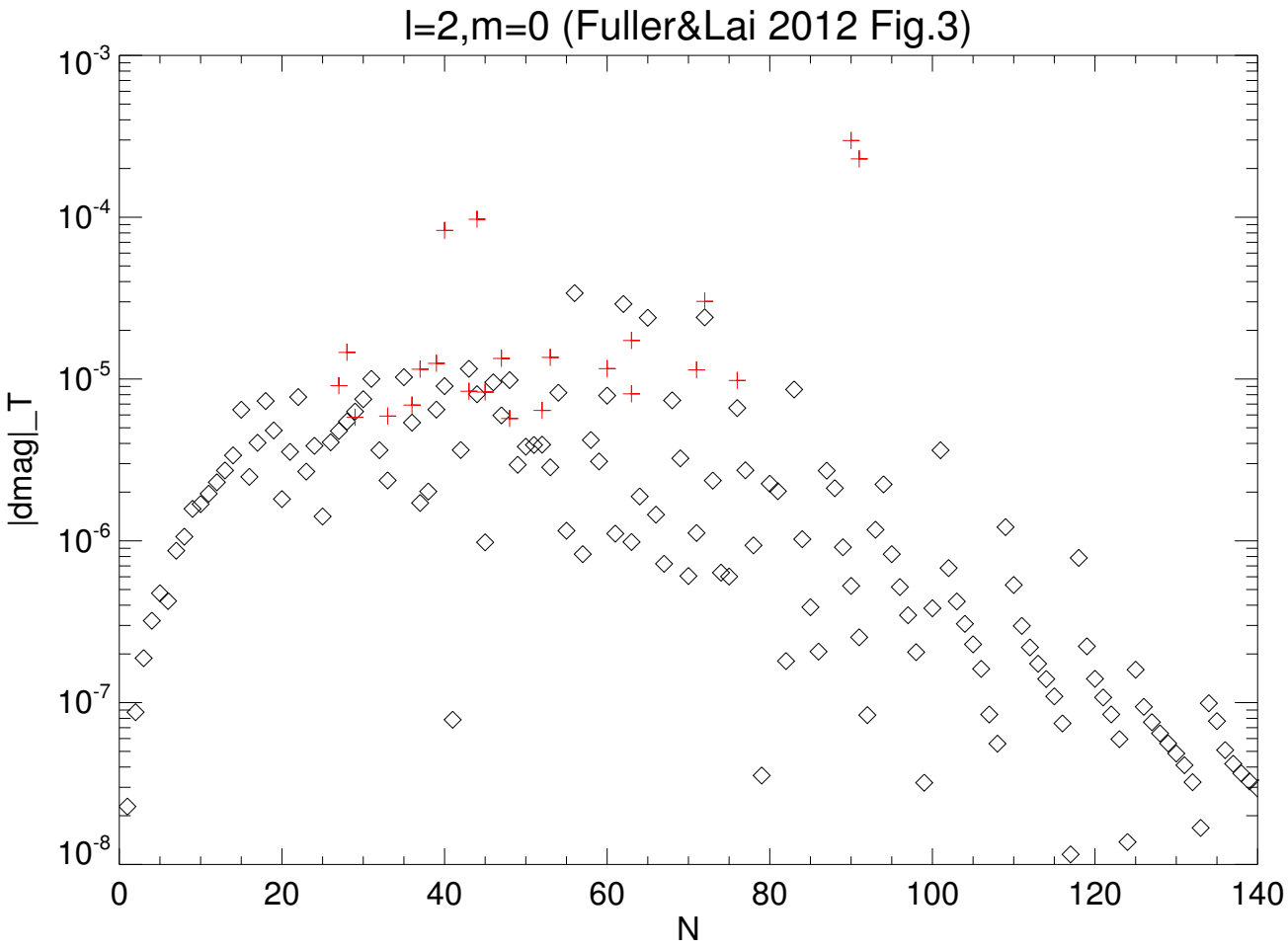

Figure 6.13 The theoretical magnitude variations (due to temperature) of $l = 2, m = 0$ modes for each orbital harmonics (Nf_{orb}) of KOI-54 from non-adiabatic calculations (diamonds). The red crosses show the observed oscillation amplitude. The magnitude variation due to geometric effects is orders of magnitudes smaller and not considered here.

6.4 Tidal Oscillations in KIC 3230227

6.4.1 Introduction

KIC 3230227 (K_p=9.002, α_{2000}=19:20:27.0253, δ_{2000}=+38:23:59.459) is an eclipsing binary, firstly included in the *Kepler* EB catalog in Slawson et al. (2011) and Prsa et al. (2011). The original catalog listed the time of eclipse minimum and orbital period as $T_0 = 54958.702188$ (BJD-2,400,000) and $P = 14.094216$ days, respectively. Later, the period was found to be half of the original value ($P = 7.0471062$ days). Uytterhoeven et al. (2011) analyzed the *Kepler* light curves of ~ 750 A- and F-type stars. Among them, KIC 3230227 was classified as an eclipsing binary with γ Doradus pulsations. Thompson et al. (2012) studied light curves of 17 heartbeat stars, including KIC 3230227. Thanks to the special light curves of HBs, they derived orbital parameters including the orbital inclination (i), eccentricity (e), and argument of periastron (ω). Armstrong et al. (2014) derived the effective temperatures of 9341 ± 350K and 7484 ± 606K for the primary and secondary, respectively, by fitting the SED (Spectral Energy Distribution) to several observed magnitudes. Niemczura et al. (2015) made a detailed analysis of their high resolution spectra of KIC 3230227. Atmospheric parameters were inferred from Na D, H Balmer and metal lines. They found $T_{\rm eff} = 8150 \pm 220$K (from Na D lines and SED), $T_{\rm eff} = 8200 \pm 100$K (from Balmer and metal lines), $\log g = 3.9 \pm 0.1$ and $v \sin i = 50 \pm 4$ km s^{-1}. They also obtained abundances for many individual elements (C, N, O, Ne, Na, Mg, etc), as listed in their Table 4. Most of these abundances are close to solar value (Asplund et al. 2009; Lodders et al. 2009). We summarize the aforementioned results in Table 6.1.

Table 6.1: Atmospheric and Orbital Parameters

Parameter	Uytterhoeven et al. (2011)	Thompson et al. (2012)	Armstrong et al. (2014)	Smullen & Kobulnicky(2015)	Niemczura et al. (2015)
$T_{\rm eff}$ (K)	7970(290)	8750	9341(350),7484(606)[1]	~ 8000	$8150(220), 8200(100)$
$\log g$ (cgs)	3.9 ± 0.3	5.0	–	$4.0, 3.5$	3.9(0.1)
$v \sin i$ (km s^{-1}) ..	–	–	–	$\sim 30, \sim 75$	50(4)
$[Fe/H]$	–	–	–	≥ 0	≈ 0
P (days)	7.0471062(175)[2]	7.04711(87)	–	7.051(1)	
T_0 (BJD-2400000)	54958.702238[3]	–	–	56311.76(03)[4]	
i (°)	–	42.79 ± 0.46	–	$66 - 71$	–
e	–	0.588(4)	–	0.60(4)	
ω (°)	–	292.1(1.2)	–	293(4)	
K_1 (km s^{-1})	–	–	–	98.5(5.4)	–
K_2 (km s^{-1})	–	–	–	104.9(6.1)	–
γ (km s^{-1})	–	–	–	$-15.7(1.7)$	–

[1]For the primary and secondary, respectively
[2]Kepler Eclipsing Binary Catalog
[3]Time of eclipse minimum from Kepler Eclipsing Binary Catalog
[4]Time of periastron passage

6.4.2 Binary Modeling

The orbital parameters of KIC 3230227 were derived from radial velocity (RV) measurements in Smullen & Kobulnicky (2015). This system was found to be composed of two A-type stars with similar masses (mass ratio $q = 0.95 \pm 0.05$), and a very eccentric orbit ($e = 0.60 \pm 0.04$, $\omega = 293 \pm 4°$). These orbital elements are also listed in Table 6.1.

Four orbital elements (P, i, e, and ω) were derived from the light curve alone in Thompson et al. (2012). It is important to note that the Kumar light curve model (Kumar et al. 1995) adopted in Thompson et al.'s work does not take into account the effects of reflection and eclipses.

A better treatment of the light curve modeling of HBs was performed for the face-on system KOI-54 by Welsh et al. (2011). These authors modeled the light curve and radial velocity curve simultaneously, taking advantage of their binary modeling tool (ELC; Orosz & Hauschildt 2000). Stellar distortions were fully modeled with the Roche equipotential, and the reflection effect from heating plus the limb and gravity darkening effect are included. To synthesize the binary light curve, NextGen atmosphere models are used to integrate numerically the flux on the stellar surface. Several techniques are adopted in ELC to improve the integration accuracy, for example, Monte Carlo sampling on the fractional pixels at eclipse horizon with Sobol sequences. Here, we use the same tool to model KIC 3230227.

The *Kepler* SAP light curves were retrieved from MAST. There are 18 quarters (Q) of long cadence data (Q0-17). Short cadence light curves are only available in quarter 1, 2, and 5. We de-trended the raw light curve in each quarter following the procedure detailed

in Guo et al. (2016). In short, the procedures include spline fitting to the long term trends, median difference corrections, outlier removal, and normalization. The de-trended light curves were then divided into 6 sections and light curve modeling was performed for each section individually.

Obvious oscillations stand out in the light curves, and they are still present in the phase-folded light curves. Their amplitudes are low enough to be treated as perturbations to the binary light curve. We adopted the period in the *Kepler* Eclipsing Binary Catalog ($P = 7.0471062 \pm 0.0000175$ days), which is based on the analysis of light curve by using the Lomb-Scargle periodogram and *kephem* software (Hambleton et al. 2013).

This system only shows a single, very narrow eclipse ($\Delta\phi \approx 0.02$ in phase) near periastron. In order to model fully the profile of eclipses, we have to use a very small step size in phase ($\delta\phi = 0.00055 = 0.2°$). This makes the light curve computation relatively expensive. Aperture contamination parameters listed in Kepler Input Catalog (KIC) are very small, ranging from 0.08% to 0.2%, and can be neglected. Based upon the effective temperatures listed in Table 6.1, the two components are likely to have radiative envelopes, thus the gravitational darkening coefficients β_1 and β_2 are set to 0.25, and bolometric albedos l_1, l_2 are fixed to 1.0.

We assume pseudo-synchronous rotation, which means the rotational frequency $f_{rot} = \sqrt{\frac{(1+e)}{(1-e)^3}} f_{orb}$ (Hut 1981). We use the orbital eccentricity $e = 0.60$ and argument of periastron $\omega_p = 293°$ in Smullen & Kobulnicky (2015) as initial values. The mass ratio q and primary semi-amplitude velocity K_1, taken from the same paper, are initially fixed to 0.95 and 98.5 km

s^{-1}, respectively. It is well known that the light curves of eclipsing binaries are only sensitive to the temperature ratio. Thus the effective temperature of the primary $T_{\rm eff1}$ is fixed to 8000K, in agreement with the spectroscopic results in Table 6.1. We fit the light curve by optimizing the following parameters: e, ω_p, i, relative radius $r_1 = R_1/a$ and $r_2 = R_2/a$, time of periastron passage T_0, and effective temperature of the secondary $T_{\rm eff2}$. The search for the χ^2 minimum was performed with the genetic algorithm *pikaia* (Charbonneau 1995), followed by a local search with the downhill simplex algorithm *amoeba*. Since ELC does not model pulsations in the light curve, the standard way of estimating uncertainties by finding the range of parameters that increases χ^2 by 1.0 from χ^2_{min} cannot be used. Instead, we adopted the standard deviation of the best-fitting parameters in 6 data sets as the 1σ errors. This is the method used by Guo et al. (2016), and it can account for possible systematic uncertainties due to light curve de-trending.

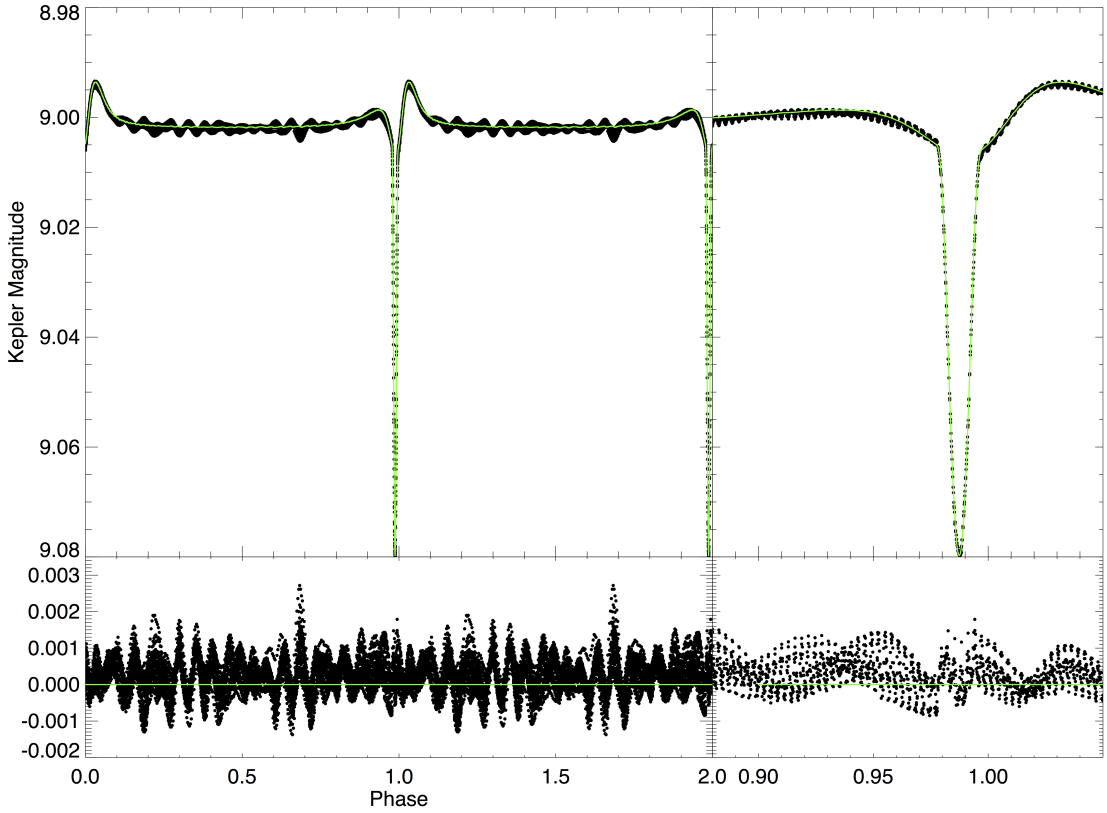

Figure 6.14 The phase-folded long cadence light curve of KIC 3230227 (dots) in Quarter 5 and 6 and the best model from ELC (green solid line). The right panel shows the light curve around the eclipses, and the bottom panels show the corresponding residuals.

The final optimized solution has essentially the same e and ω_p values as those in the RV work of Smullen & Kobulnicky (2015). The orbital inclination ($i = 73.42°$), however, is much larger than the result in Thompson et al. (2012) ($i = 43°$), and close to that in Smullen &

Kobulnicky (2015) ($i \sim 66^\circ - 71^\circ$). As shown in Figure 6.14, our light curve model matches the observations down to the level of 0.001 magnitude. The profile of the narrow eclipse is also well modeled. The secondary has slightly higher effective temperature $T_{\rm eff2} = 8177$K and smaller mass and radii ($M_2 = 1.73 M_\odot, R_2 = 1.68 R_\odot$), compared to that of the primary ($T_{\rm eff2} = 8000$K, $M_1 = 1.84 M_\odot, R_1 = 2.01 R_\odot$). The main parameters of our ELC model are listed in Table 6.2. The projected rotational velocities ($v \sin i_1 = 56.4$ km s^{-1}, $v \sin i_2 = 47.0$ km s^{-1}), under the assumption of pseudo-synchronous rotation, are in agreement with the measured $v \sin i$ from spectra as listed in Table 6.1. We found that the best-fit light curve solution from one data set or quarter can almost match the light curve of other quarters equally well. In terms of argument of periastron ω, no discernable apsidal motion was found.

Table 6.2: Model Parameters

Parameters	Primary	Secondary	System
Period (days)[1]			7.047106 ± 0.000018
Time of periastron passage, T_0 (BJD-2400000)			$54958.791621 \pm 0.000010$
Mass ratio $q = M_2/M_1$[2]			0.939 ± 0.075
Orbital eccentricity, e			0.600 ± 0.002
Argument of periastron, ω_p (degree)			293.0 ± 0.1
γ velocity (km s^{-1})			-15.7 ± 1.7
Orbital inclination (degree), i			73.42 ± 0.27
Semi-major axis ($R_\odot$), a			23.64 ± 0.95
Mass ($M_\odot$)	1.84 ± 0.18	1.73 ± 0.17	
Radius ($R_\odot$)	2.01 ± 0.09	1.68 ± 0.08	
Relative radius, R/a	0.085 ± 0.002	0.071 ± 0.002	
Gravity brightening, β	0.25^1	0.25^1	
Bolometric albedo	1.0^1	1.0^1	
$T_{\rm eff}$ (K)	8000^1	8177 ± 30	
$\log g$ (cgs)	4.10 ± 0.06	4.23 ± 0.06	
pseudo-synchronous $v \sin i$ (km s^{-1})	56.4 ± 1.4	47.0 ± 1.1	
Velocity semiamplitude K (km s^{-1})[2]	98.5 ± 5.4	104.9 ± 6.1	

[1]Fixed.
[2]Adopted from Smullen & Kobulnicky (2015).

The flux-weighted radial velocity curves from our ELC model are shown in Figure 6.15, matching the original RV measurements in Smullen & Kobulnicky (2015) very well. In the right two panels, we also show the Rossiter-McLaughlin effect during the eclipse. It can be seen that in order to measure this effect, a RV precision better than 0.5 km s^{-1} is needed.

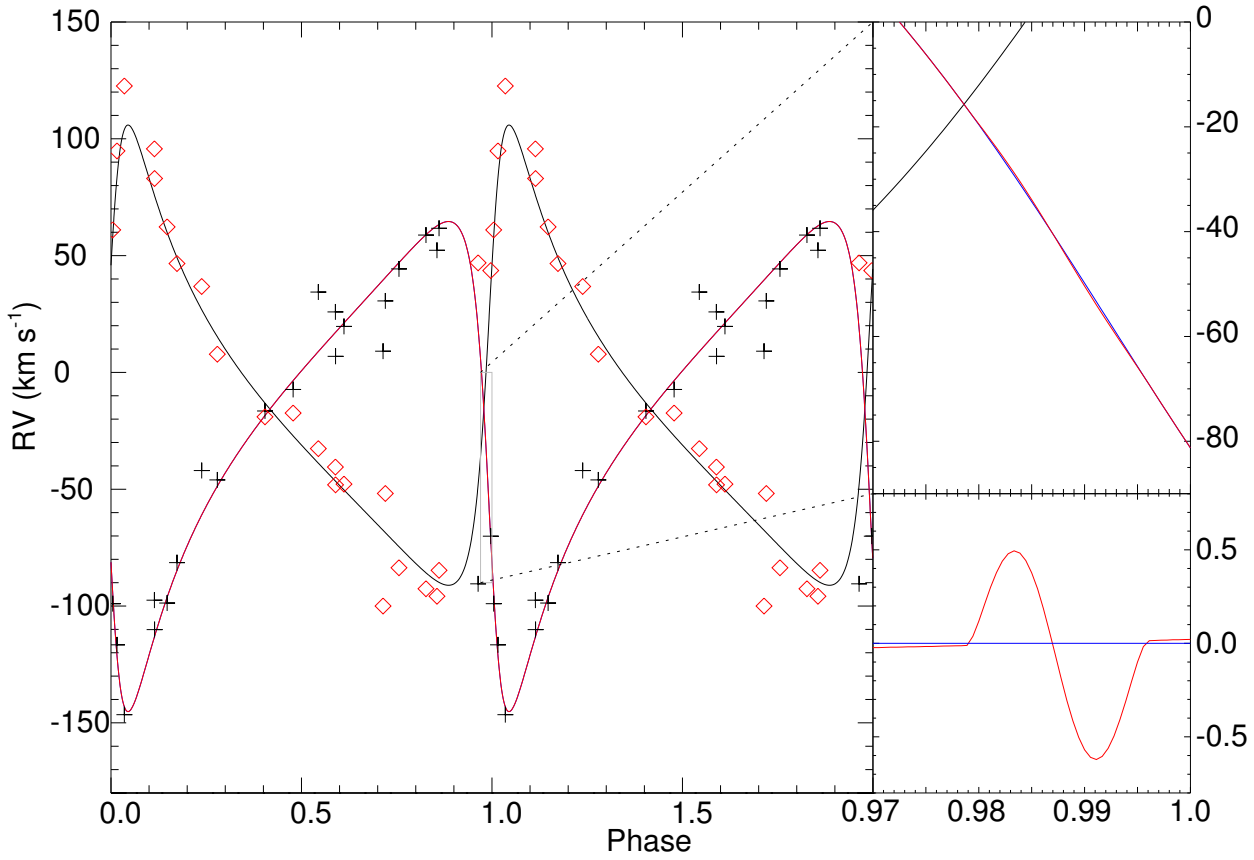

Figure 6.15 The radial velocity models of the primary (black solid) and the secondary (red solid) star from ELC. The corresponding observed radial velocities are indicated as red diamonds and black crosses. The upper right panels shows the RVs during the secondary eclipse phases. The red curve represents a flux-weighted radial velocity model of the secondary and blue curve is a simple Keplerian model. The RV residuals of the two models are shown in the lower right panel.

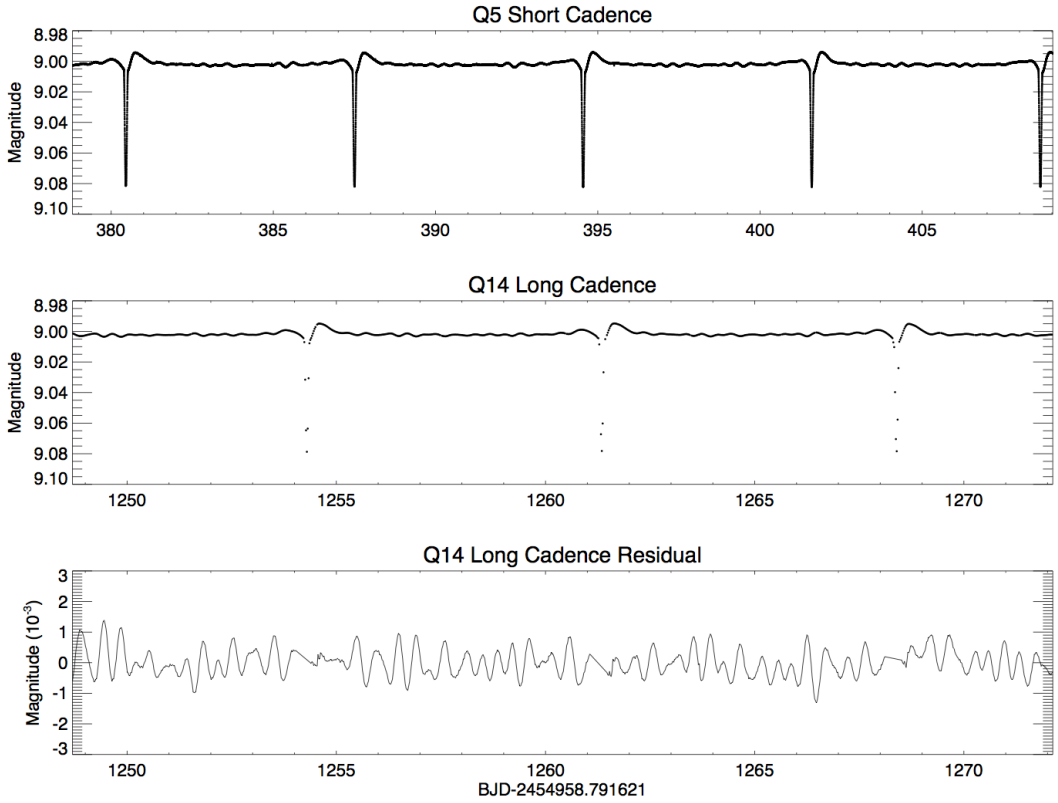

Figure 6.16 **Upper panel**: The short cadence light curve in quarter 5. **Middle panel**: The long cadence light curve in quarter 16. **Lower panel**: The light curve residuals after subtracting the best-fit binary light curve model in quarter 15. Eclipses have been masked.

6.4.3 Pulsation Characteristics

6.4.3.1 Tidally Induced Pulsations

To study the pulsations, we obtained the residuals by subtracting the best binary light curve model from the observations. Figure 6.16 illustrates the pulsational light curve in Q14, together with the original binary light curve in Q14 and the short cadence light curve in Q5. We then calculated the Fourier spectrum by using the *Period*04 package (Lenz & Breger 2005). A standard pre-whitening procedure was performed for the spectrum in each quarter. The fitting formula used is $Z + \sum_i A_i \sin(2\pi(\Omega_i t + \Phi_i))$, where Z, A_i, Ω_i, Φ_i are the zero-point shift, amplitudes of pulsations, frequencies and phases, respectively. The time t is with respect to the periastron passage: $t = \text{BJD } -2,454,958.791621$. The calculation was performed to the long cadence Nyquist frequency (24.47 d^{-1}). A similar calculation was performed on the short cadence residuals as well, but no peaks were found beyond the frequency ≈ 10 d^{-1} in the spectrum. The pulsational frequencies are actually all below 5 d^{-1}.

The amplitude spectrum calculated from residuals of quarter 1 and quarter $0 - 17$ are shown in Figure 6.17. The dominant feature in the spectrum is the equal spacing of the frequency peaks. The main pulsational frequencies and their amplitudes and phases are listed in Table 6.3. We have labeled them as f_1 to f_{10}, in the order of increasing frequency. A close examination reveals that most of these peaks are exact multiple integer times of orbital frequency ($f_{orb} = 1/7.0471062 = 0.141902\text{d}^{-1}$), for instance, f_3, f_5, f_6, f_7, f_8, f_9 and f_{10}. The orbital harmonic nature of the pulsational frequencies, together with the

high eccentricity of the binary and the masses of the stars strongly suggest that these are tidally induced pulsations. Note that the two non-orbital-harmonic frequencies f_1, f_2 can be added up to get an orbital harmonic ($f_1 + f_2 = 9.88 f_{orb} + 12.12 f_{orb} = 22 f_{orb}$). The same phenomenon was also found in the tidal oscillation frequencies of KOI-54. This can be explained by non-linear mode coupling as detailed by Burkart et al. (2012), O'Leary & Burkart (2014), and Weinberg et al. (2013). It is also interesting to note that $f_1 = 9.88 f_{orb}$ and $f_4 = 13.88 f_{orb}$ have the same fraction to the nearest orbital harmonic. The feature that nonharmonic frequencies share the common fractional parts in units of orbital frequency was discussed in detail by O'Leary & Burkart (2014) for KOI-54. This further supports the interpretation of these frequencies as the result of non-linear mode coupling.

Table 6.3: Main Oscillation Frequencies of KIC 3230227

	Frequency (d^{-1})	Amplitude (10^{-3} mag	Phase (2π)	S/N	Comment
f_1	1.40214 ± 0.00002	0.179 ± 0.027	0.97 ± 0.07	11.01	$9.88 f_{orb}$
f_2	1.71988 ± 0.00002	0.192 ± 0.022	0.34 ± 0.05	14.92	$12.12 f_{orb}$
f_3	1.84482 ± 0.00002	0.096 ± 0.021	0.32 ± 0.10	7.95	$13 f_{orb}$
f_4	1.969765 ± 0.000008	0.338 ± 0.020	0.16 ± 0.03	29.33	$13.88 f_{orb}$
f_5	2.12855 ± 0.00001	0.188 ± 0.018	0.89 ± 0.05	17.47	$15 f_{orb}$
f_6	2.41235 ± 0.00001	0.189 ± 0.016	0.39 ± 0.04	20.28	$17 f_{orb}$
f_7	2.55425 ± 0.00002	0.118 ± 0.015	0.85 ± 0.06	13.55	$18 f_{orb}$
f_8	2.69615 ± 0.00002	0.159 ± 0.014	0.37 ± 0.04	19.84	$19 f_{orb}$
f_9	2.83805 ± 0.00002	0.076 ± 0.013	0.37 ± 0.08	10.18	$20 f_{orb}$
f_{10}	2.979948 ± 0.000008	0.192 ± 0.012	0.86 ± 0.03	27.52	$21 f_{orb}$

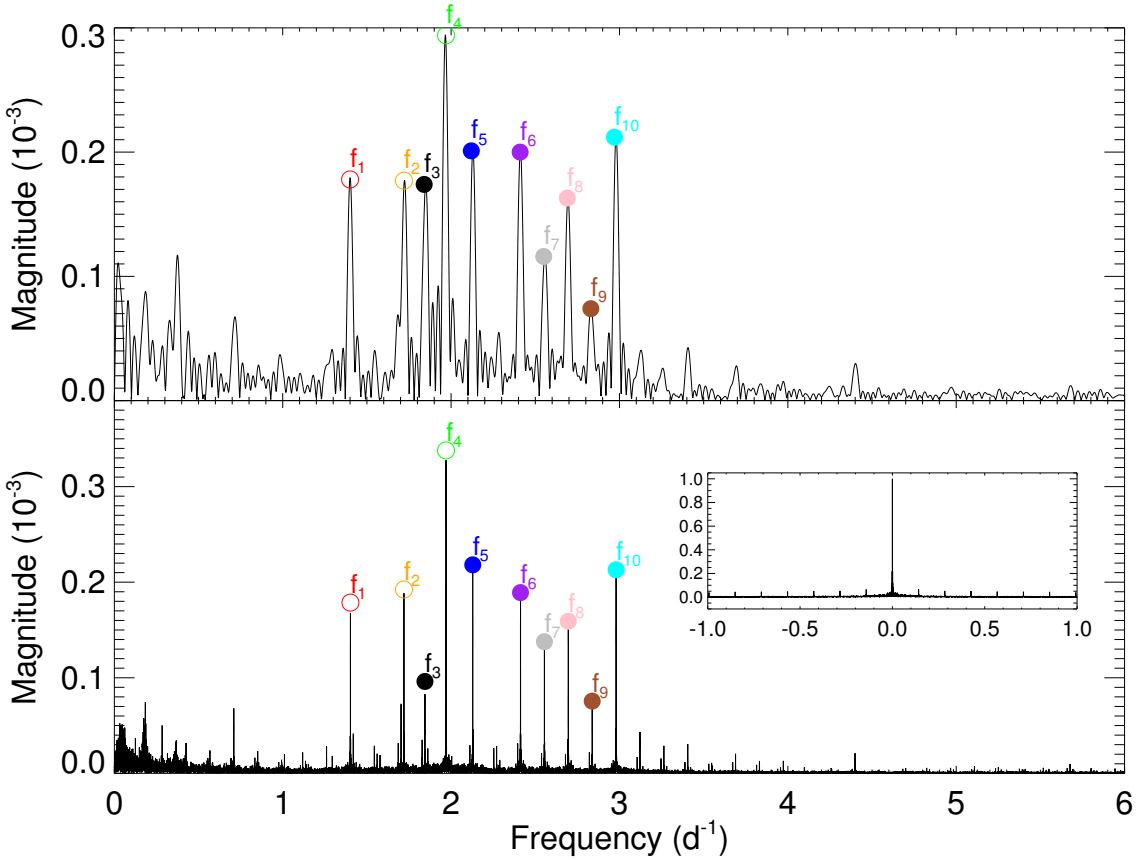

Figure 6.17 Fourier spectrum of light curve residuals with eclipses masked. The upper panel was calculated from the quarter 1 long cadence data. The lower panel presents a similar plot but using all quarters (Q0 − 17) of long cadence data. The inset shows the corresponding spectral window, and sidelobes with frequency spacing of orbital frequency can be seen. The 10 dominant frequencies listed in Table 6.3 are labeled. Filled and open circles indicate the harmonic and nonharmonic orbital frequencies, respectively.

Many frequency triplets can be seen in the spectrum, with equal spacing of orbital frequency. This can mainly be explained as side-lobes due to the spectral window. Close exam-

inations reveal that all these triplets have frequencies that are equal to $N-0.12, N, N+0.12$ times orbital frequency. Thus they can be explained as a combination of one real oscillation peak and two side-lobes due to the spectral window. The nonharmonic peaks f_1, f_2, f_4 generate side-lobes at $(N-0.12)f_{orb}$ and $(N+0.12)f_{orb}$, and the harmonic peaks generate side-lobes at Nf_{orb}. Low amplitude rotational splittings of $m=0$ modes can also exist. At high inclination, these $m=0$ modes are expected to have low amplitudes, but some triplets have rather high amplitudes which contradicts this explanation. As discussed below, the Ledoux constant C_{nl} (Ledoux 1951) is about 0.16 for the g-modes in the observed frequency range. This means the splitting δf is about $(1-0.16)f_{rot}$ for modes with frequencies much higher than f_{rot}. If we adopt pseudo-synchronous rotation $f_{rot} = 5f_{orb} = 0.71$ d^{-1}, δf is then 0.6 d^{-1}. Thus the splittings will be located at several orbital harmonics away from their central $m=0$ peak. This will make the identification more difficult. Thus the detailed analysis will be presented in a further study.

The amplitude variation of these oscillations are shown in Figure 6.18 and listed in Table 6.4. Most of the frequencies have relatively stable amplitudes over 16 quarters, with variation less than 0.05 milli-mag. The exception seems to be f_3, which decreased from 0.174 milli-mag in Q1 to 0.078 milli-mag in Q16.

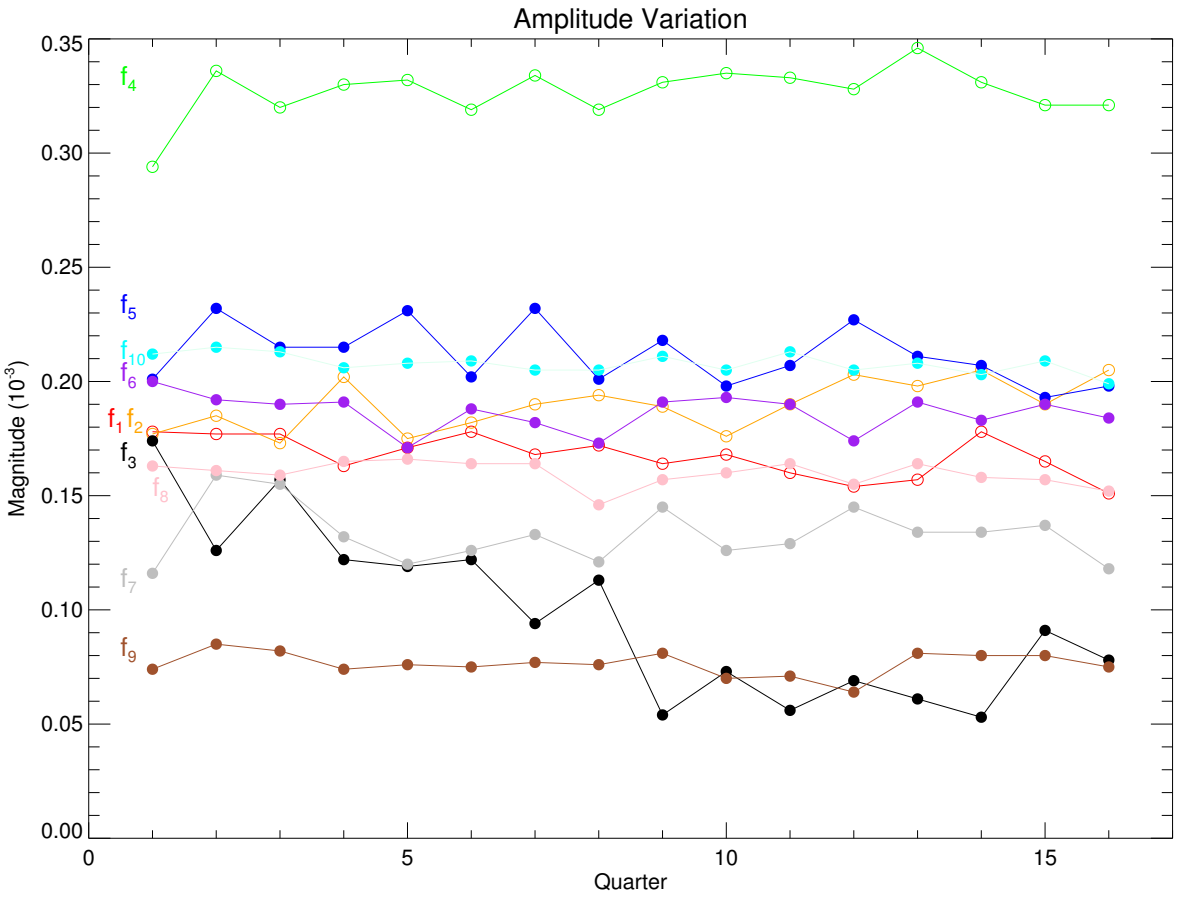

Figure 6.18 The amplitude variations of ten dominant oscillation frequencies. Filled and open circles indicate the harmonic and nonharmonic orbital frequencies, respectively.

Table 6.4: Amplitude Variations of the Main Frequencies

(10^{-3} mag)

Quarter	f_1	f_2	f_3	f_4	f_5	f_6	f_7	f_8	f_9	f_{10}
Q1	0.178	0.177	0.174	0.294	0.201	0.200	0.116	0.163	0.074	0.212
Q2	0.177	0.185	0.126	0.336	0.232	0.192	0.159	0.161	0.085	0.215
Q3	0.177	0.173	0.157	0.320	0.215	0.190	0.155	0.159	0.082	0.213
Q4	0.163	0.202	0.122	0.330	0.215	0.191	0.132	0.165	0.074	0.206
Q5	0.171	0.175	0.119	0.332	0.231	0.171	0.120	0.166	0.076	0.208
Q6	0.178	0.182	0.122	0.319	0.202	0.1881	0.126	0.164	0.075	0.209
Q7	0.168	0.190	0.094	0.334	0.232	0.182	0.133	0.164	0.077	0.205
Q8	0.172	0.194	0.113	0.319	0.201	0.173	0.121	0.146	0.076	0.205
Q9	0.164	0.189	0.054	0.331	0.218	0.191	0.145	0.157	0.081	0.211
Q10	0.168	0.176	0.073	0.335	0.198	0.193	0.126	0.160	0.070	0.205
Q11	0.160	0.190	0.056	0.333	0.207	0.190	0.129	0.164	0.071	0.213
Q12	0.154	0.203	0.069	0.328	0.227	0.174	0.145	0.155	0.064	0.205
Q13	0.157	0.198	0.061	0.346	0.211	0.191	0.134	0.164	0.081	0.208
Q14	0.178	0.205	0.053	0.331	0.207	0.183	0.134	0.158	0.080	0.203
Q15	0.165	0.190	0.091	0.321	0.193	0.190	0.137	0.157	0.080	0.209
Q16	0.151	0.205	0.078	0.321	0.198	0.184	0.118	0.152	0.075	0.199
1σ	0.027	0.022	0.021	0.020	0.018	0.015	0.015	0.014	0.013	0.012

6.4.3.2 Mode Identification from Phases

Phases of tidal oscillations contain important information on the mode properties. O'Leary & Burkart (2014) identified the two dominant pulsations in KOI-54 as $l = 2, m = 0$ modes by studying their phases. Following their treatment, we express the pulsations with the formula $\sin(2\pi(\Omega_i t + \delta_i))$ instead of cosine functions and $t = 0$ is the time of periastron passage. The phases of observed flux variation ($\delta J/J$) due to tidal oscillations that have kth times the orbital frequency are:

$$\delta = \left(\frac{1}{4} + \psi_{nlmk} + m\phi_0\right) \mod \frac{1}{2} \tag{6.3}$$

and

$$\phi_0 = \frac{1}{4} - \frac{\omega_p}{2\pi} \tag{6.4}$$

where $\omega_p = 293^\circ = 5.114$ rad is the argument of periastron from the RV and light curve analysis. In the limit of poor tuning, that is, the difference between intrinsic mode frequency of free oscillations and the nearest orbital harmonics ($\delta\omega = \omega_{nl} - kf_{orb}$) is much larger than mode damping rate (γ_{nl}), $|\delta\omega| \gg \gamma_{nl}$, we have the following approximation $\psi_{nlmk} \approx 0$, then the observed phases are then

$$\delta = \left(\frac{1}{4} + m\phi_0\right) \mod \frac{1}{2}. \tag{6.5}$$

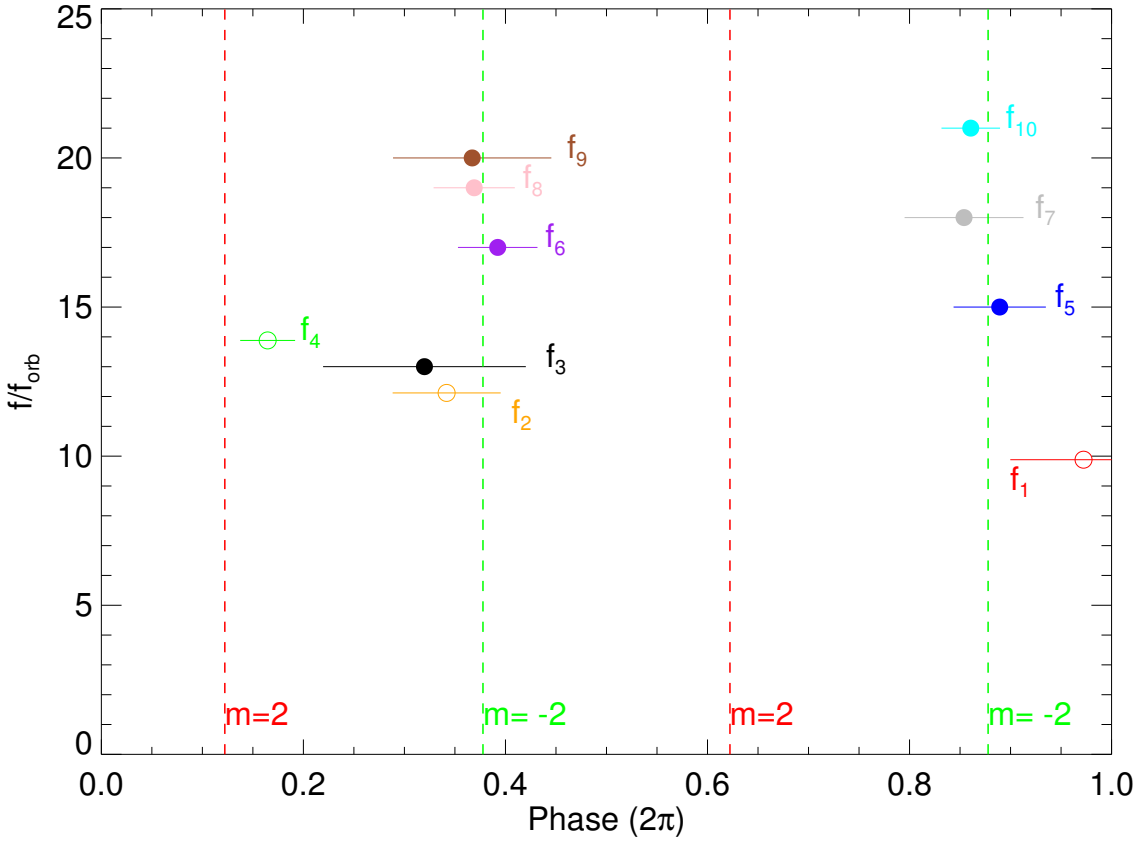

Figure 6.19 Phases of ten dominant oscillations (see Table 6.3). The 1σ error bars of phases are shown, those of frequencies are smaller than the symbols. Red and green dashed lines indicate the theoretical phases of $l = 2, m = 2$ and $l = 2, m = -2$ modes. Filled and open circles indicate the harmonic and nonharmonic orbital frequencies, respectively.

Note that if using magnitude variation, the phase will be off by π (by 1/2 if in units of 2π), since $\delta\text{mag} \propto -\delta J/J$. In Figure 6.19, we show the observed phases of main oscillations. Within uncertainties, phases of $f_2, f_3, f_5, f_6, f_7, f_8, f_9, f_{10}$ can be explained by the theoretical phases of $l = 2, m = -2$ modes ($\delta_{m=-2} = 0.38, 0.88$). The phase of f_4 is close to the predicted

phase of $m = 2$ modes ($\delta_{m=2} = 0.12$). As the time dependence of these orbital harmonic tidal oscillations is $\sin(N f_{orb} t + 2\pi\delta)$ and we cannot determine the sign of N (we can only observe $|N|$), we refrain the specification of these modes as prograde or retrograde (Burkart et al. 2012). We conclude that the observed oscillations are very likely due to $l = 2, m = |2|$ modes, in agreement with the expectations for high inclination angle of the binary ($i = 73.4°$). On the other hand, $l = 2, m = 0$ modes are expected to have low amplitudes, and none of the main frequencies have phases close to their predicted phases ($\delta_{m=0} = 0.25, 0.75$). As pointed out by O'Leary & Burkart (2014), oscillations that are in a resonance lock can have nearly arbitrary phases of pulsation. The observed phases seem to rule out this possibility.

6.4.3.3 Theoretical Flux Variations

We want to study whether the observed amplitudes of tidal oscillations agree with theory. To this end, we evolve a star of $M = 1.84 M_\odot$ with solar metallicity with MESA evolution code (Paxton et al. 2011, 2013) until its properties match the observations of the primary. The closest equilibrium model has the same radius ($R = 2.01 R_\odot$), but slightly cooler effective temperature ($T_{\rm eff}(model) = 7800$K vs. $T_{\rm eff}(observation) = 8000$K). We use parameters of the secondary ($M_2 = 1.73 M_\odot$) for the calculation of tidal forcing from the companion.

Following Fuller & Lai (2012), the Lagrangian tidal displacement $\boldsymbol{\xi}(\boldsymbol{r}, t)$ can be expressed as the sum of displacement of free oscillations $\boldsymbol{\xi}_\alpha(\boldsymbol{r})$,

$$\boldsymbol{\xi}(\boldsymbol{r}, t) = \sum_\alpha c_\alpha(t) \boldsymbol{\xi}_\alpha(\boldsymbol{r}). \tag{6.6}$$

Here α represents the mode indices which include (n, l, m). The amplitude of each mode c_α is derived from solving the forced harmonic oscillator equation (eq. 3.70) and the solution is given by eq. 3.72. The expression of $c_\alpha(t)$ involves the sum over the forcing from each orbital harmonic k, and this is from the Fourier expansion of orbital motion in the eccentric orbit (eq. 3.43, 3.44). The displacement $\boldsymbol{\xi}_\alpha$ and various other eigenfunctions of $l = 2, m = 0$ modes are calculated with the GYRE code (Townsend & Teitler 2013) in the non-adiabatic mode. We use the updated collocation method COLLOC_GL2 to solve the oscillation equations which has better performance than the Magnus solver for non-adiabatic calculations.

We use the perturbative approximation which is valid when rotation frequency ω_{rot} is much smaller than mode frequency in the zero-rotation limit (ω_{nl}). The frequencies of $l = 2, m = 2$ modes are calculated from $\omega_{nlm} = \omega_{nl} - mC_{nl}\omega_{rot}$, and the mode eigenfunctions are not changed by rotation.

Following Buta & Smith (1979), the magnitude variation of a single oscillation mode due to temperature changes has the following expression assuming pulsations are adiabatic:

$$(\Delta\mathrm{mag})_T = -1.0857\frac{\xi_r(R)}{R}\left[\frac{xe^x}{e^x-1}\frac{\Gamma_2-1}{\Gamma_2}\left(\frac{l(l+1)}{\omega^2}-4-\omega^2\right)\right]\gamma_l\sqrt{\frac{(2l+1)(l-m)!}{4\pi(l+m)!}}P_l^m(\cos i_s)e^{im\phi_0}e^{i\sigma t} \tag{6.7}$$

where $\xi_r(R)$ is the radial displacement evaluated at the stellar surface, $x = hc/\lambda kT$, i_s is the orbital inclination, $\Gamma_2 \approx 5/3$ is adiabatic index and ω is the dimensionless mode frequency given by $\omega = \omega_\alpha/\sqrt{GM/R^3}$. γ_l is bolometric limb darkening coefficient defined in eq. (39)

of Buta & Smith (1979). For an A-star similar to KIC 3230227 and flux in the *Kepler* passband, γ_l is about 0.3. The magnitude variation due to geometric effect is orders of magnitude smaller and not considered here.

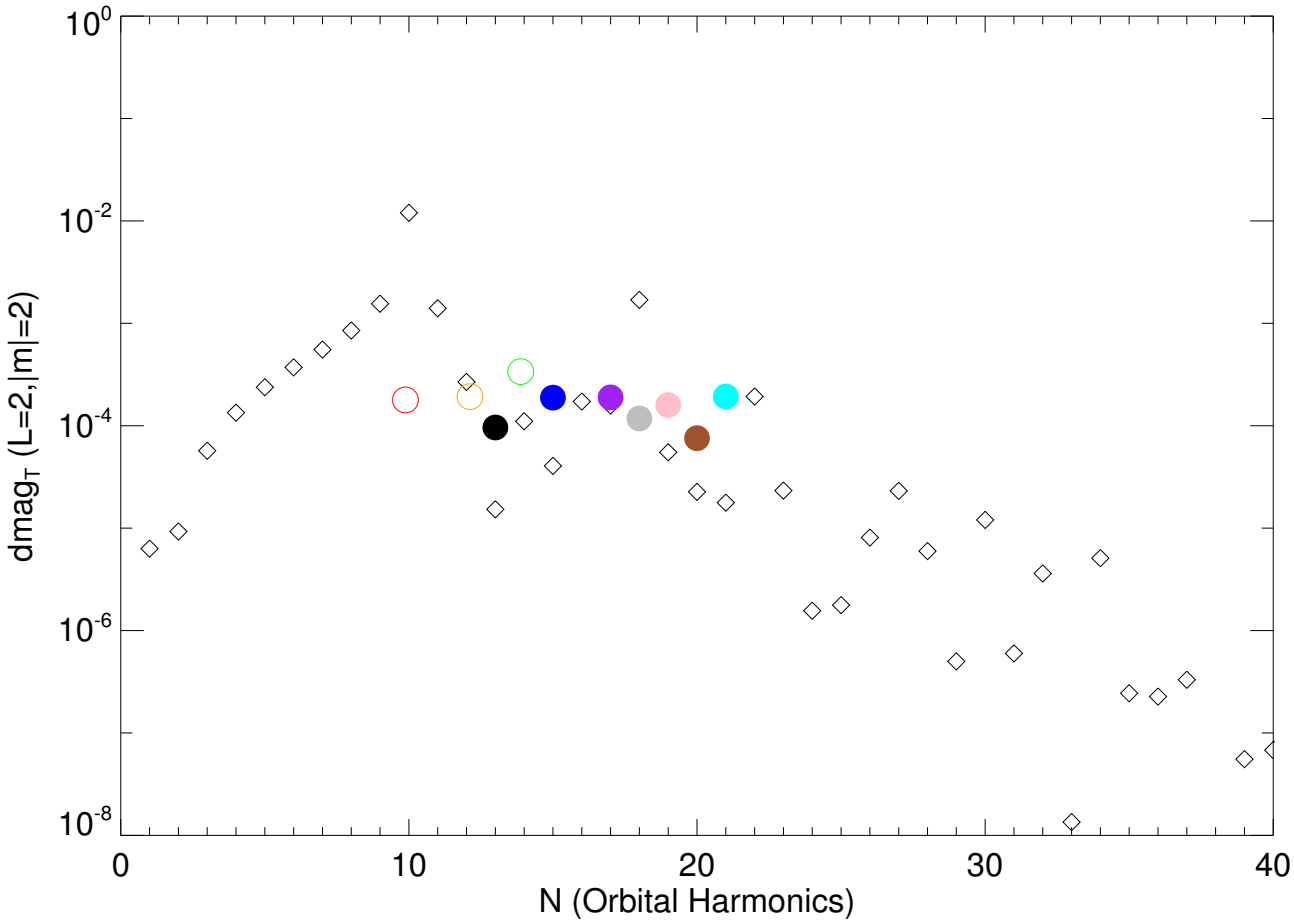

Figure 6.20 Theoretical magnitude variations of $l = 2, |m| = 2$ modes are indicated by diamonds. The observed magnitudes of oscillations are shown as color symbols. Oscillation frequencies that are orbital harmonics are indicated by the filled circles, and otherwise by open circles.

Using eq. (7) and summing up the contribution from each mode α, we calculated the magnitude variation for each orbital harmonic k for $l = 2, |m| = 2$ modes. The result is shown in Figure 6.20, together with the observed amplitudes of oscillations. The amplitudes

show various local Lorentzian-like peaks, and their amplitudes are very sensitive to the mode tuning parameter $\delta\omega = \omega_{nl} - kf_{orb}$. A stellar equilibrium model with almost the same observed parameters (radius, temperature, and mass) and slightly different mode frequencies will have quite different mode tuning. Even with this effect taken into account, the theoretical predicted mode amplitudes seem to have overall agreement with observations. It further supports the argument that the observed oscillations are due to $|m| = 2$ quadrupole modes.

6.4.4 Summary and Future Aspects

The unprecedented light curves from the *Kepler* satellite offer us opportunities to study the effect of tides on stellar oscillations. Heartbeat stars in eclipsing systems are among the best laboratories since the model independent fundamental stellar parameters such as mass and radius can be determined. We presented the study of KIC 3230227, which consists of two A-type stars in an eccentric orbit with a period of 7 days. The observed pulsations, mostly orbital harmonics, can be explained by the tidally induced $l = 2, |m| = 2$ modes. This is supported by their observed phases and amplitudes.

The fundamental parameters of KIC 3230227 are determined only to 10% in mass and 4% in radius. Further analysis could take advantage of high resolution spectra and more phase coverage in RVs. This is already in process (Kelly Hambleton, private communication). Once more accurate parameters are determined, asteroseismic modeling of these tidal oscillations can be performed, as was done in Burkart et al. (2012). To solidify the results of this work, mode identification techniques can be applied to the line profile variations as well as to the time series of multi-color photometry. It is also worthwhile studying the Fourier spectrum

more closely, identifying individual modes, characterizing rotational splittings, and analyzing the non-linear mode couplings. Another weakness of this work is that we are unable to tell which star is pulsating. A study of pulsations during eclipses may help to clarify this issue (Bíró & Nuspl 2011).

6.5 Preliminary Results for More Heartbeat Stars

Table 6.5: Parameters of Other Heartbeat Stars

Name	$T_{\rm eff1}$ (K)	$T_{\rm eff1}$ (K)	Period (days)	e	ω (deg)	K_1 (km s^{-1})	K_2 (km s^{-1})
KIC 10162999	6504(436)	5626(903)	3.4292146(62)	0.14	168	46.8	57.2
KIC 6117415	6637(379)	5571(1462)	19.7416252(765)	0.60	211	70.2	57.0
KIC 4142768	5435(359)	7698(841)	27.991603(126)	0.43	18	58.1	52.7
KIC 8456774	7182(935)	6420(792)	2.8863398(48)	0.11	185	56.4	62.8

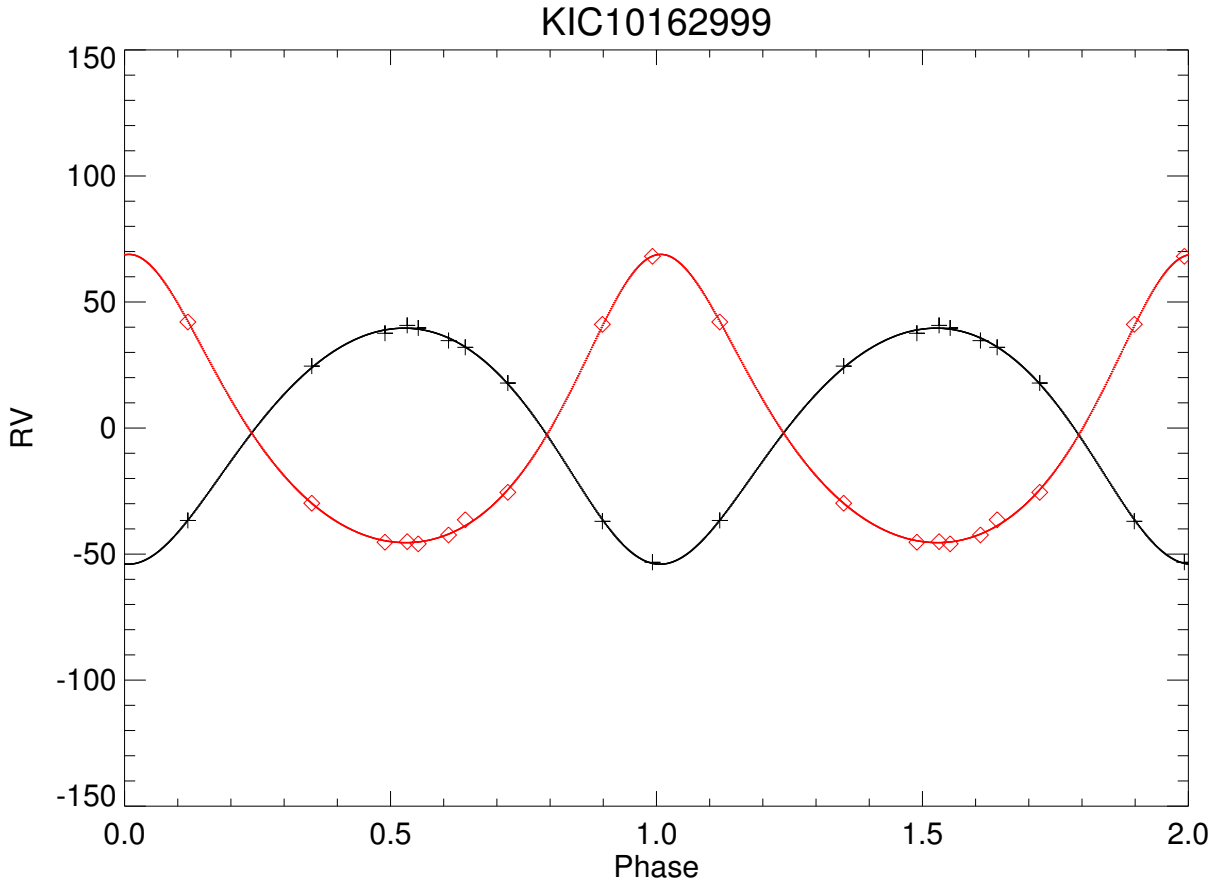

Figure 6.21 Radial Velocities of KIC 10162999 in units of km s^{-1}, derived from Keck HIRES spectra

In collaboration with Jim Fuller, we have obtained Keck HIRES spectra for 5 double-lined Kepler heartbeat stars. The detailed analysis is still under way. Here we present the preliminary analysis of 4 systems. The effective temperatures (taken from Armstrong et al. 2014) and orbital parameters are listed in Table 6.5. Individual systems are described in the following.

KIC 10162999. The RVs and light curves are shown in Figure 6.21 and Figure 6.22,

respectively. The RVs suggest that this binary has a relatively small eccentricity ($e \approx 0.14$) and two components of similar mass. The near symmetry of the light curve about periastron indicates that argument of periastron is close to 180°, in agreement with the result from RVs. A preliminary light curve model with a moderate inclination ($i \approx 40°$) seems to fit the observations very well. The Fourier spectrum of the light curve residuals is shown in Figure 6.23. The frequency peaks at 0.4788 d^{-1} and its harmonic $0.9597 = 2 \times 0.4788$ d^{-1} are probably due to rotational modulation. Since the orbital frequency is $f_{orb} = 1/3.429215 = 0.2916$ d^{-1}, the frequencies at $0.5831, 0.8748, 1.1666, 1.4582 d^{-1}$ are exactly $2, 3, 4, 5$ times f_{orb}. These are probably tidally induced oscillations.

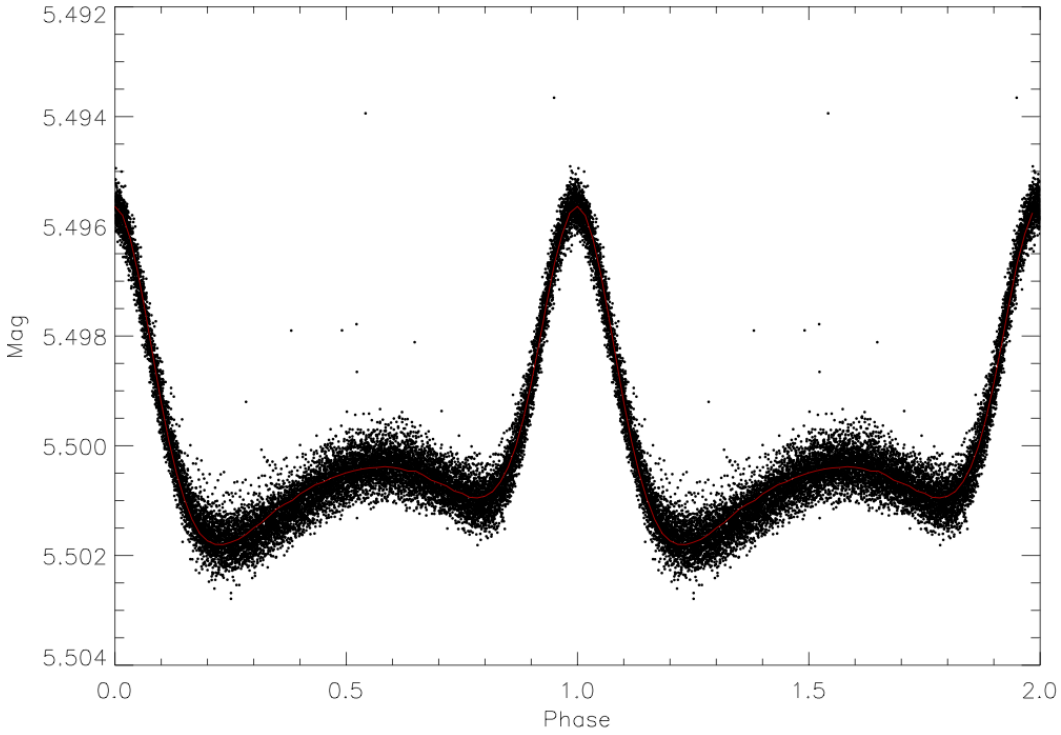

Figure 6.22 Kepler light curve of KIC 10162999 (plus an arbitrary constant in magnitude), with a preliminary ELC light curve model (red solid). The orbital inclination i is 39.35°; e and ω are fixed to spectroscopic values, see Table 6.5.

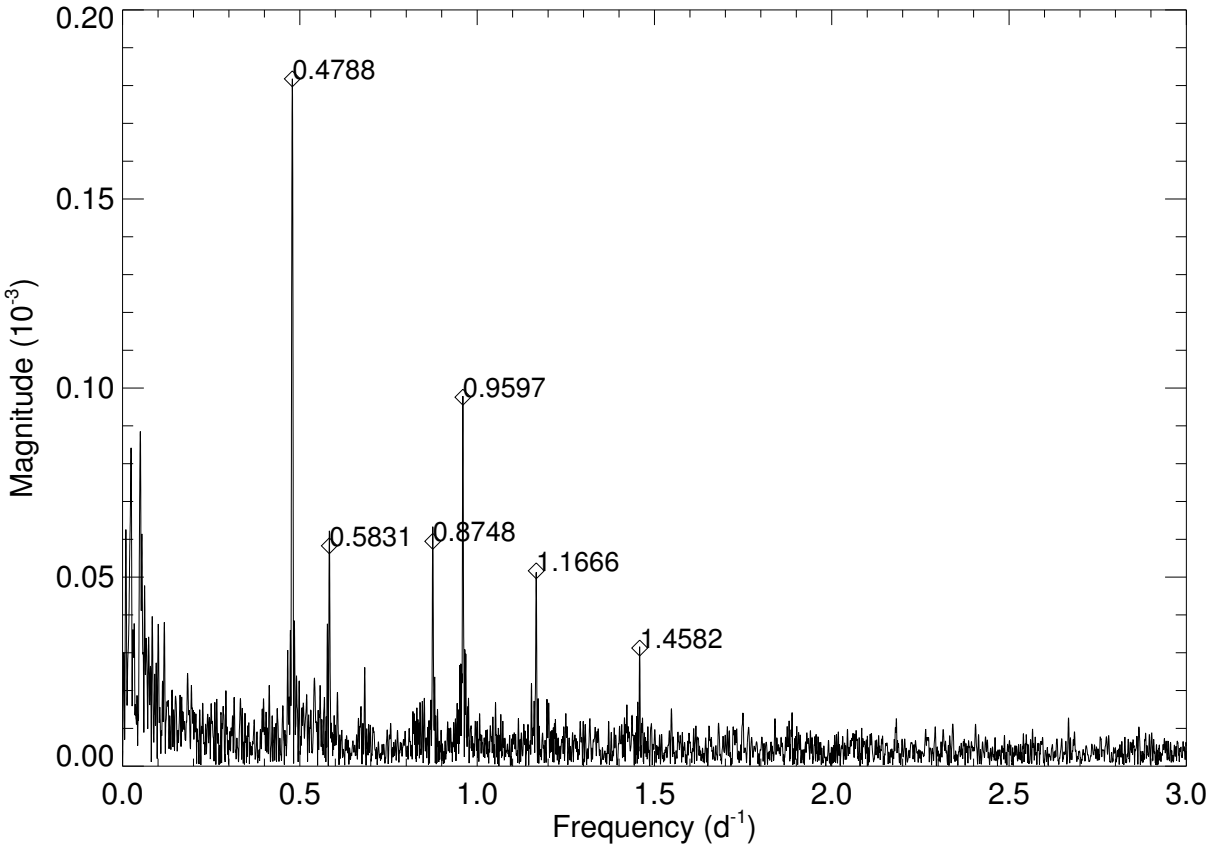

Figure 6.23 Fourier spectrum of the light curve residuals of KIC 10162999.

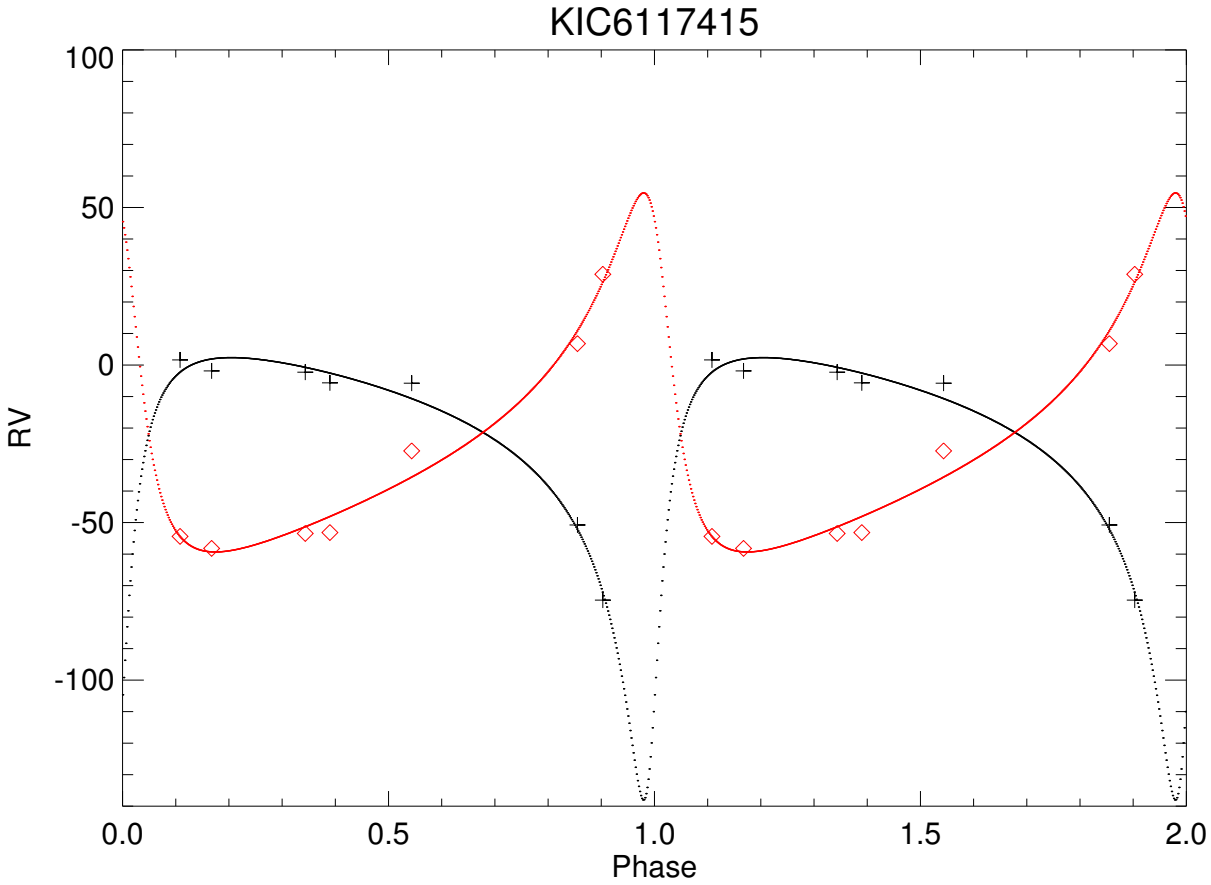

Figure 6.24 Radial Velocities of KIC 6117415.

KIC 6117415. The RVs and light curves (original and phase-folded) are shown in Figure 6.24 and Figures 6.25, 6.26, respectively. The brightness increase at periastron and the eccentricity ($e \approx 0.6$) from RVs are similar to that of the binary KIC 4544587 as shown by Hambleton et al. (2013). The Fourier spectrum of the light curve residuals (Figure 6.27) show signatures of rotational modulation.

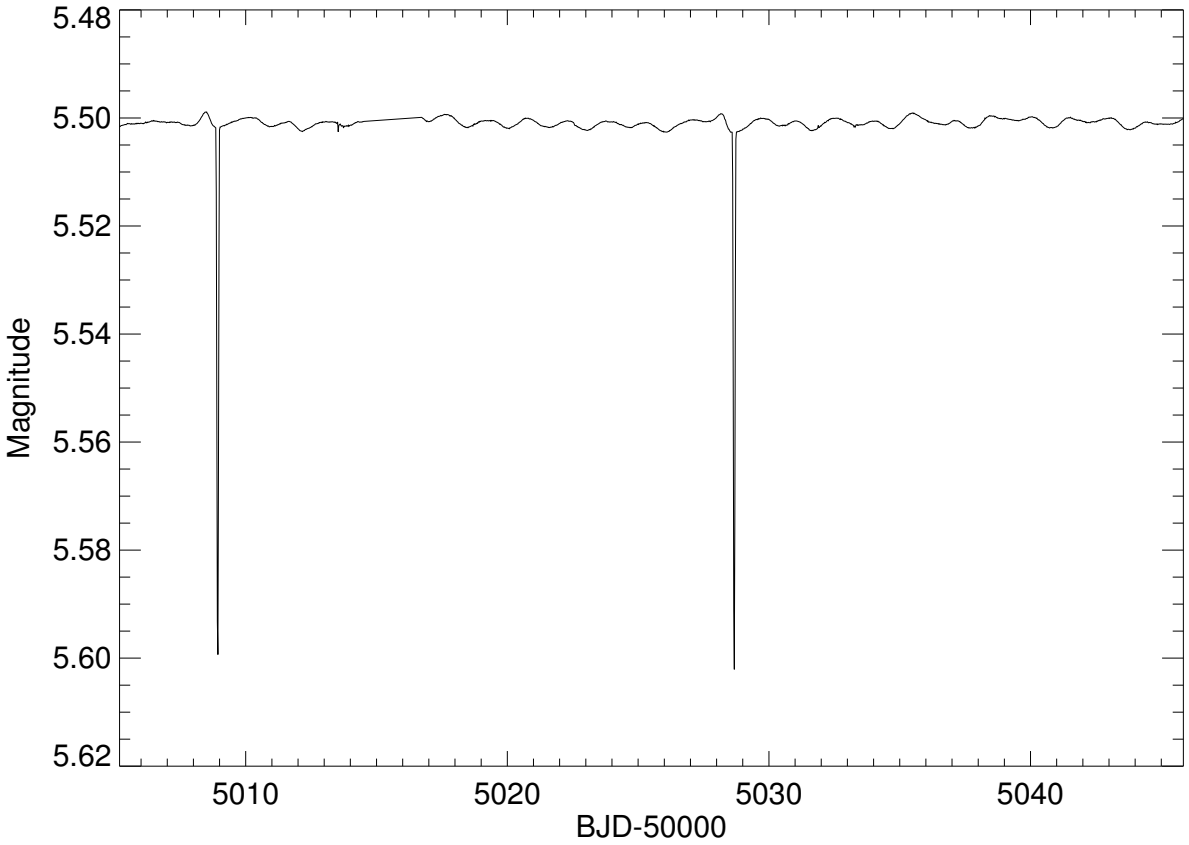

Figure 6.25 Kepler light curve of KIC6117415. Obvious pulsations can be seen in the out-of-eclipse part.

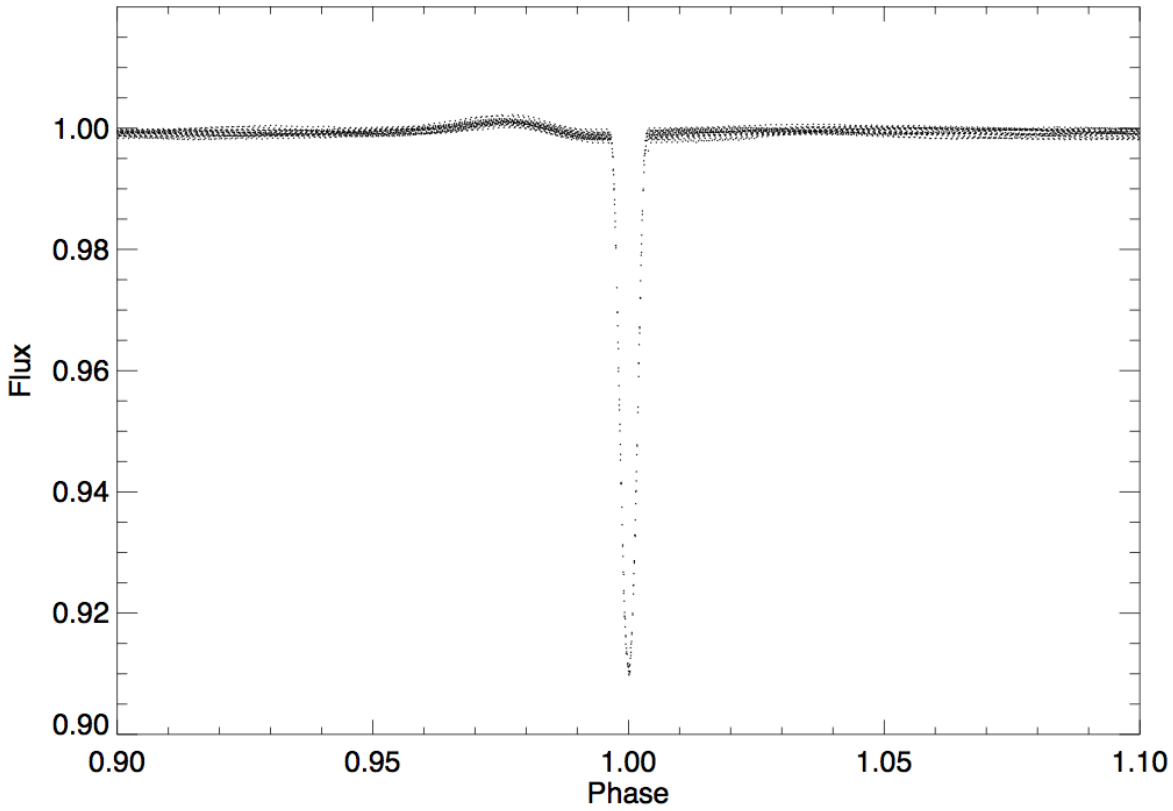

Figure 6.26 Phase folded Kepler light curve of KIC 6117415. Phases are calculated with respect to the eclipse minimum. The brightening due to reflection followed by a deep eclipse can be seen near periastron.

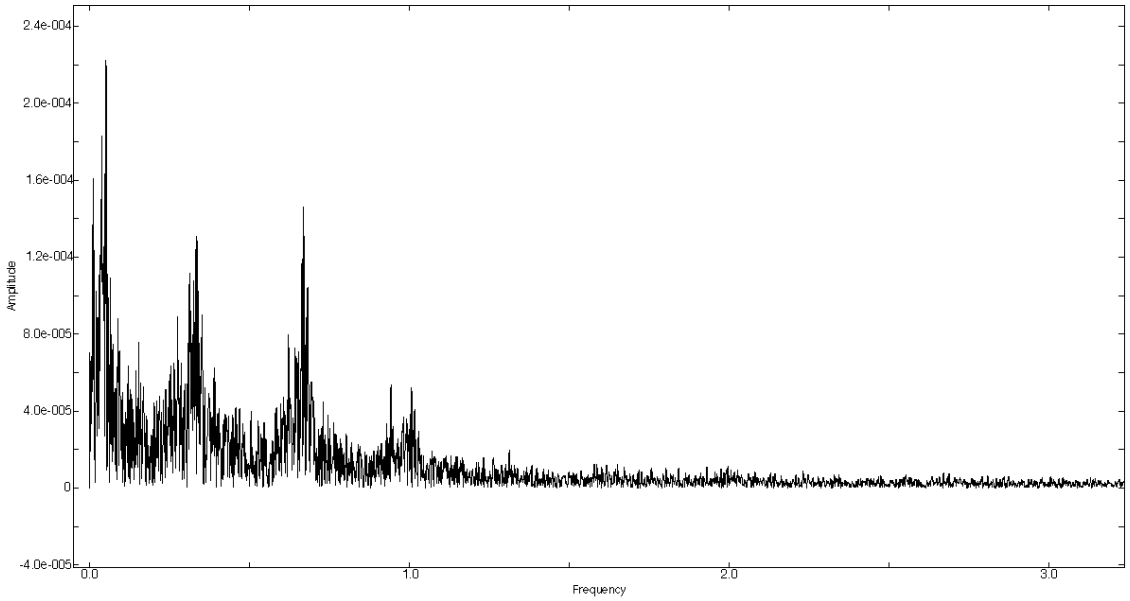

Figure 6.27 Fourier spectrum of the out-of-eclipse part of the light curve of KIC 6117415 (Amplitude vs. Frequency). The highest peak in the first frequency group has an frequency of 0.052 d^{-1}, which is close to the orbital frequency $f_{orb} = 1/19.7416252 = 0.05065$ d^{-1}. The other three frequency groups are located at $f_{group2} = 0.335, f_{group3} = 0.670, f_{group4} = 1.005$ d^{-1}. These groups are probably results of rotational modulation.

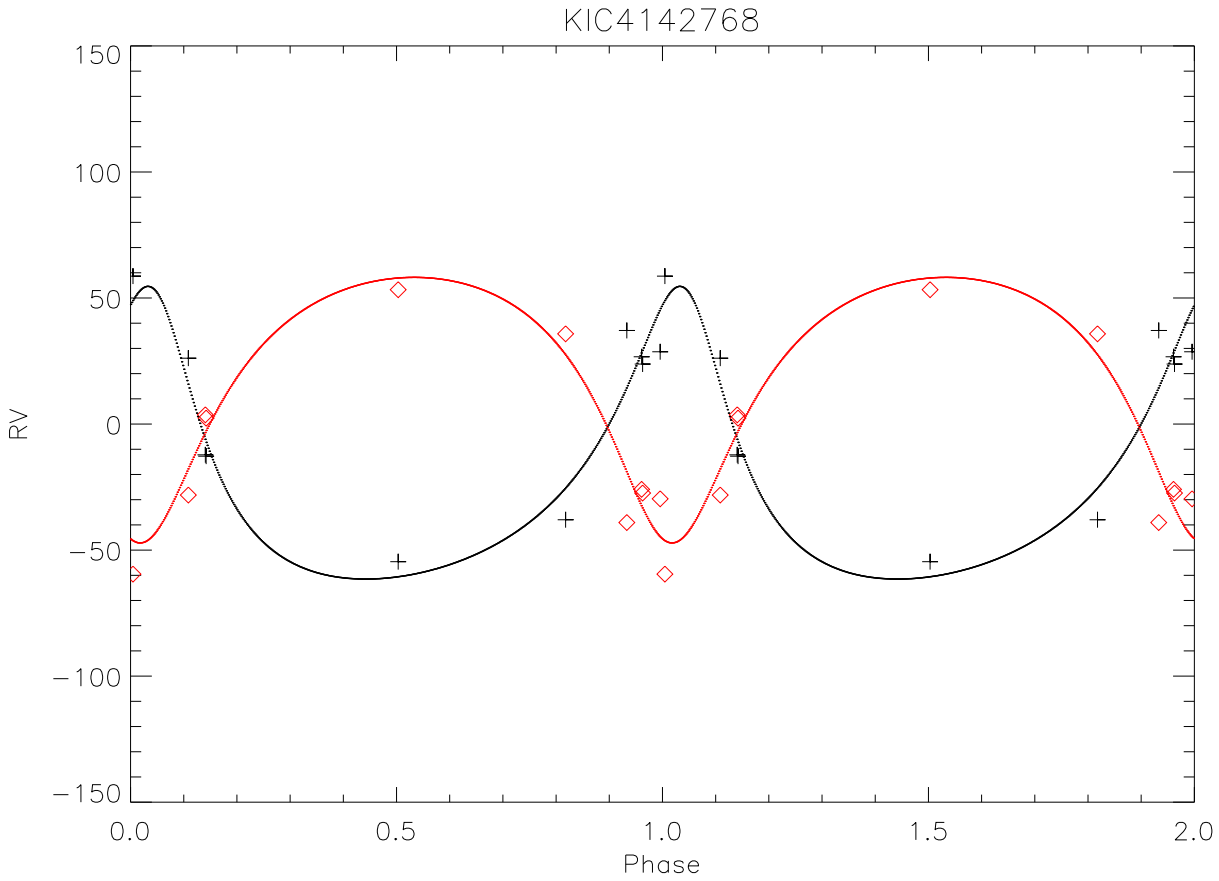

Figure 6.28 Radial Velocities of KIC 4142768

KIC 4142768. The derived RVs (Figure 6.28) show some scatter, requiring further refinement. Two deep eclipses are present in the light curve (Figure 6.29), suggesting a high inclination angle. Pulsations are obvious in the out-of-eclipse part. The Fourier spectrum (Figure 6.30) shows both strong low-frequency g-modes and high-frequency p-modes. This system is an interesting hybrid pulsator, and detailed seismic modeling is worthwhile.

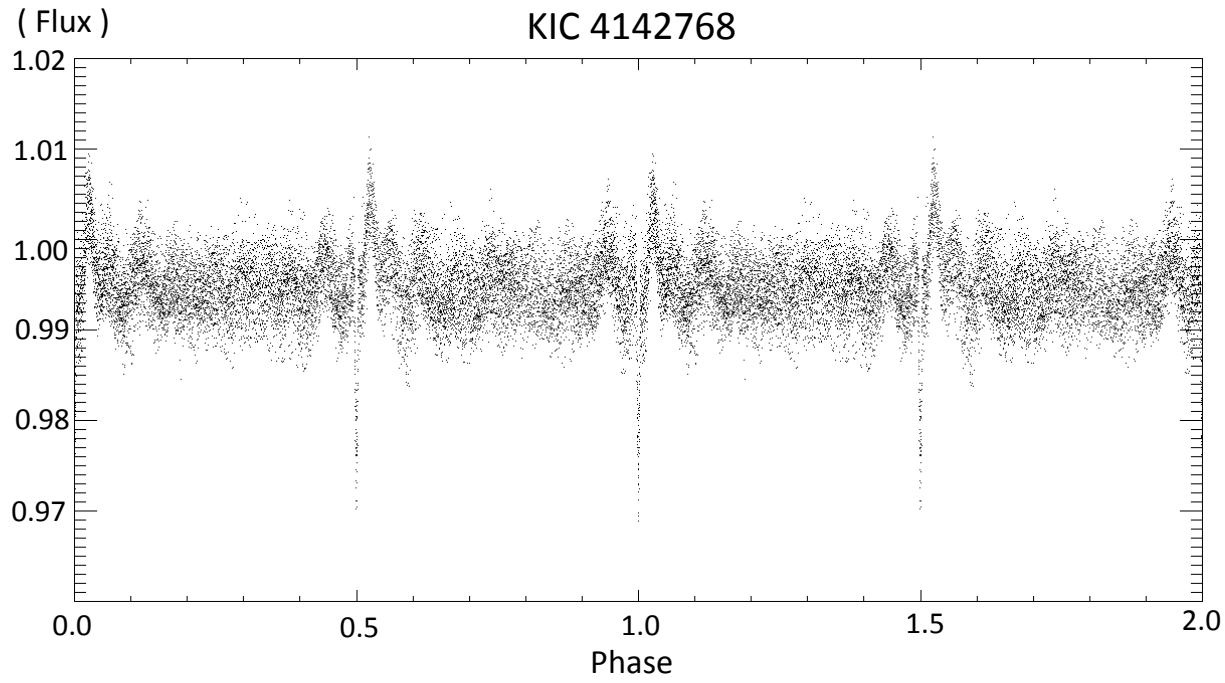

Figure 6.29 Kepler Light curve of KIC4142768

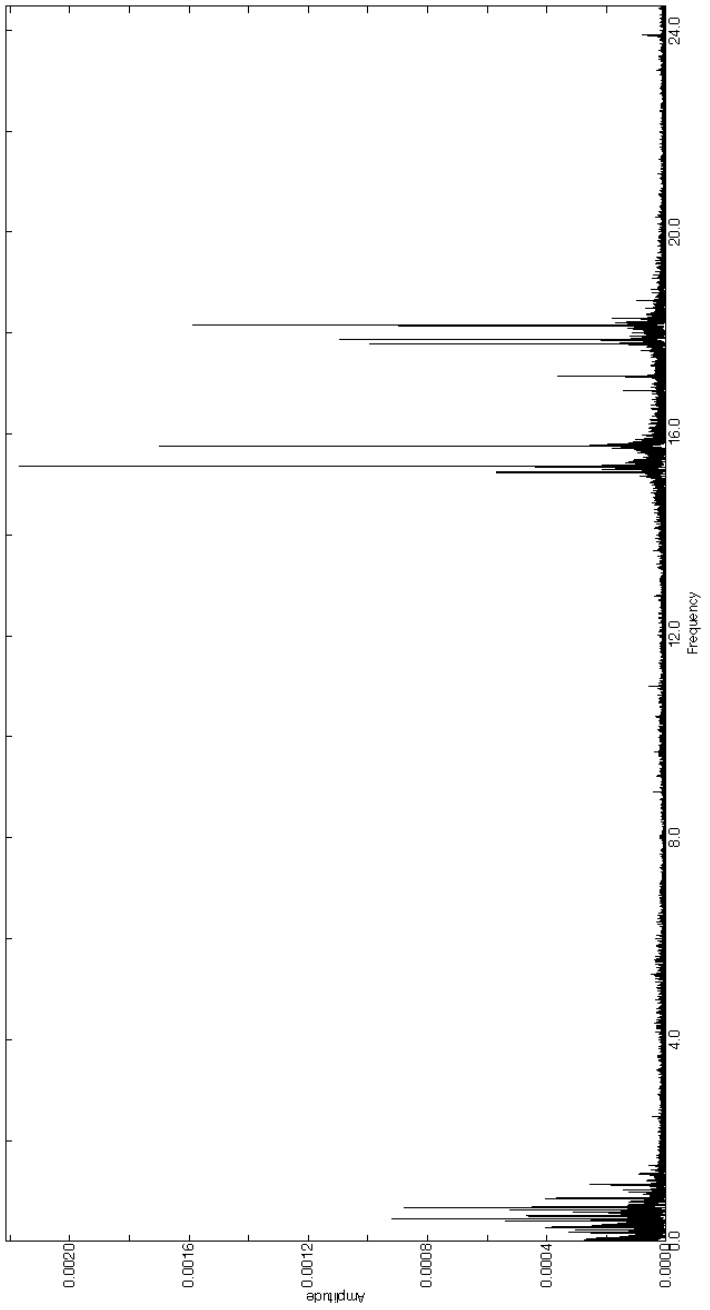

Figure 6.30 Fourier spectrum of the out-of-eclipse part of the light curve of KIC 4142768. Both low-frequency ($0 - 2$ d^{-1}) and high-frequency peaks ($15 - 19$ d^{-1}) can be seen, which are probably due to g-modes and p-modes, respectively.

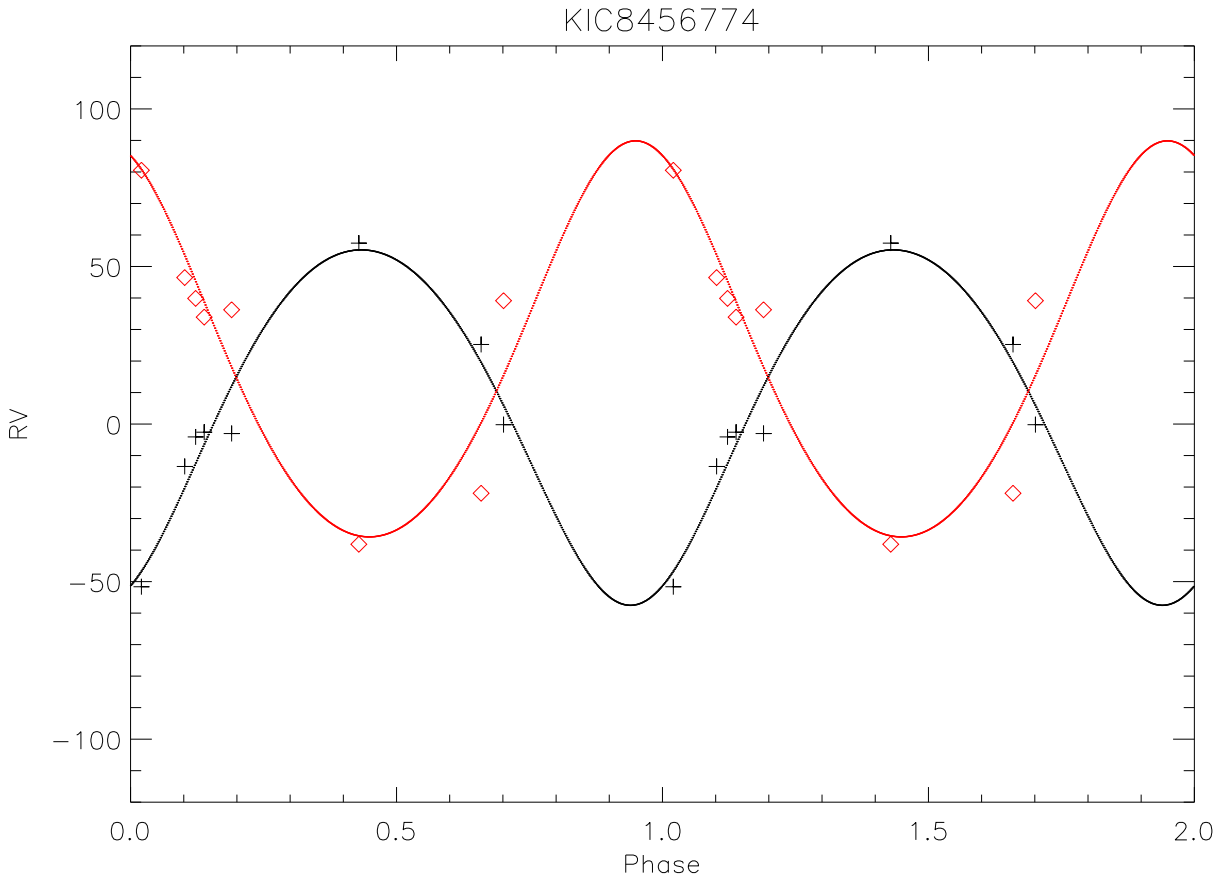

Figure 6.31 Radial Velocities of KIC 8456774.

KIC 8456774. Light curves (Figure 6.32) show symmetric periastron brightening, indicating $\omega \sim 180°$ and a low inclination angle. The broadness of the brightening suggests a relatively low eccentricity. Orbital harmonic pulsations are present. The two components have similar masses as shown in the RVs (Figure 6.31).

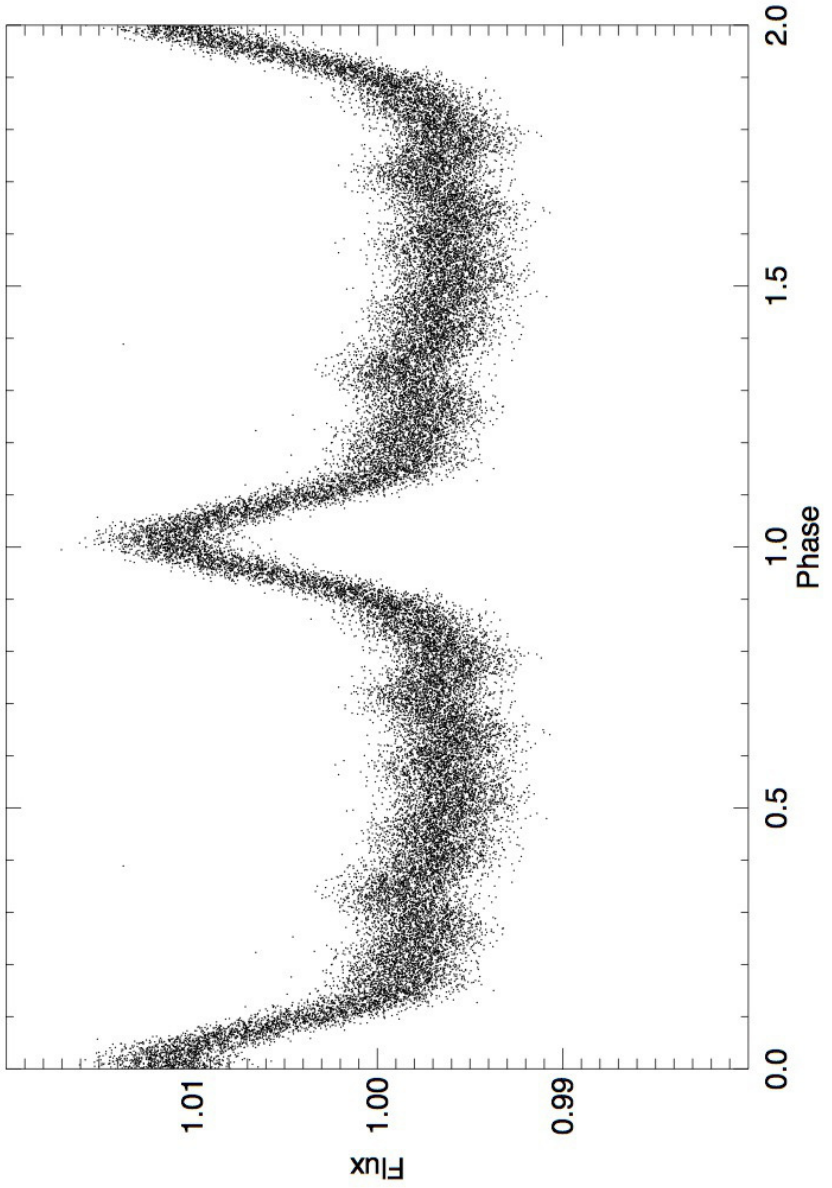

Figure 6.32 Phase folded light curve of KIC 8456774.

CHAPTER 7

Miscellaneous Case Studies of Oscillating Binaries that Contain an White Dwarf

In previous chapters, we studied the A- or F-type pulsating stars (δ Scuti, γ Dor, heartbeat stars) in binary systems. In this chapter, we extend the scope to include a Slowly Pulsating B-star with a white dwarf (WD) companion (KOI-81), as well as a cataclysmic variable (KIC 9406652). We utilize both Fourier and wavelet analysis to study their light curves. These two binaries represent the systems of which we know little about their pulsation properties. In the former one, the mass-transfer history and the fast rotation make it hard to model and identify the pulsation modes. For the latter one, due to the complications of the interactions between the accretion disk and the WD, the flux variability is quasi-periodic and a wide variety of amplitudes and timescales are present.

7.1 KOI-81: A Fast-rotating Slowly-pulsating B-Star With A Hot Companion

KOI-81 (KIC 8823868, P=23.8760923 d), was first identified as a Kepler object of interest, stars that are suspected of hosting transiting planets. Later, Rowe et al. (2010) reported that its light curve displays minima that were deeper during occultation than during transit, implying that the planetary size companions are hotter than their A- or B-type host stars. The transit and occultation light curve of KOI-81 are shown in Figure 7.1. van Kerkwijk et al. (2010) found that KOI-81 belongs to a class of beaming binaries which show the Doppler boosting phenomenon. This phenomenon reveals itself from photometry as showing a more luminous part of the light curve at one quadrature phase (when the star is approaching) than

the other (upper panel in Figure 7.1). The radial velocity semiamplitude can be inferred from Doppler boosting, and the same authors estimated that the white dwarf (WD) star of KOI-81 has a mass of $\approx 0.2 - 0.3 M_{\odot}$. The spectroscopic analysis of Matson et al. (2015) refined these results, and their derived fundamental parameters are listed in Table 7.1. Figure 7.2 illustrates a model of this system as seen projected in the sky, containing a rotationally distorted fast rotating B-star and a small, hot WD companion.

Radial velocities (RVs) of the two components in KOI-81 are presented in Figure 7.3 and Figure 7.4. The small companion contributes only a small percentage of flux, and only UV spectra from HST/COS[1] reveal its presence. Its RVs with large amplitudes are shown as open circles in Figure 7.3. RVs of the primary have very small amplitudes. Careful RV measurements are performed by using the spectra from KPNO[2], HST, and TRES[3]. The results are shown in Figure 7.4. We used both the Levenberg-Marquardt algorithm and Markov Chain Monte Carlo (MCMC) to derive the orbital parameters. Note that the MCMC method can reveal the correlations between parameters. If we only use the spectra from KPNO, the orbital parameters K_1 and γ_1 have strong correlations (Figure 7.5), due to the concentration of the KPNO observation times to phases in the first half of the orbit (Figure 7.4), the uncertainties from Levenberg-Marquardt are underestimated. When all spectra are used, the correlations are very small (Figure 7.6) and both methods (Levenberg-Marquardt and MCMC) give similar uncertainties.

[1]Hubble Space Telescope and Cosmic Origins Spectrograph

[2]Kitt Peak National Observatory (KPNO) 4m Mayall telescope and the RitcheyChretien (RC) Focus Spectrograph

[3]Tillinghast Reflector Echelle Spectrograph

Table 7.1: Fundamental Parameters of KOI 81

Parameters	Primary	Secondary
Mass ($M_\odot$)	2.916 ± 0.057	0.194 ± 0.020
Radius ($R_\odot$)	2.447 ± 0.022	0.0911 ± 0.0025
$T_{\rm eff}$ (kK)	11.7 ± 1.5	$> 19.4 \pm 2.5$
$\log g$ (cgs)	4.13 ± 0.01	5.81 ± 0.01
$V \sin i$ (km s^{-1})	296 ± 5	< 10

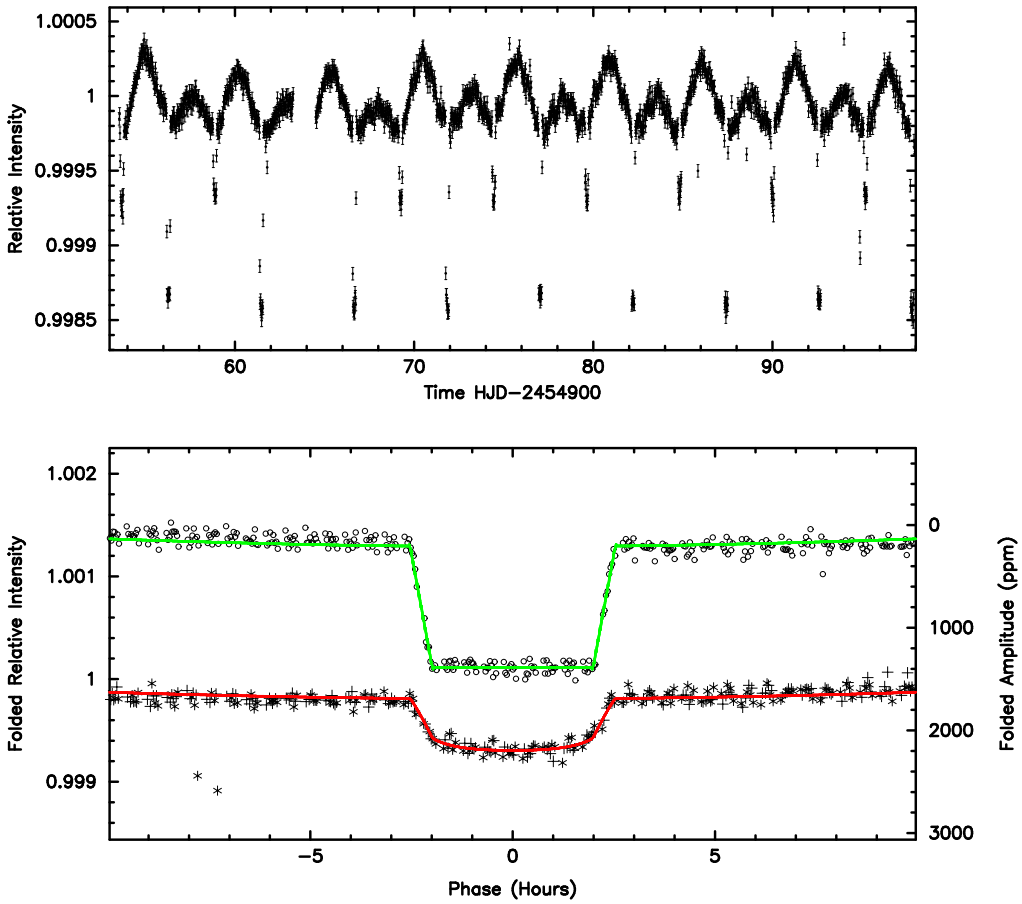

Figure 7.1 Detrended and normalized light curve of KOI-81. The upper and lower panel show the original and phase-folded version, taken from Rowe et al. (2010). The occultation of the hot companion is shown as the circles (shifted upwards for clarity). The transit light curve of the companion is indicated by the asterisks. Solid lines refer to the light curve model (red for transit and green for occultation).

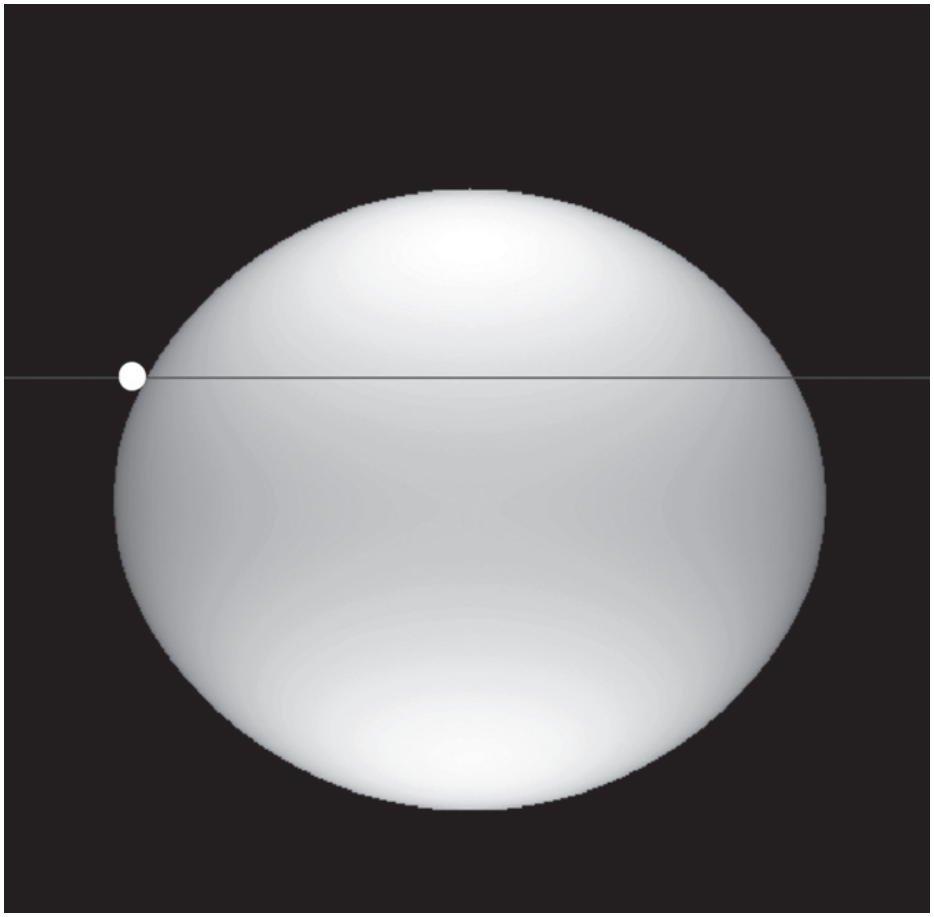

Figure 7.2 An illustration of the Roche model of KOI-81 in the Kepler bandpass. The system consists of a rotationally distorted B-star primary and a small, hot companion secondary (shown at first contact). The horizontal line indicates the modeled transit path. Figure is taken from Matson et al. (2015).

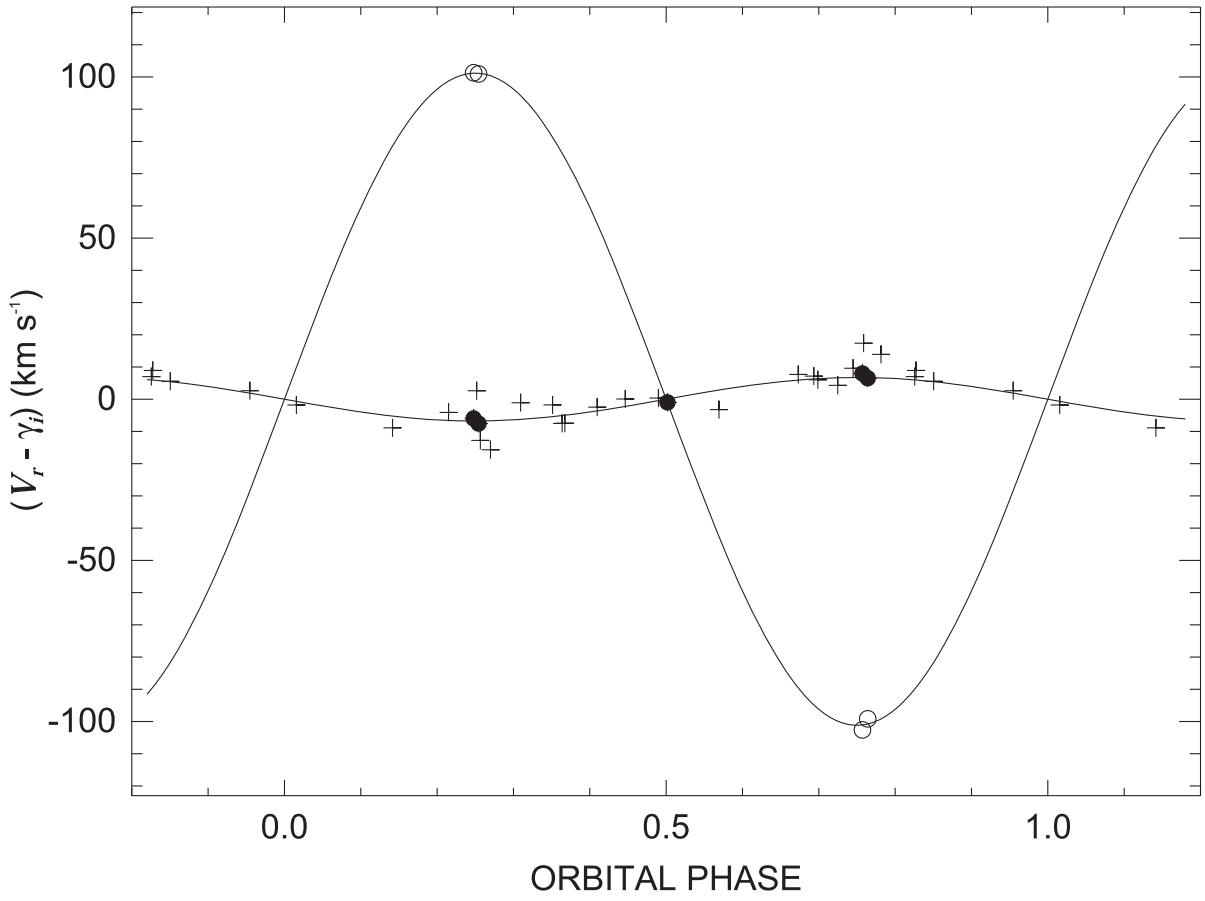

Figure 7.3 Radial velocities of KOI-81 with the best-fitting Keplerian model. RVs of the primary and secondary are indicated by crosses and filled circles. Those of the secondary are shown as open circles. Figure is taken from Matson et al. (2015).

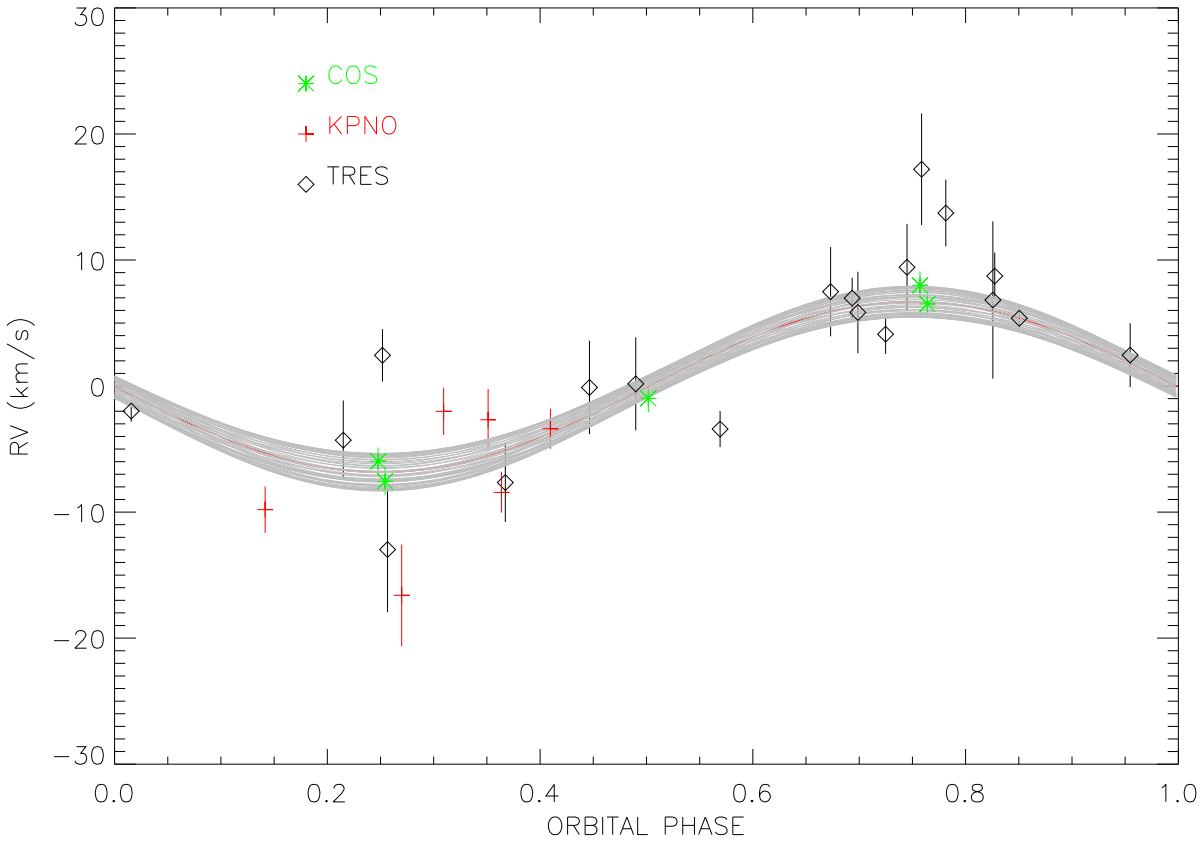

Figure 7.4 Radial velocities of the primary star of KOI-81 with the best-fit Keplerian model. The ± 2 σ credible region is filled with gray color.

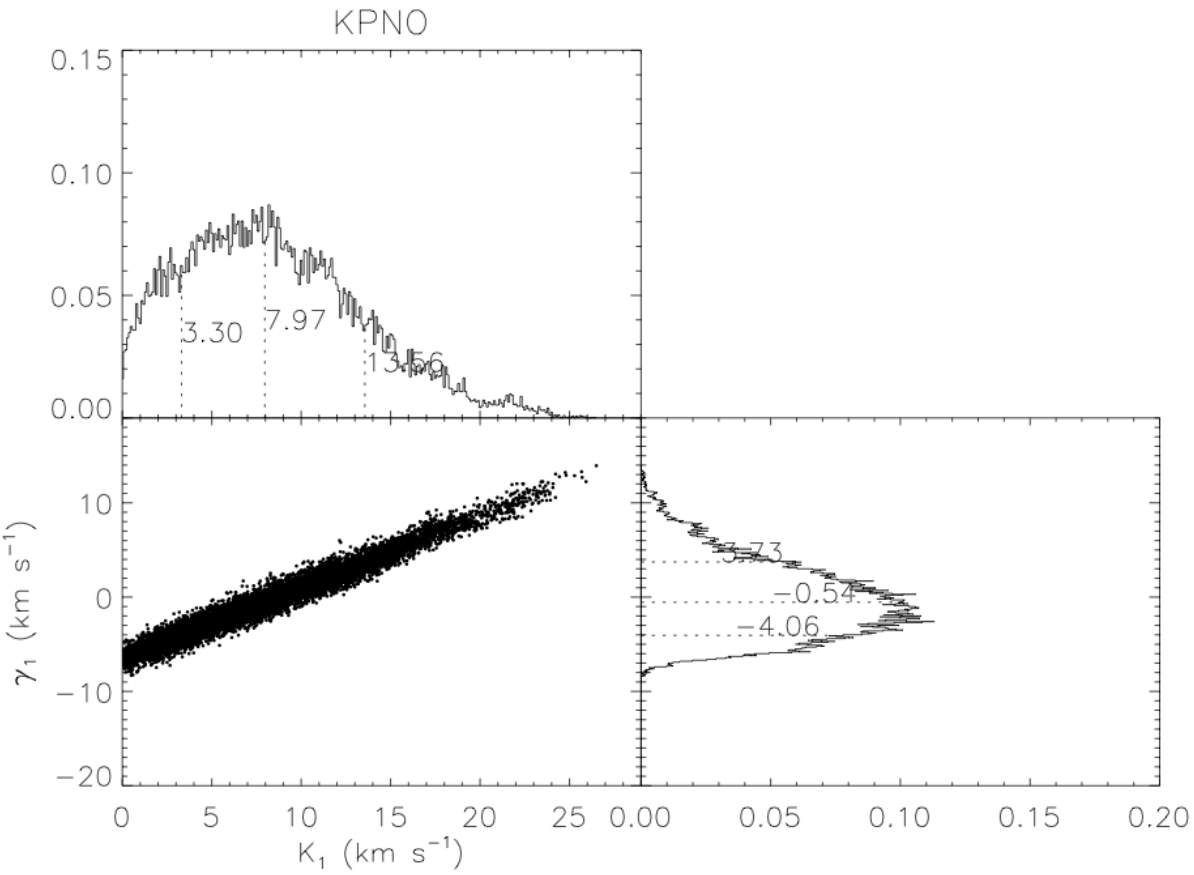

Figure 7.5 The posterior distributions of K_1 and γ_1 from the MCMC fit to KPNO radial velocities (80000 iterations). Dash lines indicate the median and ± 1 σ percentile boundary.

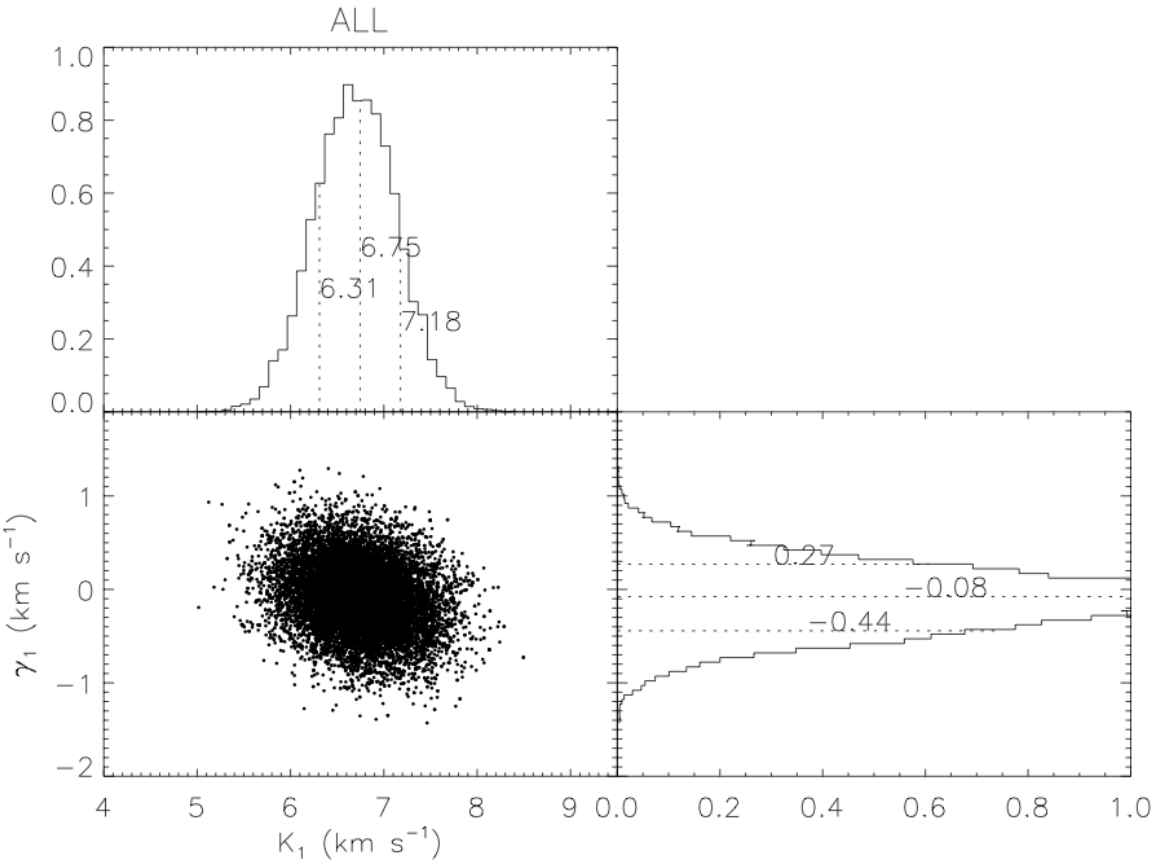

Figure 7.6 The posterior distributions of K_1 and γ_1 from the MCMC fit to the ALL (KPNO+TRES+HST/COS) radial velocities (40000 iterations). Dashed lines indicate the median and ± 1 sigma percentile boundary.

After masking the transits and occultations, we calculated the Fourier spectrum of the detrended, long cadence light curve from quarters 0 to 17 using the package Period04 (Lenz & Breger 2005). We adopted an empirical noise level by smoothing the envelope of the residual spectrum after prewhitening all significant frequencies with S/N > 3 (except for the broad rotational feature; see below). The uncertainties are calculated following Kallinger et

al. (2008). The Fourier spectrum is dominated by a very strong signal with a frequency of $f_1 = 0.722974$ cycles d^{-1} (period of 1.38318 d), and the spectrum after pre-whitening this signal is plotted in Figure 7.7. The frequencies, amplitudes, phases (relative to the epoch of central transit), and signal-to-noise ratio are listed in Table 7.2. The final column of Table 7.2 lists several numerical relations among these frequencies. One frequency (f_{12}) corresponds to the ellipsoidal (tidal) variation with twice the orbital frequency. The dominant periodicity (1.38 d) is unrelated to the orbital period, and it probably represents a strong and long-lived pulsational mode. There are also other low frequency pulsation signals in the spectrum.

The B-star primary of KOI-81 has a temperature and radius that are similar to those of the slowly pulsating B-type (SPB) stars (Pamyatnykh 1999). According to Saio (2013), most visible modes should be low degree prograde ($m < 0$) sectoral ($l = m$) g-modes and (retrograde) r-modes in rapidly rotating intermediate mass stars (assuming the time dependence of modes is $e^{i(\sigma t + m\phi)}$). For high order g-modes in rapidly rotating stars with rotational frequency Ω, if $\omega \ll |m|\Omega$ with ω being frequency in the co-rotating frame, then we expect to observe these modes at $\sigma = |\omega - m\Omega| \sim |m|\Omega$. Since sectoral prograde g-modes are expected to be most visible, we expect groups of frequencies slightly above Ω and 2Ω for $m = 1$ and 2 modes, respectively. (Modes with higher $|m|$ are expected to be less visible due to cancellation.) These frequency groups are indeed observed in several pulsating Be stars, for example, HD 163868 (Walker et al. 2005) and HD50209 (Diago et al. 2009). For KOI-81, however, no frequency groups are observed, except for a broad feature near f_5 which we interpret as differential rotation (discussed below). The criterion $\omega \ll |m|\Omega$ is not satisfied

since the observed pulsation frequency σ is comparable to or lower than Ω. The observed low ferquency pulsations are more likely due to retrograde ($m > 0$) pulsations with low m. Townsend (2005b) and Savonije (2013) argue that rapidly rotating, late-type B-stars can experience retrograde mixed modes of low azimuthal order m. Furthermore, the interpretation of the frequencies of the primary should incorporate a stellar structure model that includes the results of prior mass transfer from the WD progenitor star (Matson et al. 2015). The presence of frequency combinations also indicates that non-linear effects may be at work.

There is a broad distribution of peaks just above 2 d^{-1}, and we show an enlarged version of the Fourier amplitude in this vicinity in the top panel of Figure 7.8. A wide distribution appears around 2.04 d^{-1} that is accompanied by a strong peak at $f_5 = 2.08287$ d^{-1}. The lower panel shows the residual peaks after pre-whitening and removal of the strong f_5 signal, and this reveals the presence of several other significant peaks near f_5. This kind of broad feature with a stronger single peak at slightly higher frequency has been detected by Balona (2013, 2014) in the *Kepler* light curves of some 19% of A-type stars. Balona argues persuasively that this feature probably corresponds to the stellar rotational frequency. In his interpretation, the single strong peak corresponds to the equatorial rotational frequency and the wider peak samples the rotational frequencies at different latitudes in stars with differential rotation. Thus, following this line of argument, we may tentatively identify f_5 as the equatorial rotational frequency of the B-star in KOI-81, and thus, the rotational period is 0.48 d at the equator. Balona (2014) considers several explanations for the origin of the photometric variations including pulsation, rotational modulation by starspots, and tidal

variations induced by a co-orbiting exoplanet. We suspect that in the case of KOI-81, any co-orbiting planet would have a short period and an orbital plane similar to that of the stellar companion, so that we might expect to observe a transit signal in the f_5 folded light curve, but instead the folded light curve is approximately sinusoidal in shape. We speculate that the rotational signals in the light curve of KOI-81 and similar stars may result from long-lived vortices (Kitchatinov & Rüdiger 2009) that develop in the outer atmospheres of rotating stars due to differential rotation (similarly to the spots in the atmosphere of Jupiter).

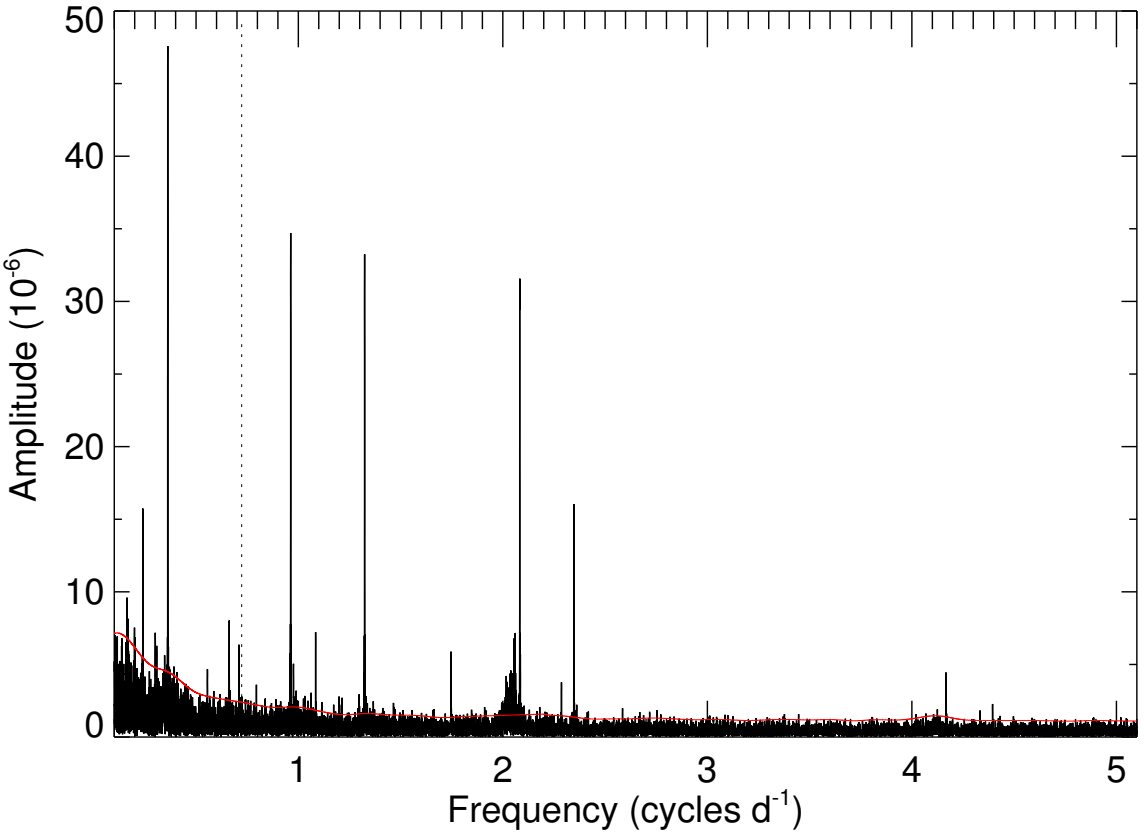

Figure 7.7 The Fourier amplitude spectrum after prewhitening the dominant peak at 0.72297 d^{-1} indicated by the dotted line. The empirical noise level is indicated by the red solid line.

Table 7.2: Significant frequencies

	Frequency (d^{-1})	Amplitude (10^{-6})	Phase (rad/2π)	S/N	Comment
f_1	0.722974 ± 0.000002	257.6 ± 4.1	0.822 ± 0.001	107.4	
f_2	1.32403 ± 0.00001	33.4 ± 2.8	0.34 ± 0.006	20.6	$f_4 + f_6$
f_3	1.08445 ± 0.00002	22.1 ± 3.2	0.98 ± 0.01	20.5	$f_1 + f_6$
f_4	0.96250 ± 0.00001	34.6 ± 3.6	0.22 ± 0.008	16.7	
f_5	2.08287 ± 0.00001	31.4 ± 2.6	0.77 ± 0.006	11.4	f_{rot}
f_6	0.36148 ± 0.00002	47.5 ± 7.7	0.28 ± 0.01	10.6	$0.5f_1$
f_7	2.34753 ± 0.00002	15.7 ± 2.3	0.36 ± 0.01	8.0	
f_8	0.70933 ± 0.00009	6.3 ± 4.2	0.96 ± 0.04	6.9	
f_9	1.74647 ± 0.00006	5.8 ± 2.3	0.15 ± 0.03	6.8	
f_{10}	2.08357 ± 0.00003	12.3 ± 2.6	0.37 ± 0.05	4.5	f_{rot}
f_{11}	4.16643 ± 0.00008	4.4 ± 2.4	0.08 ± 0.04	4.3	$2f_{rot}$
f_{12}	0.0837 ± 0.0002	10.9 ± 4.0	0.25 ± 0.02	3.2	$2f_{orb}$
f_{13}	2.08216 ± 0.00003	10.4 ± 2.6	0.09 ± 0.04	3.1	f_{rot}

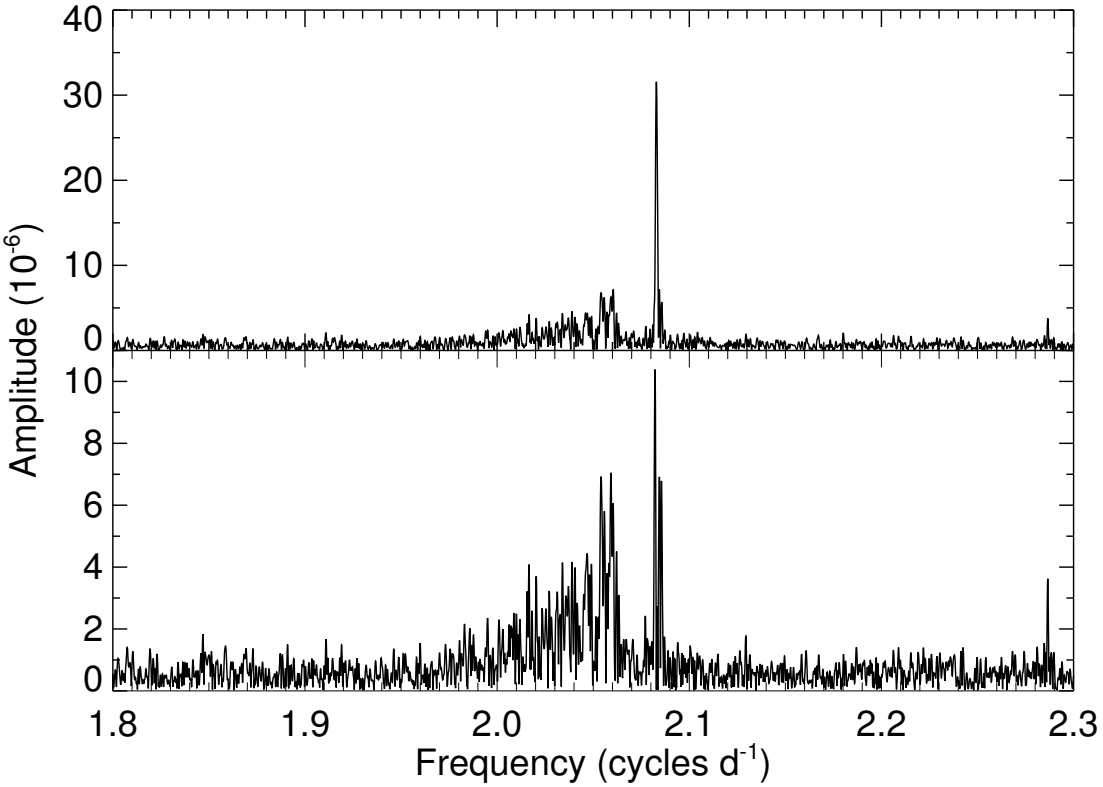

Figure 7.8 Top: The broad differential rotation feature at about $1.96 \sim 2.06$ d^{-1} and the adjacent sharp peak at $f_5 \approx 2.08287$ d^{-1}. Bottom: the same diagram but with the sharp peak prewhitened.

7.2 Variability of the Cataclysmic Variable KIC 9406652

7.2.1 Introduction

Cataclysmic variable (CV) stars are evolved, interacting binaries. The system usually consists of a cool, Roche-filling donor star and a mass-gaining white dwarf companion surrounded

by a dynamic accretion disk (Warner 1995; Hellier 2001). A wide variety of amplitudes and timescales can present in their flux variations, which are due to the processes of accretion around the disk (Honeycutt et al. 1998).

KIC 9406652 is a CV with an orbital period of 6.108 hours. It was observed by *Kepler* and the light curve shows both very rapid oscillations and long term outbursts. The fundamental parameters from a combined analysis of light curves and spectra are shown in Table 7.3. The separated individual spectra from the donor star and accretion disk are presented in the left two panels of Figure 7.9 (Gies et al. 2013). The right panel refers to the radial velocities measured from cross-correlating the absorption feature (MgH and Mg I b blend) of the donor star with a model template spectrum from the BT-Settl PHOENIX grid (Rajpurohit et al. 2013). The Hβ emission lines are used to measure the radial velocities of the WD/disk.

Table 7.3: Fundamental Parameters of KIC 9406652

Parameter	WD&Disk	System	Donor Star
Period (days)		0.2544	
q		0.83 ± 0.07	
$a \sin i$ ($R_\odot$)		1.54 ± 0.06	
i (deg)		≈ 50[1]	
K (km s^{-1})	153 ± 10[2]		167 ± 10[2]
$M \sin^3 i$ ($M_\odot$)	0.41 ± 0.04		0.34 ± 0.04
Mass ($M_\odot$)	≈ 0.9[1]		0.75[1]
Radius ($R_\odot$)	-		0.72[1]
$T_{\rm eff}$ (K)	$40,000 - 50,000$[1]	-	4390[1]

[1]Assuming the period and donor mass relation in Knigge et al. (2011)
[2]From absorption lines.

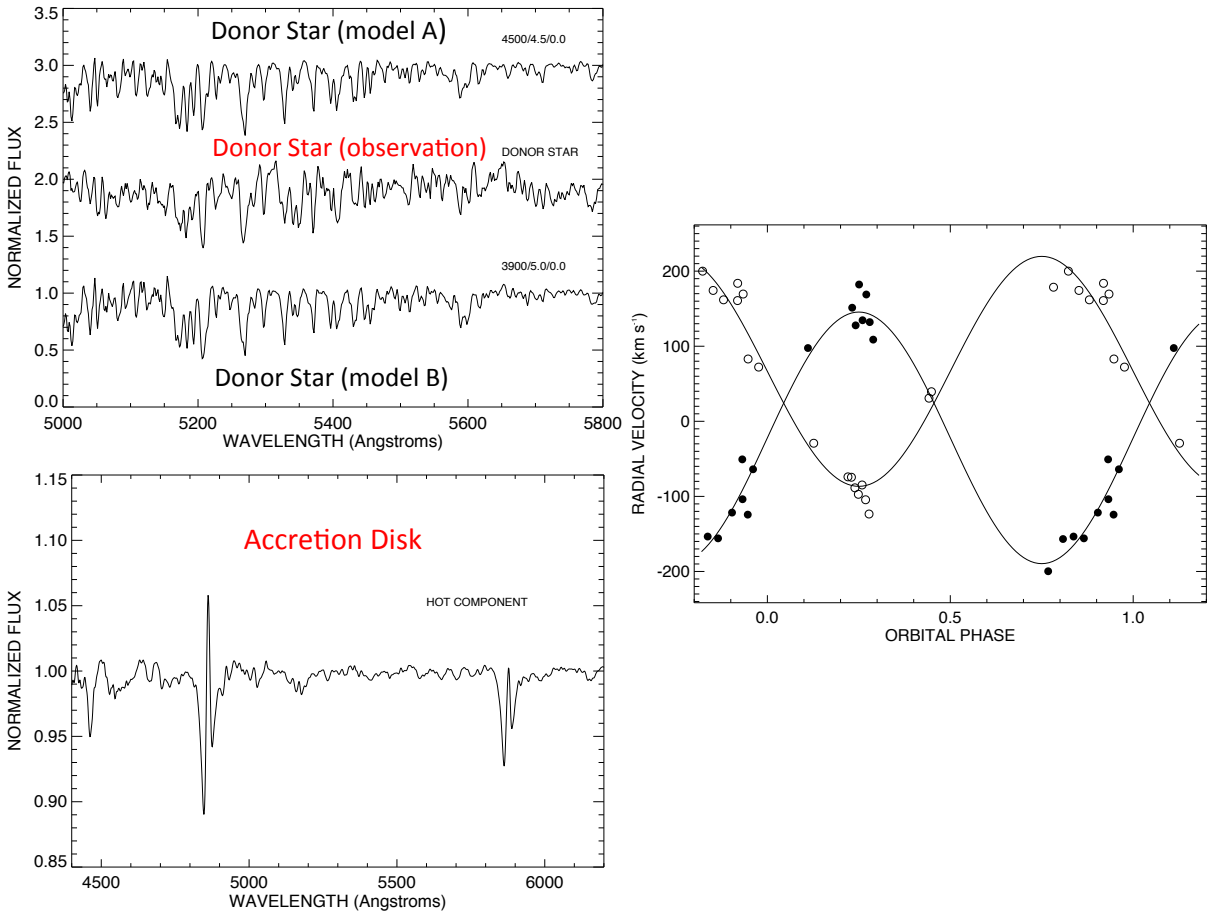

Figure 7.9 The reconstructed spectra of the donor star (upper left) and the accretion disk (lower left) of KIC 9406652. The radial velocities and best Keplerian fit are shown in the right panel. Figure is taken from Gies et al. (2013).

7.2.2 Kepler Photometry

We obtained the Presearch Data Conditioning (PDC) version of the long cadence light curve from the data archive (almost identical to the Simple Aperture Photometry version of the light curve). The entire Kepler light curve from quarters 1 through 15 is shown in the lower

panel of Figure 7.10, and Figure 7.11 contains a close up portion from quarter 7. There are both long term outbursts on timescales of weeks as well as rapid, smaller amplitude variations. The recurrence times for the outbursts vary from 27 to 84 d, and they are often (although not always) characterized by slow rise followed immediately by a sharp decline or dip. This is opposite to the fast rise and slower decline that is often observed in dwarf novae outbursts (Cannizzo et al. 2012). At peak outburst, the system is typically 0.7 mag brighter than average, while the dip minima are often 0.8 mag fainter than average. The outbursts usually have a duration of $\approx$ 7 d, although a much longer event was recorded around BJD 2455240. The fast variation (with a cycle time of about 6 h) is seen almost all the time with a full amplitude of approximately 0.2 mag (or smaller at peak outburst). The right hand panel in Figure 7.10 illustrates the periodogram for the entire Kepler light curve from quarter 1 to 15. There is a broad distribution of low frequency power that corresponds to the cyclic (but not strictly periodic) outbursts. However, there are also four significant and narrow peaks that labeled in Figure 7.10 and that have frequencies (periods) of $f_1 = 0.2421$ d^{-1} (4.131 d), $f_2 = 3.9291$ d^{-1} (6.108 h), $f_3 = 4.1714$ d^{-1} (5.753 h), and $f_4 = 7.8584$ d^{-1} (3.054 h). We also made periodograms of the light curve from each quarter separately, and the frequencies and amplitudes of the peaks nearest these mean frequencies are listed in Table 7.4 and plotted in Figure 7.12. The typical measurement uncertainties associated with the peak frequencies are 0.03 d^{-1} for quarter 1 and 0.01 d^{-1} for the subsequent quarters. We see that f_1 and f_3 grew significantly in strength up to quarter 7 while f_2 and f_4 remained approximately constant in amplitude.

In order to explore this change in the strength of the periodic signals over time, we also performed a wavelet analysis that is displayed in the central panel of Figure 7.10. We made the wavelet analysis using the package of Torrence & Compo (1998). The wavelet amplitude of a discrete time series x_n with a sampling time δt is given by a convolution of x_n with a wavelet function $\Psi((t'-t)/s)$,

$$W_n(s) = \sum_{n'=0}^{N-1} x_{n'} \Psi^* \left[\frac{(n'-n)\delta t}{s} \right] \tag{7.1}$$

where s is the wavelet scale, n is the index for the time variable, and the superscript $*$ indicates the complex conjugate. The wavelet function used here is the Morlet function defined by

$$\Psi(t/s) = \pi^{-\frac{1}{4}} \exp\left(i\omega\frac{t}{s}\right) \exp\left(-\frac{1}{2}\frac{t^2}{s^2}\right) \tag{7.2}$$

where t is the time difference and ω is a dimensionless oscillation frequency multiplier that sets the number of oscillations within the central part of the wavelet function. We adopted $\omega = 10$ which gave better frequency resolution than the default value of $\omega = 6$ in the Torrence & Compo wavelet package, but at the cost of somewhat worse temporal resolution (De Moortel et al. 2004). The wavelet scale sets the test frequency and the effective width of the time window, and a grid of scale lengths was set by the geometric series

$$s_j = s_0 2^{j\delta j}, j = 0, 1, \cdots, J.$$

We used twice the average time spacing of the Kepler long cadence data for s_0, and adopted

$\delta j = 0.25$ for a grid of values up to $J = 50$. The wavelet analysis is done in a similar way to the short-time Fourier transform (STFT) analysis, in the sense that the signal is multiplied with a wavelet function, similar to the window function in the STFT, and the transform is computed separately for different segments of the time-domain signal. The width of the window is changed as the transform is computed for every single spectral component, which is probably the most significant characteristic of the wavelet transform. Because the wavelet method is a multi-resolution analysis which was designed to overcome the resolution problem of STFT, it will give good time resolution and poor frequency resolution at high frequencies and bad time resolution and good frequency resolution at low frequencies. Furthermore, the edge effects introduced by the finite limits of the time series become progressively worse at low frequencies so that the derived wavelet power becomes unreliable within a cone of influence at the boundaries of the time series (Torrence & Compo 1998).

The wavelet power for the Kepler light curve is shown as a grayscale image in the central panel of Figure 7.10 as a function of both time and frequency. In the same way as the periodogram, most of the wavelet power occurs in the lower frequency part of the diagram, corresponding to the outbursts and dips. However, the periodic signals, f_1 to f_4, are also seen as the dark horizontal bands in the wavelet diagram. We see the same trends as documented in Figure 7.12, namely the near constancy of the signals $f_2 = 3.9291$ d^{-1} (6.108 h) and $f_4 = 7.8584$ d^{-1} (3.054 h) while the other signals $f_1 = 0.2421$ d^{-1} (4.131 d) and $f_3 = 4.1714$ d^{-1} (5.753 h) grow from near invisibility to maxima around BJD 2455400. These four frequencies are related in two ways. First, f_4 is the first harmonic of f_2 ($f_4 = 2f_2$) indicating that the f_2

signal has a non-sinusoidal shape. This is seen in Figure 7.13 (upper panel) that shows the light curve rebinned according to phase in the f_2 period. It resembles that of a low amplitude ellipsoidal binary light curve with two unequal minima. On the other hand, the shape of the f_3 signal (Fig. 7.13, lower panel) is approximately sinusoidal. The second relation is $f_1 = f_3 - f_2$. Both f_1 and f_3 share the increase in amplitude towards a maximum in quarter 7 (Fig. 7.12). We argue below that the f_2 signal is probably the orbital frequency while the f_1 signal may correspond to the precessional frequency of a tilted accretion disk.

The orbital period determined from spectroscopy is consistent with the f_2 signal from the Kepler light curve. The fact that the orbital phased light curve displays a minimum around the time of donor inferior conjunction suggests that the orbital part of the light curve variations is associated with a reflection effect, i.e., the hemisphere of the donor facing the white dwarf appears brighter. The stronger f_3 signal indicates the presence of a periodic variation that is somewhat shorter than the orbital period. Such near orbital period variations are known in many CVs through the presence of 'superhumps' in the light curve, and in some cases they appear at shorter periods.

We suggest that the precessional frequency is $f_1 = f_3 - f_2$ and that the flux variation corresponding to f_3 relates to how our view changes of the gas stream-disk interaction zone as the orbital and disk plane orientation varies.

The lower frequency signals in the periodogram of the light curve are related to the outbursts and dips that occur on a ~ 30 day timescale (Figure 7.10). These generally take the form of an outburst followed immediately by a dip. One exception was observed near

BJD 2,455,190 where a strong dip occurred before an outburst. Curiously, the next outburst that occurred near BJD 2,455,240 was also exceptional in its duration. Both of these events happened just prior to the appearance of the f_1 and f_3 signals in the periodogram (see Figure 7.10), which marks the beginning of the disk precession phase in these observations. The cause of the stunted outbursts in this system is unknown, but they may be related to cycles of changing disk mass.

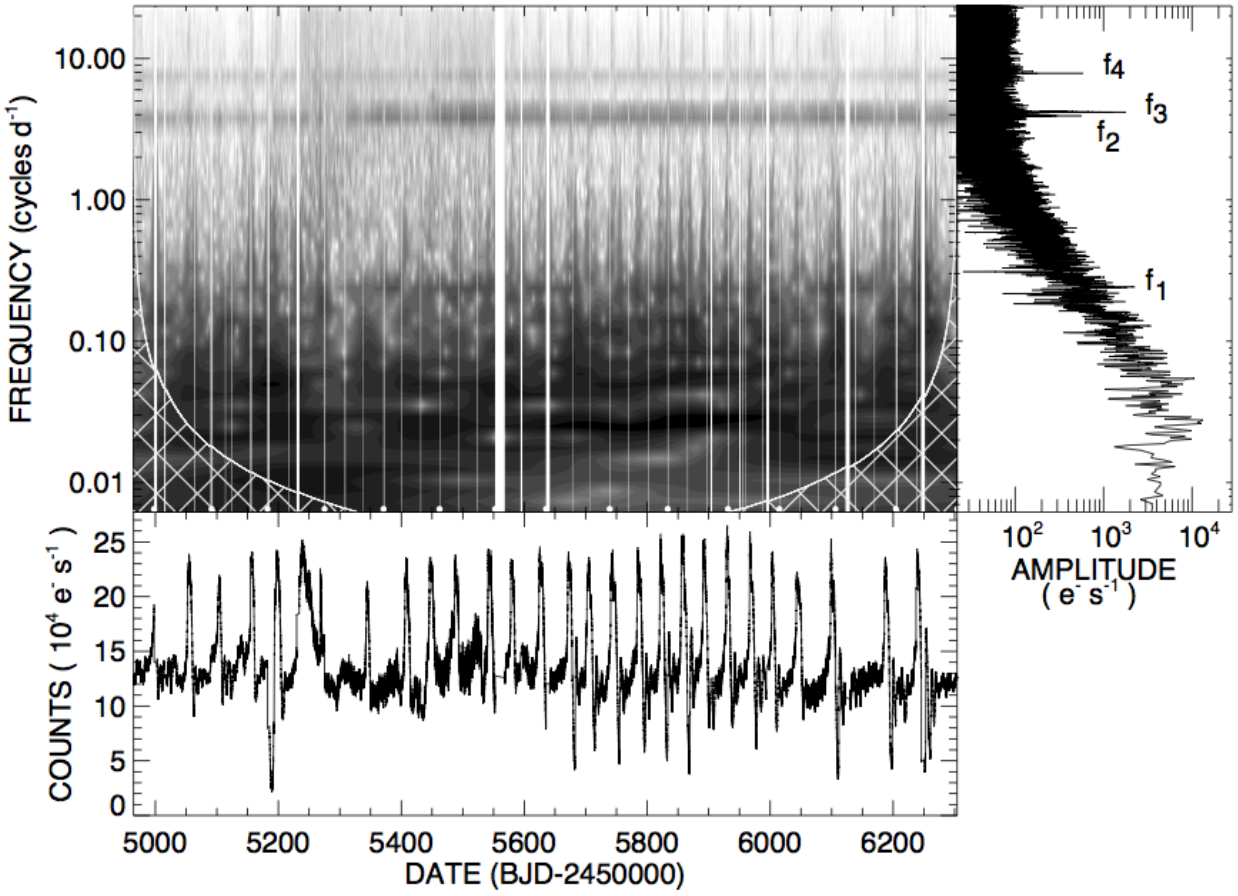

Figure 7.10 A grayscale image of the logarithm of the wavelet power as a function of time and frequency. The white dots indicate the end of each quarter (1 – 15). The panel below shows the corresponding *Kepler* light curve, and the rotated panel to the right displays the amplitude of the full sample periodogram.

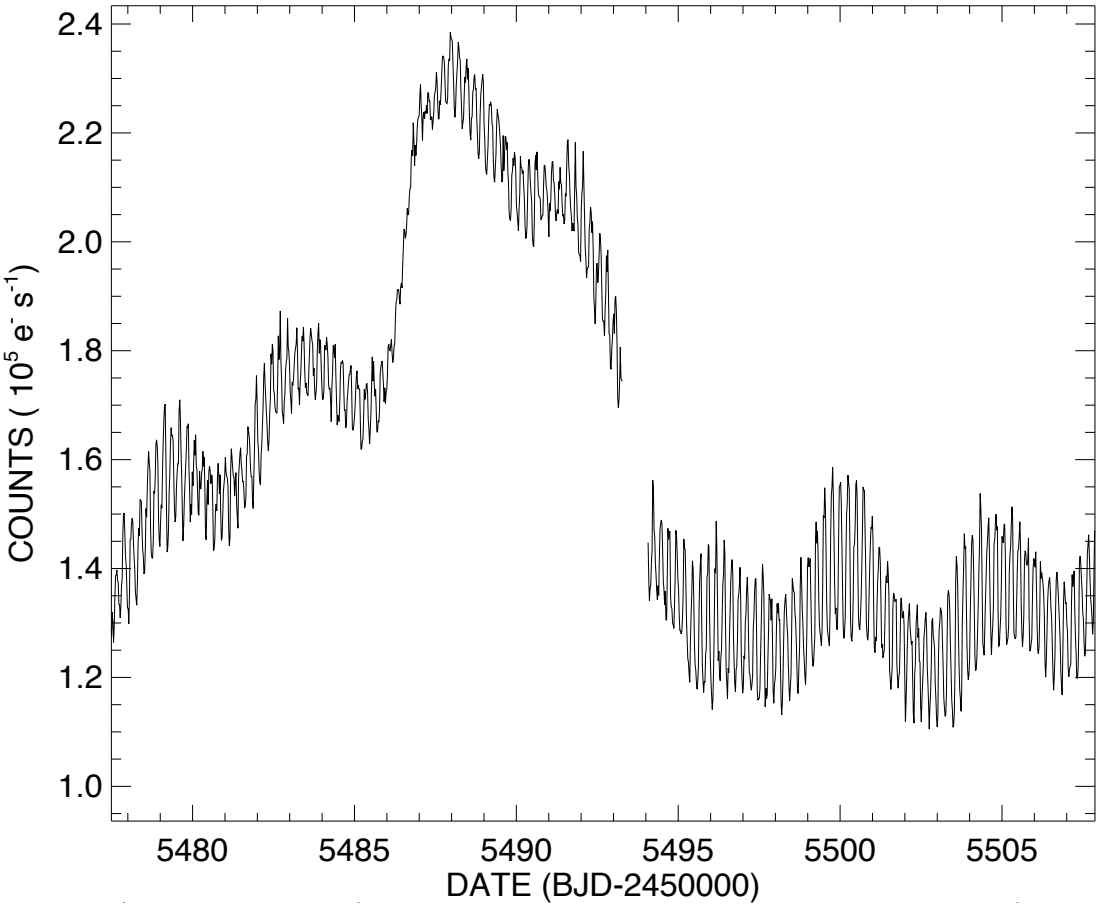

Figure 7.11 A detailed view of an outburst and rapid variations in a portion of the light curve from quarter 7.

Table 7.4: Light Curve Periodogram Results

Quarter Number	Mean Date (BJD−2,400,000)	f_1 (cycles d^{-1})	a_1 (counts)	f_2 (cycles d^{-1})	a_2 (counts)	f_3 (cycles d^{-1})	a_3 (counts)	f_4 (cycles d^{-1})	a_4 (counts)
1	54981	0.2170	643	3.9331	2172	4.1740	313	7.8571	869
2	55047	0.2421	1058	3.9360	1157	4.1949	332	7.8586	810
3	55138	0.2421	2374	3.9287	1106	4.1675	477	7.8580	842
4	55230	0.2421	3134	3.9445	1453	4.1722	530	7.8576	833
5	55324	0.2391	3046	3.9262	538	4.1674	2335	7.8595	1049
6	55417	0.2446	4008	3.9300	615	4.1737	3313	7.8586	611
7	55508	0.2406	9056	3.9289	1252	4.1707	7359	8.0973	948
8	55602	0.2424	6331	3.9304	999	4.1693	3412	7.8582	697
9	55690	0.2386	5349	3.9304	908	4.1667	3377	7.8580	828
10	55787	0.2454	6961	3.9296	1451	4.1714	3688	7.8570	607
11	55883	0.2411	4589	3.9282	1047	4.1696	3855	7.8579	706
12	55974	0.2414	7039	3.9297	995	4.1718	3005	7.8572	865
13	56061	0.2436	6766	3.9293	767	4.1717	3403	7.8556	611
14	56156	0.2509	5495	3.9269	867	4.1780	3338	7.8596	665
15	56256	0.2417	2953	3.9295	1012	4.1695	2638	7.8587	659

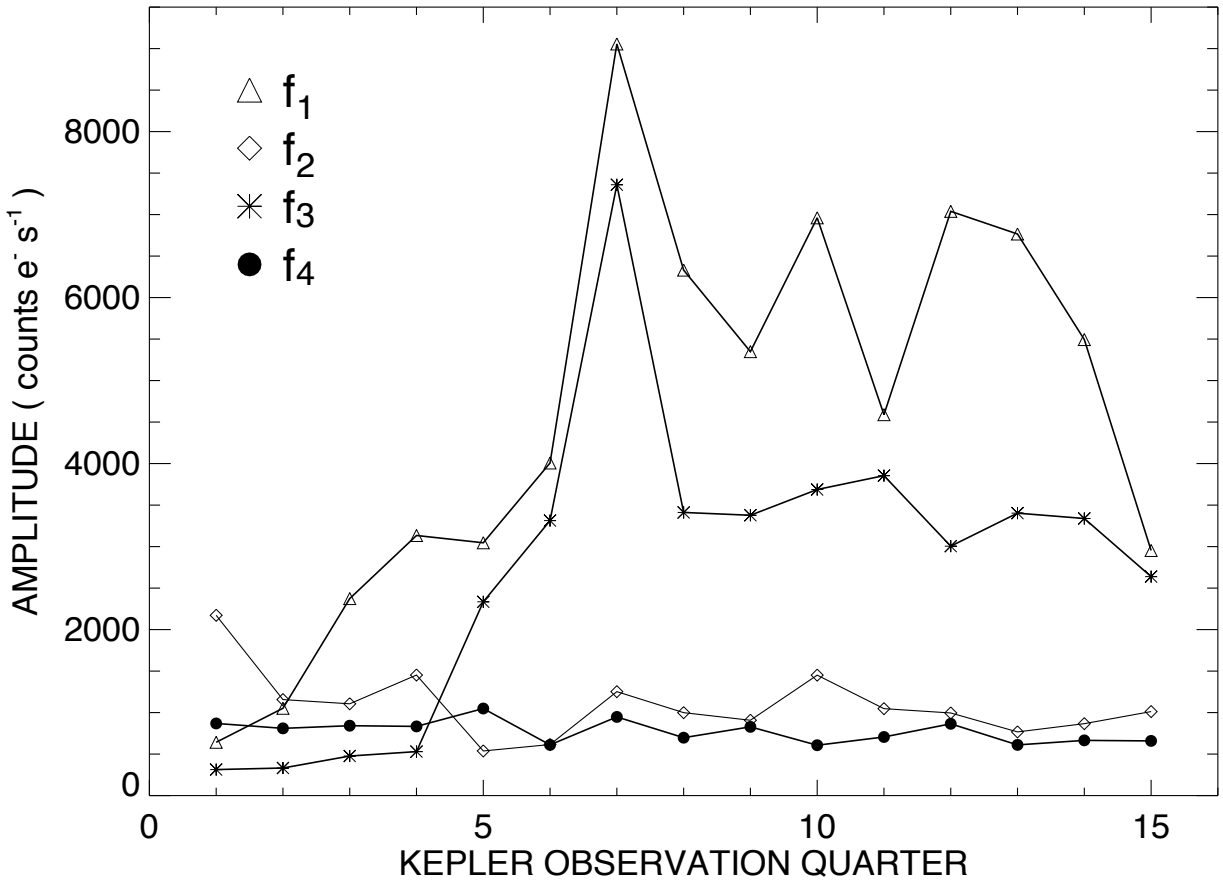

Figure 7.12 The amplitudes of one low and three high frequency signals in the periodograms of the *Kepler* light curves plotted against observing quarter number. The triangles, diamonds, asterisks, and solid circles represent the amplitudes of the f_1, f_2, f_3, and f_4 signals, respectively, that are also listed in Table 7.4.

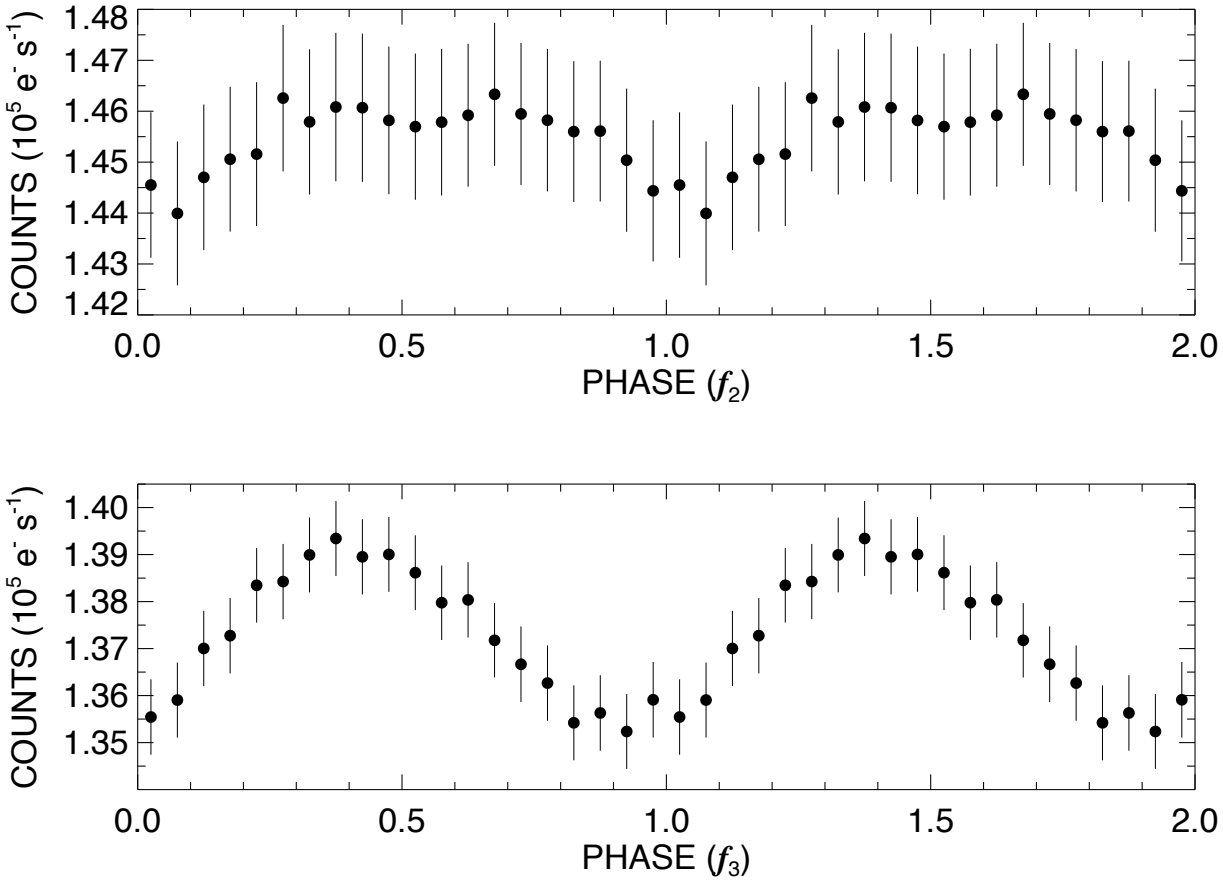

Figure 7.13 Binned light curves for the entire Q1−Q15 set for the f_2 signal (top panel) and f_3 signal (lower panel). Vertical lines indicate the standard deviation of the mean within each bin.

CHAPTER 8

Bayesian Inference with BUGS/JAGS: Applications to Binary Stars and Asteroseismology

Bayesian inference is ubiquitous in fields such as statistics and machine learning. As an attempt to bridge the gaps between astronomy and statistics, we apply the Bayesian statistical packages BUGS and JAGS to some problems in binary stars and asteroseismology, including fitting the radial velocity data, inferring atmospheric parameters from stellar spectra, etc. The problems of Bayesian experimental design and model comparison are also considered.

8.1 Introduction

A vast majority of problems in astronomy can be cast as parameter estimations. Assuming we have a vector $\boldsymbol{\theta}$ containing all parameters of a given model M, and we also have some observational data in the vector $\boldsymbol{y}$. Our goal is thus to get the posterior distribution of $\boldsymbol{\theta}$ given data: $P(\boldsymbol{\theta}|\boldsymbol{y})$, that is, the probability density of $\boldsymbol{\theta}$ given $\boldsymbol{y}$, where symbol | means 'Given'. Bayes' theorem solves this problem:

$$P(\boldsymbol{\theta}|\boldsymbol{y}, M) = P(\boldsymbol{y}|\boldsymbol{\theta}, M)P(\boldsymbol{\theta}|M)/P(\boldsymbol{y}|M). \tag{8.1}$$

Note that we explicitly show that all the probabilities are based on the assumption that model M is correct. To be more concise, we omit this default condition of 'Given model M',

$$P(\boldsymbol{\theta}|\boldsymbol{y}) = P(\boldsymbol{y}|\boldsymbol{\theta})P(\boldsymbol{\theta})/P(\boldsymbol{y}). \tag{8.2}$$

Situations of having more that one model will be discussed later in the context of Bayesian model comparison. Note that the above equation is just a direct rearrangement of the expression of the joint distribution of $\boldsymbol{\theta}$ and $\boldsymbol{y}$:

$$P(\boldsymbol{\theta}, \boldsymbol{y}) = P(\boldsymbol{\theta}|\boldsymbol{y})P(\boldsymbol{y}) = P(\boldsymbol{y}|\boldsymbol{\theta})P(\boldsymbol{\theta}). \tag{8.3}$$

$P(\boldsymbol{y}|\boldsymbol{\theta})$ is the likelihood function, usually written explicitly as a function of $\boldsymbol{\theta}$: $L(\boldsymbol{\theta})$. $P(\boldsymbol{\theta})$ is the prior distribution of $\boldsymbol{\theta}$. $P(\boldsymbol{y})$ is called Bayesian evidence or marginal likelihood, often written as Z. If the problem of parameter estimation is restricted to one model, $P(\boldsymbol{y})$ is usually ignored as it is only a normalization constant. Thus we only need to find $P(\boldsymbol{\theta}|\boldsymbol{y})P(\boldsymbol{y})$. If model comparison is needed, $Z = P(\boldsymbol{y})$ is needed and it is usually calculated in logarithmic form as $\log Z$.

We often need a point-estimate of parameter $\boldsymbol{\theta}$, and there are many different ways to summarize the result. $\boldsymbol{\theta}_{MAP}$ maximizes the posterior distribution $P(\boldsymbol{\theta}|\boldsymbol{y})$, and $\boldsymbol{\theta}_{ML}$ maximizes the likelihood $P(\boldsymbol{y}|\boldsymbol{\theta})$, and we can also use the mean $\bar{\boldsymbol{\theta}}_{mean}$ or the median $\bar{\boldsymbol{\theta}}_{median}$ of the posterior distribution.

Consider a simple curve fitting problem, and the model M can be described by a function f, with an input vector $\boldsymbol{x}$ and some model parameters $\boldsymbol{\theta}$, given by $\boldsymbol{y}_{model} = f(\boldsymbol{x}, \boldsymbol{\theta})$. $\boldsymbol{y}_{model}$ is the unknown underlying error-free model output. Assume our measurements, or data vector $\boldsymbol{y}$, are the true model outputs $\boldsymbol{y}_{model}$ added with measurement noise $\boldsymbol{e}$:

$$\boldsymbol{y} = \boldsymbol{y}_{model} + \boldsymbol{e} = f(\boldsymbol{x}, \boldsymbol{\theta}) + \boldsymbol{e}. \tag{8.4}$$

As Gaussian distribution is ubiquitously adopted, we may assume the noise $\boldsymbol{e}$ is Multivari-

ate normal distributed with a mean of zero and covariance matrix $\boldsymbol{C_e}$, $\boldsymbol{y} - \boldsymbol{y}_{model} = \boldsymbol{e} \sim N(\boldsymbol{e}|\boldsymbol{0}, \boldsymbol{C_e}) = (2\pi)^{-k/2}|\boldsymbol{C_e}|^{-1/2} e^{-\frac{1}{2}(\boldsymbol{e}-\boldsymbol{0})^T \boldsymbol{C_e}^{-1}(\boldsymbol{e}-\boldsymbol{0})}$, where $\boldsymbol{e}$ has the dimension of k. Thus the likelihood function, as a distribution of $\boldsymbol{y}$, which represents how the data are generated from the model is, $P(\boldsymbol{y}|\boldsymbol{x}, \boldsymbol{\theta}) \sim N(\boldsymbol{y}|\boldsymbol{y}_{model}, \boldsymbol{C_e}) = (2\pi)^{-\frac{k}{2}}|\boldsymbol{C_e}|^{-\frac{1}{2}} e^{-\frac{1}{2}(\boldsymbol{y}-\boldsymbol{y}_{model})^T \boldsymbol{C_e}^{-1}(\boldsymbol{y}-\boldsymbol{y}_{model})}$.

Thus the maximum likelihood solution $\boldsymbol{\theta}_{ML}$ minimizes $(\boldsymbol{y}-\boldsymbol{y}_{model})^T \boldsymbol{C_e}^{-1}(\boldsymbol{y}-\boldsymbol{y}_{model})$, and if the noise is independently distributed, $\boldsymbol{C_e}$ is then a diagonal matrix with diagonal elements σ_i^2, then $(\boldsymbol{y} - \boldsymbol{y}_{model})^T \boldsymbol{C_e}^{-1}(\boldsymbol{y} - \boldsymbol{y}_{model})$ reduces to the normal $\chi^2 = \sum_i (\frac{y_i - y_{model,i}}{\sigma_i})^2$.

The maximum posterior solution $\boldsymbol{\theta}_{MAP}$ maximizes $P(\boldsymbol{y}|\boldsymbol{\theta})P(\boldsymbol{\theta})$. If the prior distribution $P(\boldsymbol{\theta})$ is constant (e.g., the uniform distribution), then $\boldsymbol{\theta}_{MAP}$ is reduced to $\boldsymbol{\theta}_{ML}$.

8.2 Fitting Radial Velocity Curves

8.2.1 General Formulation

As an application, we fit the radial velocities of spectroscopic binaries in the aforementioned Bayesian framework. The same Keplerian problem is discussed in Gregory (2005) as well. In this specific problem, the likelihood function is

$$P(\boldsymbol{v}|\boldsymbol{t}, \boldsymbol{\theta}) \sim N(\boldsymbol{v}|\boldsymbol{v}_{model}(\boldsymbol{t}, \boldsymbol{\theta}), \boldsymbol{C_e}) \tag{8.5}$$

which can be expressed in BUGS language (Spiegelhalter et al. 1996) with the following line (if we have 20 RV data points),

$$\begin{aligned} &\#\ likelihood\ function \\ &for(i\ in\ 1:20)\{ \\ &v[i] \sim dnorm(\ modelrv[i], weight[i]\ ) \\ &\} \end{aligned} \tag{8.6}$$

where $weight[i]$ is $1/sigrv[i]^2$. Note we have assumed independent RV noise for each point. If it is necessary to consider correlated noise in RVs (a common problem in exoplanet detection from RVs), then we can specify the mean vector $modelrv[\,]$ and the covariance matrix $Cov[\ ,\ ]$ and then use a multinormal distribution:

$$v[1:20] \sim dmnorm(modelrv[], Cov[,]). \tag{8.7}$$

Cases with independent noise correspond to diagonal covariance matrices, and correlated noise will introduce off-diagonal elements.

The model RV is

$$\boldsymbol{v}_{model}(\boldsymbol{t}, \boldsymbol{\theta}) = K[\cos(\boldsymbol{\nu} + \omega) + e\cos(\omega)] + \gamma \tag{8.8}$$

where the model inputs are the HJD times $\boldsymbol{t}$, and model parameter vector is $\boldsymbol{\theta} = (T_{peri}, P, \gamma, K, e, \omega)$. The model radial velocities $\boldsymbol{v}_{model}$ are not directly related to $\boldsymbol{t}$ but directly to the true anomaly $\boldsymbol{\nu}$, and we need the following auxiliary relations for $\boldsymbol{t} \rightarrow \boldsymbol{\nu}$:

$$
\begin{aligned}
\boldsymbol{\phi} &= \frac{\boldsymbol{t} - T_{peri}}{P} \\
\boldsymbol{M} &= 2\pi\boldsymbol{\phi} \\
\boldsymbol{M} &\rightarrow \boldsymbol{E} \\
\boldsymbol{\nu} &= 2\arctan[\sqrt{\frac{1+e}{1-e}}\tan(\boldsymbol{E}/2)]
\end{aligned}
\tag{8.9}
$$

where $\boldsymbol{M}$ is mean anomaly, $\boldsymbol{E}$ is eccentric anomaly, $\boldsymbol{\phi}$ is orbital phase, and the time of periastron passage is denoted by T_{peri}. $\boldsymbol{M} \rightarrow \boldsymbol{E}$ means to get $\boldsymbol{E}$ from $\boldsymbol{M}$ by solving the Kepler equation $M = E - e\sin E$. This equation is often solved by an iterative method:

Step 1. $E_1 = M + e\sin M + [e^2\sin(2M)/2]$

Step 2. $E_0 = E_1$

Step 3. $M_0 = E_0 - e\sin E_0$

Step 4. $E_1 = E_0 + \frac{M - M_0}{1 - e\cos E_0}$

Repeat Step 2, 3, 4, until $|E_1 - E_0| < \epsilon$.

ϵ is a small criterion for convergence. We need to specify the prior distributions for the orbital parameters $P(\boldsymbol{\theta})$. For example, for uniform priors of e and ω in JAGS:

$$
\begin{aligned}
e &\sim unif(0, 1) \\
\omega &\sim unif(0, 360).
\end{aligned}
\tag{8.10}
$$

It is convenient to represent this simple parameter estimation problem by a graphical model (Figure 8.1). Nodes represent variables, and the graph structure connecting them (arrows) represents dependencies. The observed and unobserved variables are indicated by

shaded and unshaded nodes, respectively.

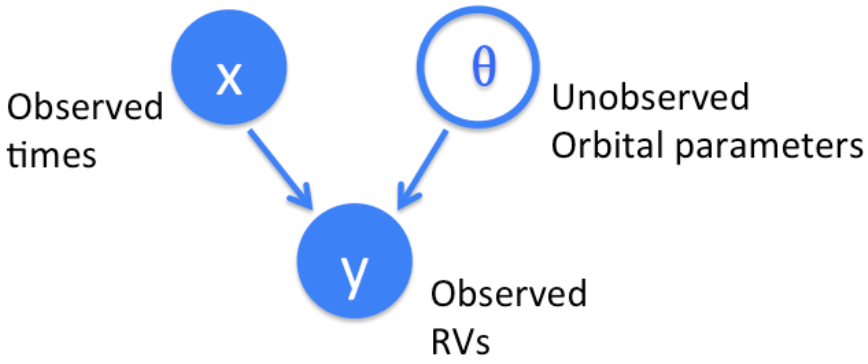

Figure 8.1 The graphical model of fitting one RV curve.

To sample from the posterior, the Markov Chain Monte Carlo (MCMC) is often performed, using the popular Metropolis-Hastings algorithm, Gibbs sampling, and their variants. We briefly summarize the two main sampling methods here. Suppose we want to sample from a probability distribution $P(\boldsymbol{\theta})$. This is often the posterior distribution $P(\boldsymbol{\theta}|\boldsymbol{y})$, but can also be any distribution. $\boldsymbol{\theta}$ is the parameter and it is a vector in p dimensions $\boldsymbol{\theta} = (\theta_1, \theta_2, \cdots, \theta_p)$. Initially, we are at $\boldsymbol{\theta}^{(0)}$ in the parameter space, and the super-script indicates the iteration number.

For the Metropolis-Hastings algorithm, we can use a Gaussian distribution centered on $\boldsymbol{\theta}^{(0)}$ with an appropriate variance to find a next proposal position $\boldsymbol{\theta}^{(1)}$. If the posterior probability is larger at $\boldsymbol{\theta}^1$, i.e., $P(\boldsymbol{\theta}^{(1)})/P(\boldsymbol{\theta}^{(0)}) > 1$, we accept the proposal step; if the posterior probability is smaller at $\boldsymbol{\theta}^{(1)}$, we do not totally reject this step but only accept this proposal step with a small probability $P(\boldsymbol{\theta}^{(1)})/P(\boldsymbol{\theta}^{(0)})$. This can be achieved by first generating a

random number $\tau \in [0, 1]$, and then accepting this proposal if $\tau < P(\boldsymbol{\theta}^{(1)})/P(\boldsymbol{\theta}^{(0)})$. The above steps are repeated to get the final Markov chain.

To use the Gibbs sampling algorithm, we assume that the conditional distributions of one $\boldsymbol{\theta}$ component i given other components $p(\theta_i|\theta_1, \theta_2, \cdots, \theta_{i-1}, \theta_{i+1}, \cdots, \theta_p)$ are given or easy to sample. We want to sample from $P(\boldsymbol{\theta}) = P(\theta_1, \theta_1, \cdots, \theta_p)$, and again we begin at $\boldsymbol{\theta}^{(0)} = (\theta_1^{(0)}, \theta_2^{(0)}, \cdots, \theta_p^{(0)})$. We can use the following iterative steps to get the next sample $\boldsymbol{\theta}^{(1)} = (\theta_1^{(1)}, \theta_2^{(1)}, \cdots, \theta_p^{(1)})$ one component by one component,

$$\begin{aligned}
\theta_1^{(1)} &\sim p(\theta_1|\theta_2^{(0)}, \cdots, \theta_p^{(0)}) \\
\theta_2^{(1)} &\sim p(\theta_2|\theta_1^{(1)}, \theta_3^{(0)} \cdots, \theta_p^{(0)}) \\
&\vdots \\
\theta_p^{(1)} &\sim p(\theta_p|\theta_1^{(1)}, \cdots, \theta_{p-1}^{(1)}).
\end{aligned} \tag{8.11}$$

Repeat the above steps, we then finally get the joint distribution $P(\theta_1, \cdots, \theta_p)$ which is just $P(\boldsymbol{\theta})$.

Some handy packages exist in the astronomical community, such as the *emcee* package in Python (Foreman-Mackey et al. 2013) and the De-MC package in IDL (Eastman et al. 2013). Here, we instead use the statistical packages JAGS (Just Another Gibbs Sampler) (Plummer 2003) and Stan (Hoffman & Gelman 2014), which are not widely used in astronomy and which implement the Gibbs sampler and Hamiltonian Monte Carlo (HMC) algorithm, respectively. The advantages of using these packages are the reduced time in coding and

easy applications of more complex hierarchical Bayesian models. The drawback is that the whole problem has to be specified in BUGS language.

A drawback in JAGS/BUGS is that nodes cannot be redefined, thus we cannot use a while loop to get E from M (the iterative method above). To overcome this problem, we need some auxiliary nodes to represent the updated M and E values in each iterative step. We have tested the iterative method above for a variety of eccentricities, and find that only a maximum of 5 iterations are needed. Note this is not a problem for Stan though, where a 'while' loop works fine as in other languages. Another advantage of Stan is that we only need several thousands of samples from the posterior due to the efficient HMC sampling algorithm, while in JAGS/BUGS we usually need tens of thousands of samples.

To use JAGS for Bayesian modeling, we need four input files:

1. *model.txt*; 2. *data.txt*; 3. *initial.txt*; 4. *script.txt*,

model.txt specifies the model (priors, likelihood, etc.) in BUGS language; *data.txt* (Figure 8.3) stores the input data and observed data in table format similar to those in R language; *initial.txt* (Figure 8.4) gives the initial values of model parameters; and finally, *script.txt* (Figure 8.5) contains the details of the Markov chain, such as how many iterations (line 17 in Fig 8.5), the number of burn-in iterations (line 8), how to thin the chains (lines $9-16$), which parameters to monitor (lines $9-16$), etc. Note that chain thinning (e.g., adopt every other points in the chain) is necessary to get independent samples since the raw samples from the Metropolis-Hastings or Gibbs algorithm are correlated.

The sampling can then be performed by the following line:

jags script.txt

The output contains the posterior chain file and the index file. Tools exist for the post analysis of these chains, e.g., the *coda* package[1] in the R language.

8.2.2 KIC 3230227: An SB2 with Good RV Phase Coverage

We apply JAGS to fit the radial velocities (RVs) of eclipsing binary KIC 3230227 (Smullen & Kobulnicky 2015). It represents an example with a good phase coverage of RVs, and in this case the model parameters have little correlation.

In Figures 8.2 to 8.5 , we show the JAGS code to fit the RVs. The result is shown in Figure 8.6, and compared with original result in Smullen & Kobulnicky (2015) in Table 8.1. The correlation plot of orbital parameters is shown in Figure 8.7, which is generated from the posterior Markov chains of JAGS. We adopt the maximum posterior estimates for the orbital parameters and their 1 σ uncertainties are derived from the $50 \pm 34\%$ percentiles.

[1]https://cran.r-project.org/web/packages/coda/index.html

```
1  model{
2  #elliptical model,fit two stars together
3  #same T0,e,  w differ by 180, diff v0 and K
4  #likelihood
5   for (i in 1:23){
6
7     rv[i]~dnorm( modelrv[i],weight[i] )
8     rv2[i]~dnorm( modelrv2[i],weight2[i] )
9
10    temp[i]<-(T[i]-T0)/per
11    inttemp[i]<-trunc(temp[i])
12    phi[i]<- temp[i]-inttemp[i]
13    M[i]<- 2.0*3.14159265359*phi[i]
14    E1[i]<-M[i]+e*sin(M[i])+e*e*sin(2.0*M[i])/2.0
15       M0a[i]<-E1[i]-e*sin(E1[i])
16    E1a[i]<-E1[i]+(M[i]-M0a[i])/(1.0-e*cos(E1[i]))
17         M0b[i]<-E1a[i]-e*sin(E1a[i])
18    E1b[i]<-E1a[i]+(M[i]-M0b[i])/(1.0-e*cos(E1a[i]))
19         M0c[i]<-E1b[i]-e*sin(E1b[i])
20    E1c[i]<-E1b[i]+(M[i]-M0c[i])/(1.0-e*cos(E1b[i]))
21
22    nu[i]<- 2.0*arctan(sqrt((1.0+e)/(1.0-e))*tan(E1c[i]/2.0))
23    modelrv[i]<- K*( cos(nu[i]+w*3.14159265359/180.)+e*cos(w*3.14159265359/180.) )+v0
24    modelrv2[i]<- K2*( cos(nu[i]+(w+180.)*3.14159265359/180.)+e*cos((w+180.)*3.14159265359/180.) )+v0
25
26    chi[i]<-(rv[i]-modelrv[i])*(rv[i]-modelrv[i])*weight[i]+(rv2[i]-modelrv2[i])*(rv2[i]-modelrv2[i])*weight2[i]
27    }
28   chi2<-sum(chi)
29
30   #prior
31   T0~dunif(-1042.71,-1040.71)
32   per~dunif(7.0,7.1)
33   e~dunif(0.3,0.8)
34   w~dunif(0,360)
35   K~dunif(20,200)
36   v0~dunif(-50,50)
37   K2~dunif(20,200)
38 }
```

Figure 8.2 The model.txt file, which contains the JAGS code used to fit the RVs of KIC 3230227.

For the orbital parameters, we assume that the primary and secondary star have the same epoch of periastron passage T_{peri}, orbital period P, eccentricity e, and systemic velocity γ (or denoted as v_0). The argument of periastron ω differs by 180°. The velocity semi-amplitude of the two stars K_1 and K_2 are assumed to range from $20 - 200$ km s^{-1}. Note the codes from line 14 to 20 are used to derive E from M, which is normally realized in a while loop.

```
#use T=t-56000.;
"T"<- c(11.6590,15.6010, 97.6850, 98.7030, 103.7920,
  107.7170,118.6710, 128.7220, 169.6730, 178.7440,
  179.6190,435.7880, 436.7110, 437.7050, 438.7160,
  439.7220,443.7160, 444.7140, 445.7090, 446.9520,
  447.6980, 467.6780, 470.7080)

"rv"<- c(-19.027, 46.931, -47.840, -83.638, -17.360,
  122.566, -48.063, 94.753, -92.616, 95.668,
   36.767, -40.507, -51.814, -84.677, 60.963,
   62.302, -100.036, -95.759, 43.633, 46.570,
   7.751, 82.977, -32.646)

"weight"<-c(0.0015889219,  0.016428129,   0.041700359, 0.032747507, 0.0097546106,
0.026716592,  0.024421694,  0.013517678,  0.025972660,0.023174025,
0.024776633,  0.027096140,  0.019333062,  0.038658704,  0.014937608,
0.030340652,  0.026115563,  0.018739567,  0.030865280,  0.024254630,
0.024784435,  0.029542862,  0.042181348)

"rv2"<- c(-16.516, -90.533, 19.696, 44.279,  -7.277,
 -146.498, 6.907, -116.552, 58.821, -97.511,
  -41.995, 25.937, 30.593, 61.699, -98.952,
  -98.713, 9.142, 52.309, -70.129, -81.418,
  -46.044, -110.124, 34.390)

weight2<-c(0.017172641, 0.027511194, 0.050362773,  0.043730139,  0.018241779,
0.038461833,  0.036461527,  0.023625004,  0.037821248,0.034989851,
0.036685345, 0.038811173, 0.030886981,  0.047965413, 0.025542752,
0.041649313, 0.037924434,  0.030224717,0.042094848, 0.036143359,
0.036657256, 0.040994156,  0.030908706)
```

Figure 8.3 The data.txt file, which contains the time of observations ($T = t - 2456000.$), the RVs of the two components (rv and $rv2$) and their weights ($1/\sigma^2_{RV}$) for KIC 3230227.

```
"T0"<--1041.20703
"per"<-7.04
"e"<- 0.5
"w"<- 290.0
"K"<-80.0
"v0"<-0.0
"K2"<-80.0
```

Figure 8.4 The initial.txt file, which contains the starting values of orbital parameters for the MCMC of KIC 3230227.

```
1 model clear
2 data clear
3 model in "model.txt"
4 data in "data.txt"
5 compile
6 inits in "initial.txt"
7 initialize
8 update 10000
9 monitor e, thin(1)
10 monitor w,thin(1)
11 monitor K, thin(1)
12 monitor v0,thin(1)
13 monitor K2, thin(1)
14 monitor T0,thin(1)
15 monitor per,thin(1)
16 monitor chi2,thin(1)
17 update 60000
18 coda *
```

Figure 8.5 The script.txt file, which specifies the needed input model (model.txt), data (data.txt), and initial values of parameters (initial.txt), as well as the details of Markov chains from the Gibbs sampler. Line 17 specifies the number of iterations, the number of burn-in iterations is in line 8, lines $9-16$ contain information on which parameters to monitor and how to thin the chains.

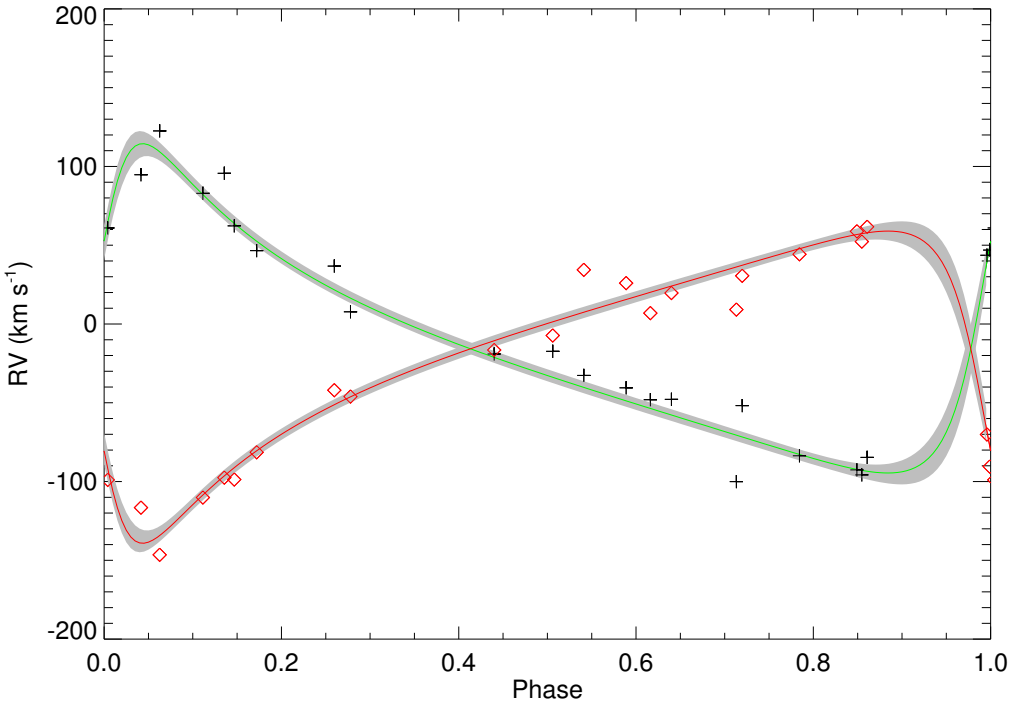

Figure 8.6 The radial velocities of KIC3230227 from Smullen & Kobulnicky (2015), with the best fit model (green and red solid lines) and the $\pm 2\sigma$ credible regions (gray shaded). Diamonds (plus signs) represent radial velocity measurements from the primary (secondary) star.

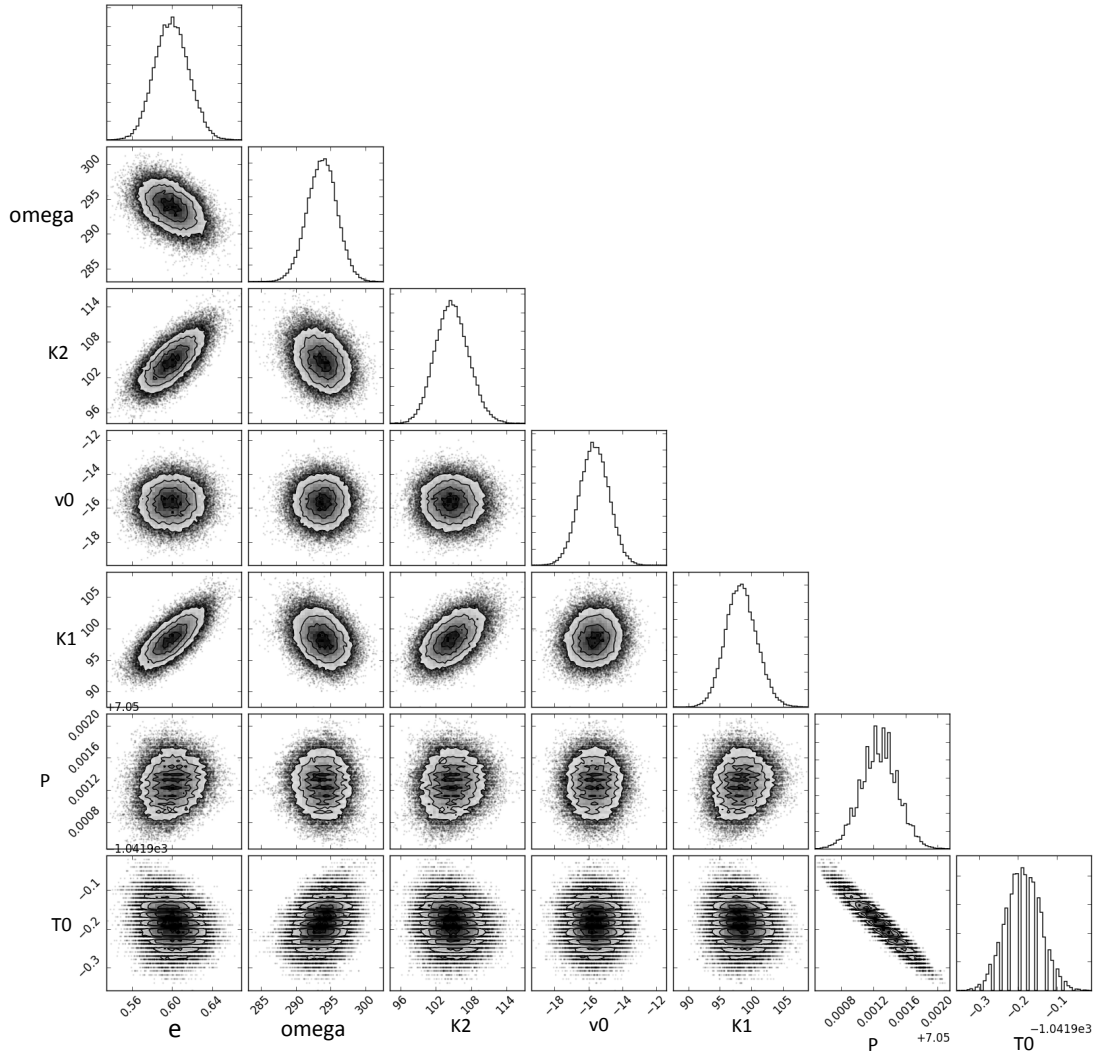

Figure 8.7 Correlation plot for the orbital parameters of KIC 3230227 from the Markov chains. The parameters on the horizontal axis (from left to right) are $e, \omega, K_2, \gamma, K_1, P$, and T_{peri}.

Table 8.1: Comparisons of Derived Orbital Elements For

KIC 3230227

Parameter	This Work	Smullen & Kobulnicky (2015)
P (days)	7.051± 0.002	7.051± 0.001
T_{peri} (HJD-2,450,000)	$4958.79^{+0.05}_{-0.04}$	6311.76 ± 0.03
e	0.60 ± 0.02	0.60 ± 0.04
ω (deg)	294 ± 2	293 ± 4
K_1 (km s^{-1})	$98.4^{+2.5}_{-2.4}$	98.5 ± 5.4
K_2 (km s^{-1})	$104.7^{+2.9}_{-2.8}$	104.9 ± 6.1
γ (km s^{-1})	-15.7 ± 0.9	−15.7 ± 1.7

8.2.3 Bayesian Experimental Design: Next Observation?

The spectroscopic follow-up of binary stars or exoplanet host stars needs a lot of telescope time. Thus it is important to optimize the observations. Given that we already have several RV data points, our question is when we shall observe for the next data point so that the parameters of interest can be mostly constrained. This is a problem of experimental design which is a common need in scientific exploration.

Following Loredo & Chernoff (2003), we consider this problem in the Bayesian framework. The likelihood function is :

$$P(v|t,\boldsymbol{\theta}) = N(v|modelv, \sigma_v^2) \tag{8.12}$$

where the $modelv$ is

$$modelv(t,\boldsymbol{\theta}) = K[\cos(\nu+\omega) + e\cos(\omega)] + \gamma. \tag{8.13}$$

It means that given the time t and orbital parameters $\boldsymbol{\theta} = (P, T_0, e, \omega, \gamma, K)$, we can fit the observed RVs (the data v), and these data are Gaussian distributed around the predictions of $modelrv$ with standard deviation σ_v (measurement errors).

We have considered the problem of inferring the posterior orbital parameters $P(\boldsymbol{\theta}|D)$ after we have the data D in the previous section. Using the terms in machine learning, we have used the training data set $D = (\boldsymbol{v}, \boldsymbol{t})$ to infer the posterior distribution of parameters $P(\boldsymbol{\theta}|\boldsymbol{v}, \boldsymbol{t})$. Note here we use bold notation for $\boldsymbol{v}$ and $\boldsymbol{t}$ since we assume we have more than one training data point (RVs). Now for a new observation performed at t_{new}, if we know the orbital parameters exactly, the predicted RV value v_{new} is just the likelihood function again,

evaluated at the t_{new}: $P(v_{new}|t_{new}, \boldsymbol{\theta}_{fixed})$. However, we do not know the orbital parameters $\boldsymbol{\theta}$ for sure, and we only have the posterior distribution of $\boldsymbol{\theta}$. Thus the predicted RV value v_{new} at t_{new} after taking into account the uncertainties of the posterior of $\boldsymbol{\theta}$ is now called the posterior predicted probability density of v_{new}: $P(v_{new}|t_{new,}D) = P(v_{new}|t_{new}, \boldsymbol{v}, \boldsymbol{t})$. We can calculate it by marginalizing over the orbital parameters $\boldsymbol{\theta}$:

$$P(v_{new}|t_{new}, D) = P(v_{new}|t_{new}, \boldsymbol{v}, \boldsymbol{t}) = \int P(v_{new}|t_{new}, \boldsymbol{\theta}) P(\boldsymbol{\theta}|\boldsymbol{v}, \boldsymbol{t}) d\boldsymbol{\theta}. \tag{8.14}$$

Since we have the posterior samples $\boldsymbol{\theta}_i$ from $P(\boldsymbol{\theta}|\boldsymbol{v}, \boldsymbol{t})$, the above integral can be estimated by the average value of $P(v_{new}|t_{new}, \boldsymbol{\theta})$ evaluated at these samples (assume N points, with $i = 1, 2, \cdots, N$).

$$\frac{1}{N} \sum_{\theta_i} P(v_{new}|t_{new}, \boldsymbol{\theta}_i) \tag{8.15}$$

The calculation of posterior predictive distribution is very easy in JAGS. After specifying

the likelihood and priors,

$$
\begin{aligned}
&\#\ likelihood\ function \\
&for(i\ in\ 1:nrv)\{ \\
&v[i] \sim dnorm(\ modelrv[i], weight[i]\ ) \\
&modelrv[i] \leftarrow (equations\ to\ get\ modelrv\ from\ t, \theta) \\
&\} \\
&\#\ priors \\
&e \sim unif(0,1) \\
&...\ (priors\ for\ other\ orbital\ parameters)
\end{aligned}
\tag{8.16}
$$

We just add two more lines of code (specifying the likelihood function again but for t_{new}):

$$
\begin{aligned}
&v_{new}[i] \sim dnorm(\ modelrv_{new}[i], weight_{new}[i]\ ) \\
&modelrv_{new}[i] \leftarrow (equations\ to\ get\ modelrv_{new}\ from\ t_{new}\ and\ \theta).
\end{aligned}
\tag{8.17}
$$

The question of when we should observe next can be answered by simply calculating the expected information gain for a new observation at t_{new}:

$$
EI(t_{new}) = -\int P(v_{new}|t_{new}, D) \log[P(v_{new}|t_{new}, D)]\ dv_{new} \tag{8.18}
$$

We already have samples from $P(v_{new}|t_{new}, D)$ (assuming N points in the Markov chain), so the above integral is just the expectation of $-\log[P(v_{new}|t_{new}, D)$ and it is approximately:

$$\overline{-\log[P(v_{new}|t_{new}, D)} \approx -\frac{1}{N}\sum_{v_{new}} \log[P(v_{new}|t_{new}, D)]. \tag{8.19}$$

Now we apply the above method to KOI-81. Assume we only have 4 RV points of the primary star from HST/COS as tabulated in Matson et al. (2015). We assume that the period $P = 23.8760923$d and $T_0 = 54976.07186$ (time of primary minimum) are known, and search for a circular orbital solution $e = 0$. The only tuning parameters are velocity semi-amplitude K and systemic velocity γ. We use uniform priors for these two parameters with the lower and upper boundaries $[0, 100]$ km s^{-1} and $[-20, 20]$ km s^{-1}, respectively. Figure 8.8 shows the RV curve from the inferred orbital parameters.

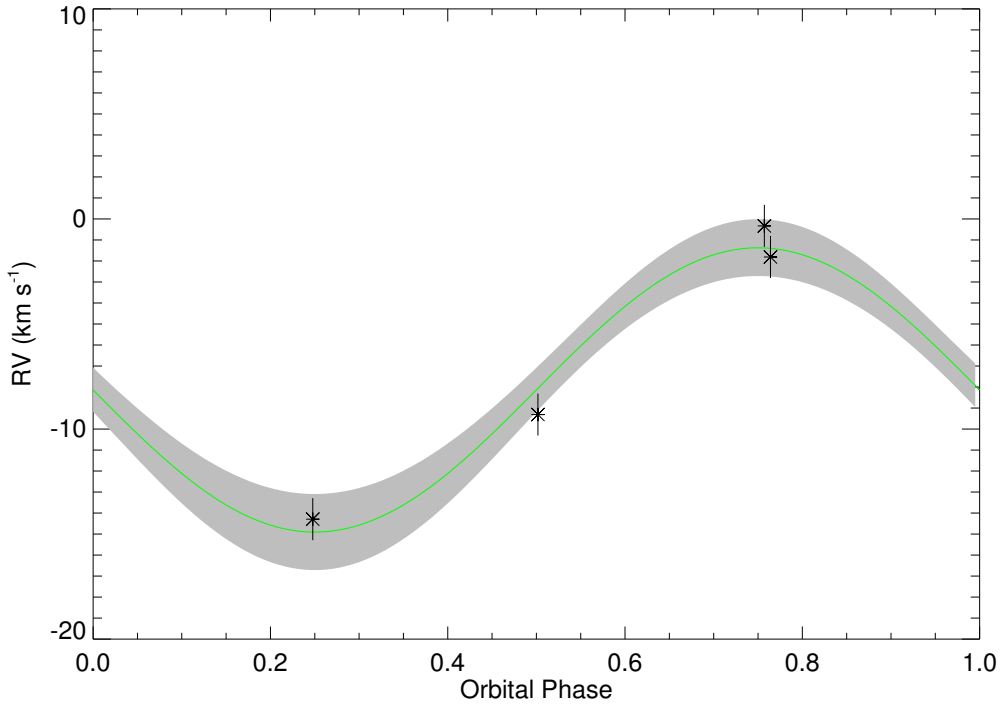

Figure 8.8 The RV data for the primary star of KOI-81 (asterisk) and the best fitting model (solid green line) with $\pm 2\sigma$ credible regions (shaded) plotted as a function of orbital phase.

We then calculate the post-predictive distribution of RVs and the corresponding expected information gain for a series of 24 new observation times (in days, since $P_{orb} \sim 24$ d). The result is shown in the following folded phase plot (Fig. 8.9). A new observation at $\phi \sim 0.2-0.3$ will bring maximum information in terms of constraining the orbital parameters K and γ.

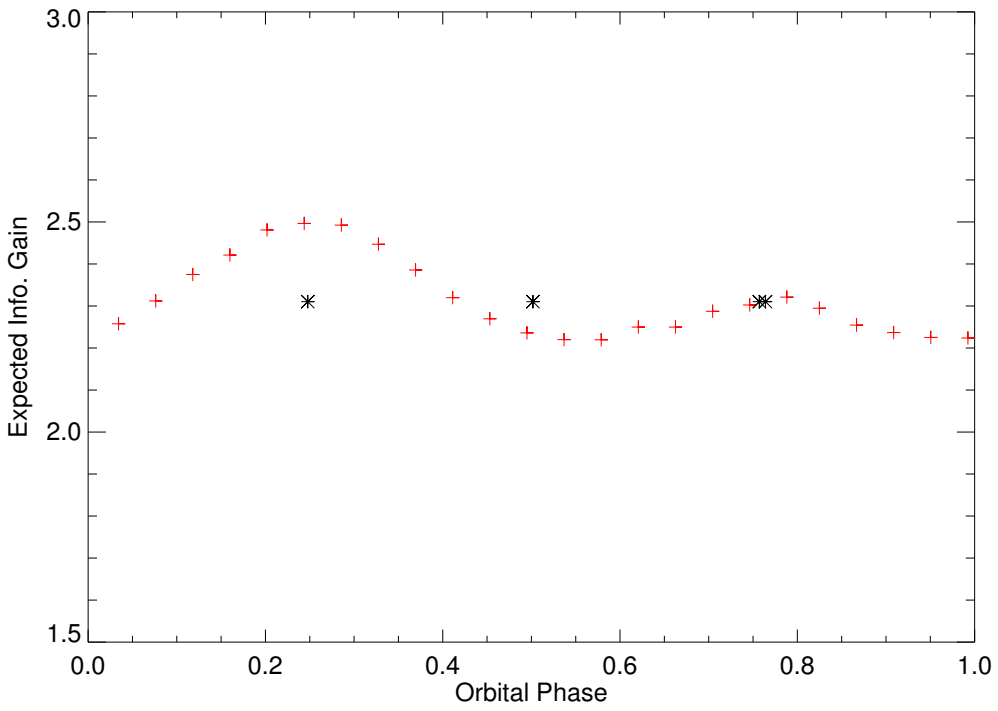

Figure 8.9 The expected information gain for 24 new observations in the phase diagram (red crosses). The asterisks indicate the RV phases of existing data. The best time to observe for the next RV point is at about $\phi = 0.2 - 0.3$, when the information gain is maximized.

As an example for eccentric systems, we also fit the RVs of the primary star in KIC3230227 as described in the last section. We optimize the six orbital parameters $P, T_{peri}, e, \omega, K, \gamma$. Their priors are all uniform distributions. Similarly, we calculated the corresponding expected information gain for the new observations. As can be seen in the following Figure 8.10, phases close to periastron passage $\phi = 1.0$ are optimal.

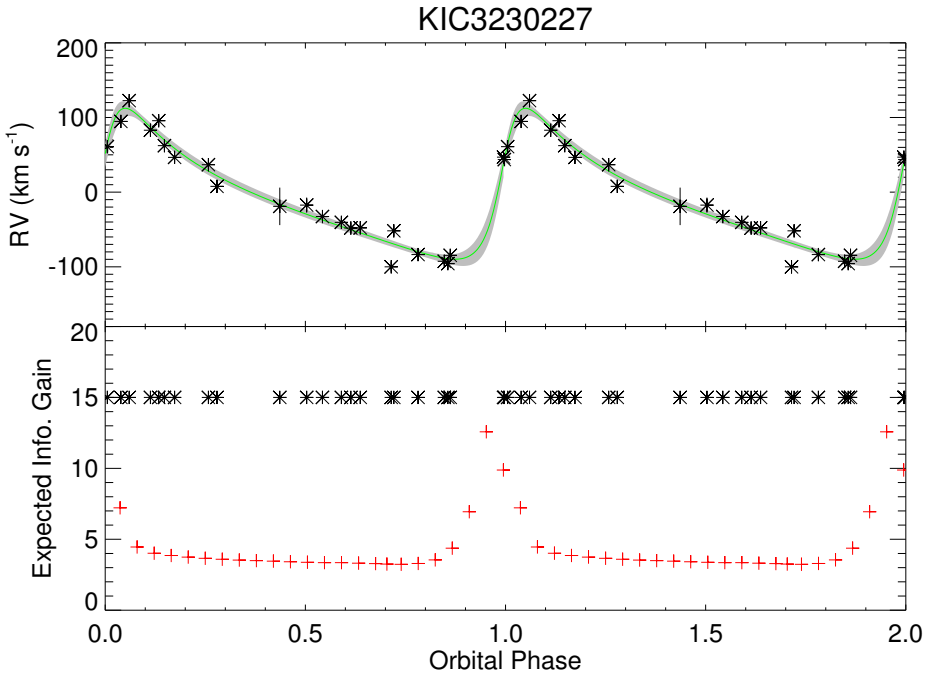

Figure 8.10 The upper panel shows the RVs of the primary star of KIC 3230227 and the best model with $\pm 2\sigma$ credible regions. The lower panel presents the expected information gain for a series of new observations in the phase diagram (red crosses). The asterisks indicate the RV phases of existing data. The best time to observe for the next RV point is at about $\phi = 0.95$, when the information gain is maximized.

Note that the information gain will be different if we want to constrain different orbital parameters. Although we can sometimes determine the next observing phase from experience (e.g., to constrain K we may need more quadrature phase observations; to constrain e we may want more measurements near periastron), it is not always clear from experience which phase to observe next. The advantage of this Bayesian experimental design is that it can

determine the best observing time quantitatively by taking into account the existing data and orbital parameters of interest. The calculation can also be updated on-the-fly once new RVs are obtained.

There are already a few studies on experimental design in literature (e.g., Ford 2008; Baluev 2008). The practical application of these methods is more complicated as more factors like instrument issues, weather, and observing availability, etc. have to be considered. As the telescope time of spectroscopic follow-up is quite expensive, it is still very worthwhile to develop and promote these techniques. It is also straightforward to extend these methods to other types of observations such as photometry, interferometry, etc.

8.3 Two More Applications

To show the potential of JAGS/BUGS and Stan, we apply them to two more problems in spectroscopic analysis and asteroseismology.

8.3.1 Fitting Stellar Spectra

To infer the atmospheric parameters of stars, it is routine to fit the observed spectra with synthetic model spectra. The model spectra are usually interpolated from large grids covering different values of $T_{\rm eff}$, $\log g$ and [M/H]. The stellar spectra are more sensitive to effective temperature, and less sensitive to surface gravity and metallicity. There are known correlations between these three parameters, and local optimizers like MPFIT or amoeba often encounter difficulty in finding the global minimum. It is more advisable to use global minimizers, for example, we have shown the results of using the genetic algorithm in Chapter

5. In this section, we will apply JAGS to the problem of inferring the $T_{\rm eff}$ and $\log g$ of stars from their spectra.

Similar to the previous section, we need to specify our likelihood function in BUGS. The likelihood function in this case does not have analytical expressions, and we can use the *interp.lin* function in JAGS to get the model spectra from grids.

As a simple example, we only consider two atmosphere parameters $T_{\rm eff}$ and $\log g$ here. It is straightforward to extend it to cases with more parameters like metallicity. We generated five grids of spectra and each grid contains 100 rows and 10 columns. Each column is the spectrum of 100 pixels, corresponding to 10 different effective temperatures stored in the array 'teffarr'. The five different grids correspond to the $\log g$ values stored in the variable $loggarr = (3.0, 3.5, 4.0, 4.5, 5.0)$. If we want to create a model spectrum with effective temperature $T_{\rm eff}$ and $\log g$, we can use this following lines to interpolate and get the spectrum value at pixel i:

$$\begin{aligned}
&modely_logg[i,1] \leftarrow interp.lin(T_{\rm eff}, \text{teffarr}, \text{grids30[i, 1 : 10]})\\
&modely_logg[i,2] \leftarrow interp.lin(T_{\rm eff}, \text{teffarr}, \text{grids35[i, 1 : 10]})\\
&modely_logg[i,3] \leftarrow interp.lin(T_{\rm eff}, \text{teffarr}, \text{grids40[i, 1 : 10]})\\
&modely_logg[i,4] \leftarrow interp.lin(T_{\rm eff}, \text{teffarr}, \text{grids45[i, 1 : 10]})\\
&modely_logg[i,5] \leftarrow interp.lin(T_{\rm eff}, \text{teffarr}, \text{grids50[i, 1 : 10]})\\
&modely[i] \leftarrow interp.lin(\log g, loggarr, modely_logg[i, 1 : 5]).
\end{aligned} \tag{8.20}$$

The whole model is specified over a wavelength grid enumerated by i :

$$
\begin{aligned}
&model\{ \\
&for(i\ in\ 1:100)\{ \\
&yobs[i] \sim dnorm(\ modely[i], weight[i]\ ) \\
&modely\_logg[i,1] \leftarrow interp.lin(T_{\rm eff}, \text{teffarr}, \text{grids30[i, 1 : 10]}) \\
&modely\_logg[i,2] \leftarrow interp.lin(T_{\rm eff}, \text{teffarr}, \text{grids35[i, 1 : 10]}) \\
&modely\_logg[i,3] \leftarrow interp.lin(T_{\rm eff}, \text{teffarr}, \text{grids40[i, 1 : 10]}) \\
&modely\_logg[i,4] \leftarrow interp.lin(T_{\rm eff}, \text{teffarr}, \text{grids45[i, 1 : 10]}) \\
&modely\_logg[i,5] \leftarrow interp.lin(T_{\rm eff}, \text{teffarr}, \text{grids50[i, 1 : 10]}) \\
&modely[i] \leftarrow interp.lin(logg, loggarr, modely\_logg[i, 1:5]) \\
&chi2[i] \leftarrow (yobs[i] - modely[i]) * (yobs[i] - modely[i]) * weight[i] \\
&\} \\
&chi2all \leftarrow sum(chi2) \\
&\\
&\#priors \\
&T_{\rm eff} \sim dunif(\ 5000.0,\ 9500.0\ ) \\
&\log g \sim dunif(\ 3.0,\ 5.0\ ) \\
&\}
\end{aligned}
\tag{8.21}
$$

Note we have assumed that the observed spectrum *yobs* is normal distributed with the

mean *modely* and variance $1/weight = 0.1^2$. We used a uniform prior distribution for $T_{\rm eff}$ and $\log g$.

We also need to specify the initial values:

$$\begin{aligned} T_{\rm eff} &\leftarrow 6000.0 \\ \log g &\leftarrow 4.2 \end{aligned} \tag{8.22}$$

and the data:

```
 teffarr <- c(5000.0,5500.0,6000.0,6500.0,7000.0,7500.0,
8000.0,8500.0,9000.0,9500.0)
loggarr<- c(3.0,3.5,4.0,4.5,5.0)
 grids30 <- structure(
 c(     0.59723,
         0.53844,
            ...
         0.93176,    0.92807),.Dim=c(100,10) )
 similarly for grids35, grids40, grids45, grids50
 # observed spectrum
yobs<- c(
  0.89360,
  ...
```

```
 0.73186)
# weight=1/sigma_{yobs}^2=1/0.1^2
weight<- c(
 100.0
 ...
 100.0)
```

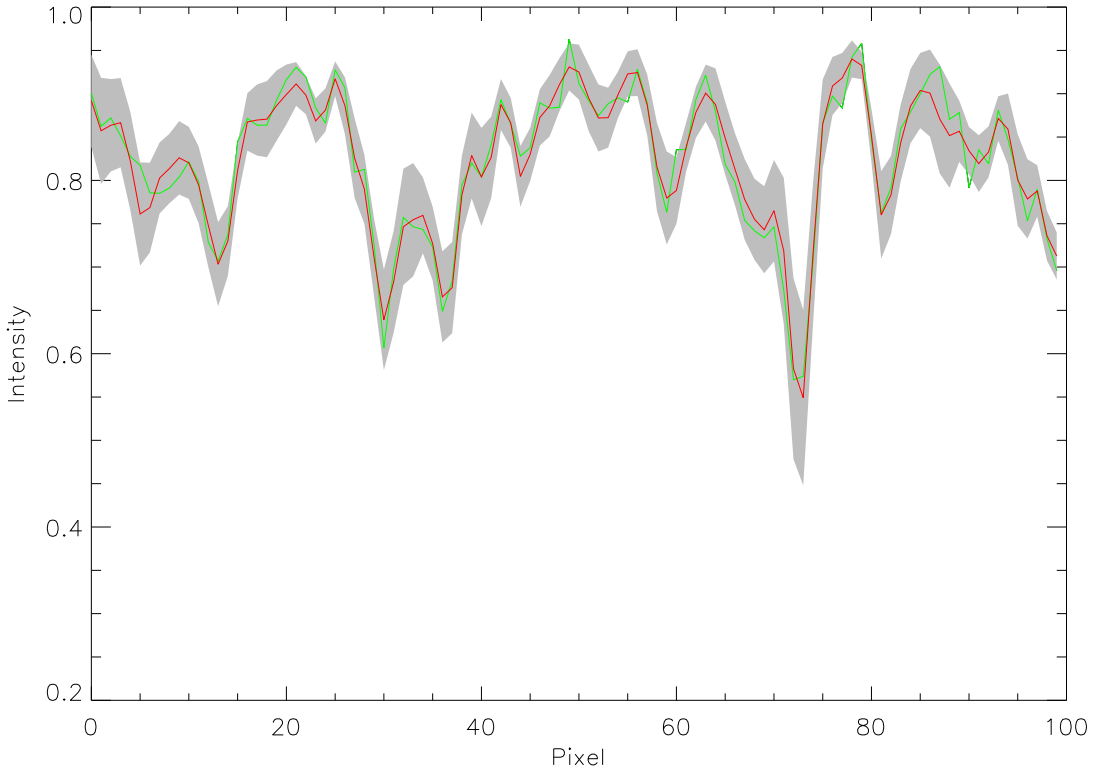

Figure 8.11 The best-fit spectrum (red solid) with parameters $[T_{\rm eff}, \log g, \log z, v \sin i]$ =[6833 K, 3.87, 0.0, 20.0 km s^{-1}] and its $\pm 2\sigma$ credible regions (gray shaded). The simulated observed spectrum $[T_{\rm eff}, \log g, \log z, v \sin i]$ =[6805 K, 4.0, 0.0, 20.0 km s^{-1}] is indicated as the green solid line. The wavelength range is from 4020.06Å to 4055.19Å.

The simulated observed spectrum shown in Figure 8.11 covers the wavelength range from 4020.06Å to 4055.19Å. It is from the UVBLUE library with a random Gaussian noise added. The resulting best model is also shown in Figure 8.11. The posterior distributions of $T_{\rm eff}$ and $\log g$ are shown in the Figure 8.12 with 80000 samples. The true value of $T_{\rm eff}$ is 6805 K and the inferred value is 6833^{+100}_{-95}K. The $\log g$ value is not very well constrained partially

because we only chose a very narrow spectral range of 100 pixels in which features are relatively insensitive to pressure. We can distinguish high $\log g$ values (> 4.4), and all low $\log g$ values fit the spectrum equally well. The true $\log g$ is 4.0, and the inferred $\log g$ is $3.87^{+0.6}_{-0.6}$.

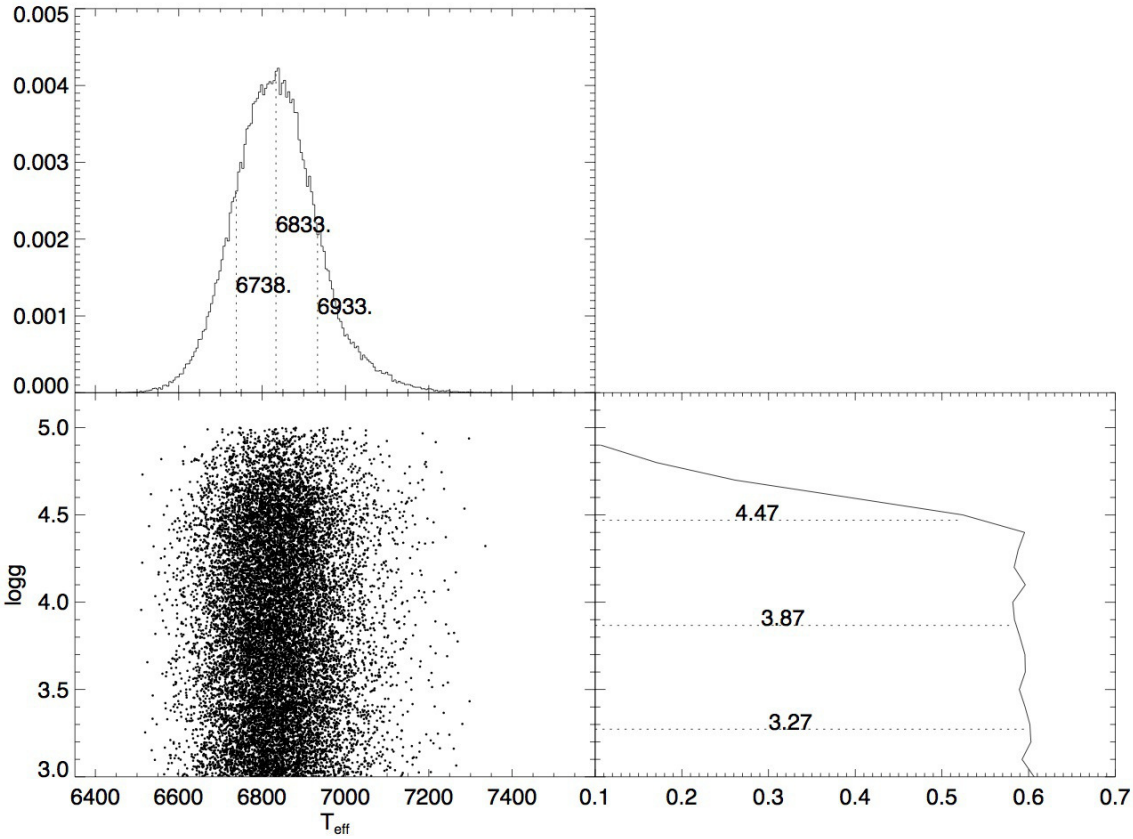

Figure 8.12 The posteriors of $T_{\rm eff}$ and $\log g$.

8.3.2 Fitting the Noise Background in the Power Spectrum Density of Solar-like Oscillators

The *Kepler* satellite observed hundreds of main sequence solar-like oscillators and tens of thousands of solar-like oscillating red giants. As a routine to analyze their oscillation spectrum, we need to fit their noise background and their Lorentzian profiles of oscillation frequencies.

The noise background in the power spectral density is generally modeled with the following equation:

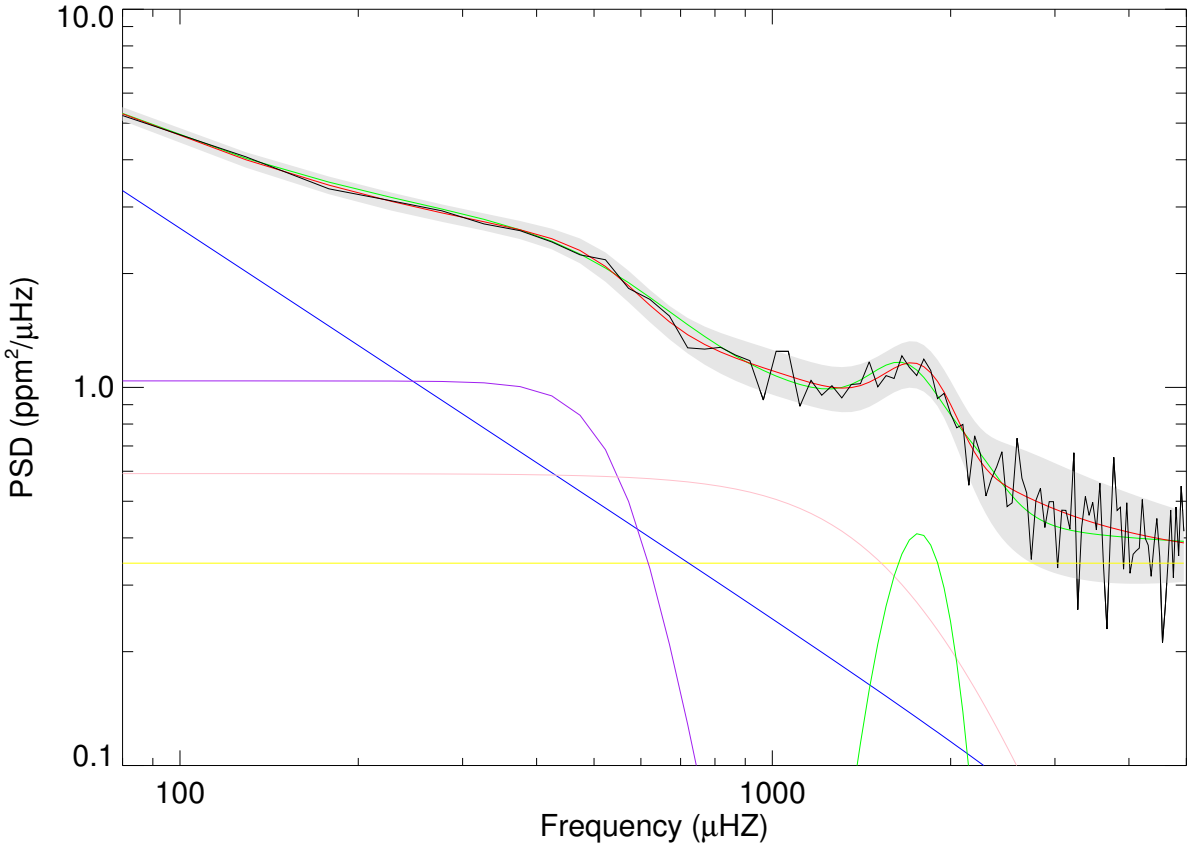

Figure 8.13 The power spectral density of a simulated solar-like oscillator, with parameters that resemble KIC 9139163 (Corsaro & De Ridder 2014). The observed PSD with noise is indicated by the black solid line. The green line is the real model without noise. The best fit model from MCMC is represented by the red solid line with the 2σ credible regions shaded. The lines in color indicate the four components (see text).

$$P(\nu, \boldsymbol{\theta}) = W + \left[\mathrm{sinc}^2\left(\frac{\pi\nu}{2\nu_{nq}}\right)\right] \times \left(a\nu^{-b} + \frac{4\tau_1\sigma_1^2}{1+(2\pi\nu\tau_1)^{c_1}} + \frac{4\tau_2\sigma_2^2}{1+(2\pi\nu\tau_2)^{c_2}} + H_{osc}\exp(-\frac{\nu-\nu_{max}}{2\sigma_{env}^2})\right). \tag{8.23}$$

The components in the equation are shown in Figure 8.13. W (yellow line) is the constant noise level. $a\nu^{-b}$ is the blue line, which represents the power law that represents slow variations caused by stellar activity. Purple and pink lines are the two Harvey-like Lorentzian profiles $\frac{4\tau_1\sigma_1^2}{1+(2\pi\nu\tau_1)^{c_1}} + \frac{4\tau_2\sigma_2^2}{1+(2\pi\nu\tau_2)^{c_2}}$; τ_1, τ_2 are the characteristic timescales; σ_1, σ_2 are the amplitudes of the signature; and c_1, c_2 are the corresponding exponents related to the decay time of the physical process involved.The Gaussian component $H_{osc}\exp(-\frac{\nu-\nu_{max}}{2\sigma_{env}^2})$ is the power excess caused by solar-like oscillations with H_{osc} as the amplitude of the oscillation envelope, and ν_{max} and σ_{env} as the corresponding frequency of maximum power and width, respectively. The $\mathrm{sinc}^2\left(\frac{\pi\nu}{2\nu_{nq}}\right)$ term, which multiplies each term except for the constant noise is the response function of the sampling rate of observed time series. The Nyquist frequency ν_{nq} of *Kepler* short cadence data is 8496.36 μHZ.

We optimize 12 parameters $\boldsymbol{\theta} = (W, a, b, \tau_1, \sigma_1, \tau_2, \sigma_2, H_{osc}, \nu_{max}, \sigma_{env})$. Following Corsaro & De Ridder (2014). we use uniform priors for these parameters except for a. A uniform prior in logarithm which is called a Jeffreys prior, $1/a$ is used in Corsaro & De Ridder (2014). We instead use a similar non-informative prior Gamma(ϵ, ϵ), and this distribution is essentially the same as Jeffreys prior when ϵ is very small. We set ϵ as 0.01.

The Bayesian inference result is shown in Figure 8.13. JAGS recovered the actual values of parameters with reasonable uncertainty estimates. The JAGS code is shown in the following.

This application of JAGS is inspired by the online notes[2] by Andres García Saravia Ortíz de Montellano at Max Planck Institute for Solar System Research. I am inclined to apply JAGS to more asteroseismic problems, for example, fitting the individual frequency profile

[2]https://research-engine.appspot.com/45001

in the power density spectrum of solar-like oscillators.

```
 model{
 pi <- 3.14159265358979
 nuNyq<- 8496.36


#likelihood
for (i  in  1:100){
 # loop over frequency index
 psd[i] ~ dnorm(  modelpsd[i],weight[i] )
 modelpsd[i] <- W
+(   sin(pi*nu[i]/(2*nuNyq))/(pi*nu[i]/(2*nuNyq)) )^2
*(  ( a*(nu[i])^(-b) )
+4.0*tau1*sig1^2 / (1.0+ (2.0* pi * nu[i]* tau1)^{c1})
+4.0*tau2*sig2^2 / (1.0+ (2.0* pi * nu[i]* tau2)^{c2})
+H_osc * exp(-(nu[i]- numax)^2/(2 * sig_env^2))  )


 chi2[i]<-(power[i]-modelpsd[i] )^2*weight[i]
 }


 chi2all <- sum(chi2)
```

```
 # priors
 W ~ dunif(0.01,1.0)
 a ~ dgamma(0.01,0.01)
 b ~ dunif(0.1,10)
 H_osc ~ dunif(0.01,1.0)
numax ~ dunif(1000.0,3000.0)
sig_env ~ dunif(50.0,400.0)


tau1~ dunif( 0.00001,0.001)
sig1~ dunif(1.0,100.0)
c1 ~ dunif(1.0,15.0)


tau2 ~ dunif( 0.00001,0.001)
sig2 ~ dunif(1.0,100.0)
c2 ~ dunif(1.0,20.0)
 }
```

8.4 Bayesian Model Comparison

We often encounter model comparison problems in binary star studies. For example, in fitting the radial velocities of binary stars, we may want to determine whether the orbit is significantly eccentric; in analyzing double-lined spectra, we may need to know if the

spectrum has one or two components. Traditionally, these questions are answered by some frequentist testing. Bayesian statistics provide a nature solution to these problems of model comparison.

8.4.1 Bayesian Evidence From Tempered Posteriors

The posterior samples from the MCMC can be used to infer the optimal parameters and uncertainties, but generally cannot be used to calculate Bayesian evidence $P(\boldsymbol{y})$ for model comparison. There is a simple way to calculate marginal likelihood called thermal dynamic integration (Gelman & Meng 1998). This method needs to do MCMC for a series of different tempered posteriors.

Let's apply this method to the problem of fitting a RV curve. Assume each RV datum point y_i is normal distributed with the mean rv_{model} and standard deviation σ_{rv}, so the likelihood function is $L(\boldsymbol{\theta}) = P(y_i|\boldsymbol{\theta}) = N(rv|rv_{model}, \sigma_{rv}^2)$, and in natural logarithm:

$$\begin{aligned} &\ln N(rv|rv_{model}, \sigma_{rv}^2) \\ &= (-\frac{1}{2}) \log(2\pi\sigma^2) - \frac{1}{2}\frac{(rv - rv_{model})^2}{\sigma_{rv}^2} \\ &= (-1) \log(\sqrt{2\pi}\sigma) - \frac{1}{2}\frac{(rv - rv_{model})^2}{\sigma_{rv}^2}. \end{aligned} \tag{8.24}$$

We assume uniform priors for the fitting parameters $\boldsymbol{\theta} = (e, \omega, K, v_0)$, so the posterior is $P(\boldsymbol{\theta}|y_i) \propto P(y_i|\boldsymbol{\theta})P(\boldsymbol{\theta}) \propto P(y_i|\boldsymbol{\theta})$. The tempered posterior is then proportional to tempered likelihood: $P(\boldsymbol{\theta}|y_i)_\beta \propto P(y_i|\boldsymbol{\theta})^\beta$, and in natural logarithm:

$$\begin{aligned}
&\ln N(rv|rv_{model}, \sigma_{rv}^2)^{\beta} \\
&= (-1)\beta \log(\sqrt{2\pi}\sigma) - \frac{1}{2}\beta \frac{(rv - rv_{model})^2}{\sigma_{rv}^2} \\
&= \text{term1} + \text{term2}
\end{aligned} \tag{8.25}$$

To calculate Bayesian evidence, we need posterior samples from a series of β in the range of $0 - 1$, where 1 corresponds to the original non-tempered posterior and 0 corresponds to the prior. The normal distribution $x \sim N(x|\mu, \sigma)$ is easily specified in BUGS language as $x \sim dnorm(\mu, 1/\sigma^2)$. An important difference in notation is that BUGS/JAGS use the precision $1/\sigma^2$ instead of variance σ^2. We use the notation $weight = 1/\sigma^2$ here.

There is no distribution in the form of $N(x|\mu, \sigma)^{\beta}$ in BUGS/JAGS. But we can bypass this problem by using the 'Zero Trick'. The key insight is that the negative log-likelihood of a sample of 0 from $Poisson(\lambda)$ is λ (the expected number of occurrence rate),

$$P(x = k) = Poisson(x|\lambda) = \frac{\lambda^k e^{-\lambda}}{k!} \tag{8.26}$$

and when we force $x = k = 0$ to be observed,

$$P(k = 0) = \frac{\lambda^0 e^{-\lambda}}{0!} = e^{-\lambda} \tag{8.27}$$

Thus, $\ln P = -\lambda$ and if the distribution λ can be expressed in BUGS language, then we

can get samples from λ with the following lines:

$$\begin{aligned} C &\leftarrow 1000 \\ \lambda &\leftarrow -(term1 + term2) + C \\ zeros &\leftarrow 0 \\ zeros &\sim dpois(\lambda) \end{aligned} \tag{8.28}$$

where C is an arbitrary constant which forces λ to be positive. So, by setting $\log \lambda$ appropriately, and forcing 0 to be observed, sampling effectively proceeds from the distribution defined by λ (Lee & Wagenmakers 2014).

Figure 8.14, 8.15, and 8.16 show the JAGS code to fit simulated RV data (20 data points), and we have used 60 different β values. After we get 60 different posterior samples, we evaluate the original non-tempered likelihood $\ln L(\boldsymbol{\theta})$ (the *realloglike* variable in the code) with these tempered samples and calculate the mean value for each (we denote it as $< \ln L(\boldsymbol{\theta}) >_\beta$). Then finally (Gregory 2010), the Bayesian evidence can be calculated from these mean values and the beta values by this integral:

$$\ln Z = \int_0^1 < \ln L(\boldsymbol{\theta}) >_\beta \, d\beta. \tag{8.29}$$

Figure 8.17 shows this integral for the aforementioned example. Below is the BUGS/JAGS code for the Keplerian problem using the tempered posteriors (compare with Figure 8.2 earlier in this chapter).

```
model{
  C<-1000
#likelihood
for(j in 1:60){
        for (i in 1:20){
        #ecc orbit RV equation
        term1[i,j]<- -1.0*beta[j]*log(sigrv[i]*sqrt(2.0*3.14159))
        term2[i,j]<-beta[j]*(-0.5)/sigrv[i]/sigrv[i]*(rv[i]-modelrv[i,j])*(rv[i]-modelrv[i,j])
        #the likelihood without tempering,this will be used for calculating evidence
        #this will return the likelihood evaluated with the tempered posterior samples
        term1_beta1[i,j]<- -1.0*log(sigrv[i]*sqrt(2.0*3.14159))
        term2_beta1[i,j]<- (-0.5)/sigrv[i]/sigrv[i]*(rv[i]-modelrv[i,j])*(rv[i]-modelrv[i,j])
        realloglike[i,j]<- term1_beta1[i,j]+term2_beta1[i,j]
        loglike[i,j]<- -(term1[i,j]+term2[i,j])+C
        zeros[i,j]~dpois(loglike[i,j])
        #rv[i]~dnorm( modelrv[i],1.0/(sigrv[i]*sigrv[i]) )
        M[i,j]<- 2.0*3.14159265359*phi[i]
        E1[i,j]<-M[i,j]+e[j]*sin(M[i,j])+e[j]*e[j]*sin(2.0*M[i,j])/2.0
                M0a[i,j]<-E1[i,j]-e[j]*sin(E1[i,j])
        E1a[i,j]<-E1[i,j]+(M[i,j]-M0a[i,j])/(1.0-e[j]*cos(E1[i,j]))
                M0b[i,j]<-E1a[i,j]-e[j]*sin(E1a[i,j])
        E1b[i,j]<-E1a[i,j]+(M[i,j]-M0b[i,j])/(1.0-e[j]*cos(E1a[i,j]))
                M0c[i,j]<-E1b[i,j]-e[j]*sin(E1b[i,j])
        E1c[i,j]<-E1b[i,j]+(M[i,j]-M0c[i,j])/(1.0-e[j]*cos(E1b[i,j]))
         nu[i,j]<- 2.0*arctan(sqrt((1.0+e[j])/(1.0-e[j]))*tan(E1c[i,j]/2.0))
        modelrv[i,j]<- K[j]*( cos(nu[i,j]+w[j]*3.14159265359/180.)+e[j]*cos(w[j]*3.14159265359/180.) )+v0[j]
        }
 }
        for(j in 1:60){
                loglike2[j]<-sum(realloglike[,j])
                #prior
                e[j]~dunif(0,1)
                w[j]~dunif(0,360)
                K[j]~dunif(0,100)
                v0[j]~dunif(-50,50)  }
}
```

Figure 8.14 The model.txt file which contains the JAGS code for Bayesian evidence calculation with samples from tempered posteriors.

```
"beta"<- c(     1.00000,    0.833333 ,   0.694444,    0.578704,  0.482253,
0.401877,    0.334898,    0.279082,    0.232568,    0.193807,
0.161506,    0.134588,    0.112157,   0.0934638,   0.0778865,
 0.0649054,   0.0540879,   0.0450732,   0.0375610,   0.0313008,
0.0260840,   0.0217367,   0.0181139,   0.0150949,   0.0125791,
0.0104826,  0.00873549,  0.00727957,  0.00606631,  0.00505526)

"phi"<-c( 0.15428758,  0.13369956,  0.36268547,  0.67910888,  0.19445006,
0.25121038,  0.75841639,  0.55761859,  0.51480292,  0.46779986,
0.087176,   0.82909544,  0.29864056,  0.03134589,  0.67800576,
0.90348903,  0.51445118,  0.53910547,  0.66432752,  0.63405676)

"rv"<- c( -0.40737435,  0.94696646,  -4.25387942,  9.16593386,  -2.26248884,
-4.61975409,  13.11834872,  3.18996153,  0.20324896,  -1.52997772,
3.94708716,  14.26057484,  -2.92849334,  8.62667192,  9.91448193,
14.64940622,  -0.09773991,  3.73381811,  7.78840173,  8.05466536)

“sigrv”<-c(  1.0,  1.0,  1.0,  1.0, 1.0,    1.0, 1.0, 1.0, 1.0, 1.0,      1.0, 1.0, 1.0, 1.0,  1.0,     1.0, 1.0, 1.0, 1.0, 1.0)

"zeros"<-structure( c(   0,  0,  0,  0,  0,  0,  0,  0,  0,  0,  0,  0,  0,  0,  0,  0,  0,  0,  0,  0,
0,  0,  0,  0,  0,  0,  0,  0,  0,  0,  0,  0,  0,  0,  0,  0,  0,  0,  0,  0,  0,  0,   0,  0,  0,  0,  0,  0,  0,  0,  0,  0,  0,  0,  0,  0,  0,  0,  0,  0,  0,  0,  0,  0,  0,  0,
0,  0,  0,  0,  0,  0,  0,  0,  0,  0,  0,  0,  0,  0,  0,  0,  0,  0,  0,  0,  0,  0,   0,  0,  0,  0,  0,  0,  0,  0,  0,  0,  0,  0,  0,  0,  0,  0,  0,  0,  0,  0,  0,  0,  0,  0,
... ...
0,  0,  0,  0,  0,  0,  0,  0,  0,  0,  0,  0,  0,  0,  0,  0,  0,  0,  0,  0,  0,  0,   0,  0,  0,  0,  0,  0,  0,  0,  0,  0,  0,  0,  0,  0,  0,  0,  0,  0,  0,  0,  0,  0,  0,  0,   0,
0,  0,  0,  0,  0,  0,  0,  0,  0,  0,  0,  0,  0,  0,  0,  0,  0,  0,  0,  0,  0,  0,   0,  0,  0,  0,  0,  0,  0,  0,  0,  0,  0,  0,  0,  0,  0,  0,  0,  0,  0,  0,  0,  0,  0,  0,   0,
0,  0,  0,  0,  0,  0,  0,  0,  0,  0,  0,  0,  0,  0,  0,  0,  0,  0,  0,  0,  0,  0,  0),.Dim=c(20,30))
```

Figure 8.15 The data009.txt file which contains the observed RVs (rv) and their uncertainties ($sigrv$) at orbital phases (phi). The *beta* variable contains the series of powers from 0 to 1. And we also need an auxiliary variable called *zeros*, which is used to calculate the tempered posteriors with the ‘zero trick’.

```
model clear
data clear
model in "model.txt"
data in "data009.txt"
compile
inits in "initial009.txt"
initialize
update 10000
monitor K, thin(1)
monitor v0,thin(1)
monitor e, thin(1)
monitor w,thin(1)
monitor loglike2,thin(1)
update 40000
coda *
```

Figure 8.16 The script.txt file. We need Markov Chains of four parameters K, v_0, e, ω as well as the log likelihood values ($loglike2$) evaluated at the tempered posterior samples.

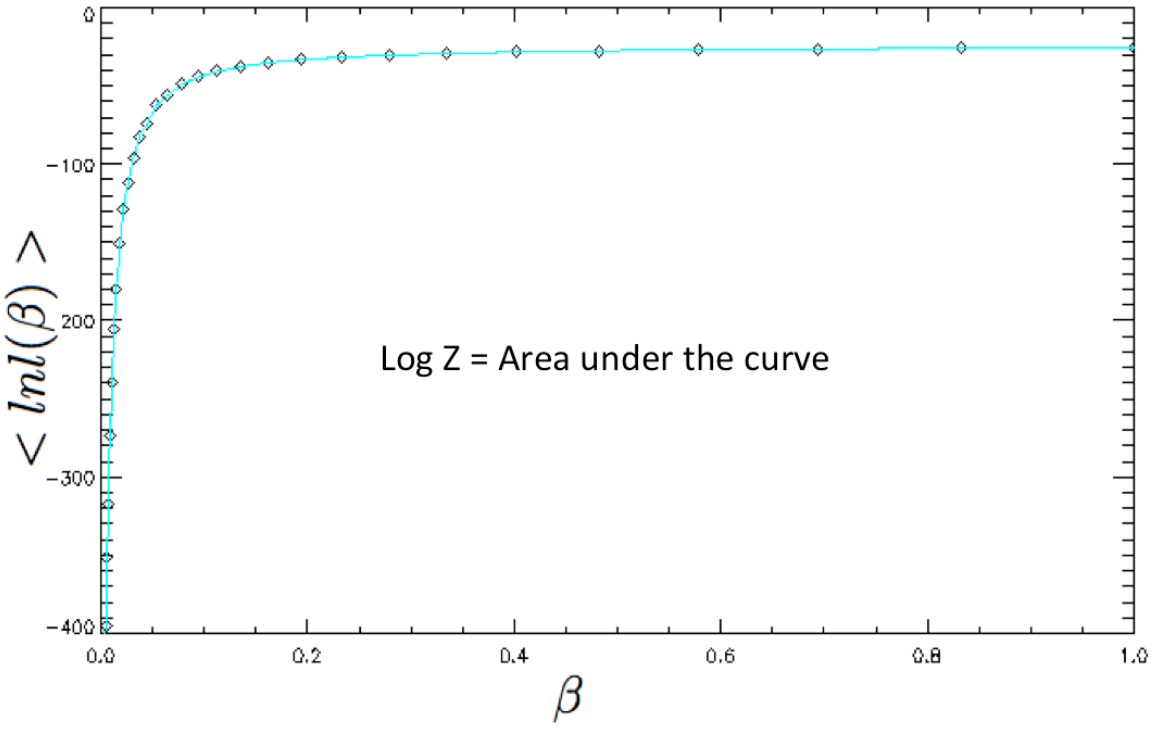

Figure 8.17 The $< \ln L(\boldsymbol{\theta}) >_\beta$ as a function of β. The log evidence is just the area under the cyan curve.

After the Bayesian evidence is calculated for each model or hypothesis (e.g., we have two models here, H_1 and H_2, for example, for a circular and elliptical orbit solutions), the model comparison can be performed by evaluating the evidence ratio, or Bayes factor:

$$BF_{12} = \frac{P(D|H_1)}{P(D|H_2)} \tag{8.30}$$

Jeffreys' scale is often used to decide which model is favored (Figure 8.18).

Bayes factor BF_{12}			Interpretation
	$>$	100	Extreme evidence for $\mathcal{M}_1$
30	–	100	Very strong evidence for $\mathcal{M}_1$
10	–	30	Strong evidence for $\mathcal{M}_1$
3	–	10	Moderate evidence for $\mathcal{M}_1$
1	–	3	Anecdotal evidence for $\mathcal{M}_1$
	1		No evidence
1/3	–	1	Anecdotal evidence for $\mathcal{M}_2$
1/10	–	1/3	Moderate evidence for $\mathcal{M}_2$
1/30	–	1/10	Strong evidence for $\mathcal{M}_2$
1/100	–	1/30	Very strong evidence for $\mathcal{M}_2$
	$<$	1/100	Extreme evidence for $\mathcal{M}_2$

Figure 8.18 The Jeffrey scale from Table 7.1 in *Bayesian Cognitive Modeling* (Lee & Wagenmakers 2014), originally in Jeffreys (1961).

This can be extended to cases of more than two models, and we then need to calculate the Bayes factor for each model pair.

8.4.2 Bayes Factor for Nested Models: Savage-Dickey Ratio

For nested models, there exists a much simpler way to calculate Bayes factors. For example, if the model H_0 is a special case of model H_1 by setting a parameter θ to a fixed value θ_0, then model H_0 is called nested in model H_1. In this case, the Bayes factor can be calculated from the Savage-Dickey ratio (Lee & Wagenmakers 2014):

$$BF_{01} = \frac{P(D|H_0)}{P(D|H_1)} = \frac{P(\theta = \theta_0|D, H_1)}{P(\theta = \theta_0|H_1)} = \frac{posterior\ at\ \theta_0}{prior\ at\ \theta_0} \tag{8.31}$$

This means we only need the posterior sample from Model H_1, and the Bayes factor is from the ratio of posterior density and prior density evaluated at θ_0.

An application of the Savage-Dickey ratio method is testing whether the RV curve is significantly elliptical, because the circular model is a special case of the eccentric model with $e = 0$.

We generated simulated RV data in the following manner: we fixed e to 0.05, randomly chose a fixed value for other orbital parameters (K, ω, v_0), and then generated 20 random phases from 0 to 1; the model RVs are calculated with the RV equation in eq. (8.8); then independent Gaussian noise is added to model RVs to get observed RVs. We then sample from the posterior of e with other orbital parameters fixed to the real values. Here we show the posterior and prior for eccentricity e in Figure 8.19. Usually a uniform prior from 0 to 1 is used for eccentricity. However, we used a Beta prior (green dotted line) here to show that the Savage-Dickey ratio method works well for any choice of prior. The Beta distribution is a very flexible distribution defined on the interval $[0, 1]$, which is appropriate for the distribution of eccentricity. Its probability density function is $P(x) = x^{\alpha-1}(1-x)^{\beta-1}/B(\alpha, \beta)$, where $B(\alpha, \beta)$ is defined with the Gamma functions by $B(\alpha, \beta) = \Gamma(\alpha)\Gamma(\beta)/\Gamma(\alpha + \beta)$.

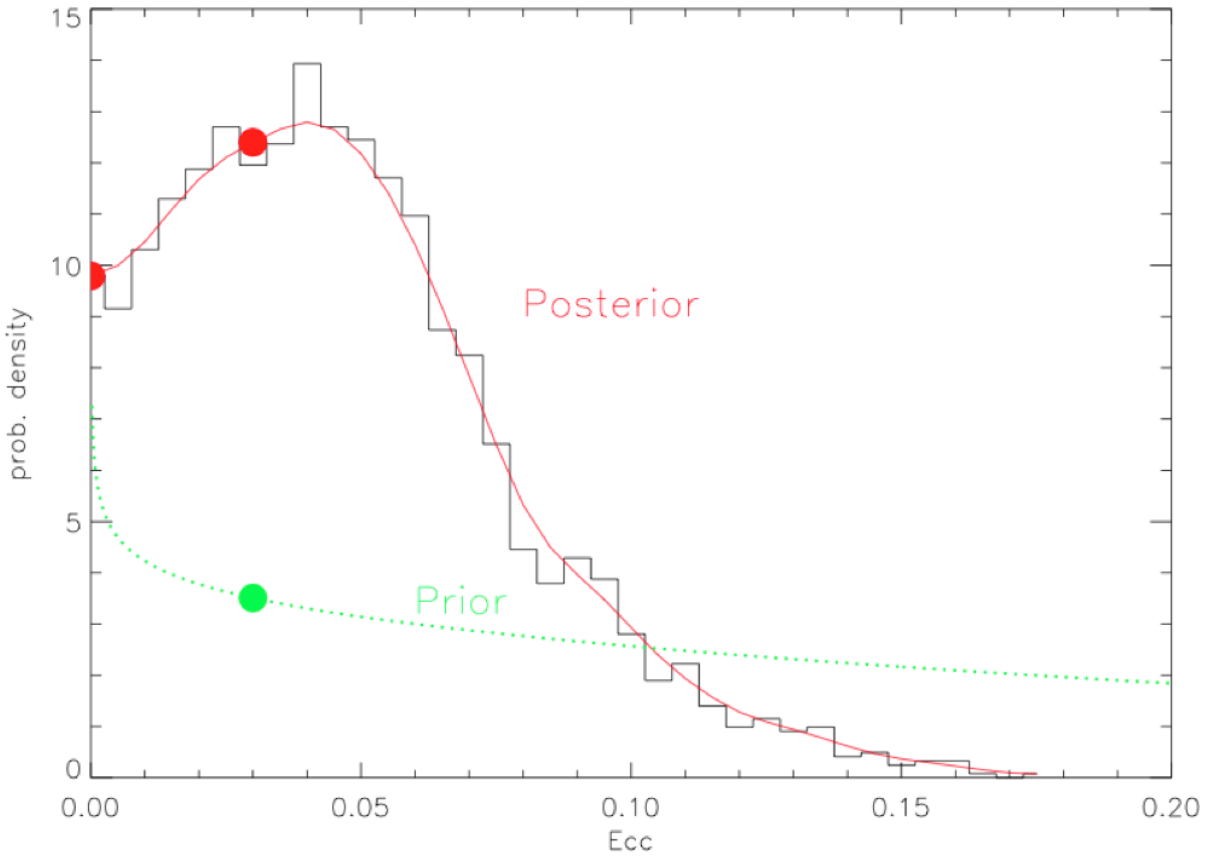

Figure 8.19 The posterior and prior distributions from fitting a RV curve with $e = 0.05$. A beta prior is used for the eccentricity e. The Bayes factor of two hypothesis $H_1 : e = 0.03$ and $H_2 : e \neq 0.03$ can be calculated by the ratio of the posterior and the prior evaluated at $e = 0.03$ (indicated by the red and green dots). And similarly for $e = 0.0$.

The Bayes factor is then the ratio of posterior and prior evaluated at e. This is shown as the dotted black line in Figure 8.20. To test the reliability of this method, we also calculated the Bayes factors from the nested sampling package MULTINEST (Feroz & Hobson 2008), which is indicated as the red solid line. There is good agreement between the Bayes factor

estimates from the two methods.

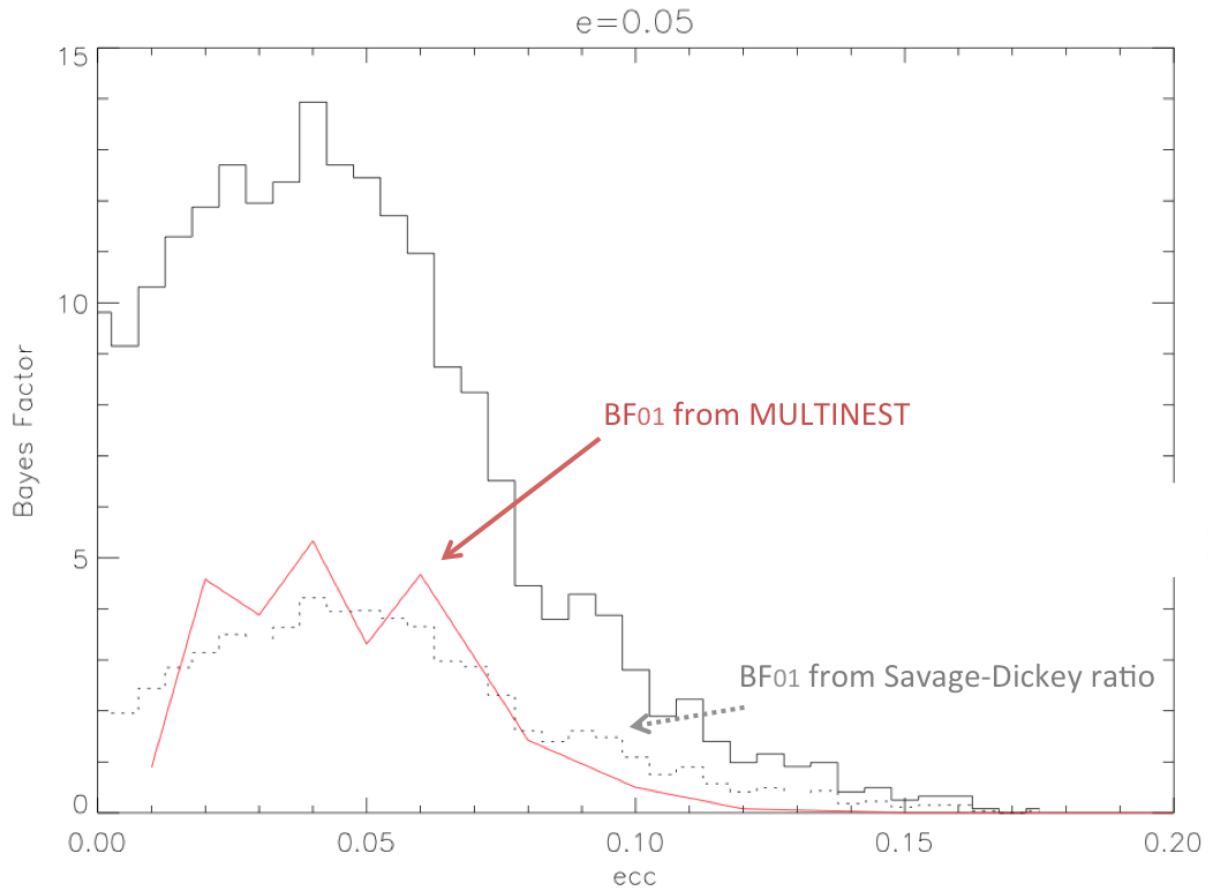

Figure 8.20 The Bayes factor BF_{01} (dotted gray) from the ratio of posterior (black solid) and prior (not shown) distribution from fitting a RV curve with $e = 0.05$. The red solid curve is the BF_{01} calculated from MULTINEST package which implemented the nested sampling algorithm to calculate Bayesian evidence.

8.5 Hierarchical Bayesian Models

Previously, we have shown the graphical model of fitting RV curve of one system, and the model function is

$$\boldsymbol{y}(\boldsymbol{t}, \boldsymbol{\theta}) = K[\cos(\boldsymbol{\nu} + \omega) + e\cos(\omega)] + \gamma \tag{8.32}$$

where the model inputs are the HJD times $\boldsymbol{t}$, and model parameter vector is $\boldsymbol{\theta} = (T_0, P, \gamma, K, e, \omega)$. Here we explicitly show each orbital parameter,

$$\boldsymbol{y}(\boldsymbol{t}, T_0, P, \gamma, K, e, \omega) = K[\cos(\boldsymbol{\nu} + \omega) + e\cos(\omega)] + \gamma. \tag{8.33}$$

Now, suppose we want to fit the RV curves of a population of stars ($i = 1, 2, 3, ...N$), and this population shares the same eccentricity distribution. To parameterize the population distribution of e, we followed Kipping (2013) and assumed a Beta distribution $P(e|a, b) = Beta(e|a, b)$. Note that Beta distribution is quite flexible and is able to represent many distributions (e.g., exponential distribution, etc.). Kipping (2013) compared several distributions for exoplanets (uniform, Rayleigh+exponential, etc.) and found that the Beta distribution best describes the observed eccentricity histogram in terms of Bayesian evidence. We assume uniform priors for other orbital parameters $(T_0, P, \gamma, K, \omega)$, and thus the prior distribution is then $P(\boldsymbol{\theta}_i, a, b) = P(e_i, a, b)P(T_{0i}, P_i, \gamma_i, K_i, \omega_i)$. Note that we have explicitly used the index i to show that the distribution is for the i^{th} system. To evaluate $P(e_i, a, b)$, the population distribution parameters a and b are treated as hyper-parameters, and we assume hyper-priors for a and b: $P(a)$ and $P(b)$. So $P(e_i, a, b) = P(e_i|a, b)P(a, b) = Beta(e_i|a, b)P(a)P(b)$. The whole parameter set is [$\boldsymbol{\theta} = (\boldsymbol{\theta}_1, \boldsymbol{\theta}_2, ...\boldsymbol{\theta}_N)$, a,b]. Assuming that each system is independent,

we can write the posterior distribution as follows,

$$\begin{aligned} P(\boldsymbol{\theta}, a, b|\boldsymbol{y}) &\propto P(\boldsymbol{y}|\boldsymbol{\theta}, a, b)P(\boldsymbol{\theta}, a, b) \\ &= P(a)P(b)\prod_i P(\boldsymbol{y}|\boldsymbol{\theta}_i, a, b)\prod_i P(\boldsymbol{\theta}_i, a, b) \\ &= P(a)P(b)\prod_i P(\boldsymbol{y}|\boldsymbol{\theta}_i, a, b)\prod_i P(e_i|a, b)P(T_{0i}, P_i, \gamma_i, K_i, \omega_i) \\ &= P(a)P(b)\prod_i P(\boldsymbol{y}|\boldsymbol{\theta}_i, a, b)Beta(e_i|a, b)P(T_{0i}, P_i, \gamma_i, K_i, \omega_i). \end{aligned} \tag{8.34}$$

We generated simulated RV data for 300 stars, and each system has different orbital parameters. We generated 300 samples from a Beta distribution $Beta(a, b) = Beta(0.867, 3.03)$ and set these values as the eccentricities. The other parameters (ω, K, v_0) are randomly sampled from uniform distribution with lower and upper bound $(0°, 360°)$, $(0, 30)$ km s^{-1}, and $(-10, 10)$ km s^{-1}, respectively. Note that without lost of generality, we assume T_0 and P are known, i.e., we assume the phases of RVs are already specified.

The following Figure 8.21 shows the graphical model for this problem. Note that the red plate (rectangle) means replication.

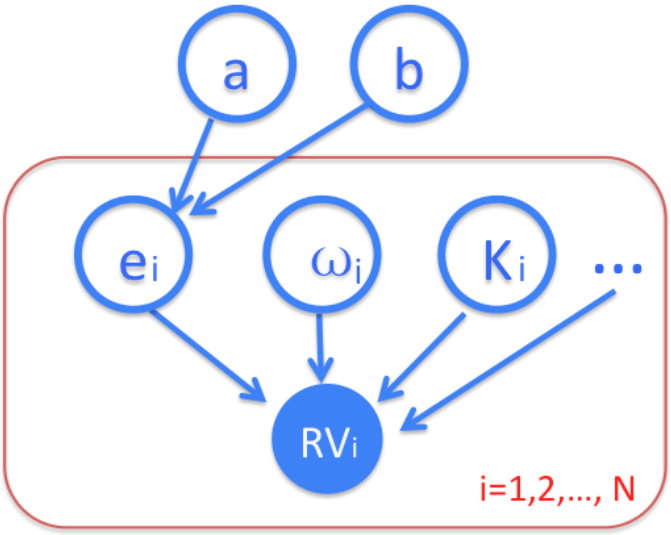

Figure 8.21 The graphical model of fitting $N = 300$ systems in order to find the population eccentricity distribution.

In BUGS language, the model can be expressed as in the following Figure 8.22.

```
model{

#likelihood
#20 data points, 300 RV datasets of stars with diff e
for(j in 1:300){
  for (i in 1:20){
  #ecc orbit RV equation

  term1[i,j]<- -1.0*log(sigrv[i,j]*sqrt(2.0*3.14159265359))
  term2[i,j]<- (-0.5)/sigrv[i,j]/sigrv[i,j]*(rv[i,j]-modelrv[i,j])*(rv[i,j]-modelrv[i,j])
  loglike0[i,j]<- term1[i,j]+term2[i,j]

  rv[i,j]~dnorm( modelrv[i,j],1.0/(sigrv[i,j]*sigrv[i,j]) )

   M[i,j]<- 2.0*3.14159265359*phi[i]
   E1[i,j]<-M[i,j]+e[j]*sin(M[i,j])+e[j]*e[j]*sin(2.0*M[i,j])/2.0
      M0a[i,j]<-E1[i,j]-e[j]*sin(E1[i,j])
   E1a[i,j]<-E1[i,j]+(M[i,j]-M0a[i,j])/(1.0-e[j]*cos(E1[i,j]))
        M0b[i,j]<-E1a[i,j]-e[j]*sin(E1a[i,j])
   E1b[i,j]<-E1a[i,j]+(M[i,j]-M0b[i,j])/(1.0-e[j]*cos(E1a[i,j]))
        M0c[i,j]<-E1b[i,j]-e[j]*sin(E1b[i,j])
   E1c[i,j]<-E1b[i,j]+(M[i,j]-M0c[i,j])/(1.0-e[j]*cos(E1b[i,j]))
   nu[i,j]<- 2.0*arctan(sqrt((1.0+e[j])/(1.0-e[j]))*tan(E1c[i,j]/2.0))
   modelrv[i,j]<- K[j]*( cos(nu[i,j]+w[j]*3.14159265359/180.)+e[j]*cos(w[j]*3.14159265359/180.) )+v0[j]
    }
 }
   for(j in 1:300){
    loglike[j]<-sum(loglike0[,j])

  #prior for e is beta distribution,with hyper params a,b
  e[j]~dbeta(a,b)
  w[j]~dunif(0,360)
  K[j]~dunif(0,30)
  v0[j]~dunif(-10,10)  }
  #hyper-prior for a,b
  a~dunif(0.1,4)
  b~dunif(0.1,8)
}
```

Figure 8.22 The JAGS code of fitting RVs of 300 systems (model.txt file).

The following Figure 8.23 presents the result. Our inferred posteriors for a and b are very close to the true values.

The traditional method to infer the eccentricity distribution is to fit the RVs of each individual system and find the point estimate eccentricity e_i for each one. Using these e_i, we generate an observed histogram for e, and we use some assumed parameterized distribution to fit the histogram. This procedure is affected by the choice of histogram bin-size. The adopted different point estimate (MAP, mean, median) for e_i will also change the shape of the histogram.

This hierarchical method has the advantage of directly inferring the distribution parameters (a and b) and thus produces more reliable results. A drawback is that problem needs a little bit more complicated formulation. BUGS/JAGS and Stan, which are designed to work with hierarchical Bayesian models, make the formulation and sampling much easier for practitioners.

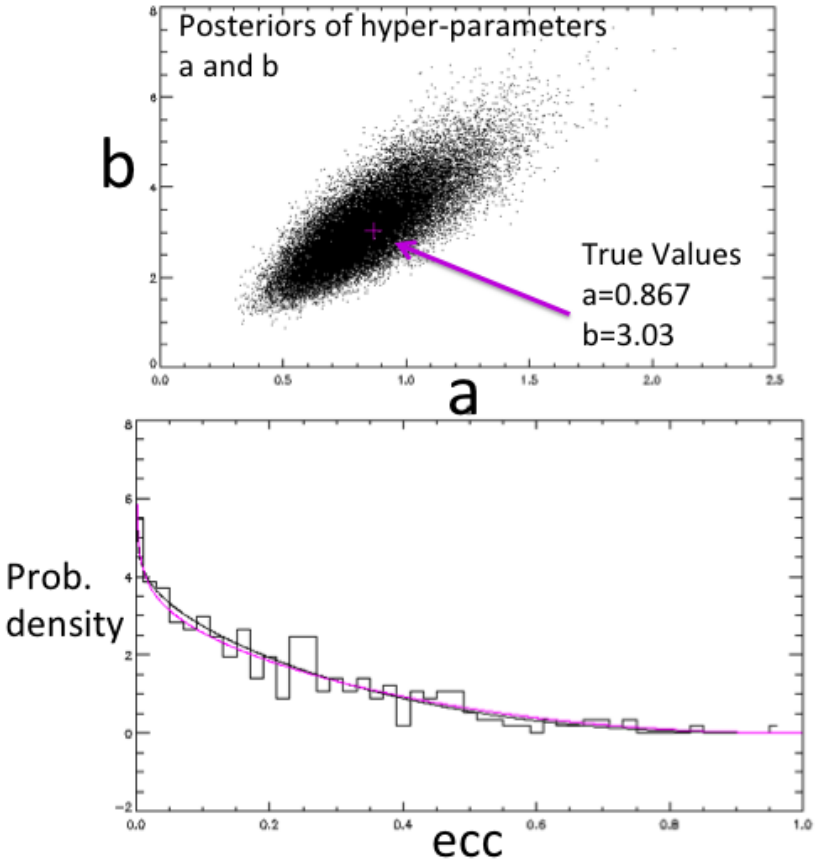

Figure 8.23 The lower panel shows the distribution of eccentricity from samples of all 300 posteriors. The black and pink solid line are the real and inferred eccentricity distribution parameterized as Beta(a, b). The upper panel shows the posterior distribution of hyper parameters a and b.

CHAPTER 9

Bayesian Spectral Tomography

We discuss the spectra separation techniques of multiple stellar systems. The current methods in the literature are essentially based on solving an over-determined, ill-posed, least squares problem either in the wavelength domain or Fourier domain. The techniques include the iterative methods and those that based on Singular Value Decomposition (SVD). First, we propose different iterative methods and test their convergence properties and speeds. We then show that by solving a revised least squares problem with regularization we can incorporate the prior knowledge of the spectra into the reconstruction process. Thirdly, we reformulate the SVD method in a more explicit elegant form by taking advantage of the properties of the circulant matrix and introduce regularization as well. Lastly, we summarize all these methods in the framework of Bayesian inference including the Tikhonov regularizations. These regularizations can improve the quality of the reconstructed spectra, and this is especially valuable for studies of systems with a faint component.

9.1 Introduction

Binary stars or multiple systems are important sources where we can get accurate stellar parameters like mass and radius (e.g., eclipsing binaries). The observed composite (double-lined) spectra cannot be analyzed in a straightforward manner as for normal single-lined spectra. Popular methods include those based on cross-correlating the observed spectra with template spectra, either one-dimensional or two-dimensional (e.g., TODCOR by Mazeh & Zucker 1994). By comparing the peak heights of cross-correlation functions, we can also

find the best spectral templates so that individual atmospheric parameters can be inferred. However, this is not always possible if the secondary component is very faint. It is often advantageous to separate the spectra of the components in multiple stellar systems, so that the nature of the faint companion can be identified (Matson et al. 2015).

The problem of spectral separation is a classical tomography problem, which has been studied extensively in other fields (geophysics, medical imaging, etc.). However, it was not introduced in the context of spectroscopic binaries until the application presented by Bagnuolo & Gies (1991). The developments of spectral separation techniques are presented in section 9.2. For a brief review, please refer to Gies (2004).

We formulate the problem of separating the component spectra of a multiple stellar system closely following Hensberge et al. (2008). The stellar system consists of K stars $k = 1...K$, and we assume the individual spectrum of each component does not depend on orbital phase. The light from each star adds up linearly to get an observed composite spectrum. We have J composite spectra b_{ji} observed at time $t_j (j = 1, 2, \cdots, J)$. The component and composite spectra are discretized onto a common grid of log-wavelength (base e) pixels: $\ln \lambda_i, i = 1, 2, \cdots, N$. The advantage of log-wavelength grid can be seen from the equation $dv/c = d\lambda/\lambda = d \ln \lambda$, and thus shifts in wavelength and velocity space are both linear. The Doppler shift of component k at t_j is β_{kj} pixels, and the light contribution factor of this star at the pixel i is represented by l_{kji}. These contribution factors satisfy the relation $(\sum_{k=1}^{K} l_{kji} = 1)$. We can usually assume a constant light ratio over all orbital phases, and l_{kji} simplifies to l_{ki}. If the light ratio is independent of wavelength, l_{ki} further reduces to l_k.

Then the composite spectra $b_j(\ln \lambda_i)$ can be related to the component spectra $x_k(\ln \lambda_i)$ by the following linear relation:

$$b_j(\ln \lambda_i) = \sum_{k=1}^{K} l_{kj}\ x_k(\ln \lambda_i - \beta_{kj}) + noise, \qquad j = 1, 2, \cdots, J. \tag{9.1}$$

Note that in order to use the above equation the component spectra need to have more pixels than N to account for Doppler shifts. Since eq. (9.1) is linear with respect to x_k, we can write it in a compact matrix form:

$$\mathbf{A}\mathbf{x} = \mathbf{b} \tag{9.2}$$

and we call it the linear tomography equation. We define $\mathbf{x}$ a $(\sum_{k=1}^{K} N_k) \times 1$ vector, concatenated by the K component spectra, of which each has N_k pixels. We call it the model vector, and it is the unknown we wish to determine. $\mathbf{b}$ is a $(N \times J) \times 1$ vector, concatenated by the J observed composite spectra, and we call it the data vector. $\mathbf{A}$ is called the design matrix, and it includes the effects of Doppler shifts and light contribution from each component. $\boldsymbol{A}$ can be treated as a linear operator that maps the model vector $\mathbf{x}$ to the data vector $\mathbf{b}$. The matrix $\mathbf{A}$ is very sparse, composed of $J \times K$ blocks, and the jk^{th} block of $\mathbf{A}$ is just a diagonal matrix with the diagonal shifted by β_{kj} pixels and multiplied by a constant l_{kj}. Please see Figure 9.1 for a detailed illustration of the structures of $\mathbf{A}$. Equation (3) shows explicitly the corresponding structure of equation (2). In Figure 9.1 we show a toy example for a binary system $K = 2$, with $J = 3$ observed composite spectra and each has $N = 8$ pixels. The star 1 and star 2 have RVs of $(-1.6, 0, 1.6)$ and $(0.8, 0, -0.8)$ pixels, flux contributions of 0.75 and 0.25, respectively. This is similar to the example in the Appendix of Hensberge et

al. (2008). We have explicitly shown the fractional pixel shifts which are represented by a linear combination of two diagonals corresponding to the upper and lower integer shifts. The design matrix has a dimension of $3N$ by $2N + 6$, and the 6 extended columns corresponds to the maximum Doppler shifts in RVs.

$$\begin{pmatrix} \mathbf{A_{1,1}} & \mathbf{A_{1,2}} \\ \mathbf{A_{2,1}} & \mathbf{A_{2,2}} \\ \mathbf{A_{3,1}} & \mathbf{A_{3,2}} \end{pmatrix} . \begin{pmatrix} \mathbf{x_1} \\ \mathbf{x_2} \end{pmatrix} = \begin{pmatrix} \mathbf{b_1} \\ \mathbf{b_2} \\ \mathbf{b_3} \end{pmatrix} \tag{9.3}$$

To illustrate the performances of different algorithms described below, we make a synthetic binary system composed of two B stars. The original component spectra are taken from the high resolution spectral library UVBLUE (Rodriguez-Merino et al. 2005), with the same effective temperature, surface gravity, and projected surface rotational velocity $T_1 = T_2 = 12000$ K, $\log g_1 = \log g_2 = 3.0$, $v \sin i_1 = v \sin i_2 = 100$ km s^{-1}. Both stars have solar metallicity and microturbulence velocity of 2 km s^{-1}. The flux contributions from the primary and secondary star are 70% and 30%, respectively. The two component spectra are shifted in accordance with their RVs and added linearly to simulate the observed composite spectra. Poisson noise with the mean value of 1/50 is added. In this example, we have 5 observed spectra corresponding to 5 pairs of RVs. These RVs range from 4 to 5 pixels.

9.2 Spectral Separation in the Wavelength Domain

9.2.1 Traditional Least Square Problems

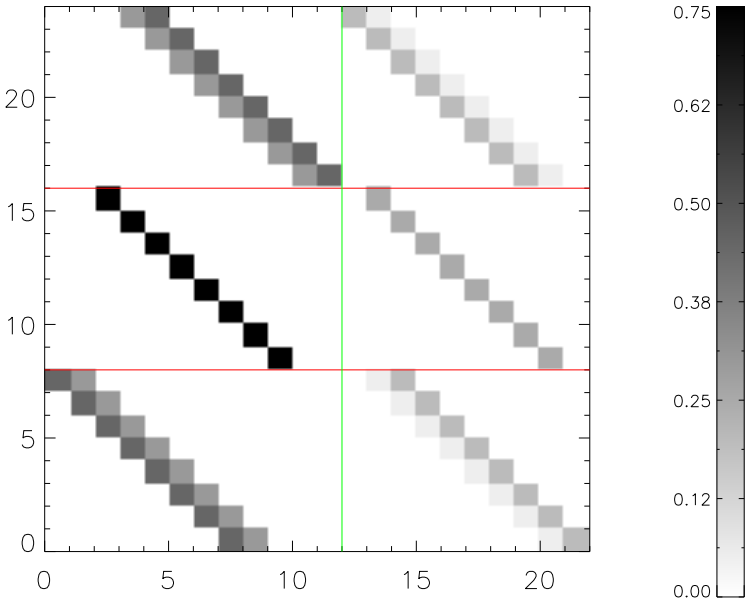

Figure 9.1 The design matrix in wavelength domain similar to Figure 1 in Hensberge et al. (2008). Fractional pixel shifts are explicitly shown. The Doppler shifts are $(1.6, 0, -1.6)$ pixels for the primary, and $(-0.8, 0, 0.8)$ pixels for the secondary. Note in the first and third row, the fractional pixel shifts are approximated by a linear combination of two adjacent integer pixels. The design matrix has a dimension of $3N$ by $2N + 6$ with $N = 8$. The 6 extended columns correspond to the maximum Doppler pixel shifts of $2 + 2 + 1 + 1$.

The spectral separation problem reduces to solving for $\mathbf{x}$ given $\mathbf{b}$ and $\mathbf{A}$ in the equation $\mathbf{Ax} = \mathbf{b}$. The naive solution of $\mathbf{A}^{-1}\mathbf{b}$ is not applicable, because matrix $\mathbf{A}$ is often rank deficient and not invertible by a direct method like Gauss elimination. Even when the inverse of $\mathbf{A}$ exists, this naive solution $\mathbf{A}^{-1}\mathbf{b}$ can greatly magnify the noise in $\mathbf{b}$, making the solution essentially meaningless. Usually $K < J$, and thus it is an overdetermined linear inverse problem in which there is no solution that satisfies equation (9.2) exactly. We can find a solution that minimizes L^2 norm of residuals. The objective function we need to minimize in this least squares case is:

$$minimize\ |\mathbf{Ax} - \mathbf{b}|^2. \tag{9.4}$$

This standard linear equation, usually in an intermediate or large scale, is often solved by an iterative method. First, we have an initial estimate of the component spectra, $\mathbf{x}^{(0)}$. We then improve the spectra at each iteration (e.g. the i^{th}) by adding a correction term, $\mathbf{x}^{(i+1)} = \mathbf{x}^{(i)} + \delta\mathbf{x}^{(i)}$. We iterate until the residual is smaller than some small number ϵ ($|\mathbf{Ax} - \mathbf{b}|^2 < \epsilon$).

Different iterative methods differ in the correction term $\delta\mathbf{x}$. Bagnuolo & Gies (1991) (BG91) solved this spectra separation problem by applying the (ILST) Iterative Least Square Technique. Their algorithm is very similar to the Kaczmarz's algorithm (Aster et al. 2012). It updates the model in the i^{th} iteration by projecting the current model $\mathbf{x}^{(i)}$ onto the hyperplane defined by the $(i+1)^{th}$ row (or column in Bagnuolo & Gies) of $\mathbf{A}$. This can be

written in a compact form following Aster et al. (2012):

$$\delta \mathbf{x}^{(i)} = \frac{b_{i+1} - \mathbf{A}_{i+1,.}\mathbf{x}^{(i)}}{\mathbf{A}_{i+1,.}\mathbf{A}_{i+1}^{T}} \mathbf{A}_{i+1}^{T} \delta \tag{9.5}$$

where δ is a factor to facilitate convergence and ranges from 0 to 1; it is similar to the learning rate in neural network optimization. $\mathbf{A}_{i+1,.}$ is the $(i+1)^{th}$ row of $\mathbf{A}$. b_{i+1} is the $(i+1)^{th}$ element of vector $\mathbf{b}$. The above equation should be compared to equations (1) and (2) in the original paper by Bagnuolo & Gies. This is essentially a gradient descent method with the search direction $\delta \mathbf{x}^{(i)}$ at iteration i along the greatest descent direction. It is similar to the ART (Algebraic Reconstruction Technique) and SIRT (Simultaneous Iterative Reconstruction Technique) algorithm widely used in the field of medical image reconstruction (Aster et al. 2012). This algorithm will converge to a local minimum close to the initial estimate.

Another iterative method, the conjugate gradient method is better suited to solve this problem. At each iteration i, instead of searching along the greatest descent direction at current position $\mathbf{x}^i$, the algorithm uses a new direction $\delta \mathbf{x}^{(i+1)}$ constructed by the current gradient and the previous search direction $\delta \mathbf{x}^{(i)}$, so that the new direction and the previous direction are orthogonal to the matrix $\mathbf{H}$ (the Hessian matrix[1]) at the current position $\mathbf{x}^i$,

$$\delta \mathbf{x}^{(i+1)} \mathbf{H} \delta \mathbf{x}^{(i)} = 0. \tag{9.6}$$

[1]Hessian matrix is a square matrix of second-order partial derivatives of a scalar-valued function. For a scalar function $f(\mathbf{x})$ with an input vector $\mathbf{x} \in R^n$, its Hessian is $\mathbf{H}_{i,j} = \frac{\partial^2 f}{\partial x_i \partial x_j}$.

The conjugate gradient iterative method has better convergence performance, and the final solution usually has smaller residuals comparing with the Kaczmarz algorithm used in BG91. The new revision such as the code lsqrCOV (Paige & Saunders 1982) developed by the Systems Optimization Laboratory at Stanford can output the covariance matrix at each iteration, which facilitates the error estimation of the reconstruction.

As an example, we use the LSQR algorithm, which is widely used in solving geophysics inverse problems, to reconstruct the component spectra of the aforementioned synthetic binary system. The squared residuals are plotted as a function of iteration number. The conjugate gradient method has a similar convergence speed but it converges to a solution with smaller squared residuals (0.145) comparing with the Kaczmarz's algorithm (0.229) used in BG91.

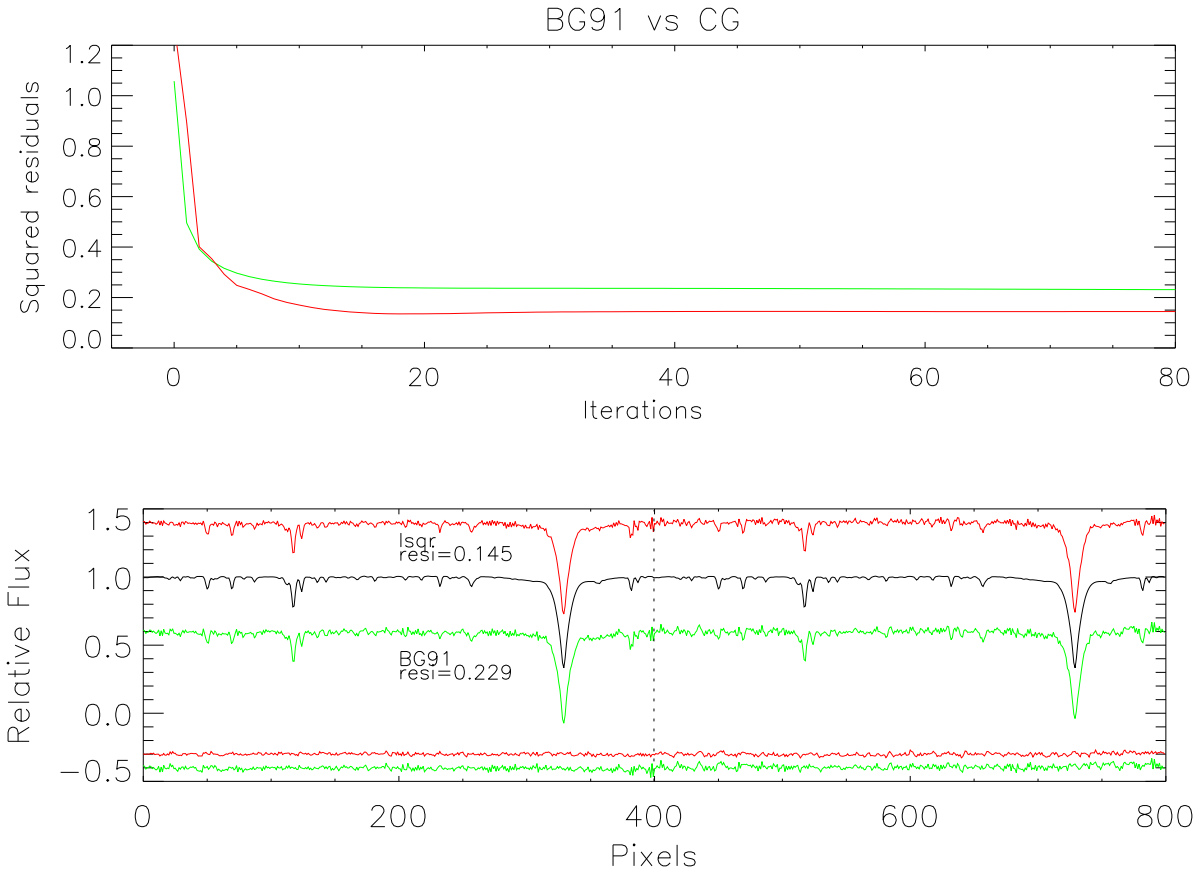

Figure 9.2 **Upper panel**: The convergence of conjugate gradient method LSQR (red) and the Kaczmarz algorithm used in BG91 (green). **Lower panel**: reconstructed spectra (star 1 on the left, star 2 on the right, separated by the dotted dividing line) by using the algorithm LSQR (red) and BG91 (green) after 100 iterations, and the real component spectra are shown in black. The residuals (two flat lines at the bottom) are indicated by the same color but shifted downwards by -0.3 and -0.4 for clarity.

It is also possible to further improve the convergence by using other iterative methods which take advantage of the non-negativity or other constraints of the matrix elements. For

a thorough discussion, please refer to Berisha & Nagy (2012).

Another important technique of solving the least squares problem is Singular Value Decomposition (SVD). SVD is a widely used technique in many different fields. Its applications can also be found in geology, image compression, image de-blurring and de-noising, etc. It was first implemented by Simon & Sturm (1994) for spectral separation. They also considered the design matrix $\mathbf{A}$ as a function of orbital parameters, and thus got the optimized orbital parameters along with reconstructed spectra $\mathbf{x}$. This procedure is since called spectral disentangling in literature. A direct implementation of SVD for large scale problems is computational expensive, and it is usually required to exploit the sparse property of the matrix $\mathbf{A}$. The innovations by Hadrava (1995) and Ilijic et al. (2004) solve equation (9.2) in the Fourier domain, which makes the computation much more efficient.

In SVD, a m by n matrix $\mathbf{A}$ is factored into three matrices,

$$\mathbf{A} = \mathbf{U}\mathbf{S}\mathbf{V}^T \tag{9.7}$$

where $\mathbf{U}$ is an m by m orthogonal matrix, $\mathbf{V}$ is an n by n orthogonal matrix, and $\mathbf{S}$ is an m by n diagonal matrix with diagonal elements called singular values. The singular values along the diagonal of $\mathbf{S}$ are customarily arranged in decreasing size $s_1 \geq s_2 \geq ... \geq s_{min(m,n)} \geq 0$. If the first p singular values are nonzero, we partition $\mathbf{S}$ as

$$\mathbf{S} = \begin{bmatrix} \mathbf{S}_p & \mathbf{0} \\ \mathbf{0} & \mathbf{0} \end{bmatrix} \tag{9.8}$$

and equation (7) simplifies to $\mathbf{A} = \mathbf{U}_p\mathbf{S}_p\mathbf{V}_p^T$, where $\mathbf{U}_p$ and $\mathbf{V}_p$ is the first p columns of $\mathbf{U}$ and $\mathbf{V}^T$. We thus have the SVD solution to equation $\mathbf{A}\mathbf{x} = \boldsymbol{b}$:

$$\mathbf{x}_{\rm SVD} = \left(\mathbf{V}_p \mathbf{S}_p^{-1} \mathbf{U}_p^T\right) \mathbf{b} = \mathbf{A}^\dagger \mathbf{b}. \tag{9.9}$$

$\mathbf{A}^\dagger$ is the pseudo-inverse matrix of $\mathbf{A}$. In practical applications, we often treat singular values that are smaller than a certain limit as zero, and we call the eq. (9.9) the truncated SVD solution. The codes *Korel* and *FDBinary* by Hadrava (1995) and Ilijic et al. (2004) are both based on truncated SVD solutions.

The uncertainties of the SVD solution can be quantified by the model resolution matrix defined by $\mathbf{R} = \mathbf{A}^\dagger \mathbf{A}$. The SVD solution $\mathbf{x}_{\rm SVD}$ is related to the true (error free) solution $\mathbf{x}_{\rm true}$ by,

$$\mathbf{x}_{\rm SVD} = \mathbf{R}\mathbf{x}_{\rm true} = \mathbf{A}^\dagger \mathbf{A} \mathbf{x}_{\rm true}. \tag{9.10}$$

It usually suffices to use the diagonal elements of $\mathbf{R}$ to infer the uncertainties. Values of 1.0 suggest full reconstruction, and the differences from unity represent the fractional uncertainties.

Note that there is an ambiguity in the least squares solution: by adding or subtracting a constant continuum from the reconstructed spectra, equation 9.2 can still be satisfied. This can be seen in the upper right panel of Fig. 9.4: there is a vertical displacement between the reconstructed component spectra (black) and the real component spectra (red). This ambiguity is related to the flux ratio, and it can usually be resolved by comparing reconstructed and model spectra.

Other methods for the reconstruction of component spectra include minimizing eq. (9.4)

by a constrained non-linear least square minimizer LBFGS (Byrd et al. 1995) as in Harries, Hilditch, & Howarth (2003). This algorithm (LBFGS) is suitable for large scale, non-linear parameter optimization problems.

9.2.2 Spectra Separation with Regularization in Wavelength Domain

In the classical spectra separation techniques, the reconstructions completely depend on the observed data (the composite spectra). In real applications, we want to incorporate our prior knowledge of the stellar spectra into the reconstruction process. One way to achieve this is to use regularization, which has been widely used in the fields such as interferometric imaging. In the classic Tikhonov regularization (Aster et al. 2012), instead of minimizing the least squares, we penalize the least squares solution by adding an extra term, representing our certain prior knowledge of the solution,

$$minimize\ |\mathbf{Ax}-\mathbf{b}|^2+\alpha^2|\mathbf{L}(\mathbf{x}-\mathbf{x}_{prior})|^2 \tag{9.11}$$

where $\mathbf{x}_{prior}$ represents the prior mean of the solution (initial estimate of component spectra), α is a scalar regularization parameter, and $\mathbf{L}$ is the Tikhonov matrix which can have different forms.

In the zeroth order Tikhonov regularization, $\mathbf{L}=\mathbf{L_0}=\mathbf{I}$ ($\mathbf{I}$ is the identify matrix), and we regularize our solution to match our prior mean $\mathbf{x}_{prior}$. In the first and second order Tikhonov regularization, $\mathbf{L}=\mathbf{L}_1$ or $\mathbf{L}_2$, where $\mathbf{L}_1$ and $\mathbf{L}_2$ are the first and second finite difference matrices:

$$\mathbf{L}_1 = \begin{bmatrix} -1 & 1 & & & & \\ & -1 & 1 & & & \\ & & \ddots & \ddots & & \\ & & & -1 & 1 & \\ & & & & -1 & 1 \end{bmatrix} \quad , \quad \mathbf{L}_2 = \begin{bmatrix} 1 & -2 & 1 & & & & \\ & 1 & -2 & 1 & & & \\ & & \ddots & \ddots & \ddots & & \\ & & & 1 & -2 & 1 & \\ & & & & 1 & -2 & 1 \end{bmatrix} \tag{9.12}$$

Note that if $\mathbf{x} \in R^n$, then the $\mathbf{L}_1$ and $\mathbf{L}_2$ are of dimensions $(N-1) \times N$ and $(N-2) \times N$, respectively. In these cases, we regularize our least squares solution so that $\mathbf{L}_1\mathbf{x}$ is close to the derivative of our prior mean $\mathbf{L}_1\mathbf{x}_{prior}$ (or convexness and concaveness $\mathbf{L}_2\mathbf{x}_{prior}$ in $2nd$ order Tikhonov regularization). The above regularized least squares problem can be written as an ordinary least squares problem:

$$minimize \quad \left| \begin{bmatrix} \mathbf{A} \\ \alpha\mathbf{L} \end{bmatrix} \mathbf{x} - \begin{bmatrix} \mathbf{b} \\ \alpha\mathbf{L}\mathbf{x}_{prior} \end{bmatrix} \right|^2 . \tag{9.13}$$

Thus we can solve this least squares problem by utilizing the SVD for the augmented matrix $\begin{bmatrix} \mathbf{A} \\ \alpha\mathbf{L} \end{bmatrix} = \mathbf{U}_p\mathbf{S}_p\mathbf{V}_p^T$, so that the solution is $\mathbf{x}_{Tikhonov} = \mathbf{V}_p\mathbf{S}_p^{-1}\mathbf{U}_p^T \begin{bmatrix} \mathbf{b} \\ \alpha\mathbf{L}\mathbf{x}_{prior} \end{bmatrix}$. A standard least squares solution to eq. (9.4) given by SVD is a mathematically correct global minimum, but it often contains some low frequency modulation which is not physical. This is due to the fact that the Doppler shifts set the velocity range over which reconstructed features are unambiguous. What we really need are continuum normalized, smooth reconstructed spectra. This is achieved this by solving eq. (9.13).

The regularization parameter α is very important. The best α should minimize $|\mathbf{x} - \mathbf{x}_{\mathbf{real}}|$ which is not known. We need a way to estimate regularization parameter α from the data at our disposal. There are several such methods such as the discrepancy principle, L-curve method, Generalized Cross Validation (Hansen 2010), Maximum Bayesian Evidence, and

hierarchical models. We use the intuitive L-curve method here. In later sections, we use Bayesian evidence to choose the appropriate regularization parameter. The L-curve diagram is a plot of squared residuals $|\mathbf{Ax} - \mathbf{b}|^2$ and the difference between the regularized solution and the prior $|\mathbf{L}(\mathbf{x} - \mathbf{x_{prior}})|^2$ for different values of the regularization parameter α. Usually a search from 10^{-2} to 10^2 uniformly in logarithm scale is satisfactory. Such a plot is shown in Figure 9.3, with best regularization parameter α marked at the point of maximum curvature. In Figure 9.4, we show the reconstructed spectra of two components for the same synthetic binary system mentioned above. In this example, we apply two prior spectra x_{prior1}, x_{prior2} for the two components. The prior spectrum can be, e.g., a flat continuum, a low order polynomial depicting the overall trend of the spectra, or some real atmosphere model. The regularization parameter α is determined by the L-Curve method. With regularization, the reconstructed spectra will then be set to the correct continuum level and have a much smaller χ^2. Note the priors on the component spectra do not have to be very good, even a very bad initial estimate with $T_{\rm eff}$, $\log g$, and $v \sin i$ off by $3000K$, 1.0 dex and 100 km s^{-1} can get a better overall reconstruction, especially if we only use its low frequency components. We have the best reconstruction when the adopted prior mean is closest to the true component spectra (the 3rd and 4th panel in Figure 9.4), which correspond to the low frequency prior and good model prior.

Figure 9.5 shows that the $\mathbf{L}_1$ and $\mathbf{L}_2$ Tikhonov regularization schemes generate smoother reconstructed spectra with reduced square errors.

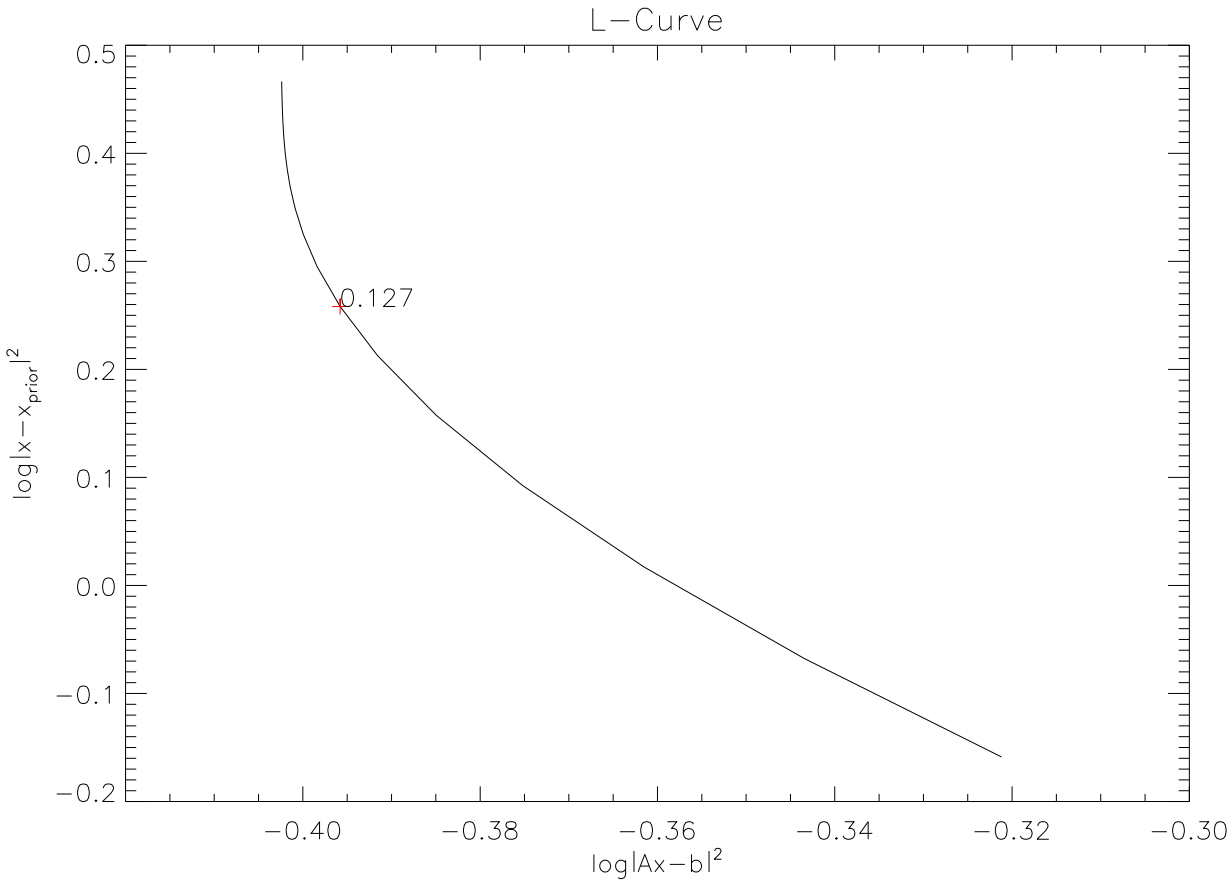

Figure 9.3 The L-Curve diagram is a log-log plot of the squared residuals $|\mathbf{Ax} - \mathbf{b}|^2$ and the square difference between the prior and the reconstructed sepctra $|\mathbf{x} - \mathbf{x_{prior}}|^2$. The best regularization parameter α corresponds to the one with the maximum curvature, indicated by the red cross with the value of 0.127. This figure corresponds to the 0th order Tikhonov regularization with a low frequency model prior (see Figure 9.4).

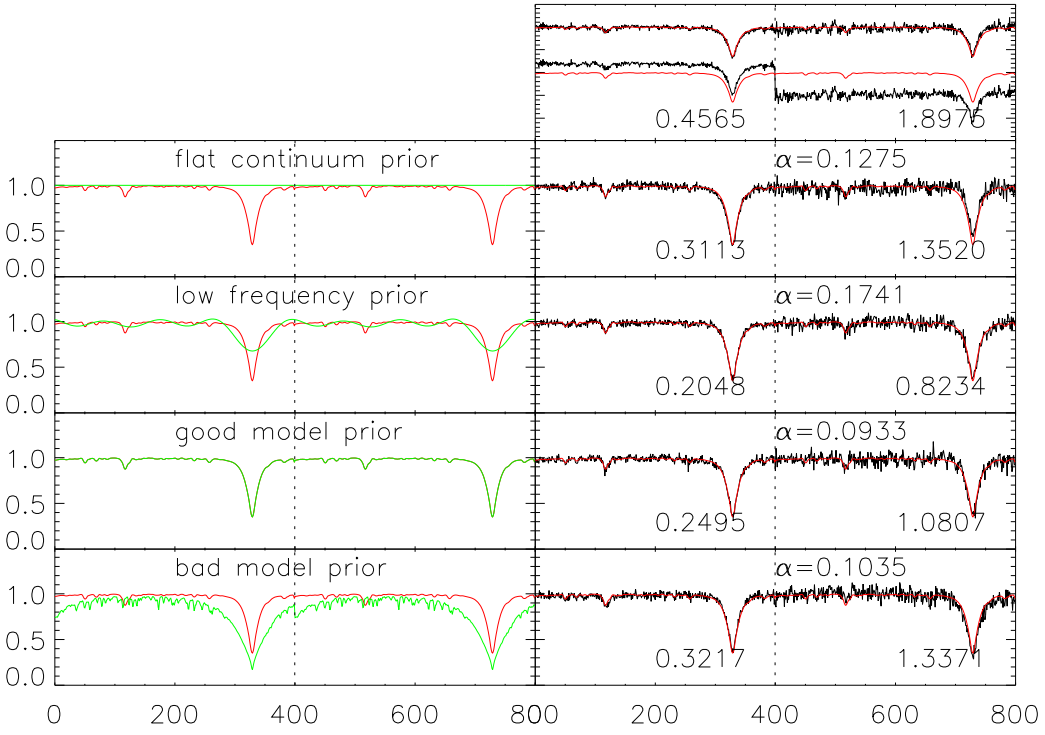

Figure 9.4 Reconstruction with 0th order Tikhonov regularization with different priors. The primary and secondary star contribute to 70% and 30% flux, respectively. The first row is a reconstruction without prior; note the reconstructed spectra have been corrected for the mean difference when comparing with models. The following rows show the prior spectra and the reconstructed spectra for 4 different priors: flat continuum; low frequency component of an atmosphere model; a good atmophere model; a bad atmosphere model with $T_{\rm eff}$ off by 3000 K, $\log g$ off by 1.0 dex and $v \sin i$ off by 100 km s^{-1}. The intrinsic true component spectra are indicated by the red lines. Green lines are priors and black lines represent the reconstruction. The two component spectrum have been concatenated into a single spectrum with the dashed line at 400 pixels separating the two components. In the second column, the best regularization parameters α are labeled and the square errors of the two component

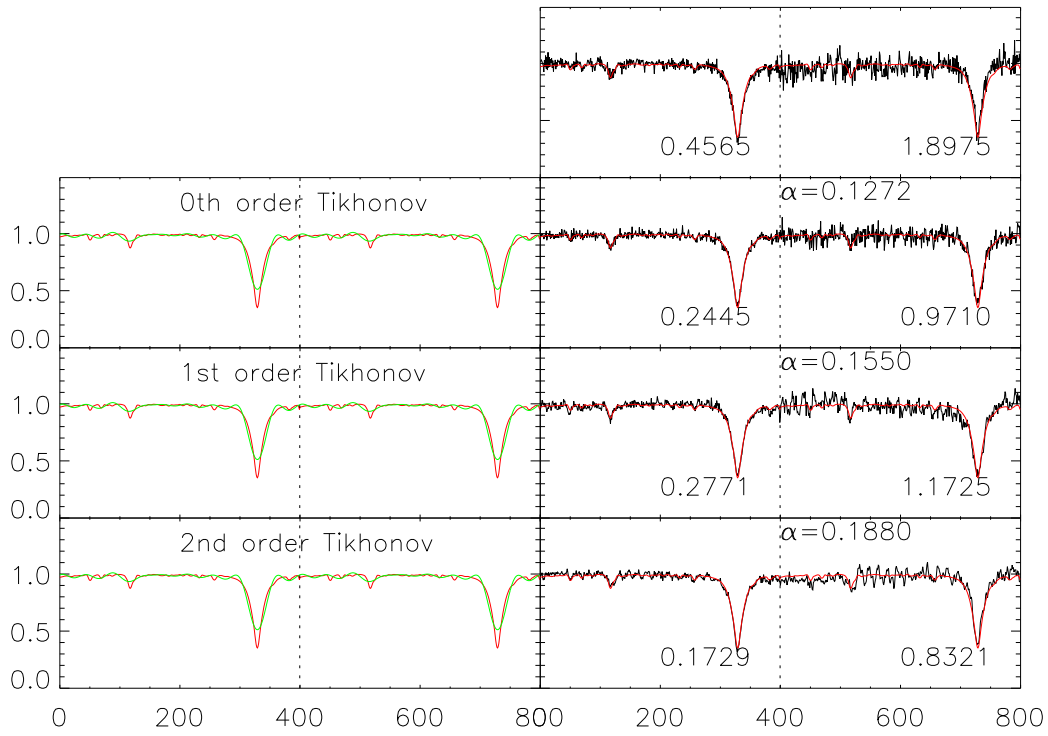

Figure 9.5 Reconstructions with 0th, 1st, and 2nd order Tikhonov regularization with the prior mean being a low frequency component of the true component spectra. The intrinsic true component spectra are indicated by the red lines. Green lines are prior means and black lines represent the reconstruction. The two component spectra have been concatenated into a single spectrum with the dashed line at 400 pixels separating the two components. In the second column, the best regularization parameter α is labeled and the square error for the two component spectra are marked at the bottom of each panel.

Direct least squares solutions from SVD usually introduce undulations in the continuum

of reconstructed spectra. This is especially the case when applied to long spectral intervals, since the input composite spectra are usually not perfectly continuum normalized. This phenomenon is dominant in the reconstructed spectrum of faint components. One way to overcome this difficulty is to use the empirical 'corridor correction' proposed in Hensberge et al. (2008). In this procedure, one of the reconstructed spectra is flipped and stacked above the spectrum of the other component. A corridor enclosed by the two spectra is then used, probably with some smoothing, to rectify the spectra to a flat continuum. Lehmann et al. (2013) split the spectra into overlapping wavelength bins, and corrected the continuum of the reconstructed spectrum at each bin and finally merged all bins and averaged overlapping parts.

We can overcome this problem by regularizing the solution with a flat prior spectrum. In Figure 9.5, we show the reconstructed spectra for the two components in KIC 9851944, which is an eclipsing binary system composed of two A stars both with effective temperature of about $7000K$ (discussed in Chapter 5). The direct least squares solutions by SVD are shown as red lines. Unphysical low frequency modulations are obvious. The 0th order Tikhonov regularization solution is shown as black lines, with flatter continuum.

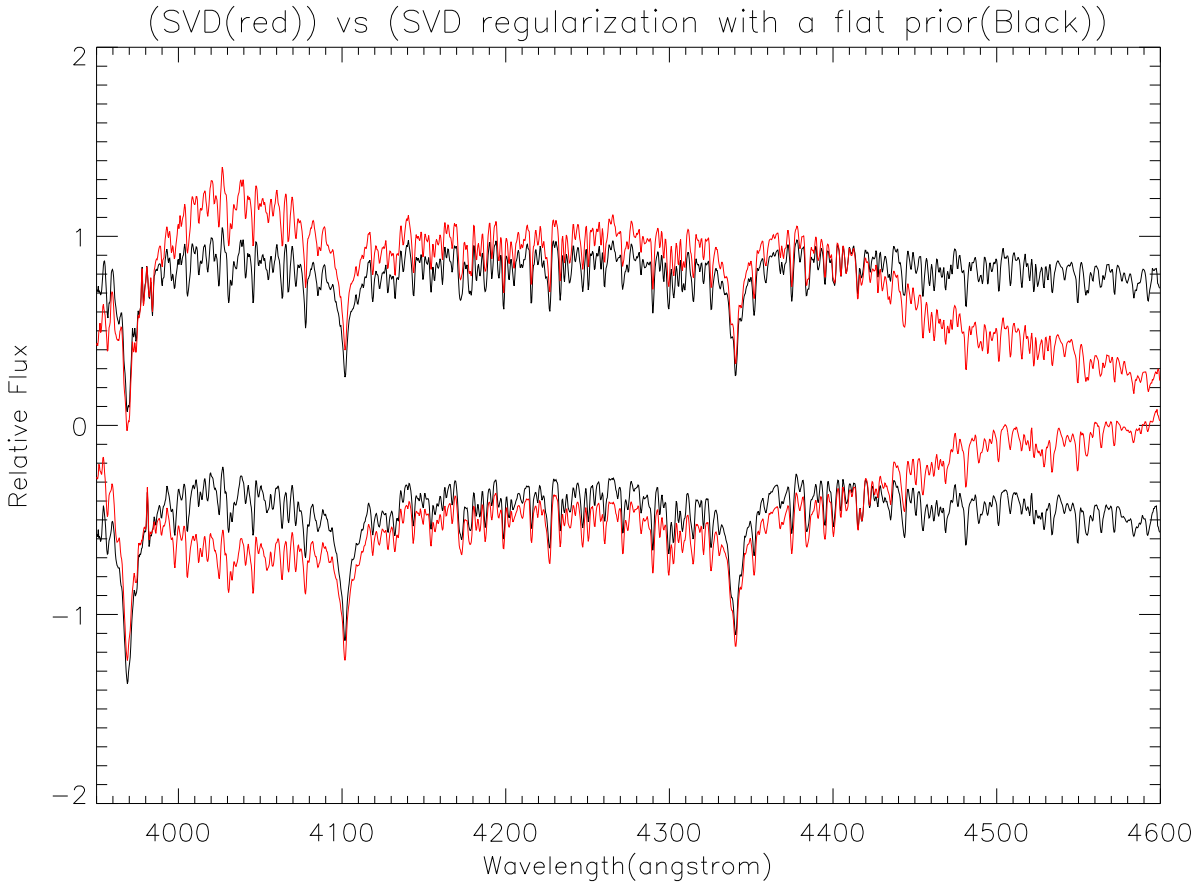

Figure 9.6 Reconstructed spectra of two components in KIC 9851944. The direct SVD solutions are represented as the red lines, while the regularized solution with a flat prior are shown as the black lines.

9.3 Spectra Separation in the Fourier Domain

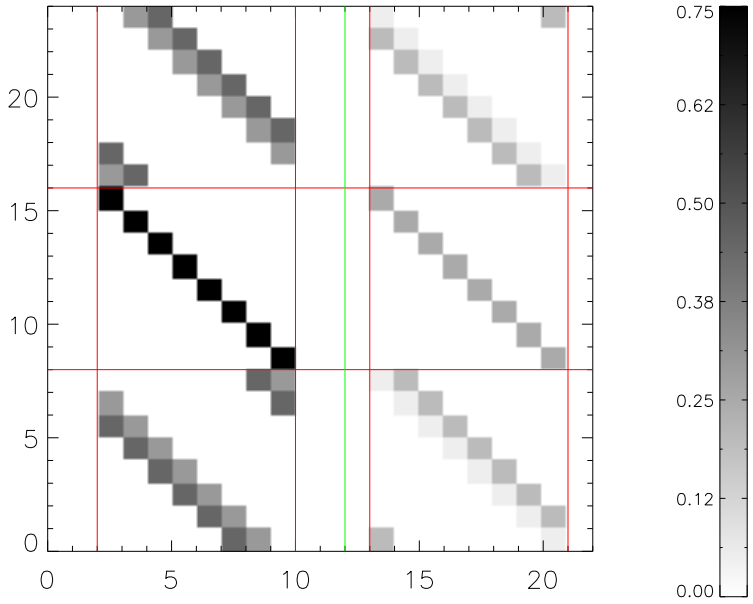

Figure 9.7 The equivalent design matrix in wavelength domain. Each square block of size 8 by 8 within the red solid lines is a circulant matrix with successive shifting rows. Only the blocks within the red lines compose the design matrix, which has a dimension of $3N$ by $2N$, with $N = 8$.

9.3.1 A Reformulation of the Fourier Method

Hensberge et al. (2008) showed that the Fourier domain method by Hadrava (1995) is equivalent to the log-wavelength (velocity) domain method. This is achieved by properly folding

the design matrix $\boldsymbol{A}$ such that each block of $\boldsymbol{A}$ is a circulant matrix. It is defined as matrices for which each row in the matrix is shifted one element to the right relative to the preceding row. In Figure 9.7, we show such a folded design matrix with circulant matrix blocks for the toy model mentioned in section 2. Figure 9.7 can be directly compared with Figure 9.1. Note that this approach makes the assumption that the spectra repeat cyclically beyond the observed boundaries, so care must be taken in interpreting the results at the wavelength extrema.

The spectral decomposition property of a circulant matrix is that it can be diagonalized by the Discrete Fourier Transform (DFT) matrix $\tilde{\boldsymbol{F}}$ (Hansen et al. 2006):

$$\boldsymbol{A} = \tilde{\boldsymbol{F}}^{*}\tilde{\boldsymbol{\Lambda}}\tilde{\boldsymbol{F}}, \tag{9.14}$$

where we use the symbol ˜ to indicate complex variables. The DFT matrix is defined that, when operating on a N by 1 vector b,

$$\tilde{\boldsymbol{F}}\boldsymbol{b} = \tilde{\boldsymbol{b}} \tag{9.15}$$

outputs $\tilde{b}$, the discrete Fourier transform of b. The matrix elements of $\tilde{\boldsymbol{F}}$ are given by

$$\tilde{\boldsymbol{F}}_{jk} = (\frac{\omega^{jk}}{\sqrt{N}})_{j,k=0,1,\cdots,N-1}, \tag{9.16}$$

where $\omega = e^{-\frac{2\pi i}{N}}$ and $i = \sqrt{-1}$. The exponent term in ω^{jk} is j times k, and should not be confused as indices. $\boldsymbol{F}^{*}$ is the inverse DFT matrix (also the conjugate of $\tilde{\boldsymbol{F}}$). It follows that $\tilde{\boldsymbol{F}}$ and $\tilde{\boldsymbol{F}}^{*}$ are unitary matrices, with the orthogonal property $\tilde{\boldsymbol{F}}\tilde{\boldsymbol{F}}^{*} = \boldsymbol{I}$. In eq. (9.14), Λ is a diagonal matrix whose elements are the eigenvalues of matrix $\boldsymbol{A}$. Since $\boldsymbol{A}$ is a circulant

matrix, its eigenvalues are fully determined by the first column, and can be calculated directly by its FFT (Hansen et al. 2006).

Using this property of circulant matrix we can reformulate the Fourier domain method in an explicit matrix form. Without loss of generality, we show the equivalence between the wavelength domain method (with a folded design matrix) and the Fourier domain method for the above toy example with a 3 by 2 design matrix. We start with eq. (9.3),

$$\mathbf{Ax} = \begin{pmatrix} \mathbf{A_{1,1}} & \mathbf{A_{1,2}} \\ \mathbf{A_{2,1}} & \mathbf{A_{2,2}} \\ \mathbf{A_{3,1}} & \mathbf{A_{3,2}} \end{pmatrix} . \begin{pmatrix} \mathbf{x_1} \\ \mathbf{x_2} \end{pmatrix} = \begin{pmatrix} \mathbf{b_1} \\ \mathbf{b_2} \\ \mathbf{b_3} \end{pmatrix} . \tag{9.17}$$

and each block of $\mathbf{A}$ is a circulant matrix (see Figure 9.7). We first block diagonalize matrix $\mathbf{A}$ by using a block diagonal matrix composed of the DFT matrix:

$$\begin{pmatrix} \tilde{\mathbf{F}}^* & \mathbf{0} & \mathbf{0} \\ \mathbf{0} & \tilde{\mathbf{F}}^* & \mathbf{0} \\ \mathbf{0} & \mathbf{0} & \tilde{\mathbf{F}}^* \end{pmatrix} . \begin{pmatrix} \tilde{\mathbf{\Lambda}}_{\mathbf{1,1}} & \tilde{\mathbf{\Lambda}}_{\mathbf{1,2}} \\ \tilde{\mathbf{\Lambda}}_{\mathbf{2,1}} & \tilde{\mathbf{\Lambda}}_{\mathbf{2,2}} \\ \tilde{\mathbf{\Lambda}}_{\mathbf{3,1}} & \tilde{\mathbf{\Lambda}}_{\mathbf{3,2}} \end{pmatrix} . \begin{pmatrix} \tilde{\mathbf{F}} & \mathbf{0} \\ \mathbf{0} & \tilde{\mathbf{F}} \end{pmatrix} . \begin{pmatrix} \mathbf{x_1} \\ \mathbf{x_2} \end{pmatrix} = \begin{pmatrix} \mathbf{b_1} \\ \mathbf{b_2} \\ \mathbf{b_3} \end{pmatrix} \tag{9.18}$$

Then multiply a block inverse DFT matrix on both sides and utilizing the orthogonal property, we find:

$$\begin{pmatrix} \mathbf{I} & \mathbf{0} & \mathbf{0} \\ \mathbf{0} & \mathbf{I} & \mathbf{0} \\ \mathbf{0} & \mathbf{0} & \mathbf{I} \end{pmatrix} . \begin{pmatrix} \tilde{\mathbf{\Lambda}}_{\mathbf{1,1}} & \tilde{\mathbf{\Lambda}}_{\mathbf{1,2}} \\ \tilde{\mathbf{\Lambda}}_{\mathbf{2,1}} & \tilde{\mathbf{\Lambda}}_{\mathbf{2,2}} \\ \tilde{\mathbf{\Lambda}}_{\mathbf{3,1}} & \tilde{\mathbf{\Lambda}}_{\mathbf{3,2}} \end{pmatrix} . \begin{pmatrix} \tilde{\mathbf{F}} & \mathbf{0} \\ \mathbf{0} & \tilde{\mathbf{F}} \end{pmatrix} . \begin{pmatrix} \mathbf{x_1} \\ \mathbf{x_2} \end{pmatrix} = \begin{pmatrix} \tilde{\mathbf{F}} & \mathbf{0} & \mathbf{0} \\ \mathbf{0} & \tilde{\mathbf{F}} & \mathbf{0} \\ \mathbf{0} & \mathbf{0} & \tilde{\mathbf{F}} \end{pmatrix} . \begin{pmatrix} \mathbf{b_1} \\ \mathbf{b_2} \\ \mathbf{b_3} \end{pmatrix} \tag{9.19}$$

The tomography equation eq. (9.3) is now written in the Fourier domain in eq. (9.20). Each block $\tilde{\mathbf{\Lambda}}_{\mathbf{jk}}$ in matrix Λ is a diagonal matrix with the diagonal elements equals to the FFT of the 1st column of the original block $\mathbf{A_{jk}}$ in matrix $\mathbf{A}$,

$$\begin{pmatrix} \tilde{\mathbf{\Lambda}}_{\mathbf{1,1}} & \tilde{\mathbf{\Lambda}}_{\mathbf{1,2}} \\ \tilde{\mathbf{\Lambda}}_{\mathbf{2,1}} & \tilde{\mathbf{\Lambda}}_{\mathbf{2,2}} \\ \tilde{\mathbf{\Lambda}}_{\mathbf{3,1}} & \tilde{\mathbf{\Lambda}}_{\mathbf{3,2}} \end{pmatrix} \cdot \begin{pmatrix} \tilde{\mathbf{x}}_{\mathbf{1}} \\ \tilde{\mathbf{x}}_{\mathbf{2}} \end{pmatrix} = \begin{pmatrix} \tilde{\mathbf{b}}_{\mathbf{1}} \\ \tilde{\mathbf{b}}_{\mathbf{2}} \\ \tilde{\mathbf{b}}_{\mathbf{3}} \end{pmatrix} \tag{9.20}$$

Then eq. (9.17) can now be decomposed into N independent equations for each frequency m, and for each m there are simply 3 equations with two complex variable unknowns.

$$\begin{pmatrix} \tilde{\lambda}_{1,1m} & \tilde{\lambda}_{1,2m} \\ \tilde{\lambda}_{2,1m} & \tilde{\lambda}_{2,2m} \\ \tilde{\lambda}_{3,1m} & \tilde{\lambda}_{3,2m} \end{pmatrix} \cdot \begin{pmatrix} \tilde{x}_{1m} \\ \tilde{x}_{2m} \end{pmatrix} = \begin{pmatrix} \tilde{b}_{1m} \\ \tilde{b}_{2m} \\ \tilde{b}_{3m} \end{pmatrix}, \; m = -N/2+1, \cdots, N/2. \tag{9.21}$$

Thus we have re-derived eq. (14) in Hensberge et al. (2008). This derivation can be trivially applied to matrix $\mathbf{A}$ of any dimensions (multiple systems, different number of observations). Note that the Fourier method assumes the spectrum is cyclically repeating which is un-physical (Hadrava 1995). This will affect the reconstruction at the extreme edges.

9.3.2 Spectra Separation in the Fourier Domain with Regularization

The regularized least squares method of spectra separation can be applied in the Fourier domain as well. In this domain, the equation $\mathbf{Ax} = \mathbf{b}$ decouples into n independent equations. Each equation has only two unknowns for a binary (or K unknowns in general) and corresponds to a Fourier frequency m ($m = -\frac{N}{2}+1, \cdots, \frac{N}{2}$, when N is even).

$$\begin{pmatrix} \tilde{\lambda}_{1,1m} & \tilde{\lambda}_{1,2m} \\ \tilde{\lambda}_{2,1m} & \tilde{\lambda}_{2,2m} \\ \tilde{\lambda}_{3,1m} & \tilde{\lambda}_{3,2m} \\ \alpha & 0 \\ 0 & \alpha \end{pmatrix} \cdot \begin{pmatrix} \tilde{x}_{1m} \\ \tilde{x}_{2m} \end{pmatrix} = \begin{pmatrix} \tilde{b}_{1m} \\ \tilde{b}_{2m} \\ \tilde{b}_{3m} \\ \tilde{x}_{prior1m} \\ \tilde{x}_{prior2m} \end{pmatrix}, \; m = -N/2+1 ... N/2. \tag{9.22}$$

This is simply an extension of eq. (9.13) in the Fourier domain. The low frequency modulation problem in the least square solution can also by solved by introducing regularization in the Fourier domain following the same procedure. The Fourier transform of the priors $\tilde{x}_{prior1}, \tilde{x}_{prior2}$ for frequency m appear in the right hand side of eq. (9.22).

In the following example, we show the advantage of regularization for a binary system with a very faint companion. KOI-81 is an eclipsing binary system composed of a fast-rotating B star and a faint and hot sub-dwarf companion. The flux ratio of the companion to the B stars f_2/f_1 is only about 0.008 in Kepler band. Matson et al. (2015) reconstructed the spectrum of the faint companion in the UV band, in which the flux ratio f_2/f_1 increases to about 0.05 at 1370 Å. Matson et al. (2015) first used a flat continuum as an initial estimate and then used a model spectrum as the starting values for their reconstruction. As the noise in the reconstructed spectrum is inversely proportional to the flux contribution, the reconstructed spectrum of the faint companion is very noisy. They were still able to identify some features, such as the Si II lines at $1295, 1297, 1299$Å, and the Si IV lines at $1394, 1403$Å. Based on these identifications, they derived a lower limit estimate for the effective temperature of the hot companion.

We did the reconstruction for the same system by using the same data. We used a prior spectrum for the faint companion, which is generated by the first 5 lowest Fourier frequencies of a model spectrum from UVBLUE library with $T_{\rm eff} = 19000$ K and $\log g = 5.0$. The prior spectrum is essentially featureless except for a dip due to the broad Lyα λ1216 line (the red line in the upper panel of Figure 9.8). The regularized reconstruction indicated by the

black line in the upper panel of Figure 9.8 shows a much smaller noise amplitude compared to the result from the BG91 algorithm (green). All lines identified in Matson et al. (2015) are also present in our reconstruction as shown in the middle and lower panels. However, the regularized solution (black) from our algorithm follows more closely to the model (red), while the BG91 result (green) deviates from the model greatly. This improvement makes it possible to identify more spectral lines.

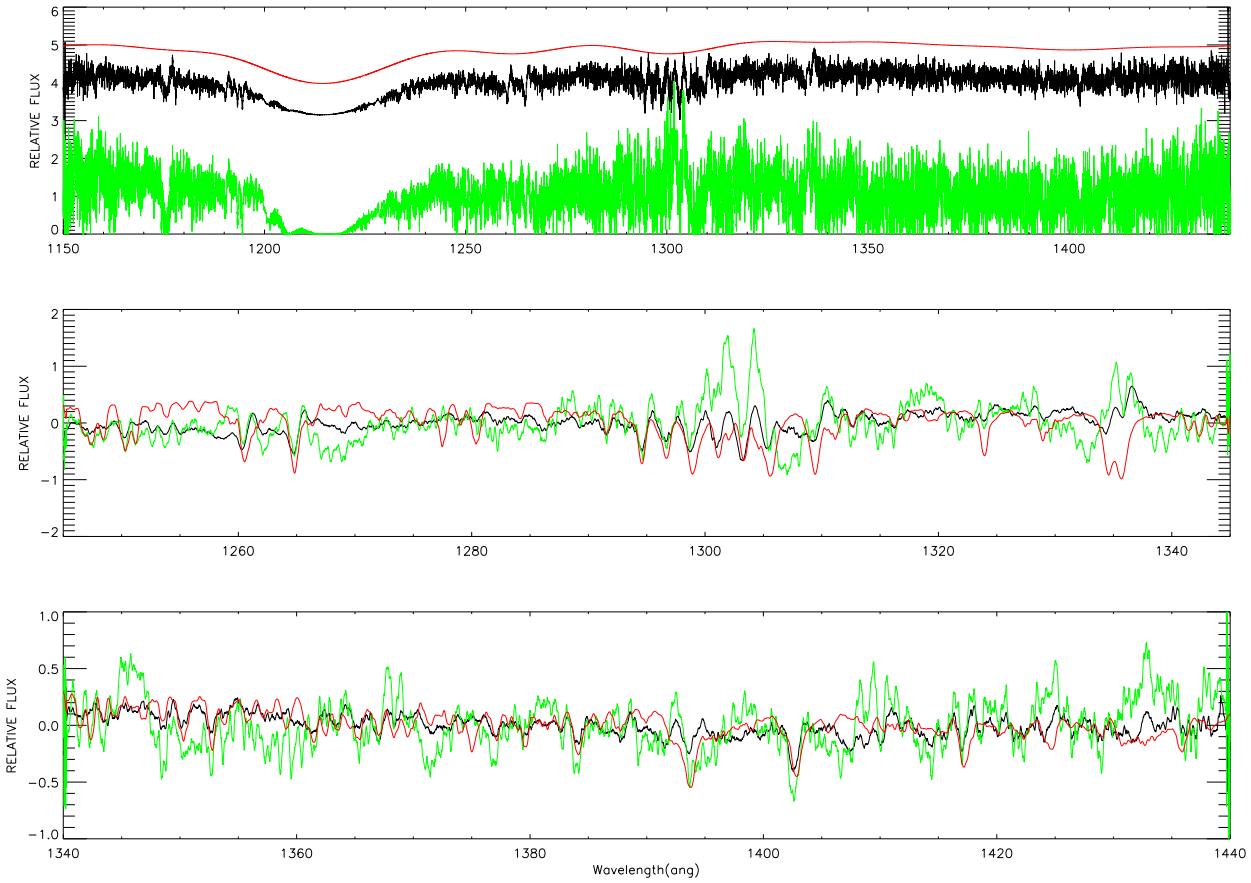

Figure 9.8 Reconstructed spectra of KOI-81 with regularization in Fourier domain. **Upper panel:** The reconstruction of the hot subdwarf star with two methods, BG91 algorithm (green), FT with regularization (black). The prior spectrum is indicated by the solid red line. **Middel & Lower panel:** comparison of the reconstructed spectrum of the hot star from the BG91 algorithm (green) and FT with regularization (black) with the model (red). All spectra have been smoothed by convolution with a box car of width 133 km s^{-1} as done by Matson et al. (2015).

9.4 Regularization in Bayesian Inference

9.4.1 Bayesian Linear Regression with Gaussian Variables

Bayesian inference is ubiquitous in statistics. It allows us to update the current probabilities as new data are acquired. It is actually an extension of the basic *and* &*or* logic and represents a basic method of reasoning.

The basic product rule in probability theory is that the joint probability of random variables $\mathbf{x}$ (model) and $\mathbf{b}$ (data) can be decomposed by the conditional probability of $\mathbf{x}$ given $\mathbf{b}$ and the probability of $\mathbf{b}$ as well as the conditional probability of $\mathbf{b}$ given $\mathbf{x}$ and the probability of $\mathbf{x}$: $p(\mathbf{x}, \mathbf{b}) = p(\mathbf{x}|\mathbf{b})p(\mathbf{b}) = p(\mathbf{b}|\mathbf{x})p(\mathbf{x})$. This leads to the bayes' theorem: $p(\mathbf{x}|\mathbf{b}) = p(\mathbf{b}|\mathbf{x})p(\mathbf{x})/p(\mathbf{b})$, where $p(\mathbf{x})$ is the prior probability distribution of the model $\mathbf{x}$. $p(\mathbf{x}|\mathbf{b})$ is the posterior distribution of $\mathbf{x}$ after we are given the new data $\mathbf{b}$. $p(\mathbf{b}|\mathbf{x})$ is often called the likelihood function if treated as a function of $\mathbf{x}$. $p(\mathbf{b})$ is a constant term called marginal likelihood or Bayesian evidence.

In the Bayesian statistical method, we treat both the concatenated component spectra $\mathbf{x}$ and concatenated observed spectra $\mathbf{b}$ as random variables. As the pixel intensities in the spectrum are photon counts, it is a Poisson process and each pixel intensity should satisfy a Poisson distribution. When the S/N is larger than, e.g., ~ 10, the distribution can be well approximated by a Gaussian as the result of the central limit theorem. Closely following the derivation in Aster et al. (2012), we assume $\mathbf{x}$ satisfies a multivariate Gaussian distribution:

$$p(\mathbf{x}) = N(\mathbf{x}|\mathbf{x}_{prior}, \mathbf{C}_X) = (2\pi)^{-\frac{n}{2}}|\mathbf{C}_X|^{-\frac{1}{2}}e^{-\frac{1}{2}(\mathbf{x}-\mathbf{x}_{prior})^T\mathbf{C}_X^{-1}(\mathbf{x}-\mathbf{x}_{prior})} \tag{9.23}$$

where n is the number of elements in $\mathbf{x}$. We use a prior model distribution $p(\mathbf{x})$ to best represent our prior knowledge of the concatenated component spectra. $\mathbf{x}_{prior}$ is the mean of this prior distribution. Our prior knowledge about the overall continuum level, the dip at some broad hydrogen lines, and other spectral features are included in $\mathbf{x_{prior}}$. $\mathbf{C}_X$ is the covariance matrix of the prior distribution, and it incorporates our prior knowledge of the correlations between different pixels in the component spectra. $|\mathbf{C}_X|$ is the determinant of $\mathbf{C}_X$. $\mathbf{\Lambda} = \mathbf{C}_X^{-1}$ is the precision matrix which is the inverse of covariance matrix.

The noise in the observed composite spectra is also modeled by a multivariate Gaussian distribution, with the mean value of zero. This is equivalent to assuming that $\mathbf{b}$ is a multivariate Gaussian, with a mean of $\mathbf{Ax}$ and covariance $\mathbf{C}_B$. The likelihood function or the conditional distribution of data given model is

$$p(\mathbf{b}|\mathbf{x}) = N(\mathbf{b}|\mathbf{Ax}, \mathbf{C}_B) \propto e^{-\frac{1}{2}(\mathbf{Ax}-\mathbf{b})^T\mathbf{C}_B^{-1}(\mathbf{Ax}-\mathbf{b})} \tag{9.24}$$

When the prior and likelihood are both Gaussians with known covariance matrices, the posterior and the Bayesian evidence can both be represented elegantly as normal distributions. Following Bishop (2006), the posterior distribution of the component spectra $\mathbf{x}$ is:

$$p(\mathbf{x}|\mathbf{b}) \propto e^{-\frac{1}{2}((\mathbf{Ax}-\mathbf{b})^T\mathbf{C}_B^{-1}(\mathbf{Ax}-\mathbf{b})+(\mathbf{x}-\mathbf{x}_{prior})^T\mathbf{C}_X^{-1}(\mathbf{x}-\mathbf{x}_{prior}))} \tag{9.25}$$

$$p(\mathbf{x}|\mathbf{b}) = N(\mathbf{x}|\mathbf{x}_{MAP}, \mathbf{C}_{X'}) \propto e^{-\frac{1}{2}(\mathbf{x}-\mathbf{x}_{MAP})^T\mathbf{C}_{X'}^{-1}(\mathbf{x}-\mathbf{x}_{MAP})} \tag{9.26}$$

$$\mathbf{x}_{MAP} = \mathbf{C}_{\mathbf{X}'}(\mathbf{A}^T\mathbf{C}_B^{-1}\mathbf{b} + \mathbf{C}_X^{-1}\mathbf{x}_{prior}) \tag{9.27}$$

$$\mathbf{C}_{X'} = (\mathbf{C}_X^{-1} + \mathbf{A}^T \mathbf{C}_B^{-1} \mathbf{A})^{-1} \tag{9.28}$$

where the mean and the mode of the posterior, which is also the best reconstructed spectrum, is $\mathbf{x}_{\mathrm{MAP}}$. Its uncertainties are contained in the covariance matrix $\mathbf{C}_{X'}$.

The Bayesian evidence (also called the marginal likelihood) is given by:

$$\begin{aligned} p(\mathbf{b}) &= N(\mathbf{b}|\mathbf{A}\mathbf{x}_{prior}, \mathbf{C}_{B'}) \\ \text{where} \quad \mathbf{C}_{B'} &= \mathbf{C}_B + \mathbf{A}\mathbf{C}_X\mathbf{A}^T. \end{aligned} \tag{9.29}$$

The evidence is usually calculated in logarithmic form,

$$\begin{aligned} \ln Z &= \ln(p(\mathbf{b})) = \ln N(\mathbf{b}|\mathbf{A}\mathbf{x}_{prior}, \mathbf{C}_{B'}) \\ &= \ln[(2\pi)^{-\frac{N}{2}} |\mathbf{C}_{B'}|^{-\frac{1}{2}} e^{-\frac{1}{2}(\mathbf{b}-\mathbf{A}\mathbf{x}_{prior})^T \mathbf{C}_{B'} (\mathbf{b}-\mathbf{A}\mathbf{x}_{prior})}] \\ &= -\frac{N}{2}\ln(2\pi) - \frac{1}{2}\ln(|\mathbf{C}_{B'}|) - \frac{1}{2}(\mathbf{b}-\mathbf{A}\mathbf{x}_{prior})^T \mathbf{C}_{B'} (\mathbf{b}-\mathbf{A}\mathbf{x}_{prior}). \end{aligned} \tag{9.30}$$

After Cholesky decomposing $\mathbf{C}_{B'}$ as $\mathbf{C}_{B'} = \mathbf{L}\mathbf{L}^T$, the determinant $|\mathbf{C}_{B'}|$ can be calculated as the product of squares of the diagonal elements of $\mathbf{L}$:

$$\ln(|\mathbf{C}_{B'}|) = \ln(\prod_i L_{ii}^2) = 2\sum_i (\ln L_{ii}). \tag{9.31}$$

Thus the tomography algorithm reduces to a problem of simple linear algebra as given in equation (9.27, 9.28). This is just a basic Bayesian linear regression with Gaussian variables. Given the importance of Gaussian distributions, we repeat the above equations (Bishop 2006;

eq. $2.113 - 2.117$) below.

Assume random variables x and b are related by the linear equation

$$\boldsymbol{b} = \boldsymbol{A}\boldsymbol{x}. \tag{9.32}$$

Suppose we are given a prior Gaussian distribution for $\boldsymbol{x}$ and a likelihood function for $\boldsymbol{b}$ given $\boldsymbol{x}$ which is also a Gaussian distribution,

$$\begin{aligned} &\text{Prior} : p(\mathbf{x}) = N(\mathbf{x}|\mathbf{x}_{prior}, \mathbf{C}_X) \\ &\text{Likelihood} : \ p(\mathbf{b}|\mathbf{x}) = N(\mathbf{b}|\mathbf{A}\mathbf{x}, \mathbf{C}_B) \end{aligned} \tag{9.33}$$

Then the posterior distributions for $\boldsymbol{x}$ and the Bayesian evidence are both Gaussians given by

$$\begin{aligned} &\text{Posterior} : \ p(\mathbf{x}|\mathbf{b}) = N(\mathbf{x}|\mathbf{x}_{MAP}, \mathbf{C}_{X'}) \\ &\quad \text{where} \quad \mathbf{x}_{MAP} = \mathbf{C}_{\mathbf{X}'}(\mathbf{A}^T\mathbf{C}_B^{-1}\mathbf{b} + \mathbf{C}_X^{-1}\mathbf{x}_{prior}) \\ &\qquad\qquad \mathbf{C}_{X'} = (\mathbf{C}_X^{-1} + \mathbf{A}^T\mathbf{C}_B^{-1}\mathbf{A})^{-1} \\ &\text{Evidence (Marginal likelihood)} : \ p(\mathbf{b}) = N(\mathbf{b}|\mathbf{A}\mathbf{x}_{prior}, \mathbf{C}_B + \mathbf{A}\mathbf{C}_X\mathbf{A}^T). \end{aligned} \tag{9.34}$$

9.4.2 Tikhonov Regularization in Bayesian Framework

Here, we show that the aforementioned Tikhonov regularization in the 0, 1, 2 order (section 9.2.2) can also be cast as the above Bayesian linear regression problem.

Assuming the different pixel values in the component spectra are independent, then the covariance matrix of the prior distribution $p(\mathbf{x})$ is $\mathbf{C}_X = \beta^2\mathbf{I}$. $\mathbf{I}$ is the identity matrix . We also assume the covariance matrix of the observed spectra vector $\mathbf{b}$ is $\mathbf{C}_B = \sigma^2\mathbf{I}$. Then the posterior (eq. 9.25) simplifies to

$$\begin{aligned} &\propto \exp\{-0.5[(\mathbf{Ax}-\mathbf{b})^T\mathbf{C}_B^{-1}(\mathbf{Ax}-\mathbf{b}) + (\mathbf{x}-\mathbf{x}_{prior})^T\mathbf{C}_X^{-1}(\mathbf{x}-\mathbf{x}_{prior})]\} \\ &= \exp\{-0.5[\frac{1}{\sigma^2}|\mathbf{Ax}-\mathbf{b}|^2 + \frac{1}{\beta^2}|\mathbf{x}-\mathbf{x}_{prior}|^2]\}. \end{aligned} \tag{9.35}$$

Thus maximizing the posterior is just a zero-order Tikhonov regularization problem:

$$minimize\ |\mathbf{Ax}-\mathbf{b}|^2 + \frac{\sigma^2}{\beta^2}|\mathbf{x}-\mathbf{x}_{prior}|^2. \tag{9.36}$$

Following the previous notation, the regularization parameter α is then given by $\alpha^2 = \frac{\sigma^2}{\beta^2}$. Thus the 0-order Tikhonov regularization parameter α is interpreted as the ratio of the noise level in the observed spectra to that in the reconstructed spectra (assuming the noise in both spectra are identical independent distributed).

For the 1st and 2nd order Tikhonov regularization, following Bui-Thanh (2012), if we set the covariance matrix of $\mathbf{x}$ as $\mathbf{C}_X = \beta^2\mathbf{SS}^T$, where $\mathbf{S} = \mathbf{L}^{-1}$ is the inverse of the difference

matrix $\mathbf{L}$ defined in eq. (9.12), then we have

$$\begin{aligned}\mathbf{C}_X^{-1} &= \frac{1}{\beta^2}(\mathbf{S}\mathbf{S}^T)^{-1} = \frac{1}{\beta^2}(\mathbf{S}^T)^{-1}(\mathbf{S}^{-1}) \\ &= \frac{1}{\beta^2}(\mathbf{S}^{-1})^T(\mathbf{S}^{-1}) = \frac{1}{\beta^2}\mathbf{L}^T\mathbf{L}\end{aligned} \tag{9.37}$$

Then the posterior reduces to:

$$\begin{aligned}&\propto \exp\{-0.5[(\mathbf{A}\mathbf{x}-\mathbf{b})^T\mathbf{C}_B^{-1}(\mathbf{A}\mathbf{x}-\mathbf{b}) + (\mathbf{x}-\mathbf{x}_{prior})^T\mathbf{C}_X^{-1}(\mathbf{x}-\mathbf{x}_{prior})]\} \\ &\text{term in } [\,] = \frac{1}{\sigma^2}|\mathbf{A}\mathbf{x}-\mathbf{b}|^2 + \frac{1}{\beta^2}(\mathbf{x}-\mathbf{x}_{prior})^T\mathbf{L}^T\mathbf{L}(\mathbf{x}-\mathbf{x}_{prior}) \\ &= \frac{1}{\sigma^2}|\mathbf{A}\mathbf{x}-\mathbf{b}|^2 + \frac{1}{\beta^2}[\mathbf{L}(\mathbf{x}-\mathbf{x}_{prior})]^T[\mathbf{L}(\mathbf{x}-\mathbf{x}_{prior})] \\ &= \frac{1}{\sigma^2}|\mathbf{A}\mathbf{x}-\mathbf{b}|^2 + \frac{1}{\beta^2}|\mathbf{L}(\mathbf{x}-\mathbf{x}_{prior})|^2.\end{aligned} \tag{9.38}$$

Thus, in general maximizing the posterior is equivalent to the Tikhonov regularization problem:

$$minimize\ |\mathbf{A}\mathbf{x}-\mathbf{b}|^2 + \frac{\sigma^2}{\beta^2}|\mathbf{L}(\mathbf{x}-\mathbf{x}_{prior})|^2 \tag{9.39}$$

We thus can set $\alpha^2 = \frac{\sigma^2}{\beta^2}$, and the above equation is then the same as eq. (9.11). We have some estimates of the measurement errors of the composite spectra $\mathbf{b}$ (the covariance matrix $\mathbf{C}_B = \sigma^2\mathbf{I}$). However, the uncertainties of the component spectrum $\mathbf{x}$, which are unknown, are harder to quantify. Thus, β can be treated as a regularization parameter, equivalent to the role of α.

Recall the definition of $\mathbf{C}_X = \beta^2\mathbf{S}\mathbf{S}^T$, where $\mathbf{S} = \mathbf{L}^{-1}$. For a vector $\mathbf{x}$ of dimension $N \times 1$, its covariance matrix $\mathbf{C}_X$ should be $N \times N$. So $\mathbf{S}$ and $\mathbf{L}$ are both $N \times N$ matrices. However, the finite difference matrix $\mathbf{L}_2$ defined in eq. (9.12) is $(N-2) \times N$. That is, $\mathbf{L}_2$ has rank of

$N-2$. Hence, if directly using $\mathbf{L}_2$ to construct the covariance matrix, the prior distribution $p(\mathbf{x})$ will be a Gaussian density in R^{N-2} which is degenerate in R^N space (Bui-Thanh 2012). The reason is that we have not specified the smoothness at the two boundary points. To this end, we define the revised form of $\mathbf{L}_2$ as

$$\mathbf{L}_D = \begin{bmatrix} \delta_1 & 0 & & & & & & \\ 1 & -2 & 1 & & & & & \\ & 1 & -2 & 1 & & & & \\ & & \ddots & \ddots & \ddots & & & \\ & & & 1 & -2 & 1 & & \\ & & & & 1 & -2 & 1 & \\ & & & & & 0 & \delta_n & \end{bmatrix} \tag{9.40}$$

We do not know the values of $\mathbf{x}$ at the two boundary points ($i = 1$ and $i = N$), and thus we assume they are Gaussian variables with a mean of zero and standard deviations of δ_1 and δ_N, respectively. Their values can be estimated assuming each point ($i = 1, \cdots, N$) has the same variance. In the process of prior elicitation via differential operators, it is a crucial to make sure that the operator is positive definite by incorporating some well-posed boundary conditions (Bui-Thanh 2012).

9.4.3 Choosing the Regulariztion Parameter by Maximizing Bayesian Evidence

To choose an appropriate regularization parameter, except for the aforementioned L-curve and cross-validation methods, we can maximize the Bayesian evidence in eq. (9.29). Thanks to the properties of Gaussians, the Bayesian evidence can be directly computed (eq. 9.30, 9.31). We denote the evidence as $\log Z = \ln(p(\mathbf{b}))$.

We consider a synthetic binary system. The two stars in the system have same atmo-

spheric parameters: $(T_{\rm eff}, \log g, [{\rm M/H}], v \sin i)$=(12000 K, 3.0, 0.0, 100 km s^{-1}). We generate five synthetic composite spectra by shifting the component spectra of star 1 and star 2 by their RVs: ${\rm RV}_1 = (-4.0, 4.5, 4.3, 4.0, 3.5)$ pixels and ${\rm RV}_2 = (4.0, -4.5, -4.3, -4.0, -3.5)$ pixels, respectively. We multiply the component spectra by their flux contribution ($f_1 = 0.6$, $f_2 = 0.4$) before the linear summation. Random Gaussian noise (with standard deviation $\sigma = 0.01$) is added to the composite spectra. Figure 9.9 shows these composite spectra and the true component spectra that are used to generate them.

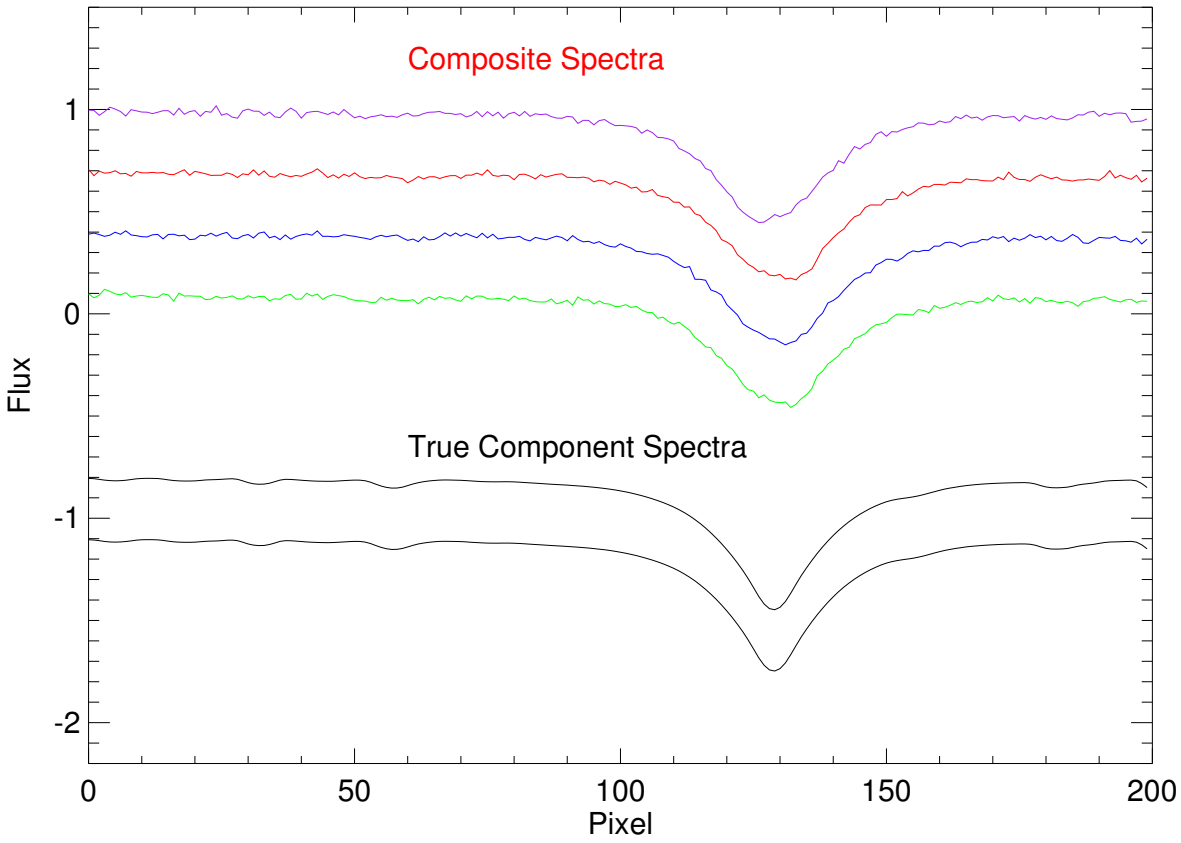

Figure 9.9 True component spectra (black) of the star 1 and star 2 in the synthetic binary system. The component spectra are shifted accroding to the RVs to generate the composite spectra (color). Only four composite spectra (out of five) are shown.

We then reconstruct the component spectra following the procedures in section 9.4.2. Assuming independent noise in the composite spectra $\boldsymbol{b}$ and treating the uncertainty of the component spectra β as a regularization parameter, the individual (component) spectra are calculated in the 0th order Tikhonov scheme. We adopt the best regularization parameter as the one that maximizes the Bayesian evidence (log Z) (eq. 9.30), and this is shown in

Figure 9.10 where red cross indicates the peak of $\log Z$ at $\beta_{best} = 0.016$.

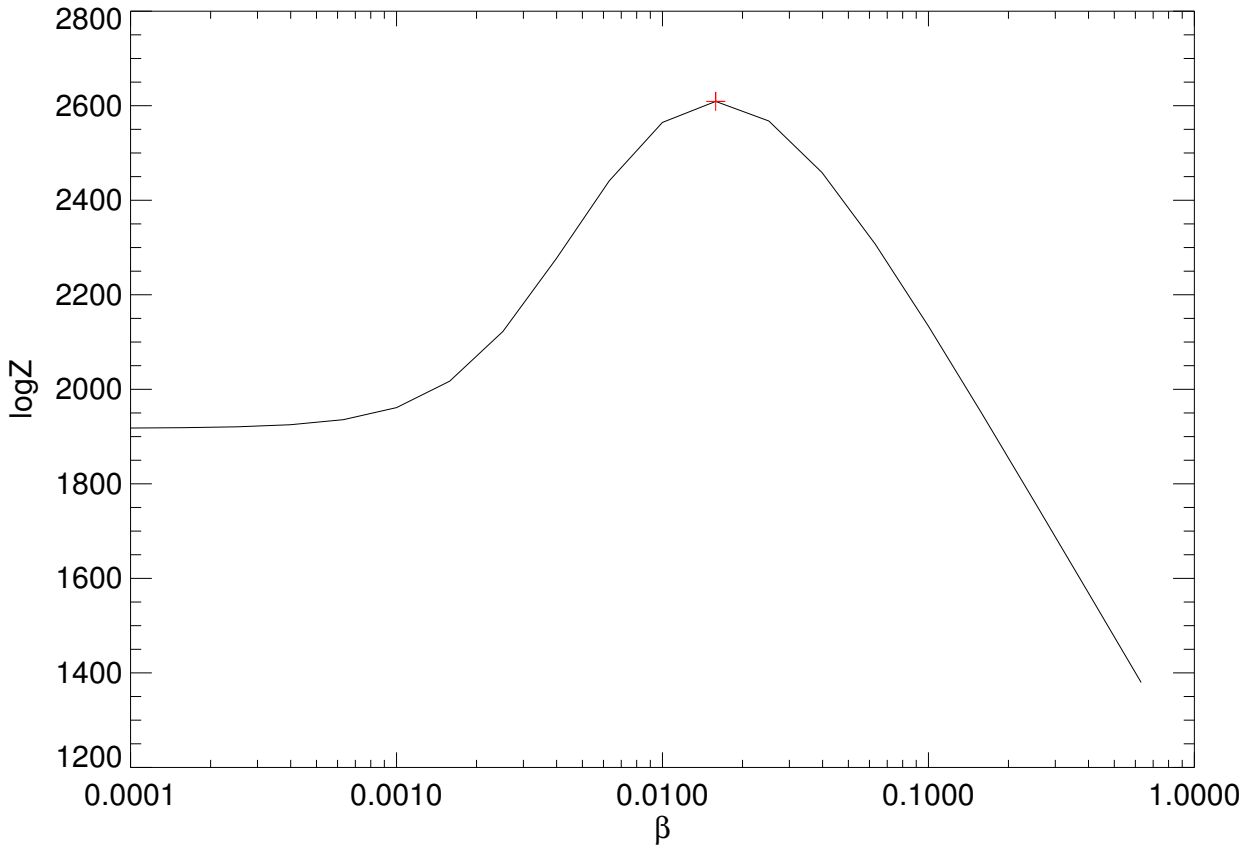

Figure 9.10 The Bayesian evidence logZ for a grid of regularization parameter β. The maximum is marked by the red cross.

The reconstructed spectra (the $\mathbf{x}_{\mathrm{MAP}}$ in eq. 9.27) are shown in Figure 9.11 as black solid lines. Two gray lines above and below are the $+2\sigma$ and -2σ uncertainties. The true component spectra are indicated by the solid red lines. In principle, the uncertainties of reconstructed spectra should roughly scaled with $1/\sqrt{N}$ times the original uncertainty in the composite spectra if the two stars have the same flux.

Bayesian evidence seems to work fine in setting an appropriate regularization parameter for this simple example. It is interesting to compare and evaluate different methods of choosing regularization parameters. This will be presented in a future study.

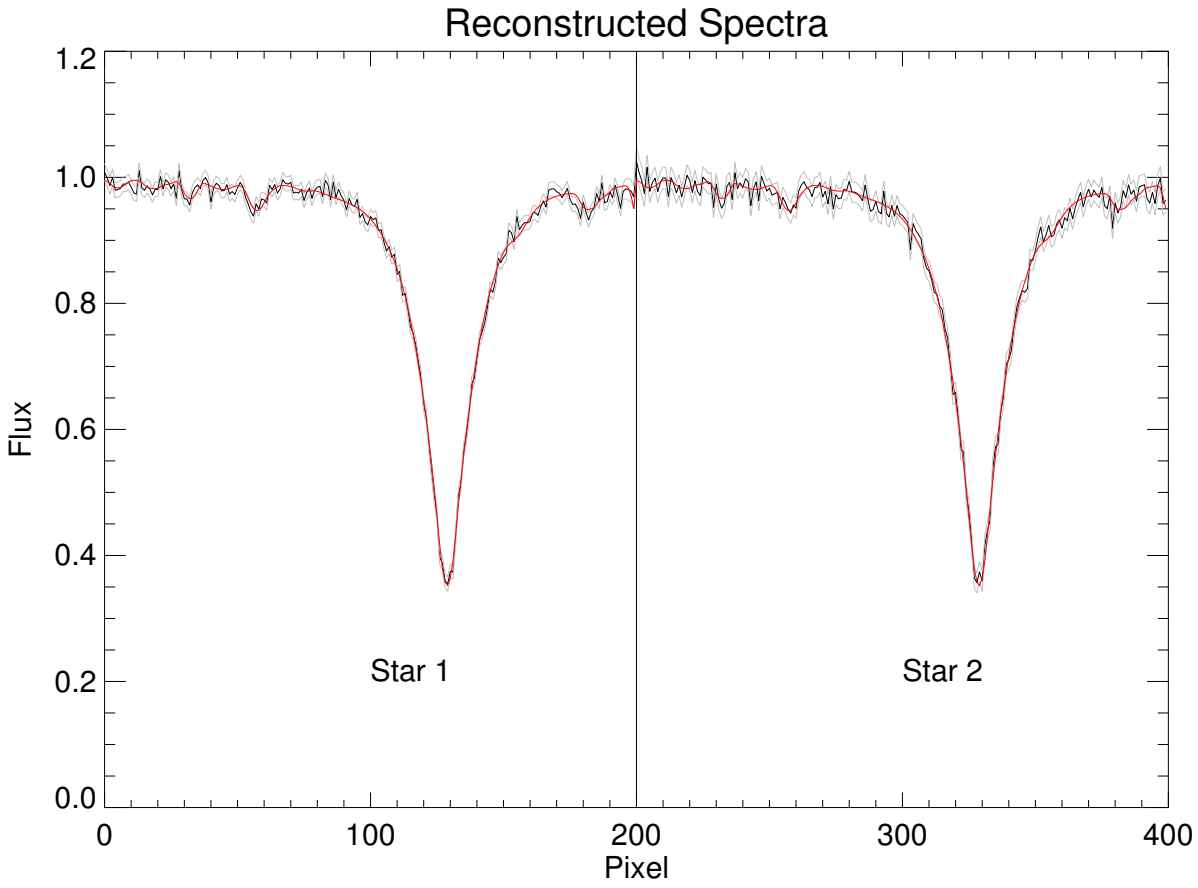

Figure 9.11 The reconstructed spectra ($\mathbf{x}_{\mathrm{MAP}}$ in eq. 9.27) for star 1 and star 2 (black solid line). Two gray lines above and below are the $+2\sigma$ and -2σ uncertainties, respectively. The true component spectra are indicated by the solid red lines.

9.4.4 Choosing the Regularization Parameter with Hierarchical Bayesian Models

The Bayesian evidence is generally very hard to calculate. Analytical forms hardly exist, and the previous section for Gaussian variables is a rare exception. In Bayesian philosophy, if we do not know anything about a parameter (regularization parameter in this case), let it be a random variable. This naturally leads to the method of hierarchical Bayesian models.

We have demonstrated that the Bayesian approach to tomographic reconstruction is equivalent to the use of α and β as regularization parameters, where $\mathbf{C}_X = \beta^2\mathbf{I}$ is the covariance of the prior distribution $p(\mathbf{x})$. Since β is a new unknown parameter, the prior distribution becomes the joint distribution of β and $\mathbf{x}$,

$$p(\mathbf{x}, \beta) = p(\mathbf{x}|\beta)p(\beta). \tag{9.41}$$

Using the Bayes' rule, the posterior is,

$$p(\mathbf{x}, \beta|\mathbf{b}) \propto p(\mathbf{b}|\mathbf{x}, \beta)p(\mathbf{x}, \beta) = p(\mathbf{b}|\mathbf{x}, \beta)p(\mathbf{x}|\beta)p(\beta). \tag{9.42}$$

With a proper sampling algorithm (e.g., MCMC), we can get the posterior samples from eq. (9.42). Thus both $\mathbf{x}$ and β are determined from data, that is, the regularization parameter is naturally chosen by the data we have, along with the reconstructed spectra $\mathbf{x}$.

In practice, we need the posterior sample for each pixel in the spectrum. To make sure of the convergence of Markov chains, usually $\sim 10^4$ iterations are needed. This makes the reconstruction relatively expensive in computational time. We only consider a toy model here. We use the same spectra desrcibed in the previous section for star 1 and star 2. Each

component spectrum has 20 pixels. We consider only three composite spectra, corresponding to $\mathrm{RV}_1 = (-4.8, 0.6, -4.4)$ pixels and $\mathrm{RV}_2 = (2.4, -0.3, 2.2)$ pixels. The flux contributions of the two stars are the same as before ($f_1 = 0.6,\ f_2 = 0.4$). The generated composite spectra and original component spectra are shown in Figure 9.12.

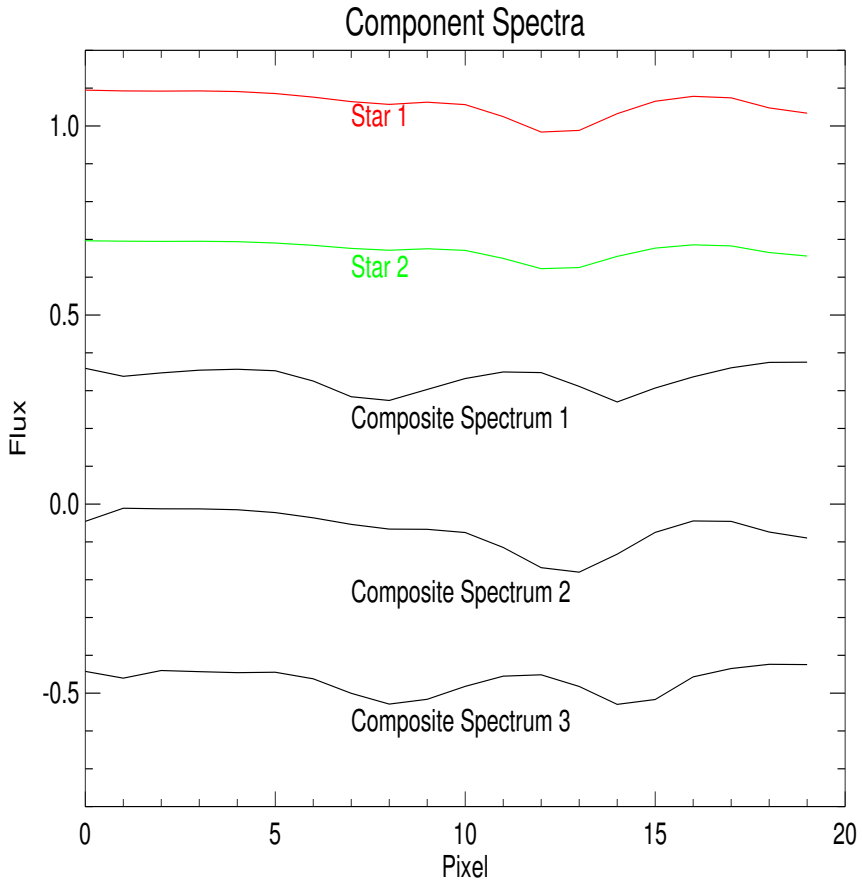

Figure 9.12 True component spectra of star 1 (red) and star 2 (green). The component spectra are shifted accroding to the RVs to generate the three composite spectra (black) that appear offset below.

The uncertainties of the composite spectra are assumed to be known, which all satisfy

a normal distribution with $\sigma = 0.02$ (independent noise), and the covariance matrix of $\boldsymbol{b}$ is $\boldsymbol{C}_B = \sigma^2 \boldsymbol{I}$. We use a flat spectrum as the prior mean for the component spectra $\mathbf{x}$ with all values equal to 1.0. The covariance matrix of the component spectra is $\boldsymbol{C}_X = \beta^2 \boldsymbol{I}$, and β is an unknown regularization parameter. We set a hyperprior on β as a Gamma distribution $p(\beta) = \text{Gamma}(0.01, 0.01)$. Note that the Gamma distribution is a commonly used, non-informative distribution for an unknown scale parameter such as the standard deviation of a Gaussian. It is very similar to the Jeffreys prior (uniform prior on a log-scale) when the two input parameters are small.

We use the Gibbs sampling implemented in JAGS to find the posterior samples of β and $\boldsymbol{x}$. The posterior distribution of hyperparameter β is shown in Figure 9.13. The reconstructed spectra (the mean or maximum posterior of $\boldsymbol{x}$: $\bar{\boldsymbol{x}} = \boldsymbol{x}_{MAP}$) are shown in Figure 9.14, with $\bar{\boldsymbol{x}} \pm \sigma_{\boldsymbol{x}}$ indicated by dotted lines.

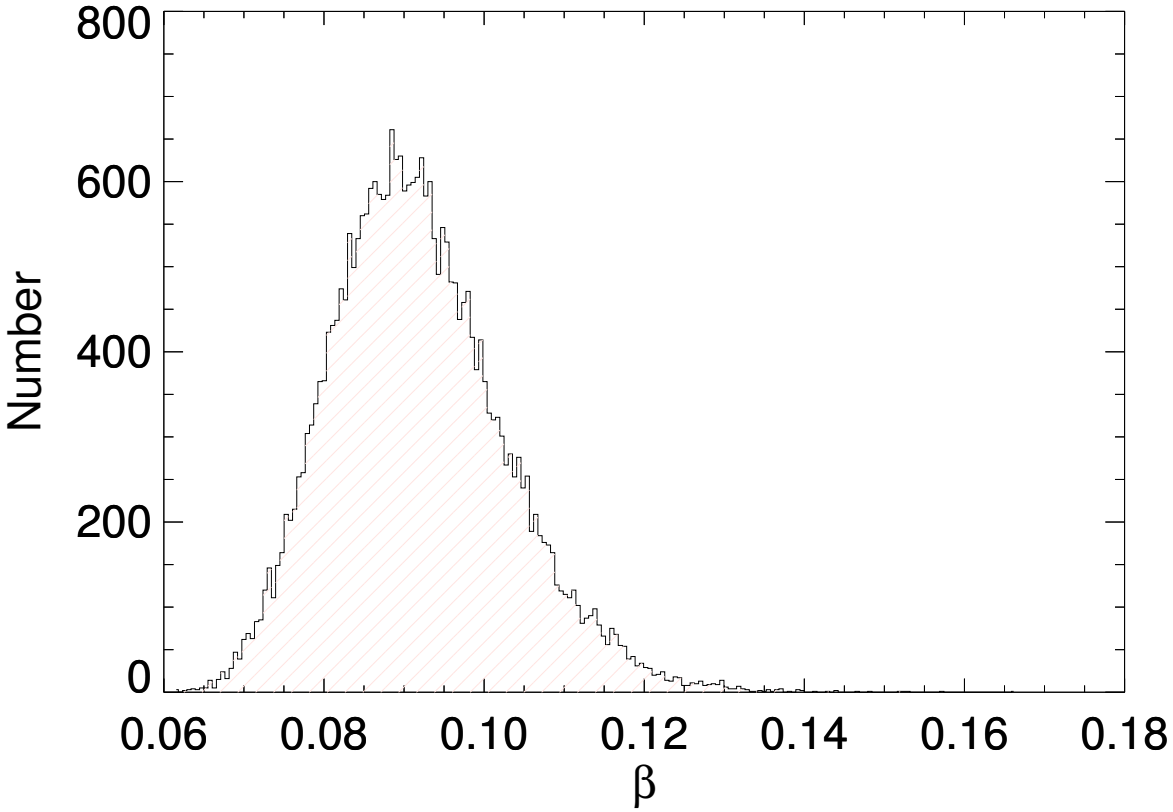

Figure 9.13 The posterior distribution of hyperparameter β (as a regularization parameter)

.

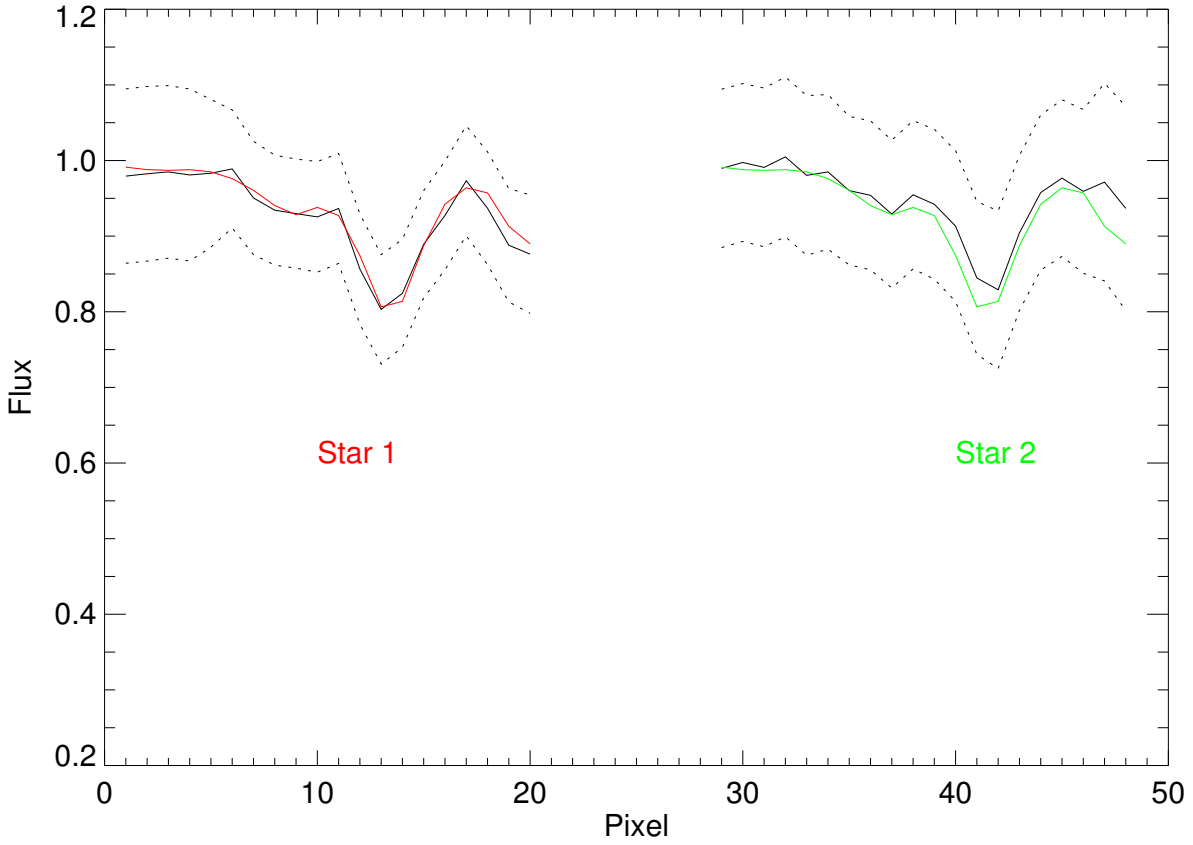

Figure 9.14 The maximum posterior solution of component spectra $\boldsymbol{x}$. Dotted lines indicate the $+1\sigma$ and -1σ percentile. True component spectra are indicated by the red and green solid lines, for stars 1 and 2, respectively.

We show the JAGS code in the following, which is a basic linear regression problem ($y = X \cdot beta$): solving for *beta* given y and X. *beta* is the component spectra vector and y is composite spectra vector. Note that we use different notations here, where previously $b = A \cdot x$, and b corresponds to y, matrix A corresponds to X, and the component spectra vector x corresponds to β. The hyperparameter β defined in the last paragraph is denoted

as *tau*. *dmnorm* in the code is the multi-normal distribution. The *inprod* function is the inner product of two vectors. Note that in JAGS the normal distribution $N(\mu, \sigma^2)$ is written as dnorm(μ,$1/\sigma^2$), i.e., JAGS uses a precision matrix instead of covariance matrix.

A Hierarchical Bayesian Model for Tomography

```
model {


#  define the identity matrix
for (l in 1:50) {
   for (j in 1:50) {
 V[l,j] <-  ifelse(l==j, 1, 0)}
}


#precision matrix, tau is unknown
for (l in 1:50) {
for(j in 1:50) {
prior.T[l,j] <- V[l,j]*tau
}
}



   # likelihood function for each pixel
for (i in 1:60){
y[i] ~ dnorm(mu[i], 1/(0.02*0.02))
mu[i]<- inprod( beta[ ], X[i, ])
```

```
}


# prior for beta (component spectra)

beta[1:50]~ dmnorm(mu.beta[ ], prior.T[ , ])


#hyperprior for tau

tau ~ dgamma(0.01,0.01)




}
```

9.5 Discussion

In practice, uncertainties in the reconstructed spectra $\boldsymbol{x}$ are from two sources. One is from the algorithm itself, which we have already characterized by the diagonal elements of covariance matrix $\boldsymbol{C}_X$ in the previous sections. The other source, however, is the design matrix $\boldsymbol{A}$. Our discussions in previous sections are all based on a fixed design matrix $\boldsymbol{A}$. Uncertainties related to the radial velocities contribute to the uncertainties of $\boldsymbol{A}$, and thus to the errors in the reconstruction $\boldsymbol{x}$. One simple way to take this into account is to use the Monte Carlo method. After deriving RVs from cross correlation, we can fit the RVs with Markov Chain Monte Carlo and get posterior samples of orbital parameters (e.g, $(P, T_0, K, e, \omega, \gamma)_i$ for $i = 1, 2, \cdots, N$, where N is the length of the Markov Chains. For each sample i, we calculate the corresponding RVs and use these to construct a design matrix $\boldsymbol{A}_i$. Thus we can perform tomography for each $\boldsymbol{A}_i$, and get many reconstructed spectra $\boldsymbol{x}_i$. The uncertainties of $\boldsymbol{x}$ are then inferred from the distribution of $\boldsymbol{x}_i$ using values at certain percentiles.

Although this chapter covers many techniques for spectral separation (tomography), a lot of work remains to be done.

1. We need to extend the hierarchical Bayesian tomography to large scale problems (a few thousands pixels).

2. Comparing and evaluating different methods of determining regularization parameters.

3. Effects of different phase coverage and numbers of RVs on the reconstruction. Hynes & Maxted (1998) did some tests for spectral disentangling and discussed briefly about phase coverage. Pál (2009) investigated the best phases for a limited number of RVs (4 or 5)

by using an analytical formula for Kepler's problem. This is related to the problem of experimental design discussed in the previous section of Chapter 8.

4. The effect of uncertainties from light ratio.

5. Quantification of the low frequency modulations in the spectra. The shape of the continuum in the raw spectra, e.g., those from an echelle spectrograph, are due to the blaze function of the gratings in the instrument. In the data reduction process, the spectra are usually normalized to the continuum and this involves de-trending with some kind of polynomial or spline. These modulations will propagate to the final reconstructed spectra.

6. Assigning better covariance matrix for the composite spectra $\boldsymbol{b}$. The Gaussian process (GP) is one of the tools for this (Rasmussen & Williams 2006). The kernel width used in the GP can be characterized from the autocorrelation of spectral pixels.

These techniques for spectral separation can be naturally applied to other linear or non-linear inverse problems, not necessarily astronomical. For example, measuring the structure of the broad emission-line region with reverberation mapping (Brewer & Elliott 2014), determining the mass density from gravitational lensing (Brewer & Lewis 2006), inferring rotational profiles from pulsation frequencies in asteroseismology (Christensen-Dalsgaard et al. 1990), various geophysical inverse problems (Snieder & Trampert 1999), inverse electromagnetic scattering problems (Cakoni et al. 2010), problems in fluid mechanics (Cotter et al. 2009), and many many more.

CHAPTER 10

Summary and Future Prospects

Asteroseismology is already a mature field for solar-like oscillating stars. Mode identification and seismic modeling for these stars are relatively straightforward and we can already perform ensemble studies (Chapter 1).

Asteroseismology of intermediate mass pulsators, e.g., the δ Scuti and γ Doradus variables is very difficult, and in most cases we cannot even identify their pulsation modes. In this dissertation, we try to tackle this problem by studying δ Scuti/γ Dor variables in eclipsing binaries (Chapter 5). The binary nature adds more complexity to analyzing their data (light curve, radial velocities, double-lined spectra), and appropriate binary modeling tools are needed (Chapter 4). The benefits are that the fundamental parameters like mass and radius can be well constrained, and we hope that more asteroseismic information will be extracted. We found that this is indeed the case for KIC 3858884, for which we can identify the fundamental radial mode. However, for KIC 9851944, the mode identification for its δ Scuti components is still inconclusive. In some binaries (e.g., KIC 8262223 in Chapter 5 and KOI-81 in Chapter 7), the prior mass transfer history poses a challenge to the evolutionary and asteroseismic modeling.

Binary stars also offer us a new asteroseismic phenomenon, i.e., the tidally excited pulsations. After presenting the theories in Chapter 3, we study several tidal pulsating eccentric binaries discovered by *Kepler* in Chapter 6. The variability caused by precession of an accretion disk around a white dwarf in a cataclysmic variable is discussed in Chapter 7.

Asteroseismology thrives thanks to the large amount of data collected by space missions. It is thus desirable to advance our treatment of data with statistical methods. We apply Bayesian statistics to some problems in binaries and asteroseismology, and it forms the contents of Chapter 8. In Chapter 9, we focus on the inverse problem (tomography) encountered in separating the spectral components of double-line spectroscopic binaries.

On the observational side, interferometry is like a missing piece of jigsaw puzzle of asteroseismology. We have obtained data with the CHARA Array interferometer (ten Brummelaar et al. 2005) for two well-studied δ Scuti stars (44 Tau and 29 Cygni). We have also obtained high-resolving-power spectra for several δ Scuti stars in the Hyades cluster. Apart from characterizing more δ Scuti/γ Dor EBs and heartbeat stars. I would also like to study solar-like oscillators such as red giants. Future space missions like TESS will target on more bright stars which are easier for spectroscopic followup. The methods and techniques presented in this dissertation, spectroscopic analysis, light curve fitting, stellar evolutionary and asteroseismic modeling can be naturally applied to exoplanet host-star systems. On the theoretical side, I would like to advance the theories in Chapter 3. This includes the tidally forced oscillations with rotation in the traditional approximation. The statistical methods presented in Chapter 8 and 9 could be applied to more problems in asteroseismology, e.g., the modeling of individual frequency profile in the power density spectrum of solar-like oscillators, the inversion of rotational splittings, etc.

THE FUTURE IS BRIGHT.

APPENDIX A

Spherical Harmonics as an Orthonormal Basis on a Sphere

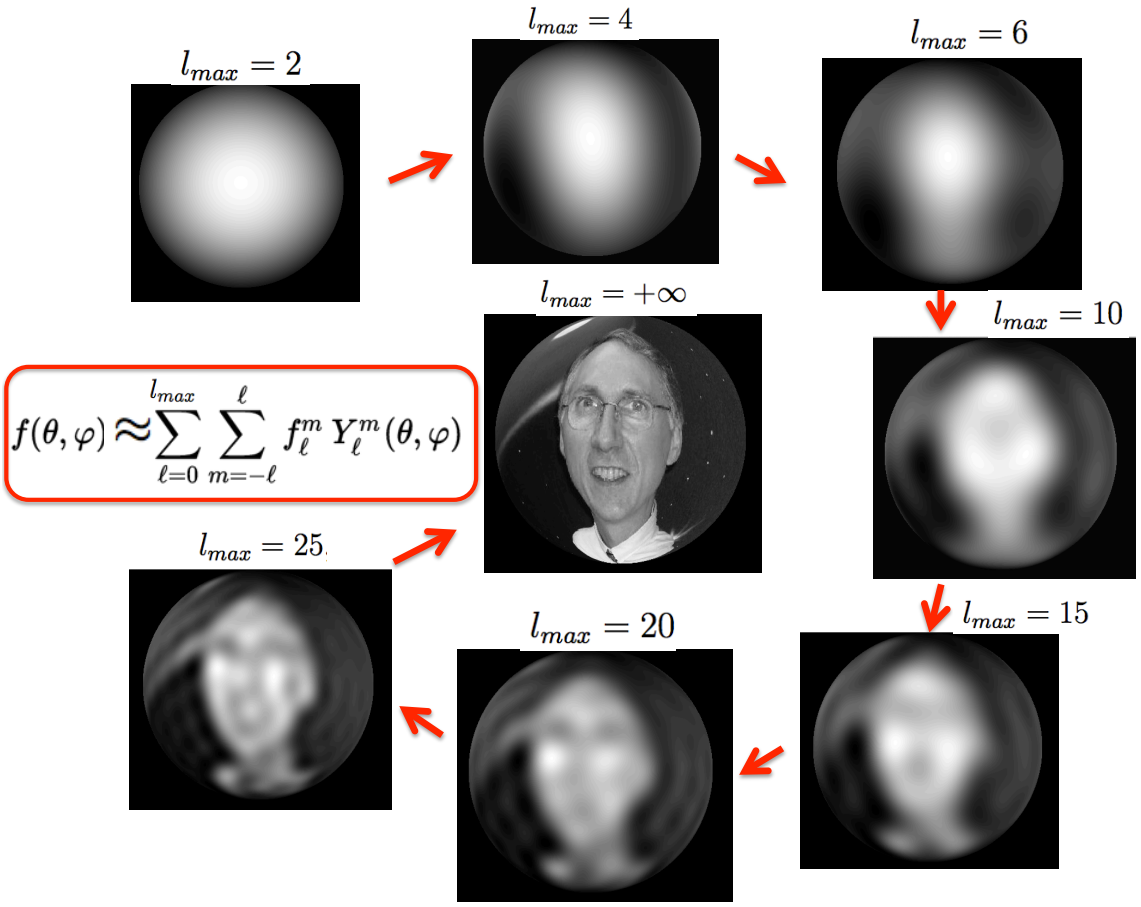

Figure A.1 On the unit sphere, any (square-integrable) function $f(\theta, \phi)$ can be expanded as a linear combination of spherical harmonics $Y_l^m(\theta, \phi)$. We approximate the original image 'Doug' on the sphere by gradually adding spherical harmonics, with maximum number $l_{max} = 2, 4, 6, 10, 15, 20, 25, +\infty$.

APPENDIX B

ELC Usage

The basic usage of ELC is to configure the two input files: *ELC.inp* and *gridloop.opt*.

The *ELC.inp* contains all the model parameters and *gridloop.opt* stores the information on the input light curve and RV curve files and details of the optimization process. In practice, I follow these steps:

1) **Estimate the main parameters that can define the system.** The effective temperatures can be found at Kepler Input Catalog, Huber et al. (2014), Armstrong et al. (2014), etc. Based on these temperatures, we can estimate the radius of stars assuming some main-sequence prior. Some estimated orbital parameters such as the period, eccentricity, inclination, T0 can be found at Kepler EB catalog[1] online maintained by the Villanova group. In practice, we usually find the effective temperature of two components from spectra, and then fix $T_{\rm eff1}$ to the spectroscopic value. The orbital period is often fixed to the value from light curve. Bolometric albedos, gravity darkening exponents are fixed to theoretical values. Limb-darkening coefficients are interpolated from tables based on the stellar temperatures and gravities.

2) **Make some trial runs of ELC to compare with the observed light curve.** Change some parameters manually and check their influence on the light curve.

3) **Determine the tuning parameters and optimization method.** Usually the parameters to optimize are among the following: e, ω, inclination,T_0, period, filling factor or fractional radii, temprat or $T_{\rm eff2}$, bolometric albedo, rotational frequency. If RVs are

[1] http://keplerebs.villanova.edu/

included in the fitting, parameters such as primK, mass ratio, systemic velocity are also optimized. The genetic algorithm is a handy optimization tool (Charbonneau 1995), and we need to set the lower and upper boundary for each parameter. We usually set broad ranges in the *gridloop.opt* file and run *geneticELC* for $200 - 400$ generations with 100 members for each generation. Alternatively, we can use the MCMC (Tegmark 2004) or de-MC sampler (Eastman et al. 2013) and we need an extra input file *MarkovELC.inp* to specify the length of chains, the number of chains and the number of iterations to skip (the burn-in part of the chain). Note that the de-MC sampler is more efficient than the ordinary MCMC algorithm. The same converged result can be reached with about 10000 samples in the de-MC method and 50000 samples in the MCMC method. For eccentric binaries, the computation is quite expensive, and we can combine the genetic algorithm with other faster optimizers like amoeba and Levenberg-Marquardt.

4) **Analyzing the results.** The parameter values and χ^2 at each generation are recorded in the *generation.XXX* files. We usually plot the χ^2 values for each tuning parameter to check if a global minimum has been found. If the parameters have converged, we usually scale the χ^2 values so that the $\chi^2_{min} \approx \nu$, where $\nu = N_{data} - N_{param}$ is the number of degrees of freedom. The $1\sigma, 2\sigma$ error bars are then found from the intersections of $\chi^2_{min} + 1.0, 4.0$ levels with the χ^2 lower envelopes. Note that this approach may underestimate the errors as the parameter correlations are not fully taken into account. For partial eclipsing systems, the light curve shape depends on $(R_1 + R_2)/a$, thus the two parameters R_1/a and R_2/a (or effectively, $f1$ and $f2$) are correlated. If we use the MCMC or de-MC optimizers in ELC, the outputs are

just Markov chains for each parameter. We need to check the convergence of the chains and then find the point estimates (usually use median values or maximum likelihood values) from the histogram of these posterior samples. Convenient packages exist for such analysis such as the *coda*[2] package in R language, and *corner*[3] package in python, etc. Other calculated parameters are stored in *ELC.parm or ELCparm.XXX* files.

[2]https://cran.r-project.org/web/packages/coda
[3]https://github.com/dfm/corner.py

APPENDIX C

Call tree of the subroutine *light curve*

- LIGHTCURVE
  - ADDDISKSPOT
  - ADDMOVESPOT
  - ADDSTARSPOT
  - ANALYTICSCALE
    - VFCN
  - BINLC
  - CHECKINPUT
    - GETOM
      - GETX
    - GETRADIUS
  - CLIPLC
  - COPRAT1
  - COPRAT2
  - COPYDISKINTY
  - COPYINTY
  - COPYTEMP
  - DELVEDARKINT2
  - DETAILREFL
    - COPYTEMP
    - IBETMAZARRAY1
    - IBETMAZARRAY2
    - ZHEIGHT
      - ZDIFF
      - ZPRIMEDIFF
  - DISKSETUP
  - DISKVISIB
    - DISKXTRAN
    - DISKYTRAN
    - INSIDECIRCLE
      - GETLINE
    - DISTORTTIME
- DISTORTTIME
- DTOPY
- DUMMYHORIZ
- DUMMYVALUES
- DUMYSKY1
- DUMYSKY2
- DWAVEY
- DXHORIZ
- EINTY
- FASTANALYTIC
  - ANALYTICG
    - ALFONE
    - CX1
    - GAMMA_LOG
    - JACOBI_POLY
  - BINLC
  - BINLCTIME
  - FILLTIME
  - GETE
  - GETREFVEL
  - SHIFTLC
    - SORT3
  - FILLTIME
  - FINDL1
    - POTEN
      - LPN
  - FINISHLC
  - FINISHRV
  - GETALFLIM
    - INSIDECIRCLE (see above)
    - XTRAN
    - YTRAN

Figure C.1 Call tree of the subroutine *lightcurve* in ELC.

```
GETANALYTICINT
    COMPUTEINTY
        GLINTY
        GNEW
        HUNT
        INDEXINTY
            LOCATE
        INGH
        INGL
        LOCATE
        TINTY
        Y2SCRATCH
    LOCATE
GETATMFLUX
    COMPUTEINTY (see above)
    LOCATE
GETATMINT
    COMPUTEINTY (see above)
    LOCATE
GETBBFLUX
    EDGECOR
        ADDPHIPAD,  SORT2
    PHIARR
GETBBLUMCOR
GETBBSIMP
GETCOORDS
    XTRAN
    YTRAN
GETDISKATMFLUX
    COMPUTEINTY,    LOCATE
GETDISKBBFLUX
    FLCB50      LOCATE
```

```
GETDISKHORIZ
    DISKXTRAN,  DISKYTRAN
    NTHETAMAXDTOPX
    SORTCIRCLE
        GETMAXVALUES
        SORT3
    GETE
    GETEXTENSION
    GETFRACS
        SORT2
GETHORIZON
    ACCHOR
        FASTPOT
            LPN
        RAD
            FINDL1,  POTEN
    ARRPROJ
    IBETLIM
    IBETMAGRADX
    IBETMAIBETLIM
    IBETMAXXLASTRING
    NEWSORTCIRCLE
        DUMR2,  GETMAXVALUES,  HUNT
        IBETMADUMT2  POLINT  SORT3
    SAVEX,  SAVEY
    XDUMMY
    XEND
    XFIRSTRING
    XTRAN,  YDUMMY
    YFIRSTRING
    YLASTRING
    YTRAN
```

Figure C.2 Call tree of the subroutine *lightcurve* in ELC (Continued).

APPENDIX D

An IDL program for Bayesian Isochrone Fitting with Padova models

```
pro padova2

;read padova isochrones for bayesian isochrone fitting

;following Jorgensen & Lindegren 2004

;/01/13/14,/09/22/15, apply to two components in EBs, G=G1*G2

;-----------------

openr,1,'isochron.dat'

d=dblarr(19,64381)

readf,1,d

close,1

;-----------------------------------------------content of the file

;1          0.00040 6.310e+07  7.80    0.15000001

;overshoot  z         age            logage   mini

;0.1500 -2.3035 3.5907  5.2264 10.529

;mact   logL   logTeff  logg  Mbol

;13.922 12.907 11.548 10.655  9.824  8.900  8.279   8.028 -9.59274740

;Umag   Bmag   Vmag    Rmag    Imag  Jmag    Hmag    Kmag   flum

;-----------------------------------------------------

overshoot=reform(d(0,*)) ;all overshoot type=1

z=reform(d(1,*))
```

```
age=reform(d(2,*))

logage=reform(d(3,*))

;corresponds to each z, logage=7.8 7.85 7.9.....10.25,increment=0.05

mini=reform(d(4,*))

mact=reform(d(5,*))

logL=reform(d(6,*))

logTeff=reform(d(7,*))

logg=reform(d(8,*))

Mbol=reform(d(9,*))

Umag=reform(d(10,*));absolute mag in U band

Bmag=reform(d(11,*))

Vmag=reform(d(12,*))

Rmag=reform(d(13,*))

Imag=reform(d(14,*))

Jmag=reform(d(15,*))

Hmag=reform(d(16,*))

Kmag=reform(d(17,*))

flum=reform(d(18,*))

;--------------------

;fix z=0.03,get G for different age
```

```
window,2,xsize=1200,ysize=600

g=where(  (abs(z - 0.03) le 0.0001)and(abs(logage -9.30) le 0.02)  )

xx=logTeff(g)

yy=logg(g)

m=mini(g)


plot,xx,yy,symsize=0.5,xrange=[4.5,3.2],yrange=[4.5,2.0],$

ystyle=1,xstyle=1,xtitle=textoidl('log(T_{eff})'),ytitle='logg',$

title='KIC9851944 isochrone fitting',/nodata


;KIC9851944 observed log(Teff),logg

xobs=3.8467 ;logTeff

yobs=3.96 ;logg

xobs2=3.839

yobs2=3.69

sigx=0.01 ;obvervation logTeff error bar

sigy=0.05

sigx2=0.01

sigy2=0.05

;-----------------component1

age=findgen(49)/49*(10.25-7.8)+7.8
```

```
Gfinal=fltarr(49)

for j=0,48 do begin

g=where(  (abs(z - 0.03) le 0.0001)and(abs(logage -age[j]) le 0.02)  )

;fix Z for now, then pick an isochrone in the age array

xx=logTeff(g)

yy=logg(g)

m=mini(g)

ng=n_elements(g)

mm=findgen(2000)/2000.0*(max(m)-min(m))+min(m)

part1=1/(sqrt(2.0*!pi)*sigx*sqrt(2.0*!pi)*sigy)

G=fltarr(1998)

 for i=1,1998 do begin

 qx=interpol(xx,m,mm[i])

 qy=interpol(yy,m,mm[i])

 chi2=(xobs-qx)^2/sigx^2+(yobs-qy)^2/sigy^2

 part2=exp(-0.5*chi2)

 G[i-1]=part1*part2*mm[i]^(-2.7)*(mm[i+1]-mm[i-1])

 endfor

Gfinal[j]=total(G)

endfor
```

```
ageGyr=10.0^age/1D9

int3=INT_TABULATED(age, Gfinal,/double)

Gfinal=Gfinal/int3 ;normalize pdf

plot,age,Gfinal,xtitle='Log(age)',$

ytitle='Probability Density',yrange=[0,15],xrange=[8.0,10.0]

;-------------------component2

age=findgen(49)/49*(10.25-7.8)+7.8


Gfinal=fltarr(49)

for j=0,48 do begin

g=where(  (abs(z - 0.03) le 0.0001)and(abs(logage -age[j]) le 0.02)  )

;fix Z now, then pick an isochrone in the age array

xx=logTeff(g)

yy=logg(g)

m=mini(g)

ng=n_elements(g)

mm=findgen(2000)/2000.0*(max(m)-min(m))+min(m)

part1=1/(sqrt(2.0*!pi)*sigx*sqrt(2.0*!pi)*sigy)

G=fltarr(1998)

 for i=1,1998 do begin

 qx=interpol(xx,m,mm[i])
```

```
 qy=interpol(yy,m,mm[i])
 chi2=(xobs2-qx)^2/sigx^2+(yobs2-qy)^2/sigy^2
 part2=exp(-0.5*chi2)
 G[i-1]=part1*part2*mm[i]^(-2.7)*(mm[i+1]-mm[i-1])
 endfor
Gfinal[j]=total(G)
endfor


ageGyr=10.0^age/1D9
int4=INT_TABULATED(age, Gfinal,/double)
print,int4
Gfinal=Gfinal/int4
oplot,age,Gfinal,linestyle=1;,xtitle='Age in Log',$
ytitle='relative Posterior Prob.'
;----------system=component1*component2
age=findgen(49)/49*(10.25-7.8)+7.8
Gfinal=fltarr(49)
for j=0,48 do begin
g=where(  (abs(z - 0.03) le 0.0001)and(abs(logage -age[j]) le 0.02)  )
;fix Z now, then pick an isochrone in the age array
xx=logTeff(g)
```

```
yy=logg(g)

m=mini(g)

ng=n_elements(g)

mm=findgen(2000)/2000.0*(max(m)-min(m))+min(m)

part1=1.0/(sqrt(2.0*!pi)*sigx*sqrt(2.0*!pi)*sigy)

part1b=1.0/(sqrt(2.0*!pi)*sigx2*sqrt(2.0*!pi)*sigy2)

G=fltarr(1998)

 for i=1,1998 do begin

 qx=interpol(xx,m,mm[i])

 qy=interpol(yy,m,mm[i])

 chi2=(xobs-qx)^2/sigx^2+(yobs-qy)^2/sigy^2

 chi2b=(xobs2-qx)^2/sigx2^2+(yobs2-qy)^2/sigy2^2

 part2=exp(-0.5*chi2)

 part2b=exp(-0.5*chi2b)


 G[i-1]=(part1*part2)*(part1b*part2b)*mm[i]^(-2.7)*(mm[i+1]-mm[i-1])

 endfor

Gfinal[j]=total(G)

endfor


ageGyr=10.0^age/1D9
```

```
int5=INT_TABULATED(age, Gfinal,/double)

Gfinal=Gfinal/int5 ;normalize the pdf

oplot,age,Gfinal,color=cgcolor('red'),$

,xtitle='System Age in Log',ytitle='Posterior Prob.'


end
```

APPENDIX E

An IDL package for spectral tomography

We have discussed in Chapter 9 various algorithms for tomographic reconstruction of spectra. Most of the algorithms are only demonstrated with toy examples of small scale. For practical applications of large scale problems, the methods in Fourier space are fast and appropriate. The *tomoft* code is about three times faster than the old *tomography.pro* program. The Bayesian methods (linear regression) can also be applied to real spectra (e.g., 1000 pixels), but one reconstruction usually takes about several minutes. The hierarchical Bayesian method currently can only be used for small scale problems (e.g., a few hundred pixels).

We attach two IDL programs for tomography in Fourier domain *tomoft* and *tomoftregu2*. The second program includes regularization.

I have tried to design the programs so that they have the same calling sequence as the old program (tomography.pro). Thus the new codes may be run by directly replacing the line containing the old tomography run (with tomography.pro):

```
TOMOGRAPHY,100,0.8,obsspec,recspec,pshift,fratio,simspec
```

with the following lines:

```
tol=1D-5

tomoft,tol,obsspec,recspec,pshift,fratio,simspec
```

If low frequency deviations appear in the reconstructions, the spectra can be renormalized using the 'corridor correction' by adding these lines:

```
;(if F2/F1=1.3,then)

f1=1.0/(1.0+1.3)

f2=1.3/(1.0+1.3)

sp1=fltarr(npix)+1.0

sp2=fltarr(npix)+1.0

z1=(sp1-1.)*f1-(rec1-1)*f1

z2=(sp2-1.)*f2*(-1.0)-((rec2-1)*f2)*(-1.0)

zmean=(z1+z2)/2.0

zmean=smooth(zmean,20)

;oplot,wave,zmean,color=cgcolor('green')

rec1corr=rec1+zmean/f1

rec2corr=rec2-zmean/f2
```

where the smoothing width parameter 20 is arbitrary and should be varied empirically.

The source codes for the two programs are listed in the following:

1 ***tomoft.pro*** (tomography in Fourier domain, algorithm in section 9.3.1)

```
pro tomoft,tol,obsspec,recspec,pshift,ratio,simspec

;a similar pro to tomograph.pro, but in FT domain,3 times faster

;NO regularization


;Inputs:--------------

;tol:  SVD singular value tolerance,
```

```
;singular values smaller than tol will be

;treated as zero, usually 1D-5

;obsspec: npix*nrv

;recspec:  npix*2; set initial values for prior spectra

;pshift:  2*nrv

;ratio:   2*nrv

;(nstar=2 for now)

;Outputs:---------------

;recspec: npix*2

;simspec: npix*nrv



yobs=obsspec

;dimension: dblarr(npix,nrv)

ydim=size(yobs,/dimension)

npix=ydim[0]

nrv=ydim[1]


pdim=size(pshift,/dimension)

nstar=pdim[0]
```

```
ym=dcomplexarr(npix,nrv);FT of the obsspec

for i=0,nrv-1 do begin

yobs(*,i)=obsspec(*,i)-mean(obsspec(*,i))

ym(*,i)=fft(yobs(*,i),/double)

endfor

;-------------------------

bet=dblarr(nrv,nstar)

bet=transpose(pshift)


L=ratio


Farr=dcomplexarr(nstar,nrv,npix)

;nrv obs spec, 2 stars,npix pixels


for i=1,nrv do begin

for j=1,nstar do begin

Lj=L(j-1,i-1)

col=dblarr(npix)

      ;npix=n_elements(col)


      temp=abs(bet(i-1,j-1))
```

```
      low=fix(temp)
      high=low+1.0

      fhigh=temp-low
      flow=1.0-fhigh

if(bet(i-1,j-1) lt 0.)then begin

  if(low eq 0.)then begin
;speciall cases when RV within[-1,0]
;2 nonzero elements are col(npix-1)and col(0)
   col(0)=flow*Lj
        col(npix-high)=fhigh*Lj
       endif else begin
        col(npix-low)=flow*Lj
        col(npix-high)=fhigh*Lj
       endelse
    endif else begin
      col(low)=flow*Lj
       col(high)=fhigh*Lj
    endelse
```

```
    ;print,i,j,'col=',col
    Farr(j-1,i-1,*)=fft(col,/double)
     endfor
   endfor

Farr=Farr*npix

x_inv=dcomplexarr(npix,nstar);ft of component spectra
ysim=dcomplexarr(npix,nrv);ft of simspec

for mm=0,npix-1 do begin
y=ym(mm,0)
for iy=1,nrv-1 do y=[y,ym(mm,iy)];form the FT(yobs)at freq=m

Fm=Farr(*,*,mm);the Fm matrix for freq=mm
;----SVD solution for each mm
la_svd,Fm,w,u,v

wfilter=w
for i=0,n_elements(w)-1 do begin
```

```
if(w[i] le tol)then begin

wfilter[i]=0.0d

endif else begin

wfilter[i]=1.0/w[i]

endelse

endfor

;for each freq=mm,x_inv is a 2 elements array

x_inv(mm,*)=v##diag_matrix(wfilter)##transpose(conj(u))##y

ysim(mm,*)=Fm##x_inv(mm,*);nrv*nstar nstar*1 =nrv*1,all complex arrays

endfor


for i=0,nstar-1 do begin

recspec(*,i)=real_part(fft(x_inv[*,i],/inverse,/double))

endfor


;ysim(npix,nrv)

simspec=dblarr(npix,nrv)


for i=0,nrv-1 do begin

simspec(*,i)=real_part(fft(ysim(*,i),/inverse,/double))

simspec(*,i)=simspec(*,i)+mean(obsspec(*,i))
```

```
;dblarr(npix,nrv)
endfor

end
```

2 ***tomoftregu2.pro*** (algorithm in section 9.3.2, calling subroutines *tomoftregu* and *findcorner*)

```
pro tomoftregu2,tol,bound,nalpha,prior,obsspec,recspec2,pshift,ratio,simspec,
resi_arr,x_xprior,alpha_arr,alphaBest
;tomoft with regularization,use tomoftergu and
;findcorner to find best regularization paramter alpha

;tol: SVD singular value tolerance, smaller than tol will be treated as zero
;bound: two elements array,lower and upper bounds of alpha,e.g. [0.01,10]
;nalpha: # of regular parameter calculated
;prior: npix*2
;obsspec: npix*nrv
;recspec2: npix*2,inital value is going to be set as prior
;pshift: 2*nrv
;ratio:  2*nrv
```

```
;----------Outputs:

;recspec2: npix*2; final recspec

;simspec: npix*nrv

;resi_arr: nalpha elements array, store the |Gx-d|^2

;x_xprior: nalpha elements array, store the |x-xprior|^2

;alpha_arr: nalpha elements array,store the regular parameters alpha

;bestalpha: the alpha adopted for final reconstruction

;

;yobs=obsspec;dblarr(npix,nrv)

ydim=size(obsspec,/dimension)

npix=ydim[0]

nrv=ydim[1]


;nalpha=20.

low=alog10(bound[0])

up=alog10(bound[1])


alpha0=dindgen(nalpha)/nalpha*(up-low)+low;low->up

alpha_arr=10.0^alpha0;


resi_arr=dblarr(nalpha)
```

```
x_xprior=dblarr(nalpha)


for al=0,nalpha-1 do begin

;alpha=0.1

alpha=alpha_arr[al]


recspec2=prior;need to reset prior, recspec2 initial values=prior

tomoftregu,tol,alpha,obsspec,recspec2,pshift,ratio,simspec

rec1=recspec2(*,0)

rec2=recspec2(*,1)


x_xprior[al]=total((rec1-prior(*,0))^2)+total((rec2-prior(*,1))^2)


sum=0.0d

for j=0,nrv-1 do begin

sum=sum+total((obsspec(*,j)-simspec(*,j))^2)

endfor

resi_arr[al]=sum


print,x_xprior[al],resi_arr[al],alpha

;alpha=-2->2, resi,xxprior,alpha saved in xyz.txt,
```

```
;and used by test_findcorner

endfor


window,18,xsize=1200,ysize=600

x=alog10(resi_arr)

y=alog10(x_xprior)

plot,x,y,psym=4,yrange=[min(y),max(y)],$

xrange=[min(x),max(x)],xstyle=1,ystyle=1,$

title='log(resi) vs log(x_xpior)',xtitle='resi',ytitle='x_xprior'


;use findcorner

findcorner,resi_arr,x_xprior,alpha_arr,alphaBest,g,kap

print,'best alpha=',alphaBest,' index=',g

oplot,[x(g)],[y(g)],psym=1,color=cgcolor('red')

for i=0,nalpha-1 do begin

str=strtrim(string(alpha_arr[i],format='(f6.3)'),2)

xyouts,[x(i)],[y(i)],str

endfor


;calculate curvature numerially

dy1=deriv(x,y)
```

```
dy2=deriv(x,dy1)

curv=abs(dy2)/(1.0+dy1^2)^1.5; Curvature

gg=where(curv eq max(curv))

;print,gg,alpha(gg)

oplot,x[gg],y[gg],psym=4,color=cgcolor('red')

window,19

plot,alpha_arr,curv,psym=1,title='alpha vs curvature'

oplot,alpha_arr,kap,psym=4,color=cgcolor('red')

;curvature from findcorner.pro approx.method

;--------------Lcurve end-----------------------------

;use the best alpha to do final tomo again

recspec2=prior

tomoftregu,tol,alphaBest,obsspec,recspec2,pshift,ratio,simspec


end


;------------------------------tomoftregu----------------------------

pro tomoftregu,tol,alpha,obsspec,recspec,pshift,ratio,simspec

;tomoft with regularization


;------------Inputs:
```

```
;tol: SVD singular value tolerance,

;smaller than tol will be treated as zero

; usually 1d-5

;alpha: regularization parameter;

;larger value->solution is closer to prior

;obsspec: npix*nrv

;recspec: npix*2; set inital values are prior spectra

;pshift: 2*nrv

;ratio:  2*nrv

;----------Outputs:

;recspec: npix*2

;simspec: npix*nrv


;set recspec initial values as prior

;tol=1d-4

;--------------

;use modelspectra as mprior ,regularization in Fourier domain

   ;modp=spmod(w,paramp)

   ;mods=spmod(w,params)

;prior: npix*nstar array

modp=recspec(*,0)
```

```
mods=recspec(*,1)

x1=modp-mean(modp)

x2=mods-mean(mods)

x1m=fft(x1,/double)

x2m=fft(x2,/double)


;the following part is the pro:

;tomoft,tol,obsspec,recspec2,pshift,ratio,simspec2


yobs=obsspec;dblarr(npix,nrv)

ydim=size(yobs,/dimension)

npix=ydim[0]

nrv=ydim[1]


pdim=size(pshift,/dimension)

nstar=pdim[0]


ym=dcomplexarr(npix,nrv);FT of the obsspec

for i=0,nrv-1 do begin

yobs(*,i)=obsspec(*,i)-mean(obsspec(*,i))

ym(*,i)=fft(yobs(*,i),/double)
```

```
endfor
;-----

bet=dblarr(nrv,nstar)
bet=transpose(pshift)
L=ratio

Farr=dcomplexarr(nstar,nrv,npix)
;nrv obs spec, 2 stars,npix pixels

for i=1,nrv do begin
for j=1,nstar do begin
Lj=L(j-1,i-1)
col=dblarr(npix)
      ;npix=n_elements(col)

      temp=abs(bet(i-1,j-1))
      low=fix(temp)
      high=low+1.0

      fhigh=temp-low
```

```
      flow=1.0-fhigh

if(bet(i-1,j-1) lt 0.)then begin

  if(low eq 0.)then begin
;speciall cases when RV within[-1,0],
;2 nonzero elements are col(npix-1)and col(0)
   col(0)=flow*Lj
        col(npix-high)=fhigh*Lj
       endif else begin
        col(npix-low)=flow*Lj
        col(npix-high)=fhigh*Lj
       endelse
    endif else begin
      col(low)=flow*Lj
       col(high)=fhigh*Lj
    endelse

    Farr(j-1,i-1,*)=fft(col,/double)
     endfor
   endfor
```

```
Farr=Farr*npix


x_inv=dcomplexarr(npix,nstar);ft of component spectra

ysim=dcomplexarr(npix,nrv);ft of simspec


II=dcomplexarr(2,2)

temp=complex(1.0,0.0)

II(0,0)=temp

II(1,1)=temp


for mm=0,npix-1 do begin

y=ym(mm,0)

for iy=1,nrv-1 do y=[y,ym(mm,iy)];form the FT(yobs)at freq=m

mprior=[x1m(mm),x2m(mm)]

Fm=Farr(*,*,mm);the Fm matrix for freq=mm

;----svd solution for each mm


Fm2=[[Fm],[alpha*II]]

ynew=[y,alpha*mprior]
```

```
la_svd,Fm2,w,u,v


wfilter=w

for i=0,n_elements(w)-1 do begin

if(w[i] le tol)then begin

wfilter[i]=0.0d

endif else begin

wfilter[i]=1.0/w[i]

endelse

endfor

;---for each freq=mm,x_inv is a 2 elements array


x_inv(mm,*)=v##diag_matrix(wfilter)##transpose(conj(u))##ynew

ysim(mm,*)=Fm##x_inv(mm,*);nrv*nstar nstar*1 =nrv*1,all complex arrays

endfor


for i=0,nstar-1 do begin

recspec(*,i)=real_part(fft(x_inv[*,i],/inverse,/double))

endfor


;ysim(npix,nrv)
```

```
simspec=dblarr(npix,nrv)


for i=0,nrv-1 do begin
simspec(*,i)=real_part(fft(ysim(*,i),/inverse,/double))
simspec(*,i)=simspec(*,i)+mean(obsspec(*,i))
;dblarr(npix,nrv)
endfor


end


;------------------------------findcorner------------------------------
pro findcorner,resi,x_xprior,reg_param,reg_corner,g,kappa
;translate from matlab code:l_curve_corner(rho,eta,reg_param)
;transform rho and eta into log-log space


;Input: --------------
;resi :|Gm-d|^2
;x_xprior :|x-xprior|^2
;reg_param: alpha array
;Output:---------------
;reg_corner :best alpha(regularization parameter)
```

```
;g : index of the best alpha

;kap : curvature at each alpha


x=alog(resi);

y=alog(x_xprior);


; Triangular/circumscribed circle simple approximation to curvature

; (after Roger Stafford)


; the series of points used for the triangle/circle

nx=n_elements(x);nx=ny

x1 = x(0:nx-3);

x2 = x(1:nx-2);

x3 = x(2:nx-1);

y1 = y(0:nx-3);

y2 = y(1:nx-2);

y3 = y(2:nx-1);

; the side lengths for each triangle

a = sqrt((x3-x2)^2+(y3-y2)^2);

b = sqrt((x1-x3)^2+(y1-y3)^2);

c = sqrt((x2-x1)^2+(y2-y1)^2);
```

```
s=(a+b+c)/2;%semi-perimeter


; the radius of each circle

R=(a*b*c)/(4*sqrt((s*(s-a)*(s-b)*(s-c))));


; The curvature for each estimate for each value which is

; the reciprocal of its circumscribed radius.

;Since there aren't circles for

; the end points they have no curvature

kappa = [0,1.0/R,0];

nk=n_elements(kappa)

curvature_max=max(abs(kappa(0:nk-1)),g);

reg_corner=reg_param(g)


end
```